The Integration of Heat Pipe Technology into Natural Ventilation Systems

Hassam Nasarullah Chaudhry

Submitted in accordance with the requirements for the degree of
Doctor of Philosophy

The University of Leeds

School of Civil Engineering

October, 2013

The candidate confirms that the work submitted is his/her own, except where work which has formed part of jointly authored publications has been included. The contribution of the candidate and the other authors to this work has been explicitly indicated on page iii. The candidate confirms that appropriate credit has been given within the thesis where reference has been made to the work of others.

Jointly Authored Publications

1. B.R.Hughes, H.N.Chaudhry, S.A.Ghani, *A review of sustainable cooling technologies in buildings*, Renewable and Sustainable Energy Reviews, Volume 15, Issue 6, August 2011, Pages 3112-3120

   Contribution from B.R.Hughes: Information on description and details of the components relating to wind towers and passive cooling.

   Contribution from H.N.Chaudhry: Review write-up of cooling technologies including night ventilation, air-conditioning, air handling units, desiccant cooling and absorption cooling systems. The summary of building cooling technologies is used in Chapter 1 (Introduction) in Section 1.1, Figure 1.3.

   Contribution from S.A.Ghani: Introduction and overview of the topic.

2. H.N.Chaudhry, B.R.Hughes, S.A.Ghani, *A review of heat pipe systems for heat recovery and renewable energy applications*, Renewable and Sustainable Energy Reviews, Volume 16, Issue 4, May 2012, Pages 2249-2259

   Contribution from H.N.Chaudhry: Review write-up of heat pipe systems including comparison between tubular heat pipes, variable conductance heat pipes, thermal diodes, pulsating heat pipes, loop heat pipes, micro heat pipes and sorption heat pipes. The schematic geometry of heat pipes are used in Chapter 2 (Literature Review) in Section 2.3.1 – 2.3.6, Figures 2.2, 2.4, 2.6, 2.7, 2.8 and 2.9.

   Contribution from B.R.Hughes: Information on computational simulations associated with heat pipes.

   Contribution from S.A.Ghani: Introduction and discussion of the topic.

3. J.K.Calautit, H.N.Chaudhry, B.R.Hughes, S.A.Ghani, *Comparison between evaporative cooling and heat pipe assisted thermal loop for a commercial wind tower in hot and dry climatic conditions*, Applied Energy, Volume 101, January 2013, Pages 740-755

   Contribution from J.K.Calautit: Design and CFD simulations of the wind tower and evaporative cooling system.

   Contribution from H.N.Chaudhry: Design and CFD simulations of the heat pipes for identifying the temperature drop using water and ethanol as the working fluid. The streamwise distance between heat pipes is used in Chapter 3 (CFD Theory and Modelling) in Section 3.6.3.

   Contribution from B.R.Hughes: Information on the CFD modelling and applying boundary conditions.

   Contribution from S.A.Ghani: Discussion of the results and scope for future work.

4. B.R.Hughes, H.N.Chaudhry, J.K.Calautit, *Passive energy recovery from natural ventilation airstreams*, Applied Energy, Volume 113, January 2014, Pages 127-140

   Contribution from B.R.Hughes: Discussion of the results and relating it to the U.K. trends of thermal comfort and average wind speeds.

   Contribution from H.N.Chaudhry: Design and CFD simulations of the heat pipes. The streamwise distance between heat pipes is used in Chapter 3 (CFD Theory and Modelling) in Section 3.6.3.

   Contribution from J.K.Calautit: Validation of the results against published literature.

Acknowledgement

I would highly wish to thank my supervisor of study, Dr. Ben Hughes for his continuous backing and encouragement throughout the year of work. Many thanks once again for providing me with the opportunity to work on this unique research. I would also like to thank Mr. Roy Trembath and Mr. John Calautit for providing vital assistance throughout the experimental phase of the research.

Finally, I would like to thank my parents and my brothers for being supportive throughout the years of my study. This would not have been possible without their motivation.

This research was made possible by a NPRP grant (NPRP 09-138-2-059) from the Qatar National Research Fund. I have taken great pleasure in undertaking the course of my study.

Abstract

The aim of this research was to integrate heat pipe technology into natural ventilation air streams to provide passive cooling in regions of hot arid climatic conditions without the use of mechanical assistance. The study used numerical and experimental techniques identified from literature to carry out the research. Design parameters of heat pipes including the working fluid and geometrical arrangement were investigated using Computational Fluid Dynamics (CFD). Flow and thermal behaviour of two-phase heat pipe working fluids including water, ethanol and R134a were investigated and their performance was quantified in terms of heat transfer and the overall effectiveness. The results showed that water has the highest cooling capability for the downstream airflow and its working performance was approximately 24% superior in comparison to refrigerant R134a and 42% higher in relation to ethanol.

The analysis further determined that for low-speed hot airstreams, heat pipe working fluid properties play an important role in enhancing heat transfer and that the specific heat capacity of the fluid was the most influential parameter in increasing convective heat transfer by 39%. Subsequent to the working fluid, geometrical arrangements of the heat pipes were studied. Using a fixed physical domain, the findings displayed that the optimum spanwise thickness between the pipes was 50mm (spanwise thickness to pipe diameter ratio of 2.5) while the optimum streamwise distance was 20mm corresponding to the streamwise distance-to-pipe ratio of 1.0. In addition, the periodic time-dependant model determined the thermal response of heat pipes in relation to external temperatures and established the relationship between source temperatures and downstream profiles.

The final part of the study validated the CFD findings through full-scale wind tunnel experimentation. Experimental testing was carried out on heat pipes using water and R134a as working fluids at varying spanwise configurations. The error patterns were found to independent of the heat pipe geometry and working fluid. The validation study determined the error range which varied between 0.6% and 18.1% for velocity, 0.7% and 18.8% for pressure and between 0.01% and 2.8% for temperature, showing a good correlation between the CFD and experimental techniques and with previous work found in published literature.

Table of Contents

List of Tables

List of Figures

Preface

The work presented in this thesis was carried out between February 2011 and October 2013 in the School of Engineering and Physical Sciences, Heriot-Watt University and the School of Civil Engineering, University of Leeds.

The outputs from this study have been published as follows:

Journal Papers:

1. B.R.HUGHES, H.N.CHAUDHRY, J.K.CALAUTIT, *Passive energy recovery from natural ventilation air streams*, Applied Energy, 113 (2014) 127-140
2. J.K.CALAUTIT, B.R.HUGHES, H.N.CHAUDHRY, S.A.GHANI, *CFD analysis of a heat transfer device integrated wind tower system for hot and dry climate*, Applied Energy, 112 (2013) 576-591
3. J.K.CALAUTIT, H.N.CHAUDHRY, B.R.HUGHES, S.A.GHANI, *Comparison between evaporative cooling and a heat pipe assisted thermal loop for a commercial wind tower in hot and dry climatic conditions*, Applied Energy, 101 (2013) 740-755
4. H.N.CHAUDHRY, B.R.HUGHES, S.A.GHANI, *A review of heat pipe systems for heat recovery and renewable energy applications*, Renewable and Sustainable Energy Reviews, 16 (2012) 2249-2259
5. B.R.HUGHES, H.N.CHAUDHRY, S.A.GHANI, *A review of sustainable cooling technologies in buildings*, Renewable and Sustainable Energy Reviews, 15 (2011) 3112-3120

Conference Papers:

1. H.N.CHAUDHRY, B.R.HUGHES, S.A.GHANI, *Computational modelling of heat transfer rates using heat pipe integrated channel section*, 4th International Conference on Applied Energy, July 5-8, 2012, Suzhou, China

2. H.N.CHAUDHRY, B.R.HUGHES, S.A.GHANI, *Computational investigation on the multiphase flow capabilities of using water and ethanol as heat pipe working fluid*, 7th Conference on Sustainable Development of Energy, Water and Environmental Systems, July 1-7, 2012, Ohrid, Republic of Macedonia

Nomenclature

u	*x*-momentum (kgm/s)
v	*y*-momentum (kgm/s)
w	*z*-momentum (kgm/s)
A	Cross sectional area (m^2)
ρ	Density (kg/m^3)
μ	Dynamic viscosity (Pas)
ε	Effectiveness of heat exchanger
k_{eff}	Effective conductivity (W/mK)
e	Elastic deformation
h	Enthalpy (J/kg)
$\vec{v}$	Fluid flow velocity (m/s)
R	Gas constant (J/kgK)
g	Gravitational acceleration (m/s^2)
q_{actual}	Heat transfer, actual (W)
q_{max}	Heat transfer, ideal (W)
q_e	Heat transfer rate to evaporator (W)
L	Latent heat of vaporisation (J/kg)
Y_j	Mass fraction of species *j*
α	Phase volume fraction
Pr	Prandtl number
p	Pressure (Pa)
r	Radius of heat pipe (m)
S_M	Source term for mass added to the continuous phase (kg)
S_t	Spanwise thickness (m)
h_{fg}	Specific enthalpy (J/kg)
$\dot{q}$	Specific heat flux (kW/m^2)
c_p	Specific heat capacity (J/kgK)
σ_t	Standard deviation
S_d	Streamwise distance (m)
τ	Stress (N/m^2)
$\bar{\bar{\tau}}$	Stress tensor (N/m^2)

σ	Surface tension (N/m)
C_{sf}	Surface/liquid parameter of Rohsenow correlation
t	Time (sec)
ΔT	Temperature difference (K)
$T_{e,inlet}$	Temperature at inlet to evaporator (K)
$T_{e,outlet}$	Temperature at outlet from evaporator (K)
k	Thermal conductivity (W/mK)
e	Turbulence dissipation rate (m^2/s^3)
k	Turbulence kinetic energy (m^2/s^2)
I	Turbulence intensity (%)
σ_k	Turbulent Prandtl number for turbulence kinetic energy
σ_e	Turbulent Prandtl number for energy dissipation rate
∇	Vector differential operator
U	Velocity (m/s)
u_c	Velocity (centre) in the test section (m/s)
$\bar{u}$	Velocity (mean) in the test section (m/s)

Chapter 1
Introduction

In order to achieve an energy-efficient world, governments, businesses and individuals must transform the building sector through a multitude of actions, which include increasing energy awareness globally. Buildings worldwide account for 40% of global energy consumption (WBCSD, 2013), and the resulting carbon footprint, significantly exceeding those of all transportation combined. Large and attractive opportunities exist to reduce building energy use at lower costs and higher returns than other sectors. These reductions are fundamental to support achieving the International Energy Agency's (IEA) target of a 77% reduction in the planet's carbon footprint against the 2050 baseline to reach stabilised CO_2 levels called for by the Intergovernmental Panel on Climate Change (IPCC).

Building energy is part of a complex system that includes transport and urban planning and has major social consequences as well as climate change impacts. The energy mix is also important in determining carbon dioxide emissions. Depending on the level of energy services, this can be 80% of the total energy (Figure 1.1), with the balance being the energy consumed in construction and demolition and the embodied energy in the materials according to the Energy Efficiency in Buildings (EEB) report (WBCSD, 2009).

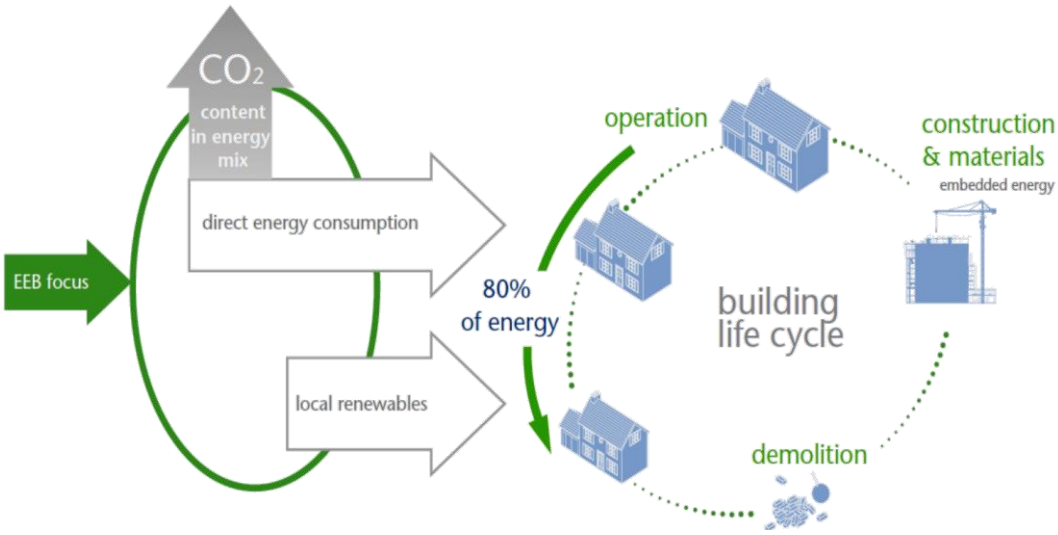

Figure 1.1 Building energy usage over lifetime (WBCSD, 2009)

On a global scale, both population and the average footprint per capita have increased since 1961. However, the relative contribution of each to the overall increased ecological footprint is different for different regions. The ecological footprint (Figure 1.2) measures humanity's demand on the atmosphere in terms of the biologically productive area and sea required to provide the resources we use and to absorb our waste. The ecological footprint (Figure 1.2) per capita involving high-income countries is significantly higher in comparison to middle and low-income countries. The largest footprint per capita increases between 1961 and 2008 were in the European Union and the Middle East/Central Asia, which increased by 1.2 and 1.1 global hectares (gha) per person (WWF, 2012).

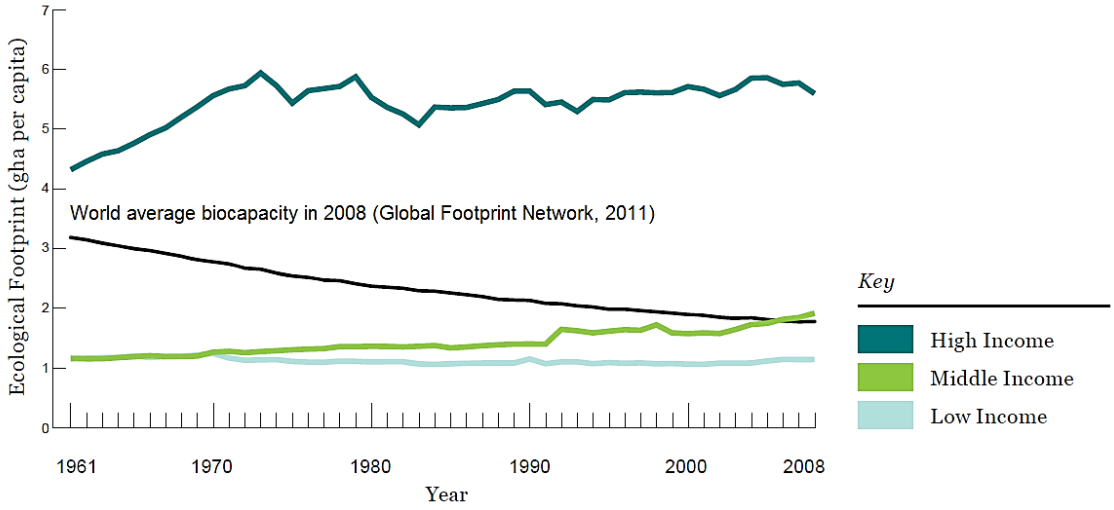

Figure 1.2 Ecological footprint per person in high, middle and low income countries between 1961-2005 (WWF, 2012)

Requirements for comfortable working conditions have resulted in an increased demand for air conditioning, likely achieved through mechanical cooling systems consuming electricity as the principal source of energy. According to a study by Deloitte, energy consumption of the Gulf Cooperation Council (GCC) countries is driven largely by home use, with almost 47% of the electricity being consumed by the residential sector (Deloitte, 2008). The Middle East region (in particular Qatar, Saudi Arabia and United Arab Emirates), is on the increase in terms of active power consumption across the global market. New construction has resulted in millions of refrigeration tons of new air-conditioning equipment being installed or planned. Over the summer months, more than 50% of the electricity demand comes from air-conditioning loads. During peak

electricity demand, closer to 100% of the peak load can be attributed to air-conditioning (Landry, 2004, Deloitte, 2008).

1.1 Mechanical cooling technologies for air-conditioning in buildings

Mechanical Heating, Ventilation and Air-Conditioning (HVAC) units are common solutions for providing effective and adequate fresh air requirements. However, active systems with complex and integral mechanisms require a high level of energy input. Electricity usage of the active building cooling systems employed at present are sometimes substantially higher at relatively low cost of equipment, thereby making them financially appealing to the building sector (Figure 1.3). The energy consumption for typical air handling units can go up to 20,000W while typical desiccant cooling systems can consume up to 55,000W of power (Hughes *et al*., 2011). Achieving the same level of ventilation and space conditioning using only natural resources (termed passive ventilation) would thus make a dramatic impact on the energy performance.

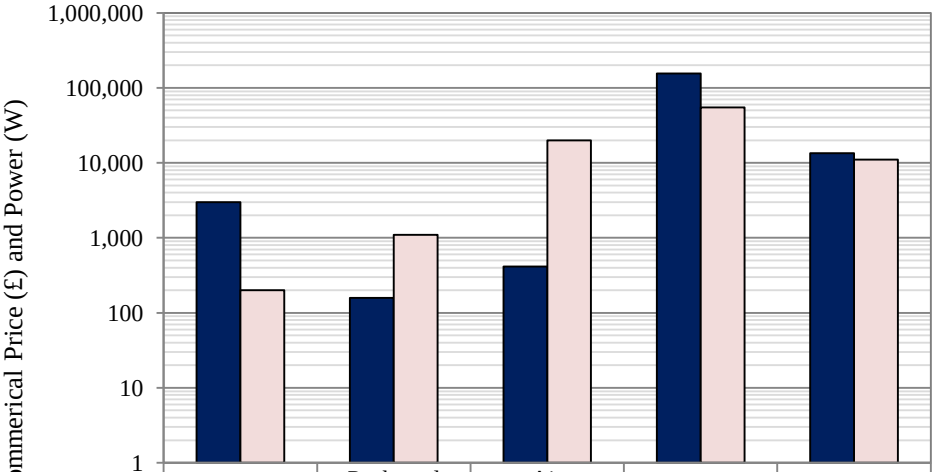

	Wind tower	Packaged terminal air conditioner	Air handling unit	Desiccant cooling	Absorption cooling
Price (£)	3,000	158	414	155,767	13,380
Power Consumption (W)	200	1,100	20,000	55,000	11,000

Figure 1.3 Comparison of cost and power of the system on the log scale (Hughes *et al.*, 2011)

In addition to electricity usage, buildings are also responsible for almost 40-50% of the world's greenhouse gas emissions (Asif, 2007). In areas of hot climatic conditions and high-humidity, ventilation is predominantly significant in reducing the discomfort levels (Givoni, 2009). From a general perspective, in regions of hot and dry climates, cooling during the day causes peak energy demands. In comparison with other time periods,

electricity consumption during the night is significantly lower due to the cooler temperatures outside.

Various strategies in buildings are already being practiced which exploit temperature and wind velocity parameters to reduce cooling loads in order to limit the expense for supplementary power consumption. In hybrid (mixed mode) ventilation, the airflow is due to wind and buoyancy through purposely installed openings in the building envelope supplemented, when necessary, by mechanical systems. One of the key mechanical components of a hybrid system includes heat exchangers for heating or cooling the outdoor supply air to requirements depending on the working configuration (Awbi, 2010).

Since the residential and commercial building sectors consume a major load of the energy consumption, there is a significant opportunity for minimising the external electricity supply using passive cooling techniques. The term passive applies here to the exclusion of energy-consuming mechanical components for carrying out the cooling operation. The urban microclimate is a major factor in the operational performance of passive cooling technologies in commercial buildings. A characteristic feature of passive cooling involves the reduction of electricity usage by active air-conditioning or by minimising heat gains through natural ventilation. Natural ventilation refers to the fresh air supply from outdoor (macro-climate) to indoors (micro-climate) through non-mechanical methods and if combined with a refrigerant-free heat transferring mechanism, can contribute in reducing the carbon footprint of new and existing dwellings.

1.2 Integration of heat pipes in natural ventilation systems

Although a lot of advancements have been made in the field of natural ventilation, they have their own limitations in terms of delivering adequate indoor cooling temperatures largely due to external climatic variations in hot countries. An energy-efficient solution for alleviating mechanical air-conditioning loads of a built environment can thus be achieved by integrating natural ventilation systems with a heat pipe heat exchanger technology. By incorporating the zero-energy working principles of heat pipes to provide the cooling duty, natural ventilation systems can become an effective and sustainable alternative in keeping the internal environment comfortable.

A heat pipe is a heat and mass transfer mechanism used in many applications ranging from petroleum, chemical, light industry and pharmaceuticals to energy and industrial productions. A heat pipe unit uses a refrigerant to carry out its heat transfer mechanism (Hellevang, 2009). However, the potential of replacing the refrigerant with a natural heat pipe working fluid such as water is vast and can lead to a significant reduction in the carbon footprint of the residential dwelling. Figure 1.4 displays the schematic of a heat pipe displaying the general method of operation.

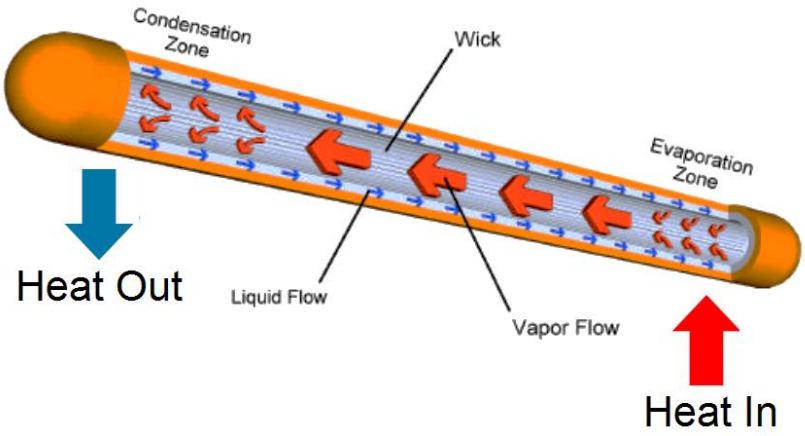

Figure 1.4 Schematic of a heat pipe highlighting its basic principles (Enertron, 2013)

High heat transfer rates are associated with boiling and condensation cycles employed by heat pipes and this have led designers and engineers to use this phenomenon for heating and cooling purposes worldwide (Holman, 1997). The unique mode of operation of heat pipes including phase change materials (PCMs) provide a better efficiency pattern over conventional heat exchangers in major operations which require effective transfer of heat (Reay and Kew, 2006). All energy transfer processes associated with heat pipes are achieved through liquid vaporisation or vapour condensation (Hellevang, 2009, Lin *et al*., 2010). The operating pressure and the type of fluid inside the heat pipe depend largely on the operating temperature of the heat pipe. Though water is a suitable natural fluid for moderate temperature ranges encountered in electronic equipment, various other fluids are used in the manufacturing of heat pipes to allow them to be used in high and medium-temperature applications (Cengel, 2006).

Crucial feature of heat pipes over other heat transfer devices such as thermal wheels is its ability to limit cross-contamination of air streams to a minimum which becomes essential in laboratories and hospitals (Cooper, 1996). In addition, heat pipes can be

used as indirect evaporative coolers, in which water is sprayed on the exhaust side of the pipe to pre-cool the supply air (Figure 1.5). (NREL, 2003).

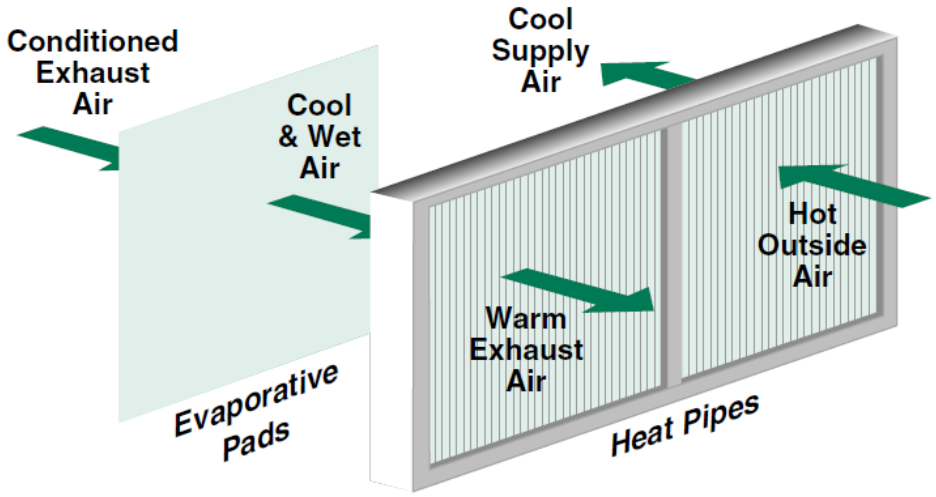

Figure 1.5 A heat pipe heat exchanger system (NREL, 2003)

Heat pipe heat exchangers offer a number of significant advantages (Ruch, 1976 and Mathur, 1991) over other types of heat exchangers. One of the foremost advantages is that in comparison to other types of heat exchangers, they require no external power to circulate the working fluid, and therefore heat can be transferred in either direction (Mathur, 2000). Heat pipe heat exchangers can be retrofitted to existing air-conditioning systems or used as stand-alone systems in new applications (Mathur, 1996).

Even with relatively small temperature differentials between the evaporator and condenser side, large amounts of heat can be transported using heat pipes because of the phase change of the working fluid inside it (Firouzfar and Attaran, 2008). A second advantage of using a heat pipe over conventional heat transfer devices is its capability to function as a nearly isothermal system, where a wide range of energy inputs can be accommodated with little change in the source temperature (Yau, 2008) thereby making it an effective mechanism in natural ventilation systems requiring sudden changes in ambient temperatures.

With escalating global demands for energy-efficient buildings, it is important that energy is not wasted. By employing a heat pipe device, thermal energy can be recovered from the warmer air stream and added to the cooler air stream. In temperate climates this allows energy saving to be realised through preheating of the outside air. Conversely, in hot climates the investments are associated with pre-cooling of the

outside air stream. Heat pipes can be arranged with air streams side by side using tubes sloping down to the warmer air. Alternatively the air streams can be stacked with the warmer air at the bottom, thus ensuring the use of the device in various orientations (SPC, 2011). Furthermore, the flexibility of heat pipes in terms of diameter and sizes make them particularly useful to be coupled with a variety of ductworks and frames or to be retrofitted into existing natural ventilation systems.

Research on emphasising the capability of heat pipes in pre-cooling warm fresh air streams to advance natural ventilation systems for buildings or residential dwellings are limited. Previous works have highlighted the use of heat pipe devices in building heat recovery and energy conservation systems although the potential for passive cooling is not well-defined, specifically in terms of optimum geometrical arrangement and choice of working fluid. This research targeted the specific areas not covered in literature (detailed in Chapter 2, Section 2.8) in order to meet the study's objectives.

1.3 Research aims and objectives

The aim of this research was to integrate heat pipe technology into natural ventilation air streams to provide passive cooling in regions of hot arid climatic conditions without the use of mechanical assistance. The study investigated the cooling duty of heat pipes when subjected to low-speed external airflows carrying ambient temperatures varying between 295K and 314K typically found in hot countries like Qatar (The Weather Channel, 2012). In order to assess the thermal performance of heat pipes, the rate of heat transfer and overall effectiveness of the device under varying design parameters was investigated.

The key objectives of this research are as follows:

1. Determine the most suitable heat pipe working fluid by comparing the fluids currently available in the marketplace (water, ethanol and R134a) based on their maximum airside cooling capability under the design conditions.

2. Determine the contribution of the fluid physical properties, namely density, thermal conductivity, dynamic viscosity and specific heat capacity to increase the cooling duty of heat pipes under the design conditions.

3. Determine the optimum spanwise arrangement between the rows of individual heat pipes by evaluating its effect on the downstream airflow and temperature profiles.

4. Determine the optimum streamwise arrangement between the columns of individual heat pipes by evaluating its effect on the downstream airflow and temperature profiles.

5. Establish a transient thermal model to determine the responsive behaviour of heat pipes in relation to rapid variations in external temperatures.

6. Validate the CFD model using experimental testing by determining the error within the accepted range of ±5% and ±17% (Ekambara *et al*., 2008, Wang, 2012).

1.4 Research methodology

Figure 1.6 displays the methodology used in this research.

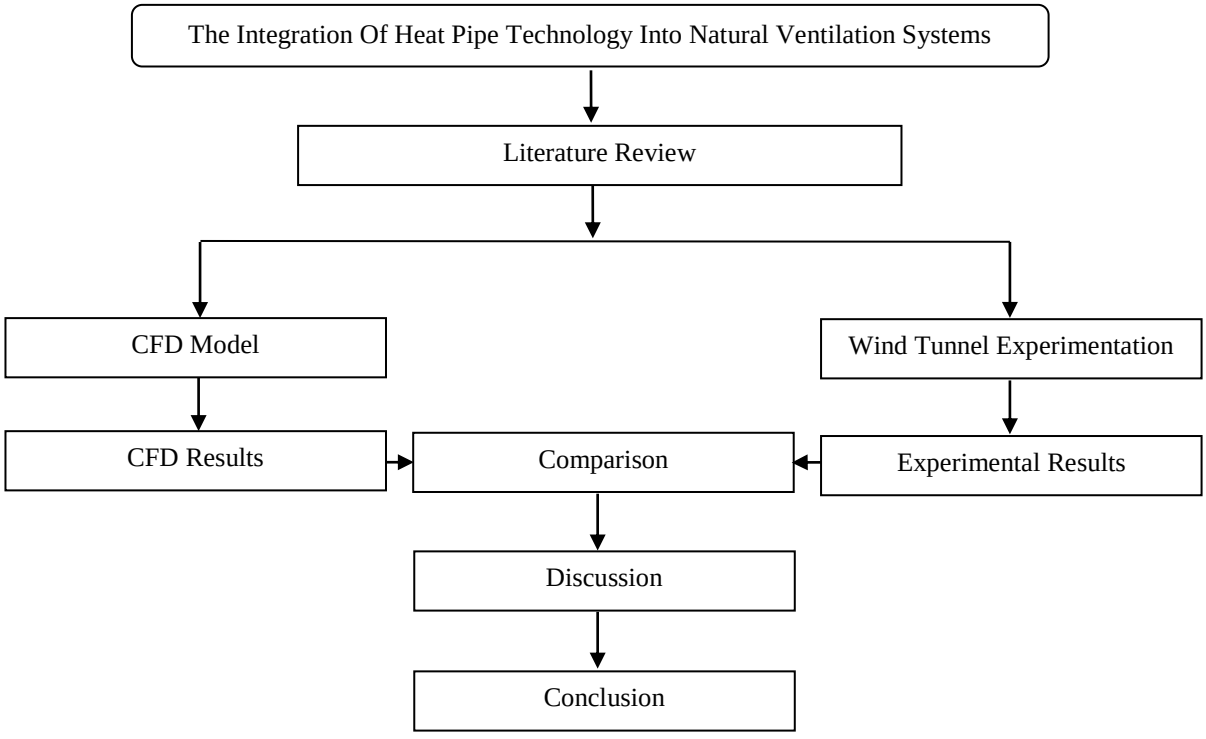

Figure 1.6 Research methodology and structure

The research methodology was divided into three phases with each phase outlining a specific area of work. The first phase of the study reviewed conventional heat pipe technologies which could be used within processes related to building energy and natural climates under the required range of operating temperatures. Current numerical and experimental techniques for analysing the performance of heat pipes are reviewed. A heat pipe heat exchanger model was designed and CFD analysis was conducted on the rate of heat transfer obtainable from using water, ethanol and R134a as internal working fluids. The effect of internal fluid properties on reducing air temperatures or cooling through convection was further investigated.

The second phase of this study investigated the effects of varying geometrical parameters on heat transfer and effectiveness of heat pipes. Spanwise thickness and streamwise distances between the rows and columns of arranged heat pipes were analysed to underline the optimum configuration. In order to determine the annual thermal performance of the heat pipe system, twelve monthly models were established with different source temperatures and wind speeds in order to calculate the overall effectiveness during each month of the year.

The third phase of this research focused on the experimental validation of the CFD predicted results. A low-speed closed-loop wind tunnel was built with the test section incorporating identical dimensions to the computational domain for accurate comparison of results. The findings obtained from the wind tunnel testing indicated the actual thermal performance of the heat pipes when exposed to low-speed hot air streams. The experimental data was therefore used to validate the CFD models subsequently drawing the study's conclusions.

1.5 Summary

The thesis is divided into 8 chapters and the summary of each chapter is listed below:

Chapter 1 provides an introduction of the present energy consumption in buildings due to active air conditioning systems and its impact on the ecological footprint. The chapter further introduces passive cooling techniques in buildings with emphasis on heat pipe heat exchanger systems and their role in heat recovery in natural ventilation. The chapter concludes with the summary of the research methodology.

Chapter 2 presents a comprehensive review of literature consisting of conventional heat pipe systems which are useful at a range of operating temperatures applicable to building energy systems. The review focuses on various numerical and experimental techniques and parametric studies that have been previously found in literature for designing and modelling heat pipes and heat pipe heat exchangers.

Chapter 3 introduces the numerical methodology which was used in this research. The first section describes the general governing equations related to fluid dynamics and heat transfer. The CFD model is then described, highlighting the physical and computational domain and applied boundary conditions. The chapter further describes the grid adaptation procedure that was used to verify the computational grid.

Chapter 4 presents the experimental methodology which was used in this research. An overview of the closed-loop wind tunnel and its components is presented. The experimental set-up is defined listing out the data acquisition devices and apparatus used for the investigation. Measurement points for recording inlet and outlet air velocity, pressure and temperature are described at both upstream and downstream locations of the heat pipe arrangement.

Chapter 5 describes the numerical results of the current study. The findings included the determination of the most suitable current working fluid alongside the optimum spanwise and streamwise arrangement between the heat pipes under the operating temperatures. Furthermore, the chapter shows the effect of internal fluid properties on the general cooling duty of the heat pipes working under low-speed natural airstreams. The final section analyses the overall effectiveness of the heat pipe system during each month of the year for Doha, Qatar (The Weather Channel, 2012).

Chapter 6 outlines the experimental results of the research. Experimental tests were conducted on copper-water and copper-R134a heat pipes under stabilised source and sink conditions. The heating elements were normalised to various steady-state temperatures followed by a transient investigation in order to understand the actual thermal performance of the heat pipes at different operating conditions. The chapter includes transient infrared images and smoke generation test results for thermal visualisation.

Chapter 7 displays the detailed comparison of the CFD results using experimental data. The variations in air velocity, pressure and temperature findings are quantified to determine the uncertainty percentage between the two techniques. In addition, the work compares the variation range of the results generated to published numerical and experimental data from previous literature.

Chapter 8 concludes the findings of this research by comparing against the key objectives in order to meet the defined aim of the study.

Chapter 2
Literature Review

2.1 Introduction

The consumption of external energy in buildings can be categorised into two primary means, to keep the interior comfortable for occupants through using HVAC systems and secondly, to run the required domestic applications, (all of which leading to an increase in resultant global CO_2 emissions). For countries incorporating hot and dry climatic conditions, the electricity demand from air-conditioning loads can reach above 50% (Landry, 2004). Increasing fuel costs and environmental concerns have thus given constant scope for advancing research and development in the field of energy-efficient space cooling techniques to minimise the dependence on mechanical intervention.

Passive or natural ventilation systems are appropriate alternative solutions to mechanical methods in maintaining the fresh-air and thermal comfort requirements of a built environment. However, at present, the key limiting factor of implementing these systems in hot countries includes insufficient delivery of indoor temperatures due to their complete dependence on outdoor climates. In order to confront the subject, there is a need for incorporating heat transfer mechanisms within natural ventilation systems in order to carry out the cooling duty. If integrated with heat pipes as heat transfer devices, the overall effectiveness of natural ventilation technology can be enhanced in terms of providing adequate indoor temperatures.

Heat pipes function on a closed-loop heat transfer cycle without requiring external electricity for its operation, thereby making itself entirely adaptable for use within natural ventilation systems. Retrofitting heat pipes into heat exchangers for the purpose of pre-cooling and heat recovery has become an important economic consideration since the utility of heat pipes for environmental management is cost effective and environmentally sound. This chapter conducts a comprehensive review into the conventional heat pipe systems currently available and outlines previous literature on existing numerical and experimental studies related to the technology. The literature review was conducted in order to fulfil the research gap associated with existing

parametric studies on heat pipes, specifically targeting the optimum geometrical arrangements and the significance of the internal working fluid on heat transfer.

2.2 Basic characteristics of heat pipes

Since the first basic heat pipe concept was proposed by Gaugler (1944), heat pipes have been widely applied to a variety of both simple and complex designs for space and terrestrial applications. Heat pipes are devices used for efficient transport of heat over large distances. Under typical operation, a metal container such as aluminium or copper contains a small amount working fluid pressurised to its saturation point. The heat transfer system is based on the continuous cycle of evaporation and condensation process. When heat is applied to the outer area of the tube, the liquid inside the tube boils and vaporises into a gas that moves through the tube seeking a cooler location where it condenses, giving off its latent heat. Using capillary action, the wick transports the condensed liquid back to the evaporation section (Faghri, 1986).

For gravity-assisted heat pipes, the liquid is condensed back to the evaporator section by means of gravity (Hagens *et al.,* 2007). The appropriate choice of working fluid along with the inclination angle is therefore a major factor in heat transfer obtainable from heat pipes (Song *et al.*, 2008). When used in the 90° or vertical orientation, the temperatures at the condenser region of the heat pipes can be maintained by using a constant cold water or ice bath (Naphon, 2010) in a fixed control volume. Figure 2.1 displays the schematic of a gravity assisted heat pipe operating with the evaporator section at the bottom and the condenser section at the top.

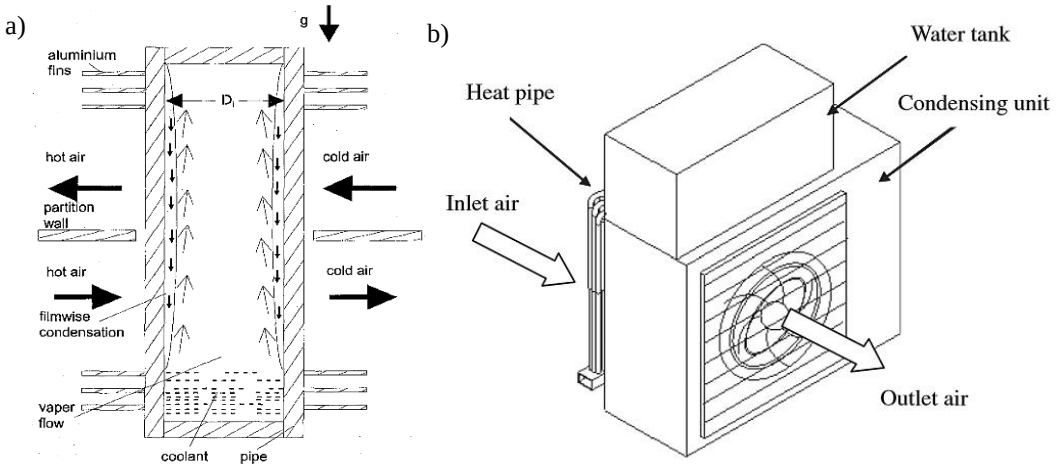

Figure 2.1 Schematic of: a) a heat pipe heat exchanger in a vertical position (Beckert and Herwig, 1996) b) condenser unit with a heat pipe set in vertical position (Naphon, 2010)

Heat pipes transfer only sensible energy from one airstream to another. In heat pipe applications, the supply and exhaust air streams are next to one another, although some modified or split heat pipes allow the air streams to be separated. Heat pipes do not have moving parts, and failure of the entire unit is infrequent due to minimal risk of corrosion and wear. Space efficiency is another typical characteristic of heat pipes as they can be manufactured in various dimensions depending on the configuration of the energy system.

Heat pipes are energy-efficient passive devices and do not consume fossil fuels and other environmentally hazardous resources for carrying out its operation, thereby making itself extremely suitable for use in natural ventilation air streams. There are various heat pipe systems currently available which are applicable to operating temperatures associated with building energy applications.

2.3 Conventional heat pipe systems

Existing heat pipe technologies range from the conventional tubular designs to the more complex systems incorporating the sorption phenomenon. This section reviews the existing heat pipe configurations and emphasises on the obtained temperature profiles and heat transfer measurements.

2.3.1 Tubular heat pipes

Tubular or cylindrical heat pipes are the most uncomplicated type of passive heat transfer devices commercially available for use or retrofit into many terrestrial applications for heat transport over variable distances. Optimum working is achieved when the heat pipes are exposed to clean air streams while working under forced convection flows. The standard operational principle is based on capillary or gravity assisted action and the performance is measured in equivalent thermal conductivity and heat transfer duty.

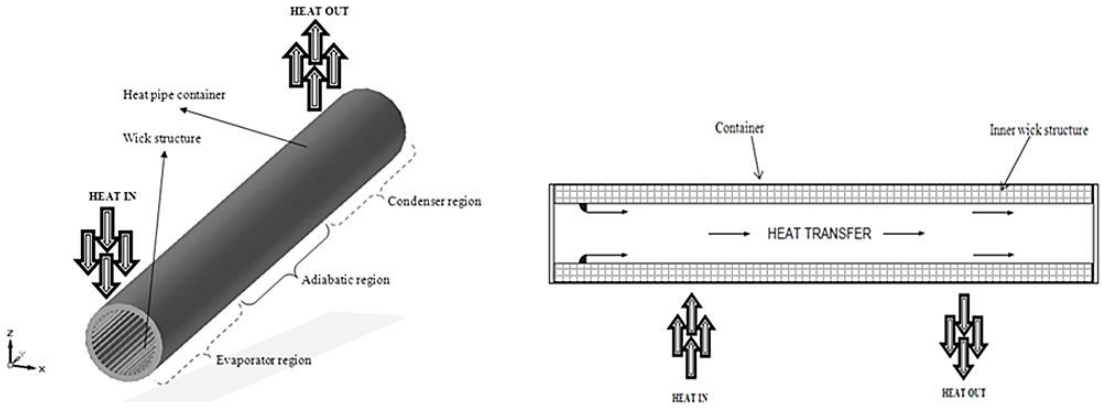

Figure 2.2 Schematic of a tubular heat pipe (Chaudhry *et al*., 2012)

Figure 2.2 displays the schematic of a tubular heat pipe. Joudi and Witwit (2000) carried out work to improve the thermal performance of gravity assisted conventional wickless heat pipes. An experimental study was carried out on a modified copper heat pipe with the introduction of an adiabatic separator. The heat pipe under test was fixed in a rig and coupled with several measuring devices including a digital amp meter and voltmeter in order to calculate the input power. The heat pipe was insulated with glass wool to minimise heat losses to the environment. The condenser flow rate was kept constant and the temperature was monitored at 23±2ºC and the power input was increased steadily to obtain gradual thermocouple readings. The outcome from the study highlighted useful results with respect to the addition of an adiabatic separator in the heat pipe. The study revealed an approximate increase of 35% in heat transfer coefficient in comparison to conventional heat pipes. The investigation concluded that the addition of an adiabatic separator eradicated the effect of inclination angles above 45º and decreased the heat pipe working temperature.

Liao *et al.* (2007) analysed the thermal performance of a smooth carbon steel-water heat pipe in comparison to its internally finned equivalent. Influencing parameters including the inclination angle, working temperatures and heat flux formed the basis of the investigation. The experimental set-up comprised of a fibre glass coated carbon steel pipe with a flat band heater for providing heat flux to the evaporator section. The apparatus was placed on an adjustable workbench for alteration of inclination angles and thermocouples were linked to the data logging system for output results. The work showed that under experimental conditions, the heat transfer coefficient of the internally finned heat pipe was increased by 50-100% in comparison to the smooth heat pipe.

Shabgard and Faghri (2011) developed a steady-state analytical model for cylindrical heat pipes subjected to a constant heating flux. The proposed model coupled two-dimensional heat conduction in the heat pipe's surface wall along with the liquid flow in the wick and the vapour hydrodynamics. Constant fluid thermophysical properties along with axisymmetric heating and cooling were assumed in the model. The heat pipe was constructed out of copper and distilled water was used as the internal working fluid. The evaporator section comprised of 4 heating elements, each measuring at total length of 0.0635m. The condenser length was kept fixed at 0.3m. Figure 2.3 displays the cross-sectional view of the cylindrical heat pipe with multiple heat sources.

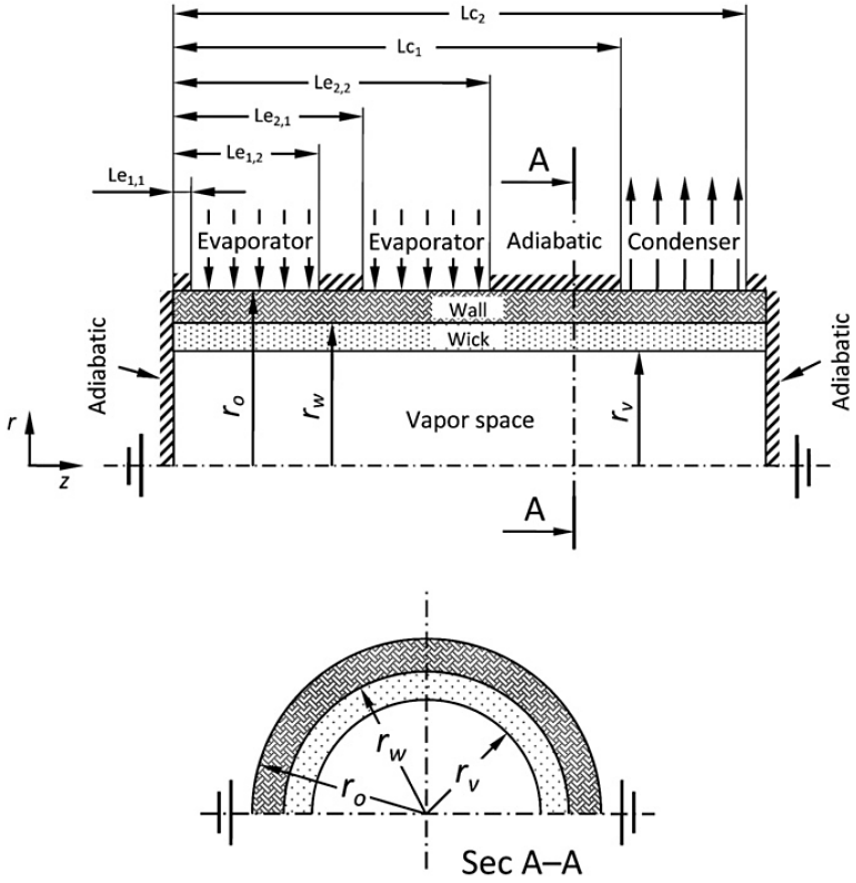

Figure 2.3 Cylindrical heat pipe with multiple heat sources (Shabgard and Faghri, 2011)

The results of the analytical model were compared to full numerical simulations previously conducted by the authors and good correlation was observed. The work found that in certain cases exclusion of the axial heat conduction in the surface wall can cause an error of more than 10% in the calculated pressure drops in heat pipes. The benefit of the analytical model developed in the study was to aid in alleviating the computational time using full numerical solutions.

2.3.2 Thermal diodes

A simple thermal diode can be a thermosiphon in which the gravitational force supplies the irregularity when positioned appropriately. A variety of aerospace and ground based applications make use of thermal diodes. The device is also used in modern renewable energy systems particularly where heat transfer in one direction is a requirement. However, due to the high initial capital expenditure and complexity in retrofitting such systems, commercialisation and interest has increased only steadily. Figure 2.4 displays the schematic of a thermal diode.

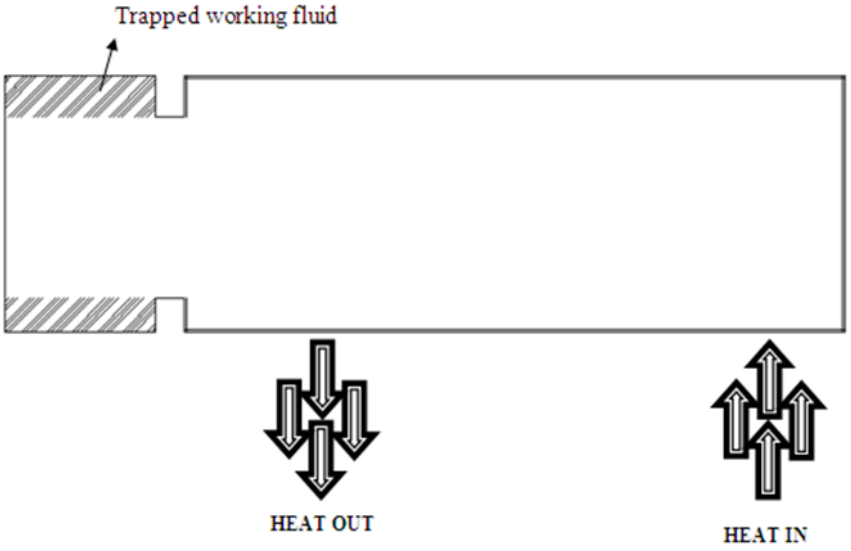

Figure 2.4 Schematic of a thermal diode (Chaudhry *et al*., 2012)

Omer *et al.* (2001) analysed a thermoelectric refrigeration system integrated with thermal diodes to study the performance of Phase Change Materials (PCMs). The fabricated system built for test included a 150W thermoelectric refrigeration system. The performance of the proposed system was compared to another similar system without integrated thermal diodes. The findings established the feasibility of thermal diodes between the thermoelectric cells and the PCM in order to prevent heat leakage. The results further displayed an improved performance of the system incorporating thermal diodes in the storage ability of the thermoelectric refrigeration system in comparison to its counterpart.

Varga *et al.* (2002) carried out tests to evaluate the performance of thermal diode panels incorporating heat pipes for passive cooling in buildings in Portugal. The manufactured

experimental set-up included nine copper/water bent heat pipes with a diameter of 12.7mm welded to aluminium sheets along with the thermal diode panels. The thermal and physical properties were tested using a finite element heat transfer model combined with an optimisation procedure for both forward and backward heat transfer. The work concluded the agreement of the applied model with the experimental procedure. In addition, the results displayed a significant increase in the forward heat transfer results in comparison to its backward counterpart.

Fang and Xia (2010) studied the thermal performance of a novel Bidirectional Partition Fluid Thermal Diode (BPFTD) for the function of providing solar heating. The BPFDT was a water tank integrated with a thermal insulation partition along with a movable control blade (Figure 2.5).

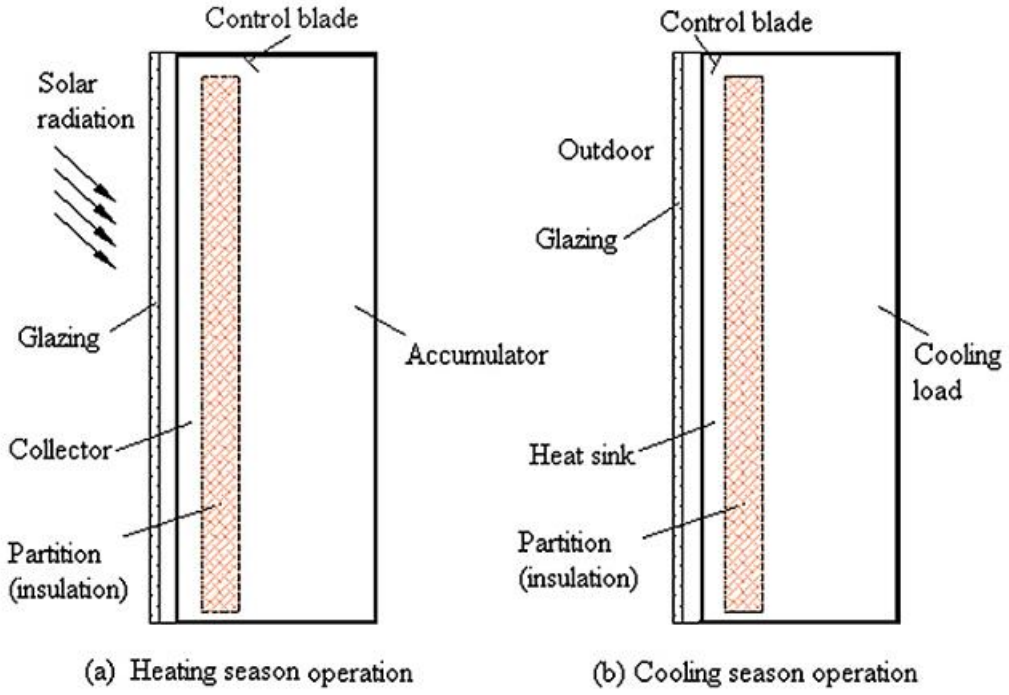

Figure 2.5 Bidirectional partition fluid thermal diode (Fang and Xia, 2010)

The working operation during heating season comprised of the collector absorbing solar energy, subsequently heating the liquid in it to a temperature higher than that in the accumulator, thereby producing a pressure head to turn the blade around the axis to open the upper channel. During the cooling season, the blade was moved manually to the other side of the upper channel to create the opposite pressure head in order to turn the blade. The experimental analysis was carried out by testing the BPFTD with two

identical hot boxes with similar wall configuration and comparisons were established with a water-wall of optimum thickness. Test results yielded that the BPFTD had a higher heating performance compared to its water-wall counterpart with additional findings confirming an increase in heat supply of around 140% when a single glazing cover without night ventilation is utilised when compared to the water-wall.

Rhee *et al.* (2010) investigated the temperature stratification in a solar hot water storage tank. The experiment proposed four different storage tank designs involving thermal diodes for its operation. The results of the test examined that the so-called express-elevator design displayed the highest amount of stratification during both heating and cooling periods in comparison to the other proposed designs. Consequently, the work concluded the bright future scope of optimising the geometric parameters of thermal diodes to obtain an improved rate of stratification.

2.3.3 Pulsating heat pipes

A pulsating (oscillating) heat pipe consists of a regular curving channel, evacuated and filled with the working fluid. Heat is transported through the latent heat of vapour and through the sensible heat transferred by the liquid slugs. When the tube on the evaporator section of the heat pipe is put under thermal load, the working fluid evaporates thus increasing the vapour pressure and formation of bubbles and transferring the liquid towards the condenser section where cooling results in a reduction of vapour pressure and condensation of bubbles in the section. The increase and decrease of bubbles in the two sections lead to an oscillating or pulsating motion within the capillary tube. However, the total weight of the cyclic loop limits its ability to be retrofitted into existing systems.

Qu and Ma (2007) investigated the principal factors involved in start-up of oscillating motions in a pulsating heat pipe including superheat and heat flux level on the evaporator section and the cavity size on capillary inner surface. The experimental investigation comprised of a glass prototype with a total length of 300mm and the evaporator section of 90mm along the constant inlet temperature of 296K. The findings of the theoretical analysis confirmed that the performance at start-up can be improved by controlling the vapour bubble type and using a rougher surface.

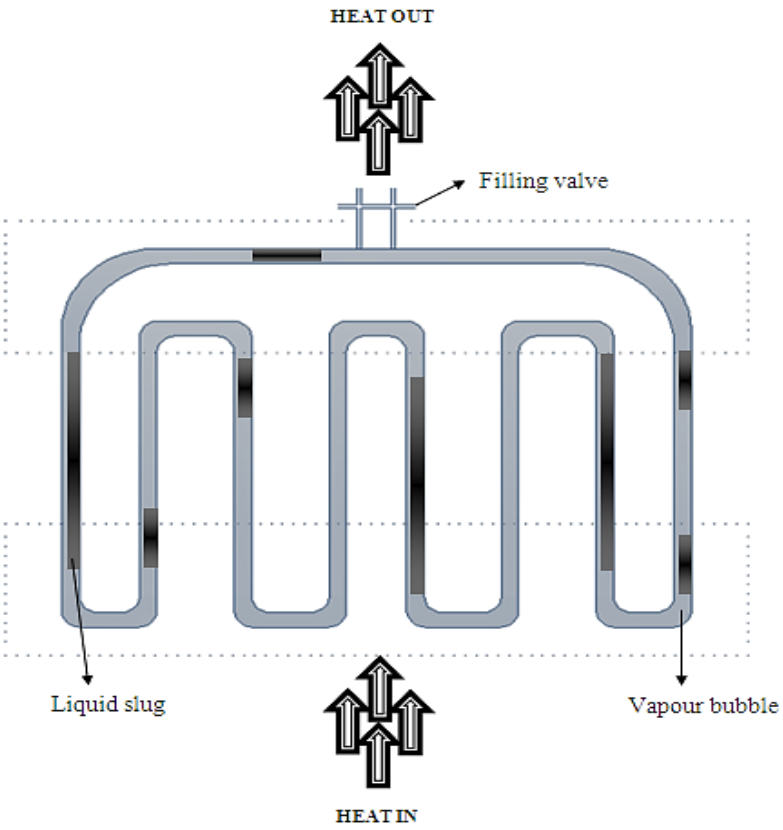

Figure 2.6 Schematic of a pulsating heat pipe (Chaudhry *et al*., 2012)

The schematic of the pulsating heat pipe is displayed in Figure 2.6. Yang *et al.* (2008) carried out work on estimating the thermal performance of closed loop pulsating heat pipes by conducting experiments on copper tubes of varying inner diameters and filling ratios. The system comprised of 40 copper tubes with the inner diameters of 1mm and 2mm and the vertical bottom heated, vertical top heated and the horizontal orientations were compared. The investigation findings displayed that the closed loop pulsating heat pipe with the vertical bottom heating gives the best performance with 2mm inner diameter and 50% fill ratio while the orientation effects were negligible for the 1mm inner diameter tube.

Wang *et al.* (2009) studied the thermal performance of heat transport of the four-turn pulsating heat pipe by comparing various working fluids with water. The experimental analyses were based on two operating orientations (vertical and horizontal) of a copper tube with an external diameter of 2.5mm. FS-39E microcapsule working fluid and Al_2O_3 nano-fluid were used for the test. The outcome of the investigation proved that the functional working fluids increased the heat-transport ability of the heat pipe when compared with water.

2.3.4 Loop heat pipes

Loop Heat Pipes (LHP) employ the characteristics of a conventional heat pipe but have an advantage in terms of its ability to transfer thermal energy over a larger space without any constraint on the path of the liquid or vapour lines and also in terms of a greater heat flux potential and robust operation (Reay and Kew, 2006). For this reason, LHPs are fast becoming typical devices to meet the global demand of control of thermal difficulties of high-end electronics. A capillary force in the evaporator section drives the operation for the LHP requiring no auxiliary power input. The main limiting factor for these cycles includes supplementary power requirements for mechanically pumped loops. Figure 2.7 displays the schematic of a loop heat pipe.

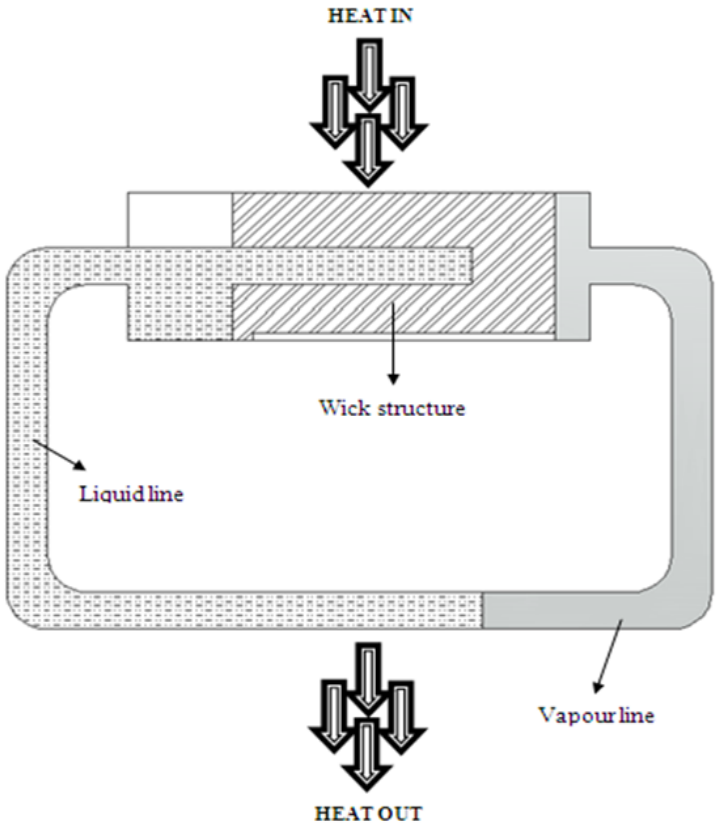

Figure 2.7 Schematic of a loop heat pipe (Chaudhry *et al*., 2012)

Kaya and Goldak (2006) investigated the heat and mass transport in order to study the capillary porous structure of the LHP. A finite element method for the evaporator cross section based numerical code was developed to solve the mass and energy equations and the solutions included an all-liquid and vapour-liquid wick cases. The results highlighted that at high heat loads, the boiling initiation under the evaporating meniscus

is very unlikely since the liquid contact with the fin decreases significantly. The investigation concluded that in order to increase the heat transfer limit for boiling, the elimination of non-condensable gases along with a very good contact at the fin-wick interface is essential.

Zhao *et al.* (2010) carried out work on developing a novel LHP solar water heating system for a characteristic dwelling in Beijing in order to facilitate efficient transportation and conversion of solar heat into hot water. A numerical model was developed to monitor the overall thermal performance of the system and various parameters such as the heat pipe loop and the façade integrated solar absorber were considered for influencing results. The findings indicated that the system efficiency decreases with increasing the mean temperature of water flow and efficiency of the thermal system increases with increase in the ambient temperature. The results further confirmed that the optimum operating temperature for the heat pipe is around 345K.

Wang *et al.* (2011) conducted experimentation based on a flat LHP under low-heat power input to understand the control of compensation chamber and the evaporator on the start-up behaviour. The testing system comprised of locating the standard K-type thermocouples, DC stabilised power supply along with an isothermal cooling water tank for experimentation. The results indicated that the LHP has the potential of start-up under low heat power of 6W. The results also confirmed that the LHP has a better start-up performance under low-power with an increasing thickness of the capillary interlayer.

2.3.5 Micro heat pipes

Micro Heat Pipes (MHPs) are used in applications where small to medium heat transfer rates are desirable. The rate of cooling achieved from the MHP is significantly lower compared to forced convection systems. However, the capability to control temperatures in environments of varying heat loads along with its compact size allows it to be used in various applications (Reay and Kew, 2006).

Lefe`vre and Lallemand (2006) investigated the heat transport capability of a flat MHP with the location of heat sources and heat sinks. A two-dimensional model containing a porous wick medium to behave as a capillary structure was incorporated with a three-dimensional thermal model to study the heat conduction of both the liquid and vapour

phases. The thermal model evaluated the capability to calculate the heat flux generated solely by the wall heat conductance.

Do *et al.* (2008) predicted the thermal performance of a flat micro heat pipe comprising of a rectangular grooved wick structure. A mathematical model was developed taking the influence of the contact angle, liquid-vapour interfacial shear stress and the amount of liquid charge. One-dimensional conduction equation for the wall and the augmented Young-Laplace equation were solved. The examined results revealed that the heat transport rate increases slowly as the liquid charge increases. The findings displayed the optimisation of the grooved wick structure highlighting the maximum heat transport rate of 128W under the optimum conditions of the height and groove width. The schematic arrangement is displayed in Figure 2.8.

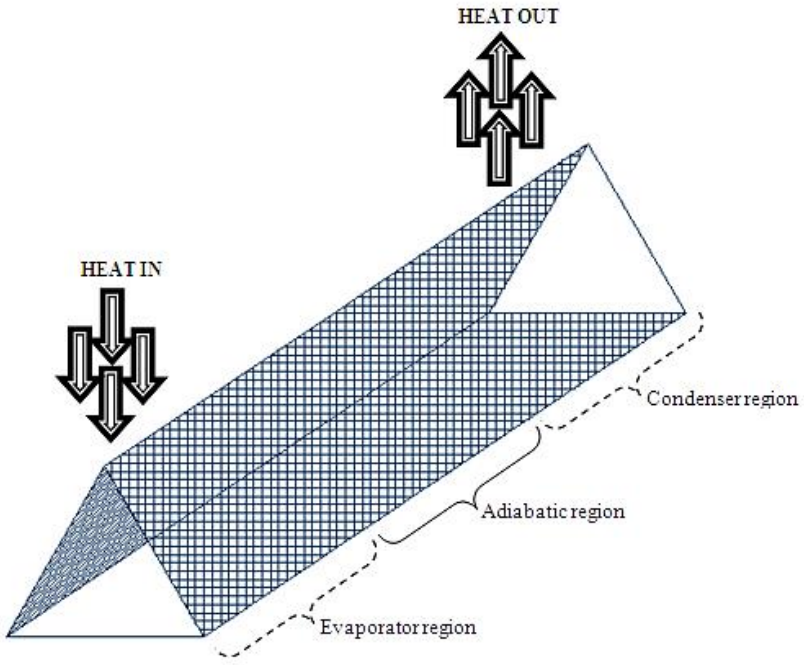

Figure 2.8 Schematic of a micro heat pipe (Chaudhry *et al*., 2012)

Hung and Seng (2011) carried out work on studying the thermal performance in terms of the heat transport capability of star-groove micro-heat pipes particularity with the influence of the geometrical design. A one-dimensional steady state numerical model was developed to solve the continuity, momentum and energy equations of the liquid and gas phases. The comparison results of the study yielded that the star-groove micro-heat pipe have a better performance characteristic compared to the conventional

polygonal micro-heat pipe due to its ability to provide a higher capillary rate by the flexibility in reducing the corner apex angle.

2.3.6 Sorption heat pipes

The sorption heat pipe is a device which employs the sorption phenomenon on the heat pipe to improve the heat transport ability. Similar to the loop heat pipe, sorption heat pipes can also be used in terrestrial applications since it comprises of similar evaporator and condenser along with the working fluid. Furthermore, the literature highlights that the integrity of the sorption cooler with a loop heat pipe provides higher heat fluxes and evaporator thermal resistances. However, the intricate sorption cycle limits the use of this type of system for ventilation and building applications.

Vasiliev and Vasiliev Jr. (2004) conducted an in-depth study on sorption heat pipes as a heat transfer device and highlighted the potential in order to be utilised in cryogenic fluid storage due to its high heat transport ability. The investigation was based on an experimental set-up, comprising of a sorption cooler and a capillary pumped evaporator for both sorption and loop heat pipe arrangement. The results of the experiment revealed that the heat transfer by the sorption heat pipe was in excess of 12kW/m^{2}K, an increase of three times in comparison to a loop heat pipe. Figure 2.9 displays the schematic of a sorption heat pipe.

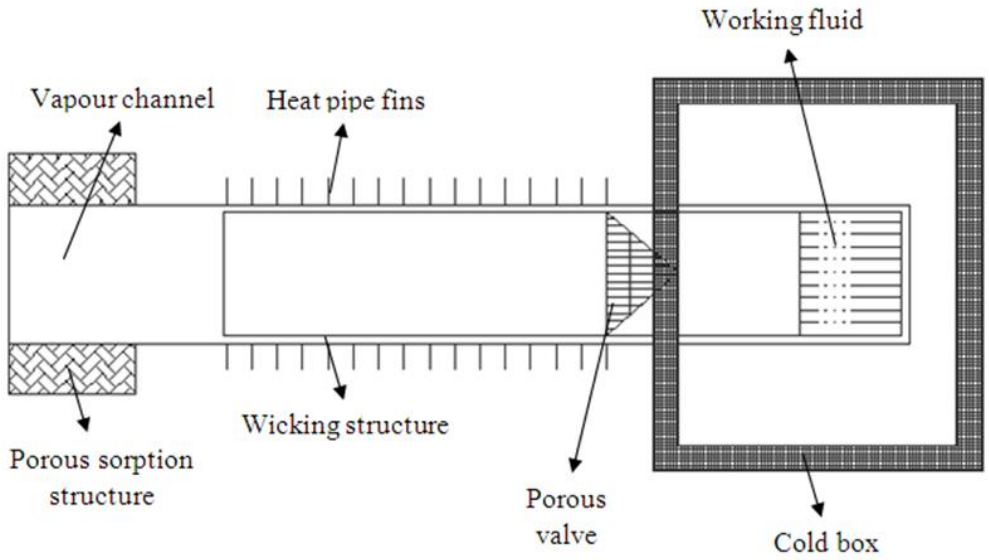

Figure 2.9 Schematic of a sorption heat pipe (Chaudhry *et al*., 2012)

A further study by Vasiliev and Vasiliev Jr. (2005) included the use of sorption heat pipes as a thermal control device for space and ground applications. The work emphasised the use of sorption heat pipes as an enhanced heat and mass transfer device due to its insensitivity to gravitational acceleration forces. Similar, to the loop heat pipes, the dominant mode of heat transfer was through the evaporation of liquid inside the porous structure. The study revealed that the efficiency obtainable for this type of system is the highest at heating loads of 200W/cm^2 or more. Figure 2.10 displays the schematic of the sorption heat pipe used in the study.

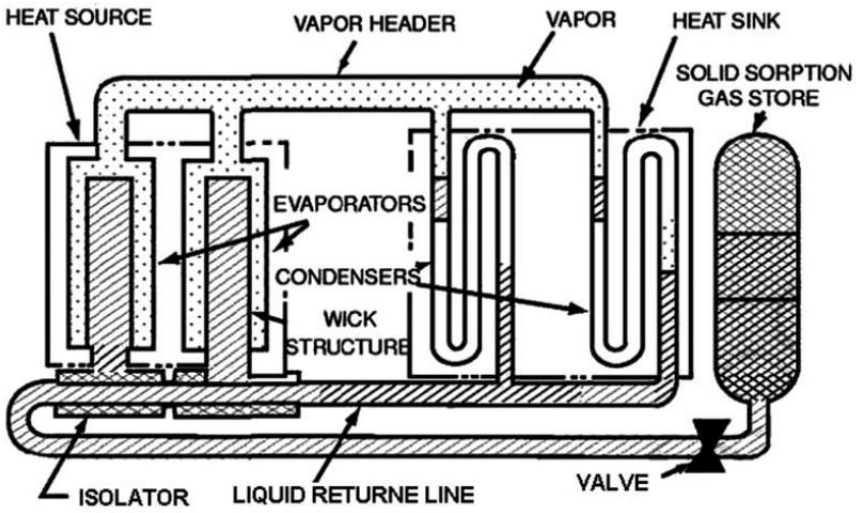

Figure 2.10 Sorption heat pipe (Vasiliev and Vasiliev Jr., 2005)

For the existing conventional heat pipe systems used in terrestrial applications, it is considered that each system has its own advantages and limitations based largely on operating conditions. The complexity of the heat pipe cycle is an important factor when considering its retrofit capabilities in natural ventilation systems. The review therefore categorised the general working operation of existing heat pipe cycles using schematic illustrations and previous related works on the subject.

2.4 Parametric studies on heat pipes

The thermal performance of heat pipes depend on various internal and external parameters ranging from the compatibility of the working fluid to the geometrical arrangement of the pipes within the physical domain. This section of the chapter consolidates existing literature related to the general working parameters associated with heat pipes in terms of assessing flow characteristics and heat transfer.

2.4.1 Internal working fluid investigations using heat pipes

Previous studies obtained from literature have highlighted the use of natural liquids and refrigerants as heat pipe working fluids in a broad range of applications within the range of intermediate working temperatures, appropriate to areas of hot natural climates.

Abou-Zian *et al*., (2000) designed and constructed a two-phased closed thermosiphon in order to predict its thermal conductivity performance characteristics under stationary and vibrated conditions. Water and R134a were used as working fluids. The copper pipe had an internal and outer diameter of 23mm and 25mm while measuring 900mm in total length. The evaporator section was heated through an electric heater having a power of 1500W. The condenser section was cooled using flowing water through an annular jacket measuring 250mm in length. The vibration frequencies were in the range between 0 and 4.33Hz. The results of the work depicted a maximum heat transport of stationary water-copper thermosiphon at 1100kW/m^2 while the R134a charged thermosiphon displayed 190kW/m^2. It was found out that the effect of vibration on the wickless pipes was different for both fluids due to their different thermophysical properties.

De Leeuw *et al*., (2006) carried out work on comparing the performance of a heat pipe heat exchanger to a conventional water-cooled heat exchanger. R134a was used as the working fluid and the study analysed the overall heat transfer under inlet mass flow rates varying from 0.4kg/sec to 2kg/sec. The temperature of the hot channel was kept between 40-70°C while ambient air was used as the cold sink keeping temperatures regulated between 20-50°C. A mathematical model was developed in order to predict the heat transfer performance and a good correlation was observed when the results were compared against published pool boiling and filmwise condensation models at low Reynolds number. The overall heat transfer at the evaporator side was measured between 10 and 40W/m^2K with the temperature distribution being indicative of proper fluid filling ratio. The study emphasised that the testing conditions were kept similar to countries experiencing warmer climates with the constant possibility in applying heat pipe based cooling technology in practice.

Savino *et al.* (2009) investigated the effect of surface tension variation with temperature to highlight the performance of self-rewetting fluids in comparison to ordinary fluids in wickless heat pipe systems. Temperature profiles using thermographic images were developed by conducting laboratory experiments on glass tubes containing alcohol and

1-heptanol aqueous solution. Computed volume fractions at different time intervals were obtained (Figure 2.11).

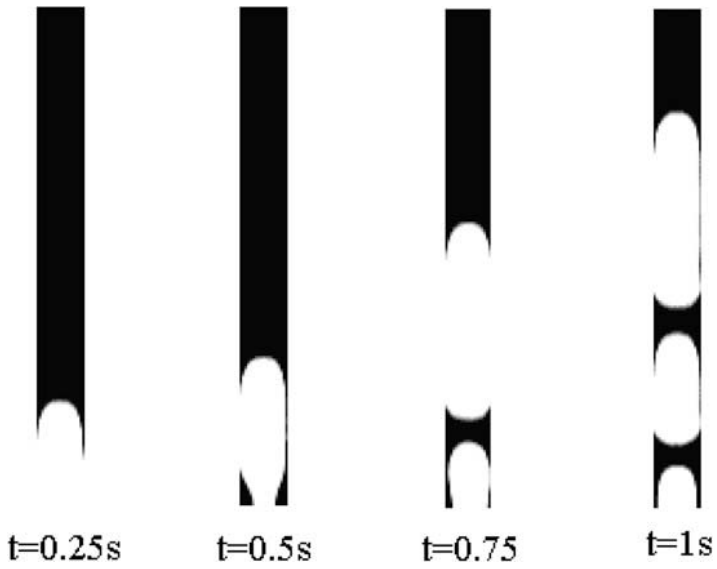

Figure 2.11 Slug boiling behaviour in water under normal gravity conditions (Savino *et a*l., 2009)

The results of the study demonstrated that under normal gravity conditions, the evaporation process continues periodically since when one detached vapour bubble rises, another one is formed simultaneously in the boiling film. It was observed that the ordinary fluid (ethanol) exhibited a decreasing linear dependency on the temperature while the self-rewetting fluid (heptanol) showing a non-linear dependence. The work confirmed that for the self-rewetting fluid the evaporation region contains more liquid in comparison to water, which also implies spontaneous liquid supply to higher temperature region. The detailed study emphasised the potential of efficient heat transfer by introducing new working self-rewetting fluids on the binary mixtures based on Water/Ammonia and Water/Ethylene Glycol for various applications.

Wong *et al*. (2011) analysed the evaporator resistance performance of heat pipes charged with water, methanol and acetone as working fluids. A sintered two layer copper wick was used and uniform heating was applied to the copper base plate at the evaporator section. The condenser section was kept at constant cold temperature using a water jacket at 20°C. The evaporator resistance was determined using the temperature difference between the copper plate and the vapour under and above the evaporator section. The findings of the work revealed that maximum heat loads for water were superior to methanol and acetone. The work concluded that the values for heating loads

correlated well with their figure of merit highlighting the superiority of water over the compared fluids.

Yau and Foo (2011) carried out a comparative study on evaporator heat transfer characteristics involving R134a, R22 and R410A as heat pipe working fluids. The work was based on investigating the potential of a rotating heat pipe heat exchanger to be used in HVAC applications for energy conservation. The experimental set-up comprised of an evaporator air temperature of 40°C while the condenser temperature was kept constant at 10°C with an airflow rate across the test chambers at 0.0075m^3/sec. The heat transfer characteristics of the completely inclined heat pipes are displayed in Figure 2.12.

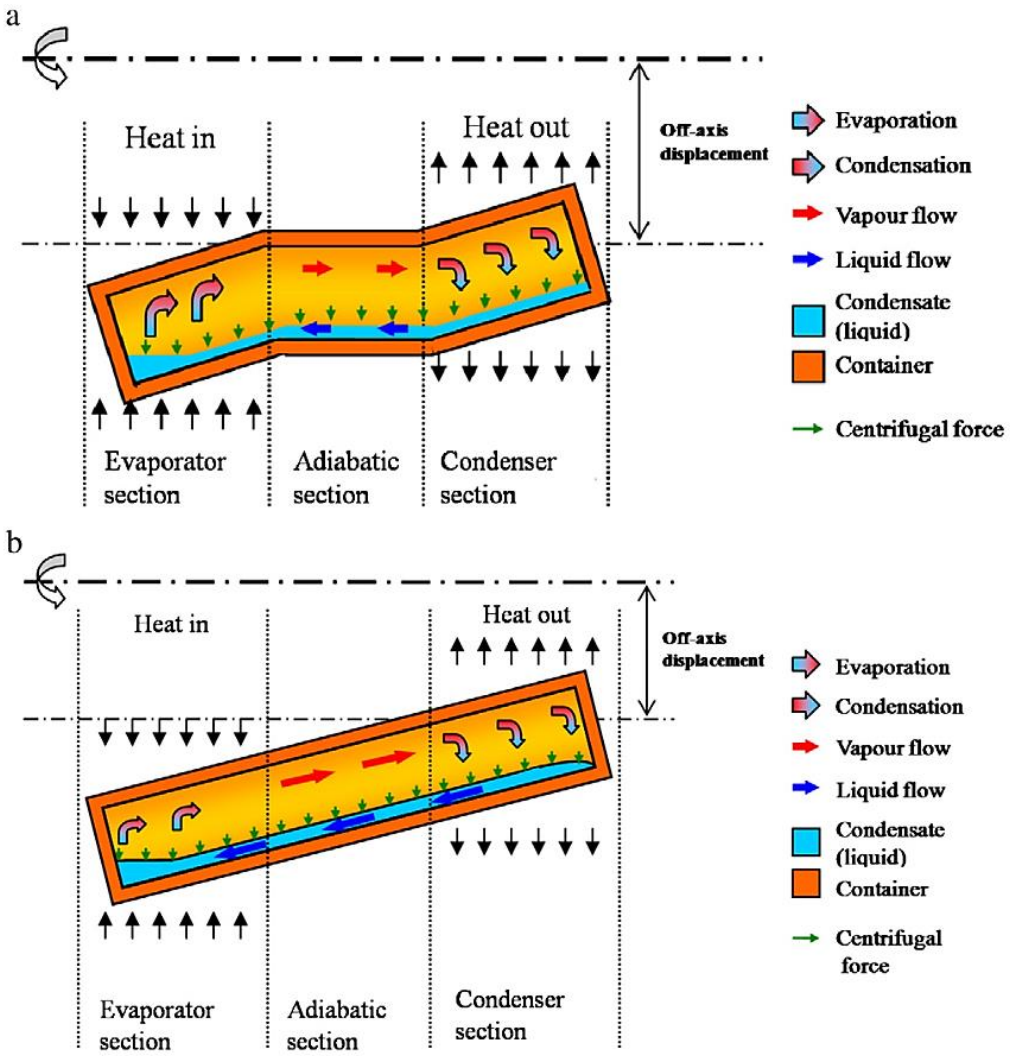

Figure 2.12 a) Fluid flow in rotating heat pipe with inclined condenser and evaporator sections at certain off-axis displacement b) Fluid flow in fully inclined rotating heat pipe at certain off-axis displacement (Yau and Foo, 2011)

The work demonstrated that in general, heat pipes showed increased heat transfer with increased rotational speeds and radial displacement. However, the heat transfer enhancement on the evaporator of the fully inclined rotating heat pipe was inferior to the straight and parallel counterpart. The results further depicted that R410A refrigerant displayed a superior performance in liquid return wherein its low viscosity property allowed the heat pipe to perform to a higher heat transfer capacity. The study depicted that R134a was the most economical and had the lowest saturation pressure among the compared refrigerants. The work determined the scope of using heat pipes for building applications and cooling of machineries.

Typical operating temperatures for heat pipe systems found in terrestrial applications range from 293K to 393K. The choice of working fluid is a major contemplation in identifying appropriate heat pipe assemblies. The Figure of Merit or Merit No. is therefore a useful indicator in determining the maximum heat transport capability in terms of the internal fluid properties. The Merit No. is based on the heat pipe working fluid properties and is a ratio of liquid density, surface tension, latent heat of vaporisation to the dynamic viscosity.

Chaudhry *et al*. (2012) compared different heat pipe working fluids in terms of their Merit No. for particular use in building and ventilation systems. Water, ammonia, acetone, pentane and heptane were equated based on their thermophysical fluid properties and the review study revealed that water incorporated the highest Merit No. in relation to other working fluids. At an operating temperature of 293K, the Merit No. for water was 1.78×10^{11}, which was an order higher than ammonia which incorporated a Merit No. of 7.02×10^{10}. In addition, with an increasing operating temperature gradient from 293K to 393K, water displayed an increase in Merit No. of 64% while other working fluids displayed a reduction in Merit No. as the operating temperatures were increased. The study identified the scope of further research into comparison between available heat pipe working fluids in order to evaluate the ideal candidate for use under the working temperatures suitable for natural ventilation.

Apart from the heat pipe internal working fluid, common heat transfer enhancement parameters include the application of fins and identifying the most suitable alignment between the pipes. The following sections review previous works related to the function

of fins on pipes along with comparative studies conducted between staggered and inline arrangement in terms of increasing the thermal performance of the system.

2.4.2 Use of fins or extended surfaces on heat pipes and heat exchangers

The key purpose of integrating fins or extended surfaces on heat pipes or heat exchanger set-up comprises of increasing of the available surface area in order to ensure maximum contact time between the fluid flow and pipe surface. Previous studies have highlighted this aspect and its influence in augmenting the overall heat transfer.

A mathematical investigation into the use of fins as a means to increase heat transfer was conducted by Lane and Heggs, (2005). A generalised equation was developed to study the temperature profile along the length of the fin of various profiles including tapered, trapezoidal and inverted trapezoidal or dovetail fin. The work established that the heat flows through the fins having the same base thickness increase as the values of fin tip length factor become larger, thereby analytically establishing that the tapered fin inducing the lowest heat flow while the dovetail fin having the largest. The work recommended the use of dovetail fin profile over the longitudinal rectangular fin arrangement for use in double pipe heat exchanger applications.

Pin fins are often used in heat exchangers as effective elements for enhancement of heat transfer. Sahiti *et al.*, (2008) derived the heat transfer and pressure drop characteristics of a double-pipe pin fin heat exchanger using a mathematical model (Figure 2.13).

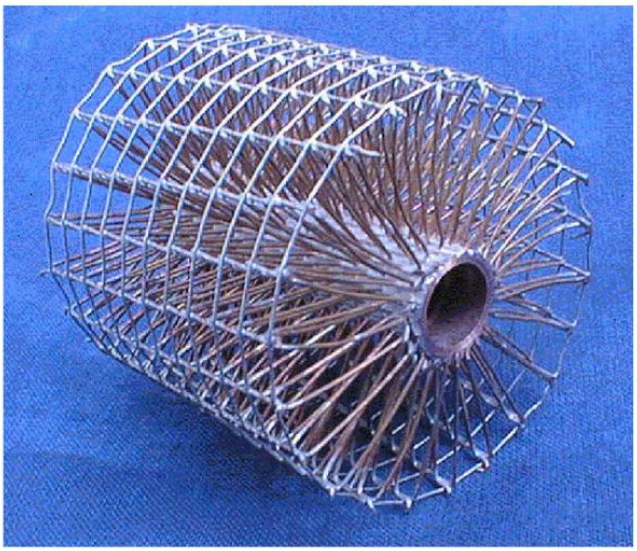

Figure 2.13 Core element of the pin fin heat exchanger (Sahiti *et al.*, 2008)

The model related the entropy generation as a function of the Reynolds number for different heat exchanger pin lengths. The double-pipe heat exchanger was operated in the counter-flow mode. The unit was built from two pipes measuring 920mm in length, incorporating the inner one of copper and the outer one of stainless steel. Around the inner pipe, a copper wire mesh provided pin-like fins with a 0.7mm diameter and 28.2mm length. A staggered pin arrangement was used for the investigation. The study showed that from a thermodynamic viewpoint, larger numbers of passages with smaller pin height in the given frontal area of heat exchanger are more preferred than less heat exchanger passages with larger pin heights.

Liang and Hung (2010) investigated the thermal performance of fins used as heat sinks on U-shaped heat pipes. The mode of operation of the heat pipe was conduction and the optimum range of operating heat loads based on thermal resistance analysis of the heat sink was characterised. The heat pipe was constructed out of copper and having a diameter of 6mm. The evaporator and condenser sectional lengths were identical at 120mm each. Radial fins were used on the pipes and the schematic arrangement is illustrated in Figure 2.14.

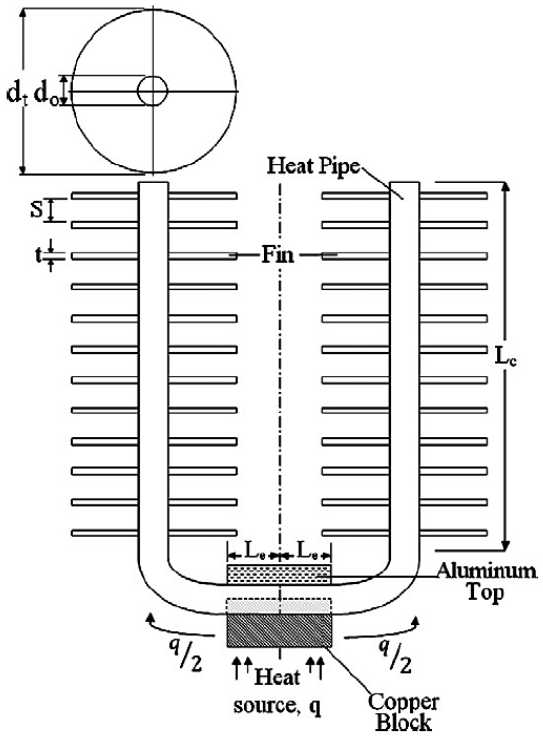

Figure 2.14 Heat sink of radial fins with embedded U-shaped heat pipe (Liang and Hung, 2010)

The heating elements used in the study included a power rating of 300W and K-type thermocouples were used to carry out the temperature measurements. The thermocouples were attached to the condenser sections to measure its temperature in response to ambient conditions. The findings displayed that the effectiveness of fins decreased at low heating power since the heat transfer to the pipe was reduced thereby decreasing heat dissipation from the fins to the surroundings. The results depicted that the heat pipe operated efficiently at the heating power ranges from 30W to 70W with the identification of the optimum heat pipe heat transport rate of 50W.

Aris *et al.*, (2011) carried out work on analysing the performance of a delta wing-type surface protrusion to enhance heat transfer through forced convection flows using heat pipes. The experimentation was carried out at two different fixed delta wing designs including thin delta wings and three-dimensional delta wing tabs as vortex generator designs. Figure 2.15 displays the physical domain of the vortex generator fin stack.

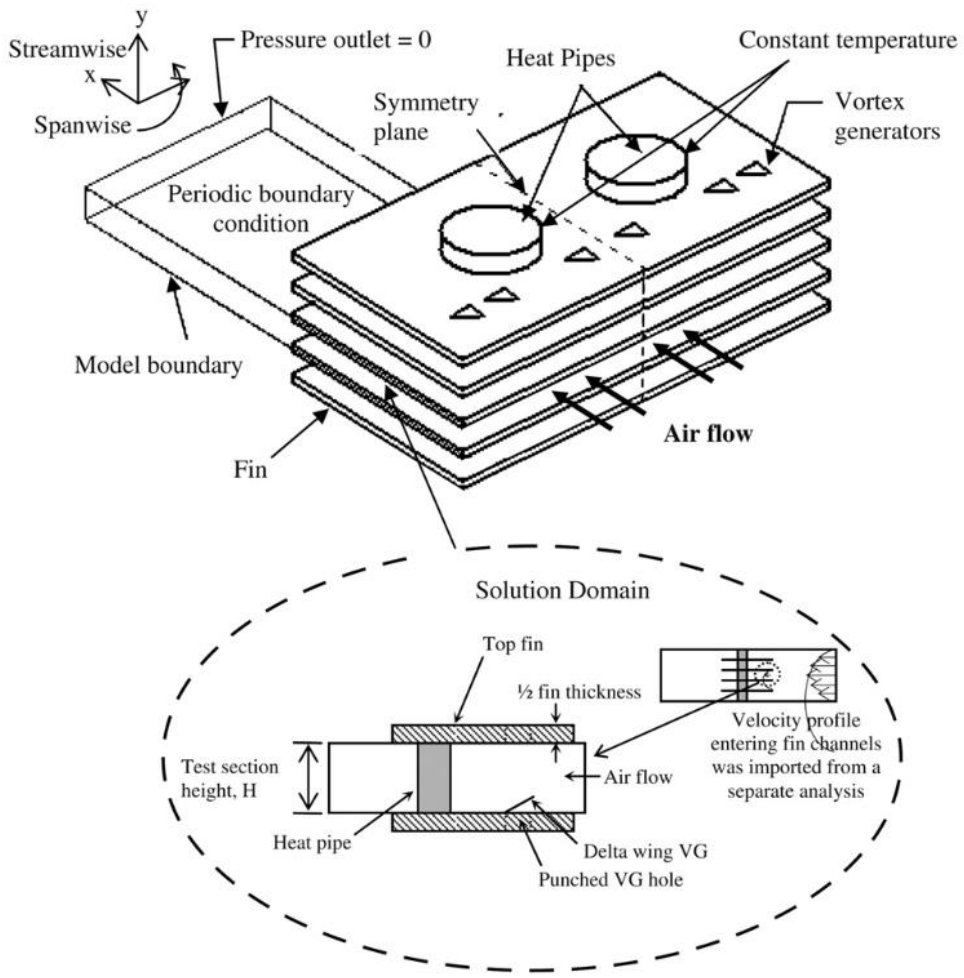

Figure 2.15 Physical domain of the vortex generator fin stack (Aris *et al.*, 2011)

Air was supplied from a fan and directed to flow into the test section through a 10mm x 50mm x 800mm rectangular cross-sectional duct. The Reynolds number for the experiment was based on the characteristic length of the channel and was within the range of 330 to 960. The work revealed that the fixed delta wings were found to enhance heat transfer by as high as 37% with a maximum increase in flow pressure loss of 15% compared to plain finned surfaces.

A review by Mochizuki *et al.*, (2011) indicated that the appropriate use of fins can significantly increase the air cooling capability of heat pipes and that radial fin extrusions gave a higher fin-air heat transfer coefficient in comparison to parallel fin extrusions. Zhang *et al.*, (2012) investigated the fluid flow characteristics for shell side of a double-pipe heat exchanger with helical and pin fin arrangements. The experimental study used a Laser Droplet Anemometer (LDA) to conduct the measurements under the cylindrical coordinate system. The helical channel of a shell side was milled from a solid Perspex cylinder. For the shell side enhanced with pin fins, six pins were adhered into the helical channel periodically along the centreline within one pitch (Figure 2.16).

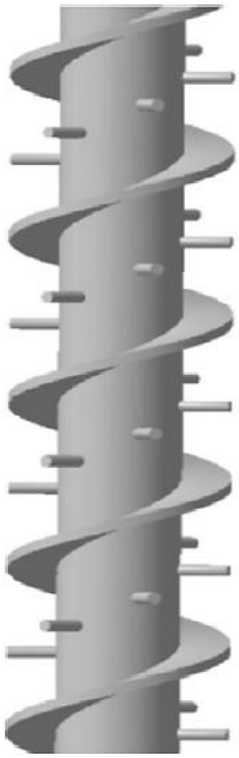

Figure 2.16 Inner tube of a heat exchanger with helical fins and pin fins (Zhang *et al.*, 2012)

The total length of the test section was 520mm while the inner diameter of the tube was 90mm. The radius of the centreline was 35mm and the thickness of the helical pins was 10mm. Water was used as the working fluid and was allowed to flow through the helical channel. The range of mass flow rate used in the tests was between 32 kg/hr to 1,370 kg/hr. The behaviour of the fluid flow in the shell side of the heat exchanger with and without pin fins was investigated. For the shell side only with helical fins, the study revealed that the maximum axial velocity region occurs near the outer wall of the channel. In comparison to the flow without pins, the fluctuation of the velocity of the channels with fins was quicker. The work concluded that pin fins help in significantly increasing the turbulence of the flow, which assists in enhancing heat transfer.

2.4.3 Geometrical arrangement using staggered and inline arrays

A wide range of studies have been carried out in order to comprehend the thermal behaviour of heat pipes when arranged in a staggered or an inline grid. Generally, staggered arrangements have been found to be more effective than the inline method (Van Fossen, 1981, Metzger *et al*., 1984, Chyu *et al*., 1998, Rallabandi *et al*., 2011, Karthikeyan and Rathnasamy, 2011).

Kendu and Das (2009) analytically investigated the performance of flat fins in heat exchangers for both staggered and inline arrangements. Design optimisation parameters including the longitudinal distance (S_l) and transverse distance (S_t) between the pipes were investigated and its effect on the efficiency of the heat exchanger was analysed. At a constant fin surface area, the findings of the study showed that for both configurations (staggered and inline), the performance of the heat exchanger is influenced by the S_l/S_t dimensionless ratio. The results of the work revealed that the staggered pin performance was always superior in comparison to the inline configuration at S_l/S_t ratios over 1. Furthermore, the investigation concluded that an equilateral triangular array for staggered arrangement resulted in maximum heat transfer irrespective of fin volume and thickness. Figure 2.17 displays the schematic representation of the fin tube heat exchanger with both inline and staggered grid arrangement.

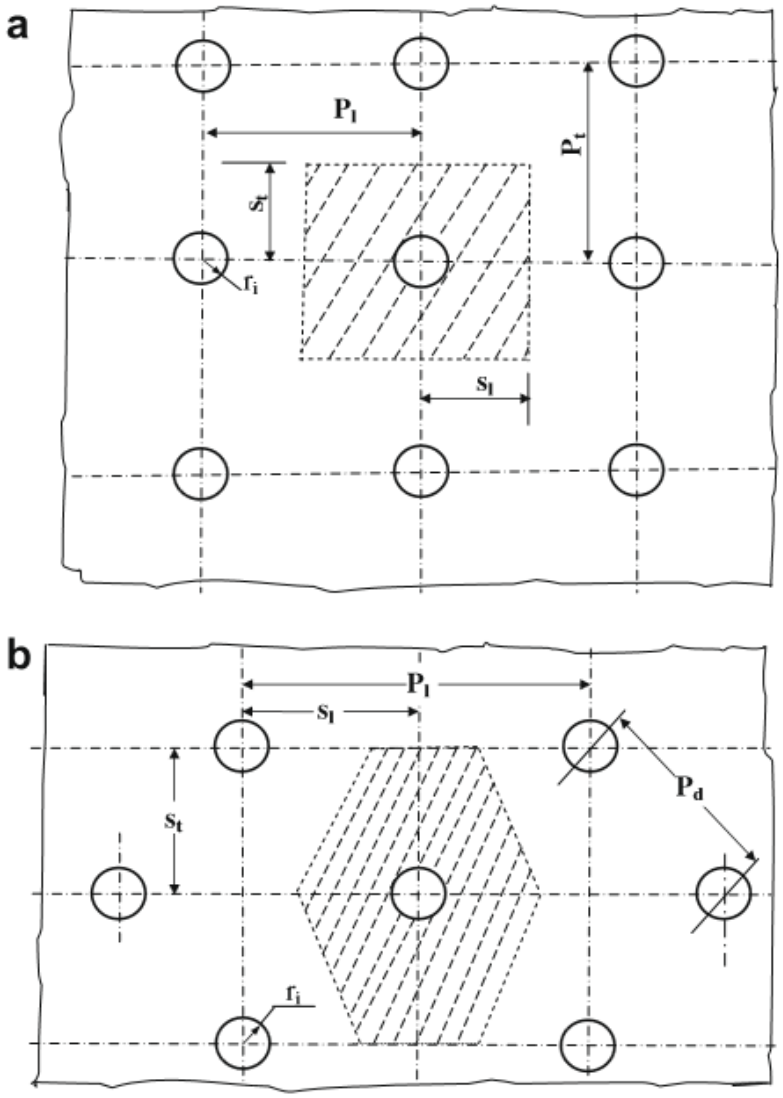

Figure 2.17 Schematic representation of fin tube heat exchanger in: a) inline arrangement b) staggered arrangement (Kendu and Das, 2009)

Yodrak *et al.*, (2010) carried out work on analysing the thermal performance of heat pipes when arranged in both staggered and inline grids. The heat pipe comprised of an evaporator and condenser length of 0.15m along with an adiabatic section of 0.05m. Water was used as the internal working fluid and the internal diameter of the steel heat pipe tube was 0.02m. The arrangement comprised of a total of 8 rows with 6 tubes in each row.

Measurements were recorded at the inlet and outlet of the evaporator and condenser section when a steady-state was achieved wherein the temperatures normalised. K-type thermocouples were used as instrumentation for temperature measurement. The mass flow rate of the incoming fluid to the evaporator section was 0.0098 kg/sec. The results

of the study established that when the tube arrangement was changed from inline to staggered arrangement, the heat transfer increased from 1,996W to 2,273W. This was primarily due to the staggered arrangement incorporating a larger frontal area of heat pipes than the inline arrangement. Figure 2.18 displays the geometrical parameters of the heat pipes in both staggered and inline arrangements.

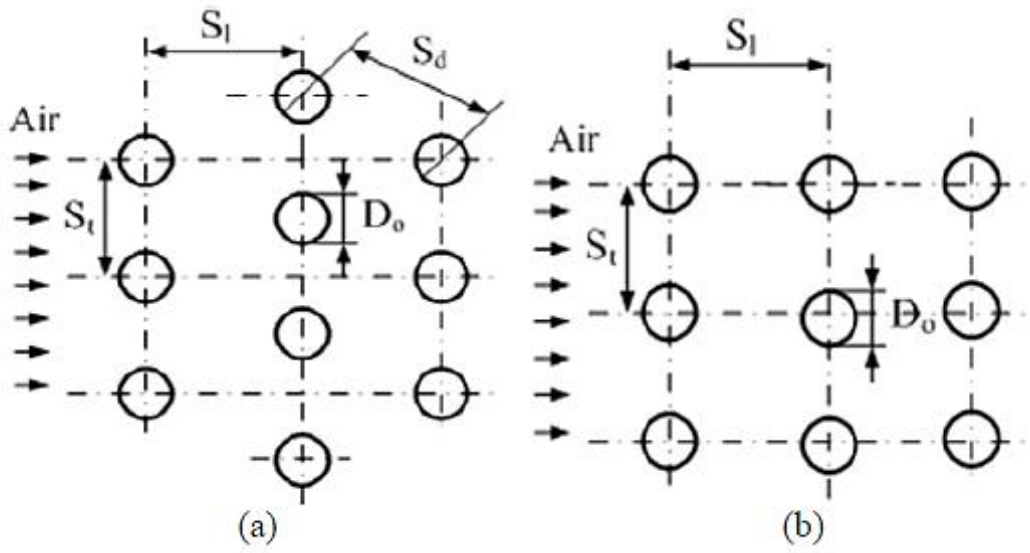

Figure 2.18 Geometrical parameters of heat pipes in: a) staggered arrangement b) inline arrangement (Yodrak *et al.*, 2010)

Further to the study carried out by Aris *et al.*, (2011) on using fins to enhance heat transfer, the work also investigated the thermal performance of heat pipes arranged under staggered and inline grid structures. The analysis was based on forced convection cooling, thereby indicating the use of heat pipes to carry out the heat duty. The findings indicated that a staggered arrangement of three-dimensional wings as extended surfaces with an aspect ratio of four and an angle of attack of 14° gave the highest enhancement in heat transfer in comparison to the inline arrangement.

Karthikeyan and Rathnasamy (2011) studied the convective heat transfer of pin-fin arrays using the staggered and inline arrangement. The tests were conducted for various mass flow rates of air (Reynolds number ranging from 2,000 to 25,000. The cylindrical cross-section of the pin-fin array included a diameter of 10mm with an overall height of 90mm. A uniform plate heater with a power capacity of 1,500W was used to provide heating temperatures and temperature recordings were undertaken using thermocouples at the inlet and outlet of the evaporator section. The experimental results showed that

the staggered pin-fin array significantly enhanced heat transfer as a result of higher turbulence and downstream pressure drop. At a Reynolds number of 4,000, the heat transfer rate using staggered array was approximately 35W higher than the inline arrangement.

2.4.4 System behaviour using parallel-flow, counter-flow and cross-flow and air exchanges

The basic function of any heat exchanger is to transport heat from one fluid to another. General operating mechanism of a heat exchanger can thus be simplified as a hollow tube with one fluid running through it and another stream of fluid flowing by on the outside. In the case of heat pipes, the internal working fluid transfers heat by the process of evaporation and condensation when air temperatures exceed above and fall below saturation levels. Previous studies have highlighted the influence of the method of operation of the heat exchanger on its heat transfer capabilities.

Hsieh and Huang (1990) compared the working performance of a heat pipe heat exchanger in counter-flow and parallel-flow arrangements. The study outlined the behaviour of the system in terms of heat transfer and pressure drop patterns. The heat exchanger comprised of 6 rows of water charged heat pipes in a staggered arrangement. The evaporator and condenser lengths were 0.305m each while the diameter of the pipe was 0.0337m. The results drew three distinct conclusions, thereby revealing that for a definite geometrical alignment, counter-flow mode of operation provides a higher heat transfer than parallel-flow arrangement. In terms of pressure drop, the work stated that the staggered grid indicated a higher airside drop in pressures and has a significant influence on thermal performance in comparison to inline arrays.

A range of existing studies have identified and highlighted the adequate functioning of heat pipe heat exchangers when subjected to counter-flow air streams under forced convection flows (Noie-Baghban and Majideian, 2000, El-Baky and Mohamed, 2007, Yau and Ahmadzadehtalatapeh, 2010).

An investigation of a double-pipe helical heat exchanger was performed by Rennie and Raghavan (2005) in both parallel-flow and counter-flow arrangements. The heat exchanger was constructed out of standard copper tubing and the outer diameter of the pipes was 15.9mm with a wall thickness of 0.8mm. The flow rate of the fluid entering at

333K was controlled and measured between 100 cm^3/min and 1,500 cm^3/min. The transient test was conducted for 120 seconds following the normalisation of temperatures. K-type thermocouples were used to record temperature measurements. The findings of the study revealed that heat transfer rates were significantly higher in the counter-flow configuration due to the larger average temperature difference between the two working fluids

Mishra *et al.*, (2006) investigated the dynamic thermal behaviour of a cross-flow heat exchanger due to perturbations in temperature and flow conditions. The numerical analysis was based on single-phase fluids with fixed thermophysical properties. Figure 2.19 displays the schematic representation for the cross-flow heat exchanger module used in the study.

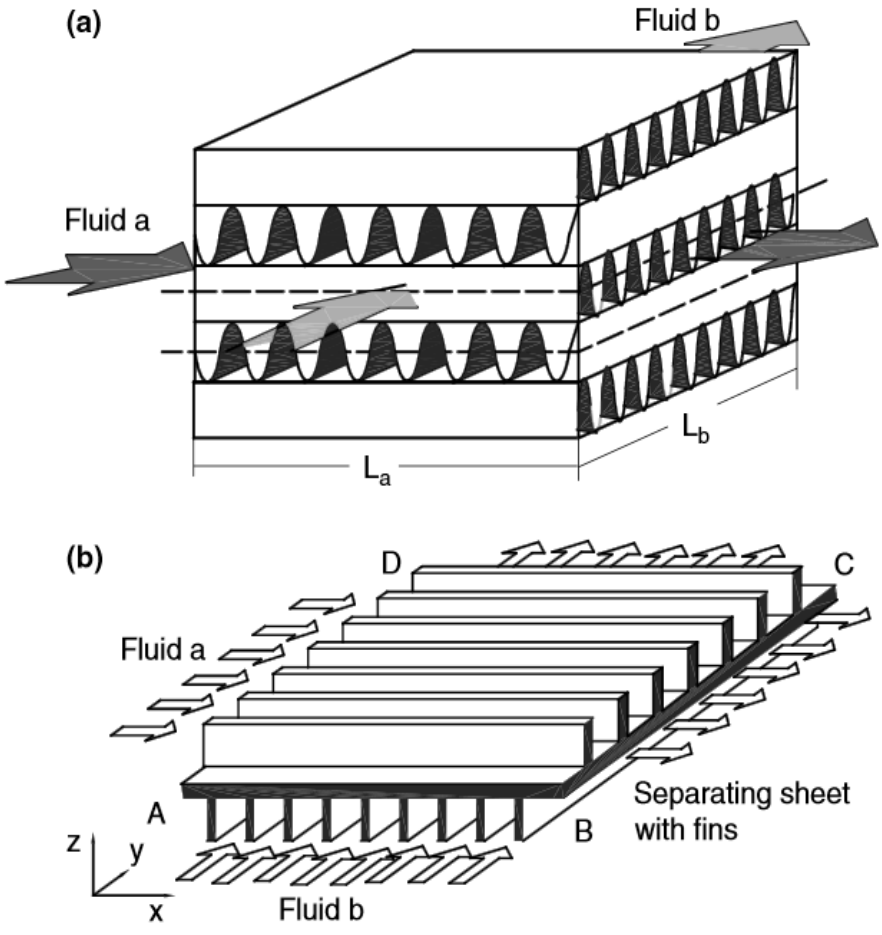

Figure 2.19 Cross-flow heat exchanger in: a) schematic representation b) symmetric module for analysis (Mishra *et al.*, 2006)

Adiabatic conditions were assumed for the heat exchanger shell and heat transfer per surface area was kept constant. The findings highlighted that the mean exit temperature of both fluids increase or decrease with the simultaneous increase or decrease in flow rate of the two fluids. Furthermore, the increase or decrease in exit temperatures was dependent upon the relative magnitude of the disturbance provided to the two fluids. The work concluded that an increase in mean exit temperatures was observed when the disturbance was more in hot fluid, while a decrease was observed with larger disturbances being observed in cold fluid.

2.5 Numerical simulation techniques used for heat pipe heat exchangers

Following the review of literature involving current heat pipe technologies along with parametric studies on working fluid and geometrical arrangement, this section further examines computational studies that have been carried out to comprehend the internal behaviour of heat pipes. Extensive numerical simulations have been conducted on various heat pipe arrangements displaying two-phase flow patterns to highlight the broad scope of the technology for use in various passive and active applications as reviewed earlier. Viable numerical codes have developed into useful tool for determining specific and precise results for the overall performance of various multiphase flow patterns and phase change behaviours.

Shao and Riffat (1997) investigated the performance of a heat recovery system based on a heat pipe arrangement at different positions inside passive stacks for natural ventilation systems. The FLUENT solver was used for CFD coding to simulate flow losses in the ventilation stack by solving the mass and energy conservation equations. The domain mapped by a uniform dimensionless grid of 50x100 comprised of the two-dimensional geometry of the exhaust stack and the building space to understand the buoyancy flow in the room. The boundary conditions included a constant external and internal stack wall temperature of 288 and 293K.

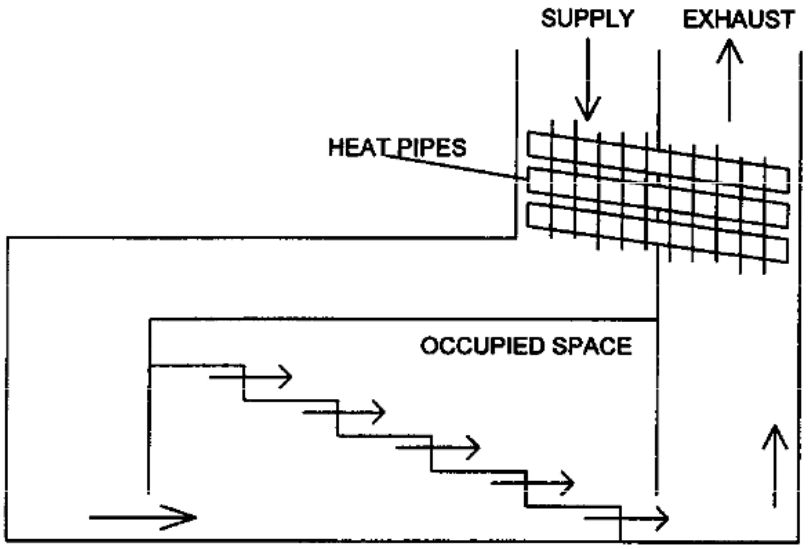

Figure 2.20 Heat pipe heat recovery system in a natural ventilation stack (Shao and Riffat, 1997)

Figure 2.20 displays the physical domain of the heat pipe heat recovery system in a natural ventilation stack. The findings from the computational simulation displayed that the average vertical velocity in the stack is 0.223m/s along with a pressure differential of in excess of 29Pa obtained between the inlet and outlet. Further, the investigation proved that the insertion flow loss is higher when the heat pipes are located at the bottom of the vertical stack compared to the top and is inversely proportional to the insertion pressure loss. It was noted that the heat pipes did not cause a significant reduction of stack flow.

Lin *et al.* (2005) investigated the potential of heat pipe heat exchangers for use in dehumidification processes to understand the performance of the system. The FLOTHERM numerical code in conjunction with Microsoft Excel commercial package was used for CFD simulation of a drying cycle in the dehumidification process using characteristic air properties with an inlet temperature variation between 308-323K along with a relative humidity of 100% and a volume flow rate variation between 6-8l/sec. The heating and condensing regions were defined in the domain for the calculation of fluid parameters and properties for the simulation. Values for the cuboids representation of heat pipes with thermal conductivity, specific heat capacity and density were obtained.

The predicted results confirmed the performance of the system at various operating conditions and showed that a significant improvement in dehumidification process was

possible using the heat pipe solution with higher condensate rates obtained at higher inlet flow rates and temperatures. However, the results further established that the heat transport in the heat pipe decreased with increasing flow rate signifying the potential of a heat exchanger using auxiliary power can work with better efficiency at higher flow rates.

Previous works involving numerical codes to predict multiphase flow patterns in pipes have been carried out by Ekambara *et al*. (2006, 2008). The studies included volume-averaged multiphase simulations of bubbly flow in horizontal pipes. Eulerian-Eulerian multiphase model was incorporated alongside two *k-e* models were used in the study wherein the first model incorporated constant bubble size while the second model included population balance. A structured grid was generated on the walls of the pipe with the mesh refined in the specific areas of the pipe.

Good quantitative agreement was observed for both models with experimental data with mean and maximum error of ±5% and ±17% for constant bubble size model. The results indicated that maximum volume fraction was achieved near the upper pipe wall and an increase in gas volume flow rate had an increasing impact on the volume fractions. Figure 2.21 displays the contour plots of simulated gas volume fractions and axial liquid velocity at the outlet of the pipe.

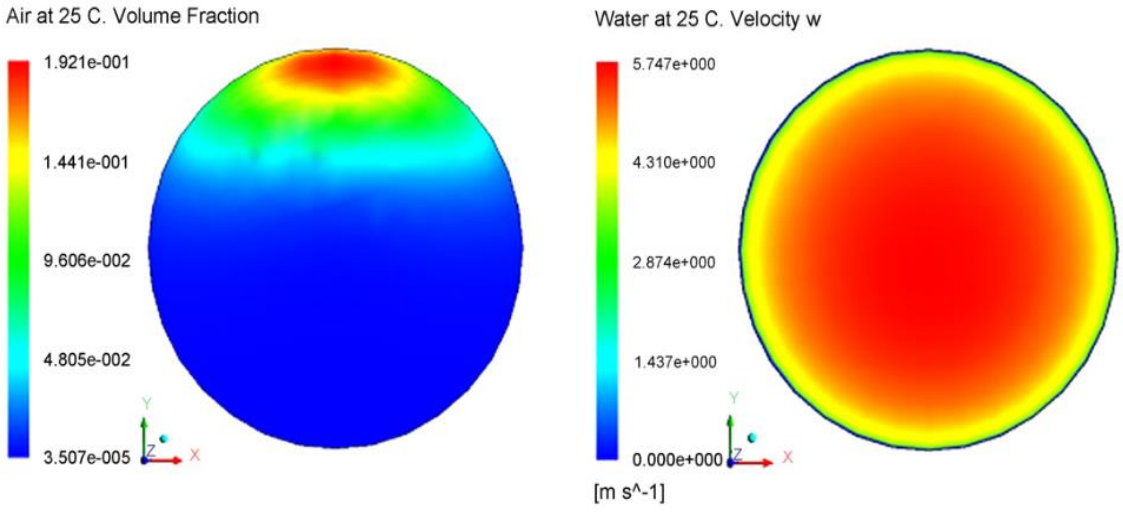

Figure 2.21 Contour plots of simulated gas volume fraction and axial liquid velocity at the outlet of the pipe (Ekambara *et al*., 2008)

Dimensionless parameters such as Reynolds number and Prandtl number are a useful indicator into understanding heat transfer from flows around bluff bodies. Sahu *et al*.,

(2009) carried out work on determining the heat transfer from a heated square cylinder in an unsteady flow regime. The Reynolds number was varied between 60 and 160 while the Prandtl number variation included from 0.7 to 50 in order to study a range of incoming two-dimensional flow conditions. A semi-explicit finite volume method was used to solve the unsteady Navier-Stokes equations. The findings of the study indicated that an increase in Nusselt number is directly proportional to the increase in Reynolds and Prandtl number The results further depicted that the front surface of the cylinder exhibit the highest value of the surface average Nusselt number.

Alizadehdakhel *et al.* (2010) studied the operation of a thermosiphon by simulating two-phase flows using FLUENT 6.2 commercial CFD code and validating the results with an experimental set-up using various operating parameters (Figure 2.22). A two-dimensional geometry was modelled using the Gambit software with the domain consisting of a total number of 47,124 and 14,361 grids for the fluid and the solid region. The Volume of Fraction (VOF) (Hirt and Nichols, 1981) method was established for flow modelling.

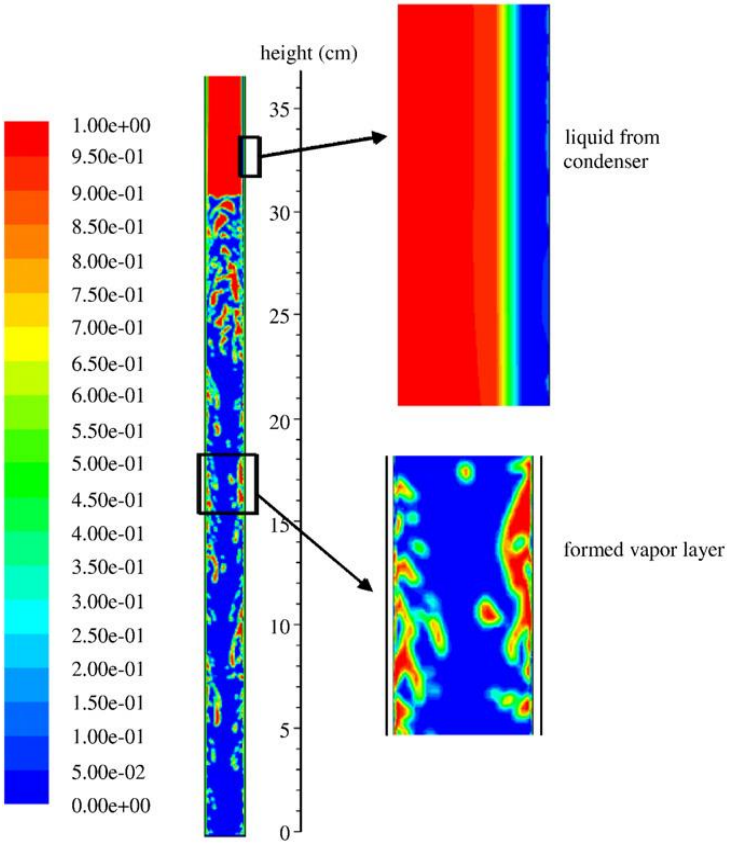

Figure 2.22 Contour plots of vapour volume fraction in the evaporation section (Alizadehdakhel *et al*., 2010)

The numerical work applied various heat flux values obtained from the experiments as the heat inlet to the evaporator section and a vapour pressure of 1.72kPa at 288K was applied to water in the gaseous phase. Good agreement was achieved between the CFD and experimental temperature profiles across the length of the pipe. The experimental results confirmed that increasing of the inlet heat flow from 350W to 500W greatly enhances the overall performance of the thermosiphon. The conclusions of the study revealed that complex heat and mass transfer phase changes can be effectively modelled and a greater perceptive of the phase change is observed using CFD.

Saber and Ashtiani (2010) investigated the thermal efficiency and evaporator performance of a heat pipe heat exchanger using the CFD finite volume principles. The *k-e* turbulence model was applied to the heat exchanger geometry consisting of 12 tubes each placed in six rows. Four different design cases (with and without baffles) were studied to compare and optimise the velocity and thermal distribution at the start of the heat exchanger. Temperature and flow profiles were analysed and the results of the study concluded the effectiveness of using short baffles to avoid bypass flows and improve temperature distribution.

Rahmat and Hubert (2010) developed a triangular two-phase model of a micro-heat pipe to study the heat and mass transfer inside the three-dimensional micro channel. Ansys CFX-5.7.1 commercial software was used for solving the unsteady flow equations. The channel geometry was divided into three identical portions to incorporate the evaporator and condenser section behaviour. The length of the evaporator and condenser section was 0.67cm. The meshed model comprised of 560,000 elements while the average working fluid volume of the elements was $310\mu m^2$. The fluctuation of convergence results with respect to various fill ratios and boundary condition type was investigated for precise performance. The findings showed that the effective thermal conductivity of 3,333W/ºC was obtained for the micro channel at a fill ratio of 25%.

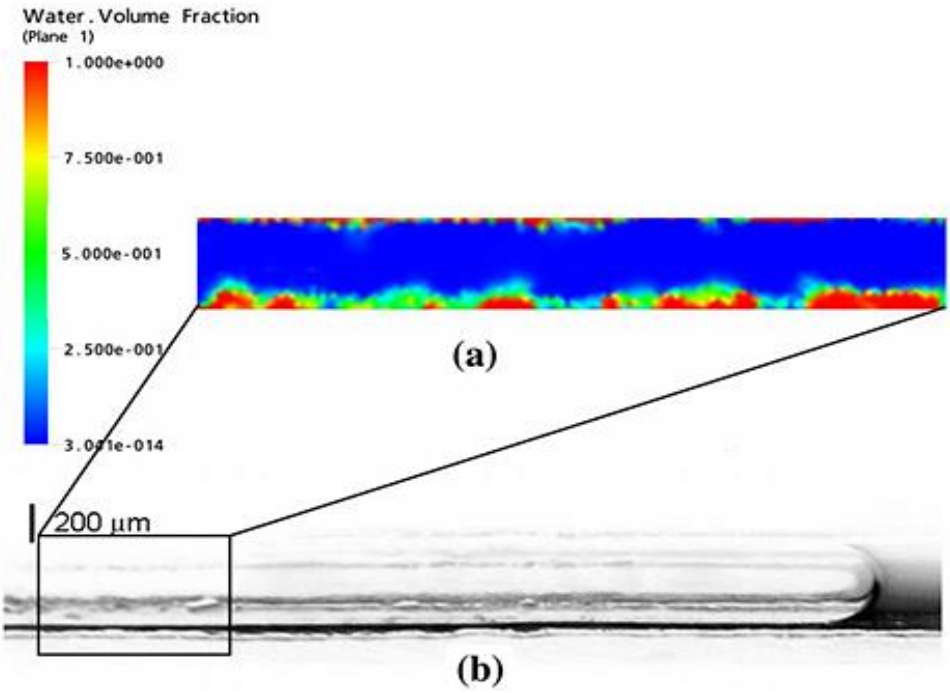

Figure 2.23 a) Water volume fraction in the evaporator section at the plane of symmetry. b) Experimental observation of liquid/gas interface in a triangular micro heat pipe (Rahmat and Hubert, 2010)

Figure 2.23 displays the water volume fraction in the evaporator section along with the experimental observation of liquid/gas interface. Furthermore, the results of the numerical analysis concluded that an increase in liquid fill ratio causes an increase in the effective length of the heat pipe. The investigation confirmed a good agreement between the computational findings with relevant literature with an error of 5.5%, highlighting the capability of commercial finite element codes in order to successfully simulate two-phase flows.

Hemadri *et al.* (2011) conducted a study on the feasible utility of pulsating heat pipes in thermal radiator systems for terrestrial and space applications. The experiment was conducted on aluminium and mild steel radiator plates with and without embedded pulsating heat pipe arrangement aligned in three distinct orientations. Surface mounted flat mica heater of known dimensions was used for heat generation at varying thermal input between 50 and 150W. The outcome drawn from the investigation included spatial thermography and the effects of orientation. It was observed that the pulsating heat pipe arrangement provided limited improvement to the rate of isothermalisation (thermal equilibrium) due to the high base thermal conductivity of the aluminium plate. The results further displayed the increase in domination of gravitational forces at low heat

input of for the vertical orientation with heater position upwards for both plates. The work highlighted the potential of pulsating heat pipes in efficient thermal management for space and terrestrial sectors.

Ranjan *et al.* (2011) conducted numerical analysis on the study of flat heat pipes or vapour chamber by solving the vapour and liquid flow using three-dimensional Navier-Stokes continuity, momentum energy equations to understand the effect of varying wick microstructure on evaporation and condensation sections of the heat pipe. Temperature and flow contours were computed by a device-level numerical macro-model unaided and coupled with wick-level micro-model to account for the evaporation heat transfer rate in the pores of general sintered-powder wick structures using the commercial FLUENT solver. The coupled model incorporated corrections to the evaporative mass flow rates at the liquid-vapour interface based on local contact angle of liquid in the wick. An effective conductivity value of 40W/mK was assumed for the macro-model while the convective heat transfer boundary conditions for the micro-model consisted of a constant inlet temperature and pressure to investigate the liquid meniscus between copper wires. The results based on the two models (coupled and non-coupled) indicated that the thermal resistance by the liquid-vapour interface increases affecting the performance of the vapour chamber as the device is decreased in magnitude.

Heat transfer materials like water, ethylene glycol, engine oil, aluminium, copper and silver have been widely used in numerous important fields, such as heating, ventilating, air-conditioning systems, micro-electronics, transportation, manufacturing and nuclear engineering. Nasrin *et al*., (2012) investigated the effects of solid volume fraction and Prandtl number on buoyancy driven heat transfer of water-Al_2O_3 nano-fluid in a closed enclosure. A square chamber was differentially heated with the left and right walls having different temperatures while keeping the top and bottom walls adiabatic. The Navier–Stokes and energy equations were solved numerically using the finite element technique. Thermophysical properties of water were taken at a Prandtl number of 6.2. The influence of Prandtl number on velocity and temperature profile was investigated. The findings showed that the nanoparticle with the highest solid volume fraction and Prandtl number displayed the most effective enhancing performance of the heat transfer rate.

Hughes *et al.*, (2013) carried out a numerical investigation on scrutinising the performance of a heat pipe integrated heat exchanger for heat recovery in natural ventilation air streams. The computational domain comprised of 13 tubular heat pipes with an outer diameter of 20mm and a total length of 500mm, subjected to an incoming air velocity of 0.25m/s. FLUENT V14.0 commercial code was used to simulate the multiphase flow incorporating the Euler-Euler approach coupled with *k-e* turbulence model for flow and thermal analysis. Mass transfer phenomenon for phase interaction between the vapour and liquid species was carried out using the evaporation–condensation mechanism involving fluid saturation temperature of 293K. Water was used as the heat pipe working fluid while the condenser section of the heat exchanger was used as the passive heat recovery system from fresh air streams. Figure 2.24 displays the liquid mass flow of the internal fluid within the heat pipes.

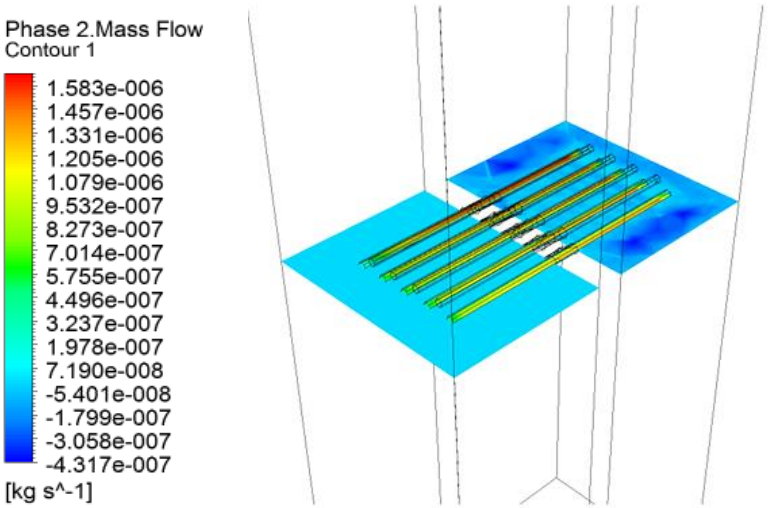

Figure 2.24 Liquid phase mass flow inside heat pipes (Hughes *et al.*, 2013)

The results of the study showed the system was capable of increasing the heat pipe working fluid temperature from 293K (20°C) to 296.3K (23.3°C). Maximum sensible heat transfer for the airstream at the condenser section was 115W. The numerical model was validated against previous experimental literature and a good correlation was observed between the results with a maximum error percentage of 16%. The work concluded with the deduction that energy recovery using no mechanical intervention aids in reducing the overall energy consumption of the ventilation system. In addition, the work highlighted the proficiency of using CFD as a numerical tool for predicting the thermal performance of heat pipes under convection air streams.

2.6 Experimental studies on analysing heat pipe heat exchangers

In order to quantify the performance of heat pipe systems, experimental evaluation using custom-built testing rigs is often carried out. This section reviews the literature associated with experimental studies relating to heat pipes and heat pipe heat exchanger technologies.

Noie-Baghban and Majideian (2000) carried out work on the design and build of a heat pipe arrangement to be installed in a heat pipe heat exchanger for the purpose of heat recovery in hospital and laboratory buildings where high air change is a primary requirement. The experimental set-up is illustrated in Figure 2.25.

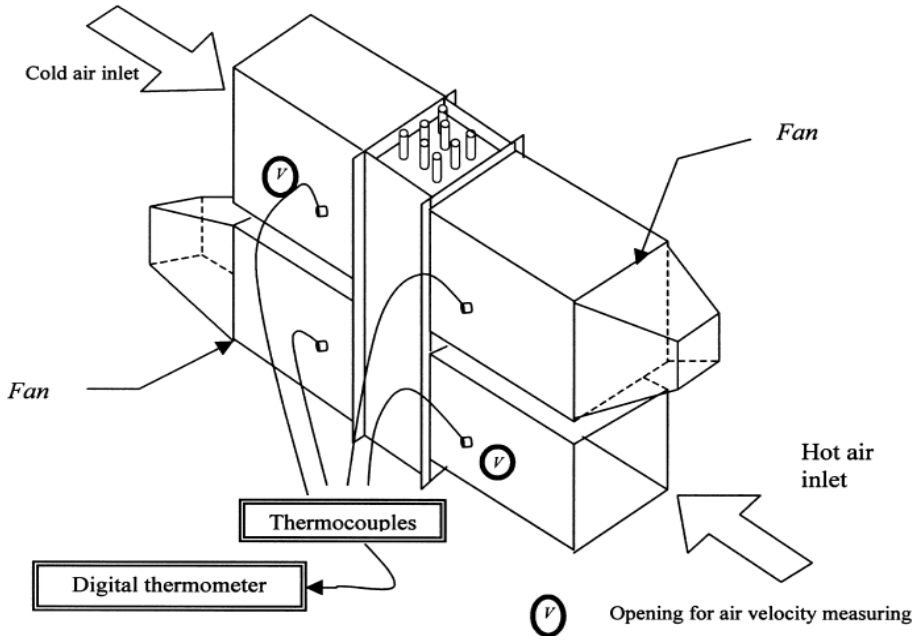

Figure 2.25 Schematic of the heat pipe heat exchanger and test rig (Noie-Baghban and Majideian, 2000)

The experimental apparatus included a test-rig comprising of two fans to deliver a flow rate of 0.103m^3/s through evaporator and condenser. Eight copper pipes with an outside diameter of 15 mm, inside diameter of 9 mm and length of 600 mm were used along with three types of wicks including the 50 mesh nickel, 250 mesh nickel and 100 mesh stainless steel. Inlet air velocity was kept constant at 2.3m/s while the inlet temperatures to the evaporator and condenser sections were monitored at 328K and 290K. K-type thermocouples were used for temperature measurements. A mathematical model was developed to validate the experimental findings. The work concluded a good correlation between the mathematical and experimental results with respect to the heat transfer rate

in the evaporator section of 100W. Further, the study highlighted the importance of using finned heat pipes and increasing the number of rows along with insulation capability in increasing the overall effectiveness of the system.

Riffat and Zhu (2003) carried out an experimental investigation on the use of heat pipes as an indirect evaporative cooler. An indirect evaporative cooler incorporating cylindrical heat pipes with fins and a porous ceramic was analysed. The copper heat pipe tubes consisted of an outer diameter of 20mm and a total length of 950mm with the evaporator section of 350mm (Figure 2.26). Distilled water was used as the working fluid. The experiments were based on analysing the cooling capacity with respect to different ceramic properties and the results indicated an increase in the cooling capacity by 4.89% as the ceramic porosity increased. Furthermore, the findings highlighted a decrease in the cooling capacity by 1.03W/m^2 as the ceramic wall thickness increased, thus concluding the thickness of ceramic to be a minimum for higher efficiency.

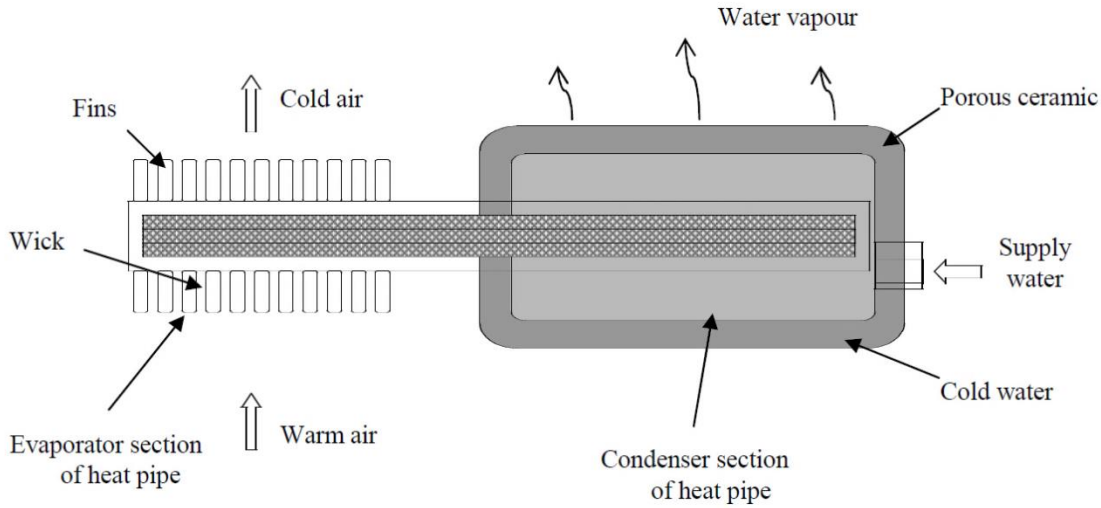

Figure 2.26 Indirect evaporative cooling using heat pipes (Riffat and Zhu, 2003)

El-Baky and Mohamed (2007) investigated the overall effectiveness of heat pipe heat exchangers for heat recovery through external air-conditioning systems in buildings in order to reduce the cooling load. A mathematical model was developed based on the experimental set-up which included the two air ducts of 0.3 x 0.22m^2 sectional areas along with the heat pipe arrangement comprising of 25 copper tubes with the evaporator and condenser section of 0.2m and the adiabatic section of 0.1m. R-11 was used as a working fluid at a saturation temperature of 303K. Inlet fresh air temperatures to the

evaporator section were taken as 305K, 309.2K and 313K while the temperature of return air was maintained at 299K. The inlet fresh air mass flow rate was 0.4kg/sec.

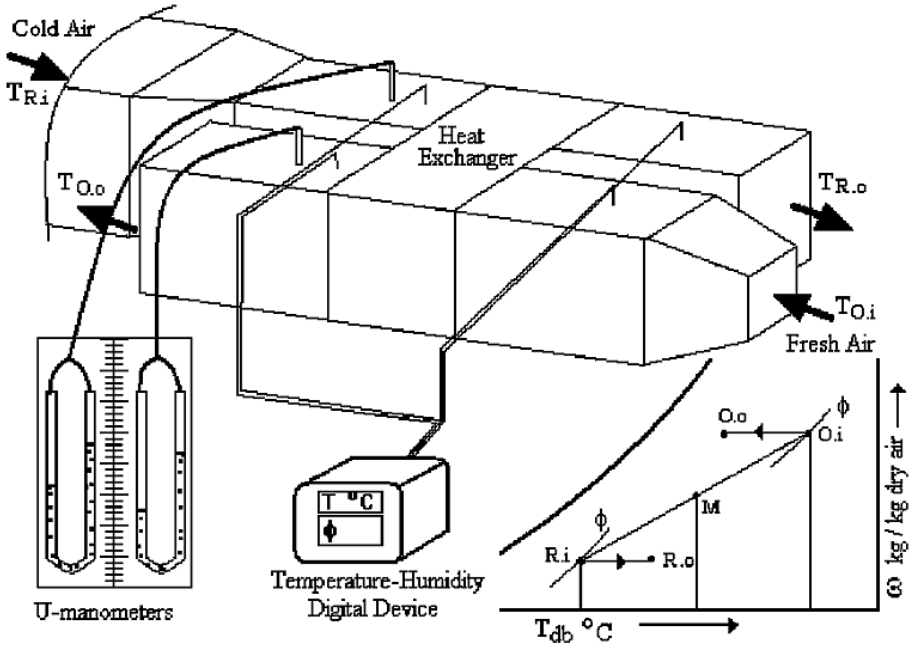

Figure 2.27 Air ductwork and measuring instrumentation for testing of the heat pipe heat exchanger (El-Baky and Mohamed, 2007)

The thermal performance of the system (Figure 2.27) was analysed for varying fresh air inlet mass flow rates and temperatures stream. The results of the work depicted an average heat transfer of 50W per heat pipe while the average heat transfer coefficient was calculated at 29W/m^{2}K. The findings of the study further revealed that effectiveness and heat transfer rates are influenced with the increase in fresh air inlet temperature. The study also revealed that the mass flow rate ratio has a significant effect of temperature change of fresh air and heat recovery rate is increased by approximately 85% with the increase in fresh air inlet temperature.

2.6.1 Wind tunnel experimentation on heat pipes

Alongside the custom-built testing rigs for experimental evaluation of heat pipes, wind tunnels have also been commonly employed to analyse the performance of novel heat pipe heat exchanger systems. Elnaggar *et al.* (2011) carried out an experimental and numerical study of a U-shaped heat pipe system to be used as a cooling component. The analysis was carried out in both natural and forced convection modes using a heat input varying from 4W to 24W and air velocity variation between 1m/s and 4m/s. An open-

circuit wind tunnel was used for testing the performance of heat pipes. The schematic of the experimental set-up is displayed in Figure 2.28.

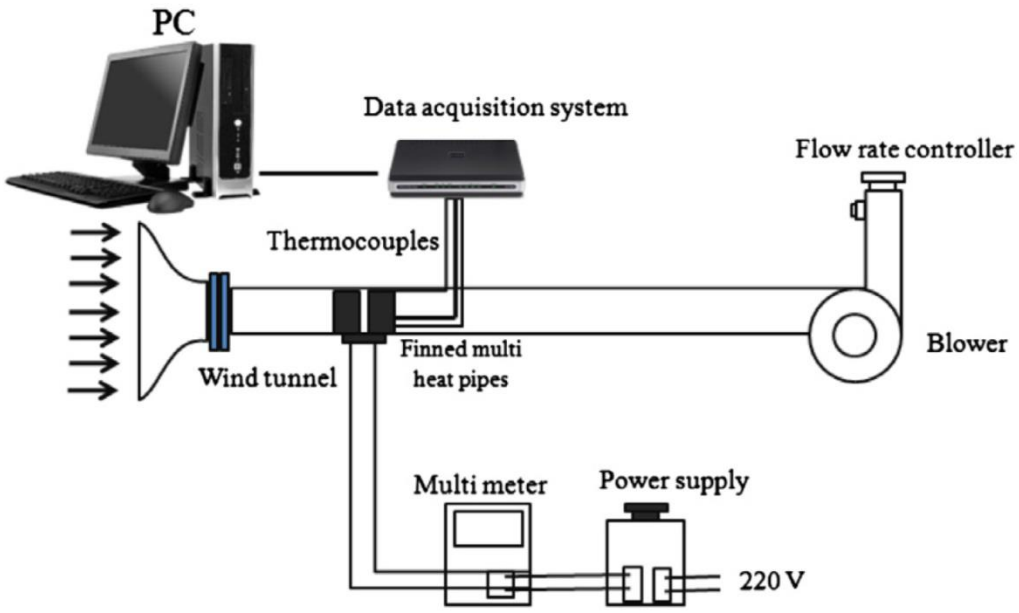

Figure 2.28 Wind tunnel experimental set-up for testing of U-shaped heat pipes (Elnaggar *et al*., 2011)

K-type thermocouples were used for measuring air temperatures, connected to the data acquisition system. The findings from the work highlighted that the air velocity and power input have important effect on the performance of heat pipes. The total thermal resistance decreases with an increase in heat input and coolant velocity. In addition, the study emphasised that the heat pipe orientation plays an imperative role and that the vertical mounting can the heat pipe overall effectiveness in comparison with the horizontal arrangement since gravitational forces facilitate in heat transfer through vertical orientation. The lowest value of the total thermal resistance obtained was 0.181°C/W when the coolant velocity was 3m/s and heat load measuring 24W.

Wang (2012) investigated the performance of flat and embedded heat pipes using wind tunnel experimentation technique. The dimensions of the flat heat pipe thermal module were 118 x 18 x 16mm^3, which was subjected to a heating power of 180W. The maximum static pressure to which the pipes were exposed was 360Pa, with the mean air velocity kept constant at 3.5m/s. The heat pipes were exposed to an ambient temperature of 45°C (318K). T-type thermocouples were used to record the temperature measurement readings. Figure 2.29 displays the wind tunnel experimental set-up highlighting the inclination angles of the test specimen.

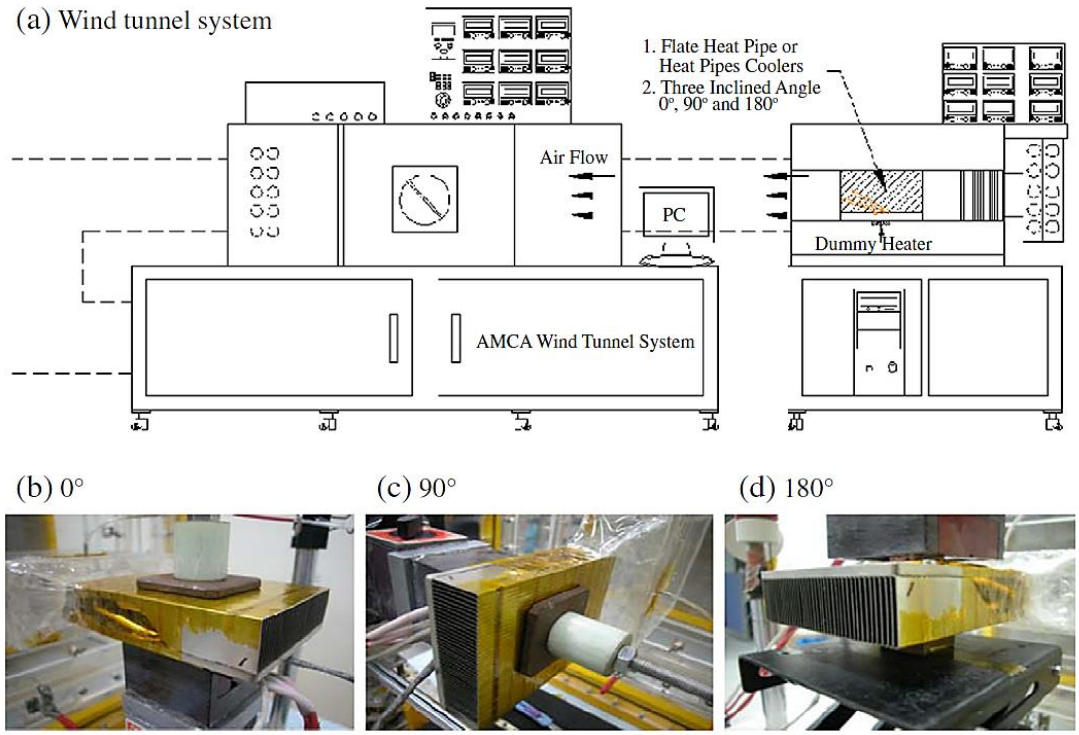

Figure 2.29 a) Wind tunnel experimental equipment b) testing angle of 0° c) testing angle of 90° d) testing angle of 180°

At a heating power of 180W, the findings of the study indicated that the thermal resistance of heat pipes was at its highest at 0.277°C/W an inclination angle of 0° and at its lowest value of 0.259°C/W at an inclination angle of 180°, thus highlighting its best thermal performance at that angle. The experimental results were compared with the numerical simulation using the *k-e* turbulence model and good correlation was obtained between the two quantities, establishing an error percentage within 5%.

Peng *et al.* (2013) conducted an experimental study on the heat transfer performance of an aluminium Flat Plate Heat Pipe (FPHP) with fins. A variety of performance tests of FPHP were carried out with different air flow velocities ranging from 1.5 m/s to 6 m/s and working fluid filling ratios ranging from 10% to 50%. The vapour chamber was made of aluminium and was constructed out of two flat plates with 2.5mm thickness and a frame size measuring 80mm x 75mm x 15mm. Figure 2.30 displays the experimental set-up. The testing apparatus comprised of a wind tunnel, a 300W heating source to provide the required inlet temperatures connected to the data acquisition system. The wind tunnel had a rectangular cross section throughout the test section measuring 60mm in height and 75mm in width.

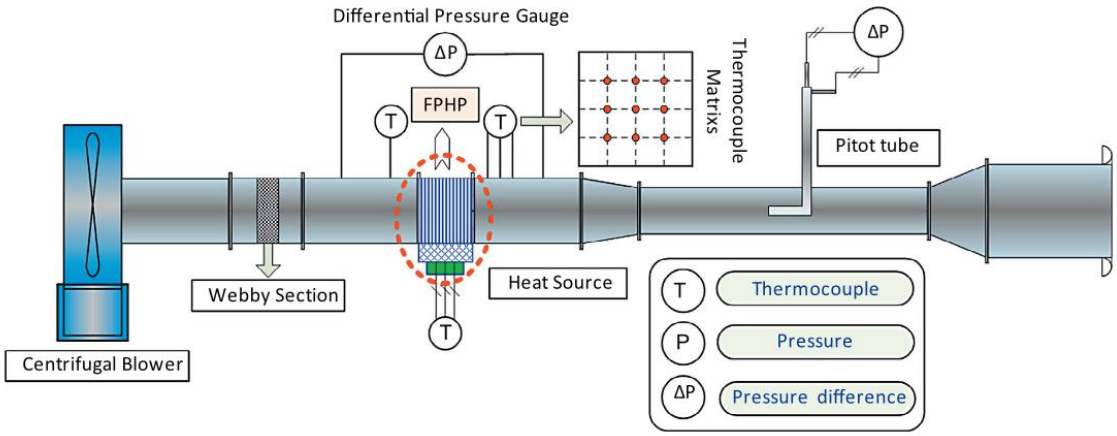

Figure 2.30 Wind tunnel set-up for testing of flat plate heat pipes (Peng *et al*., 2013)

Thermocouples used in the experiment were T-type with an experimental uncertainty of ±0.1K. The results of the work showed the influence of airflow rate and filling ratio on start-up and heat transfer of flat plate heat pipes. The findings revealed that the start-up time is reduced with an increase in the level of applied heat flux. Furthermore, the study depicted that at lower filling ratios, the amount of working fluid is not sufficient to carry out the heat transfer resulting in a dry out. The work recommended that an appropriate filling ratio and vacuum degree should be chosen for improving heat dissipation of the system.

Zhang *et al.,* (2013) experimentally investigated the heat recovery characteristics of a flat micro-heat pipe heat exchanger using Al_2O_3 nanoparticules with a diameter of 20nm in R141b as the working fluid. An array of 16 heat pipes was used with each heat pipe measuring 340mm by 30mm by 2mm in dimensions. Equal lengths of evaporator and condenser sections were used at 140mm each. The experimental set-up comprised of two individual ducts fitted to blowers to supply the temperatures to the evaporator and condenser sections. Figure 2.31 displays the experimental testing facility for the heat pipe heat exchanger. The ducts were equipped with thermal insulating material to minimise heat transfer to the surrounding air. Temperature at the evaporator section was varied between 300K and 313K while the temperature at the condenser section was maintained at 297K.

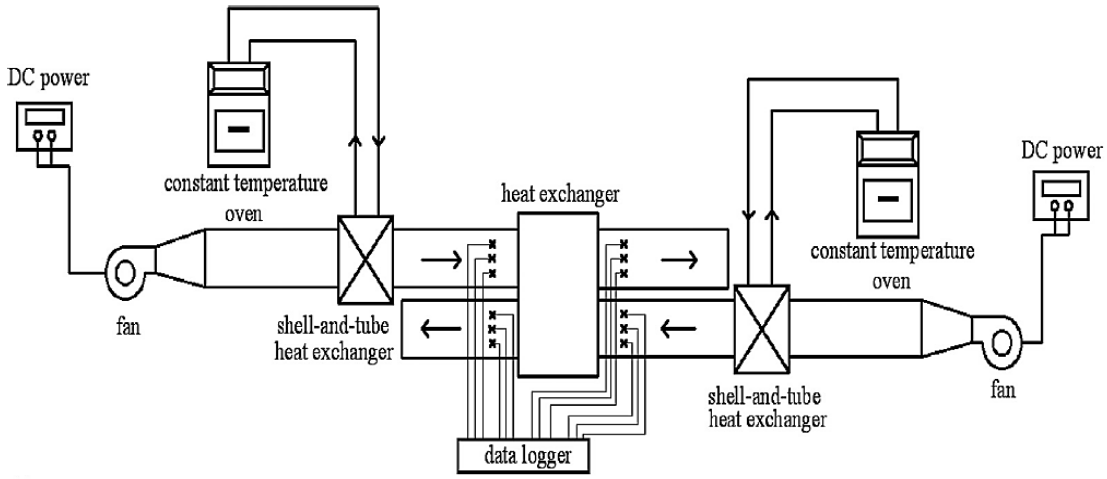

Figure 2.31 Experimental facility for testing of heat pipe heat exchanger (Zhang *et al*., 2013)

The results of the experimental study displayed that the overall effectiveness of heat pipes was increased with an increase of evaporator temperature, regardless of the volume. The maximum effectiveness reached was approximately 58.2% at an inlet air temperature of 313K (40°C) when the air volume flow rate was 120m^3/h. The experimental results further showed that using 0.01% volume of Al_2O_3 nanoparticles as a working fluid could greatly enhance heat transfer effectiveness compared with conventional R141b as the working fluid.

2.7 Heat pipes in air-conditioning and heat recovery systems

The use of heat exchangers incorporating heat pipes in building and air-conditioning sectors have been emphasised in literature to decrease the operational costs of the system in order to reach energy saving capacity (Wei and Hongjun, 2010). Mathur (1996) investigated the impact on overall energy consumption of treating ventilation air by retrofitting a heat pipe heat exchanger unit. Using the climatic conditions of St. Louis, Missouri, an in-depth performance investigation was carried out for the year round operation of the HVAC system equipped with the heat exchanger. The heat exchanger comprised of six rows of heat pipes in a horizontal orientation with an effectiveness of 60%. The findings of the study revealed that a heat pipe heat exchanger may be effectively used for increasing the efficiency of the existing HVAC systems.

Gan and Riffat (1998) studied the effectiveness of using heat pipe heat recovery units for naturally ventilated buildings. Experimental work was carried out inside a testing chamber which was divided into two zones with a horizontal partition. Supply air

entered through the lower zone and return air was extracted from the upper zone. A heat pipe heat recovery unit was housed in the supply and exhaust ducts for exchange of heat between the supply and exhaust air streams. The results displayed that external air velocities have a significant effect on the performance of the heat pipe heat recovery unit wherein the effectiveness decreases with increasing air speeds. The work concluded that the effectiveness of the unit was 17% superior using two banks of heat pipes compared to a single bank.

Wan *et al*., (2007) conducted a study on the use of heat pipe integrated air-handling coil on energy consumption in central air-conditioning systems in buildings. In order to quantify the performance of heat pipe air-handing coil on the energy savings at a fixed indoor design temperature, an office building with the area of 2,673m^2 in Guangzhou, China, was selected for the investigation. Under the required design conditions, the study showed that the energy consumption in a central air-conditioning system using heat-pipe air-handling coil was considerably lower than a conventional central air-conditioning system. For a fixed relative humidity of 50% Rh and an indoor temperature in the range of 22–26°C, the rate of energy savings in the office building was estimated at 23.5–25.7% for cooling load and 38.1–40.9% for total energy consumption, displaying a significant energy saving capability.

Yau and Ahmadzadehtalatapeh (2010) reviewed the utility of pipe heat exchangers as an energy recovery unit in air conditioning systems in tropical climates. The review included literature from previously published work on the vertical and horizontal orientations of heat pipes. Figure 2.32 displays a 3-row thermosiphon heat exchanger test facility used for convective heat transfer. The work concluded that the application of heat pipe heat exchangers for both horizontal and vertical orientations in terms of dehumidification purposes and energy saving is recommended for tropical climates as a highly efficient heat recovery unit. The investigation further highlighted the use of thermosiphon and double heat pipe heat exchanger units in heating, ventilation and air-conditioning systems for reducing energy consumption rates in tropical climatic behaviour.

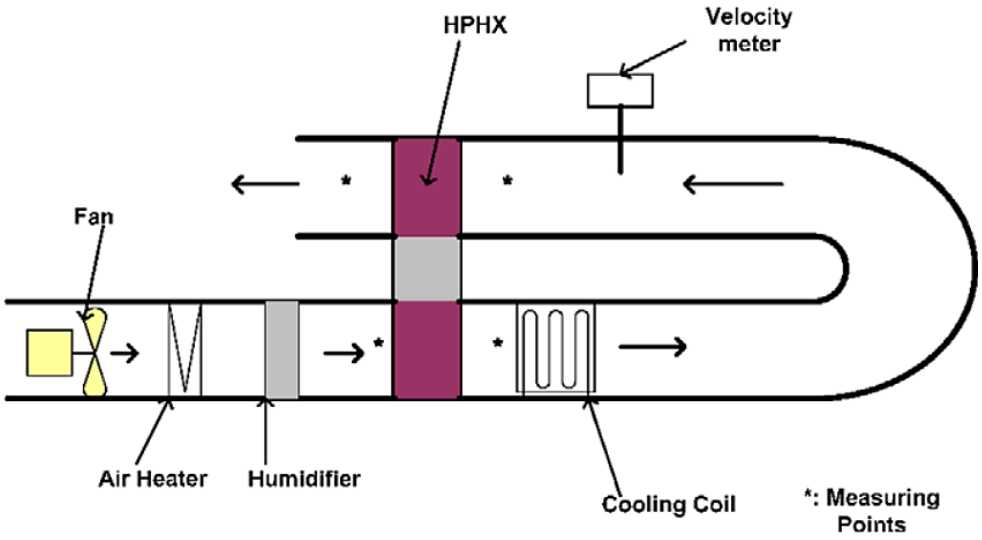

Figure 2.32 Schematic of a 3-row thermosiphon heat exchanger testing rig (Yau and Ahmadzadehtalatapeh, 2010)

Wu *et al.*, (2011) investigated the potential of using gravity-assisted wickless heat pipes or thermosiphons as cold energy storage systems for cooling data centres. The emphasis of the study dealt with reducing electricity consumption of the facility. A large heat load of 8,800kW was applied on the thermosiphon modules. The work revealed that the system was capable of taking up to 60% of the total cooling load with a payback time of approximately 3 and a half years. In addition, with the reduction of external power consumption, the work revealed that up to 10.4 kilotons of carbon dioxide emissions can be reduced per year. However, when operating with thermosiphon units, it must be ensured that the temperatures at the condenser section or the cold interface must be lower than the evaporator end.

Further work into the integration of heat pipes in energy management and renewable energy based systems was carried out by Singh *et al.*, (2011). The work outlined an energy conservation technology for cooling of data centres, cold storage, waste heat recovery and automotive dashboard cooling by using gravity assisted wickless heat pipes (or thermosiphons) and capillary pumped loop. The evaporator and condenser lengths used in the study were 90mm and an inlet air velocity of 1.8m/s was provided to cool the condenser section in order to keep the heat pipes functioning. Figure 2.33 presents the correct mode of operation when the ambient temperatures are below the inlet cold energy storage temperature to the evaporator section of the thermosiphon.

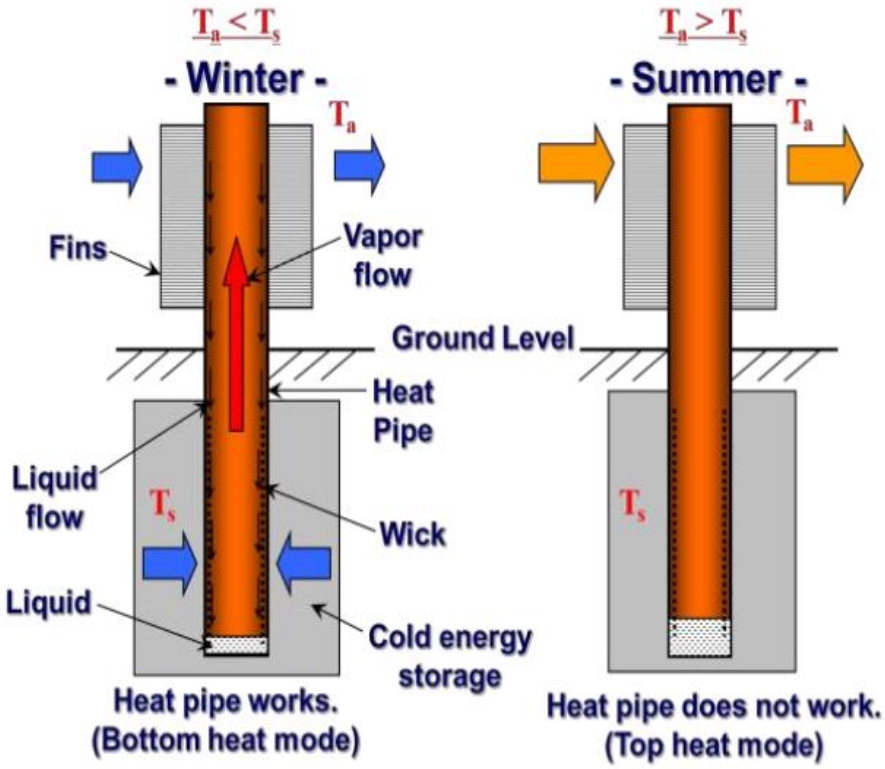

Figure 2.33 Thermosiphon diode characteristics (Singh *et al*., 2011)

The findings suggested that a heat pipe heat exchanger with 118 heat pipes, designed for an operational temperature of 303K, can effectively dissipate 30kW of heat from data centres for most of the year. Moreover, the work concluded that the proposed heat pipe based cooling systems incorporate natural ambient cold energy and therefore eliminating the running costs involved. Besides, since heat pipes do no release greenhouse gas emissions into the atmosphere, the employment of these devices help in reducing the carbon footprint of a building application.

A review into the utility of heat pipe heat exchangers as indirect evaporative coolers was conducted by Duan *et al*., 2012. The work indicated the potential of indirect evaporative cooling technology as an alternative to conventional mechanical compression refrigeration systems for air-conditioning in buildings. The study revealed that the heat pipe incorporated indirect evaporative cooling can be combined with a direct evaporative cooler or/and chill water coil to form a hybrid system. Within such a hybrid system, the configuration of heat pipe can be of any type ranging from thermosiphon, flat plate and capillary pumped loop heat pipe.

The uses of gravity assisted heat pipes for environmental management are a very cost effective, logical and environmentally sound strategy (Cooper, 1996). One of the reasons for that is that heat pipe heat exchangers function more efficiently in vertical orientation (90° from ground level) due to the guarantee of an unhindered condensate return to the evaporator section (Beckert and Herwig, 1996).

Heat pipe heat exchangers have been commonly used in energy systems to recover heat from the exhaust air streams and transfer it to the supply fresh air stream thereby reducing active pre-heating requirements (Noie-Baghban and Majideian, 2000, El-Baky and Mohamed, 2007). The heat recovery effectiveness decreases as the external air speed increases due to lack of contact time between the air stream and the heat pipes (Riffat, 1997). The exploration of heat pipes and their applications in thermal management have been widely recognised. Depending on their application area, they can operate over a wide range of temperatures with a high heat-removal capability.

In relevance to building economics, previous studies of using a heat pipe heat exchanger for energy recovery in air-conditioning streams have indicated a payback time of 3 years on recovery profit (Sanaye and Talaee, 2009) making the technology to appeal financially. Heat pipe heat exchangers are readily employed as a heat recovery unit in air-conditioning systems for the built environment although the prospect of achieving passive cooing from natural ventilation air streams is not well-established.

2.8 Research gap

The review of the existing literature and research covered an extensive range of numerical and experimental work to assess the effectiveness of current heat pipe heat transfer techniques. Previous works have highlighted the use of heat pipe devices in building heat recovery and energy conservation systems alongside comparative studies on internal working fluids and appropriate geometrical arrangement parameters. However, the following was not resolved in the literature review:

- There was little study that investigated the capability of heat pipes as a passive cooling mechanism for treating fresh air streams in natural ventilation systems.

- There was little work that defined a thorough comparison between natural and refrigerant heat pipe working fluids for the range of operating temperatures suited to hot climates.

- There was little work that examined the individual physical properties of heat pipe internal working fluids and its influence on enhancing convective heat transfer.

- There was little attempt to increase the convective heat transfer of a heat pipe heat exchanger by varying the actual spanwise configuration between the rows of the heat pipes by using numerical and experimental techniques.

- There was little attempt to increase the overall effectiveness of a heat pipe heat exchanger by varying the actual streamwise configuration between the columns of the heat pipes.

- There was no relevant study that defined a periodic time-dependant thermal response model for a heat pipe system in relation to the rapid variations in external operating temperatures.

This study used the numerical and experimental techniques, identified through the literature review to carry out the research objectives. The closed-loop heat transfer system involving heat pipes was designed and built to achieve passive exchange of heat by incorporating a heat source and a cold sink position, integrated to form a continuous cycle. Design parameters were investigated including the geometrical arrangement of the heat pipe matrix, ideal working fluid for the range of operating temperatures and the influence of fluid properties on overall heat transfer and cooling of hot natural airstreams. The dynamic thermal response of heat pipes in relation to variation in external temperatures was further analysed and a correlation between numerical and experimental findings was presented. In order to achieve the key objectives, the following work was carried out:

- The use of complete heat pipe geometry for CFD multiphase simulation using phase volume fractions (Alizadehdakhel *et al.*, 2010).

- The use of Euler-Euler multiphase approach incorporated with *k-e* turbulence model for numerical investigation of the heat pipe heat exchanger domain (Ekambara *et al*., 2008, Alizadehdakhel *et al.*, 2010).

- Systematic examination of the internal fluid's thermophysical properties to optimise heat transfer and effectiveness of the heat pipe heat exchanger (Nasrin *et al*., 2012).

- Geometrical variation of the heat pipe assembly to establish the effect on air flow and temperature profile (Kendu and Das, 2009, Yodrak *et al.*, 2010).

- Validation of CFD techniques using wind tunnel as an experimental method for testing the built heat pipe heat exchanger system (Elnaggar *et al*., 2011, Peng *et al.*, 2013).

- Attaining a quantitative agreement within a maximum error percentage of ±5% and ±17% between the CFD and experimental models (Ekambara *et al*., 2008, Wang, 2012).

2.9 Summary

The technological development of research into the application of heat pipes for effective heat transport is rapidly increasing through the use of advanced computation and complex experimentation techniques. Even though heat pipes are extensively used in heat recovery applications, their capability for cooling natural or fresh airstreams is not been fully understood. This chapter reviewed previous literature related to the current developments and technologies used in energy transfer through heat pipes. The review highlighted that conventional heat pipe systems are particularly suited to building applications and can be utilised under natural operating temperatures. Existing studies on numerical and experimental techniques used in simulating and testing the performance of heat pipe systems were defined. The review further described previous work related to comparison between different heat pipe internal working fluids along with the various performance-affecting geometrical parameters. The chapter concluded by identifying the research gap to be accomplished through this study.

Chapter 3
CFD Theory and Modelling

3.1 Introduction

Following the identification of the research aims, this chapter describes the numerical methodology used in this study. The computational or numerical investigation was carried out using Computational Fluid Dynamics (CFD). CFD is a scientific tool for predicting fluid flow, heat and mass transfer along with phase change and various other phenomena related to fluid dynamics by solving the mathematical equations using numerical algorithms (ANSYS, 2011). The use of CFD in analysing different aspects related to fluid behaviour is vast. The advantage of carrying out CFD simulations over experimentation is the ability to predict design verifications or modifications without the expense of requiring physical modifications, thereby saving cost and time. In addition, due to the high level of detail generated by the results, the technology has been widely applied to various engineering applications. This chapter describes the CFD theory and modelling including the generation of the computational domain which was used in for carrying out the numerical investigations.

3.2 Numerical model

FLUENT 14.0 commercial code was used to simulate the flow with coupled heat and mass transfer analysis on the geometry matrix. FLUENT is a general purpose commercial CFD package for modelling fluid flow and heat transfer in complex geometries. It supports different mesh types including both 2D triangular and quadrilateral along with 3D tetrahedral, hexahedral, pyramid, wedge and hybrid mesh.

The three basic simulation procedures adapted by FLUENT include pre-processor, solver and a post-processor. The pre-processor step starts with an attempt to create a Computer Aided Design (CAD) wire-frame geometry for the fluid flow physical domain. Once the geometry is created, the surfaces are connected into volume sub-blocks and the meshed grid is generated depending on the configuration. After successfully reading the meshed file within FLUENT solver, essential steps must be

taken to check and rescale the grid where appropriate. Using the set boundary conditions, the flow field is initialised by the solver and the solution is calculated.

Based on the set convergence criterion, the iterations are carried out until a solution is obtained. The post-processor then allows writing the case and data files along with displaying and printing the simulation results. FLUENT editor offers domain geometry and grid display, velocity vector plots, contour plots and particle tracking. It is imperative to validate the numerical results using experimental data or any previously published literature in order to evaluate the solution. Figure 3.1 displays the logical sequence from the formation of a computer-aided geometry to achieving the numerically processed results.

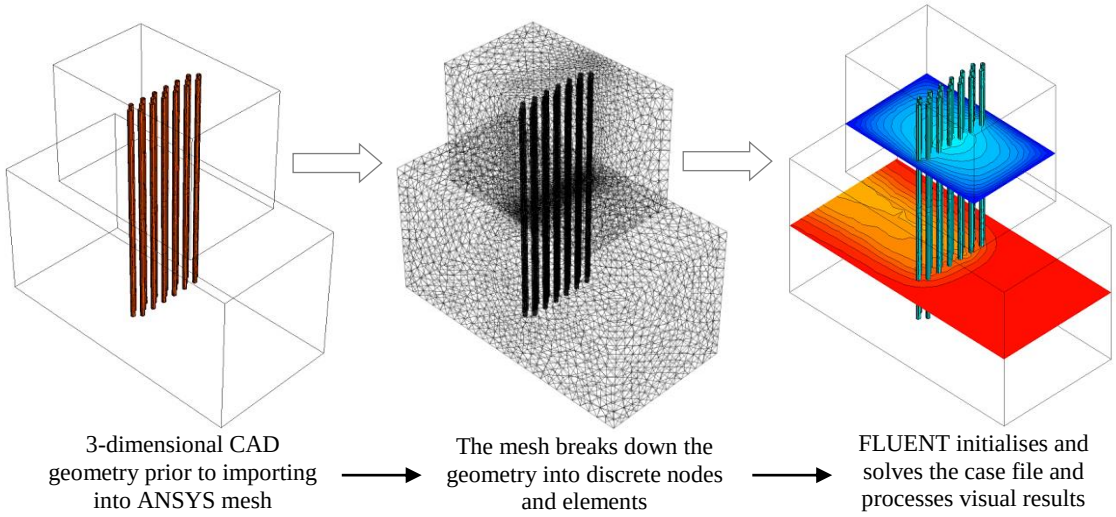

Figure 3.1 Geometry cycle from a 3D CAD to a solved case using FLUENT

3.2.1 Governing equations

The basic governing equations of fluid flow represent the mathematical statements of the conservation laws of physics (Versteeg and Malalasekera, 1995):

- The mass of fluid is conserved.
- The rate of change of momentum equals the sum of the forces on a fluid particle (Newton's second law).
- The rate of change of energy is equal to the sum of the rate of heat addition to and the rate of work done on a fluid particle (first law of thermodynamics).

Figure 3.2 displays a fluid element to which the conservation laws are applied. The six faces are labelled *N, S, E, W, T* and *B* which stand for North, South, East, West, Top and Bottom. The centre of the element is located at the position (x, y, z). Variations in mass, momentum and energy of the fluid element due to fluid flow across its boundaries leads to the fluid flow equations. All fluid properties are functions of space and time and density, pressure, temperature and velocity vector need to be written as $\rho(x, y, z, t)$, $p(x, y, z, t)$, $T(x, y, z, t)$ and $\mathrm{u}(x, y, z, t)$ (Versteeg and Malalasekera, 1995).

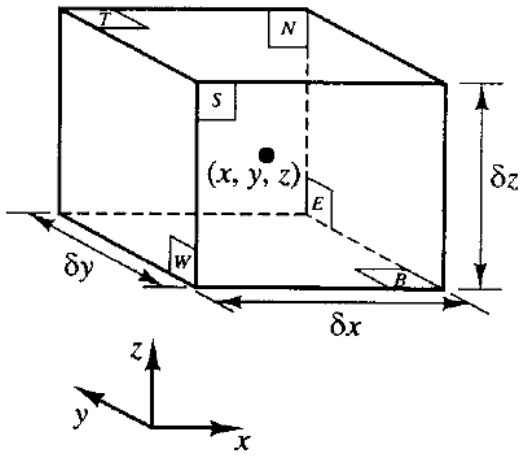

Figure 3.2 Fluid element for conservation laws (Versteeg and Malasekara, 1995)

3.2.1.1 Mass conservation or continuity equation

The mass conservation equation is also known as the continuity equation. The law of mass conservation equation is that the mass of a controlled volume will remain constant, regardless of any process acting inside the system. The controlled system can change form, but cannot be destroyed. The general form (eqn.1) of the partial differential equation of the continuity equation can be written as follows (ANSYS, 2011):

$$\frac{\partial \rho}{\partial t} + \nabla(\rho \vec{v}) = S_m \qquad \text{(eqn.1)}$$

where:

$$\nabla = \frac{\partial}{\partial_x} + \frac{\partial}{\partial_y} + \frac{\partial}{\partial_z} \qquad \text{(eqn.2)}$$

The source S_m is the mass added to the continuous phase from the dispersed second phase and any user defined sources.

3.2.1.2 Momentum conservation equation

Newton's second law states that the rate of change of momentum of a fluid particle equals the sum of forces acting on it. In this case, there are two types of forces acting on fluid particles including body forces (gravity, centrifugal and electromagnetic) and surface forces (pressure, viscous, shear and normal). The rate of increase of (x, y, z) momentum per unit volume of a fluid particle is given by:

$$\rho \frac{Du}{Dt}, \qquad \rho \frac{Dv}{Dt}, \qquad \rho \frac{Dw}{Dt}$$

The body forces overall effect is by the source terms S_{Mx}, S_{My}, S_{Mz} of the x-component, y-component and z-components of the momentum equation. Based on this principle, the momentum conservation equation can be written as follows (Versteeg and Malalasekera, 1995).

The x-component of the momentum equation is found by setting the rate of change of change of x-momentum of the fluid particle equal to the total force in the x-direction on the element due to surface stresses and the rate of increase of x-momentum due to sources as formulated in eqn.3.

$$\rho \frac{Du}{Dt} = -\frac{\partial p}{\partial x} + \frac{\partial \tau_{xx}}{\partial x} + \frac{\partial \tau_{yx}}{\partial y} + \frac{\partial \tau_{zx}}{\partial z} + S_{Mx} \qquad \text{(eqn.3)}$$

Similarly, the y-component of the momentum equation is formulated in eqn.4.

$$\rho \frac{Dv}{Dt} = -\frac{\partial p}{\partial y} + \frac{\partial \tau_{xy}}{\partial x} + \frac{\partial \tau_{yy}}{\partial y} + \frac{\partial \tau_{zy}}{\partial z} + S_{My} \qquad \text{(eqn.4)}$$

While the z-component of the momentum equation is formulated in eqn.5.

$$\rho \frac{Dw}{Dt} = -\frac{\partial p}{\partial z} + \frac{\partial \tau_{xz}}{\partial x} + \frac{\partial \tau_{yz}}{\partial y} + \frac{\partial \tau_{zz}}{\partial z} + S_{Mz} \qquad \text{(eqn.5)}$$

3.2.1.3 Energy equation

The energy equation is derived from Newton's first law which states that the rate of change of energy inside a fluid element is equal to the rate of heat added to the fluid element and the work done on fluid element (ANSYS, 2011). The energy equation used in this study can be written as formulated in eqn.6.

$$\frac{\partial}{\partial t}(\rho E) + [\vec{v}(\rho E + p)] = \nabla\left[k_{eff}\nabla T - \sum_j h_j \vec{J_j} + \left(\overline{\overline{\tau_{eff}}} \times \vec{v}\right)\right] + S_h \qquad \text{(eqn.6)}$$

Where: k_{eff} is the effective conductivity, $\overrightarrow{J_J}$ is the diffusion heat flux of species *j*, S_h includes the heat of chemical reaction and other volumetric heat sources that are user defined. In the above equation:

$$E = h - \frac{p}{\rho} + \frac{v^2}{2} \quad \text{(eqn.7)}$$

Where sensible enthalpy *h* is defined for an ideal gas as:

$$h = \sum_j Y_j h_j \quad \text{(eqn.8)}$$

And for incompressible as:

$$h = \sum_j Y_j h_j + \frac{P}{\rho} \quad \text{(eqn.9)}$$

3.2.1.4 Navier-Stokes equations for a Newtonian fluid

The Navier-Stokes equations are used to define the fluid flow viscous stress τ_{ij}. In many fluid flows, the viscous stresses can be expressed as functions of local deformation rate (or strain rate). In three-dimensional flows, the local rate of deformation is composed of the linear deformation rate and the volumetric deformation rate. In a Newtonian fluid, the viscous stresses are proportional to the rates of deformation (Versteeg and Malalasekera, 1995). The three linear elongating deformation components are:

$$e_{xx} = \frac{\partial u}{\partial x}, \qquad e_{yy} = \frac{\partial v}{\partial y}, \qquad e_{zz} = \frac{\partial w}{\partial z}$$

The six shearing linear deformation components are:

$$e_{xy} = e_{yx} = \frac{1}{2}\left(\frac{\partial u}{\partial y} + \frac{\partial v}{\partial x}\right), \qquad e_{xz} = e_{zx} = \frac{1}{2}\left(\frac{\partial u}{\partial z} + \frac{\partial w}{\partial x}\right), \qquad e_{yz} = e_{zy} = \frac{1}{2}\left(\frac{\partial v}{\partial z} + \frac{\partial w}{\partial y}\right)$$

The volumetric deformation is given by eqn.10.

$$\frac{\partial u}{\partial x} + \frac{\partial v}{\partial y} + \frac{\partial w}{\partial z} = \nabla V \quad \text{(eqn.10)}$$

Where the x-component of Navier-Stokes equation is formulated in eqn.11.

$$\rho \frac{Du}{Dt} = -\frac{\partial p}{\partial x} + \nabla(\mu grad u) + S_{Mx} \quad \text{(eqn.11)}$$

The y-component of Navier-Stokes equation is formulated in eqn.12.

$$\rho \frac{Dv}{Dt} = -\frac{\partial p}{\partial y} + \nabla(\mu grad v) + S_{My} \quad \text{(eqn.12)}$$

The z-component of Navier-Stokes equation is formulated in eqn.13.

$$\rho \frac{Dw}{Dt} = -\frac{\partial p}{\partial z} + \nabla(\mu grad w) + S_{Mz} \qquad \text{(eqn.13)}$$

3.2.2 Multiphase model

A large number of flows encountered in real-life systems are a mixture of phases. In multiphase flows, a phase can be defined as an identifiable class of material that has a particular inertial response to and interaction with the flow and the potential field in which it is immersed. Liquid-vapour multiphase flow regimes are commonly characterised as bubbly, slug or stratified flows. Figure 3.3 displays the various multiphase flow regimes which can be solved using CFD (ANSYS, 2011).

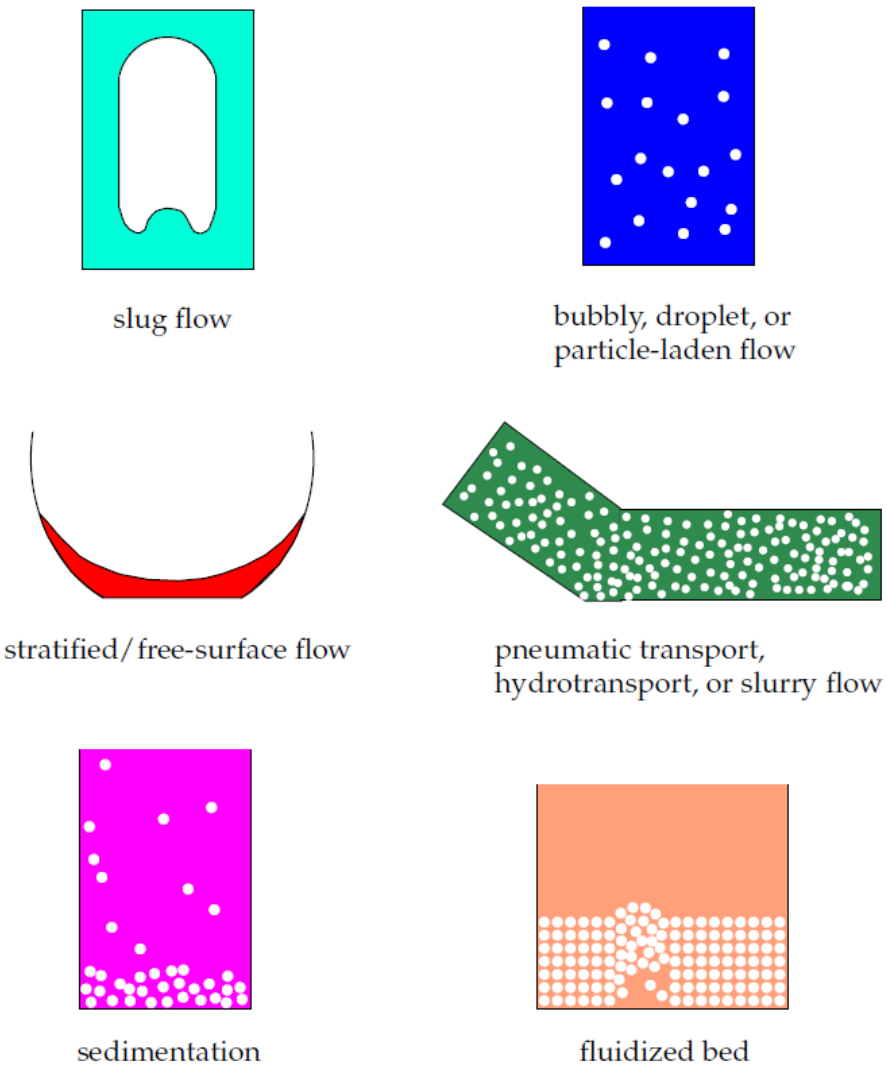

Figure 3.3 Multiphase flow regimes (ANSYS, 2011)

Based on use in previous literature (Ekambara *et al*., 2008, Alizadehdakhel *et al.*, 2010), the Euler-Euler approach was used in this study, where different phases were treated mathematically as interacting. Since the volume of a phase cannot be occupied by the other phases, the concept of phasic volume was introduced and assumed to be continuous functions of space and time and their sum being equal to one. The three available models in the Euler-Euler method include Volume of Fluid (VOF), Mixture and Eulerian models. The Eulerian multiphase model was not used due the complexity of a solution being limited by convergence behaviour (ANSYS, 2011).

3.2.2.1 Volume of Fluid (VOF) model

The VOF model is a surface-tracking technique applied to a fixed mesh. It is designed for two or more immiscible fluids where the position of the interface between the fluids is of interest. In the VOF model, a single set of momentum equations is shared by the fluids, and the volume fraction of each of the fluids in each computational cell is tracked throughout the domain (ANSYS, 2011). As a result, the velocity inlet boundary conditions are shared for both sets of fluid phases. For this reason it was not deployed during this study, but described here for completeness.

3.2.2.2 Mixture model

The Mixture model solves for the mixture momentum equation and prescribes relative velocities to describe the dispersed phases. Accordingly, velocity inlet boundary conditions are applicable to both liquid and vapour phases of the fluid. The Mixture model was therefore used to solve the governing equations considering its extensive use in the study of particle transport of two-phase flows through pipes (Ekambara *et al*., 2008, Easa and Barigou, 2009). The Mixture model is a simplified multiphase model that can be used to model multiphase flows where the phases travel at different velocities, but assume local equilibrium over short spatial length scales.

Mass transfer phenomenon for phase interaction between the vapour and liquid species was carried out using the evaporation-condensation mechanism involving the fluid saturation properties. The evaporation-condensation model is a systematic model (Lee, 1979) with a physical basis and solves the mass transfer based on the following temperature regimes as formulated in eqn.14 and eqn.15.

If $T > T_{sat}$ $\dot{m}_{e\to v} = coeff \times \alpha_l \rho_l + \left(\frac{T-T_{sat}}{T_{sat}}\right)$ (eqn.14)

If $T < T_{sat}$ $\dot{m}_{e\to v} = coeff \times \alpha_v \rho_v + \left(\frac{T-T_{sat}}{T_{sat}}\right)$ (eqn.15)

Where; $\dot{m}_{e\to v}$ represents the rates of mass transfer from the liquid phase to the vapour phase, α and ρ are the phase volume fraction and density.

3.2.3 Turbulence model

The standard *k-e* transport model (Launder and Spalding, 1972) which is frequently used for incompressible flows (Chung, 2002) was used to define the turbulence kinetic energy and flow dissipation rate within the model. The use of the standard *k-e* transport model on cylindrical pipe flows has been found in previous works (Ekambara *et al*., 2006, Saber and Ashtiani, 2010) as has been the approach of integrating Eulerian-Eulerian multiphase simulations alongside (Ekambara *et al*., 2008). The turbulence kinetic energy, *k*, and its rate of dissipation, *e*, are obtained from the following transport equations formulated in eqn.16 and eqn.17.

$$\frac{\partial}{\partial t}(\rho k) + \frac{\partial}{\partial x_i}(\rho k u_i) = \frac{\partial}{\partial x_j}\left[\left(\mu + \frac{\mu_t}{\sigma_k}\right)\frac{\partial k}{\partial x_j}\right] + G_k + G_b - \rho\epsilon - Y_M + S_k \quad \text{(eqn.16)}$$

$$\frac{\partial}{\partial t}(\rho e) + \frac{\partial}{\partial x_i}(\rho e u_i) = \frac{\partial}{\partial x_j}\left[\left(\mu + \frac{\mu_t}{\sigma_e}\right)\frac{\partial e}{\partial x_j}\right] + C_{1e}\frac{e}{k}(G_k + C_{3e}G_b) - C_{2e}\rho\frac{e^2}{k} + S_e \quad \text{(eqn.17)}$$

Where; G_k represents the generation of turbulence kinetic energy due to the mean velocity gradients, G_b represents the generation of turbulence kinetic energy due to buoyancy. Y_M represents the contribution of fluctuating dilatation in compressible turbulence to the overall dissipation rate. C_{1e}, C_{2e} and C_{3e} are constants, σ_k and σ_e are the turbulent Prandtl numbers for *k* and *e*. S_k and S_e are the user-defined source terms.

3.2.4 Rate of evaporation

This section of the chapter states the equations that were used to calculate the rate of evaporation of the heat pipe working fluid along with the equations used for calculating the convective heat transfer of air. The study used the commonly employed Rohsenow (Welty *et al.*, 2007) correlation formulated in eqn.18 for investigating the nucleate boiling heat transfer, the temperature differential obtained above saturation and the rate of evaporation of the two working fluids at their saturation properties.

$$\dot{q} = \mu_L h_{fg} \left(\frac{g(\rho_L - \rho_V)}{\sigma}\right)^{1/2} \left(\frac{c_{p,L}\Delta T}{C_{sf} h_{fg} Pr_L}\right)^3 \quad \text{(eqn.18)}$$

Using the cross-sectional area of the pipe, the boiling heat transfer was calculated using eqn.19.

$$q = \dot{q} \times A \quad \text{(eqn.19)}$$

Under steady state conditions, the rate of evaporation was therefore calculated using eqn.20.

$$\dot{m} = \frac{q}{h_{fg}} \quad \text{(eqn.20)}$$

Temperature dependant parameters were analytically modelled to determine the variation in thermal transport properties of the fluids. Considering a saturation temperature of 293K and using the properties of water and ethanol (Reay and Kew, 2006), the applied heat flux was calculated. The geometrical cross-section area of the cylindrical heat pipe was 0.000201m^2. At a saturation temperature of 293K, boiling heat transfers of 26.2kW, 151.4kW and 109.4kW for water, ethanol and R134a were determined using a constant heated surface temperature of 323K for the study. C_{sf} values for water-copper, ethanol-chromium and water-R134a surface combinations were taken as 0.013, 0.0027 and 0.0073 (Rao, 2001, Jabardo *et al.*, 2004).

3.2.5 Heat transfer and overall effectiveness

Thermal performance of a heat pipe heat exchanger is quantified by using heat transfer rate or cooling capacity with respect to the inlet airflow. For a constant pressure or constant flow process, the temperature differential of air, upstream and downstream of the heat pipes is directly proportional to the heat transfer due to convection. The rate of heat transfer at the evaporator section is formulated in eqn.21 (Noie-Baghban and Majideian, 2000, El-Baky and Mohamed, 2007).

$$q_e = \rho_G U A C_{p,G} \left(T_{e,inlet} - T_{e,outlet}\right) \quad \text{(eqn.21)}$$

Where q_e represents the heat transfer in the evaporator section, ρ_G represents the density of air, *U* represents the velocity of air, *A* represents the cross-sectional area, $C_{p,G}$ represents the specific heat capacity of air, $T_{e,inlet}$ represents the temperature at the inlet and $T_{e,outlet}$ represents the temperature at the outlet.

The efficiency of heat pipes is determined using the concept of heat exchanger overall effectiveness. The effectiveness of a heat exchanger is the ratio of actual rate of heat transfer by the heat exchanger to the maximum possible heat transfer rate between the air streams (Kays and London, 1984) as formulated in eqn.22.

$$\varepsilon = \frac{q_{actual}}{q_{max}} = \frac{T_{e,inlet} - T_{e,outlet}}{T_{e,inlet} - T_{c,inlet}} \quad \text{(eqn.22)}$$

As heat transfer takes place through both conduction and convection from working fluids, Prandtl number is often used as a dimensionless parameter to identify the ratio of momentum boundary layer to thermal boundary layer. The Prandtl number (eqn.23) is the ratio of momentum to thermal diffusivity of a fluid and is an important control variable in thermal convection (Majumder *et al*., 2002).

$$Pr = \frac{C_p \mu}{k} \quad \text{(eqn.23)}$$

The Prandtl number was used as a guideline in order to determine whether heat transfer through convection was dominant over pure conduction while investigating heat pipe internal fluid properties.

3.3 Computational domain

The purpose-built heat pipe geometry was constructed in order to carry out the numerical simulations alongside achieving direct experimental validation. The model was designed according to the wind tunnel test section (described in Chapter 4) incorporating identical dimensions. 19 cylindrical heat pipes of exact specification were used, which were oriented vertically at an angle of 90° to the ground. The inner and outer diameter of the heat pipes were 0.015m and 0.016m. The generic geometrical parameters of the heat pipe heat exchanger are illustrated in Table 3.1.

Table 3.1 Geometric parameters of the teat pipe heat exchanger model

Property	**Value**
Outer diameter of the heat pipe (m)	0.016
Inner diameter of the heat pipe (m)	0.015
Length of the heat pipe (m)	0.80
Cross-sectional area of the heat pipe (m^2)	0.0002
Length of the test section (m)	1.00
Width of the test section (m)	0.50

The cross-sectional dimensions of the test-rig were 0.5m x 0.5m with a total length of 1.0m as displayed in Figure 3.4.

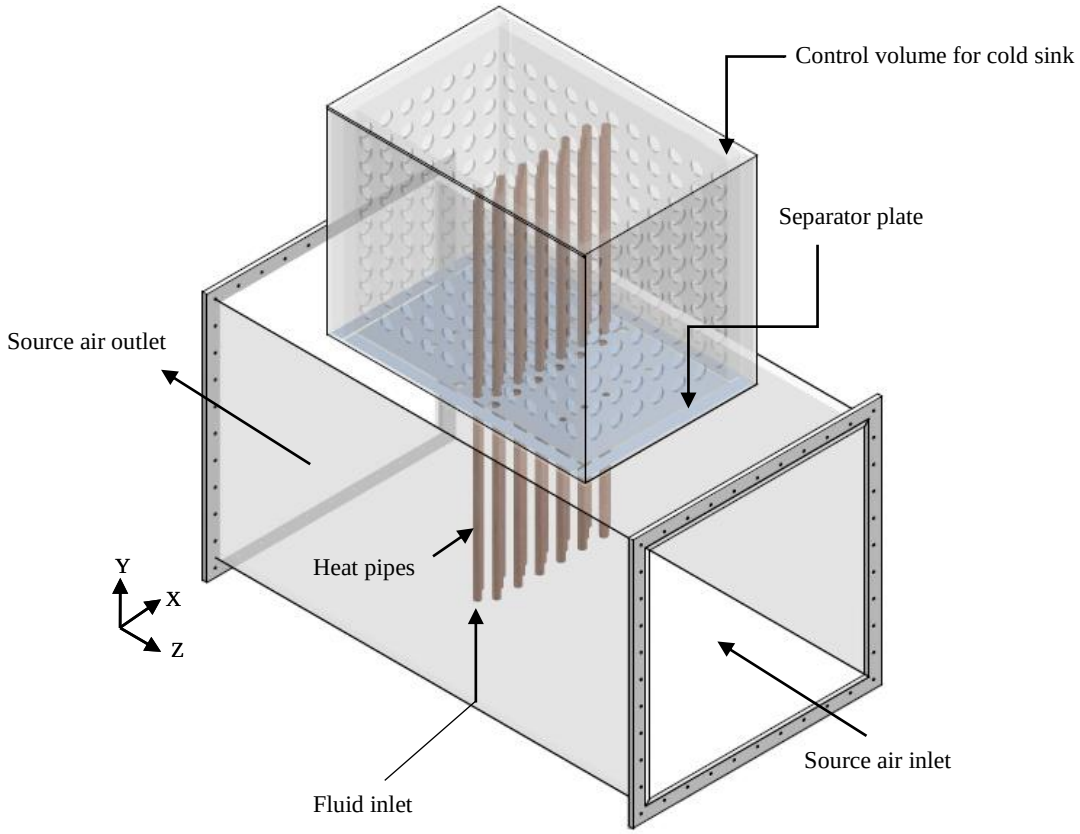

Figure 3.4 Heat pipe arrangement in the testing rig

The evaporator section of the heat pipe was located inside the test section where it was exposed to hot inlet airside temperatures while the condenser section was kept at steady sink conditions below saturation using a fixed control volume. The control volume of the cold sink measured 0.6m by 0.4m with a height of 0.5m, the cross-sectional area of which was calculated at 0.24m^2. The heat pipe internal working fluid was fed in through the bottom of the heat pipes at its specified saturation temperature and pressure. The separator plate was located at the centre of the two sections to distinguish the hot and cold air streams.

All geometries were created using the commercial Solid Edge ST CAD software package. The set-up comprised of cylindrical heat pipes assembled in three rows and arranged in a staggered grid configuration (Van Fossen, 1981, Metzger *et al*., 1984, Chyu *et al*., 1998, Rallabandi *et al*., 2011, Karthikeyan and Rathnasamy, 2011) with the row and column spacing subjected to numerical investigation. The evaporator and

condenser section lengths were kept identical at 400mm each. The detailed plan view of the heat pipe arrangement is displayed in Figure 3.5 with all dimensions specified in mm.

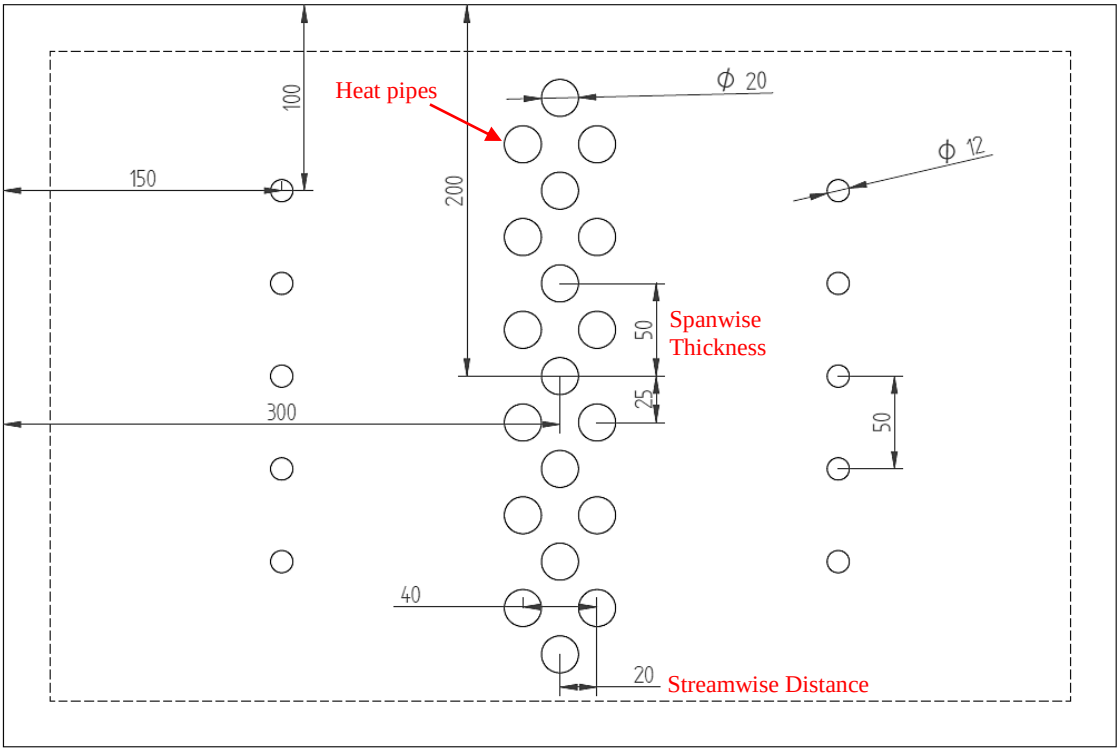

Figure 3.5 Plan view of the test-plate indicating the spanwise thickness and streamwise distances of the heat pipe configuration

3.4 Mesh generation

Mesh generation is one of the most important processes in CFD simulation. The quality of the mesh plays a significant role on the accuracy of results and the stability of the solution. A mesh or grid is the representation of the continuous physical surface and volume of an object through a set of discrete *x*, *y*, *z* coordinates. Each cell forms a control volume into which the domain is broken up. The boundary of a cell is known as a face while the boundary of a face is known as an edge.

There are two types of mesh generation schemes available including structured mesh and unstructured mesh. All interior vertices in a structured mesh have an equal number of adjacent elements. Structured meshes typically contain all quadrilateral (2D) or hexahedral (3D) elements. Each cell (element) in the grid can thus be addressed by a unique index (*i*,*j*,*k*). Algorithms employed to create such meshes generally involve complex iterative smoothing methods which attempt to align elements with boundaries

or physical domains (Ridley, 2010). Common terminologies associated with a two and three-dimensional computational domains are displayed in Figure 3.6 (Bakker, 2002).

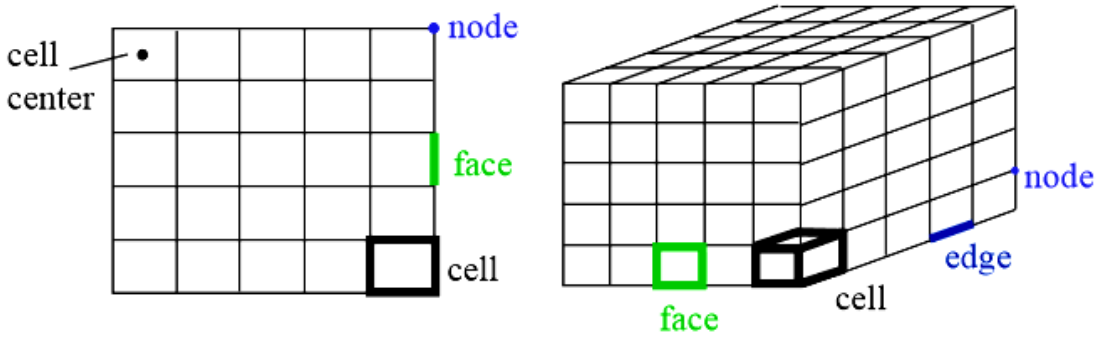

Figure 3.6 General terminologies associated with a 2D and 3D computational domain (Bakker, 2002)

Unstructured meshes do not have the requirement that all interior vertices must have an equal number of adjacent elements and therefore allow any number of elements to meet at a single vertex. As an unstructured solver, ANSYS FLUENT uses internal data structures to assign an order to the cells, faces, and grid points in a mesh and to maintain contact between adjacent cells. Therefore, it does not require *i,j,k* indexing to locate neighbouring cells. This provides flexibility in using the best mesh topology as the solver does not force an overall structure or topology on the mesh (ANSYS, 2011). Other acceptable mesh structures in FLUENT include mixed or hybrid meshes, an example of which is illustrated in Figure 3.7.

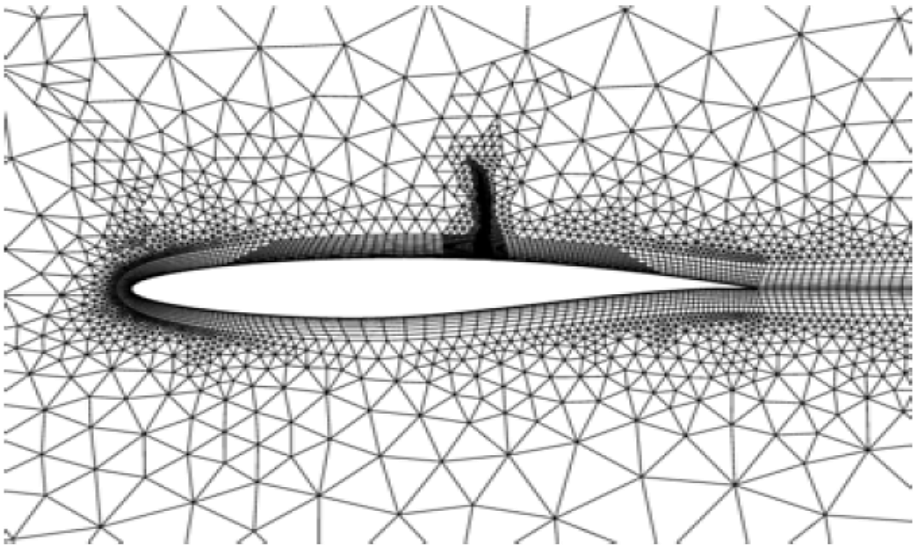

Figure 3.7 Hybrid triangular/quadrilateral mesh with hanging nodes (ANSYS, 2011)

For the investigated computational domain, patch independent CFD tetrahedron and hexahedral meshing technique was applied on the channel while hexahedral elements were applied on the heat pipes wherein the boundary conditions applied on the edges and vertices. The patch independent mesh algorithm for tetrahedron elements is based on the subsequent spatial subdivision algorithm which ensures refinement of the mesh where essential, but retains larger elements where feasible, therefore allowing faster computing times. The meshed model comprised of 160,736 nodes and 778,932 combined tetrahedral and hexahedral elements (Figure 3.8) to obtain a balance between the run time and the resolution in the channel axial direction.

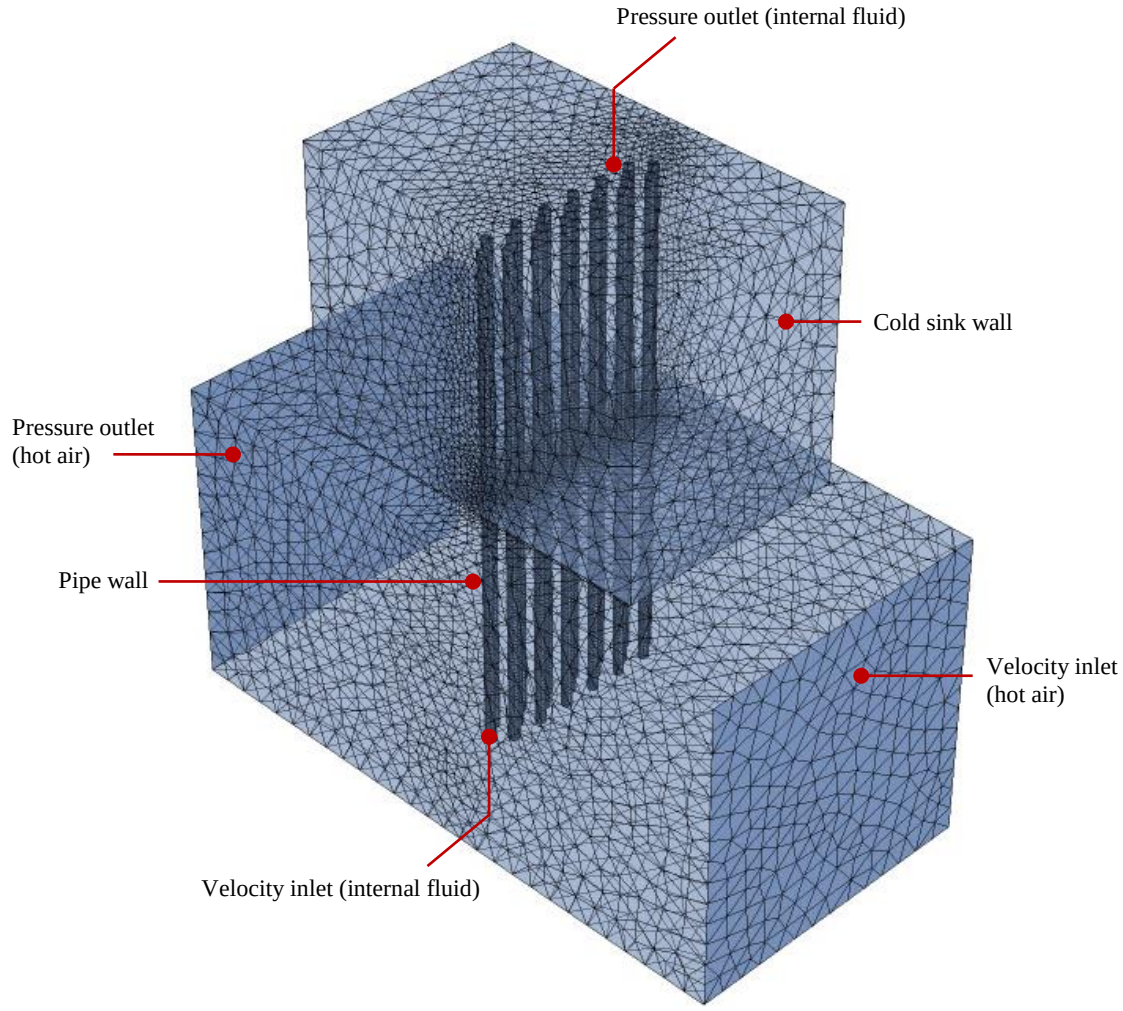

Figure 3.8 Generation of computational mesh on geometry surfaces

The maximum and minimum sizes of the mesh elements were obtained at 7.33×10^{-2} m and 3.66×10^{-4} m while the maximum face sizing was 3.66×10^{-2} m. Higher resolution of mesh was used on the heat pipes (near wall mesh refinement) and in close proximity

while lower resolution was used further away from the subject in order to obtain superior precision of results (Figure 3.9).

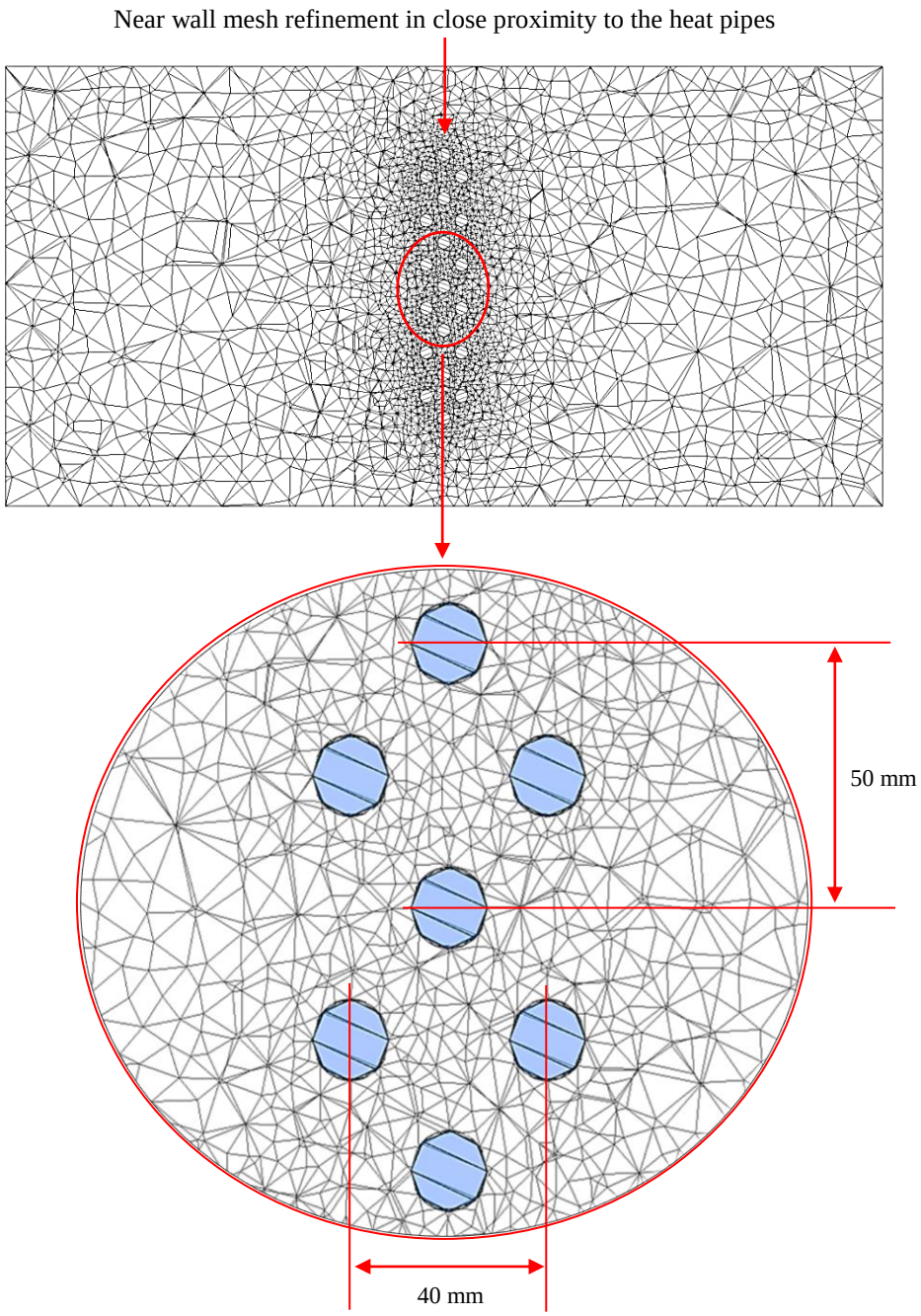

Figure 3.9 Schematic showing high resolution used in the proximity of the pipes, and lower resolution at a larger distance away from the pipes

A total of 7,799 hexahedral elements were applied on the heat pipe tubes (Ekambara *et al*., 2008) with the grid lines perpendicular to the wall surfaces for accurately resolving the viscous and thermal boundary layer (Figure 3.10).

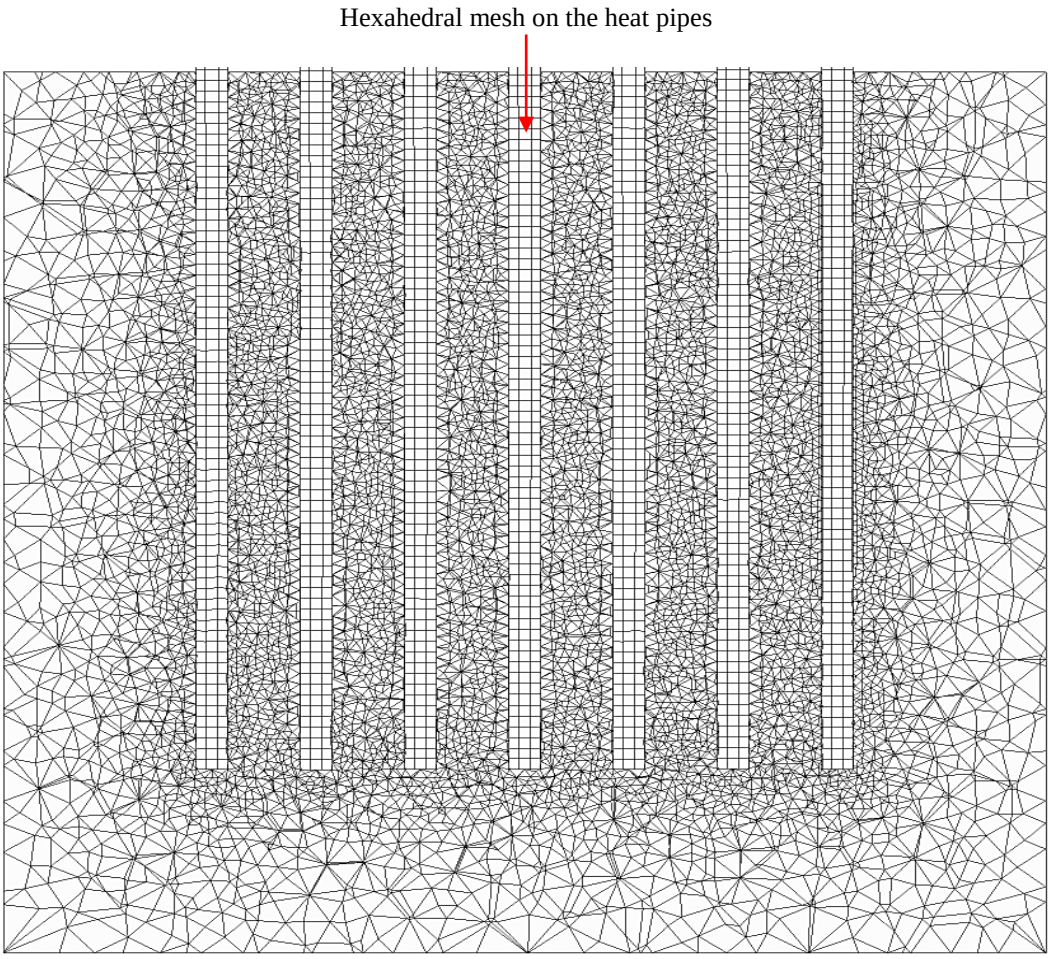

Figure 3.10 Generation of hexahedral mesh on the heat pipe tubes

The y^+ is a non-dimensional wall distance for a wall-bounded flow commonly used in boundary layer theory and can be defined by eqn.24.

$$y^+ = \frac{u_* y}{v} \qquad \text{(eqn.24)}$$

Where u_* is the friction velocity at the nearest wall, y is the distance to the nearest wall and v is the kinematic viscosity of the fluid. The critical y^+ values of the grid on the walls of the heat pipe were in the range of 28 and 45, with the average weighted average across the axial length of the heat pipe tubes being 37 remained as per the recommended range which constitutes to $y^+ > 30$ in the entire domain (Versteeg and Malalasekera, 1995, ANSYS, 2011).

Figure 3.11 displays the variation in y^+ values over the axial length of the heat pipe.

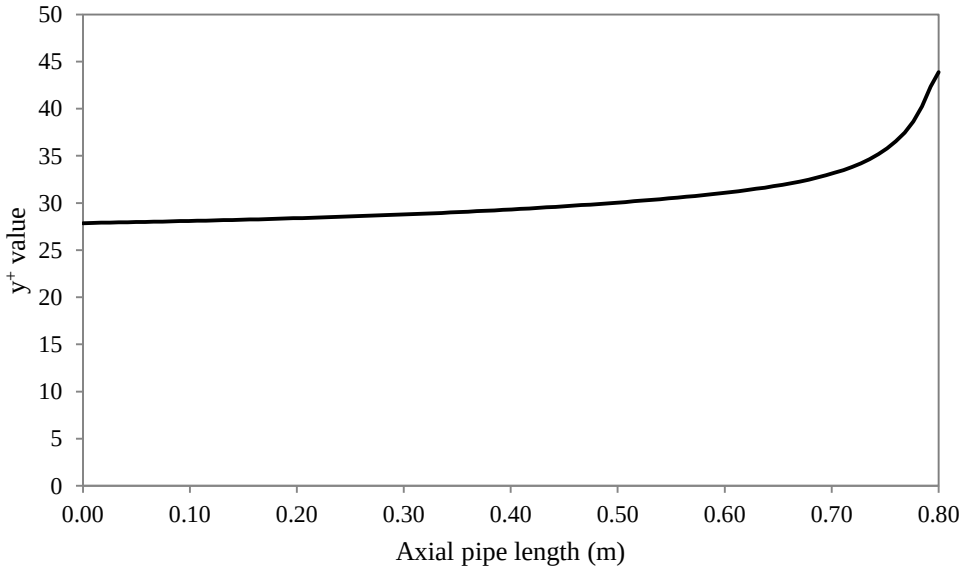

Figure 3.11 y^+ values across the axial length of the pipe

3.5 Grid verification

In order to verify the numerical models, grid verification is carried out to determine the variation in results over increasing mesh sizes. Basic concepts associated with mesh refinement deals with the refinement and evaluation of elements where the posterior error indicator is larger than the preset criterion, while mesh enrichment considers running higher order polynomials till the solution is expected to improve with a fixed mesh (Chung, 2002). Grid verification was carried out using mesh refinements (*h-method*) in order to optimise the distribution of mesh size *h* over a finite element.

Area weighted average is described as the average of a quantity, computed by dividing the summation of the product of the selected filed variable and the facet area by the total area of the surface. The complete computational domain was split and refined in two particular areas, the channel wall and immediate surrounding zone; and the wall of the heat pipe. Each stage was continued until an acceptable compromise was reached between: number of elements; computational time to solve; and the posterior error indication.

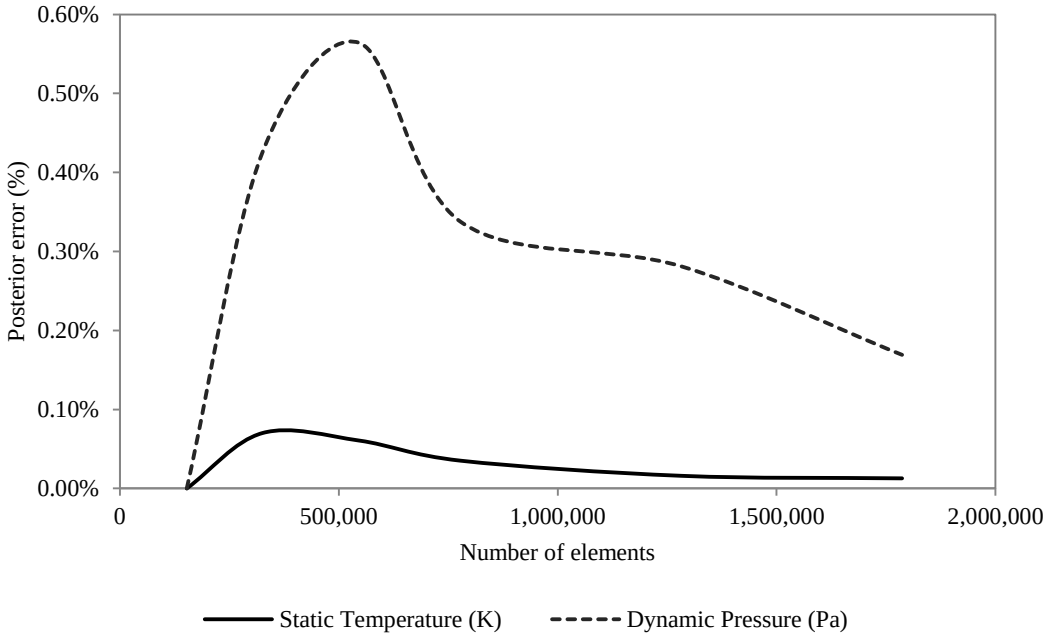

Figure 3.12 Error reduction at increasing number of elements

Figure 3.12 displays the variation in posterior error at increasing number of elements. Area weighted average of the static temperature and the dynamic pressure at the outlet of the test section were taken as the parameters for calculating the posterior error. The grid verification process increased the number of elements by 1,633,816. The maximum posterior error was 0.56% (dynamic pressure) and 0.06% (static temperature) using 546,730 elements. At 778,932 elements the error indication between refinements was dropped to below 0.5% for both variables; coupled with the computational time, made it an acceptable compromise. Table 3.2 displays the posterior error with respect to increasing number of elements and as observed, the error percentage dropped below 0.5% in the final three stages of refinement.

Table 3.2 Posterior error with increasing number of elements

Nodes	**Elements**	**Static Temperature (K)**	**Posterior error (%)**	**Dynamic Pressure (Pa)**	**Posterior error (%)**
41,656	152,782	313.88	0.00%	3.511	0.00%
74,035	325,627	313.66	0.07%	3.526	0.43%
121,496	546,730	313.47	0.06%	3.546	0.56%
160,736	778,932	313.36	0.04%	3.558	0.34%
264,704	1,282,765	313.31	0.02%	3.548	0.28%
662,736	1,786,598	313.27	0.01%	3.542	0.17%

The grid verification process was carried out to determine the stability of the CFD model prior to validation of the study's findings against existing published literature and experimental methods, which will be described in Chapter 7.

3.6 Boundary conditions

This section of the chapter details out the boundary conditions that were applied to the CFD model for all numerical investigations that were carried out.

3.6.1 Comparison between water, ethanol and R134a as heat pipe fluids

The first step of the CFD investigation established a comparison between the working fluids in terms of their airside cooling capability. Water, ethanol and R134a were used as heat pipe internal fluids to determine the rate of sensible heat transfer and overall effectiveness of the heat exchanger.

The applied boundary conditions on the heat pipe (Figure 3.13) included a constant heated surface temperature of 323K, applied upstream and downstream wall faces of the heat pipe vertices. Saturation temperature was kept constant at 293K for all three fluids. Inlet axial mass flow rate values were 1.07×10^{-2} kg/sec, 1.69×10^{-1} kg/sec and 3.41×10^{-1} kg/sec for water, ethanol and R134a which were obtained from the analytical model at the applied specific heat flux. Liquid phases of the working fluid were set as secondary and vapour phases were set as the primary.

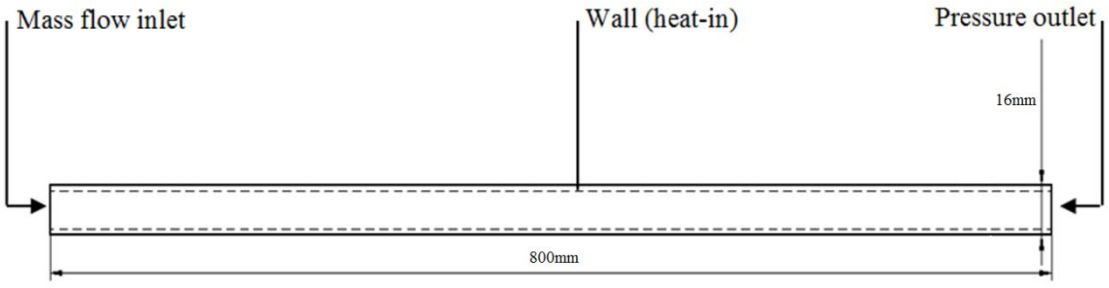

Figure 3.13 Heat pipe sectional specifications and boundary conditions

The range of temperature dependant properties of the three working fluids in terms of density and dynamic viscosity are tabulated in Table 3.3, Table 3.4 and Table 3.5 (Reay and Kew, 2006).

Table 3.3 Physical temperature dependant properties of water

Property	Phase	T=293K	T=298K	T=303K	T=308K	T=313K	T=318K	T=323K
Density (kg/m^3)	Liquid	998.2	996.7	995.3	993.8	992.3	989.9	987.7
	Vapour	0.020	0.028	0.035	0.043	0.050	0.070	0.090
Dynamic Viscosity (Ns/m^2)	Liquid	1.0E-03	9.1E-04	8.3E-04	7.4E-04	6.5E-04	6.1E-04	5.6E-04
	Vapour	9.6E-06	9.8E-06	1.0E-05	1.0E-05	1.0E-05	1.1E-05	1.1E-05

Table 3.4 Physical temperature dependant properties of ethanol

Property	Phase	T=293K	T=298K	T=303K	T=308K	T=313K	T=318K	T=323K
Density (kg/m^3)	Liquid	789.5	785.3	781.0	776.3	771.5	766.9	762.2
	Vapour	0.215	0.298	0.38	0.465	0.550	0.635	0.720
Dynamic Viscosity (Ns/m^2)	Liquid	1.3E-03	1.1E-03	1.0E-03	9.4E-04	8.7E-04	7.2E-04	7.2E-04
	Vapour	8.8E-06	8.9E-06	9.1E-06	9.3E-06	9.4E-06	9.5E-06	9.7E-06

Table 3.5 Physical temperature dependant properties of R134a

Property	Phase	T=293K	T=298K	T=303K	T=308K	T=313K	T=318K	T=323K
Density (kg/m^3)	Liquid	1,225.3	1,206.7	1,187.5	1,167.5	1,146.7	1,125.1	1,102.3
	Vapour	27.78	32.35	37.53	43.42	50.08	57.66	66.27
Dynamic Viscosity (Ns/m^2)	Liquid	2.1E-04	1.9E-04	1.8E-04	1.7E-04	1.6E-04	1.5E-04	1.4E-04
	Vapour	1.1E-05	1.2E-05	1.2E-05	1.2E-05	1.3E-05	1.3E-02	1.4E-05

Using the physical properties of the fluids, an analytical comparison between water, ethanol and R134a was established in terms of the rate of evaporation and boiling heat transfer parameters. Keeping a constant heat pipe saturation temperature of 293K, the rate of evaporation and the boiling heat transfer of the fluid inside was calculated at increasing temperatures above saturation. The rate of evaporation was the greatest for R134a with a value of 3.41×10^{-1} kg/sec when the source temperature was 323K. Water displayed the lowest rate of evaporation and consequently the boiling heat transfer of the compared fluids. Ethanol displayed the greatest boiling heat transfer at a source temperature of 323K with a value of 151.4kW. The calculations were thus used to predict the evaporation mass flow rate of the fluids inside the heat pipe as an inlet boundary condition. The graphical representation of the comparison between the three heat pipe working fluids is displayed in Figure 3.14.

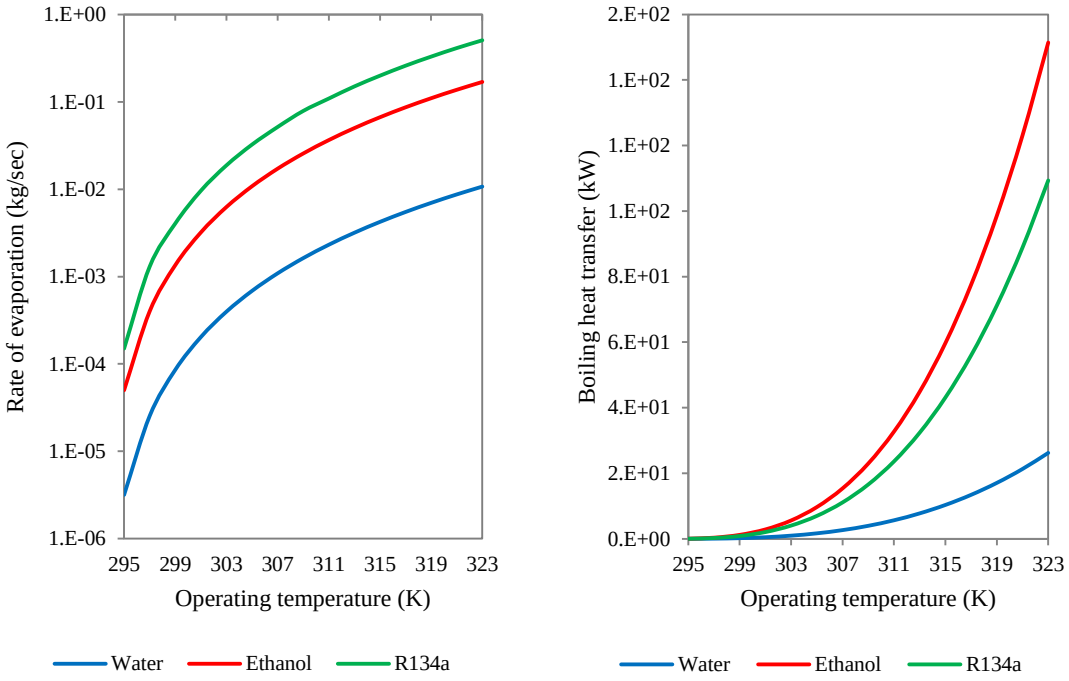

Figure 3.14 Rate of evaporation and boiling heat transfer at increasing operating temperatures

The SIMPLE (Vasquez and Ivanov, 2000) algorithm was used for pressure-velocity coupling in order to incorporate the mass transfer terms implicitly into the general matrix and to solve for corrections of pressure and velocity sequentially. Second Order Upwind discretisation scheme was used to obtain the face fluxes for all cells, including those near the interface. Upwinding indicates that the face value of a cell is derived from quantities in the cell upstream, or upwind, relative to the direction of the normal velocity (ANSYS, 2011).

In addition to analysing the internal behaviour of the three working fluids within a heat pipe, their thermal performance on decreasing air temperatures from a hot natural airstream was investigated. The applied boundary conditions on the heat exchanger computational domain comprised of an initial air velocity of 2.3m/s perpendicular to the hot channel. The cross-sectional area of the test section was 0.25m^2 thereby indicating a Reynolds number of 62,299 (a mass flow rate of 0.631kg/sec) of air at the evaporator section through convection. Table 3.6 indicates the summarised applied boundary conditions applied on the heat pipe heat exchanger.

Table 3.6 Applied boundary conditions on the heat pipe model

Parameter	**Value / description**
Multiphase model	Mixture model
Viscous model	k-epsilon
Near-wall treatment	Enhanced wall functions
Phase 1	Vapour
Phase 2	Liquid
Saturation temperature	293K
Inlet source temperature	305K, 308K, 314K
Inlet sink temperature	288K
Inlet air velocity	2.3m/s
Velocity formulation	Absolute
Solver type	Pressure based
Gravity	-9.81m/s^2 (Y direction)

The inlet speed of 2.3m/s was kept fixed for all analysed fluids in order to achieve a direct comparison with experimentally obtained results. The control volume of the cold sink located directly above the evaporator section was set to a temperature of 288K and was used as the condenser section of the heat pipes. The inlet and outlet temperature values were used in order to computationally obtain the rate of heat transfer and effectiveness of the heat pipe heat exchanger. Gravitational acceleration of -9.81m/s^2 was applied across the two channels in the Y direction. Metal surfaces for heat pipe walls included copper for water and R134a and chromium for ethanol for compatibility with the working fluids. The heat pipe heat exchanger was investigated at three different air temperatures, namely 305K, 308K and 314K, while the inlet temperature for cold channel remained constant at 288K. The operating or saturation temperature was kept constant at 293K.

3.6.2 Effect of internal fluid properties on convective heat transfer of air

In order to further enhance heat transfer due to convection using heat pipes, the internal fluid properties were investigated. Individual properties of existing heat pipe internal working fluids were initially obtained at a fixed operating temperature of 20°C or 293K (Reay and Kew, 2006, F2 Chemicals, 2012).

Temperature dependant properties of water were used as a benchmark model while sixteen additional models were developed with variation in density, thermal conductivity, dynamic viscosity and specific heat capacity values. The available fluid

properties were obtained from literature to outline a range of values under which typical heat pipe working fluids operate. Table 3.7 displays the internal physical properties for available heat pipe working fluids. Further details on fluid properties are provided in Appendix D.

Table 3.7 Physical properties of available heat pipe working fluids at 293K

Working fluid	**Density (kg/m^3)**	**Thermal conductivity (W/mK)**	**Dynamic viscosity (Pas)**	**Specific heat capacity (J/kgK)**
Acetone	790	0.181	3.2E-04	2,160
Ammonia	610	0.286	2.2E-04	4,758
Ethanol	788	0.169	1.3E-03	2,470
Flutec PP2	1,801	0.607	1.8E-03	1,000
Heptane	683	0.140	4.3E-04	2,219
Methanol	793	0.204	6.1E-04	2,534
Pentane	626	0.138	2.4E-04	2,177
R134a	1,225	0.085	2.1E-04	1,405
Water	998	0.603	1.0E-03	4,182

Using the properties of water as a baseline, four individual numerical investigations were carried out for each fluid property to determine its impact on the convective heat transfer of air. Source and sink temperatures were kept constant at 314K and 288K along with the inlet air velocity of 2.3m/s to allow for a fair comparison. Saturation temperature was kept constant at 293K throughout all stages of the numerical investigation. Each individual fluid property was systematically varied at one time keeping the other three parameters fixed to understand the effect on convective heat transfer and hence determine the most influential parameter on increasing the efficiency of heat pipes. Table 3.8 and Table 3.9 display the variation in density, thermal conductivity, dynamic viscosity and specific heat capacity used in the analysis.

Table 3.8 Boundary conditions for individual testing on material properties including density and thermal conductivity

Working fluid	**Density (kg/m^3)**	**Working fluid**	**Thermal conductivity (W/mK)**
Test 1	600	Test 5	0.1
Test 2	700	Test 6	0.3
Water	998	Water	0.6
Test 3	1,200	Test 7	0.8
Test 4	1,800	Test 8	1.0

Table 3.9 Boundary conditions for individual testing on material properties including dynamic viscosity and specific heat capacity

Working fluid	Dynamic viscosity (Pas)	Working fluid	Specific heat capacity (J/kgK)
Test 9	1.0E-05	Test 13	1,000
Test 10	1.0E-04	Test 14	2,000
Water	1.0E-03	Water	4,182
Test 11	1.0E-02	Test 15	5,000
Test 12	1.0E-01	Test 16	6,000

The variation in density ranged between 600kg/m^3 to 1,800kg/m^3 while the variation in thermal conductivity was between 0.1W/mK and 1W/mK. Dynamic viscosity was varied between 1x10^{-5} Pas and 1x10^{-1} Pas while the final investigated property was the specific heat capacity which varied between 1,000J/kgK and 6,000J/kgK.

Alongside the four fluid properties considered, the latent heat of vaporisation is another key component in convective heat transfer. This property was not included in the current study due to the inadequate computational capability of the software resource in calculating this property. However, this investigation is included in the future works (Chapter 8, Section 8.3) and described here for completeness.

The impact of fluid properties on the dimensionless Prandtl number and its relation to the temperature gradient was further determined. The molecular Prandtl number of air was taken as 0.74 while the Effective Prandtl number using the turbulence model was 0.85 (ANSYS, 2011). In summary, the influence of heat pipe internal working properties on convective heat transfer of air and the Prandtl number formed the basis of this section of the numerical investigation.

3.6.3 Geometrical variation - spanwise thickness

Following the identification of the most suitable working fluid, the next step of the computational investigation was to identify the optimum spanwise thickness (St) between the rows of the heat pipes. The streamwise distance was kept fixed at 20mm (Calautit *et al*., 2013, Hughes *et al*., 2013) between the columns of the heat pipes. Water was used as a heat pipe working fluid in this case in the heat exchanger model. Five computational models were developed which included variations in spanwise thickness

ranging from 44mm to 52mm which was the maximum distance that could be reached using the available width of the test section (Figure 3.15).

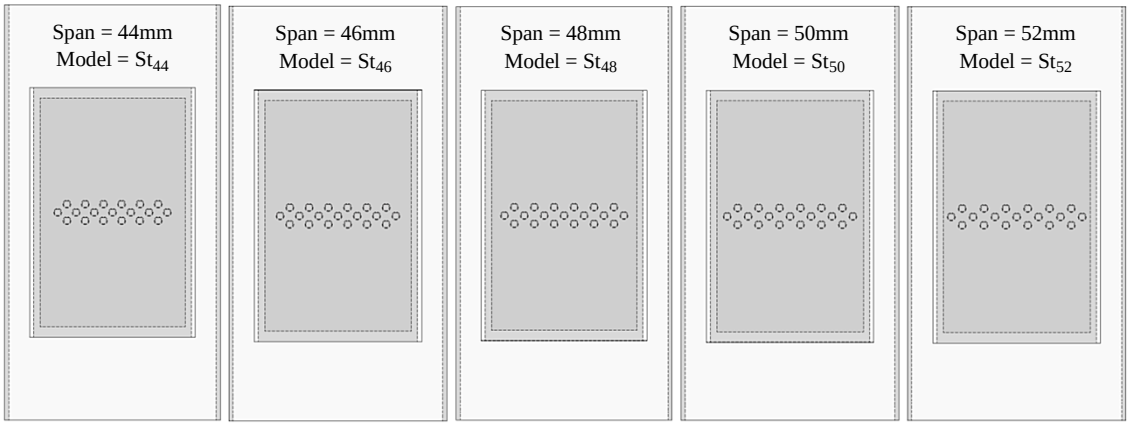

Figure 3.15 Physical domain illustrating the spanwise thickness for the analysed models

The total number of pipes used was 19 for all the cases to allow for a fair comparison between all models. Inlet source and sink temperatures were set to 314K and 288K while the heat pipe operating temperature was kept constant at 293K. The inlet air speed at the evaporator section was fixed at 2.3m/s in order to validate the CFD model using experimental methods which will be discussed in the following chapters. The condenser wall temperatures were set to 288K to replicate the control volume of the cold sink.

Table 3.10 indicates the ratio of increasing spanwise thicknesses to the diameter of the heat pipe groove. The ratio of St/D was increased from 2.2 to 2.6 while the ratio of Sd/D was kept fixed at 1.0.

Table 3.10 Spanwise thickness models

Model	**D (mm)**	**St (mm)**	**Sd (mm)**	**St/D**	**Sd/D**
St_{44}	20.0	44.0	20.0	2.2	1.0
St_{46}	20.0	46.0	20.0	2.3	1.0
St_{48}	20.0	48.0	20.0	2.4	1.0
St_{50}	20.0	50.0	20.0	2.5	1.0
St_{52}	20.0	52.0	20.0	2.6	1.0

3.6.4 Geometrical variation - streamwise distance

The next step of the numerical analysis was to identify the optimum streamwise distance (Sd) between the columns of heat pipes. The spanwise thickness (St) was kept

constant at 50mm while the streamwise distance was increased from 20mm to 40mm in 5mm increments (Figure 3.16). Water was again used as a heat pipe working fluid in this case in the heat exchanger model. In order to conduct a fair assessment, all boundary conditions were kept identical to the ones used for the comparison of spanwise thickness models.

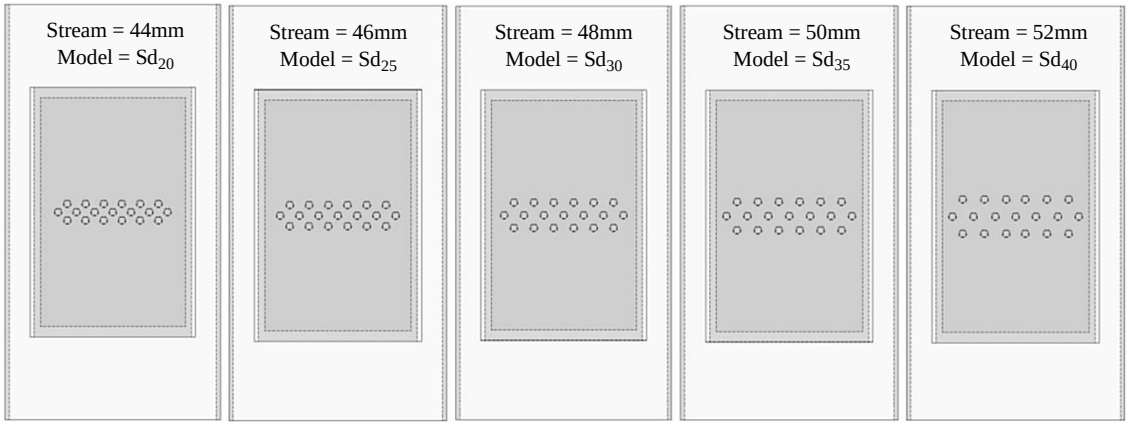

Figure 3.16 Physical domain illustrating the streamwise distance for the analysed models

Table 3.11 indicates the ratio of increasing streamwise distances to the diameter of the heat pipe groove. The ratio of Sd/D was increased from 1.0 to 2.0 while the ratio of St/D was kept fixed at 2.5.

Table 3.11 Streamwise distance models

Model	**D (mm)**	**St (mm)**	**Sd (mm)**	**St/D**	**Sd/D**
Sd_{20}	20.0	50.0	20.0	2.5	1.00
Sd_{25}	20.0	50.0	25.0	2.5	1.25
Sd_{30}	20.0	50.0	30.0	2.5	1.50
Sd_{35}	20.0	50.0	35.0	2.5	1.75
Sd_{40}	20.0	50.0	40.0	2.5	2.00

3.6.5 Monthly thermal models with varying temperatures and wind speeds

Following the initial simulations involving a comparison between working fluids along with variation in heat pipe geometrical arrangement, a further twelve models were developed which included the weather source data for mean monthly temperatures to investigate the effectiveness of the heat exchanger in response to varying source conditions. The city of Doha with coordinates of latitude at 25° 15´ North and longitude

at 51° 34´ East was taken as the location of case-study and the monthly mean peak temperature values were obtained (The Weather Channel, 2012).

The purpose of the established numerical models were to replicate the monthly source temperatures in order to determine the heat pipe heat exchanger's thermal performance to meet the thermal loads of 301.15K (ASHRAE 55, 2004) of typical indoor environmental operative temperature conditions. At a heat pipe operating temperature of 293K, the summary of the source temperatures which were used for the models are displayed in Table 3.12.

Table 3.12 Boundary conditions for the monthly climatic models

Month	**Source temperature (K)**	**Operating temperature (K)**	**Differential (K)**
January	294.99	293.15	1.84
February	295.94	293.15	2.79
March	300.89	293.15	6.74
April	304.95	293.15	11.80
May	311.02	293.15	17.87
June	314.04	293.15	20.90
July	314.15	293.15	21.00
August	313.63	293.15	20.48
September	311.32	293.15	18.17
October	307.86	293.15	14.71
November	302.55	293.15	9.40
December	296.83	293.15	3.68

The heat pipe operating temperature was kept constant at 293K which was lower than the lowest mean temperature to understand the effects of rate of heat transfer at all source temperatures and hence to investigate the performance of the device. The cold sink temperatures were also kept fixed at 288K for all the twelve models to depict the function with varying monthly temperatures throughout the year. The simulation was carried out at two different inlet wind speeds which included 1.0m/s and 2.3m/s. With a characteristic length of 0.5m, the Reynolds number of the incoming flow varied between 27,086 (wind speed of 1.0m/s) and 62,299 (wind speed of 2.3m/s). The two different wind speeds were used to obtain a comparison in terms of rate of heat transfer and the overall heat exchanger effectiveness at dissimilar climatic conditions.

Fixed measurement points were located on the axial plane situated 0.15m upstream and downstream of the heat pipes. A total of 7 measurement points were located in the

evaporator section with 2 upstream and 5 downstream of the flow domain to analyse the temperature variation recorded as the external air transfers its heat to the pipes. The points were horizontally spaced in 0.05m intervals. The vertical distances were set to 0.25m from the top of the testing rig which was the centre of the heat exchanger evaporator section. The coordinates of measurement points are displayed in Figure 3.17.

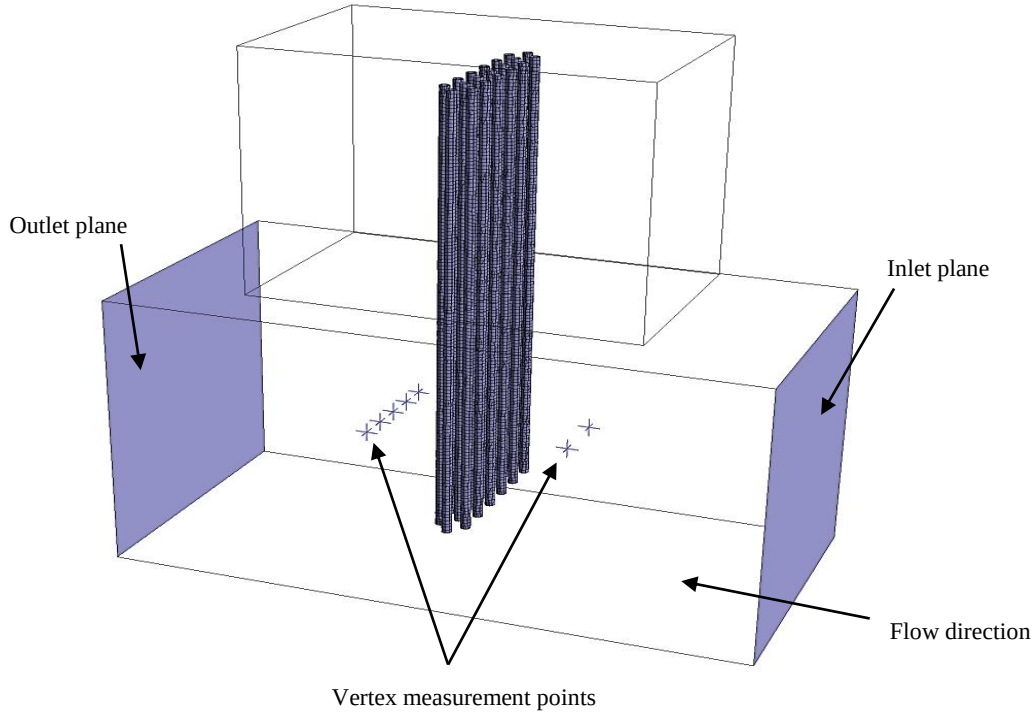

Figure 3.17 Locations of vertex measurement points on the computational domain

In order to evaluate the performance of heat pipes, fundamental fluid flow parameters including velocity, pressure and temperature were initially assessed prior to calculating the total rate of heat transfer or the cooling capacity obtainable from the physical domain of the arranged heat pipes.

3.7 Computational error and uncertainty

Due to the constant advancement in the capabilities of CFD in modelling complex physical processes and alleviating the dependence on experimental testing, the needs for developing rigorous model validation methodologies are rising. A CFD code solves the turbulence flow and auxiliary heat transfer models by computing variables at only a finite number of locations as defined by the user. Thus, modelling using this

computational technique is prone to certain levels of both error and uncertainties in solutions (The American Institute of Aeronautics and Astronautics Guide, 1998).

For ventilation processes involving heat transfer, an analysis highlighting an example of verification and validation of a CFD based *k-e* turbulence model was presented by Srebric and Chen, (2002) using air temperature and mean velocity as the parameters. While the computational velocities agreed well with the experimental data, the CFD code under-predicted the air temperatures with an uncertainty of 0.4°C (0.4K) as displayed in Figure 3.18. However, the consistency of the predicted computational trends confirms as an acceptable indicator for the solution to be satisfactory. The conclusive remarks from the work underlined the capability of the CFD code of simulating displacement within a built environment involving heat transfer although the degree of validation is essential (Oberkampf and Trucano, 2002)..

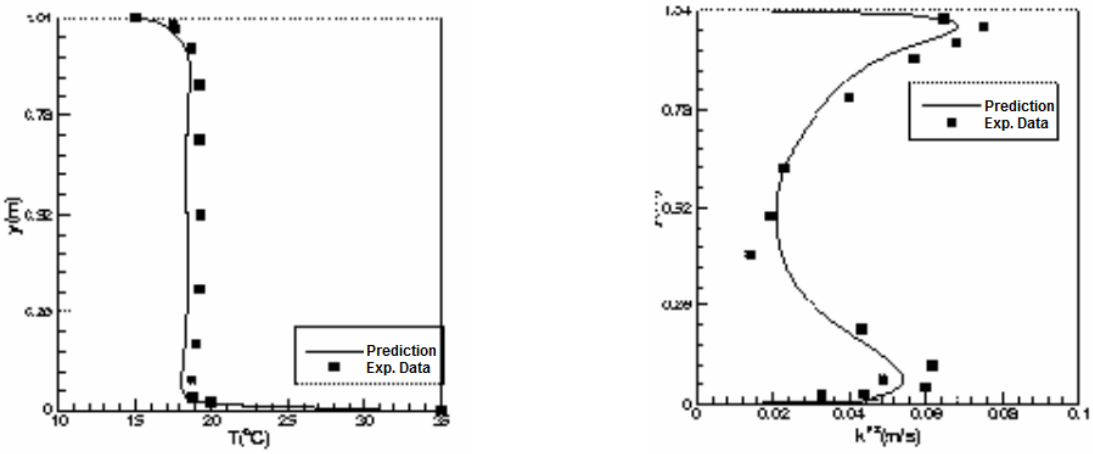

Figure 3.18 Validation of computed mean temperature and turbulence kinetic energy with experimental data (Srebric and Chen, 2002)

Computational investigations involving Euler-Euler multiphase scheme and *k-e* turbulence models have illustrated good quantitative agreement with experimental data indicating a mean and maximum error of ±5% and ±17% (Ekambara *et al*., 2008). Comparing results generated using CFD with experimental data is the most important part of reporting a CFD analysis for computational domains including flow, heat and mass transfer. Errors and uncertainties associated with CFD are usually evaluated by performing validation studies to illustrate that error trends as a function of their parameters remain systematic over the entire computational domain (Mehta, 1996, Roache, 1997, Lee, 2003). Hence, the fundamental strategy of validation is to identify

suitable experimental data in order to ensure the degree of accuracy associated with the numerical model and to quantify the error and uncertainty in the simulation (Chen and Srebric, 2002). With reference to the present study, a comprehensive comparison between the CFD and experimentally generated results is detailed in Chapter 7 – Comparison between CFD and Experimentation.

3.8 Summary

This chapter outlined the numerical methodology which was applied to the current study. The governing equations were presented, followed by the computational models and heat transfer equations which were used in the investigation. The FLUENT 14.0 commercial code which was used to simulate the flow with coupled heat and mass transfer analysis on the geometry matrix was described. The physical domain used to carry out the CFD investigation was detailed. In order to verify the CFD model, a grid verification procedure was carried out to determine the variation in results over increasing mesh sizes. Furthermore, the applied boundary conditions used to carry out all the analysis on the computational domain were defined. In summary, this chapter described the methodology from generating the physical domain of the heat pipe heat exchanger geometry to the process of applying the boundary conditions for numerical simulations in order to predict the performance of heat pipes within the computational domain.

Chapter 4
Experimental Set-Up and Procedure

4.1 Introduction

This chapter describes the experimental method that was used in this study. In order to undertake the experimental testing, a closed-loop low-speed wind tunnel was designed and commissioned in the School of Civil Engineering at the University of Leeds. The experimental work comprised of both qualitative and quantitative data analysis to determine the working performance of heat pipes by evaluating air velocity, pressure and temperature profiles upstream and downstream of the test section. Since the entire design of the wind tunnel was a part of the current study, the flow non-uniformity inside the test section along with turbulence intensity and temperature profiles were first characterised to comprehend its behaviour prior to proceeding with the study's experimentation.

The chapter further outlines the data acquisition devices that were used for taking point measurements and recording data. K-type thermocouples were used and connected to the data logging system in order to record time-dependant temperature measurements. In addition, the experimentation process incorporated a thermal visualisation technique which was carried out using an infrared thermal imaging camera. The final section of the chapter details the experimental procedure used for conducting both steady-state and transient experimentation on heat pipes.

4.2 Overview of the low-speed closed-circuit wind tunnel

The wind tunnel consisted of an overall plan length of 5.6m with a test section of the height, width and length of 0.5m, 0.5m and 1.0m. The method of operation of the tunnel was closed-circuit or return-flow, in which air that passed through the test section was drawn back into the fan and recirculated into the test section repeatedly. Guide vanes were used to turn the air flow around the corners of the wind tunnel while reducing the turbulence. The contraction, diffuser, test section and two corners were located at floor level and the return legs set with the axial fan are positioned vertically above the test section.

The elevation plan of the low-speed closed-loop wind tunnel is displayed in Figure 4.1. The transparent test section was designed in accordance with the dimensions used in the CFD set-up (Chapter 3 – CFD Theory and Modelling) in order to achieve an accurate evaluation of the results.

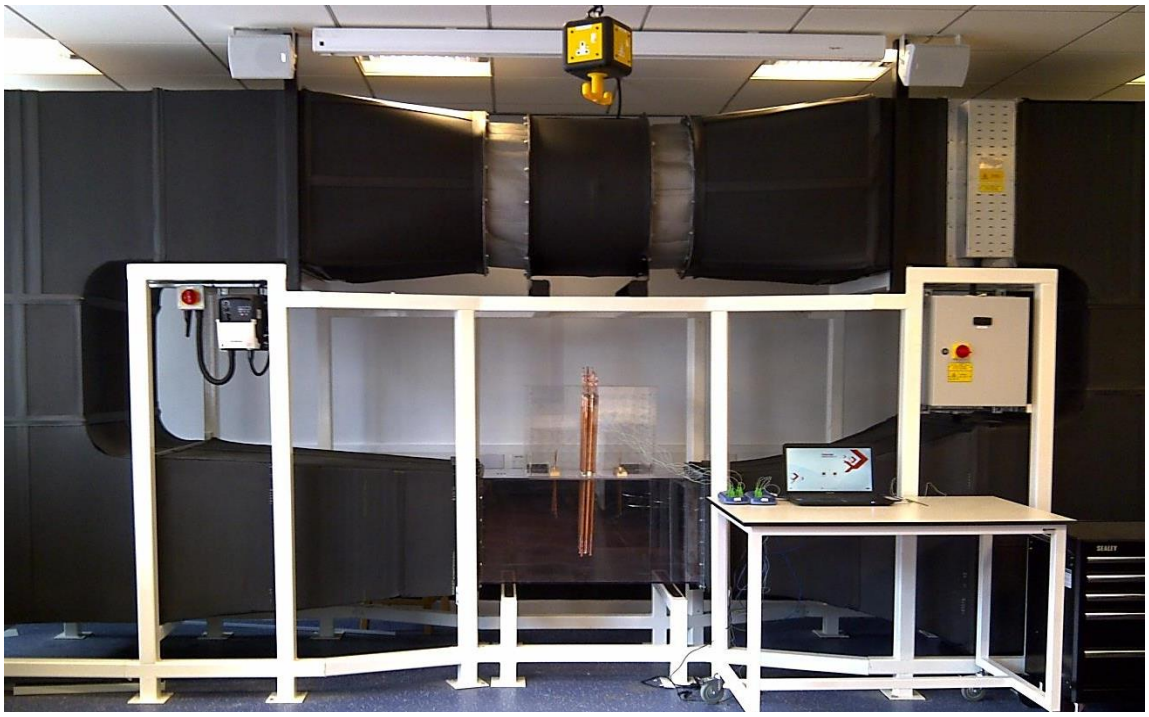

Figure 4.1 University of Leeds closed-loop wind tunnel side elevation

A 2.1kW, 710mm axial variable-revolution fan was used to deliver the required stationary air-flow within the test section which varied between 2-15 m/s. The air coming out of the tunnel exhaust was recirculated into the supply end of the tunnel to continue the closed-loop cycle. Variable-intensity heating elements of 15kW were positioned after the axial fan and prior to the first corner in order to generate the required static air temperatures for experimentation involving temperature variations. The wind tunnel facility was intended to be used for a wide range of applications including architectural and environmental aerodynamics. Hence it was essential that the flow quality in the test section met the standards for wind engineering studies. Figure 4.2 displays the schematic of the wind tunnel.

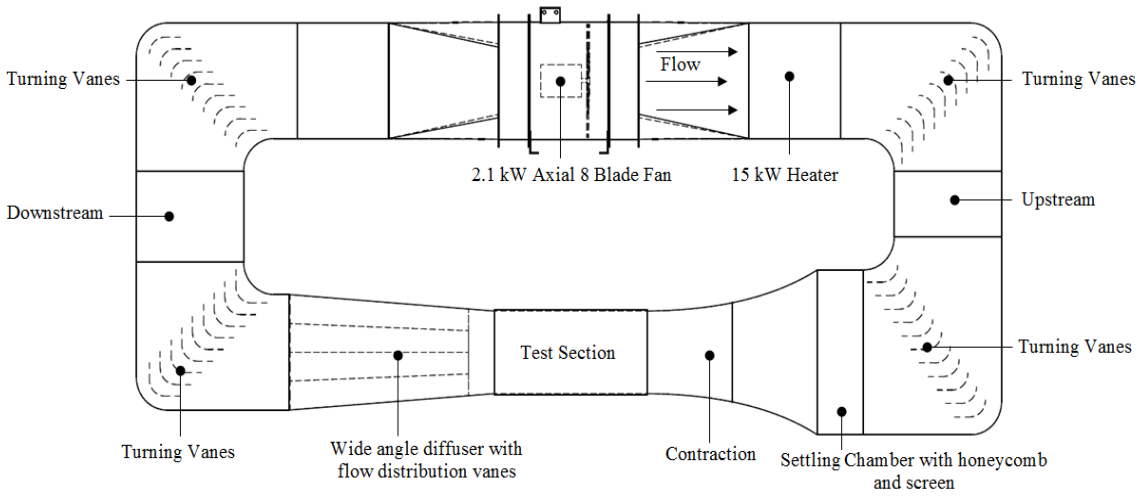

Figure 4.2 Schematic of the wind tunnel design and components

A summary of the wind tunnel design components and specifications are tabulated in Table 4.1.

Table 4.1 Summary of the design specification and dimensions of wind tunnel components

Component	**Basic Dimensions (mm)**	**Specification**
Test Section	500 (w) x 500 (h) x 1,000 (l)	Square cross-section,
Contraction	1,000 x 1,000 (inlet) / 500 x 500 (outlet)	4:1 ratio
Diffuser	500 x 500 (inlet) / 1,000 x 1,000 (outlet)	3:1 ratio, 8˚conical angle
Round to Rectangle Duct	700 (diameter) / 1,000 x 700 (outlet)	Anti-vibration
Settling Chamber	1,000 (w) x 1,000 (h) x 400 (l)	Honeycomb, wire mesh
Axial Fan	700 (diameter)	2.1 kW

4.3 Wind tunnel components and pressure loss profile

Design of individual wind tunnel components is one of the most important parameters in achieving a uniform airflow with minimal effect of turbulence. This section of the chapter briefly describes the major components used in the assembly of the closed-loop wind tunnel.

4.3.1 Test section

The rectangular test section had cross-sectional dimensions of 0.5m by 0.5m with a cross-sectional area of 0.25m^2. A large test section was desirable for the purpose of conducing experimentation involving a greater range of blockage sizes. The hydraulic diameter (D_H) of the test section was 0.5m. At an average wind speed of 3m/s in Doha,

Qatar (Weather History for Doha, Qatar, 2012), the air velocity of 10m/s was selected as a guide for a scaling factor of 1:10. Hence, the Reynolds Number was estimated at $264x10^3$ while the volume-flow rate inside the test section was calculated as $2.28m^3/s$ ($8{,}208m^3/hr$). The pressure and head loss coefficient for the test section was estimated at 0.91 and 4.64m. Figure 4.3 displays the dimensions of the test section which was designed and formed out of polycarbonate. The material was used due to its low friction and high heat resistance alongside being transparent to provide better flow visualisation.

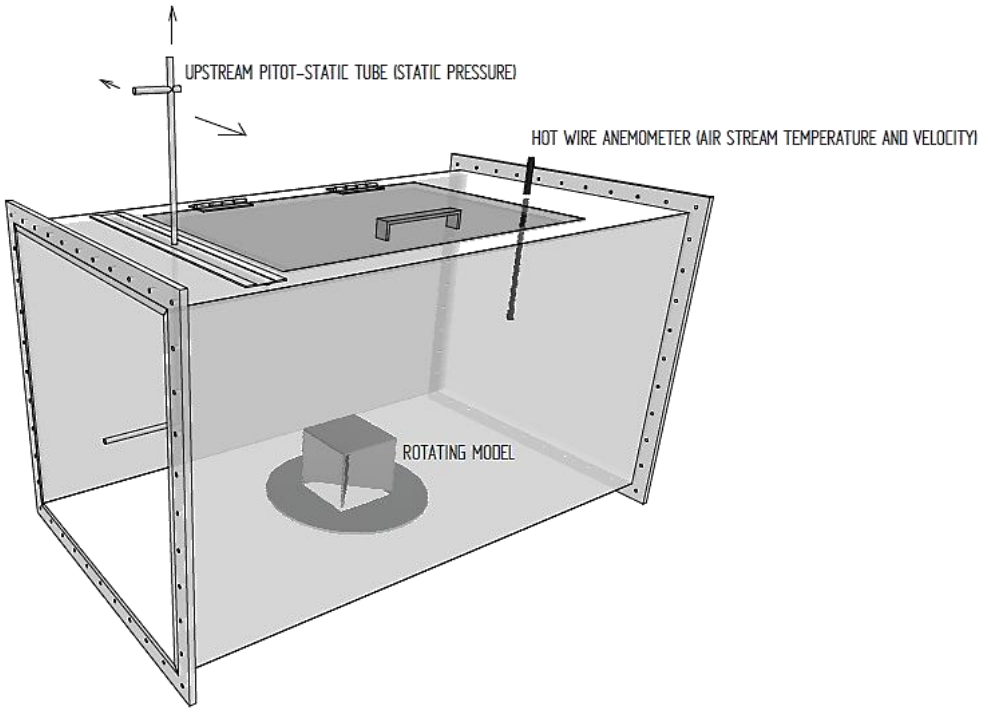

Figure 4.3 Design of the test section for the closed-loop wind tunnel

4.3.2 Contraction section

The contraction is a crucial section of a wind tunnel. The most widely accepted method for an engineering contraction includes a combination of two blended cubic arcs, each having its apex at one end of the contraction. When the dimensions of upstream and downstream contraction sections are fixed, the location of the matched points becomes the only parameter to establish the entire wall shape (Morel, 1997). Large contraction ratios are advantageous but require higher construction and running costs besides possible problems of noise and separation near the ends. Therefore contraction ratios between 6 and 9 are generally used for small wind tunnels (Mehta and Bradshaw, 1979).

The contraction section takes the flow from settling chamber to the test section while typically increasing the average speed by factors in the range of 6-10. To allow for a longer test section, the contraction section must have the ability to accelerate the flow with minimum separation and boundary layer growth, while decreasing non-uniformity and turbulence of its exit velocity into the test section, all attained within the shortest possible distance to make it desirable (Barlow *et al*., 1999). Further flexibility in design of wind tunnel contractions were demonstrated with the use of CFD to enable rapid testing of designs with varying curvature profiles in order to optimise contractions of arbitrary cross-section and wall profile. Numerical modelling allocates for design optimisation since experimental validations are performed after the construction (Sargison *et al*., 2004).

The designed wind tunnel for this study consisted of a test section connected to a contraction upstream with a contraction ratio of 4:1 in order to meet the maximum allowable space requirements within the Building Physics Laboratory. The cross-sectional dimensions of the contraction were 1m by 1m with an inlet area of $1m^2$. Figure 4.4 displays the design of the contraction section.

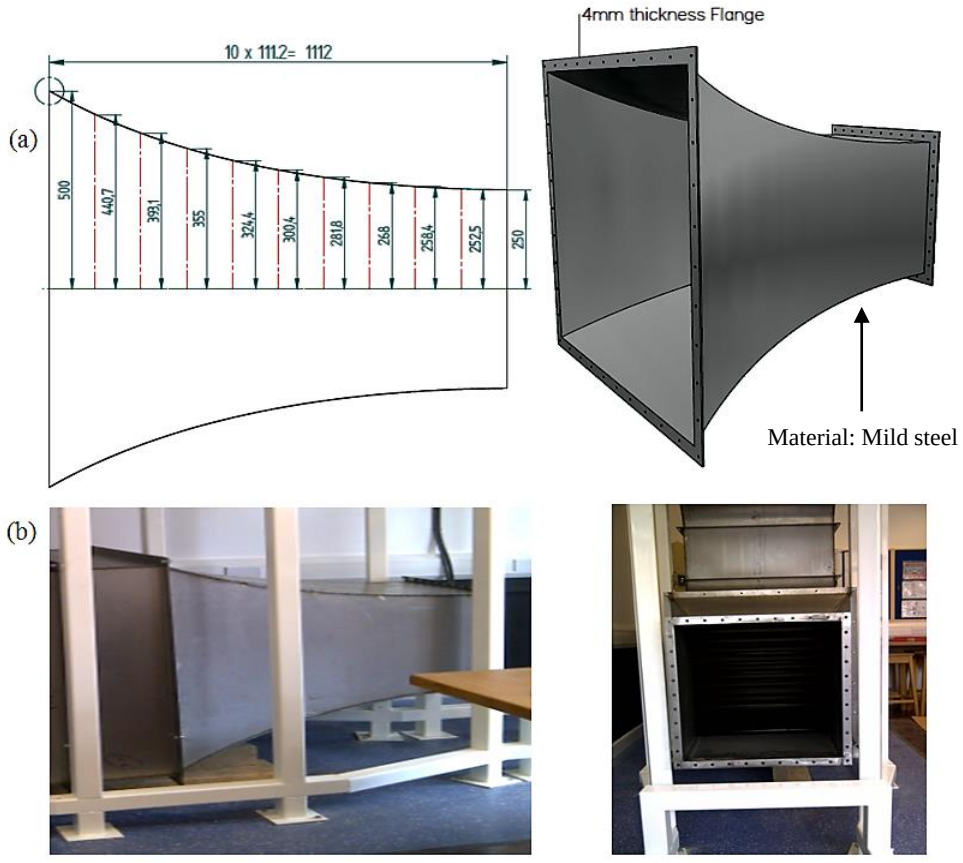

Figure 4.4 Design of the contraction section for the closed-loop wind tunnel

4.3.3 Diffuser section

Minimum energy loss corresponds to maximum pressure recovery. It is generally desirable to reduce the speed in the shortest possible distance without incurring flow separation (Barlow *et al.*, 1999). The diffuser of a closed-loop wind tunnel normally extends from the downstream end of the test section to the third corner of the tunnel. The conical expansion angle (θ_e) is the total angle formed by the walls of a circular diverging cone. The Area Ratio is defined as the ratio of largest cross-sectional area to the smallest. In the case of the diffuser, the Area Ratio is the ratio of outlet area over the inlet area. The Area Ratio along with diffuser angle 2θ, number of screens n, and the sum of all loss coefficients resemble the four most important parameters while considering the design of diffusers (Figure 4.5) (Mehta and Bradshaw, 1979).

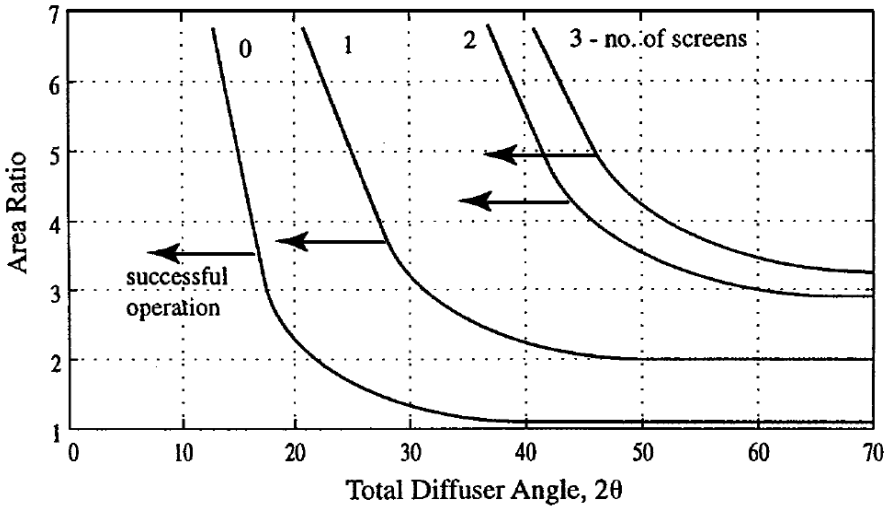

Figure 4.5 Design boundaries for diffusers with screens (Mehta and Bradshaw, 1979)

For the present study, the test section was connected to a diffuser channel downstream with a diffuser area ratio of 3:1 and the equivalent conical angle of 8° which was within the recommended range (Sahin *et al.*, 1995, Gan and Riffat, 1996, Mehta and Bradshaw, 1979, Barlow *et al.*, 1999). The cross-sectional dimensions of the diffuser were 1m by 1m with an inlet area of $1m^2$. Therefore, the velocity in the diffuser and the head loss was estimated as 3.26m/s and 0.24m. Figure 4.6 displays the design of the diffuser section.

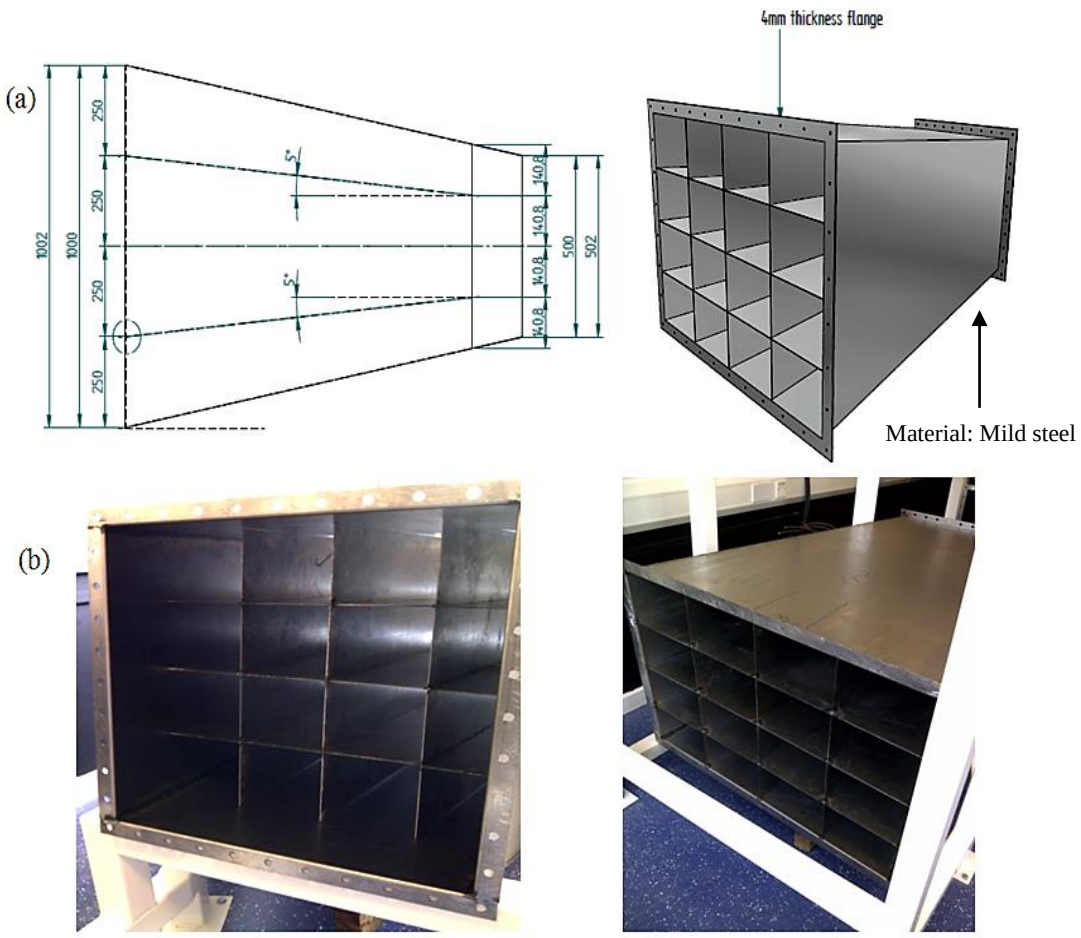

Figure 4.6 Design of the diffuser section for the closed-loop wind tunnel

4.3.4 Guide Vanes

In order to circumvent large losses and to maintain uniform flow throughout the circuit, the corners are equipped with guide or turning vanes. An unfilled 90° corner generates large eddy formations on the inner wall immediately downstream of the corner itself. Many wind tunnels use quarterly vanes of circular profile with prolongation at the trailing edge, having a minimum pressure-loss coefficient at a pitch value in between the range of 0.33 and 0.35 (Klein *et al.*, 1930).

The pitch is defined as the ratio between the spacing between vanes and the chord length. Appropriate design of the corners is critical since the four combined corners of a conventional closed circuit wind tunnel account for approximately 60% of the total losses within the tunnel (Barlow *et al.*, 1999). For the current design, the guide vanes were used to turn the air flow around the corners of the wind tunnel while reducing the

turbulence and power loss. Figure 4.7 displays the three-dimensional representation of the wind tunnel guide or 90° turning vanes.

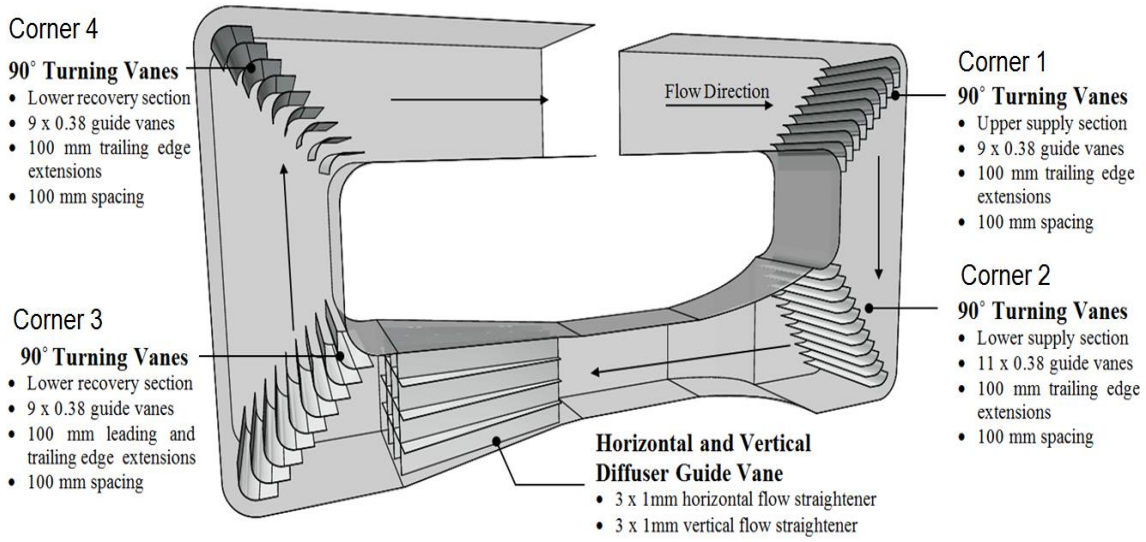

Figure 4.7 Three-dimensional representation of wind tunnel guide vanes

For the current design, guide vanes with a chord length of 157mm excluding the leading and trailing edges and a leading edge-to-leading edge spacing of 100mm are positioned at all 4 corners to straighten the flow and avoid areas of re-circulation. The guide vanes section was designed with the aim of minimising the pressure drop for flow in the 90˚ bends. The pitch value for the turning vanes in all four corners of the wind tunnel was 0.38.

4.3.5 Honeycomb flow straightener

Due to the insufficient length of the settling chamber located at the upstream of the contraction section, a honeycomb mesh in combination with a screen was installed to reduce the turbulence of the flow prior to entering the test section. The basic specifications of the hexagonal mesh included a cell size of 12.7mm with a material thickness of 0.127mm. The depth of the honeycomb was measured at 160mm. Therefore the reduction area into honeycomb area ratio was calculated at 0.961. The honeycomb and screen combination has been useful in eliminating the turbulence as found in several works from literature (Mehta, 1985, Soltani *et al*., 2010).

Figure 4.8 displays the diffuser section which was designed and built for the current closed-loop wind tunnel.

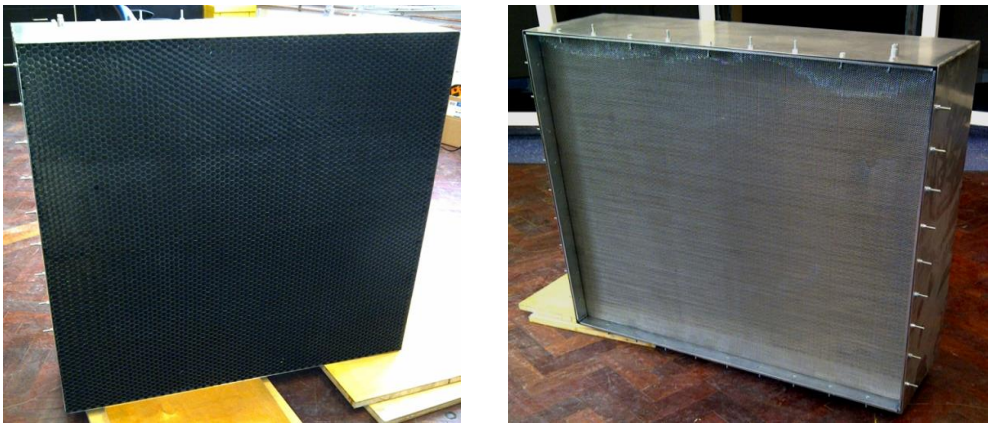

Figure 4.8 Design of the honeycomb screen flow straightener for the closed-loop wind tunnel

4.3.6 Total pressure loss

The total pressure loss coefficients and head losses were obtained for upstream and downstream wind tunnel sections alongside the corner vanes are summarised in Table 4.2. The total head loss for the wind tunnel was calculated at 13.35m providing a total pressure loss of 140.1Pa. Further details on the sectional pressure loss of the wind tunnel are provided in Appendix A.

Table 4.2 Summary of sectional pressure head losses

Wind tunnel section	Loss coefficient	Head loss (m)
First corner	0.65	0.35
Upstream horizontal duct	1.00	0.54
Upstream vertical duct	1.00	0.54
Downstream horizontal duct	1.00	0.54
Downstream vertical duct	1.00	0.54
Second corner	0.65	0.35
Contraction	-	3.97
Test section	0.91	4.64
Diffuser	0.45	0.24
Third corner	0.65	0.35
Fourth corner	0.65	0.35
Annular inlet	-	0.05
Annular outlet	0.09	0.94

Pressure loss calculations were conducted for a range of speeds measuring from 1m/s to 20m/s in the test section in order to plot a set of data within the desirable range. The

pressure loss curve at corresponding test section volume flow rates is displayed in Figure 4.9. The two parameters were found to be in direct proportion to each other. The volume flow rate displayed a linear increase with increase in test section velocities while the pressure loss was depicted to increase in an exponential behaviour.

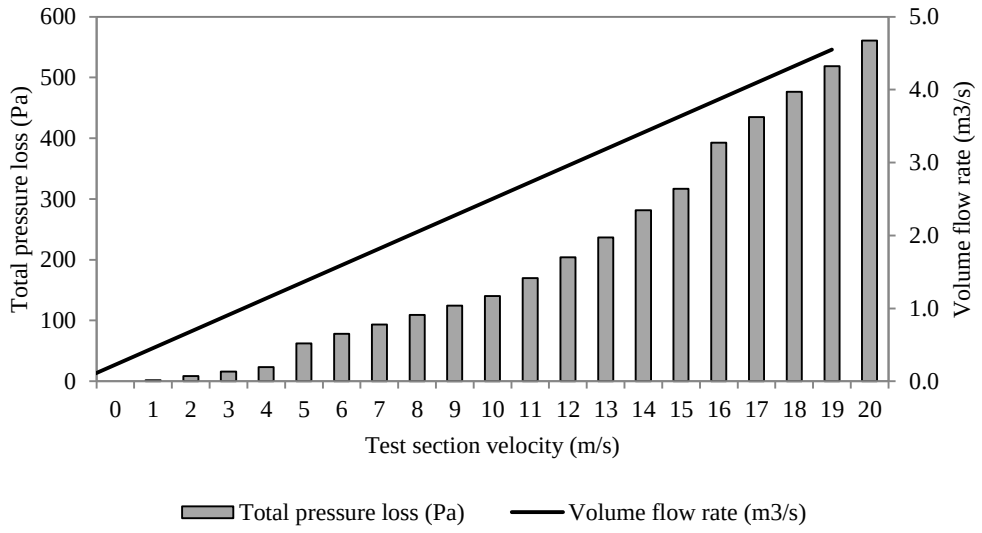

Figure 4.9 Pressure loss curve at corresponding test section flow rate

4.4 Characterisation of air flow profile and turbulence intensity

Prior to carrying out the experimentation, it was necessary to characterise the wind tunnel in order to evaluate the flow non-uniformity and turbulence to meet the recommended guidelines of below 1% (Barlow *et al*., 1999, Sedov, 1997). Performance testing on the wind tunnel assembly was conducted at five different fan input frequencies ranging from 10Hz to 50Hz. A total of 9 points were located across the test section as tabulated in Table 4.3.

Table 4.3 Co-ordinates of the measurement points for wind tunnel characterisation

Profile	**X (m)**	**Y (m)**	**Z (m)**
P1	0 - 1	0.125	0.125
P2	0 - 1	0.125	0.250
P3	0 - 1	0.125	0.375
P4	0 - 1	0.250	0.125
P5	0 - 1	0.250	0.250
P6	0 - 1	0.250	0.375
P7	0 - 1	0.375	0.125
P8	0 - 1	0.375	0.250
P9	0 - 1	0.375	0.375

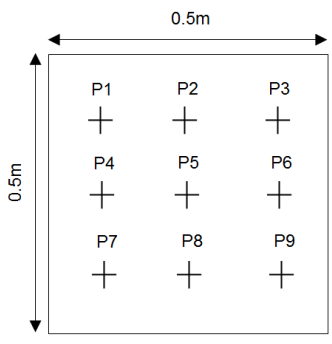

The hot-wire anemometer yielded mean air speed and its time-based equivalent. The average sectional velocity over the local value was used to estimate the non-uniformity coefficient for each point given by eqn. 25 (Sedov, 1997).

$$e = \frac{\Delta u}{\bar{u}} = \frac{u_i - \bar{u}}{\bar{u}} \qquad \text{(eqn.25)}$$

Where u_i represents the actual air velocity at the measurement point i and $\bar{u}$ represents the mean air velocity of all the points.

The level of turbulence intensity (I) in a wind tunnel can be expressed as a ratio of the standard deviation of the velocity fluctuations to mean stream velocity. The turbulence level can be defined as equated in eqn. 26.

$$I = \frac{\sigma_u}{\bar{u}} \qquad \text{(eqn.26)}$$

Where σ_u represents the standard deviation of the air velocity and $\bar{u}$ represents the mean air velocity of all the points.

Time based mean equivalent of the velocities were noted at each measuring point and a comparison was established against other points. Figure 4.10 displays the velocity profile at varying fan frequencies prior to adding the honeycomb section.

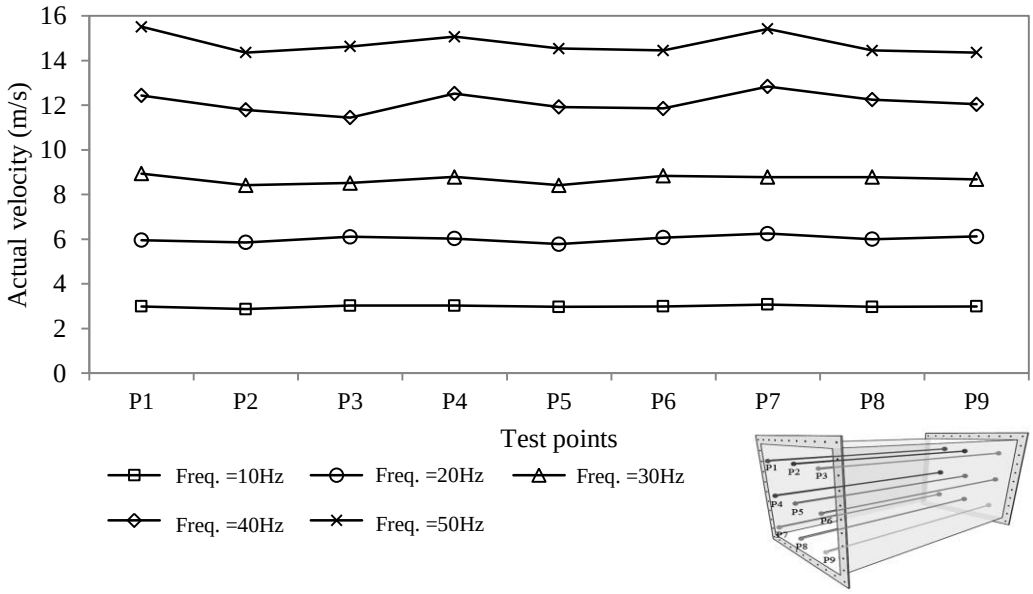

Figure 4.10 Velocity profiles in the test section at increasing fan frequencies before the addition of honeycomb section

A high variation in velocities was recorded at the measurement points with the mean non-uniformity obtained at 6.6%. Increasing values of measured variation occurred at

high frequencies with a maximum value recorded at 11.4%. It was observed that the turbulence in the velocity profiles increased as the fan inlet pressures was increased which was expected as the flow sheared away rapidly after contact with the 90° turning vanes which were located at the immediate upstream of the settling chamber. The detailed wind tunnel calibration results are provided in Appendix C.

With respect to Figure 4.11 the variation in actual test section velocity after adding the honeycomb structure is displayed. A honeycomb section in combination with a screen was thus installed to improve the overall flow performance. As expected, the honeycomb section assisted in straightening the flow considerably. A low variation was detected at all measuring points with a mean non-uniformity of 0.9% across all the points in the test section which is in the recommended range for wind tunnels (Sedov, 1997). At 10Hz or the minimum frequency, the mean non-uniformity was measured at 1.0% and it was observed that the variation reduced as the air velocities were increased. At 50Hz or the maximum fan frequency, a mean non-uniformity value of 0.7% was measured across the test section.

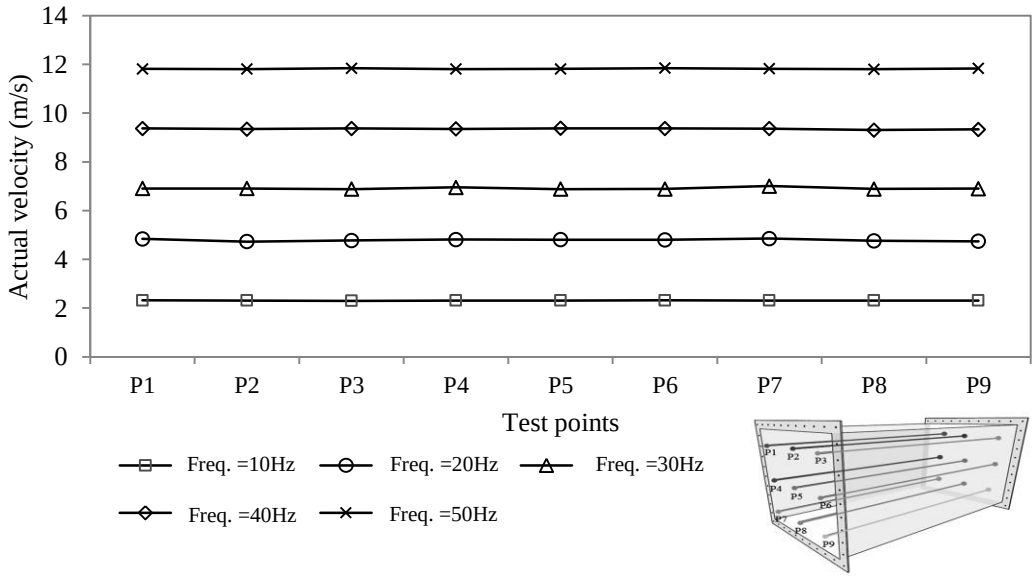

Figure 4.11 Velocity profiles in the test section at increasing fan frequencies after the addition of honeycomb section

Velocity measurement (u_c) at the centre of the wind tunnel test section was recorded and a ratio against the mean test section velocity $(\bar{u})$ was established to highlight the non-uniformity coefficient at the centre. Figure 4.12 (a) displays the turbulence intensity (I) before and after the addition of the honeycomb screen.

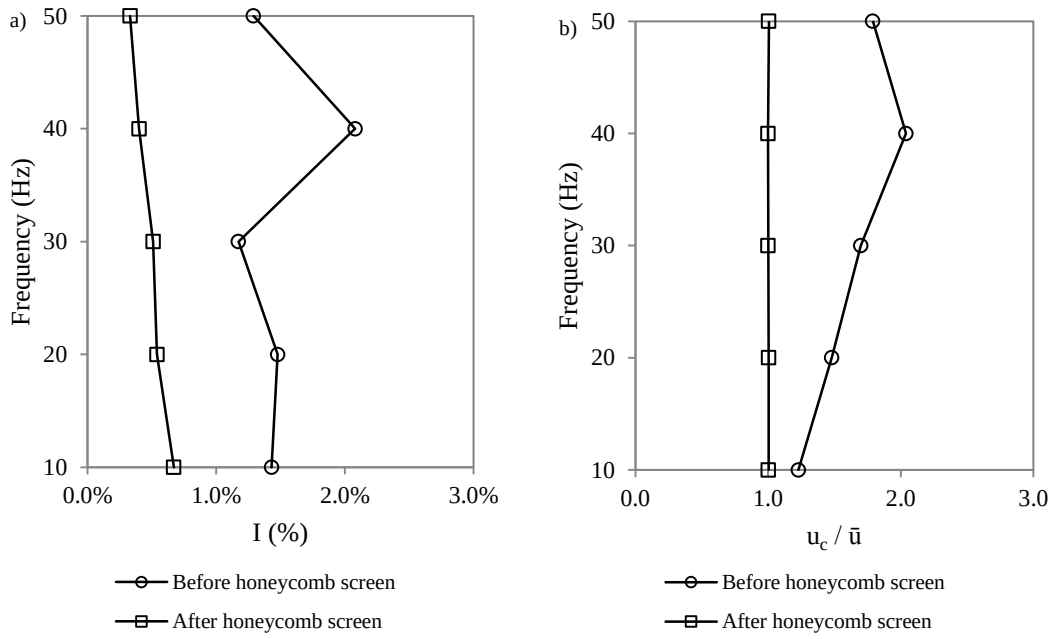

Figure 4.12 Variation of: a) I (%) and b) $u_c/\bar{u}$ at increasing fan frequencies

The mean value of turbulence intensity before the addition of the honeycomb screen was measured at 1.49%. The turbulence intensity however decreased to below 1% following the addition of the honeycomb screen. A steady decrease was observed as the fan frequencies were increased. Figure 4.12 (b) represents the variation of $u_c/\bar{u}$ before and after the addition of the honeycomb screen. The maximum non-uniformity coefficient at the centre of the test section was measured at 2.04 at 40Hz prior to the addition of honeycomb screen while the values remained consistent at 1.0 after the addition of honeycomb screen, confirming the uniform flow at the centre of the test section.

A total of 15 separate experimental test-runs were conducted for each test point with 3 individual tests for each fan frequency in order to get a precise approximation of the velocity variations. The pressure readings displayed a balanced trend with minimal variation between the different measurement points. At 10Hz, the mean pressure was measured at 4.16Pa which increased to 18.73Pa at 20Hz. At a maximum fan input frequency of 50Hz, the mean pressure value was measured at 102.74Pa. Figure 4.13 displays the variation in pressure profiles at increasing fan frequencies.

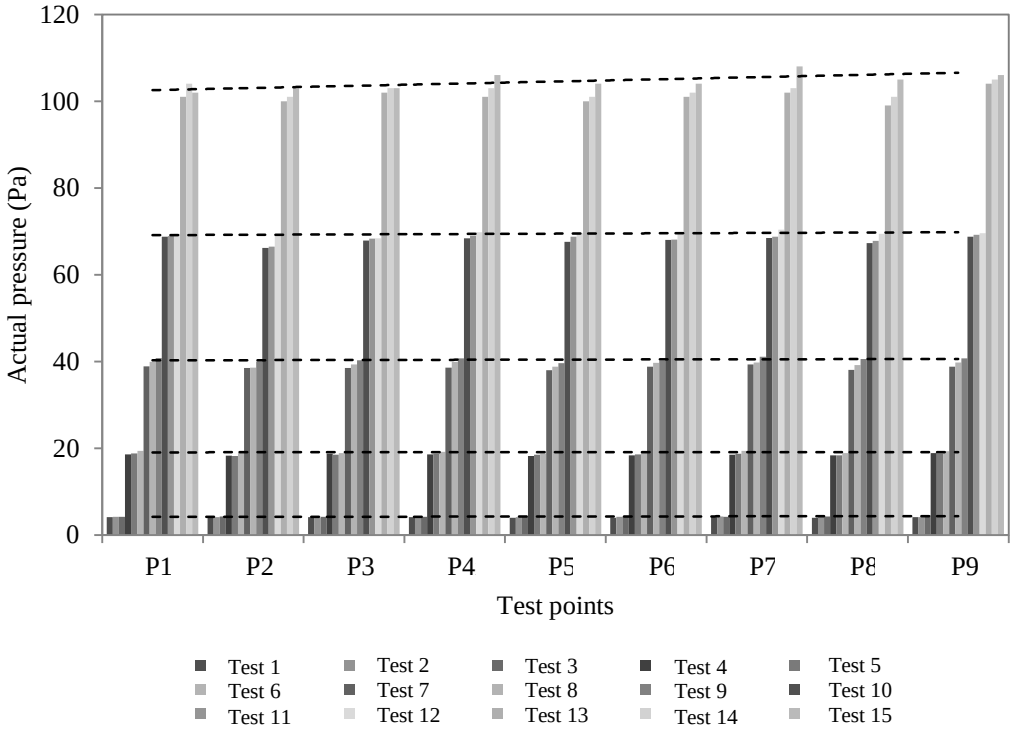

Figure 4.13 Pressure bars in the test section at increasing fan frequencies

The overall turbulence intensity (*I*) at the test points across the test section was further measured for flow characterisation of the wind tunnel. 15 individual tests were conducted once again wherein time averaged mean velocity values were noted and the standard deviation was calculated. The turbulence in the test section was highest at 0.97% and the mean value was calculated at 0.49%. The lowest value of turbulence intensity was recorded at 0.19%. The measured turbulence values did not exceed 1% at any of the points which was in the recommended range as found from literature (Barlow *et al.*, 1999).

The mean value of turbulence intensity at 10Hz or minimum fan frequency was 0.61% and it was observed that the turbulence levels decreased as the fan pressure increased. At the maximum fan frequency of 50Hz, the mean turbulence levels were calculated at 0.47%. Figure 4.14 displays the plot of turbulence intensity values obtained at the measurement points for all individual tests.

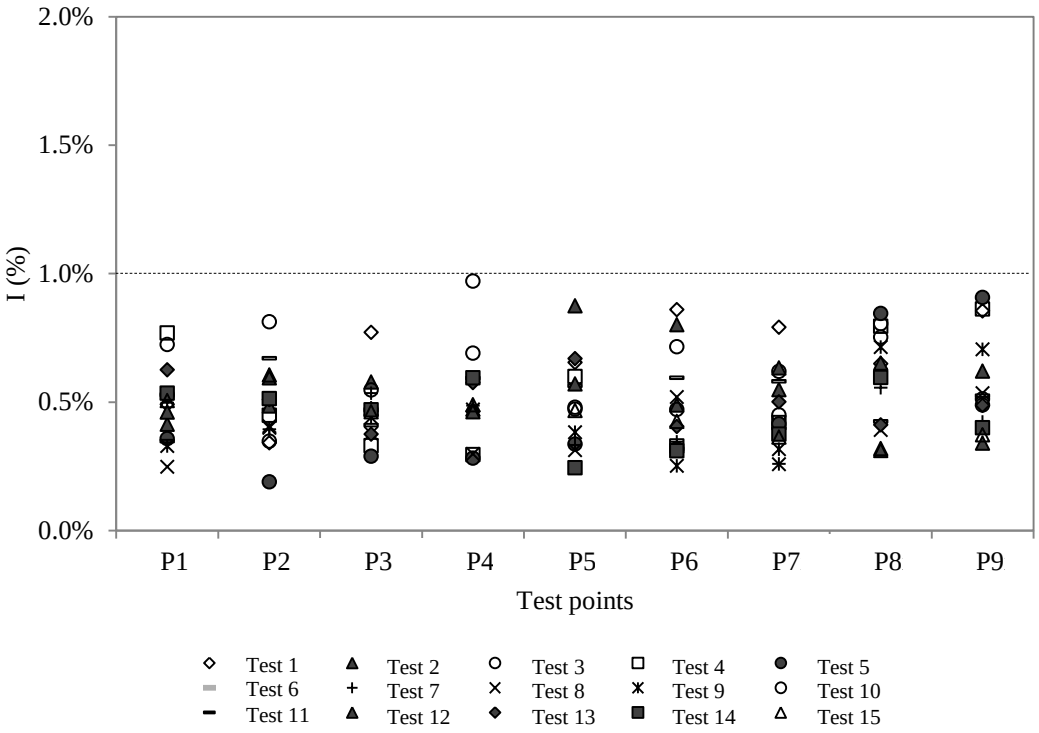

Figure 4.14 Turbulence intensity calculated at the measurement points

4.5 Characterisation of air flow profile under varying temperatures

Since the study's experimentation involved thermal analysis, it was essential to characterise the wind tunnel in response to high temperature airflows. The effects of temperature on air velocity were therefore examined to determine its impact on non-uniformity of the flow. The inlet temperature in the wind tunnel was varied starting from the 293K (or 20°C) under ambient conditions and increased up to 323K (or 50°C).

The test was conducted at a fan frequency of 10Hz thereby classifying the operation of the wind tunnel at its lowest working speed of 2.3m/s. The actual velocity readings at the measurement points were measured and the minimum non-uniformity was observed at 20°C, recorded at 1.0%. The non-uniformity increased to 1.1% at 30°C while the maximum non-uniformity was observed at 50°C, recorded at 1.3%. In general, the velocity profiles were observed to behave uniformly across all operating temperatures shown in Figure 4.15.

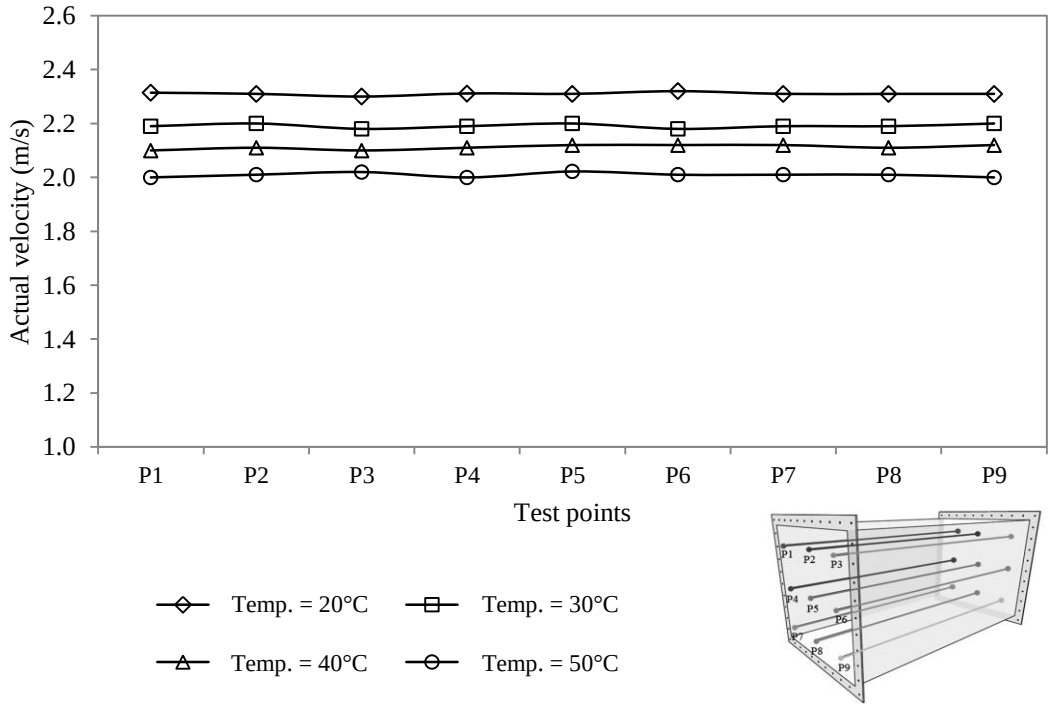

Figure 4.15 Velocity profiles at increasing operating temperatures

Velocity measurement (u_c) at the centre of the wind tunnel test section was recorded and a ratio against the mean test section velocity $(\bar{u})$ was established to highlight the non-uniformity at the point. Figure 4.16 (a) displays the variation of $u_c/\bar{u}$ and I (%) against increasing fan frequencies at constant temperature. As observed, the turbulence intensity decreases as the fan frequencies are increased, confirming a superior working performance of the wind tunnel at higher wind speeds. The ratio of $u_c/\bar{u}$ remained steady at approximately 1 for all frequencies indicating that the flow variation at the centre of test section remained constant at all equivalent wind speeds.

Figure 4.16 (b) depicts the variations as the operating temperature was increased and as observed, the turbulence intensity percentage was increased by 0.19% as the temperature was increased from 20°C to 50°C. This was expected as the increasing kinetic energy of the air particles increased the corresponding turbulence intensities of the particles (Cochran, 2002). The ratio of $u_c/\bar{u}$ increased as the actual velocity values decreased from the mean at increasing temperatures to maintain the energy balance of the system.

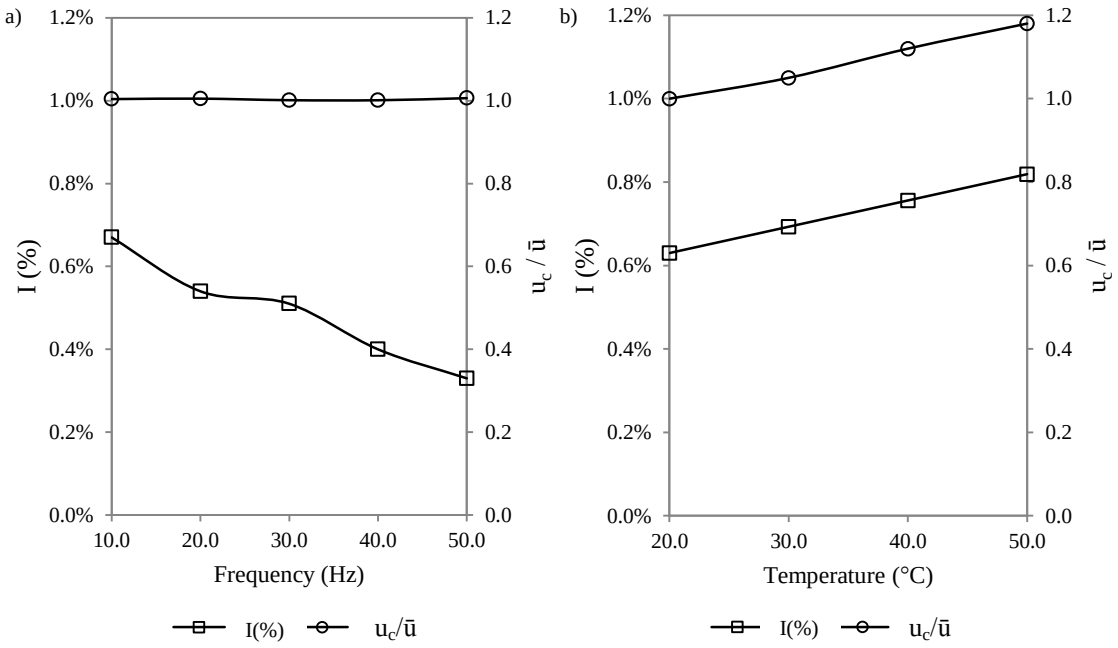

Figure 4.16 Variation of $u_c/\bar{u}$ and I (%) at: a) increasing fan frequencies b) increasing operating temperatures

A measurement of mean velocity across the test section of the wind tunnel was taken at operating temperatures ranging from 20°C up to 50°C. This was done to determine the percentage reduction in velocity with the increase in temperature, the results of which are tabulated in Table 4.4.

Table 4.4 Velocity reduction percentage at increasing wind tunnel operating temperature

Operating temperature (°C)	**Operating temperature (K)**	**Mean velocity (m/s)**	**Mean reduction (%)**
20	293	2.37	0.0%
22	295	2.34	1.3%
24	297	2.31	2.5%
26	299	2.30	3.0%
28	301	2.27	4.2%
30	303	2.25	5.1%
32	305	2.22	6.3%
34	307	2.20	7.2%
36	309	2.17	8.4%
38	311	2.15	9.3%
40	313	2.12	10.5%
42	315	2.09	11.8%
44	317	2.06	13.1%
46	319	2.04	13.9%
48	321	2.03	14.3%
50	323	2.01	15.2%

A steady decrease in velocity was observed as the operating temperatures were increased highlighting an inverse relationship between the two parameters as illustrated in Figure 4.17.

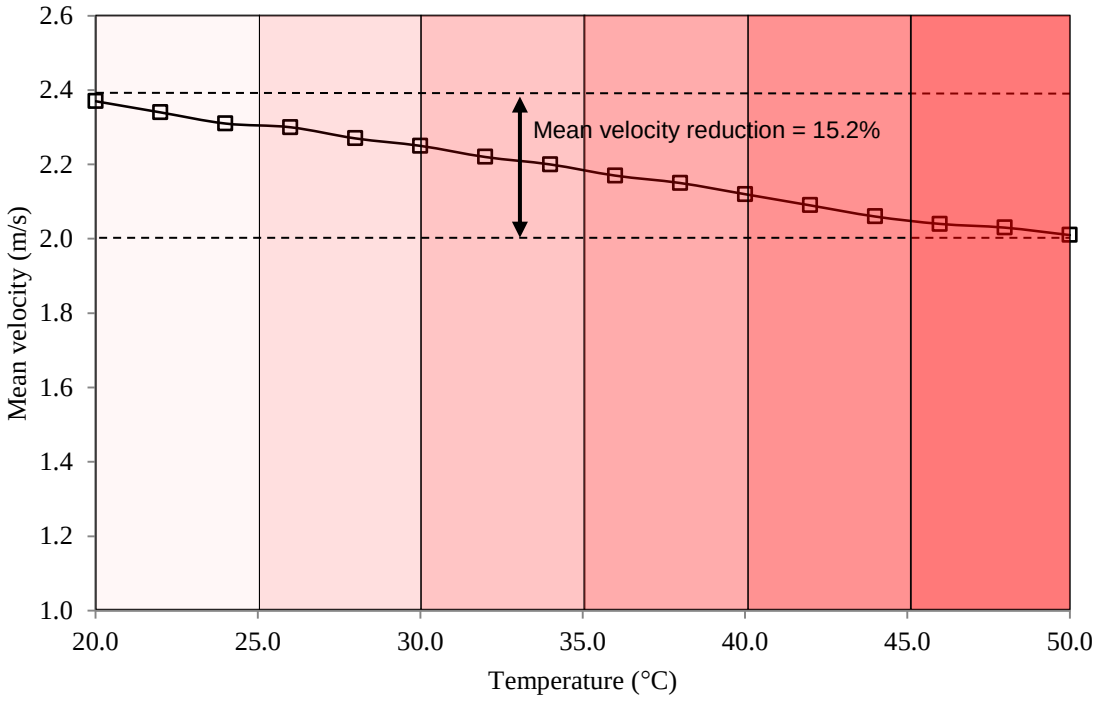

Figure 4.17 Relationship between mean velocity and wind tunnel operating temperature

The total decrease in mean air velocity was 0.36m/s from 2.37m/s at 20°C to 2.01m/s at 50°C. As a result, the mean velocity reduction was obtained as 5.1% at 30°C, which increased to 10.5% at 40°C and the maximum velocity reduction was observed at 50°C at 15.2%. The colour schemes highlight the increasing temperatures by a factor of 5°C.

4.6 Characterisation of air temperature profile

In addition to the characterisation of air velocity, the temperature variations in the test section were also measured. A transient test was conducted for 300 seconds using K-type thermocouples located at the measuring points for recording temperatures. Two sets of experiments were conducted; one with the heating elements turned off and the other with heating elements turned on. The test was conducted at increasing fan frequencies. Table 4.5 displays the mean temperature profiles obtained with respect to the fan frequencies along with the standard deviation (σ_t) and actual temperature

variation percentage. At lower fan frequencies, the variation percentage of temperatures was the lowest with 0.49% measured for 10Hz.

Table 4.5 Mean test section temperature variation at increasing fan frequencies

Freq. (Hz)	Max. temp. (°C)	Min. temp. (°C)	Mean temp. (°C)	σ_t	Variation (%)
10.00	19.96	19.86	19.92	0.03	0.49%
20.00	20.27	20.04	20.16	0.07	1.14%
30.00	20.74	20.36	20.57	0.12	1.86%
40.00	21.52	20.95	21.28	0.16	2.66%
50.00	22.67	21.70	22.22	0.29	4.33%

It was observed that both the actual temperature values along with the standard deviation increased as the fan frequency increased. This was expected due to the heat produced by rotating friction of the fan blades. The standard deviation (σ_t) of temperature recorded was maximum at 50Hz with a value of 0.29, at which the temperature variation was 4.3%. The graphical representation of the results is plotted in Figure 4.18.

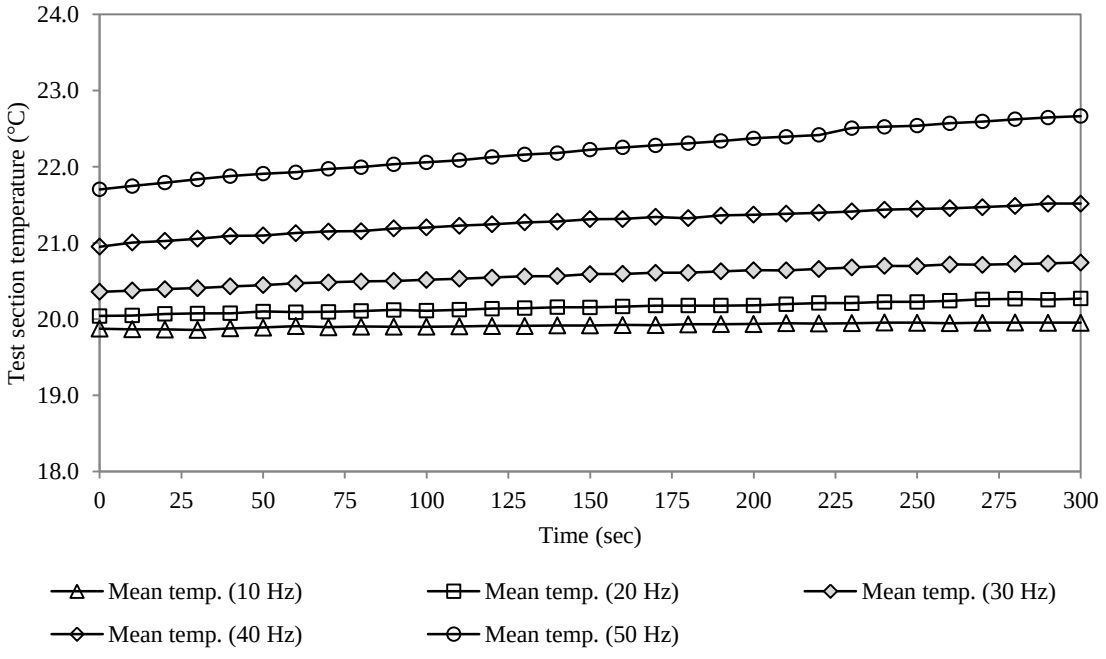

Figure 4.18 Mean test section temperatures at increasing fan frequencies without heating elements

4.7 Heat losses and generation of thermal boundary layer profile

The final wind tunnel characterisation test was conducted on determining the heat losses and variation associated with the test section temperature at a varying inlet temperature

from the heating elements. The transient results are plotted in Figure 4.19. The test was conducted at 10Hz (velocity of 2.3m/s) and the heating elements were turned on and off in a parabolic profile to understand the variation as the temperature increases and decreases. Furthermore, the characterisation yielded the heat losses from the test-section when the wind tunnel was in operation. An additional thermocouple was located at the immediate outside the test-section (distance of 0.1m) within the ambient laboratory environment in order to quantify the variation in temperature thereby providing a measure of heat losses to the surroundings.

The transient assessment was conducted for the duration of 600 seconds. The average variation in temperature was noted at 5.4% during the run-time of 600 seconds. In general, the variation in temperature profile was found to be below 10% during the entire duration of the experiment. The mean σ_t was recorded at 1.16 with over the entire duration of the experiment. The deviation was at its highest during the first 200 seconds of run-time and the values were noted converge in the range of 1.0 once the set-point temperature produced by the heating elements normalised.

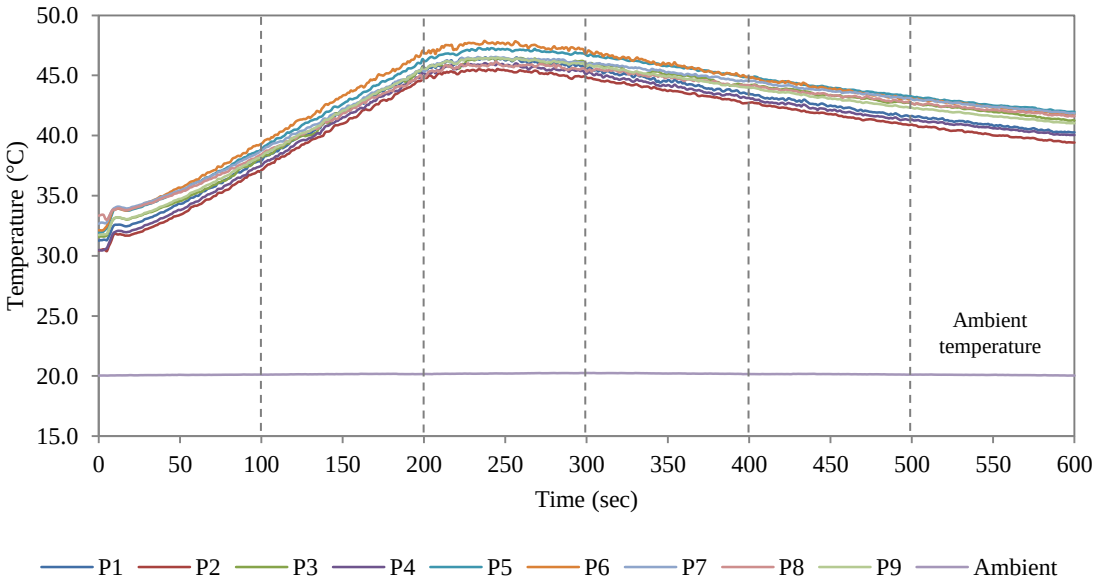

Figure 4.19 Time dependant air temperature profile in the test section at varying inlet temperatures

With respect to the heat losses, the average room temperature during the duration of the test was recorded at 20.17°C while the maximum temperature was recorded at 20.25°C when the heating elements reached their maximum point, thus indicating a differential of 0.08°C. Using the U value (overall heat transmission coefficient) for the test-section

wall surface as 4.9W/m^{2}K (PXTD 236, 2013), the heat loss through each wall was calculated at 0.19W, thus making the heat losses negligible for the experimentation.

A comparison was established between the CFD predicted thermal boundary layer to the experimentally obtained values. The tests were conducted at test section temperatures of 20°C and 50°C. Figure 4.20 (a) displays the graphical representation of the streamwise variation of the vertical temperature profile in the test section at 20°C while the profile at 50°C is depicted in Figure 4.20 (b).

Thermal stratification effects were observed to be more influential when the temperature was increased to 50°C. Temperature gradient at the walls of the test section was higher in comparison to that of the flow in the middle of the test section due to the thermal effects of the wall. It was noted that at a test section operating temperature of 20°C, the thermal boundary layer profile does not vary greatly. The thermal boundary layer thickness was 0.04m. Good correlation was observed between the numerically predicted and experimentally measured quantities.

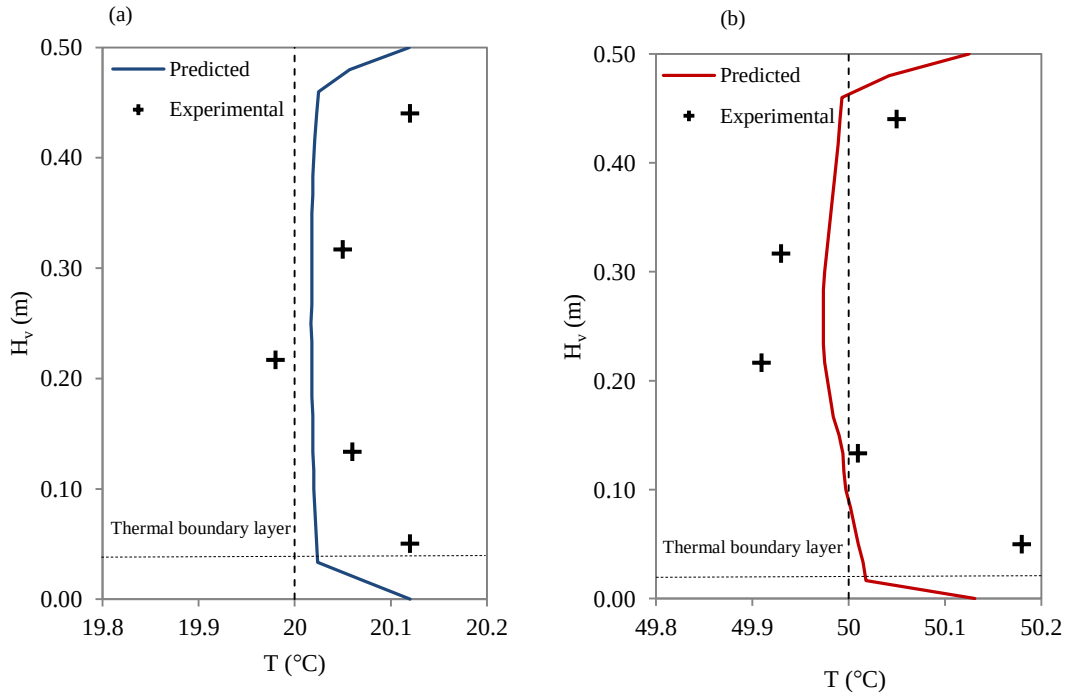

Figure 4.20 Streamwise variation of the vertical temperature profile at: a) 20°C b) 50°C

Due to the friction caused by the heating elements and the fan blades, the operating temperature in the test section was found to increase with increasing frequencies. An increase of 2.3°C was observed from the nominal temperature value of 20°C at a fan

frequency of 50Hz while a larger increase of 5.8°C was observed from the nominal temperature value of 50°C at the same frequency. The rate of increase in temperature was found to be directly proportional to the increase in fan frequency and the inlet temperature of the wind tunnel. Figure 4.21 displays the mean operating temperature in the test section with respect to increasing fan frequencies.

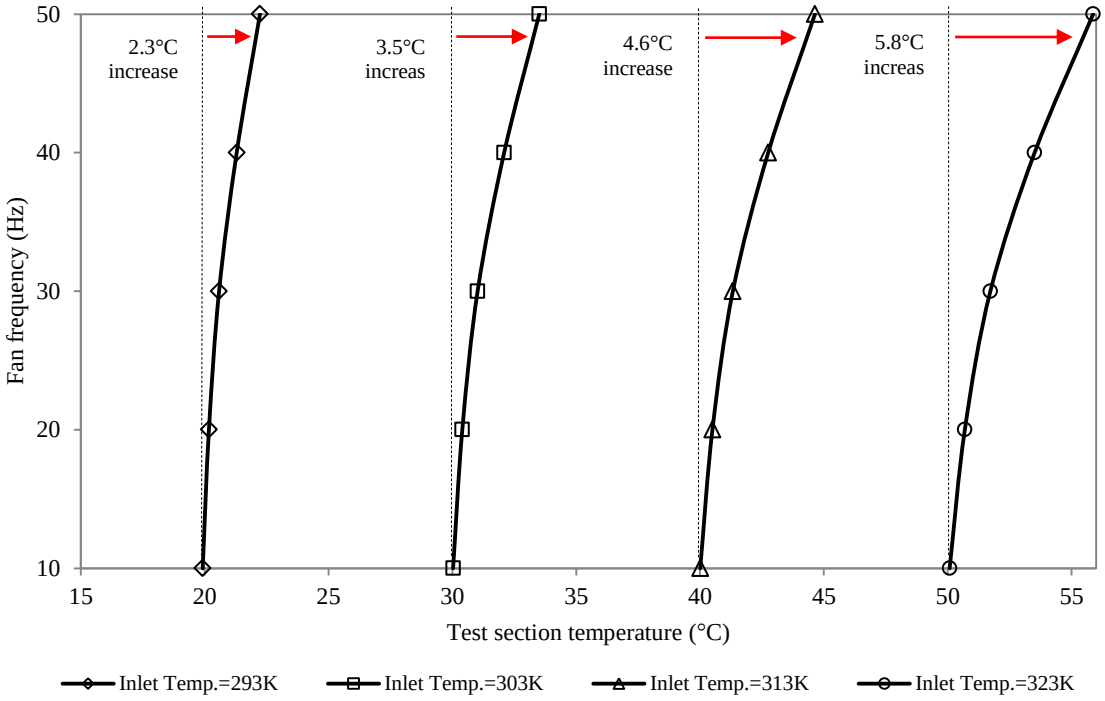

Figure 4.21 Test section mean operating temperature at increasing fan frequencies

The characterisation testing was repeated thrice at 10Hz in order to analyse the error associated with experimental uncertainties since the study's testing involved the operation of the wind tunnel at its lowest frequency. The error associated with the velocity parameter between the three test runs at 10Hz was 1.6%. With regards to the temperature measurements, the error associated with the temperature variations between the three test runs was recorded at 0.5%.

The wind tunnel characterisation study revealed that the velocity non-uniformity coefficient in the test section was 0.9% while the mean turbulence intensity was 0.49%. Furthermore, the characterisation study showed that mean variation in test section temperatures in response to heating elements was 5.4%. Further details on the numerical flow and thermal characterisation of the wind tunnel are provided in Appendix B.

4.8 Data acquisition devices

Subsequent to the characterisation of flow and thermal profiles within the wind tunnel, this section of the chapter details the data acquisition devices that were used for recording measurement readings and conducting the actual heat pipe experimentation.

4.8.1 Temperature measurements

Thermocouples are the most extensively used temperature sensors since they are cheap, interchangeable and can measure a wide range of temperatures. The PICO Type K Thermocouple (exposed wire, Polytetrafluoroethylene (PTFE) insulated) with a tip diameter of 1.5mm and a tip temperature range between -75°C to 250°C were used for the present study. The maximum allowable measurement uncertainty of the device at 0°C was 0.5°C while the maximum allowable uncertainty was 0.6°C at a temperature of 50°C. The thermocouples were connected to a TC-08 Thermocouple Data Logger which included a USB interface and had a capacity of 8 thermocouple channels. The high (20-bit) resolution ensured that the TC-08 could detect minute changes in temperature.

4.8.2 Infrared thermography

A FLUKE Tir1 Thermal Imager was used to capture the thermal images of air and heat pipe temperatures at different intervals. The measurement range of the FLUKE Tir1 thermal imaging camera was -20 to 100°C at an accuracy of ±2°C. The dimensions of the unit measured 270 x 130 x 150cm with the results being displayed on a 9.1cm screen. The FLIR-$T650_{SC}$ was a second infrared camera used for detecting thermal and visual images. The 640 × 480 infrared detector incorporated 0.03°C sensitivity and ±1°C accuracy resulting in high resolution and image quality for precise readings on small targets.

4.8.3 Velocity measurements

The digital hot-wire anemometer (TESTO 425) was used for measuring readings of air velocity. The accuracy of the sensor was ±0.03m/s at a resolution of 0.01m/s. The hot-wire anemometer was placed perpendicular to the flow and the uncertainty was ±0.08m/s for a velocity value of 1m/s and ±0.43m/s for the velocity reading of 8m/s. The uncertainty was ±1.03m/s for velocity values over 20m/s according to the

calibration certificate. Figure 4.22 displays the plot of the upper and lower uncertainty values for the hot-wire anemometer. The error uncertainties in recording the measurements were higher at lower speeds with a maximum of 7.4% at 1m/s. The mean error in measurements due to uncertainties was measured at 5.2% between speeds ranging from 1m/s to 20m/s.

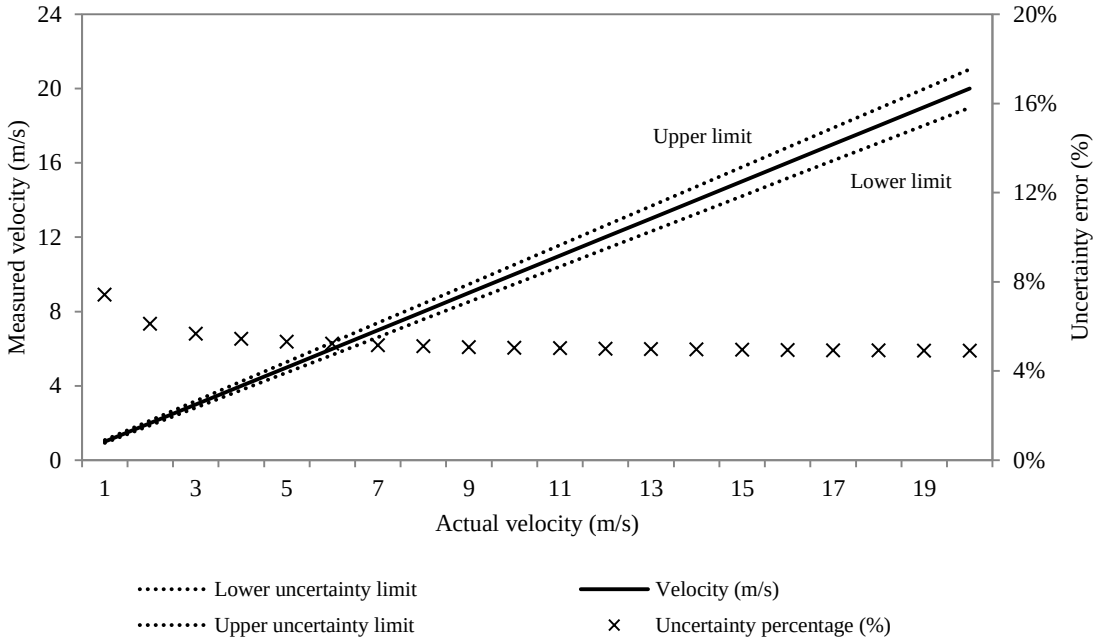

Figure 4.22 Measurement uncertainties recorded from the hot-wire anemometer

4.8.4 Pressure measurements

The dynamic pressure readings were recorded using DPM ST650 micro manometer connected to the Model 166T telescoping stainless steel pitot tube having of a standard 1/8 inch tip diameter. The measurement uncertainties associated with the device was ±1.0% of the reading at 22°C. Further details on the calibration of the data acquisition devices are provided in Appendix C, Section C.6, C.7 and C.8.

4.9 Experimental apparatus

This section of the chapter describes the design specifications of the experimental apparatus comprising of the heat pipes and the cold sink.

4.9.1 Cylindrical heat pipes

Cylindrical copper heat pipes were manufactured as per the design specifications. The heat pipes were charged with water and R-134a as the working fluids comprising of 2/3rd of the evaporator length, thus indicating a fluid volume of 0.000054m^3. The working sub-atmospheric pressures were set to saturation and at an operating temperature of 293K. The heat pipes were vacuum sealed at the end of the tube with the end cap incorporating a diameter of 3mm greater than the actual pipe diameter. Figure 4.23 displays the sealed heat pipes which were used in the experimental study.

Figure 4.23 Vacuum sealed copper heat pipes

The total length of the heat pipes was 800mm and the sections were separated in the centre using a connecting plate allowing identical evaporator and condenser sectional lengths of 400mm each. The dimensions of the evaporator and condenser sections and the main parameters of the manufactured heat pipes are displayed in Figure 4.24.

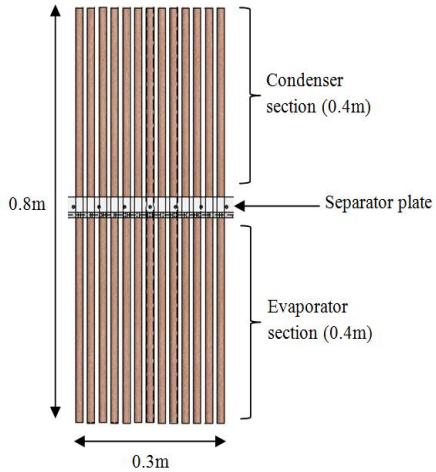

Description of the manufactured heat pipes

Parameter	Value / description
Nos.	19
Pipe material	Copper
Pipe diameter	15.9 mm
Evaporator length	400 mm
Condenser length	400 mm
Total length	800 mm
Working fluid	Water / R134a
Working temperature	0-100°C
Orientation	Vertical (90°)

Figure 4.24 Main parameters of the manufactured heat pipes

4.9.2 Cold sink

The cold sink or cold interface acted as the condenser section for the heat pipes and was assigned a control volume measuring 598mm by 398mm with a height of 455mm. In order to supply the cold temperature, air holes measuring 30mm in diameter were drilled in all four corners of the sink and flexible ice pockets were slotted within to generate the required temperatures and allow the cold air to escape through the holes and on to the heat pipes. The dimensions of the cold sink are displayed in Figure 4.25.

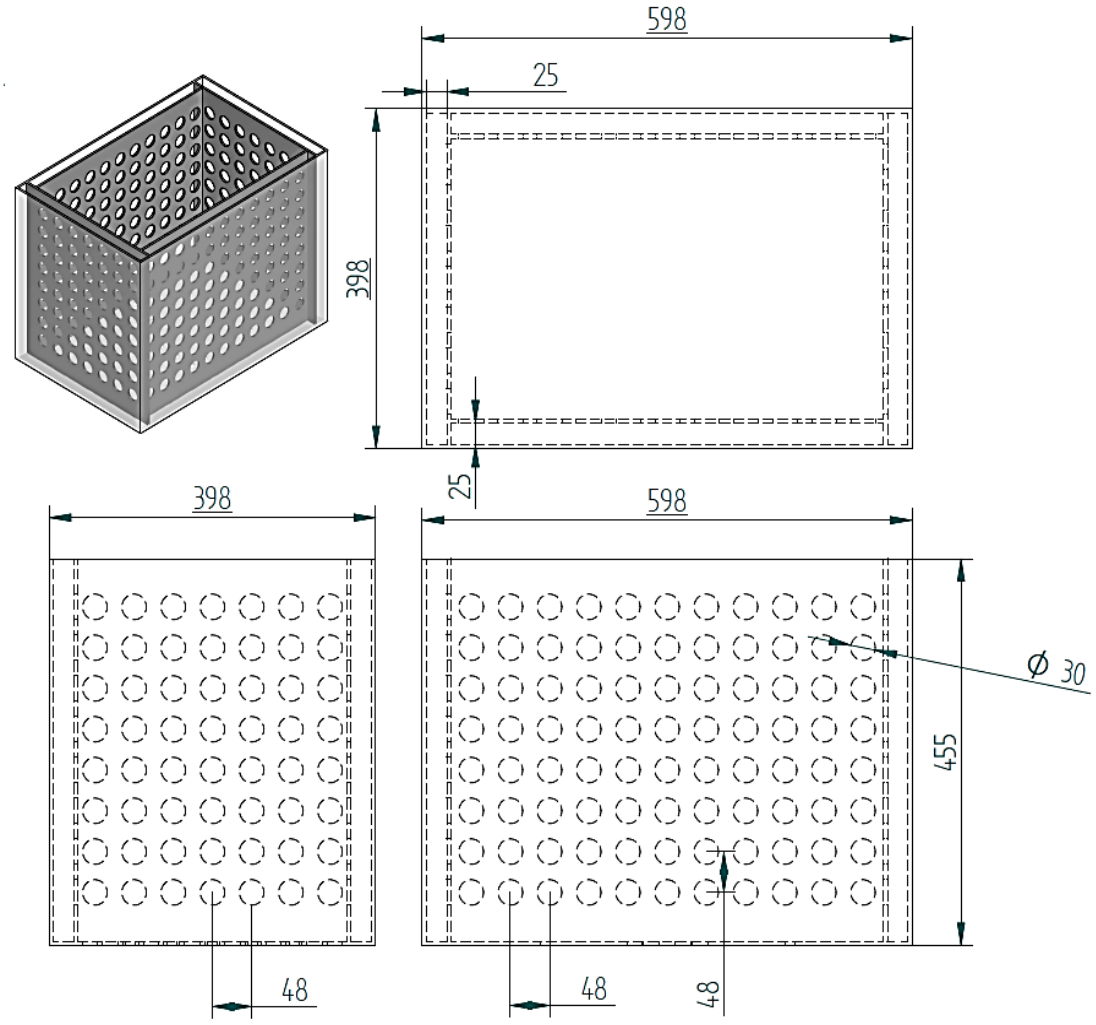

Figure 4.25 Geometrical dimensions of the cold sink

The cold sink was manufactured out of polycarbonate due to its low friction properties and its ability to withstand low temperatures. The performance of the cold sink was first determined in order to depict the stabilisation time for maintaining sink temperatures, the experimental set-up of which is provided in the next section.

4.10 Experimental set-up

This section of the chapter describes the set-up used for conducting the various experimental tests. One of the major features of this investigation was to set-up a test rig capable of adequately quantifying the thermal performance of a heat pipe heat exchanger against a range of working conditions. As a result, the designed wind tunnel was capable of achieving air temperatures ranging from 293K to 323K and air velocities ranging from 2.3m/s to 11.8m/s. The experimental set-up ensured the scope of testing a range of various climatic conditions alongside validating the numerical results.

4.10.1 Test set-up for monitoring the thermal behaviour of the cold sink

The first step of the experimental phase was to monitor the thermal behaviour of the cold sink with respect to time. Figure 4.26 displays the set-up and apparatus used for conducting the transient test on the cold sink.

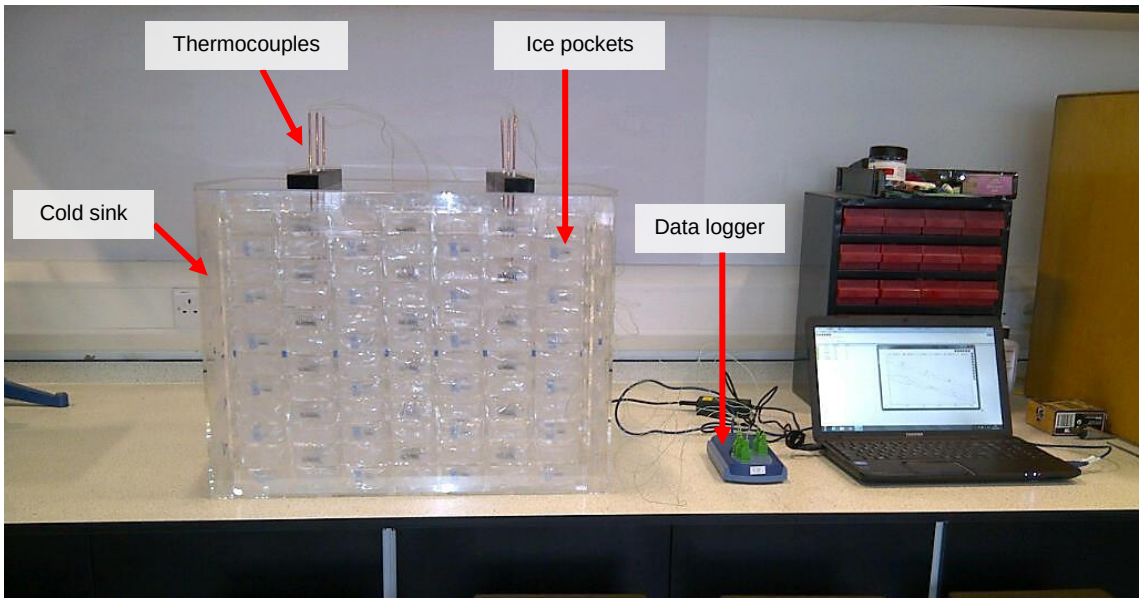

Figure 4.26 Experimental set-up for testing of the cold sink

Since the wind tunnel was capable of producing heated temperatures within the control volume in the test section, it was essential that the heat sink requirements were met accordingly in order to ensure that the efficient working of the closed-loop heat pipe cycle. The control volume of the cold sink measured 0.6m by 0.4m with a height of 0.5m, the cross-sectional area of which was calculated at 0.24m^2. The cooling process was carried out by positioning sealed ice pockets on all 4 walls of the control volume,

transferring the cold temperature to the entire physical domain. Each ice pocked had a fill volume of 12ml and a total of 49 ice pockets were used per side of the cold sink.

Temperature measurements were carried out on the empty chamber by connecting 6 K-type thermocouples upstream and downstream of where the heat pipes would be eventually positioned. A transient test was conducted for approximately 5 hours starting from when the sealed ice pockets were initially positioned and ending when the ice pockets were completely melted.

4.10.2 Test set-up for monitoring the thermal behaviour of the heat pipes

Following the performance monitoring of the cold sink, the heat pipes were tested for correct functionality. Figure 4.27 displays the set-up and apparatus used for conducting the transient test on heat pipes.

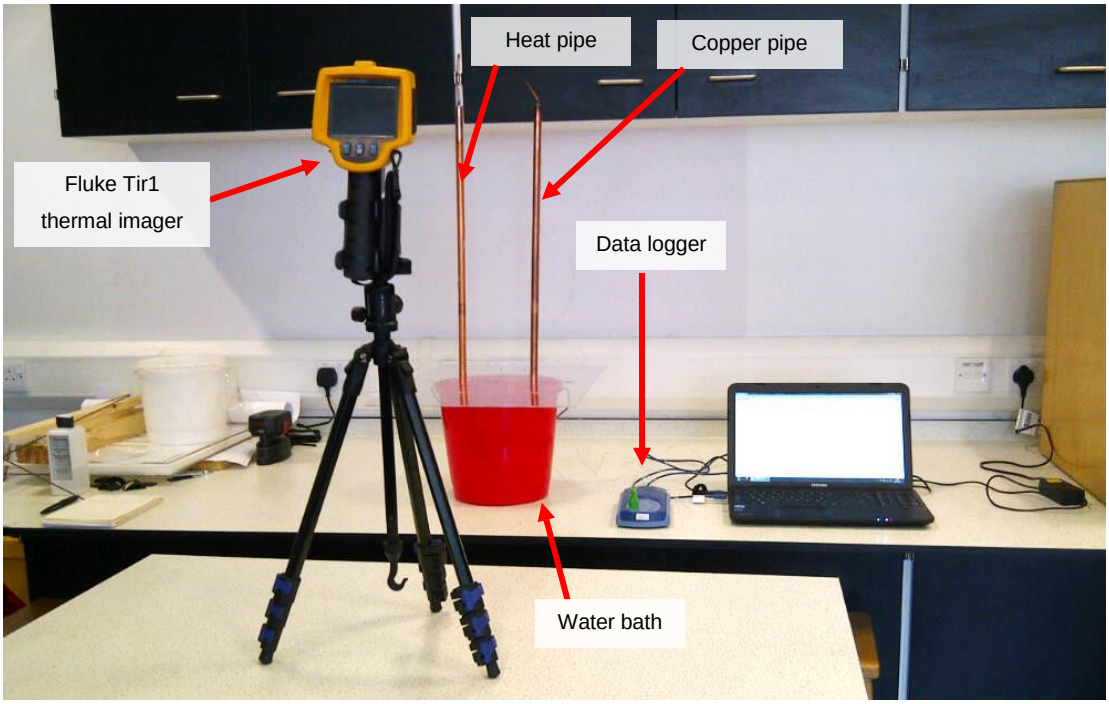

Figure 4.27 Experimental set-up for testing of heat pipes

The emerging surface temperature of a heat pipe was compared against an ordinary copper pipe in order to visualise the thermal conductivity in response to a heated medium. The pipes measured 16mm in diameter with a total length of 800mm. The pipes were placed in a warm water bath at a temperature of approximately 55°C or 328K. A K-type thermocouple was attached to the surface of both pipes and the transient temperature test was conducted for 200 seconds. The rise in the temperature of

both pipes were noted and compared and infrared thermographic images were taken using the Fluke Tir1 Thermal Imager.

4.10.3 Test set-up for evaluating the performance of the heat pipes

The test section of the wind tunnel was used as the testing rig for carrying out the experimentation. The set-up comprised of 19 cylindrical heat pipes arranged vertically at an angle of 90° with respect to ground. The separator plate was located at the centre of the pipes providing an evaporator and condenser sectional lengths of 400mm. Seven K-type thermocouple exposed wires were located upstream and downstream of the heat pipes for recording temperatures and the values were logged using the data acquisition system and connected to the computer.

The data logger comprised of a total of sixteen channels or ports which meant that up to sixteen thermocouple readings were possible during a single test run, out of which seven were used on measuring the air temperatures due to convection. Two thermocouple wires were also attached to the heat pipe surface (one at the evaporator end and one at the condenser end) in order to measure its thermal response when conducting the transient testing for a period of 24 hours. The wind tunnel axial fan with variable motor was able to provide air speeds ranging up to 12m/s while the heating elements provided temperatures up to 323K which was essential for carrying out the experimentation. All other openings unused during the test-run were sealed to prevent hot air from escaping and mixing with the ambient.

Two distinct sets of experimentation were carried out on the heat pipes with the first one being normalised steady-state and the second one involving transient evaluation. Initially, normalised air temperature tests were conducted wherein the source temperature streams at the evaporator section were varied according to a desired set-point temperature. The condenser section of the heat pipe was kept at a steady sink temperature ranging between 288K and 291K.

Using an inlet air speed of 2.3m/s, each test run was carried out for 200 seconds following the stabilisation of heating elements at the set-point level. Tests were carried out at three different heating temperatures including 305K (32°C), 308K (35°C) and 314K (41°C) in order to validate the CFD model at different source temperatures found in Doha, Qatar for the months of November, April and June (The Weather Channel,

2012). The heat pipes were arranged in three different spanwise thicknesses ranging from 48mm to 52mm. Water and R134a were used as the heat pipe internal fluids and were tested systematically one at a time during the run-time. In total, eighteen individual test-runs were conducted in the first experimental phase with nine separate runs for each working fluid.

The second set of experimental testing included a dynamic thermal model replicating the hourly temperatures for 21st June, 2012 found in Doha, Qatar (Weather History for Doha, Qatar, 2012). Inlet temperatures from the heating elements were varied every 1,800 seconds as per the available climatic data and the thermal performance of the heat pipes were monitored by connecting thermocouples upstream and downstream of the physical domain. The transient investigation was conducted in order to determine the responsive behaviour of the heat pipes in relation to external temperature variations between the evaporator and condenser sections over a period of 24 hours or 86,400 seconds.

Figure 4.28 and Figure 4.29 illustrate the experimental set-up for the performance evaluation of the heat pipes in relation to varying inlet temperature conditions.

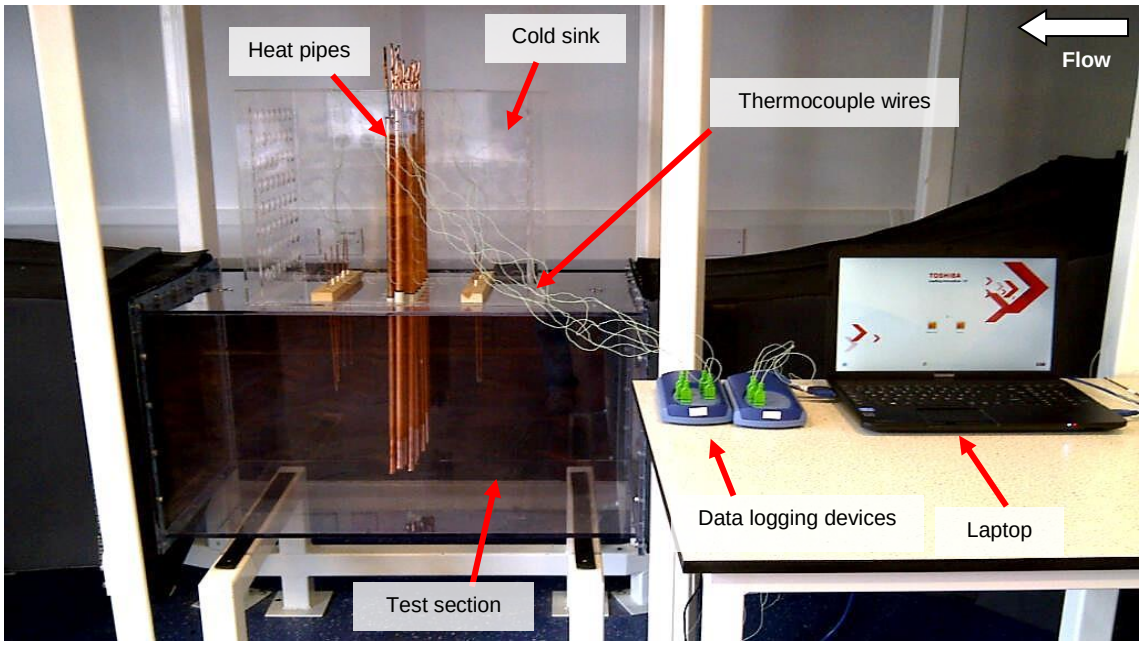

Figure 4.28 Experimental set-up for heat pipe testing (front view)

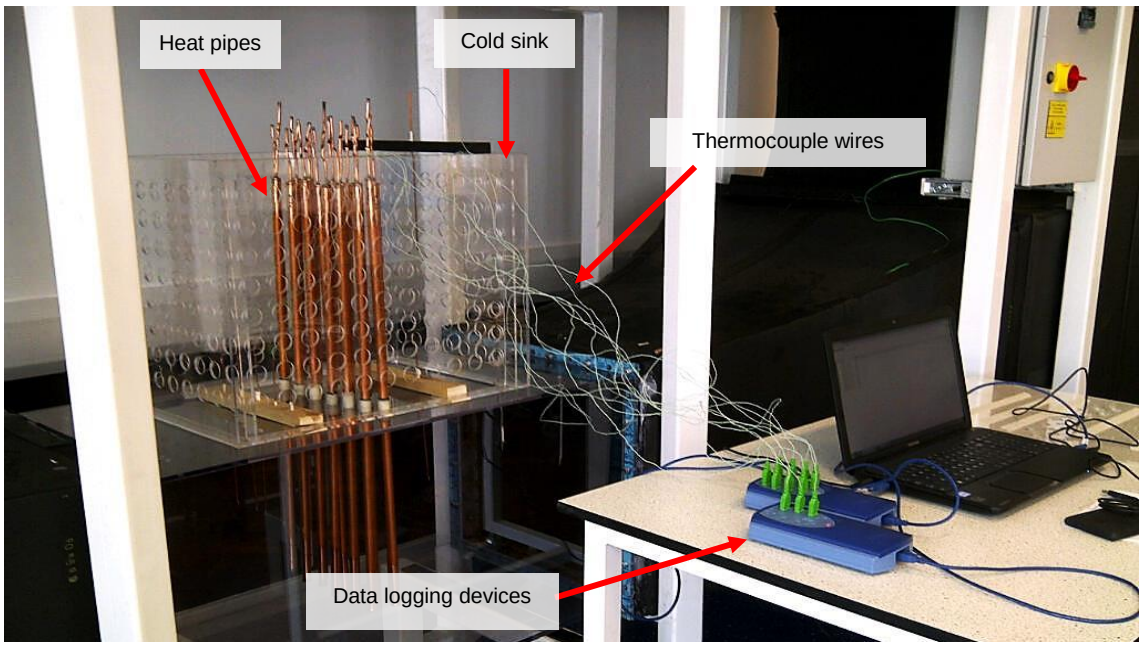

Figure 4.29 Experimental set-up for heat pipe testing (isometric view)

Thermocouple locations were kept identical to the CFD measuring points in order to compare the readings. The origin was the base of the test section directly underneath the central heat pipe. Thermocouples were located 0.15m upstream and downstream of the heat pipes (X-direction), spaced 0.05m apart in the Z-direction. The Y-direction was kept constant at 0.25m. Table 4.6 displays the values of the measurement co-ordinates in the X, Y and Z direction.

Table 4.6 Co-ordinates of the measurement points

Profile	X (m)	Y (m)	Z (m)
I_1	-0.15	0.25	0.05
I_2	-0.15	0.25	-0.05
O_1	0.15	0.25	0.10
O_2	0.15	0.25	0.05
O_3	0.15	0.25	0.00
O_4	0.15	0.25	-0.05
O_5	0.15	0.25	-0.10

The schematic view of the thermocouple wire locations in the X and Z direction along with their connection to the data logging device and the computer is further illustrated in Figure 4.30.

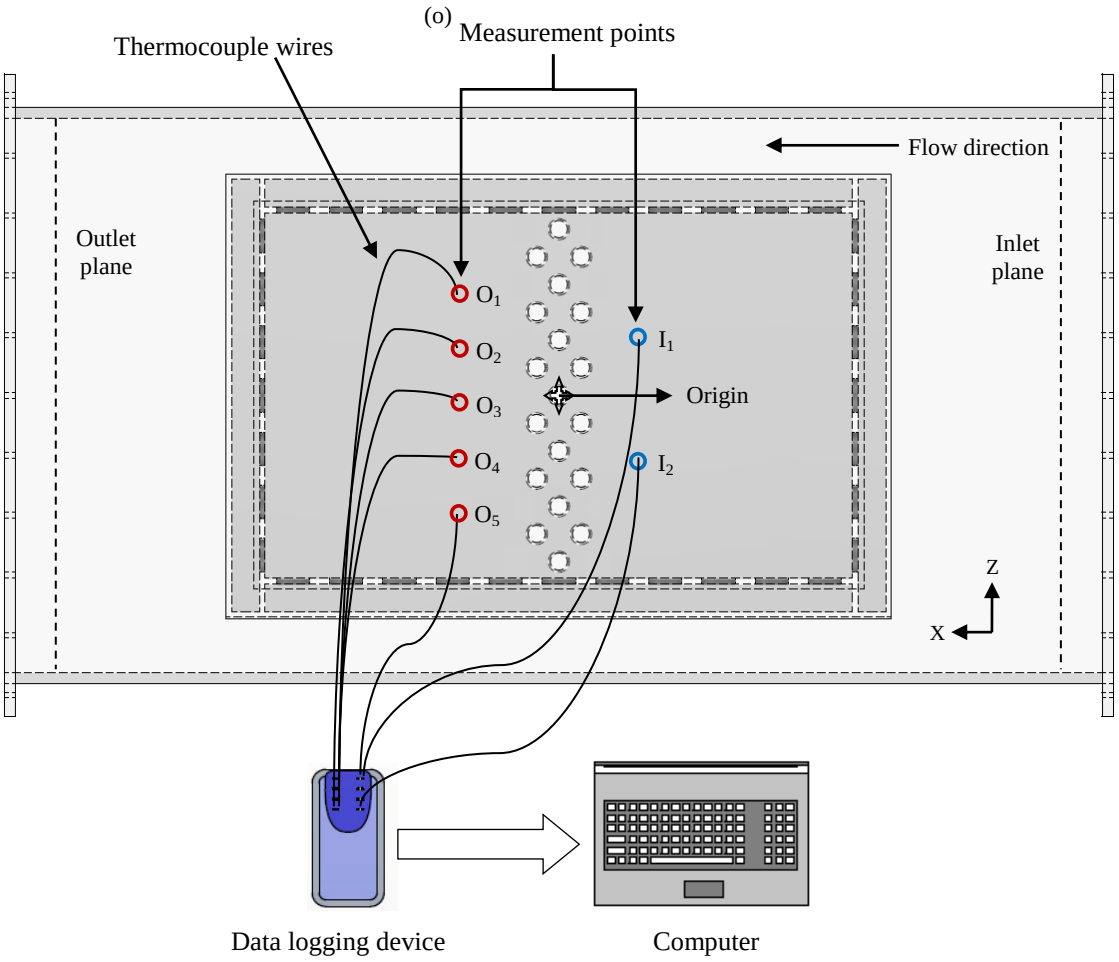

Figure 4.30 Schematic representation of thermocouple positions

4.11 Summary

This chapter described the method used for carrying out the experimentation phase of the study. A closed-loop wind tunnel was designed and commissioned and was characterised for its flow and thermal profile. The major components of the wind tunnel testing rig were labelled and the overall pressure loss was summarised. In addition, the work underlined the improved flow quality of air through the test section after the addition of the honeycomb and screen device. The study confirmed that the velocity non-uniformity coefficient in the test section was reduced from 6.6% to 0.9% after adding the flow straightener while mean turbulence intensity was 0.49% which was under the acceptable range associated with wind tunnels. The mean reduction in

velocity was 15.2% as the temperature was increased from 20°C to 50°C while the average variation in test section temperatures in response to heating elements was recorded at 5.4% (further information detailed in Appendix B and C).

The fluid flow and thermal evaluation was conducted primarily to comprehend the profiles of the test section prior to carrying out heat transfer experimentation. The chapter further illustrated the data acquisition devices and apparatus which were used for measuring and recording data along with the experimental set-up that was created for conducting the tests. Individual test-runs including stabilised steady-state and transient evaluation were described. Measurement point locations for velocity, pressure and temperature recordings were provided in order to achieve a direct comparison with the numerical results which will be discussed in the following chapters.

Chapter 5
CFD Results

5.1 Introduction

This chapter details the results obtained from the CFD investigation on heat pipes operating under typical temperature conditions found in Doha, Qatar for natural ventilation. The computational analysis studied a range of design parameters including the heat pipe working fluid and characteristic arrangement and determined their influence on the downstream flow and thermal profiles. The chapter establishes a comparison between water, ethanol and R134a as the heat pipe working fluids and determines their thermal performance in terms of internal behaviour and in response to external airstreams. Based on the most suitable working fluid, a relationship between the fluid properties and total heat transfer is further determined, the findings of which are displayed in section 5.3.

In addition, this chapter describes the impact of varying spanwise and streamwise distances between the heat pipes on the downstream air temperature. Quantification of results was achieved by measuring air velocity, pressure and temperature at the assigned measurement locations. Using the optimum working fluid and arrangement, the final section of this chapter presents the findings underlining the proportionality between varying source temperatures and wind speeds and quantifying the annual effectiveness of heat pipes using the temperature data for Doha, Qatar (The Weather Channel, 2012).

5.2 Comparison between water, ethanol and R134a as heat pipe fluids

The first step of the computational investigation was to identify the optimum heat pipe working fluid. This section of the chapter evaluates the thermal and flow profiles obtained from the comparison between water, ethanol and R134a as heat pipe working fluids at the applied boundary conditions. Subsequent to determining the internal behaviour of the three fluids, external air temperature profiles were investigated and the rate of heat transfer was estimated at a saturation temperature of 293K. The comparison was used to determine the ideal working fluid to be used for the remainder of the study.

5.2.1 Internal fluid flow and thermal profiles

Figure 5.1 shows the liquid phase volume fractions for analysis of water, ethanol and R134a as heat pipe working fluids. It was observed that the phase development of ethanol was the greatest, followed by R134a while water displayed the lowest ratio of volume fractions during the simulation. The images were tilted vertically in order to compare the three working fluids side by side. The bottom side of the contour exemplifies the region closest to the pipe wall and the volume fraction was concentrated at that point (Rahmat and Hubert, 2010) for all fluids, confirming the appropriate operation of the evaporation process.

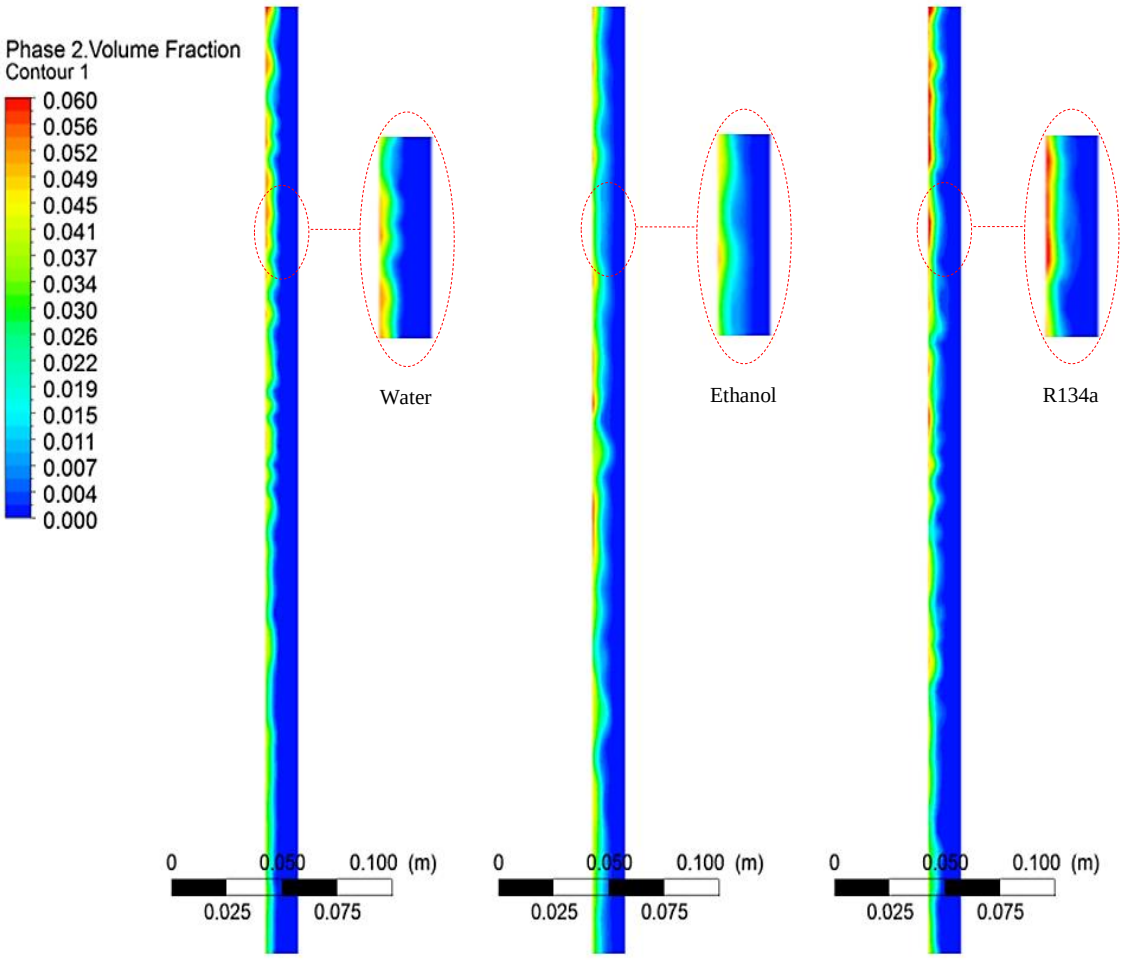

Figure 5.1 Contour levels of fluid volume fractions

Figure 5.2 displays the temperature contour plots of the three heat pipe working fluids. The wall source temperature was set to 323K while the saturation temperature was kept constant at 293K for all fluids. It was observed that water initiated the flow from its

saturation temperature of 293K and the temperature increased to a mean value of 307K when in contact with the walls of the heat pipe. However, this trend was not observed for ethanol and R134a was much higher temperature levels were noted for the two working fluids. The maximum fluid temperature of ethanol was 383K while the maximum temperature obtained for R134a was 408K.

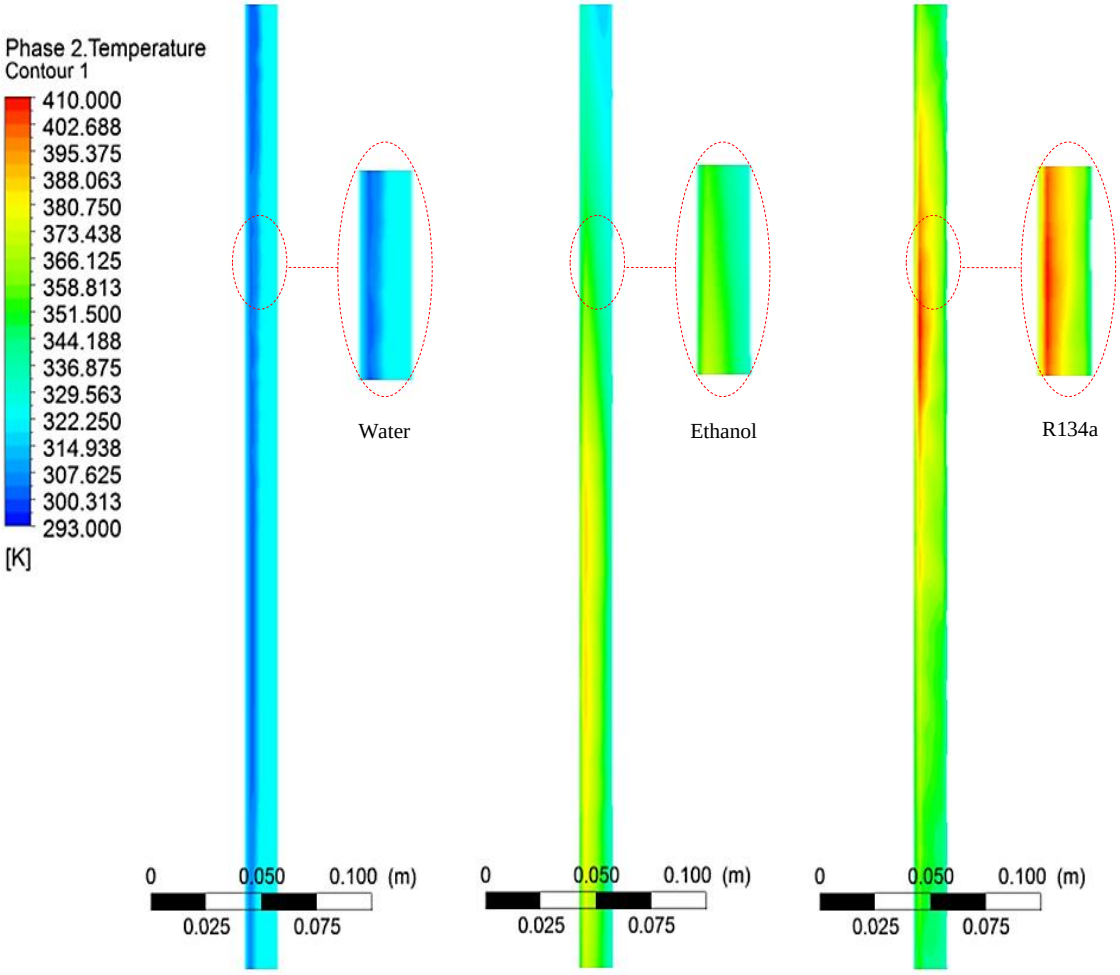

Figure 5.2 Contour levels of fluid temperature

Internal flow profiles for water, ethanol and R134a are displayed in Figure 5.3. A slug flow pattern was observed for ethanol as it displayed the highest velocity of 0.12m/s in comparison to the other working fluids. The velocity profile of water was noted to be predominantly through the heat pipe walls rather than across the entire cross-sectional face of the tube. The velocity profile of ethanol and R134a were dissimilar due to the effects of dynamic viscosity (μ). Ethanol incorporated a dynamic viscosity of 1.26×10^{-3} Pas at 293K which was superior to the dynamic viscosity of R134a at 2.09×10^{-4} Pas. In summary, the CFD investigation determined that all three heat pipe working fluids

characterised different patterns of volume fraction formation, thermal behaviour and velocity profiles in response to the defined source temperature.

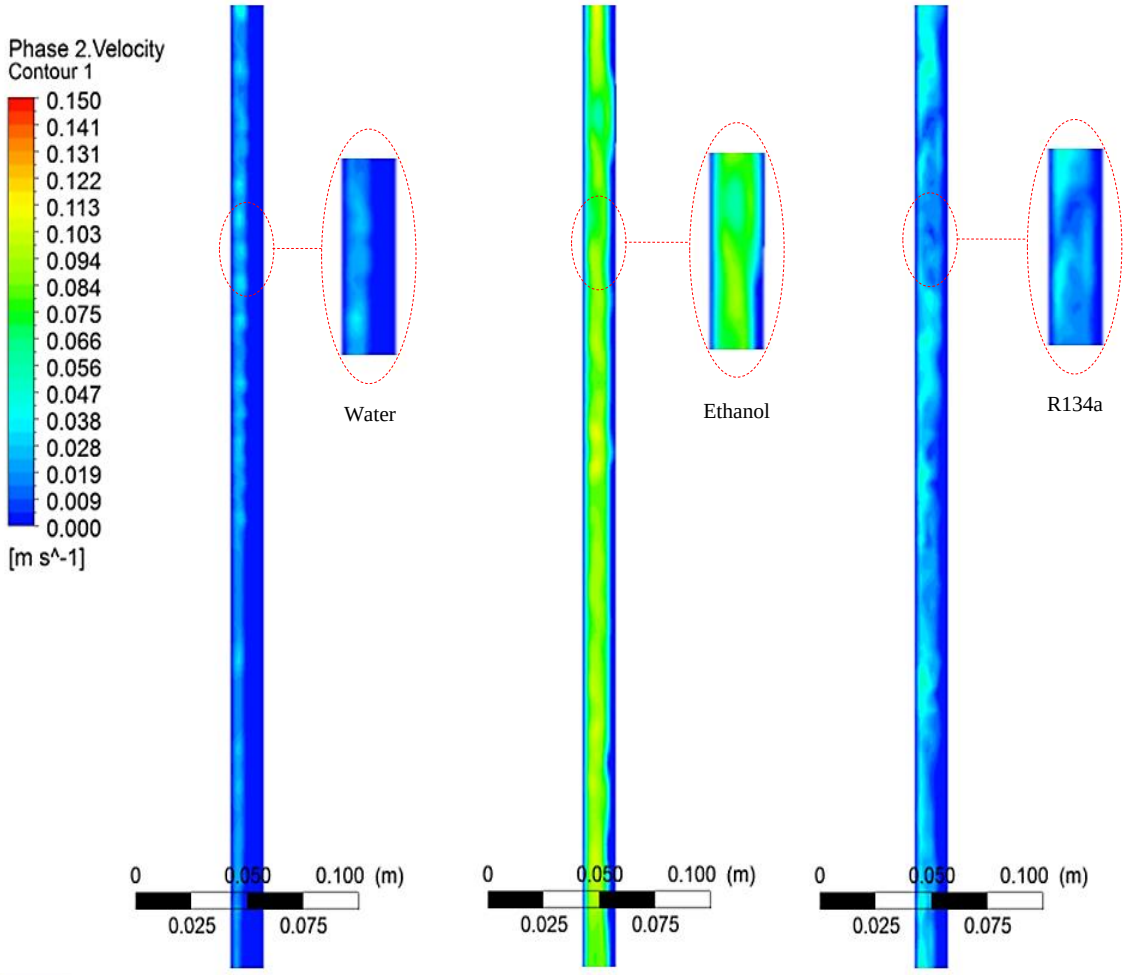

Figure 5.3 Contour levels of fluid velocity

A line was constructed across the bottom wall of the heat pipes to plot the volume fractions of the three working fluids on a logarithmic scale. Figure 5.4 displays the graphical representation of the volume fractions of the three heat pipe working fluids over the axial length of the heat pipes. As observed, the formulation of liquid phase of water volume fraction was the lowest in comparison to R134a and ethanol with the volume fraction of ethanol being the highest. The maximum value of the volume fraction for ethanol was 0.069 which was higher than that of R134a at 0.014. The lowest volume fraction was obtained for water which was estimated at 0.002. It was noted that the volume fractions for all three heat pipe working fluids remain stabilised for the entire axial length of the pipe with minimum fluctuations.

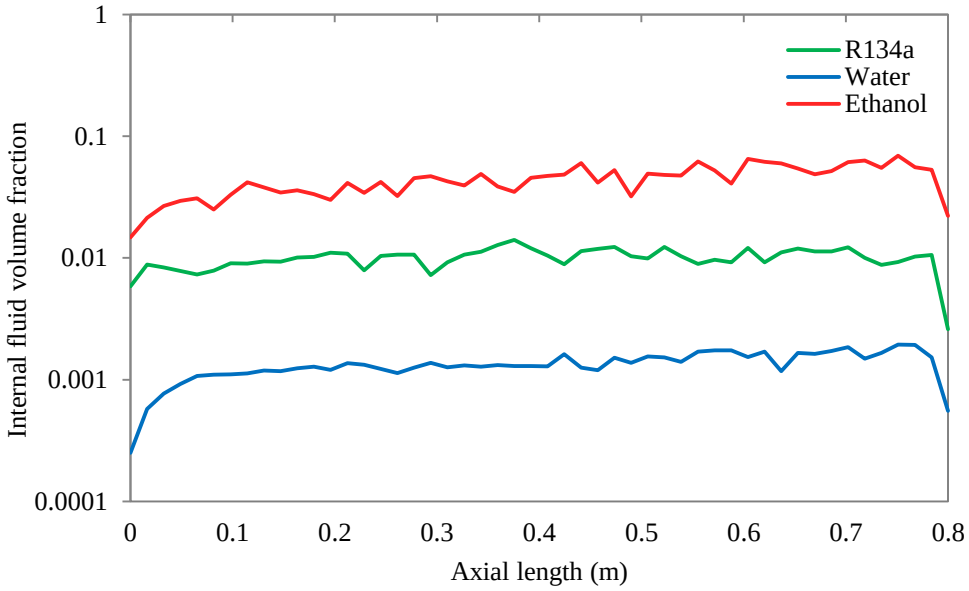

Figure 5.4 Comparison between volume fractions over the axial length of the pipe

The temperature profile of water, ethanol and R134a as heat pipe working fluids is further displayed in Figure 5.5.

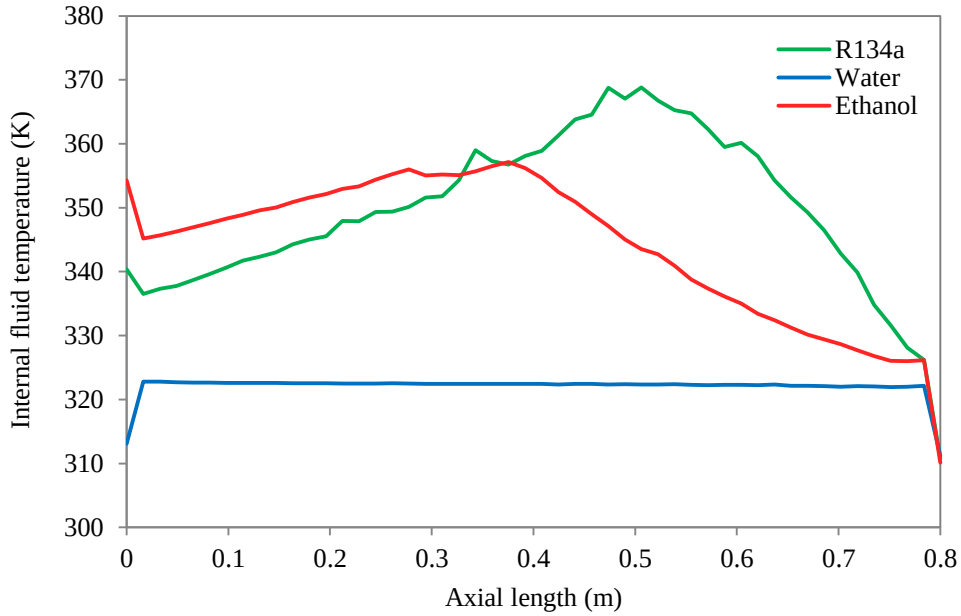

Figure 5.5 Comparison between temperature profiles over the axial length of the pipe

The wall temperatures were set to 323K and it was observed that water maintained the inlet temperature over the entire axial length of the heat pipe. The inlet saturation temperature of 293K rapidly normalised to the wall temperature as water evaporated

into its vapour phase. A parabolic increase in temperature was observed for both ethanol and R134a with ethanol reaching its maximum value at 357.1K while R134a reaching its maximum temperature at 368.8K. However both fluids displayed a downward gradient in temperature across the axial length of the pipe, showing an inverse parabolic relationship.

5.2.2 Air temperature profiles

Following the internal investigation involving flow behaviour of the heat pipe working fluids, air temperature analyses were performed along the axial and radial length of test section for all three working fluids to comprehend the difference in the working performance. Figure 5.6, Figure 5.7 and Figure 5.8 display the air temperature profile along an axial plane constructed in the evaporator and condenser region of the test section for water, ethanol and R134a. The upper and lower limits of the contour levels were set from the heat pipe condenser or sink temperature of 288K to the applied source temperature of 314K. It was observed that water charged heat pipes exhibited the greatest air temperature reduction in comparison to ethanol and R134a.

The simulation predicted that the air temperatures decreased at downstream locations as the flow came in contact with the heat pipes. The minimum value of downstream air temperature along the evaporator section was 311.9K for water while ethanol and R134a displayed greater values of downstream air temperatures at 312.9K and 312.5K. The greatest temperature reduction was obtained at 2.1K for water as the heat pipe working fluid, indicating its superior thermal performance over other working fluids. Simultaneously, the values of air temperatures were increased in the condenser section of the heat exchanger due to the transfer of heat out of the heat pipe in that region. Maximum air temperatures along the axial length of the condenser section were calculated at 293.1K for water while maximum condenser temperature predicted using ethanol and R134a were 291.5K and 291.7K. The steady-state simulation for the three working fluids was run for a unit heat pipe cycle.

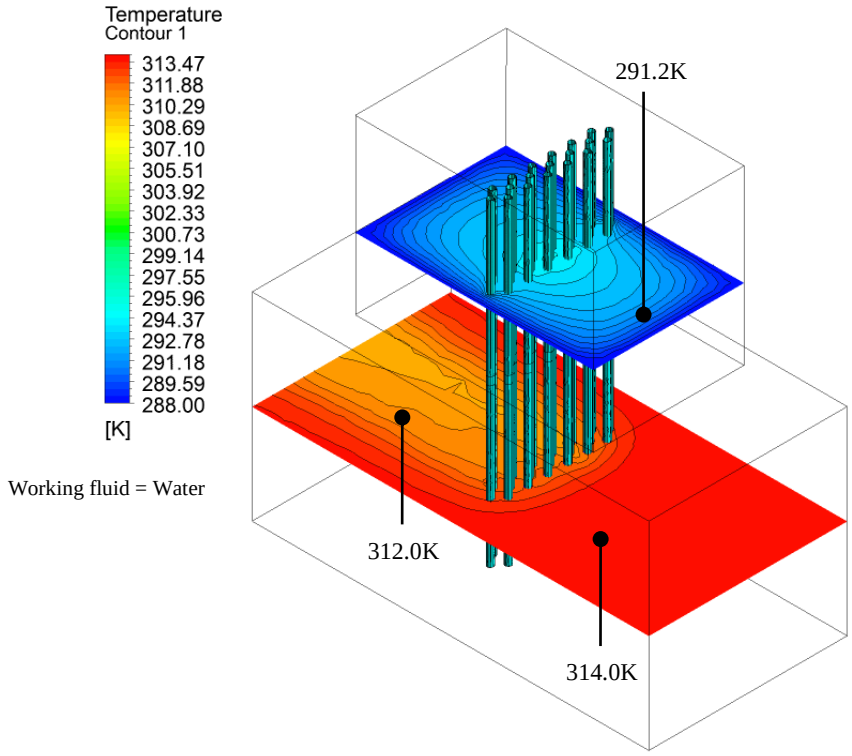

Figure 5.6 Contours levels displaying air temperature across the axial length of the heat exchanger using water as the working fluid

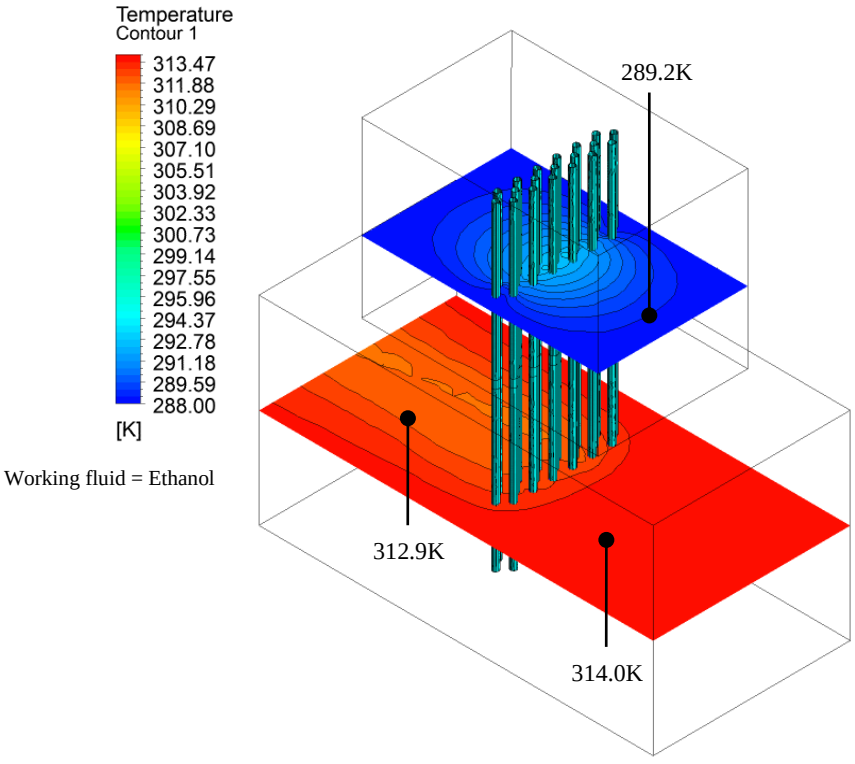

Figure 5.7 Contours levels displaying air temperature across the axial length of the heat exchanger using ethanol as the working fluid

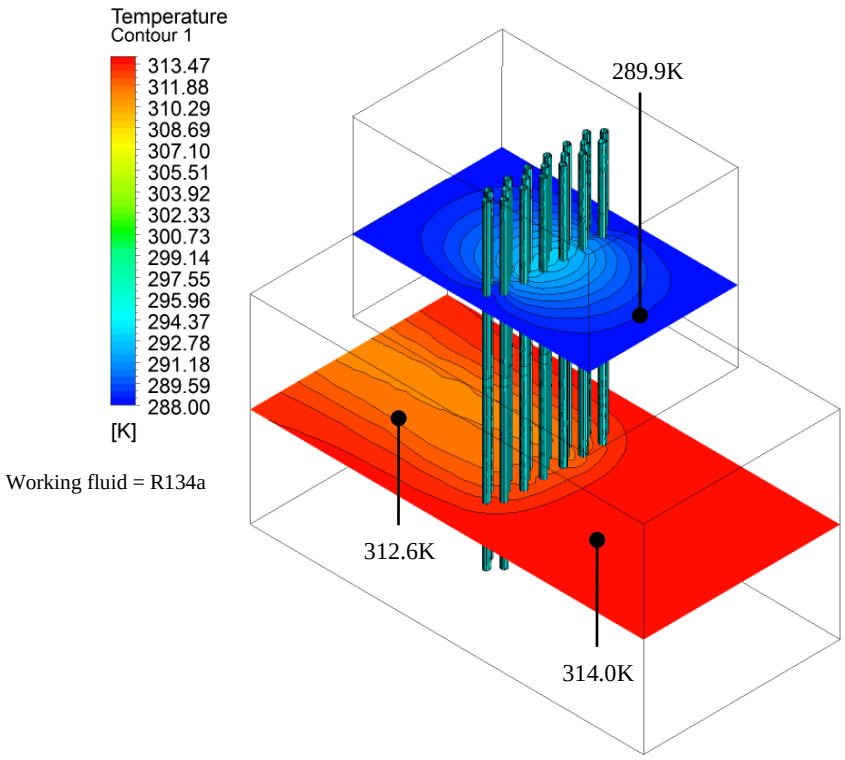

Figure 5.8 Contours levels displaying air temperature across the axial length of the heat exchanger using R134a as the working fluid

In order to obtain an in-depth comparison between the working fluids, thermal analyses were carried out at different source temperatures. The source temperatures used for the investigation were 305K, 308K and 314K corresponding to the monthly temperatures of November, April and June found in Doha, Qatar (The Weather Channel, 2012). A plane was created at 150mm downstream of the heat pipe arrangement and across the entire radial circumference of the test section.

With reference to Figure 5.9, the thermal profile at a source temperature of 305K is obtained. The maximum reduction in temperature using water as the working fluid was 1.4K with a temperature value of 303.6K. Ethanol displayed the thermal transfer with a temperature reduction of 0.8K while R134a indicated a temperature reduction of 1.1K. The analysis showed that for a source temperature value of 305K, the reductions in air temperature were the lowest for all working fluids due to the lower difference between source and sink conditions.

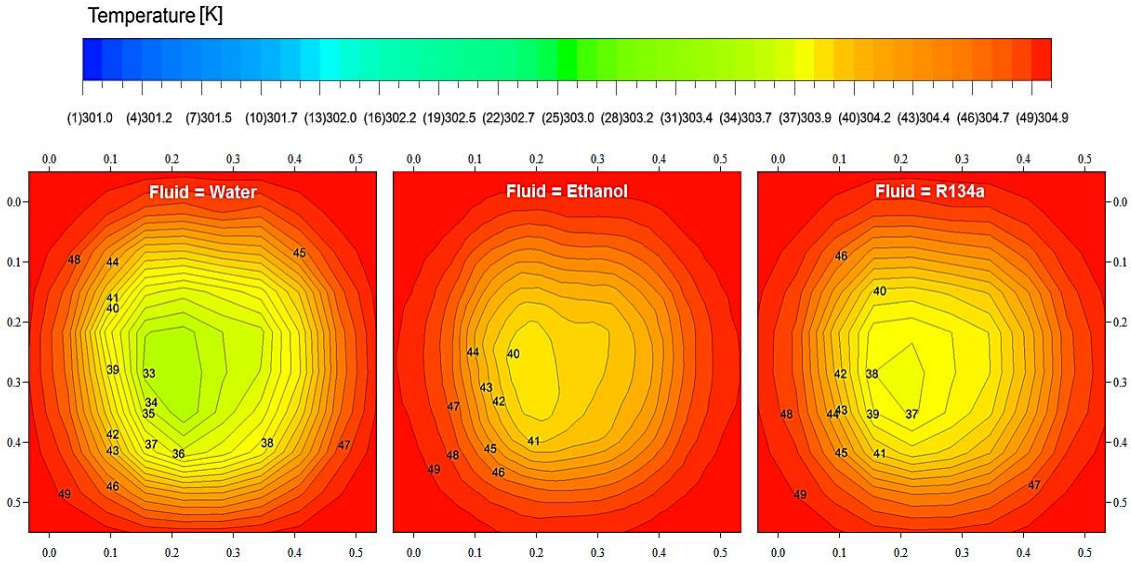

Figure 5.9 Thermal profile of the working fluids at source temperature of 305K

Thermal profiles of the three working fluids at a source temperature of 308K are displayed in Figure 5.10. The trend was similar to the one obtained at a source temperature of 305K as water displayed the highest reduction in air temperatures of all the compared fluids. Temperature reductions from all working fluids were increased as the source temperature was increased with water indicating a reduction of 1.6K at a source temperature of 308K.

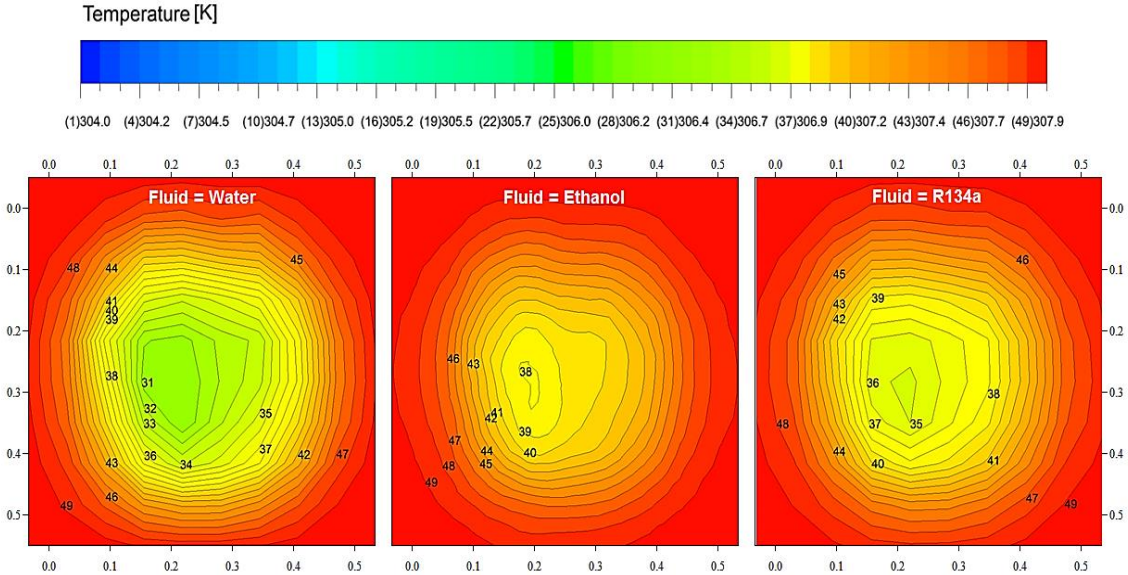

Figure 5.10 Thermal profile of the working fluids at source temperature of 308K

The contour levels of air temperatures obtained downstream of the heat pipes at a source temperature of 314K are displayed in Figure 5.11. All fluids displayed their greatest

temperature reduction of air as the differential between the source temperature and heat pipe operating temperature was the maximum. Water indicated the greatest air temperature reduction of approximately 2K. It was noted that the temperature pattern observed for all working fluids remained relatively similar for all analysed source temperatures.

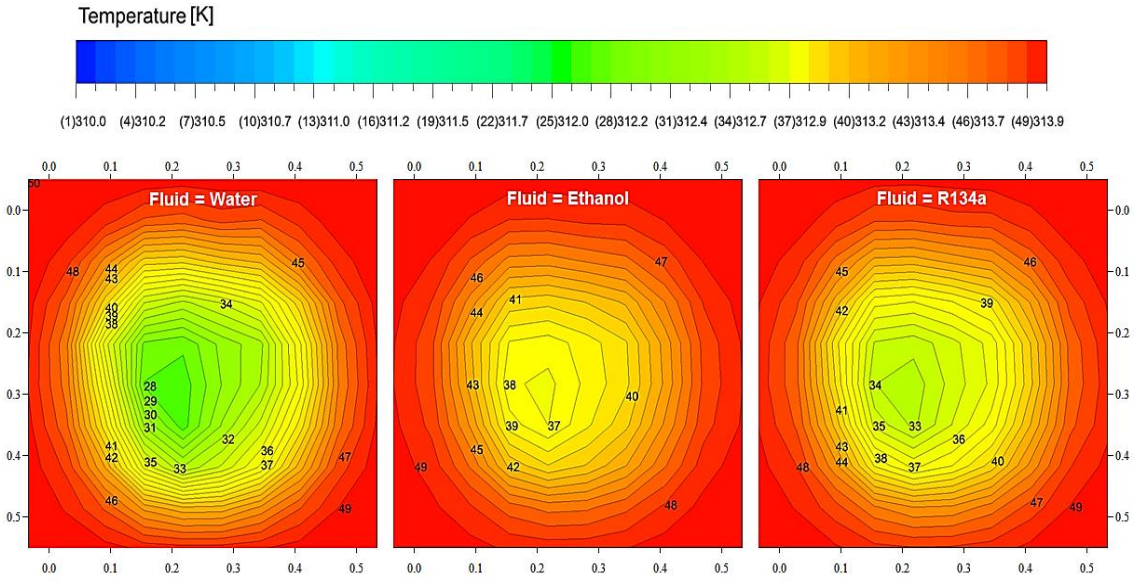

Figure 5.11 Thermal profile of the working fluids at source temperature of 314K

The continuous variations of air temperature profiles along the axial length of the test section are illustrated in Figure 5.12. The cross-sectional area of the test section was $0.25m^2$, indicating an inlet volume flow rate of $0.58m^3$/sec for all investigated cases. At a source temperature of 305K, the minimum downstream values obtained for water, ethanol and R134 were 303.4K, 304.2K and 303.9K. For all three source temperatures, water displayed the greatest temperature reduction in comparison to ethanol and R134a. Air temperature reductions obtained from the three working fluids at a source temperature of 314K were greatest due to a higher temperature differential between source and heat pipe operating temperature. The maximum temperature reduction was achieved at 2K using water while the lowest temperature reduction was achieved using ethanol at 1.5K from the inlet.

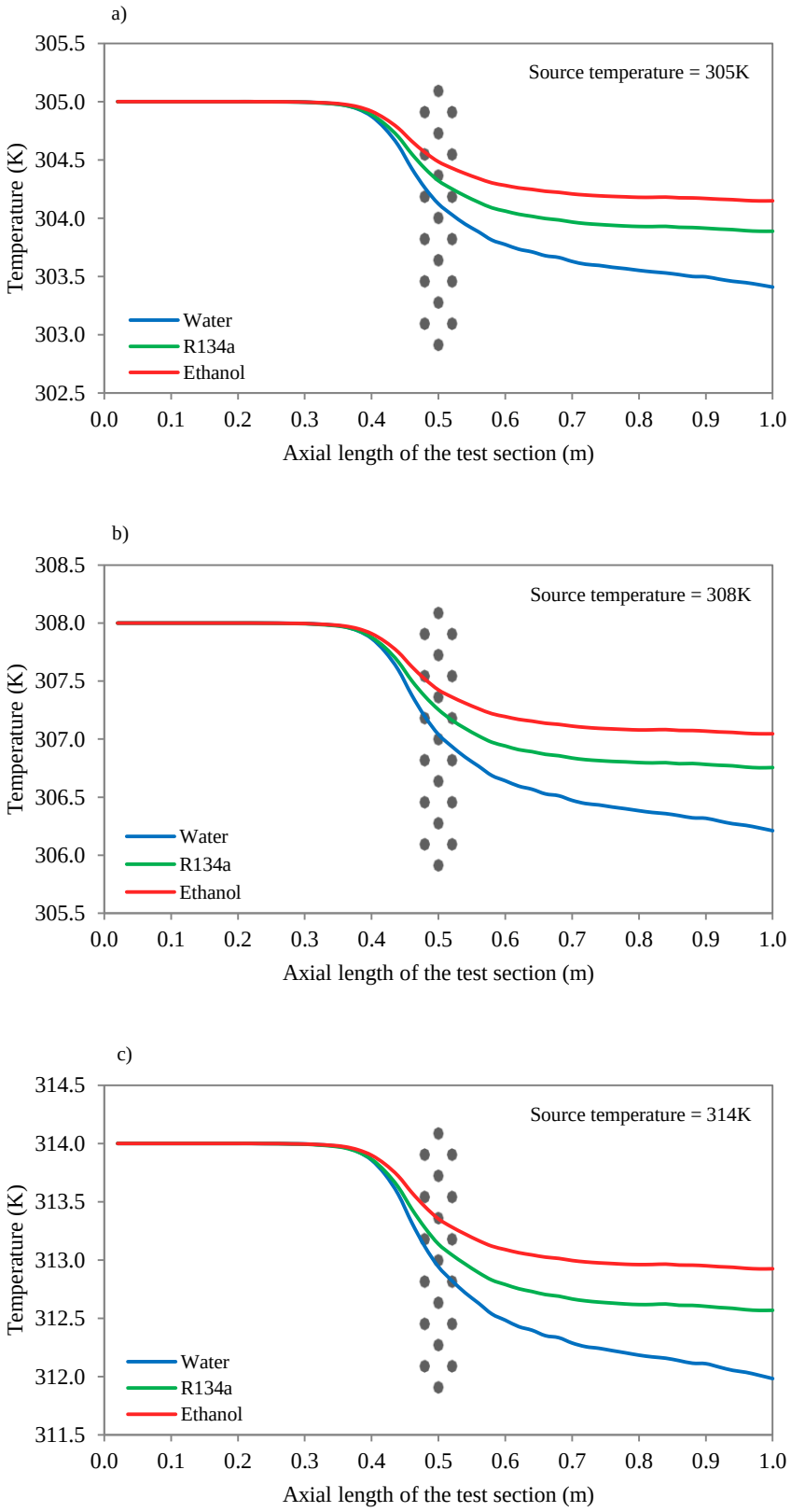

Figure 5.12 Variation in air temperature across the axial length of the evaporator section at source temperatures of: a) 305K b) 308K c) 314K

Figure 5.13 displays variation in air temperatures across the radial length of the test section.

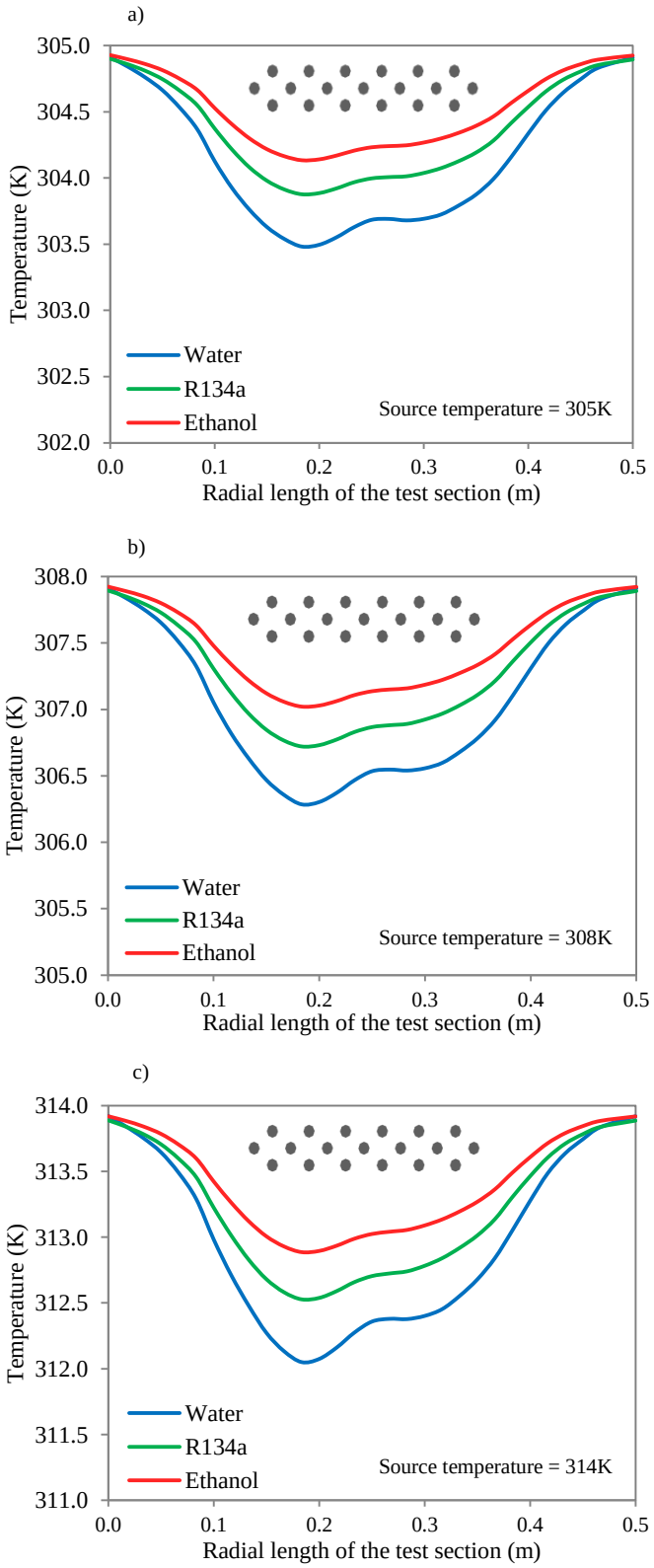

Figure 5.13 Variation in air temperature across the radial length of the evaporator section at source temperatures of: a) 305K b) 308K c) 314K

The plot was determined on a line constructed along the radius of the test section at 150mm downstream of the heat pipe arrangement. A consistent thermal profile was observed for all three working fluids different source temperatures. The greatest radial temperature reduction was estimated at approximately 2K for water at a source temperature of 314K while the lowest reduction was noted for ethanol at 0.7K at a source temperature of 305K. The temperature profiles displayed a parabolic trend as the temperatures obtained downstream of the heat pipes were lower than those obtained at the walls of the test section, the region that did not accommodate heat pipes.

5.2.3 Total cooling capacity and overall effectiveness

The cooling capacity or rate of heat transfer (q_e) and overall effectiveness (ε) of the heat pipe heat exchanger was calculated using eqn.27 and eqn.28 (full definition mentioned in Chapter 3, Section 3.2.5) for the three working fluids in water, ethanol and R134a at the measurement locations.

$$q_e = \rho_G U A C_{p,G}\left(T_{e,inlet} - T_{e,outlet}\right) \quad \text{(eqn.27)}$$

$$\varepsilon = \frac{q_{actual}}{q_{max}} = \frac{T_{e,inlet} - T_{e,outlet}}{T_{e,inlet} - T_{c,inlet}} \quad \text{(eqn.28)}$$

Where q_e represents the heat transfer in the evaporator section, ρ_G represents the density of air, U represents the velocity of air, A represents the cross-sectional area, $C_{p,G}$ represents the specific heat capacity of air, ε represents the heat exchanger effectiveness, $T_{e,inlet}$ represents the temperature at the inlet, $T_{e,outlet}$ represents the temperature at the outlet and $T_{c,inlet}$ represents the inlet temperature to the condenser or the temperature of the cold sink.

Measurement points were used, at the inlet (I_1 and I_2) and outlet (O_1 – O_5) of the heat pipes (Chapter 3, Section 3.6.4) to quantify the results at the three operating temperatures. Table 5.1 displays the findings obtained using water as the working fluid. The heat transfer was directly proportional to the temperature differential between upstream and downstream locations.

The highest heat transfer was obtained for point O_2 at 1,155W using a source temperature of 314K. The highest heat transfer using a source temperature of 308K was 983W while the highest heat transfer using a source temperature of 305K was only

873W. The maximum heat exchanger effectiveness was calculated at 8.94%. Temperature readings at measurement points I_1 and I_2 were determined to be very similar to the inlet values since those points were located upstream of the heat pipes.

Table 5.1 Sensible heat transfer and effectiveness at the measurement locations for water as the working fluid

Source temp.	Point	Temperature (K)	Heat transfer (W)	Effectiveness (%)
305 K	I_1	304.97	17.25	0.18%
	I_2	304.96	23.00	0.24%
	O_1	303.66	768.71	7.86%
	O_2	303.48	873.93	8.94%
	O_3	303.67	764.69	7.82%
	O_4	303.68	758.94	7.76%
	O_5	303.82	678.44	6.94%
308 K	I_1	307.96	22.86	0.20%
	I_2	307.96	22.86	0.20%
	O_1	306.51	851.57	7.45%
	O_2	306.28	983.02	8.60%
	O_3	306.51	851.57	7.45%
	O_4	306.54	834.43	7.30%
	O_5	306.71	737.27	6.45%
314 K	I_1	313.97	17.50	0.12%
	I_2	313.96	23.34	0.15%
	O_1	312.31	985.94	6.50%
	O_2	312.02	1,155.12	7.62%
	O_3	312.32	980.10	6.46%
	O_4	312.38	945.10	6.23%
	O_5	312.59	822.59	5.42%

Following the determination of heat transfer and effectiveness using water, Table 5.2 displays the quantification of results using ethanol as the heat pipe working fluid. Ethanol displayed the lowest transfer of thermal energy in comparison to water and R134a. The highest heat transfer was obtained 661W at a source temperature of 314K while the heat transfer dropped to 440W at 305K.

The maximum heat exchanger effectiveness was calculated at 5.18%. In general, the point O_2 consistently displayed the lowest air temperature results or the maximum values of heat transfer through convection for all working fluids.

Table 5.2 Sensible heat transfer and effectiveness at the measurement locations for ethanol as the working fluid

Source temp.	Point	Temperature (K)	Heat transfer (W)	Effectiveness (%)
305 K	I_1	304.98	10.00	0.12%
	I_2	304.97	15.00	0.18%
	O_1	304.23	385.12	4.53%
	O_2	304.12	440.04	5.18%
	O_3	304.22	390.28	4.59%
	O_4	304.25	375.04	4.41%
	O_5	304.23	385.14	4.53%
308 K	I_1	307.97	16.32	0.15%
	I_2	307.97	16.32	0.15%
	O_1	307.13	473.19	4.35%
	O_2	307.00	543.90	5.00%
	O_3	307.12	478.63	4.40%
	O_4	307.17	451.44	4.15%
	O_5	307.29	386.17	3.55%
314 K	I_1	313.96	23.85	0.15%
	I_2	313.97	17.89	0.12%
	O_1	313.03	578.41	3.73%
	O_2	312.89	661.89	4.27%
	O_3	313.01	590.34	3.81%
	O_4	313.07	554.56	3.58%
	O_5	313.22	465.11	3.00%

The tabulation of the heat transfer findings using R134a as the heat pipe working fluid is displayed in Table 5.3.

Table 5.3 Sensible heat transfer and effectiveness at the measurement locations for R134a as the working fluid

Source temp.	Point	Temperature (K)	Heat transfer (W)	Effectiveness (%)
305 K	I_1	304.97	17.94	0.18%
	I_2	304.97	17.94	0.18%
	O_1	303.98	610.07	6.00%
	O_2	303.85	687.83	6.76%
	O_3	303.98	610.07	6.00%
	O_4	304.02	586.15	5.76%
	O_5	304.15	508.39	5.00%
308 K	I_1	307.96	23.99	0.20%
	I_2	307.96	23.99	0.20%
	O_1	306.86	683.58	5.70%
	O_2	306.69	785.52	6.55%
	O_3	306.85	689.58	5.75%
	O_4	306.89	665.59	5.55%
	O_5	307.06	563.65	4.70%
314 K	I_1	313.95	29.90	0.19%
	I_2	313.96	23.92	0.15%
	O_1	312.72	766.75	4.93%
	O_2	312.52	885.18	5.69%
	O_3	312.69	783.50	5.04%
	O_4	312.75	747.62	4.81%
	O_5	312.94	633.98	4.08%

A maximum value of 885W was obtained for point O_2 using a source temperature of 314K, while the heat transfer decreased to 687W at a source temperature of 305K. The maximum heat exchanger effectiveness was calculated at 6.76%. The summarised results for the average rate of sensible heat transfer at measurement locations for all investigated fluids are tabulated in Table 5.4. Keeping the inlet mass flow rate constant at 0.63kg/sec for all cases, the heat transfer due to convection was only influenced by the temperature differential upstream and downstream of the heat pipes. The highest temperature reduction was 1.68K at a source temperature of 314K using water as the working fluid. The increase in heat transfer was 209W for water when the source temperature was increased from 305K to 314K. Ethanol and R134a also specified an increase in heat transfer as the source temperature was increased with Ethanol indicating an increase of 163W while R134a showing a rise of 175W.

Table 5.4 Rate of heat transfer calculated for the three compared heat pipe working fluids

	Source = 305 K		**Source = 308 K**		**Source = 314 K**	
Fluid	**Heat transfer (W)**	**ΔT (K)**	**Heat transfer (W)**	**ΔT (K)**	**Heat transfer (W)**	**ΔT (K)**
Water	768.94	1.34	851.57	1.49	977.77	1.68
R134a	600.50	1.00	677.58	1.13	763.41	1.28
Ethanol	395.04	0.79	466.67	0.86	570.06	0.96

In order to determine the working performance of a heat pipe heat exchanger, the overall effectiveness results were quantified for all working fluids. The results for overall effectiveness of the heat exchanger are summarised in Table 5.5. It was observed that the heat pipe effectiveness was the highest at a source temperature of 305K for all three heat pipe working fluids. The effectiveness was calculated on the temperature ratio between the sensible energy transferred to the maximum theoretical energy transfer possible. The maximum heat exchanger effectiveness was calculated for water at 7.9% while ethanol and R134a indicated a maximum effectiveness of 4.7% and 5.9% at 305K.

Table 5.5 Overall effectiveness calculated for the three compared heat pipe working fluids

Working fluid	**Effectiveness (%) at 305K**	**Effectiveness (%) at 308K**	**Effectiveness (%) at 314K**
Water	7.87%	7.45%	6.45%
R134a	5.91%	5.65%	4.91%
Ethanol	4.65%	4.29%	3.68%

The graphical representation of the comparison between water, ethanol and R134a in terms of heat transfer capability and effectiveness is displayed in Figure 5.14. The rate of heat transfer was observed to be in direct proportionality with the increasing source temperatures for all working fluids. Due to its higher latent heat of vaporisation and airside temperature reduction, water consistently displayed superior heat transfer compared to ethanol and R134a at all source temperatures.

On average, water highlighted a superior heat exchanger effectiveness of 1.8% in comparison to R134a and a 3.1% in comparison to ethanol. The highest level of effectiveness for all three working fluids was determined at a source temperature of 305K due to a lower temperature differential between the source and sink temperatures.

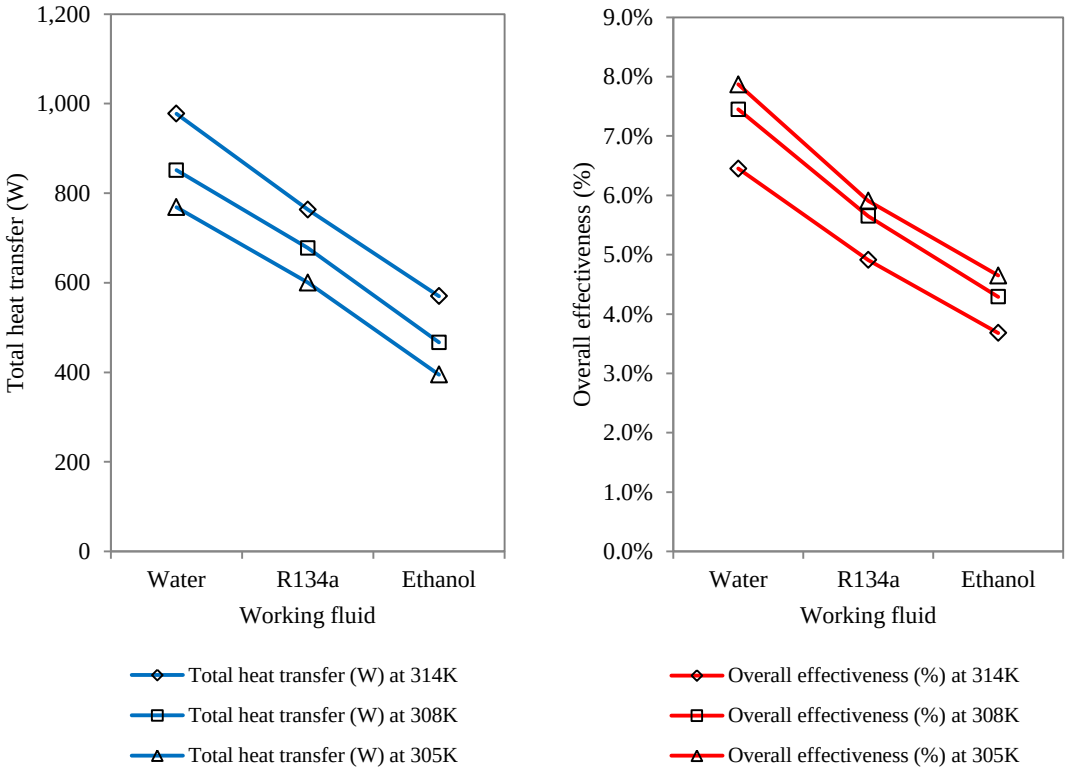

Figure 5.14 Comparison between water, R134a and ethanol in terms of rate of heat transfer and overall effectiveness

5.3 Effect of internal fluid properties on convective heat transfer

Following the findings from the previous section which identified water as the optimum working fluid, this section of the chapter describes the impact of internal fluid properties on heat transfer under convection flows. Water was taken as the benchmark fluid and physical properties including the density, thermal conductivity, dynamic

viscosity and specific heat capacity were analysed to quantify its corresponding effect on the rate of heat transfer.

5.3.1 Temperature dependant properties of existing heat pipe fluids

Individual properties of existing heat pipe internal working fluids were initially obtained at a fixed operating temperature of 20°C or 293K (Reay and Kew, 2006, ANSYS, 2011, F2 Chemicals, 2012). Using the available data, the fluid properties were systematically varied in order to determine their impact on the rate of heat transfer. Figure 5.15, Figure 5.16, Figure 5.17 and Figure 5.18 display the variation in density, thermal conductivity, dynamic viscosity and specific heat capacity of the available heat pipe working fluids.

Figure 5.15 shows the variation in density (ρ) for the existing working fluids. The lowest density was 610kg/m^3 for ammonia while the highest density was obtained for Flutec PP2 at 1,801kg/m^3. Water, which was used as the benchmark working fluid, had the second largest density at 998kg/m^3. The range of densities from minimum to maximum was 1,190kg/m^3.

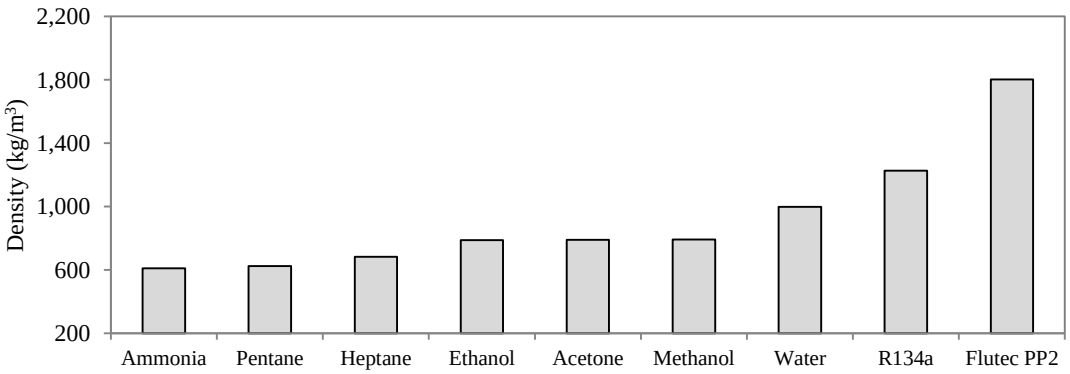

Figure 5.15 Variation in density for available heat pipe working fluids

Figure 5.16 displays the thermal conductivity (k) of the available heat pipe working fluids. Flutec PP2 had the greatest thermal conductivity of 0.61W/mK which was similar to that of water. The lowest thermal conductivity was obtained for R134a at 0.09W/mK. The difference in thermal conductivity or the range from minimum to maximum was calculated at 0.52W/mK.

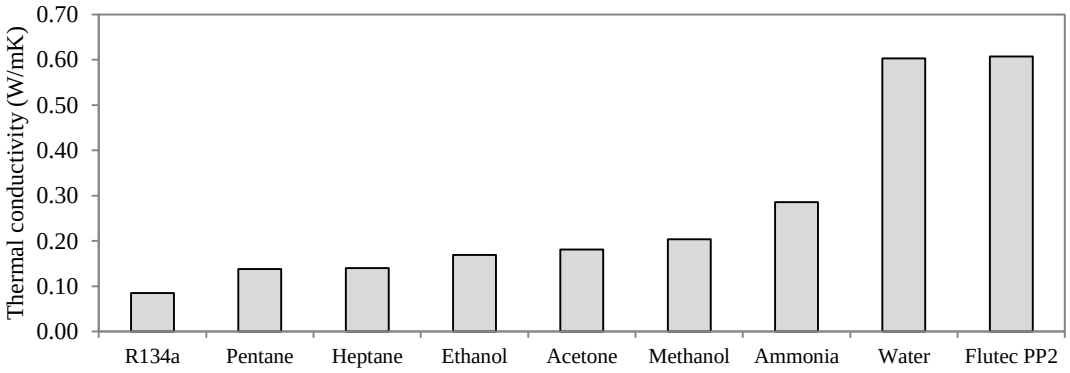

Figure 5.16 Variation in thermal conductivity for available heat pipe working fluids

The variation in dynamic viscosity (μ) for available working fluids is displayed in Figure 5.17. The highest dynamic viscosity was obtained for Flutec PP2 at 1.79x10^{-3} Pas while R134a indicated the lowest fluid viscosity of 2.09x10^{-4}Pas. The range of available fluid viscosities from minimum to maximum was calculated at 1.58x10^{-3} Pas.

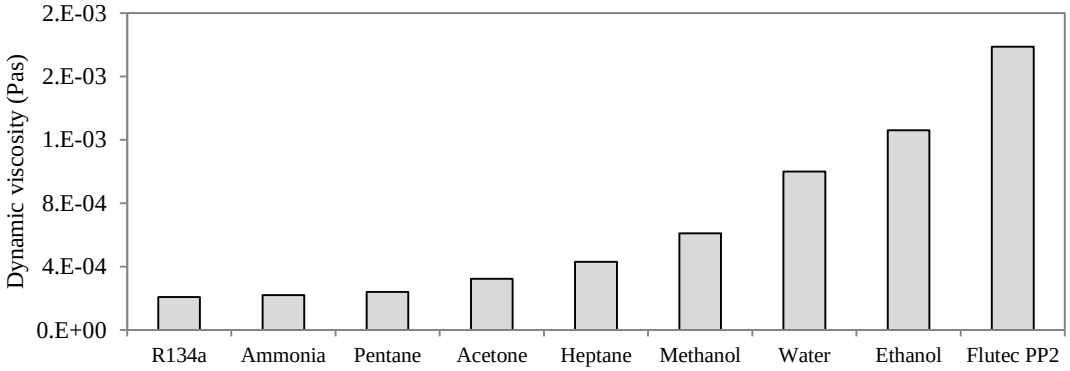

Figure 5.17 Variation in dynamic viscosity for available heat pipe working fluids

Similarly, the final investigated fluid property was the specific heat capacity (c_p) as displayed in Figure 5.18. Ammonia displayed the largest specific heat capacity of 4,758kJ/kgK which was 576kJ/kgK higher than water. Flutec PP2 displayed the lowest specific heat capacity of 1,000kJ/kgK. Therefore, working range between minimum and maximum was calculated at 3,758kJ/kgK. The purpose of illustrating the properties of existing fluids was to comprehend the working range associated with heat pipe working fluids.

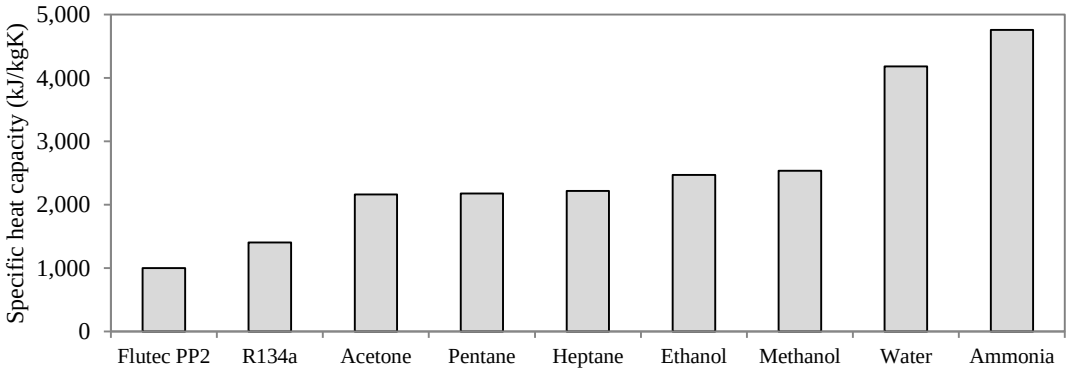

Figure 5.18 Variation in specific heat capacity for available heat pipe working fluids

A plane was constructed 150mm downstream of the heat pipe arrangement along the circumference of the test section. Using the properties of water as a heat pipe working fluid, the corresponding relationship between air temperature and effective Prandtl number was established. The effective Prandtl number was essentially the ratio involving the sum of laminar and turbulent viscosity and thermal conductivity components. The molecular Prandtl number of air at 314K was 0.74 while the Effective Prandtl number using the turbulence model was 0.85 (Montgomery, 1947, ANSYS, 2011). Figure 5.19 displays the relationship between air temperature and Prandtl number

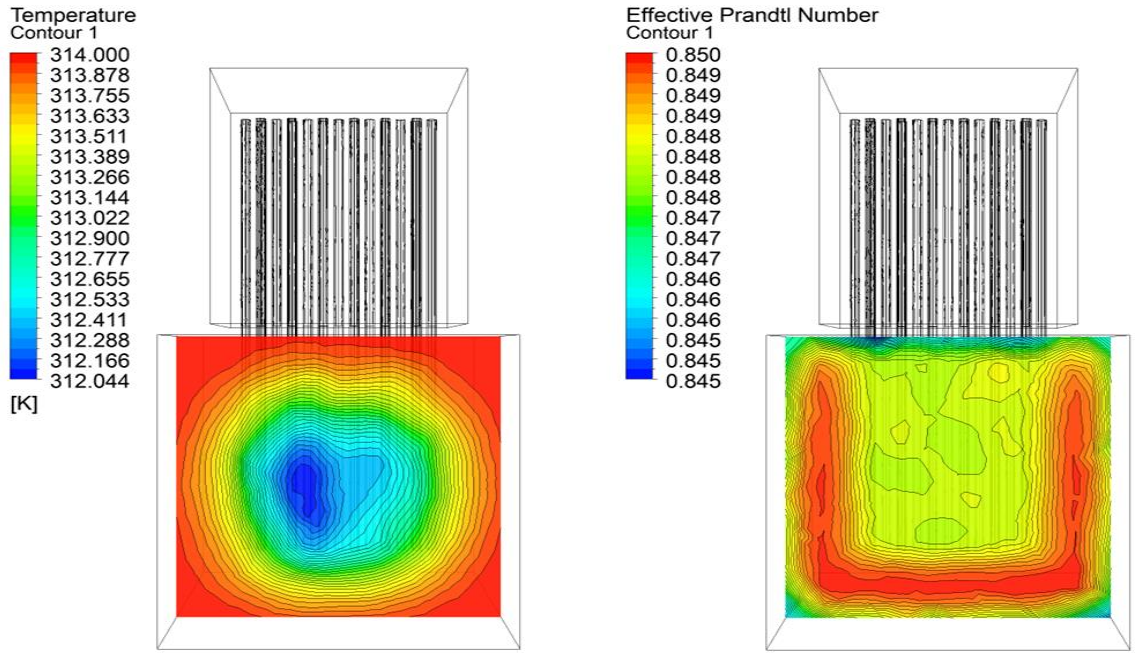

Figure 5.19 Relationship between air temperature and Effective Prandtl number using water as the heat pipe working fluid

It was observed that both the air temperature and the Prandtl number was the highest at 314K and 0.850 near the walls of the test section which were out of proximity of the heat pipes. Conversely, the air temperature and the Prandtl number were reduced to 312K and 0.847 in the areas at the immediate downstream of the heat pipes along the centre of the test section. The study confirmed that the Prandtl number was inversely proportional to the temperature gradient between the fluid temperature and the temperature of the wall (Kakac *et al*., 2004).

The source and sink temperatures of 314K and 288K along with the inlet velocity of 2.3m/s were kept constant for all analysed cases. Four individual tests were conducted on each fluid property with tests 1-4 comprising of the variation in density (ρ), tests 5-8 comprising of the variation in thermal conductivity (k), tests 9-12 comprising of the variation in dynamic viscosity (μ) and tests 13-16 comprising of the variation in specific heat capacity (c_p) (Chapter 3, Section 3.6.5). Each of the above fluid property was varied one at a time while keeping the other properties constant, the findings of which are described in depth in the following discussion sections

5.3.2 Effect of density on heat transfer

This section illustrates the numerical results obtained by varying the density of the heat pipe working fluid while keeping the other properties constant. The range of densities was taken from 600kg/m^3 to 1,800kg/m^3 with the density of water being 998kg/m^3 at an operating temperature of 293K. A plane was constructed through the axial length of the heat pipes and the contour levels of Prandtl number at varying densities are displayed in Figure 5.20. Area weighted average of the Prandtl number was taken across the plane and a similar profile was observed at varying fluid density values. The Prandtl number was 0.857 for the baseline model using the fluid properties of water. It was noted that the Prandtl number decreased by 0.002 as the density was increased to 1,800kg/m^3 indicating the minimal influence of fluid density of the parameter.

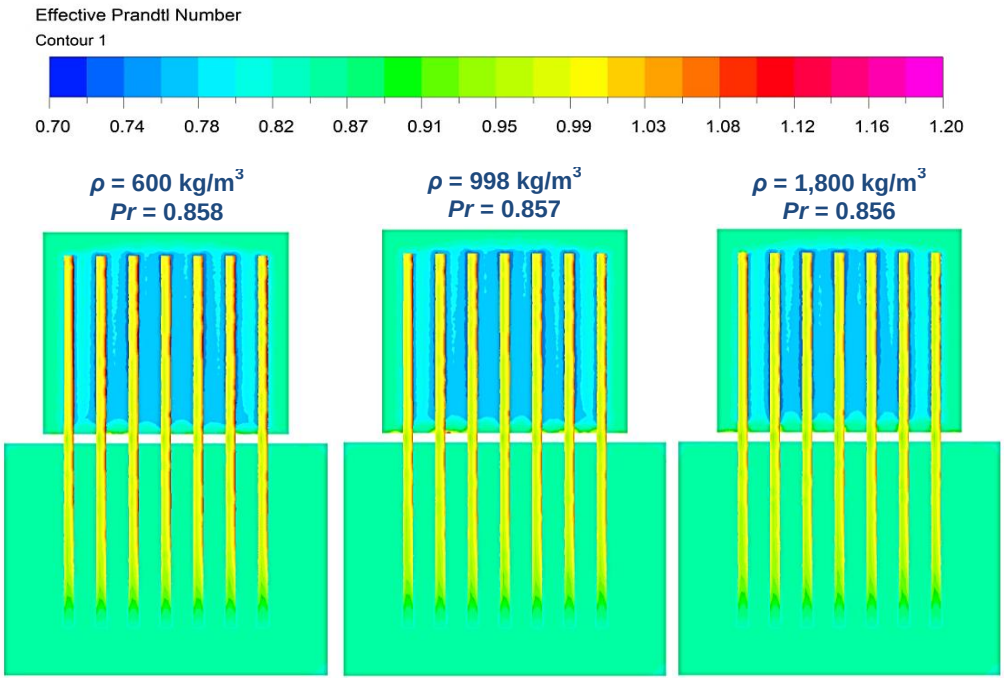

Figure 5.20 Effective Prandtl number across the axial plane of the heat pipe at varying fluid density

Table 5.6 shows the summary of findings obtained for the heat transfer and Prandtl number at varying densities for tests 1 to 4 (Chapter 3, Section 3.6.5). The maximum net heat transfer of 416.18W was indicated for a fluid density of 700kg/m^3, at which the Prandtl number was 2.02. Water displayed the lowest value of heat transfer at 414.46W at a Prandtl number of 1.99. The difference between the minimum and maximum values of convective heat transfer was 1.72W for fluid density variation between 600 and 1,800kg/m^3.

Table 5.6 Net heat transfer and Prandtl number for varying fluid density

Working fluid	Density (kg/m^3)	Heat transfer (W)	Prandtl number
Test 1	600	415.47	2.036
Test 2	700	416.18	2.021
Water	998	414.46	1.991
Test 3	1,200	415.33	1.979
Test 4	1,800	415.51	1.961

The graphical representation of the variation in convective heat transfer of air between the inlet and outlet of the test section along with the corresponding Prandtl number of the heat pipe working fluid is displayed in Figure 5.21. It was noted that the variation in the Prandtl number remained fairly constant for the variation in density with a range of

0.075 obtained between the minimum and maximum value. The trend in heat transfer represented a third order polynomial indication with a maximum increase of 1.72W recorded from water baseline model.

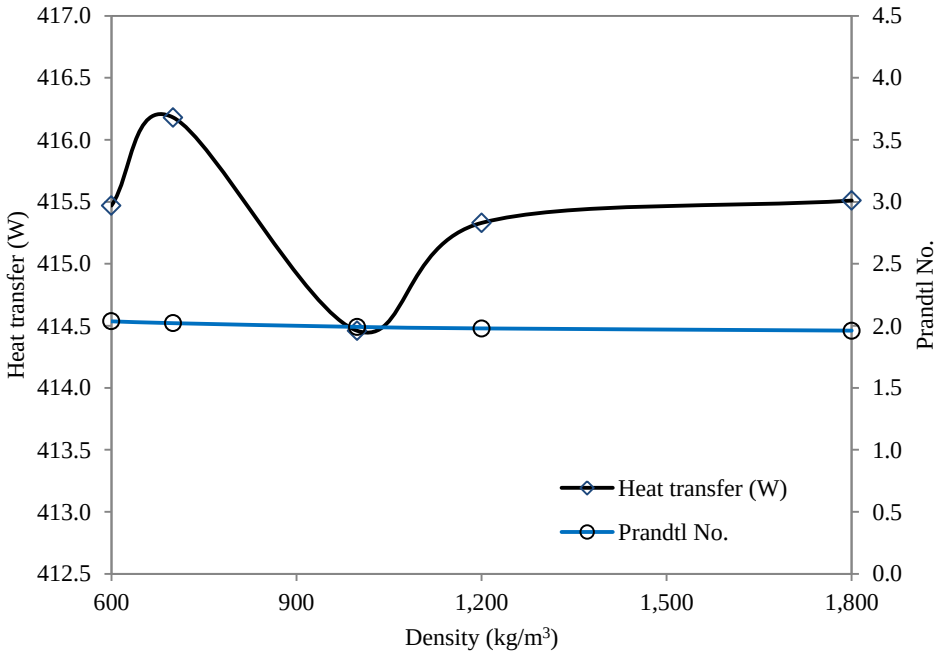

Figure 5.21 Relationship between convective heat transfer and Prandtl number at increasing fluid density

5.3.3 Effect of thermal conductivity on heat transfer

This section displays the numerical results obtained by varying the thermal conductivity of the heat pipe working fluid while keeping the other properties constant. The range of thermal conductivity was taken from 0.1W/mK to 1.0W/mK with the thermal conductivity of water being 0.6W/mK at an operating temperature of 293K.

Figure 5.22 displays the contour levels of the effective Prandtl number at values of thermal conductivity including 0.1, 0.6 and 1.0W/mK. A similar profile was obtained once again for the Prandtl number with a maximum value of 0.858 noted for a thermal conductivity of 0.1W/mK. This was slightly higher than the value for water (thermal conductivity of 0.6W/mK) which indicated a Prandtl number of 0.857.

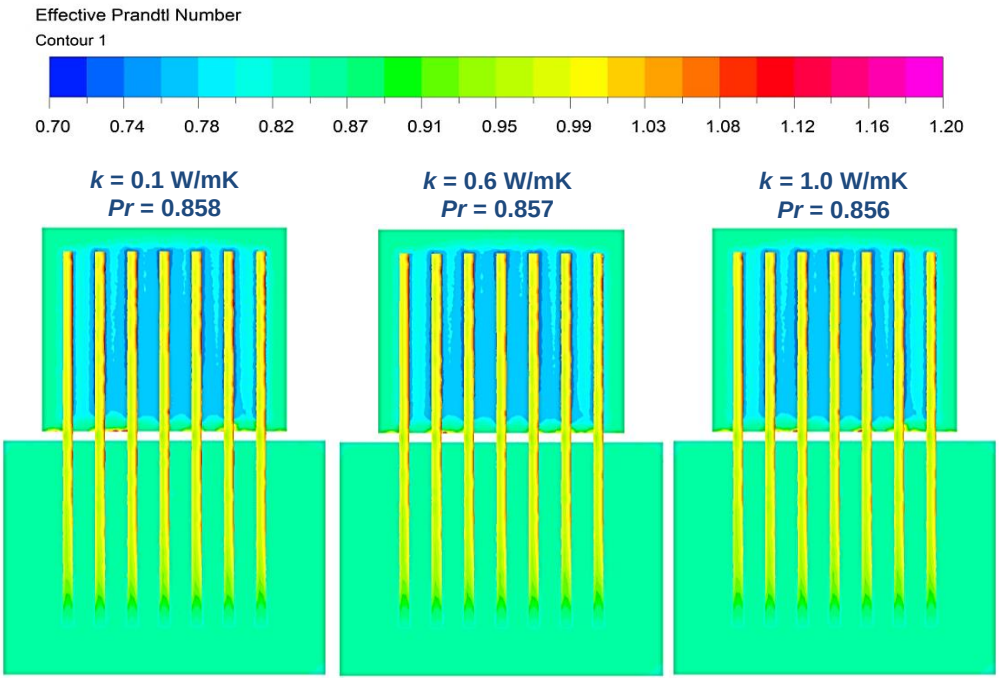

Figure 5.22 Effective Prandtl number across the axial plane of the heat pipe at varying fluid thermal conductivity

The quantification of the results obtained for tests involving variation in thermal conductivity are tabulated in Table 5.7. The maximum value of convective heat transfer was obtained when the thermal conductivity was 0.3W/mK at 415.50W while the minimum value was recorded for water model at 414.46W. The Prandtl number decreased in inverse proportion as the thermal conductivity was increased indicating the greater influence of thermal diffusion in comparison to diffusion through momentum.

Table 5.7 Net heat transfer and Prandtl number for varying fluid thermal conductivity

Working fluid	Thermal conductivity (W/mK)	Heat transfer (W)	Prandtl number
Test 5	0.1	415.49	2.042
Test 6	0.3	415.50	2.021
Water	0.6	414.46	1.991
Test 7	0.8	415.48	1.972
Test 8	1.0	415.49	1.952

The graphical representation of the findings comparing heat transfer and Prandtl number are displayed in Figure 5.23. A variation of 1.04W was recorded between the five tests while the variation in Prandtl number was determined at 0.09. The trend followed a similar pattern to the one obtained for tests involving varying densities. The maximum increase in convective heat transfer from the benchmark water model was 1.04W at a

thermal conductivity of 0.3W/mK, at which the Prandtl number of the heat pipe fluid was 2.02. In general, the Prandtl number remained relatively constant at increasing values of thermal conductivity with a maximum difference of 0.09 between the minimum and maximum value.

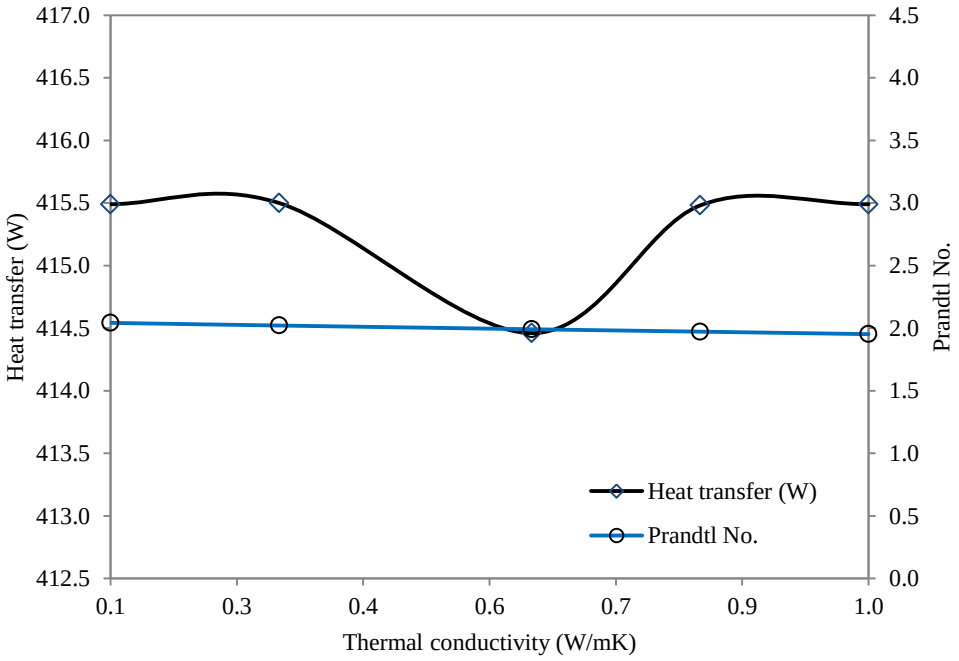

Figure 5.23 Relationship between convective heat transfer and Prandtl number at increasing fluid thermal conductivity

5.3.4 Effect of dynamic viscosity on heat transfer

The findings relating the dynamic viscosity of the heat pipe working fluid to the convective heat transfer of air are displayed in this section. The range of dynamic viscosity was taken from $1x10^{-5}$ Pas to $1x10^{-1}$ Pas with the dynamic viscosity of water being $1x10^{-3}$ Pas at an operating temperature of 293K.

Figure 5.24 displays the variation in effective Prandtl number across the axial plane of the heat pipes. A sharp increase in Prandtl number was noted when the dynamic viscosity was increased to $1x10^{-1}$ Pas. The area weighted average Prandtl number of the plane was 1.4, which was 0.54 greater than what was obtained at a dynamic viscosity of $1x10^{-5}$ Pas. In general, the Prandtl number increased as the dynamic viscosity of the fluid increased.

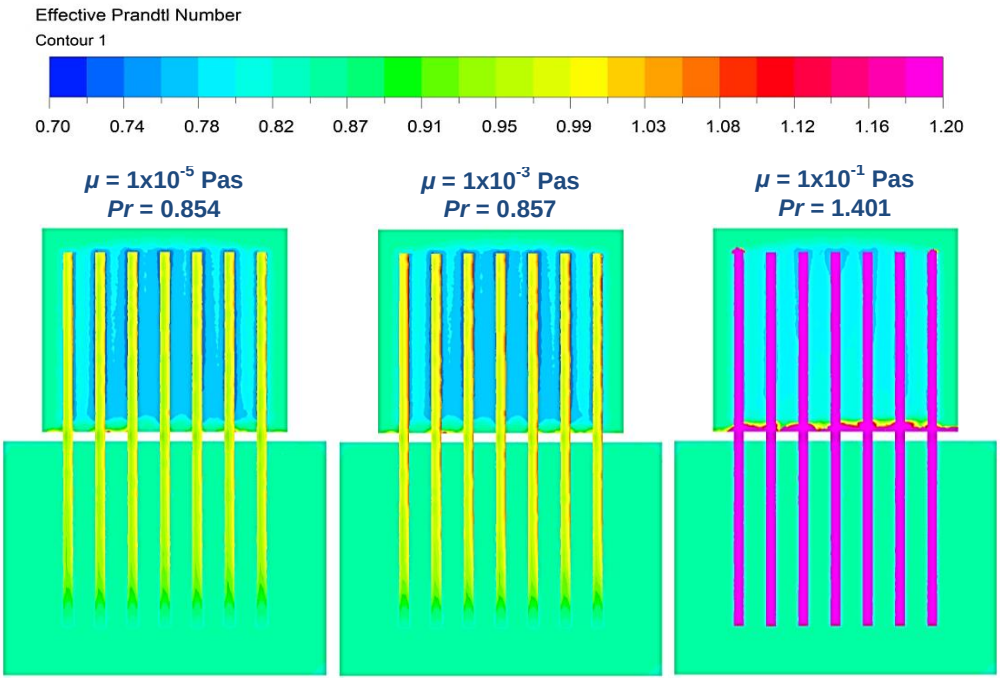

Figure 5.24 Effective Prandtl number across the axial plane of the heat pipe at varying fluid dynamic viscosity

Table 5.8 quantified the results obtained for the convective heat transfer of air and the Prandtl number of the heat pipe working fluid. The maximum value of the convective heat transfer was obtained at 415.48 when the dynamic viscosity was $1x10^{-1}$ Pas. Correspondingly, the highest Prandtl number was also obtained at this dynamic viscosity with a value of 4.1. This was expected as the Prandtl number is directly proportional to the dynamic viscosity parameter. It was observed that while the Prandtl number increased sharply from 0.96 to 4.11 (dynamic viscosity increase from $1x10^{-5}$Pa to $1x10^{-1}$ Pas), the effect on convective heat transfer was less significant with an increase of only 0.99W noted between the minimum and the maximum value.

Table 5.8 Net heat transfer and Prandtl number for varying fluid dynamic viscosity

Working fluid	Dynamic viscosity (Pas)	Heat transfer (W)	Prandtl number
Test 9	$1.0x10^{-5}$	414.49	0.962
Test 10	$1.0x10^{-4}$	414.43	0.963
Water	$1.0x10^{-3}$	414.46	1.991
Test 11	$1.0x10^{-2}$	414.62	2.170
Test 12	$1.0x10^{-1}$	415.48	4.108

Figure 5.25 illustrates the graphical representation of the convective heat transfer of air from inlet to outlet of the test section and the corresponding Prandtl number of the heat

pipe working fluid. A large increase in Prandtl number was observed when the dynamic viscosity was $1x10^{-1}$ Pas, confirming the maximum convective heat transfer out of the conducted tests on fluid viscosities. The maximum increase in convective heat transfer of air from the benchmark water model was 1.02W when the dynamic viscosity was $1x10^{-1}$ Pas. A direct proportionality was recorded between convective heat transfer and the Prandtl number at increasing values of dynamic viscosities to enhance diffusion through momentum.

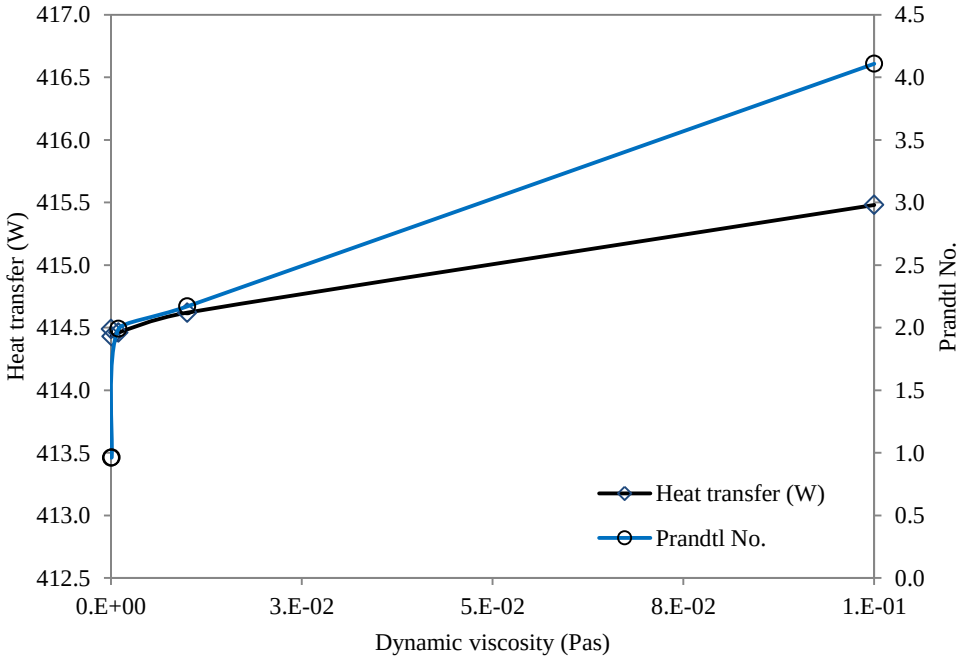

Figure 5.25 Relationship between convective heat transfer and Prandtl number at increasing fluid dynamic viscosity

5.3.5 Effect of specific heat capacity on heat transfer

The final set of testing involved the variation in the specific heat capacity of working fluids and determining its impact on heat transfer through convection. The specific heat capacity was taken from 1,000J/kgK to 6,000J/kgK with the specific heat capacity of water being 4,182J/kgK at an operating temperature of 293K. Figure 5.26 displays the variation in effective Prandtl number across the axial plane of the heat pipes. As observed, the Prandtl number increased from 0.829 to 0.864 as the specific heat capacity was increased from 1,000J/kgK to 6,000J/kgK. Since the Prandtl. No. was directly proportional to the specific heat capacity of the fluid; this trend was expected and was clearly visible from the figure.

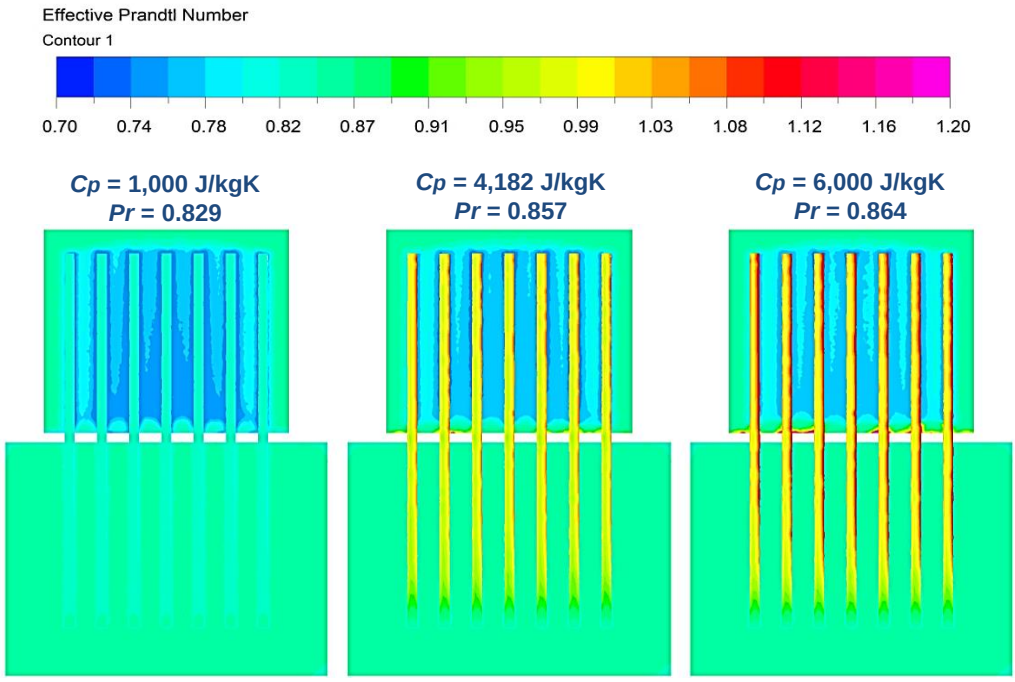

Figure 5.26 Effective Prandtl number across the axial plane of the heat pipe at varying fluid specific heat capacity

Table 5.9 indicates the findings for tests 13 to 16 (Chapter 3, Section 3.6.5) involving the variation in specific heat capacity of fluid while keeping the other properties constant. The effect on heat transfer and Prandtl number was noted and it was observed that the specific heat capacity had the greatest influence on convective heat transfer. A maximum value of 416.89W was obtained at a specific heat capacity of 6,000J/kgK while the minimum value of 413.18W was obtained at a specific heat capacity value of 1,000J/kgK. Similarly, the Prandtl number increased from 0.77 to 2.69 in direct proportion to the increase in specific heat capacity of the fluid.

Table 5.9 Net heat transfer and Prandtl number for varying fluid specific heat capacity

Working fluid	**Specific heat capacity (J/kgK)**	**Heat transfer (W)**	**Prandtl number**
Test 13	1,000	413.18	0.769
Test 14	2,000	413.22	1.153
Water	4,182	414.46	1.991
Test 15	5,000	416.38	2.306
Test 16	6,000	416.89	2.690

The graphical representation of findings is displayed in Figure 5.27. An increase of 2.43W was obtained from the benchmark water model to when the specific heat capacity was increased to 6,000J/kgK. This was the most significant heat transfer

enhancement from all investigated material properties. It was shown that heat transfer through convection and Prandtl number increase in direct proportion as the specific heat capacity of the fluid is increased. According to theory, an increase in specific heat capacity and dynamic viscosity increases the Prandtl number and the present numerical study applied the same principles in order to enhance the heat transfer of air through the use of pipe working fluids.

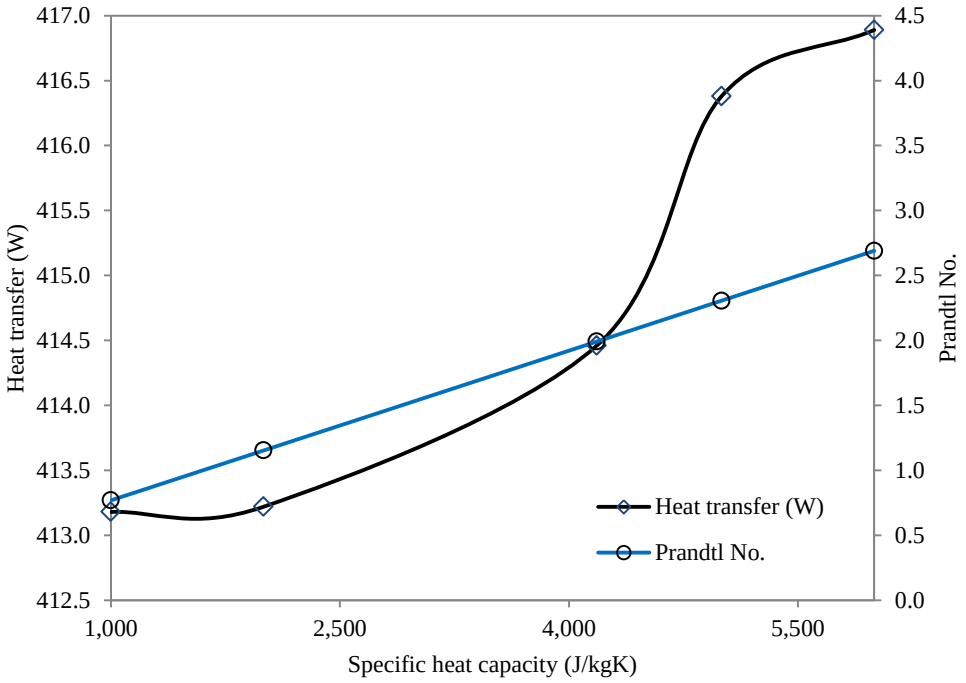

Figure 5.27 Relationship between convective heat transfer and Prandtl number at increasing fluid specific heat capacity

This section's findings predicted the influence of the material properties on the convective heat transfer and its relation to the Prandtl number. From the perspective of cooling a natural airstream carrying a high temperature of 314K, the results determined the impact of internal fluid on heat transfer through convection. Under the operating conditions, the specific heat capacity was found to be the most influential parameter with a 39% enhancement (increase of approximately 4W) in convective cooling while density was found to augment heat transfer by approximately 28%. Dynamic viscosity and thermal conductivity were the least dominant parameters with both affecting an increase of approximately 17%. Figure 5.28 displays the graphical representation displaying the enhancement in overall energy transfer through convective cooling for each individual fluid property in relation to the original water properties.

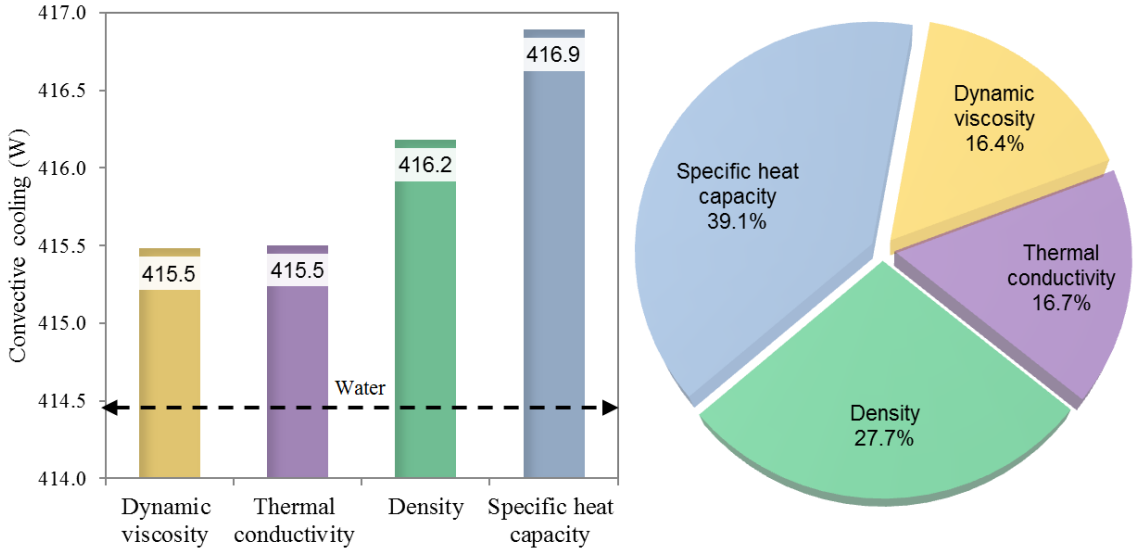

Figure 5.28 Increase in heat transfer through convective cooling for investigated fluid properties

5.4 Geometrical variation - spanwise thickness

In addition to underlining the influence of internal working fluid and its properties, the effect of heat pipe characteristic arrangement on their working performance was established. Using water as the fluid, this section describes the results obtained from the five computational models that were developed incorporating spanwise thickness (S_t) ranging from 44mm to 52mm in increasing intervals of 2mm. The models were created in order to determine the optimum spanwise thickness between the heat pipes.

5.4.1 Air velocity, pressure and temperature profiles

The computational model predicted the air velocity, pressure and temperature profiles upstream and downstream of the heat pipes within the test section. Based on the evaluation of the greatest temperature reduction, the optimum heat pipe configuration in terms of spanwise thickness was determined. A horizontal plane was constructed across the axial length of the test section at a height of 0.25m. Figure 5.29 displays the velocity streamlines along with pressure and temperature contours obtained.

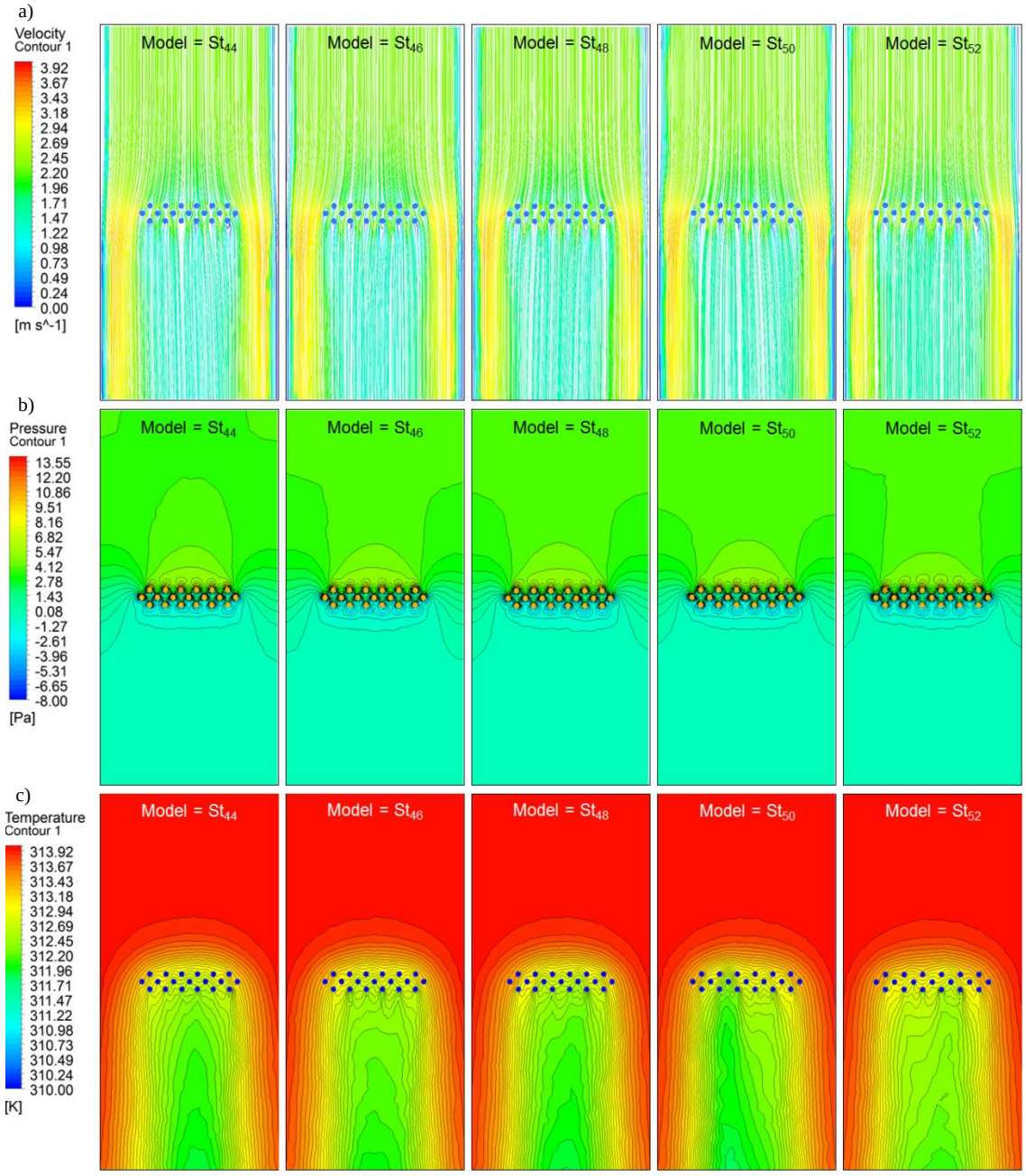

Figure 5.29 Contour levels displaying air: a) velocity b) pressure c) temperature for the analysed spanwise thickness models

It was observed that all models displayed a relatively similar profile to each other for the three parameters. With respect to Figure 5.29 a), the velocity profiles obtained show that the velocity increases as it shears away from the circular heat pipes. The inlet velocity was set to 2.3m/s and the air velocity increased further as it travelled along the sides of the heat exchanger channel. This trend was noticeable in all analysed models irrespective of the spanwise thickness. The air velocity however was found to decrease downstream of the heat pipes.

The static pressure contours for all models are shown in Figure 5.29 b). A maximum positive airside pressure was created as the air stream came in direct contact with the surface of the 1st row of heat pipes. This was due to the force being directly perpendicular to the area of interaction. As a result, a negative pressure was created on the opposite end at the immediate downstream of the heat pipes where the air velocity increased due to the streamlined body of the heat pipes. There was a decrease in positive pressure as the spanwise thicknesses were increased confirming an inverse relationship between the two quantities.

The temperature contour levels are highlighted in Figure 5.29 c). As observed, the air temperature decreased due to the transfer of heat between the air stream and the heat pipes. Since the air velocity was higher on either side of the bank of the pipes, the temperature was observed to be higher on the sides of the channel in comparison to the temperature obtained at the immediate downstream of the heat pipes. It was noted that all analysed models were capable of achieving a temperature reduction, the detailed quantification of which is provided in the following discussion.

An in-depth quantification of results, including the variation in air velocity, pressure and temperature behaviour is displayed in Figure 5.30, Figure 5.31, Figure 5.32, Figure 5.33 and Figure 5.34. Each figure highlights the trend obtained for the air velocity and temperature before and after contact with the heat pipes spaced in various spanwise arrangements.

Figure 5.30 displays the variation in air velocity before and after contact with the heat pipes for St_{44} (spanwise thickness = 44mm) model. The velocity increased to 2.49m/s from an inlet velocity of 2.3m/s as the air stream flows around the first row of pipes. The velocity subsequently decreased as the air stream was in contact with the 3rd row of heat pipes and a reduction of 51.9% was observed along the axial length of the heat exchanger channel. The mean air speed was calculated to be 1.76m/s. The maximum and minimum pressures were 7.18Pa and 0.22Pa, highlighting an overall pressure drop of 45.9%. The air temperature variation is represented on the secondary axis to obtain a comparison with the air velocity. The inlet temperature was set to 314K which was dropped to its minimum value of 312K due to the sensible heat transfer between the air and heat pipes. A mean temperature value of 312.9K was observed and the overall reduction was noted at 0.62%.

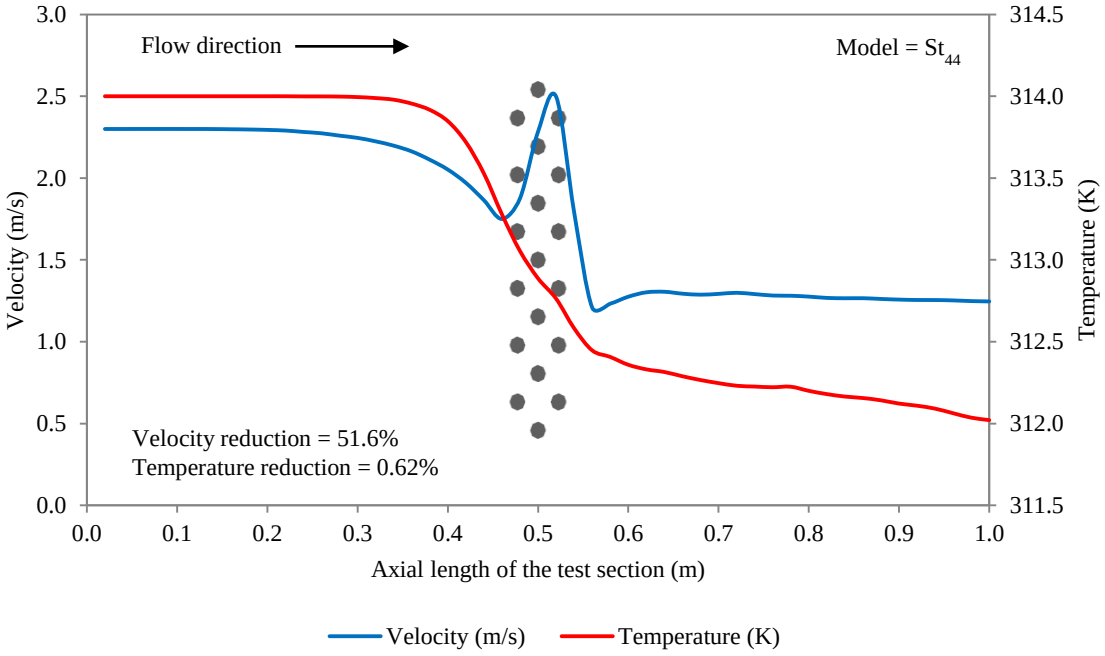

Figure 5.30 Variation in air velocity and temperature profile before and after contact with heat pipes for St_{44} model

Figure 5.31 displays the graphical representation of the variation in the three investigated parameters for St_{46} (spanwise thickness = 46mm) model. The general trend found in air velocity, pressure and temperature was similar to the St_{44} model. The mean air velocity was obtained at 1.79m/s which was 0.03m/s higher than the St_{44} model thereby highlighting that the increase in spanwise thickness had a direct impact on the velocity of air stream. The reduction in total pressure was noted to be higher as well with a pressure drop of 7.5Pa obtained over the axial length of the test section. The velocity and pressure had an impact on the temperature reduction as a mean value of 313K was obtained, thereby indicating the reduction in temperature of 0.63%.

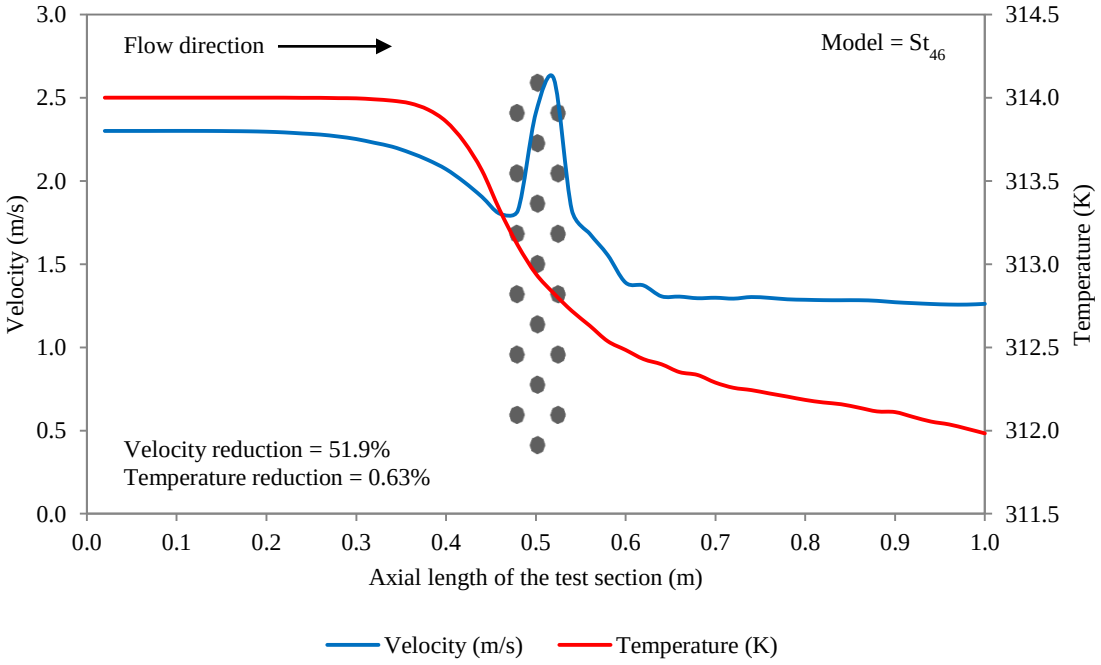

Figure 5.31 Variation in air velocity and temperature profile before and after contact with heat pipes for St_{46} model

The maximum air velocity across all analysed models was obtained for the St_{48} (spanwise thickness = 48mm) model at 2.64m/s as displayed in Figure 5.32.

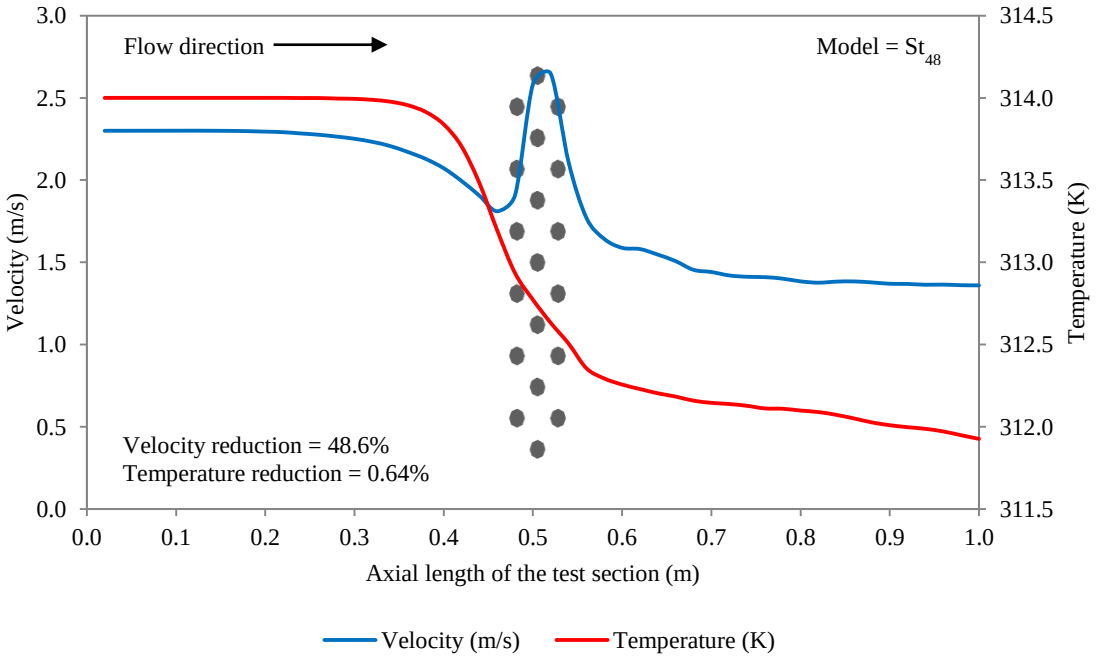

Figure 5.32 Variation in air velocity and temperature profile before and after contact with heat pipes for St_{48} model

The mean velocity was calculated at 1.86m/s as a reduction percentage of 48.6% was calculated. The velocity pattern however remained similar to all other analysed models. The mean air pressure was determined at 3.91Pa across the length of the test section. With respect to the temperature variation, a reduction of 2K from the inlet source temperature was obtained for the St_{48} model. The minimum temperature recorded was 312.0K which indicated a reduction of 0.64% which was superior to both St_{44} and St_{46} models.

Figure 5.33 displays the quantified results for air velocity and temperature for the St_{50} (spanwise thickness = 50mm) model. The spanwise thickness of 50mm did not influence a reduction in velocity like the earlier models as a mean velocity value of 1.89m/s was obtained. This was 0.13m/s greater than the St_{44} model. In addition, the static pressure values were also reduced with the maximum value obtained at 7.06Pa (0.12Pa lower than the St_{44} model). With respect to the airside axial thermal profile, the St_{50} model displayed the optimum results in terms of temperature reduction as a minimum temperature value of 311.8K was obtained, highlighting a temperature drop of 2.2K or 0.67%.

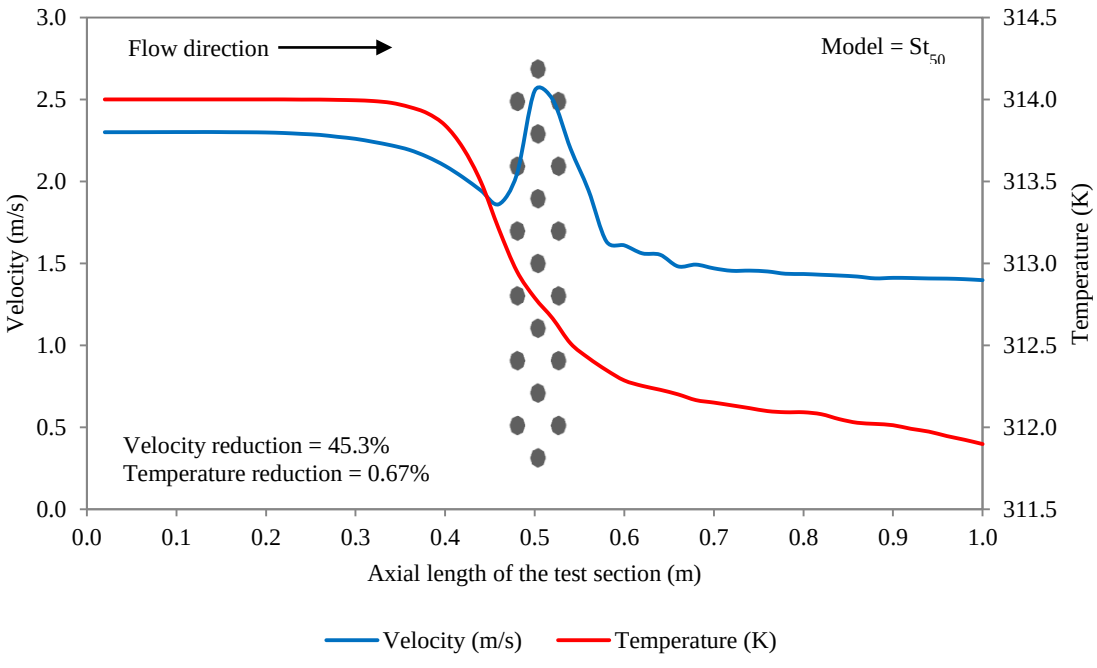

Figure 5.33 Variation in air velocity and temperature profile before and after contact with heat pipes for St_{50} model

The maximum allowable spacing possible from the current test section geometry incorporated heat pipes with a spanwise thickness of 52mm. Figure 5.34 displays the findings obtained from the St_{52} (spanwise thickness = 52mm) model. The reduction in velocity decreased further with a mean value of 1.88m/s obtained. The maximum velocity value was predicted at 2.48m/s which was 0.18m/s greater than the inlet velocity of 2.3m/s. The mean pressure value was recorded at 4.09Pa with a drop of 41.3% along the axial length. A maximum reduction of 1.8K or 0.59% in air temperature was obtained with the mean temperature value determined at 313.1K. Temperature reduction using the St_{52} model was the lowest in comparison to all other models. From all analysed models it was concluded that the St_{50} model provided the greatest reduction in sensible air temperatures across the axial length of the test section.

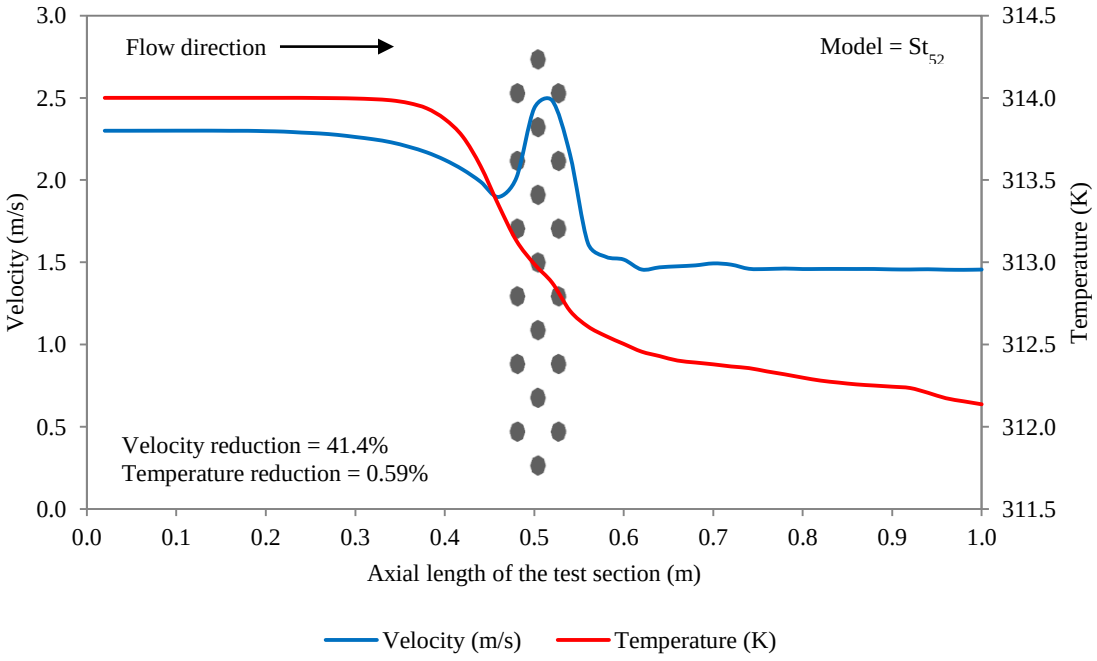

Figure 5.34 Variation in air velocity and temperature profile before and after contact with heat pipes for St_{52} model

A comparison between all analysed models in terms of variation in air velocity, pressure and temperature across the radial length of the test section is displayed in Figure 5.35. A line was constructed 150mm downstream of the heat pipe arrangement in order to determine the parametric profiles of the compared variables. The line was constructed along the entire radial length of the test section measuring 0.5m.

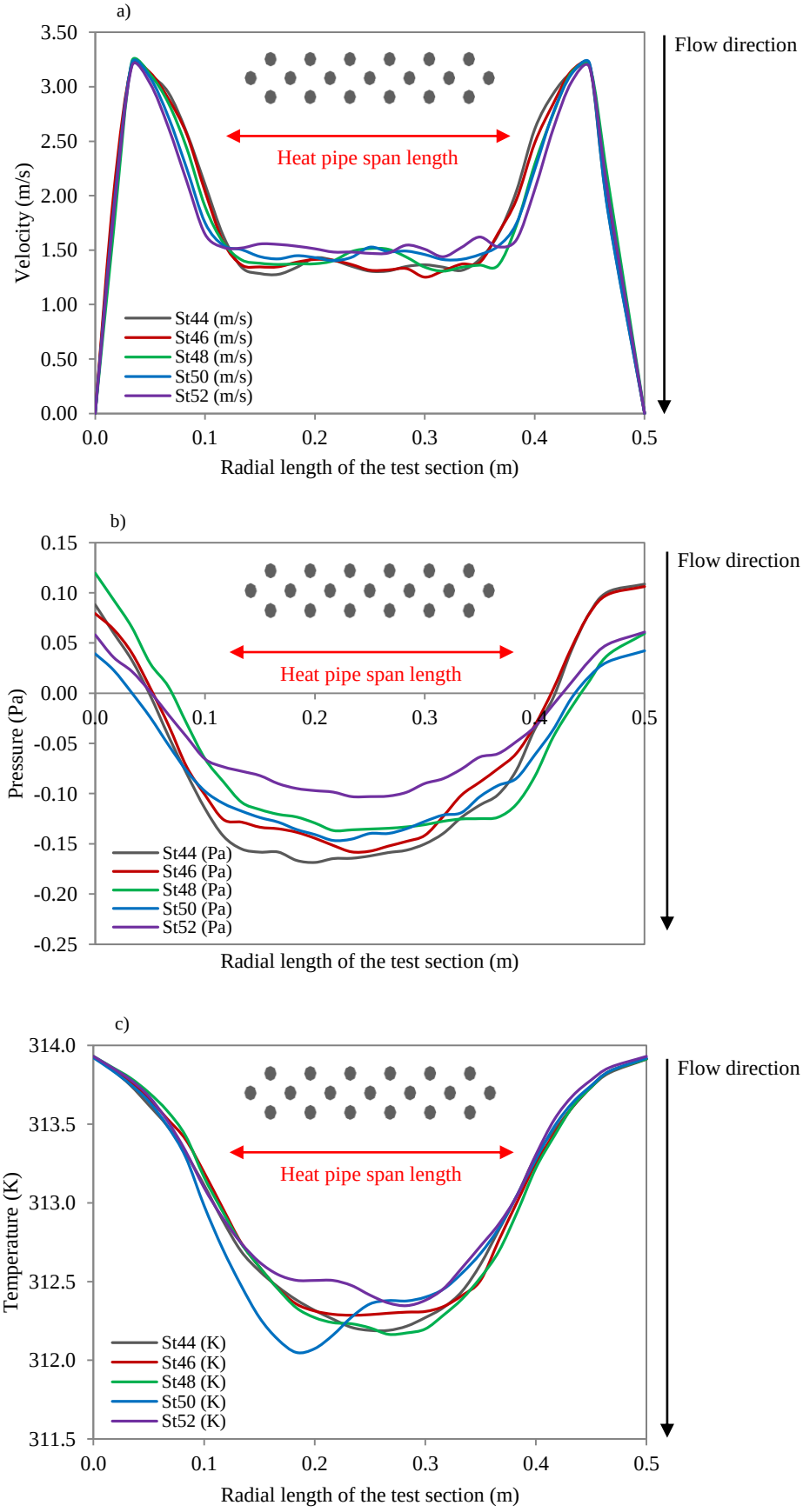

Figure 5.35 Variation in air: a) velocity b) pressure c) temperature across the radial length of the test section of all analysed models

Figure 5.35 a) displays the air velocity profile for all models across the radial length of the test section. As observed, the velocity is zero near the walls and reaches its maximum value at both sides of the bank of the heat pipe tubes. The velocity is reduced at the immediate downstream of the heat pipes at which it normalises at approximately 1.5m/s, which was 0.7m/s lower than the inlet velocity of 2.3m/s. Due to the streamlined cross-section of the heat pipes, it was noted that all analysed models displayed a similar trend to each other with minor variations in air velocity paths.

Variation in air pressure profiles are displayed in Figure 5.35 b). It was observed that the pressure drop decreased as the spanwise thicknesses were increased, thus confirming an inverse relationship between the two quantities. As a result, a maximum pressure drop was obtained for St_{44} model, for which the lowest static pressure value was -0.17Pa. This was due to the minimum spanwise thickness between the arranged heat pipes. In addition, a minimum pressure drop was determined for the St_{52} model with a static pressure value of -0.10Pa. The pressure profiles were at its minimum values at immediate downstream of the heat pipes while higher pressure gradients were observed along the sides of the bank of heat pipes.

Figure 5.35 c) shows the radial variation in air temperatures as it comes in contact with the heat pipes. At an inlet temperature of 314K, it was observed that all analysed models were capable of achieving a mean reduction of approximately 1.6K. Air temperature near the walls of the test section were higher than the immediate downstream of the heat pipes due to insufficient heat transfer near the walls. The St_{50} model was found to achieve the largest reduction in temperature with a minimum temperature value of 312.1K (approximately 2K lower than the source temperature of 314K) while the lowest reduction was estimated for the St_{52} model with a minimum temperature value of 312.5K. However, a similar temperature profile was predicted for all analysed models with minor variations.

Measurement points were constructed in order to quantify the airside velocity, pressure and temperature data. Two points were created at the inlet, upstream of the heat pipes (I_1 and I_2) while five points were created downstream at the outlet ($O_1 – O_5$) of the heat pipes (Chapter 3, Section 3.6.4). Table 5.10 displays the parametric values of air velocity, pressure and temperature at the measurement locations. Air temperatures at the point O_3 were consistently lower than other points since it was located centrally

downstream of the bank of heat pipe tubes and was the least affected by the air stream passing through the sides of the channel.

The lowest temperature value recorded was 312.02K for the St_{50} model at the point O_3. Similarly, the highest air velocity value was recorded at 1.57m/s at O_4 for the St_{52} model due to the maximum spanwise thickness between the heat pipes allowing minimal blockage to the path of the air stream. The pressure was found to be in direct proportion to the velocity as the maximum value of 1.368Pa was also observed for the St_{52} model at the point O_5.

Table 5.10 Air velocity, pressure and temperature values for all analysed models at the measurement locations

Model	Point	Velocity (m/s)	Pressure (Pa)	Temperature (K)
St_{44}	I_1	2.18	3.09	313.96
	I_2	2.19	3.05	313.96
	O_1	1.28	1.02	312.60
	O_2	1.38	1.31	312.33
	O_3	1.32	1.13	312.24
	O_4	1.35	1.23	312.39
	O_5	1.31	1.09	312.48
St_{46}	I_1	2.18	3.06	313.96
	I_2	2.18	3.04	313.96
	O_1	1.34	1.22	312.64
	O_2	1.42	1.21	312.32
	O_3	1.34	1.09	312.29
	O_4	1.30	1.02	312.31
	O_5	1.37	1.33	312.44
St_{48}	I_1	2.18	3.08	313.95
	I_2	2.18	3.06	313.96
	O_1	1.38	1.29	312.64
	O_2	1.37	1.27	312.29
	O_3	1.51	1.42	312.23
	O_4	1.39	1.44	312.18
	O_5	1.34	1.24	312.43
St_{50}	I_1	2.19	3.09	313.97
	I_2	2.20	3.08	313.96
	O_1	1.46	1.38	312.31
	O_2	1.44	1.39	312.02
	O_3	1.48	1.50	312.32
	O_4	1.50	1.41	312.38
	O_5	1.42	1.25	312.59
St_{52}	I_1	2.21	3.07	313.97
	I_2	2.21	3.08	313.97
	O_1	1.54	1.62	312.66
	O_2	1.52	1.56	312.51
	O_3	1.48	1.44	312.45
	O_4	1.57	1.54	312.35
	O_5	1.56	1.68	312.63

Table 5.11 summarises the mean values of the air velocity and temperature for all analysed models at the measurement locations. Keeping a constant inlet air temperature of 314K for all cases, the mean outlet temperature obtained from the St_{50} model was the lowest at 312.32K. St_{52} model displayed the highest mean outlet temperature of 312.52K. A direct proportionality was obtained between the increasing spanwise thickness and the outlet air velocities as the increase in spanwise thickness distance from 44mm (St_{44} model) to 52mm (St_{52} model) increased the mean outlet velocity from 1.33m/s to 1.53m/s.

Table 5.11 Summary of the mean parametric values obtained for spanwise thickness models

Model	Mean inlet velocity (m/s)	Mean outlet velocity (m/s)	Δv (m/s)	Mean inlet temperature (K)	Mean outlet temperature (K)	ΔT (K)
St_{44}	2.18	1.33	0.97	313.97	312.41	1.59
St_{46}	2.18	1.35	0.95	313.97	312.40	1.60
St_{48}	2.18	1.40	0.90	313.96	312.35	1.65
St_{50}	2.20	1.46	0.84	313.96	312.32	1.68
St_{52}	2.21	1.53	0.77	313.96	312.52	1.48

The graphical illustration highlighting the mean outlet air velocity and temperature at measurement locations for all spanwise thickness models is displayed in Figure 5.36.

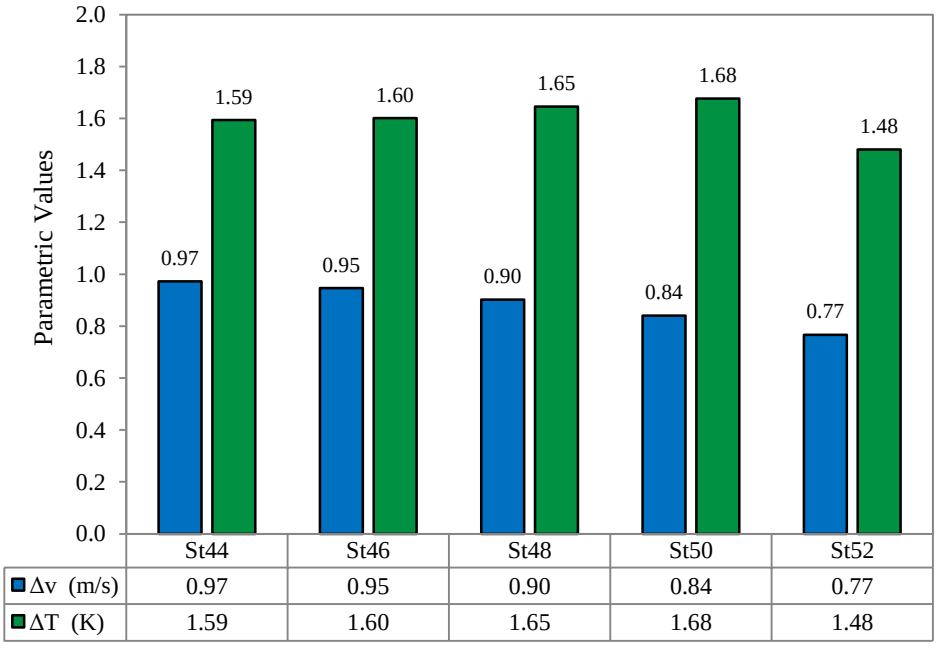

Figure 5.36 Bar chart representation of the difference in air velocity and temperature for spanwise thickness models

As observed from the figure, the St_{50} model displayed the largest reduction of 1.68K in temperature in comparison to other models. The largest velocity reduction was obtained for the St_{44} model due to the minimum spanwise thickness out of all the compared models. The highest velocity reduction was calculated at 0.97m/s. Conversely, the lowest airside velocity reduction was obtained for the St_{52} model due to the increased spanwise thickness between the heat pipes. Using the inlet velocity of 2.3m/s, the lowest velocity reduction was calculated at 0.77m/s.

5.4.2 Total cooling capacity and overall effectiveness

This section determined the cooling capacity (rate of heat transfer) and heat pipe effectiveness achieved from the analysis of all five spanwise thickness models. Measurement points were used, at the inlet (I_1 and I_2) and outlet ($O_1 – O_5$) of the heat pipes (Chapter 3, Section 3.6.4). The heat transfer and effectiveness was calculated using eqn.27 and eqn.28. The values of heat transfer alongside the heat exchanger effectiveness across the measurement points were obtained and are displayed in Table 5.12.

In general, the measurement locations O_2 and O_3 displayed superior values of heat transfer due to the minimal influence of the air stream passing through the sides of the test section. The maximum value of heat transfer in the evaporator was obtained at 1,155.12W for the St_{50} model, at which the corresponding heat exchanger effectiveness was 7.62%. The heat exchanger effectiveness was found to be directly proportional to the temperature differential or the rate of heat transfer. It was noted that the heat exchanger effectiveness was below 10% for all measurement points. This was due to the high inlet velocity of 2.3m/s allowing convection with less contact time between the air stream and the heat pipes.

Table 5.12 Sensible heat transfer and effectiveness for spanwise thickness models at the measurement locations

Model	Point	Heat transfer (W)	Effectiveness (%)
St_{44}	I_1	25.09	0.12%
	I_2	23.34	0.12%
	O_1	818.50	5.15%
	O_2	974.27	5.73%
	O_3	1,026.78	5.96%
	O_4	940.43	6.35%
	O_5	888.51	5.27%
St_{46}	I_1	23.92	0.12%
	I_2	23.34	0.15%
	O_1	794.58	6.50%
	O_2	980.10	7.62%
	O_3	999.36	6.46%
	O_4	986.52	6.23%
	O_5	910.68	5.42%
St_{48}	I_1	29.17	0.19%
	I_2	23.34	0.15%
	O_1	793.42	5.23%
	O_2	997.61	6.58%
	O_3	1,032.61	6.81%
	O_4	1,061.78	7.00%
	O_5	915.93	6.04%
St_{50}	I_1	17.50	0.16%
	I_2	23.34	0.15%
	O_1	985.94	5.24%
	O_2	1,155.12	6.46%
	O_3	980.10	6.59%
	O_4	945.10	6.50%
	O_5	822.59	6.00%
St_{52}	I_1	17.50	0.17%
	I_2	17.50	0.15%
	O_1	781.75	5.40%
	O_2	869.26	6.42%
	O_3	904.26	6.77%
	O_4	962.60	6.20%
	O_5	799.25	5.86%

The summarised area-weighted averaged results for the evaporator net heat and mass transfer are displayed in Table 5.13. The highest mean overall effectiveness was calculated at 5.60% for the St_{50} model while the lowest mean overall effectiveness was calculated at 4.67% for the St_{52} model. The highest rate of heat transfer in the test section was 768.17W for the St_{50} model. The table further highlights the values of net mass transfer of air between the inlet and outlet of the evaporator test section. The mean values were found to be in the order of 10^{-7} thereby confirming the appropriate mass transfer of air between the inlet and the outlet surfaces.

Table 5.13 Summary of the mean heat and mass transfer values obtained for spanwise thickness models

Model	Evaporator net heat transfer (W)	Evaporator net mass transfer (kg/sec)	Overall effectiveness (%)
St_{44}	714.35	1.78E-08	5.21%
St_{46}	719.44	1.19E-07	5.24%
St_{48}	748.58	1.01E-06	5.46%
St_{50}	768.17	5.96E-08	5.60%
St_{52}	640.15	2.98E-07	4.67%

A graphical representation of the heat and mass transfer results are displayed in Figure 5.37. The values are plotted on a logarithmic scale in order to visually compare the difference in the analysed parameters. As observed, the rate of heat transfer for all models is obtained in the order of 10^3 while the values of mass transfer are in the order ranging from 10^{-6} to 10^{-8}.

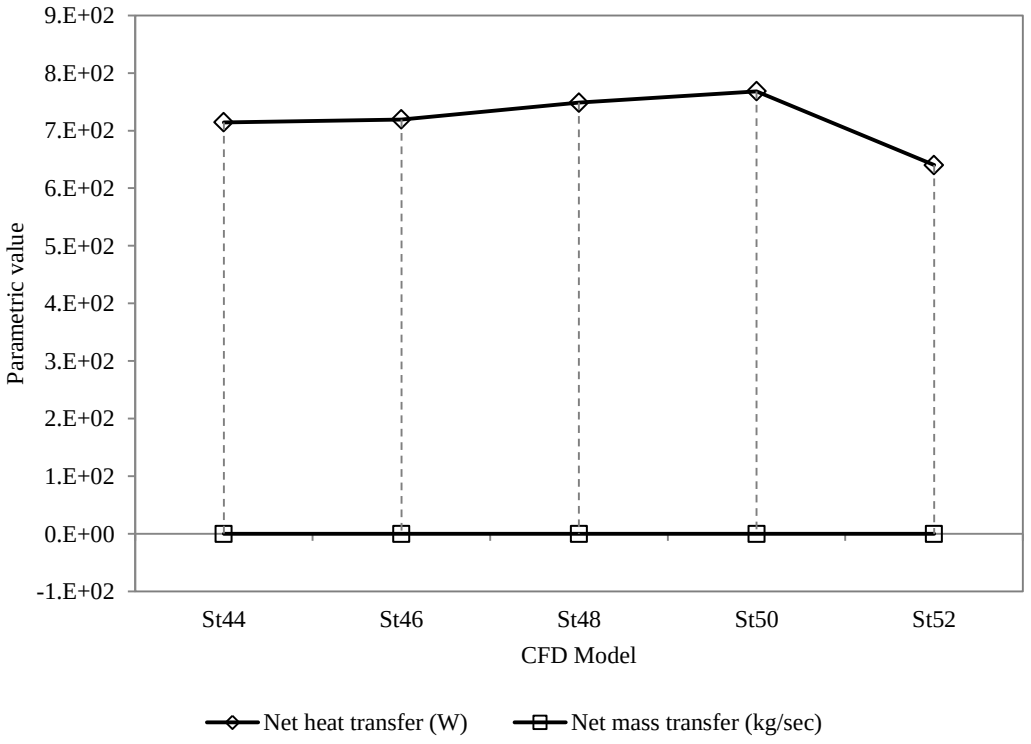

Figure 5.37 Logarithmic scale representation of evaporator net heat and mass transfer rate

The area-weighted averaged cooling capacity or heat transfer upstream and downstream of the heat pipes was further evaluated. A graphical illustration of the comparison between total cooling capacity and overall heat exchanger effectiveness for all analysed models is further displayed in Figure 5.38. Since all other influencing parameters were kept constant, the rate of heat transfer and effectiveness were directly proportional to the temperature difference of the airstream upstream and downstream of the heat pipes.

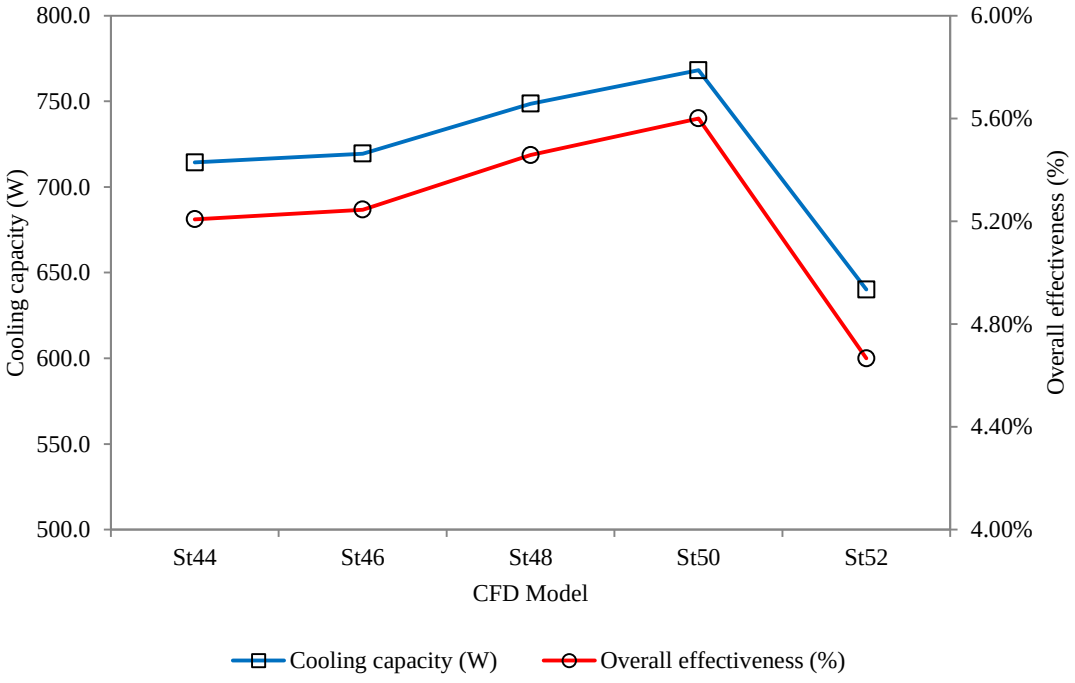

Figure 5.38 Relationship between cooling capacity and overall heat exchanger effectiveness for spanwise thickness models

The peak effectiveness of the heat exchanger was approximately 5.6% for the St_{50} model, at which the area-weighted heat transfer or cooling capacity was determined at approximately 768W. A parabolic profile was obtained from the five compared CFD models with a spanwise thickness of 50mm corresponding to the optimum heat pipe arrangement. The overall effectiveness was found to decrease on either side of the St_{50} model and was at its lowest when the spanwise thickness was increased to 52mm. As discussed earlier, the general low percentage of heat exchanger effectiveness was due to the large incoming air velocity of 2.3m/s directly perpendicular to the pipe surface, therefore providing minimal contact time for heat transfer between the air stream and the heat pipes.

5.5 Geometrical variation - streamwise distance

Following the identification of the optimum spanwise thickness for the heat pipe arrangement, this section of the results describes the findings for the ideal streamwise distance (S_d) between the rows of heat pipes. Using water as the internal working fluid and a span length of 50mm, the results from five computation models incorporating streamwise distances from 20mm to 40mm are discussed.

5.5.1 Air velocity, pressure and temperature profiles

The computational investigation predicted the air velocity, pressure and temperature profiles upstream and downstream of the heat pipes within the test section. Based on the evaluation of the greatest temperature reduction, the optimum heat pipe configuration in terms of streamwise distance was determined. Figure 5.39 displays the air velocity streamlines along with air pressure and temperature contour levels for each of the analysed models.

Figure 5.39 a) displays the air velocity streamlines and due to the streamlined cross-section of the cylindrical tubes, a similar velocity trend to varying spanwise thickness models was obtained once again. The inlet velocity was kept constant at 2.3m/s for all cases and the findings showed that the velocity increased by approximately 0.9m/s at both ends of the bank of the tubes. A decrease in air velocity was noted at the immediate downstream of the heat pipes due to the contact period between the fluid and the pipe surface. With respect to Figure 5.39 b), the static pressure contours for all models are highlighted. Positive pressure regions were created at the upstream of the rows of heat pipes for all analysed models with a mean value of 4.1Pa. Correspondingly, the downstream locations of the heat pipes experienced a region of negative pressures with a mean value of -0.3Pa noted across all models.

Temperature contour levels are illustrated in Figure 5.39 c). The temperature of air decreased as the stream passed over the pipes due to the transfer of heat between the air stream and the heat pipes. Maximum temperature reduction was noted at the immediate downstream locations of the heat pipes where the air velocity was the lowest indicating a direct proportionality between the two quantities. Simultaneously, there was no temperature reduction on either side of the bank of the pipes since there was no contact between the airstream and the heat pipes.

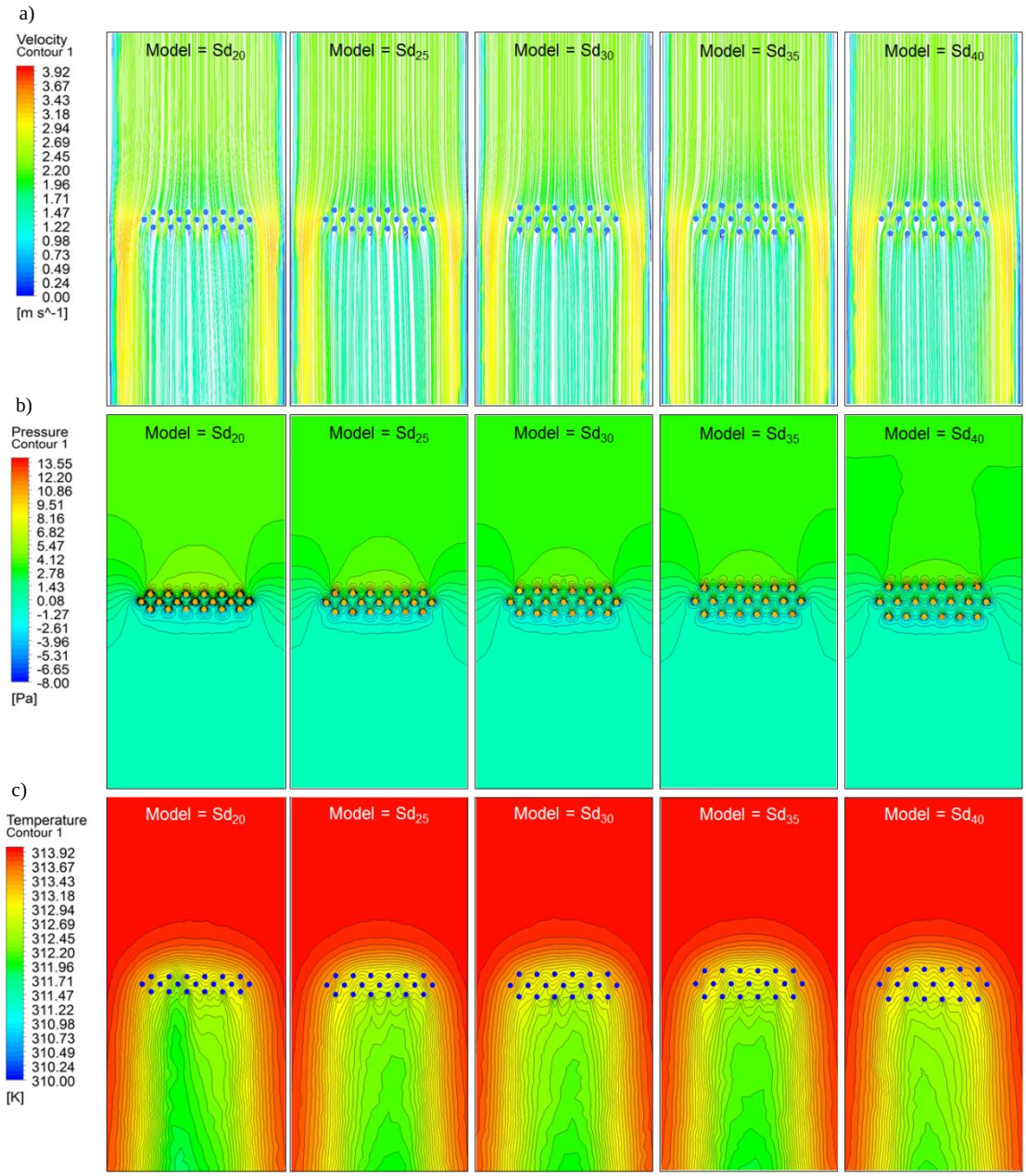

Figure 5.39 Contour levels displaying air: a) velocity b) pressure c) temperature for the analysed streamwise distance models

For Sd_{20} (streamwise distance = 20mm) model, the variation in air temperature and velocity across the axial length of the test section is displayed in Figure 5.40. At an inlet velocity of 2.3m/s, the maximum velocity value was determined at 2.55m/s as the airstream came in contact with the 1st row of heat pipes. Overall, the air velocity was reduced by 45.3%. With respect to the airside axial thermal profile, the Sd_{20} model displayed the optimum results in terms of temperature reduction as a minimum temperature value of 311.8K was estimated, highlighting a temperature drop of 2.2K or 0.67%.

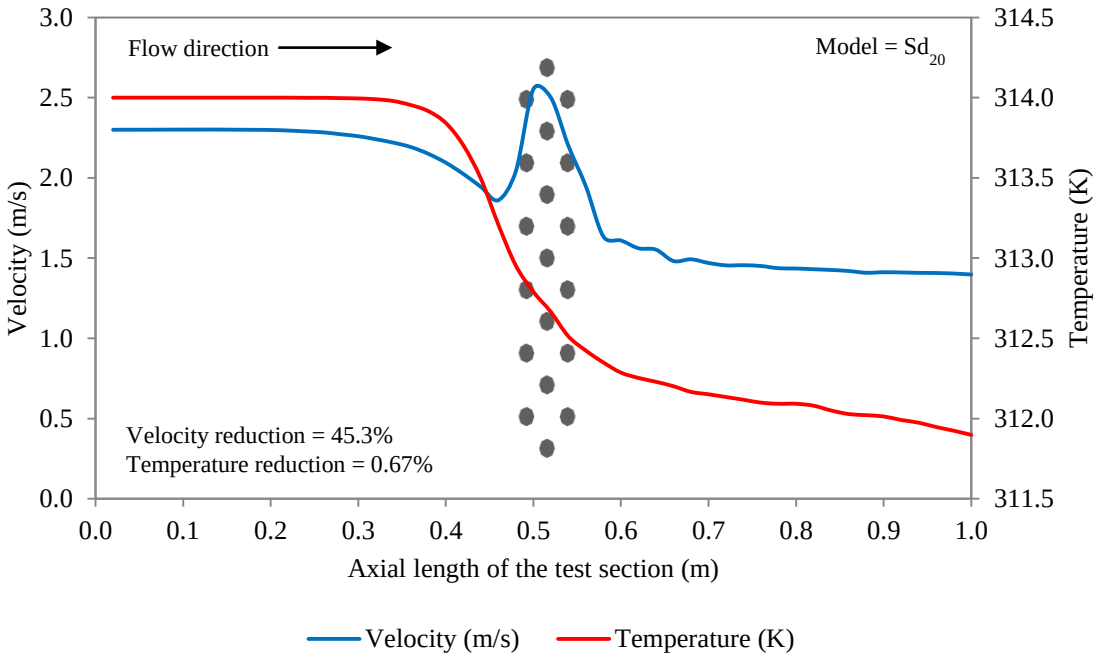

Figure 5.40 Variation in air velocity and temperature profile before and after contact with heat pipes for Sd_{20} model

Figure 5.41 displays the quantification of air velocity and temperature results for the Sd_{25} (streamwise distance = 25mm) model.

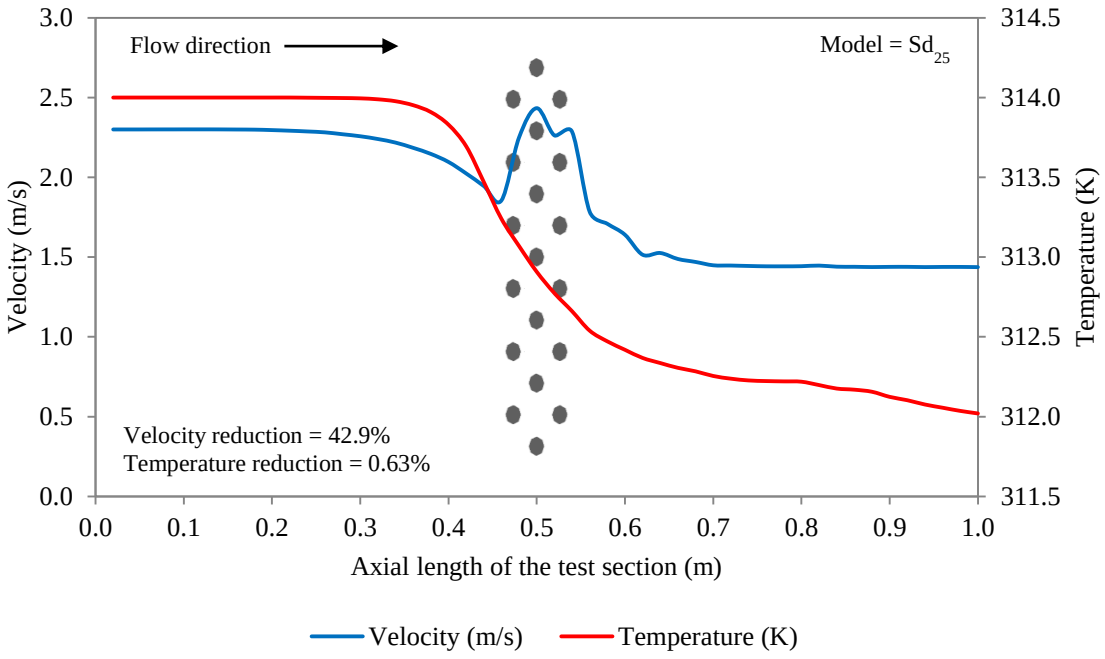

Figure 5.41 Variation in air velocity and temperature profile before and after contact with heat pipes for Sd_{25} model

The trend in velocity profile was dissimilar to the Sd_{20} model with a maximum velocity value of 2.43m/s obtained prior to the 1st row of heat pipes. As the Sd/D (streamwise distance to pipe diameter) ratio increased above unit to 1.25, the formation of the second velocity peak became evident, thereby indicating a reduction in contact time between the air stream and the heat pipes. The minimum velocity value was estimated at 1.43m/s as the airstream came in contact with the three rows of heat pipes. Inlet temperature was set to 314K and a reduction percentage of 0.63% was noted for the Sd_{25} streamwise distance model in comparison to 0.67% for the Sd_{20} model.

Figure 5.42 shows the air velocity and temperature trend for the Sd_{30} (streamwise distance = 30mm) model. Like the Sd_{25} model, two distinct velocity peak points were observed as the streamwise distance between rows was increased to 30mm. This effect was predominantly due to the increasing distances between the individual rows, providing time for the airstream to reach regions of high velocities on two instances. The maximum air velocity was determined at 2.54m/s while the mean air velocity was 1.91m/s. The temperature profile continued to indicate a lower reduction in air temperature with increasing streamwise distances as a reduction 1.96K or 0.62% was calculated.

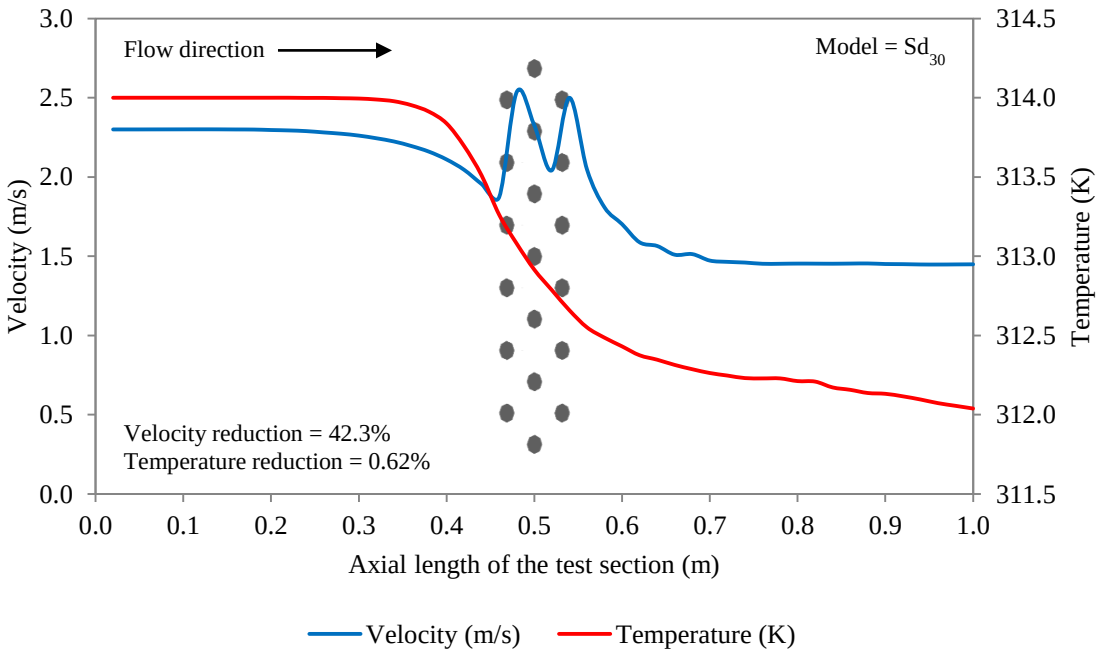

Figure 5.42 Variation in air velocity and temperature profile before and after contact with heat pipes for Sd_{30} model

The streamwise distance was further increased to 35mm and the quantified air velocity and temperature results for Sd_{35} (streamwise distance = 35mm) model are displayed in Figure 5.43. Once again, two velocity peaks were formed at the start of the 1st and 3rd row of heat pipes. The highest velocity was noted at 2.51m/s which was 0.02m/s lower than the Sd_{30} model. The velocity was found to decrease to a minimum value of 1.45m/s downstream of the heat pipes. The air temperature decreased from the inlet value of 314K to approximately 312K after contact with the heat pipes. The temperature profile obtained from the Sd_{35} model was very similar to the Sd_{30} model as a reduction percentage of 0.61% was calculated.

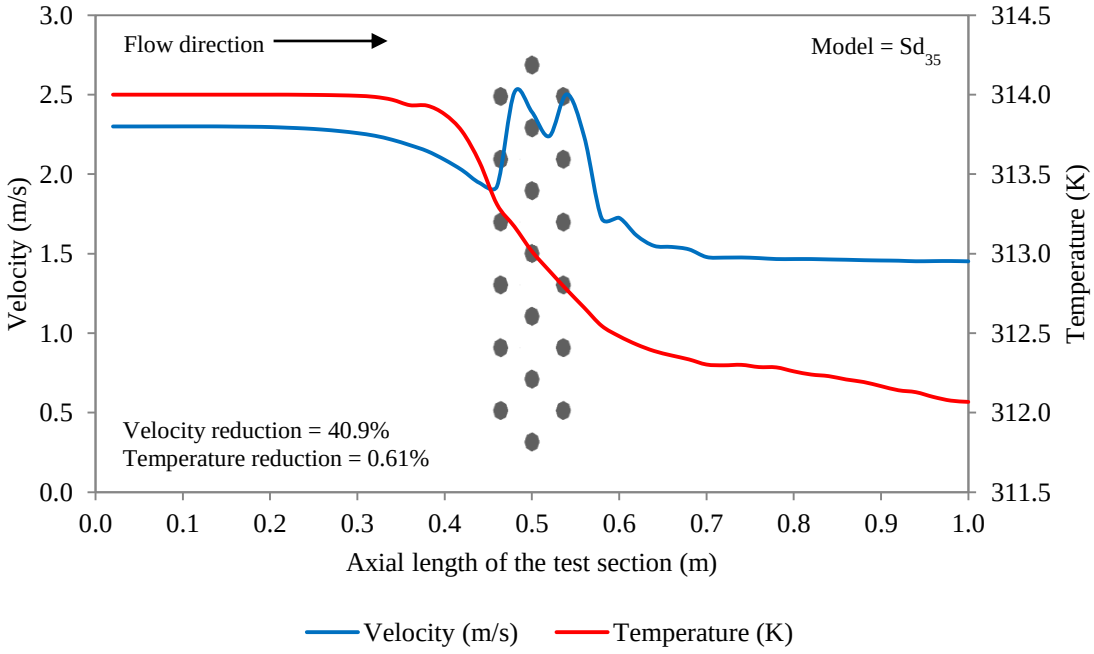

Figure 5.43 Variation in air velocity and temperature profile before and after contact with heat pipes for Sd_{35} model

The maximum streamwise distance analysed from the current geometry was 40mm or twice the pipe diameter. Figure 5.44 displays the findings obtained from the Sd_{40} (streamwise distance = 40mm) model. A maximum velocity value of 2.46m/s was noted at the upstream of the 1st row of heat pipes. This arrangement provided the lowest reduction in air velocity as a reduction percentage of only 40% was obtained. This was due to the increased spacing between the rows of the heat pipes with the Sd/D (streamwise distance to pipe diameter) ratio of 2.0. With respect to the thermal profile, the Sd_{40} model indicated the lowest reduction in air temperatures, calculated at only 1.83K or 0.58%. From all analysed models it was concluded that the Sd_{20} model

provided the greatest reduction in air temperatures across the axial length of the test section.

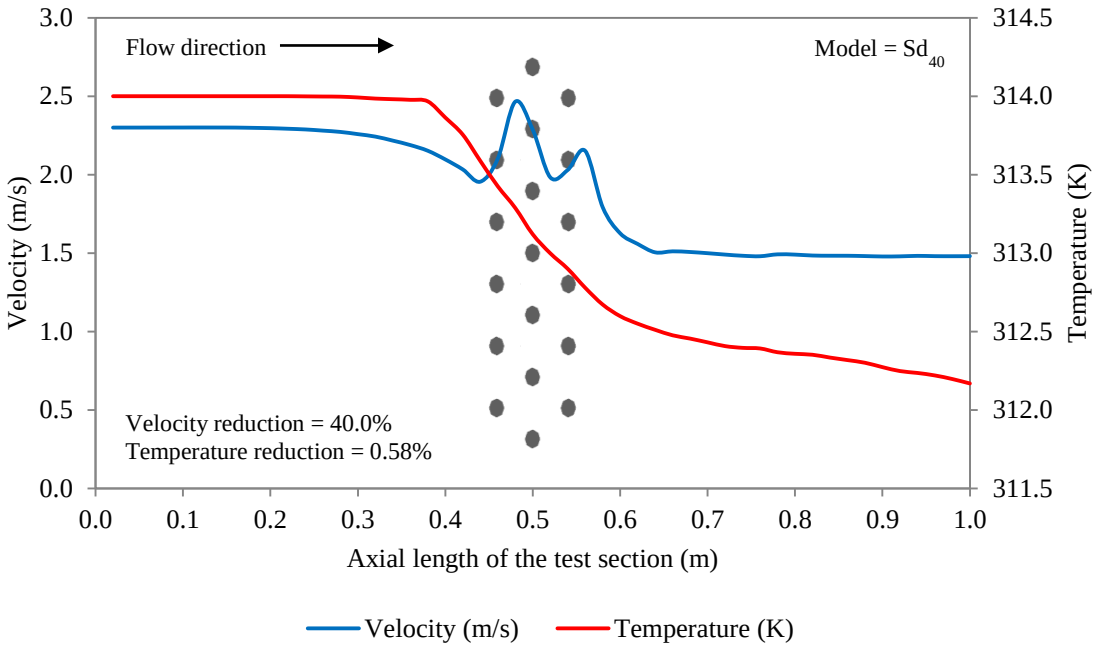

Figure 5.44 Variation in air velocity and temperature profile before and after contact with heat pipes for Sd_{40} model

Table 5.14 summarises the mean values of the air velocity and temperature for all streamwise distance models at the measurement locations. Keeping a constant inlet air temperature of 314K for all cases, maximum temperature difference (ΔT) was obtained for the Sd_{20} model at 1.68K. In general, the temperature differentials decreased as the streamwise distance increased with the lowest ΔT calculated for the Sd_{40} model at 1.55K. An inverse proportionality was thus established between the decreasing temperature reductions and the increasing streamwise distances between the rows of heat pipes.

Table 5.14 Summary of the mean parametric values obtained for streamwise distance models

Model	**Mean inlet velocity (m/s)**	**Mean outlet velocity (m/s)**	**Δv (m/s)**	**Mean inlet temperature (K)**	**Mean outlet temperature (K)**	**ΔT (K)**
Sd_{20}	2.20	1.46	0.84	313.96	312.32	1.68
Sd_{25}	2.20	1.50	0.80	313.96	312.33	1.67
Sd_{30}	2.19	1.50	0.80	313.97	312.42	1.58
Sd_{35}	2.19	1.51	0.79	313.97	312.43	1.57
Sd_{40}	2.19	1.55	0.75	313.97	312.45	1.55

In addition, the analysis determined that the mean outlet velocity increased from 1.46m/s to 1.55m/s as the streamwise distance was increased from 20mm to 40mm. The maximum reduction in air velocity (Δv) was calculate for the Sd_{20} model at 0.84m/s while the minimum reduction in air velocity was depicted at 0.75m/s for the Sd_{40} model. The bar graph representation of the parametric reductions in air velocity and temperature for all analysed streamwise distance models are displayed in Figure 5.45.

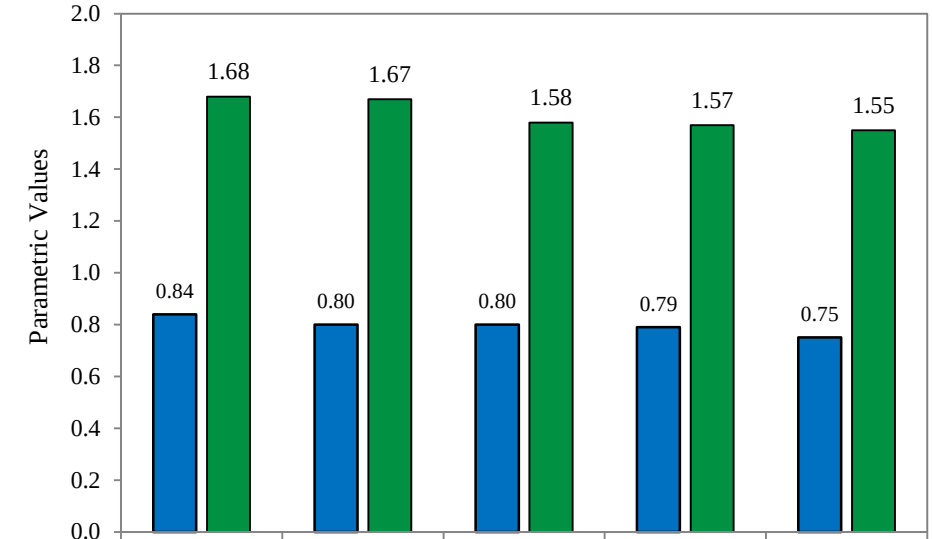

	Sd20	Sd25	Sd30	Sd35	Sd40
Δv (m/s)	0.84	0.80	0.80	0.79	0.75
ΔT (K)	1.68	1.67	1.58	1.57	1.55

Figure 5.45 Bar chart representation of the difference in air velocity and temperature for streamwise distance models

5.5.2 Total cooling capacity and overall effectiveness

Similar to the spanwise arrangement models, the area-weighted averaged cooling capacity or heat transfer, upstream and downstream of the heat pipes was further evaluated. This section established the quantified results for the cooling capacity (rate of heat transfer) and effectiveness obtained from the analysis of all five streamwise distance models. The heat transfer and effectiveness was calculated using eqn.27 and eqn.28. The summarised findings for heat transfer and overall heat pipe effectiveness are displayed in Table 5.15. The highest mean overall effectiveness was calculated at 5.6% for the Sd_{20} model while the lowest mean overall effectiveness was calculated at 5.0% for the Sd_{40} model. The highest rate of heat transfer in the test section was 768.17W for the Sd_{20} model. A variation of 82.3W was achieved between the highest and lowest rate of heat transfer from the compared models.

Table 5.15 Summary of the mean heat transfer values obtained for streamwise distance models

Model	Evaporator net heat transfer (W)	Overall effectiveness (%)
Sd_{20}	768.17	5.60%
Sd_{25}	764.25	5.57%
Sd_{30}	705.46	5.14%
Sd_{35}	698.93	5.10%
Sd_{40}	685.87	5.00%

The graphical representation of the cooling capacity and heat pipe effectiveness results are plotted Figure 5.46. The total cooling capacity or heat transfer was directly proportional to the overall effectiveness of the heat pipe system since all other parameters apart from air temperature were kept constant throughout the investigation. Since the temperature differential reduced as the streamwise distances increased from 20mm (Model Sd_{20}) to 400mm (Model Sd_{40}), a decreasing gradient was observed for both total heat transfer rate and overall effectiveness of the heat pipe heat exchanger.

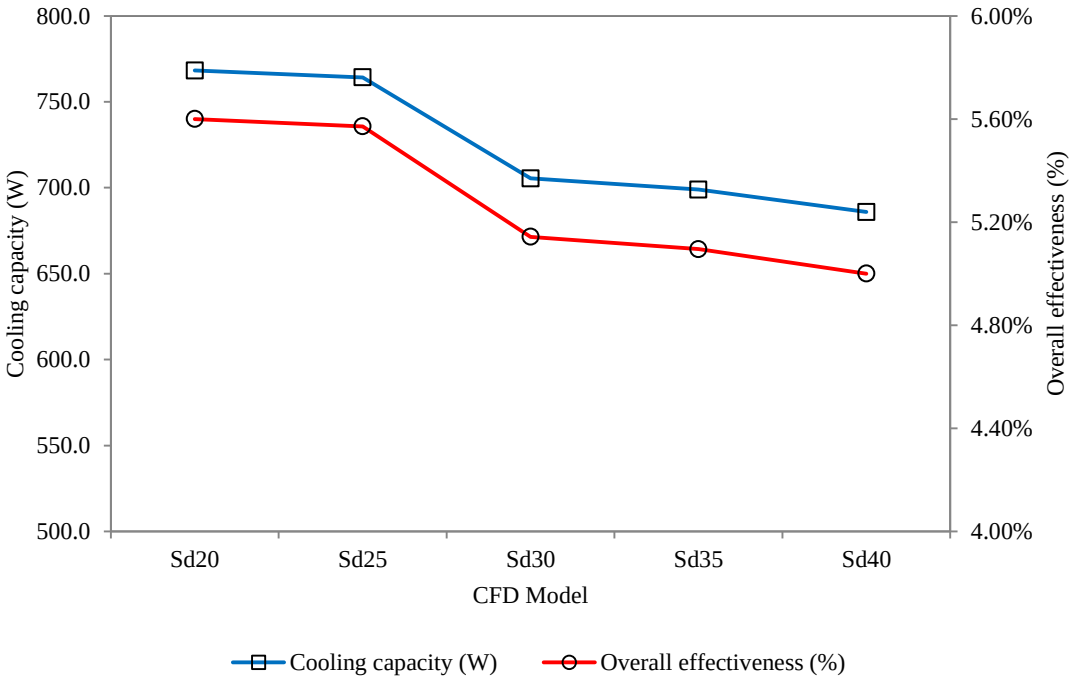

Figure 5.46 Relationship between cooling capacity and overall heat exchanger effectiveness for streamwise distance models

To summarise, the findings from the previous two sections (Section 5.4 and 5.5) of this chapter revealed that the optimum spanwise thickness between heat pipes was 50mm with a St/D (spanwise thickness to pipe diameter) ratio of 2.5 while the optimum

streamwise distance was calculated at 20mm at which the Sd/D (streamwise distance to pipe diameter) ratio was 1.0.

5.6 Monthly thermal models with varying temperatures and wind speeds

Subsequent to determining water as the ideal working fluid along with the optimum characteristic arrangement, this section provides results emphasising on the annual thermal performance of the heat pipe system. The city of Doha with coordinates of latitude at 25° 15´ North and longitude at 51° 34´ East was taken as the location of case-study and the monthly mean temperature values were obtained (The Weather Channel, 2012). Twelve steady-state models were developed to replicate the monthly mean source temperatures in order to determine the heat pipe heat exchanger's thermal performance to meet the thermal loads, of achieving 301.15K (ASHRAE 55, 2004). The analysis was carried out at two external wind speeds including 1.0m/s and 2.3m/s in order to determine the overall effectiveness under varying temperature and velocity conditions.

5.6.1 Air velocity, pressure and temperature profiles

Using a spanwise thickness of 50mm and a streamwise distance of 20mm as the spacing between individual heat pipes, air temperatures were determined across the axial and radial length of the test section in order to visualise the temperature differential for each month of the year. Figure 5.47 displays the variation in air velocity, pressure and temperature across the axial length of the test section for the month of July. The source temperature for July was 314.2K as the contour levels represent the aerodynamic and thermal profile of the heat exchanger at air velocities of 1.0m/s and 2.3m/s.

As observed from the velocity contours in Figure 5.47 a), the air accelerated across both sides of the bank of the heat pipes in the test section due to the spherical body of the tubes. The velocity was reduced at the immediate downstream of the three rows of heat pipes. The subsequent static pressures for both cases are displayed in Figure 5.47 b). A higher positive pressure was created upstream of the heat pipes due to the higher inlet velocity of 2.3m/s while lower static air pressures were obtained at a velocity of 1.0m/s.

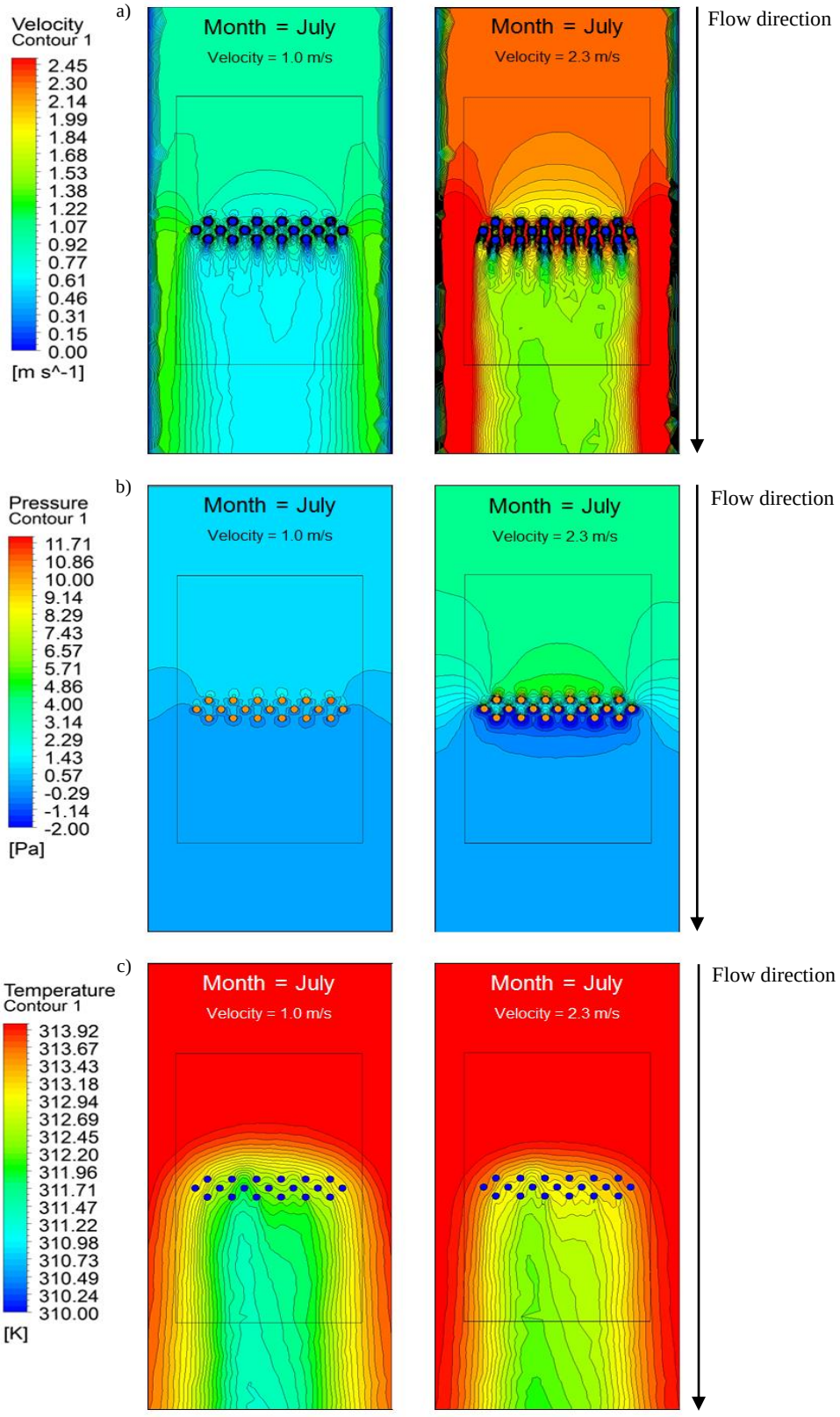

Figure 5.47 Contour levels displaying air: a) velocity b) pressure c) temperature for the month of July

Temperature contour levels are displayed in Figure 5.47 c). Keeping the source temperature constant at 314.2K for the month of July, a greater reduction in downstream

temperatures was observed when the air velocity was 1.0 m/s. This was mainly due to the increase in contact time between the air streams passing over the three rows of heat pipes. Figure 5.48 displays the contour levels of air temperature upstream and downstream of the heat pipes for the month of July and November. The contours were drawn at an air inlet velocity of 1.0m/s. It was observed that the heat pipes were able to lower the inlet air temperatures during both months of the year with a greater heat transfer capability in the month of July. The source temperature in July was 314K which was 11.5K higher than the source temperature in November. Two planes were created along the radius of the test section at a distance of 0.2m upstream and downstream from the heat pipe arrangement. The mean temperature drop (ΔT) recorded between the two planar locations was approximately 2.5K for July and 1.5K for November. The operating range for heat pipes was larger in July thus confirming the efficiency of the system to deliver greater transfer of heat during the hotter months of the year.

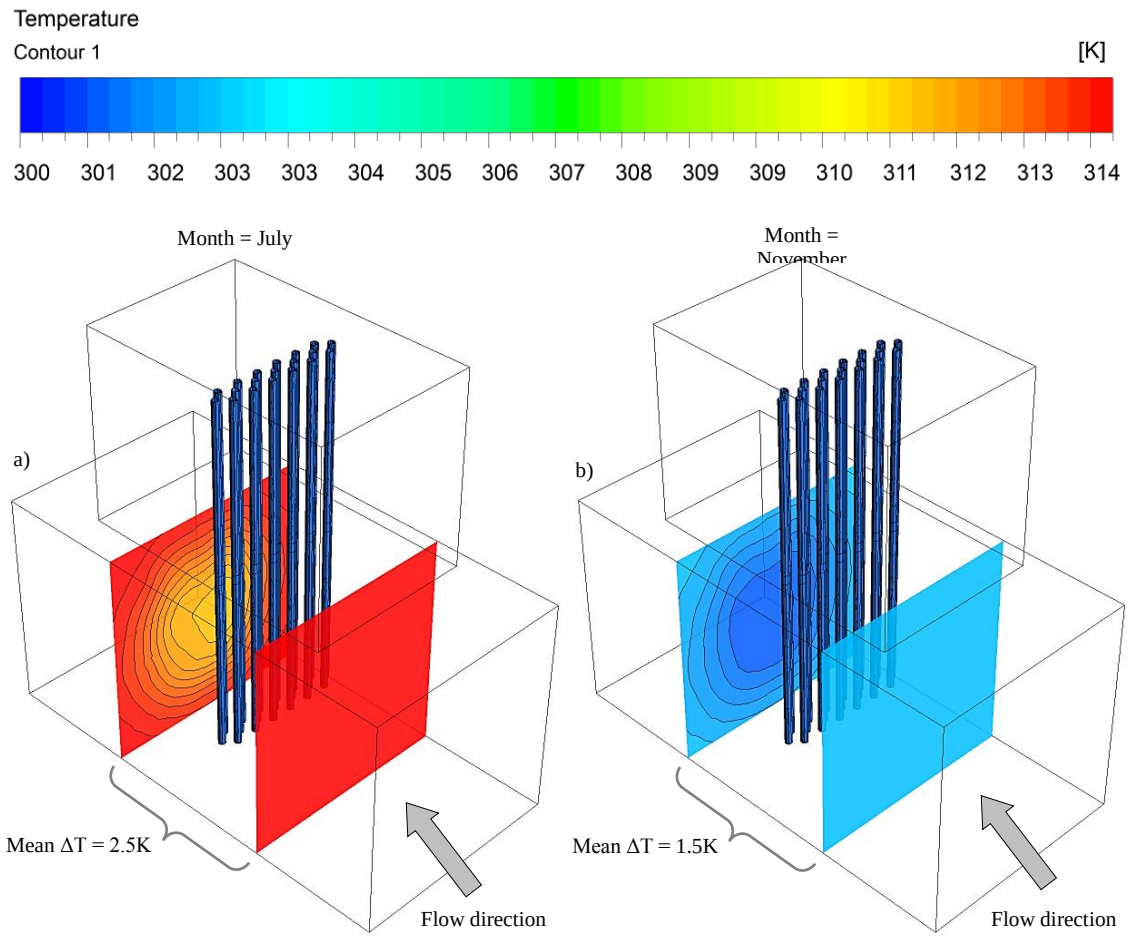

Figure 5.48 Contour levels displaying upstream and downstream air temperatures for the month of: a) July b) November

The graphical representation of air temperature distribution across the axial length of the test section is displayed in Figure 5.49 for an inlet air velocity of 1.0m/s. It was observed that the heat pipe system was capable of reducing air temperatures during the months ranging from March to November, when the source temperatures were higher than 301K. This was due to the difference between the source temperatures and operating internal fluid temperature being approximately 7K or higher and in line with typical operation of heat pipes which require a temperature drop of at least 5K for correct functionality (Nemec *et al.*, 2010). The maximum temperature reduction was achieved in the month of July at 2.81K as the difference between the source and heat pipe operating temperature was at its maximum. During months ranging from December to February, the heat pipe system was found to be non-effective due to the inadequate temperature difference between the airstream and the heat pipe operating temperature.

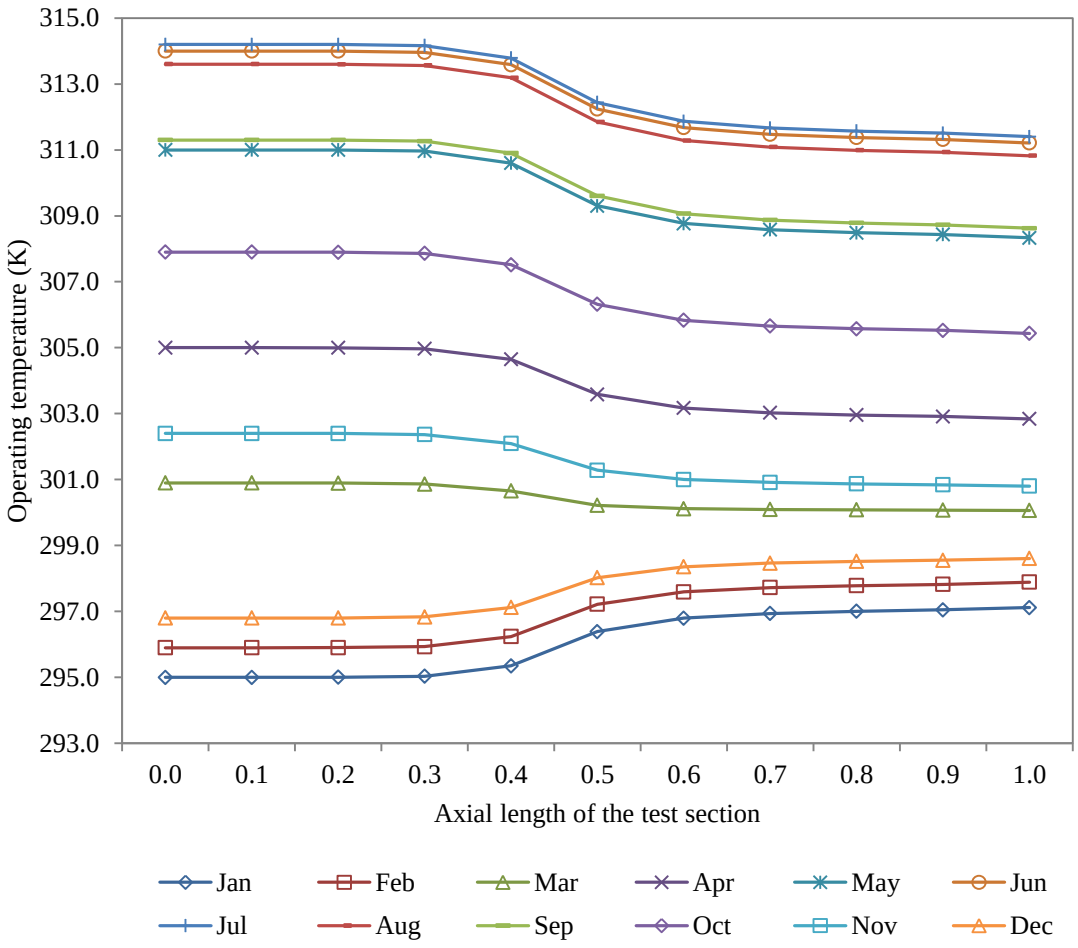

Figure 5.49 Variation in air temperature across the axial length of the evaporator section at a velocity of 1.0m/s

The temperature distribution across the axial length of the test section for an inlet air velocity of 2.3m/s is highlighted in Figure 5.50. Temperature differentials at this velocity were lower in comparison to those obtained at 1m/s. The maximum temperature differential was noted for the month of July with a reduction of 2.01K which was 0.8K lower than what was achieved for the month at an inlet velocity of 2.3m/s.

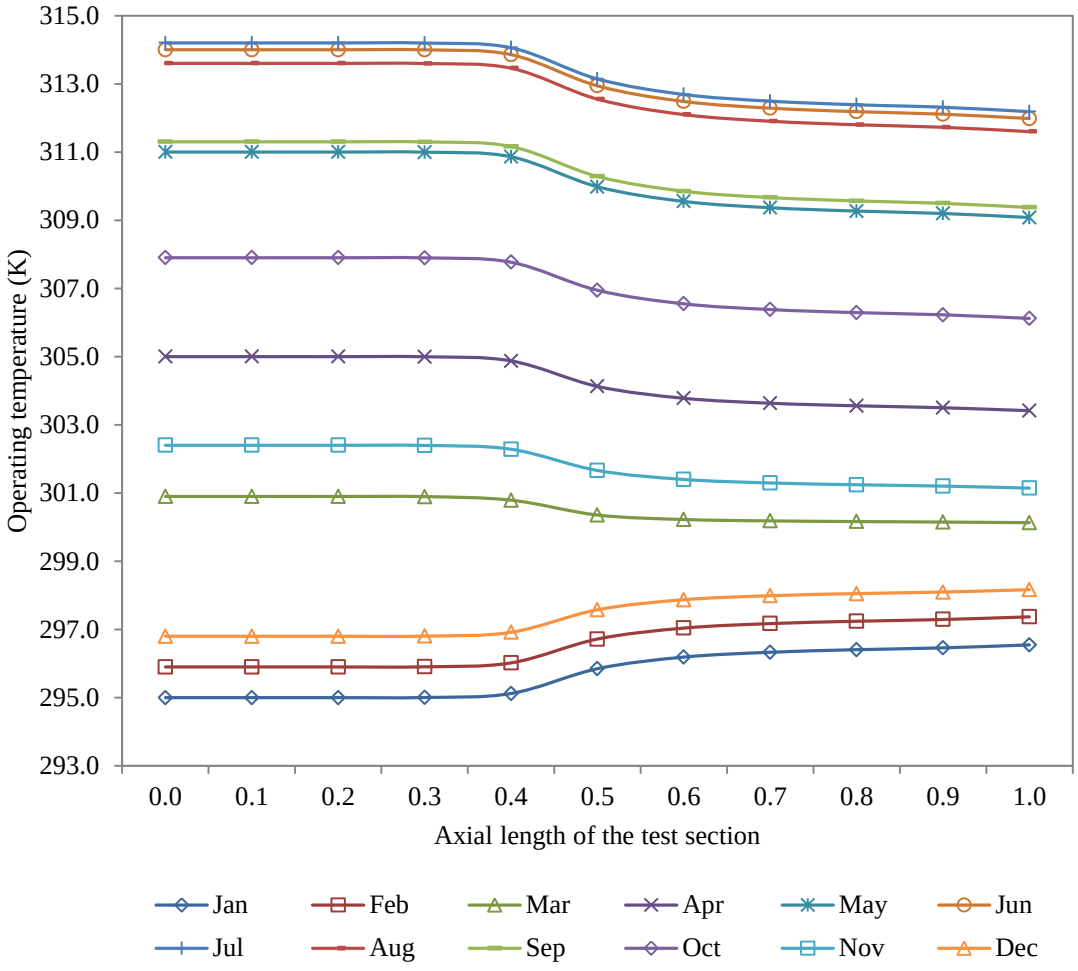

Figure 5.50 Variation in air temperature across the axial length of the evaporator section at a velocity of 2.3m/s

The upper limit of the operating temperature range for indoor spaces resulting in occupancy metabolic rates between 1.0 and 1.3met was set to 301.15K (ASHRAE 55, 2004) while the mean air temperatures downstream of the heat pipes were recorded at the measurement points. The limit was set only as a guideline in order to determine the effectiveness of the heat pipes.

Table 5.16 indicates the summarised results of the temperature differentials obtained using heat pipes for each month of the year. The operating temperature was kept constant at 293K for the study while the source temperatures were varied as per the reference monthly temperatures. Measurement points were used in order to determine the upstream and downstream airstream temperatures as it came in contact with the heat pipes.

As observed, the ΔT or the temperature differentials at a velocity of 1.0m/s were greater than those obtained at a velocity of 2.3m/s. The greatest temperature reduction was 2.5K achieved during months ranging from June to August while the lowest temperature reduction was achieved in the month of March at 0.7K. The positive sign of ΔT indicates a decrease in downstream temperature from the original source temperature while the negative sign of ΔT shows vice-versa.

Table 5.16 Heat pipe downstream temperature at varying source temperatures

Month of the year	**Jan**	**Feb**	**Mar**	**Apr**	**May**	**Jun**	**Jul**	**Aug**	**Sep**	**Oct**	**Nov**	**Dec**
Source temperature (K)	295	296	301	305	311	314	314	314	311	308	303	297
Operating temperature (K)	293	293	293	293	293	293	293	293	293	293	293	293
ASHRAE Standard 55, 2004 (K)	301	301	301	301	301	301	301	301	301	301	301	301
ΔT (K) at velocity of 1.0 m/s	-1.9	-1.8	0.9	1.9	2.4	2.5	2.5	2.5	2.4	2.2	1.5	-1.6
ΔT (K) at velocity of 2.3 m/s	-1.3	-1.2	0.7	1.4	1.6	1.7	1.7	1.7	1.6	1.5	1.1	-1.2

A graphical illustration of relationship between the source and heat pipe downstream temperature is displayed in Figure 5.51. A comparison between air temperatures obtained at 1.0m/s and 2.3m/s was compared as a bar graph. It was observed that the heat pipes performed better in terms of temperature reduction when the airstream velocity was 1.0m/s. However, the temperature difference using the heat pipe arrangement was not significant in order to meet the ASHRAE set-point level of 301.15K for the months ranging from April to October.

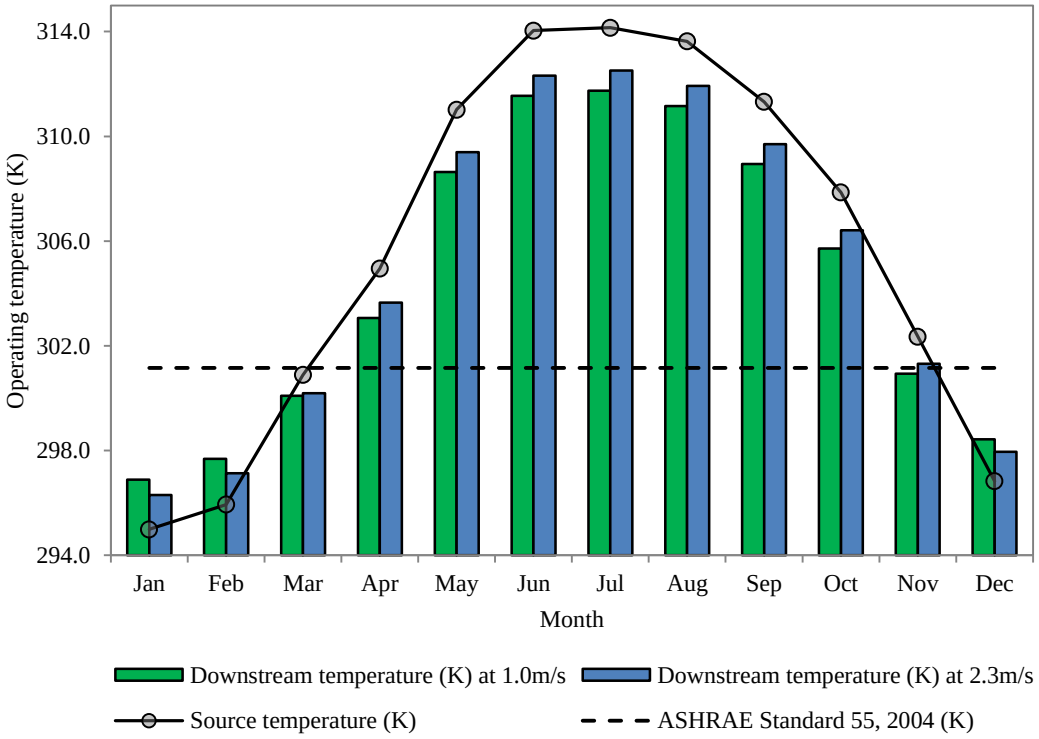

Figure 5.51 Air temperature differentials obtained using inlet velocity of 1.0m/s and 2.3m/s

5.6.2 Total cooling capacity and overall effectiveness

At an incoming inlet air velocity of 1.0m/s, the highest rate of heat transfer or cooling capacity at the measurement points was obtained at 644W for the month of July, when the source temperature was 314.2K. The corresponding effectiveness was calculated at 9.4%. The heat pipe heat exchanger was found to be the most efficient during the month of April with an effectiveness of 11.36%. It was imperative to note that the heat transfer increased when the inlet velocity was increased to 2.3m/s. According to theory, heat transfer due to convection increases when the inlet mass flow rates are increased, thus the values were as anticipated. However, due to a lower reduction in downstream temperatures, the overall effectiveness of the heat pipe heat exchanger was reduced.

The maximum effectiveness was obtained for the month of April at 7.92%, a reduction of 3.44% from the figure calculated at the velocity of 1.0m/s. The positive sign of heat transfer and effectiveness indicate a decrease in downstream temperatures from the original source temperatures while the negative signs show an increase in air temperature. The summarised results obtained for the inlet air velocities of 1.0m/s and 2.3m/s are tabulated in Table 5.17 and Table 5.18.

Table 5.17 Heat transfer and overall effectiveness at inlet velocity of 1.0m/s

Month	Heat transfer (W)	Effectiveness (%)
January	-502.89	-27.03%
February	-475.72	-22.51%
March	217.80	6.22%
April	509.50	11.36%
May	615.71	10.24%
June	640.64	9.44%
July	644.15	9.40%
August	641.92	9.55%
September	616.98	10.12%
October	577.21	10.99%
November	393.66	10.18%
December	-441.78	-18.55%

Table 5.18 Heat transfer and overall effectiveness at inlet velocity of 2.3m/s

Month	Heat transfer (W)	Effectiveness (%)
January	-750.84	-18.66%
February	-718.22	-15.65%
March	431.73	5.53%
April	772.10	7.92%
May	912.86	6.97%
June	955.34	6.45%
July	976.78	6.41%
August	922.56	6.52%
September	912.14	6.87%
October	853.12	7.50%
November	636.81	7.57%
December	-673.10	-13.16%

A comparison between total rates of heat transfer for the two investigated inlet air velocities is displayed in Figure 5.52. An inverse parabolic curve was noted with the greatest heat transfer results produced in the month of July. It was observed that the heat transfer was directly proportional to the temperature difference between the source and heat pipe operating conditions. Negative values were obtained from months ranging from December to February indicating the transfer of heat in the opposite direction. On average, the rate of heat transfer increased by 279W or 34% when the inlet air velocity was increased from 1.0m/s to 2.3m/s. The maximum effect on heat transfer was an increase of 332W for the month of July while minimum increase was determined at 213W for the month of March.

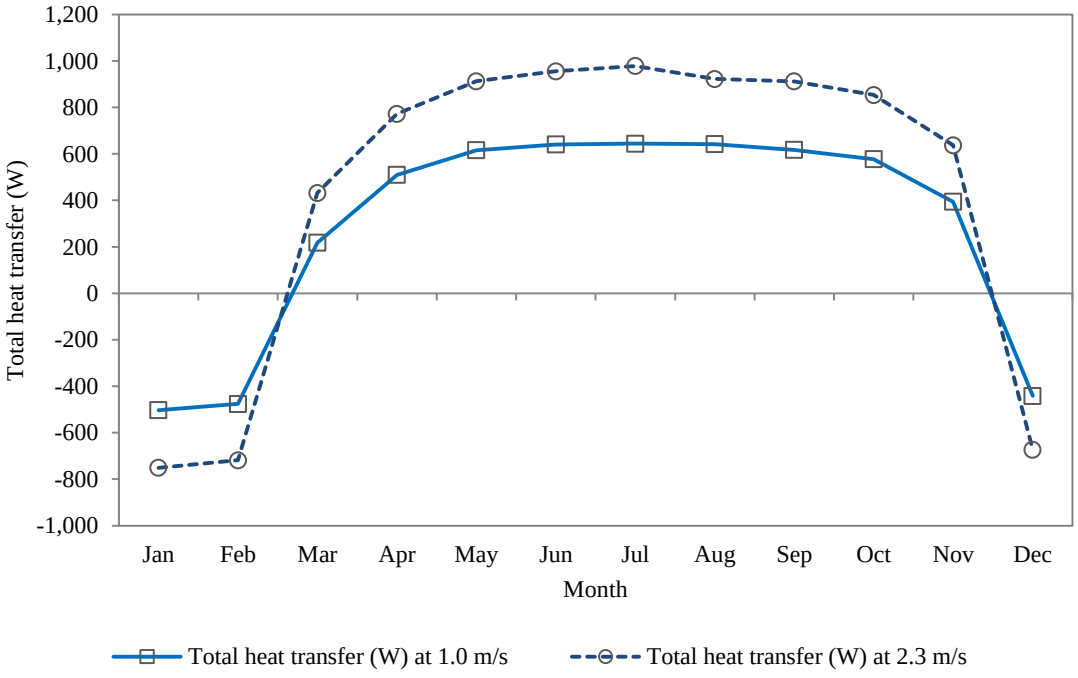

Figure 5.52 Annual thermal performance of the system in terms of total heat transfer

A graphical representation of the overall heat exchanger effectiveness for each month of the year is displayed in Figure 5.53.

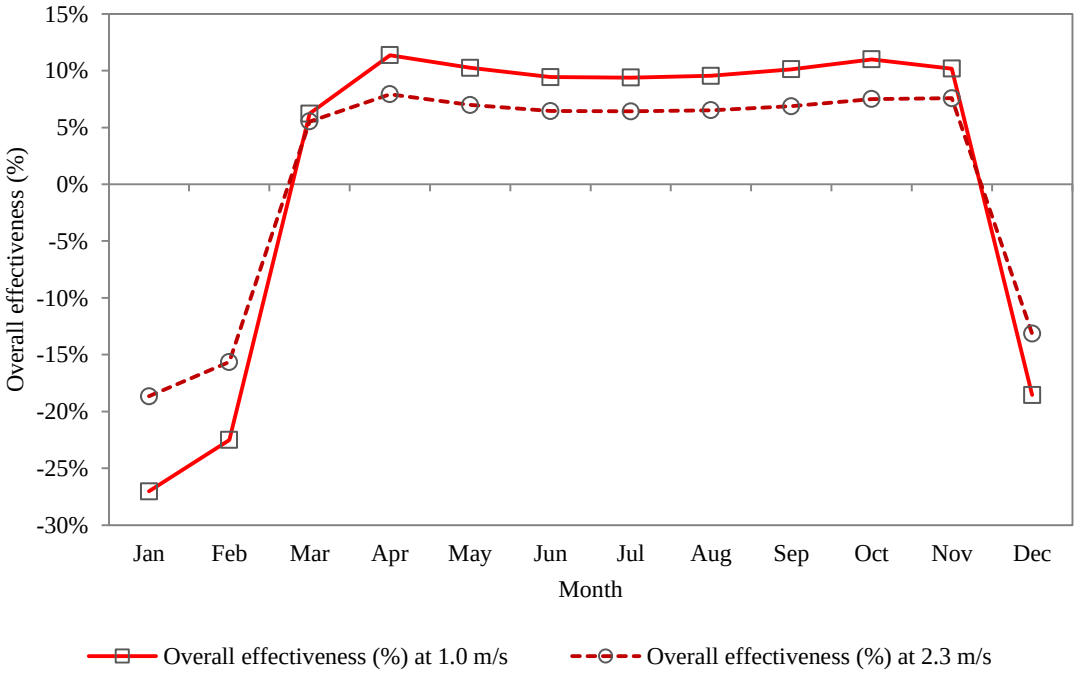

Figure 5.53 Annual thermal performance of the system in terms of overall effectiveness

The highest overall effectiveness value of 11.4% was obtained for the month of April at the inlet air velocity of 1.0m/s while the lowest overall effectiveness was obtained at 5.5% for the month of March at the inlet velocity of 2.3m/s. In general, the performance of the heat exchanger decreased when the velocity was increased confirming an inverse proportionality between the two parameters. On average, the overall effectiveness decreased by 29% when the inlet air velocity was increased from 1.0m/s to 2.3m/s highlighting the significance of air velocity on the operation of heat pipes.

5.7 Summary

This chapter described the numerical results obtained from the present study. A comparison was established between water, ethanol and R134a as heat pipe working fluids for use natural ventilation air streams. The results showed that water indicated a superior heat exchanger effectiveness of 1.8% and 3.1% in comparison to R134a and ethanol. Subsequent to determining water as the optimum working fluid, this chapter highlighted the effect of heat pipe internal working fluid on the Prandtl number and the heat transfer through convection of air.

Using water as the benchmark case, density, thermal conductivity, dynamic viscosity and specific heat capacity was varied systematically. The investigation determined that heat transfer was most influenced by the fluid's specific heat capacity as an increase of approximately 4W or 39% was obtained. Keeping a fixed computational domain and using water as the internal working fluid, the rate of heat transfer and effectiveness of the heat pipe system was analysed through variation in spanwise and streamwise characteristic lengths. At an optimum streamwise distance of 20mm (Sd/D ratio=1.0), the optimum spanwise arrangement between heat pipes was determined to be 50mm (St/D ratio=2.5).

In order to establish the overall effectiveness of the heat pipe system over varying source temperatures, monthly thermals models were created wherein the city of Doha, Qatar was used as the case-study reference. The highest rate of heat transfer or temperature differential was obtained for the month of July at a source temperature of 314.2K. Moreover, a superior performance of the system was confirmed when the velocity was reduced from 2.3m/s to 1.0m/s due to the increase in contact time between air and the heat pipes, increasing the overall effectiveness by 29%.

Chapter 6
Experimental Results

6.1 Introduction

This chapter describes the full-scale experimental results obtained using the wind tunnel test facility. The heat pipes were placed inside the test section according to the spanwise and streamwise arrangements analysed during the CFD study. The experimental investigation was carried out to determine the effectiveness of heat pipes using two design parameters namely spanwise arrangements and working fluids. The copper heat pipes used water and R134a as the working fluids and a comparison was made at source temperatures of 32°C (305K), 35°C (308K) and 41°C (314K) corresponding to the mean monthly temperatures of November, April and June in Doha, Qatar (The Weather Channel, 2012).

Furthermore, this chapter highlights the trends obtained from the thermal surface visualisation analysis, which was carried out using infrared thermal imaging camera. In addition to the steady-state testing, the chapter presents the results for the transient temperature test which was conducted to investigate the climatic response characteristics of heat pipes over a period of 24 hours. The findings from the transient thermal model aided in determining the behaviour of heat pipes in direct response to varying air temperature gradients.

6.2 Calibration of the test equipment

This section of the chapter describes the calibration of the test equipment that was used for conducting the experimentation. The cold sink and the heat pipes were calibrated for their working behaviour in order to determine their thermal characteristics.

6.2.1 Monitoring the thermal behaviour of the cold sink

Prior to conducting the tests on heat pipes, it was essential to monitor the performance of the cold sink in order to determine its stabilisation time. The thermal behaviour of the cold sink was monitored for a period of four and a half hours due to the melting time of ice pockets which were located on all four corners of the control volume. Temperature

measurements were carried out on the control volume of the sink by connecting 6 K-type thermocouples upstream and downstream of where the heat pipes would be inserted. Channels 1-6 represent the 6 thermocouple channels used for temperature measurements. At start-up, it was observed that the temperature gradient started to decrease when the sealed ice pockets were installed. The temperature dropped to a mean value of 7.5°C (or 280.5K) at which it stabilised. The stabilised temperature was recorded for 133 minutes corresponding to 2.2 hours. This information was used to determine the length of time for carrying out the experimentation involving heat transfer from heat pipes. The temperatures started to increase after 2.7 hours into the test as the ice pockets began to melt at room temperature. A steady increase in gradient was then observed until the conclusion of the experiment. The results of the transient test are displayed in Figure 6.1.

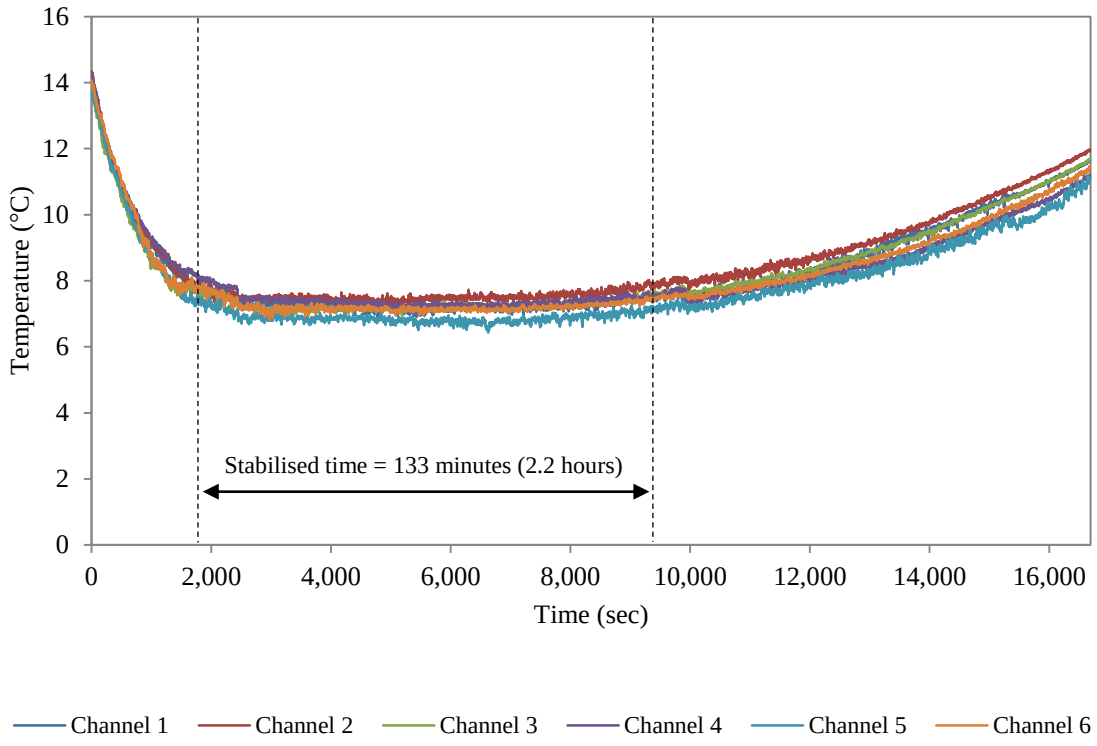

Figure 6.1 Time-dependant temperature readings recorded inside the cold sink

Figure 6.2 displays the infrared image taken from the thermal imaging camera relating the temperature of the cold sink to the ambient environment. The minimum temperature in the cold sink was recorded at 5°C due while the ambient temperature was recorded at 20°C. Considering the heated temperature inside the test section of the wind tunnel to be

in excess of 30°C, the temperature difference between the evaporator and condenser sections of the heat pipes were in the required range for carrying out heat transfer investigations using heat pipes (Nemec *et al.*, 2010).

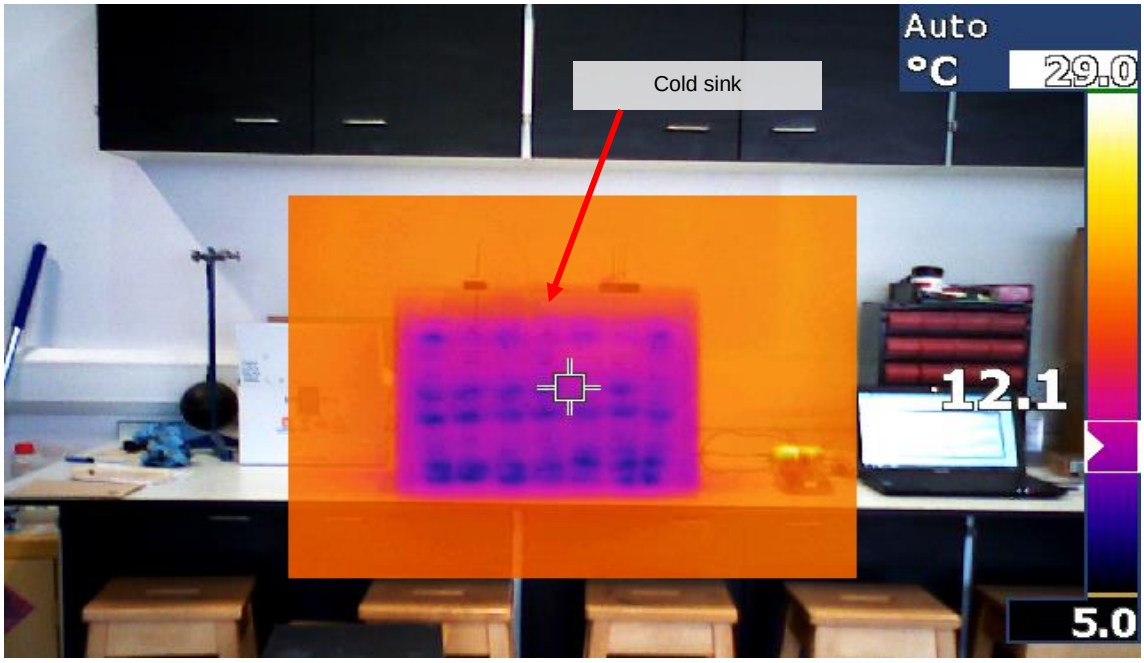

Figure 6.2 Temperature of the cold sink in comparison to the ambient generated using FLUKE Tir1 thermal imaging camera

6.2.2 Monitoring the thermal behaviour of the heat pipes

In order to calibrate the heat pipes, they were compared to unfilled copper pipes and the thermal behaviour was monitored. Both pipes were placed in a warm water bath, maintained at 55°C or 328K. K-type thermocouples were attached to both pipes to record the surface temperatures due to conduction as the pipes came in contact with the warm water bath. The transient test was conducted for 200 seconds with a settling time of approximately 50 seconds prior to delivering heat.

Figure 6.3 displays the comparison of temperature results between a heat pipe and an ordinary copper pipe. As expected, the thermal performance of a heat pipe in response to conduction was significantly superior to that of a copper pipe. The surface of a heat pipe reached the input water temperature of 55°C in approximately 100 seconds while the copper pipe increased the temperature to a maximum of 30°C.

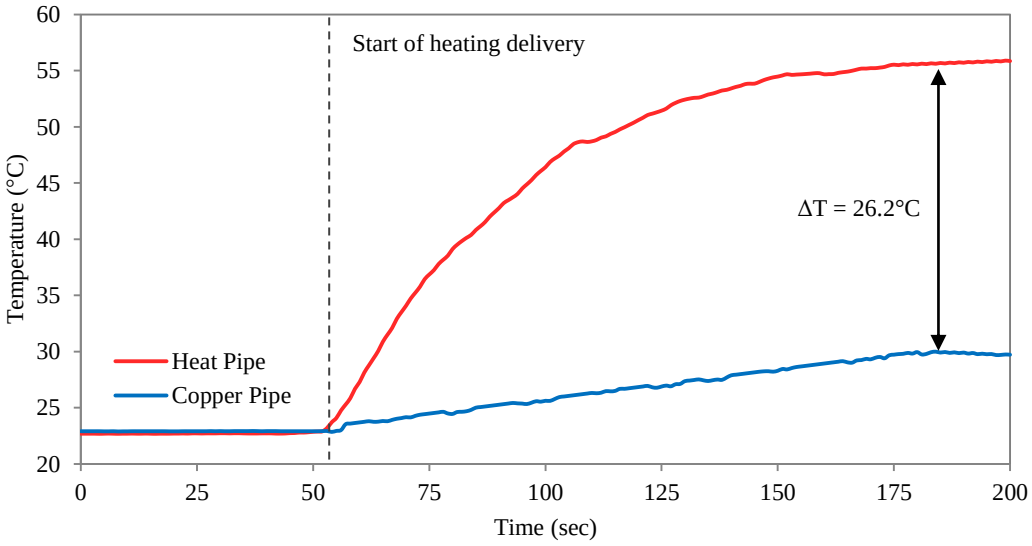

Figure 6.3 Time-dependant temperature readings recorded on the surface of the pipes

Infrared thermographic images were taken to visualise the difference in transient temperatures between the two pipes. Figure 6.4 displays the variation in the surface temperature of a heat pipe and a copper pipe over the 200 seconds of run-time. The ambient temperature increased from 22.6°C (or 295.6K) at the start of the test to 23.7°C (or 296.7K) after 200 seconds due to transfer of heat from the pipes. The contour levels confirm the superior thermal response of a heat pipe in comparison to a copper pipe in transferring heat from one location to another.

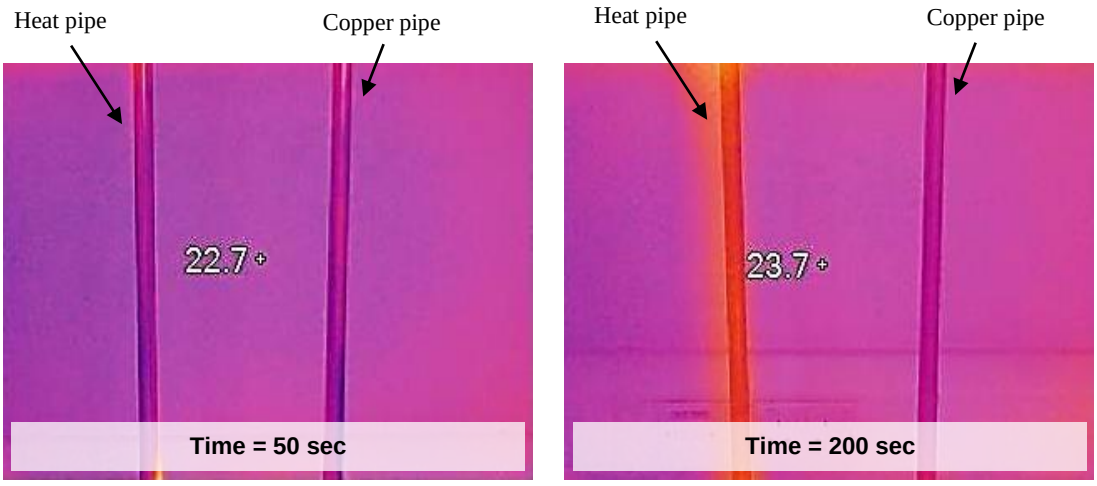

Figure 6.4 Surface temperature formation of a heat pipe in comparison to a copper pipes generated using FLUKE Tir1 thermal imaging camera

6.3 Surface temperature visualisation

The first phase of the study's experimental findings was to illustrate the parametric visualisation for surface temperature fields. Figure 6.5 displays the image of the experimental set-up prior to setting up the thermal image in order to comprehend the situation of heat pipes within the flow domain.

Figure 6.5 Image of the experimental set-up prior to setting up the thermal image

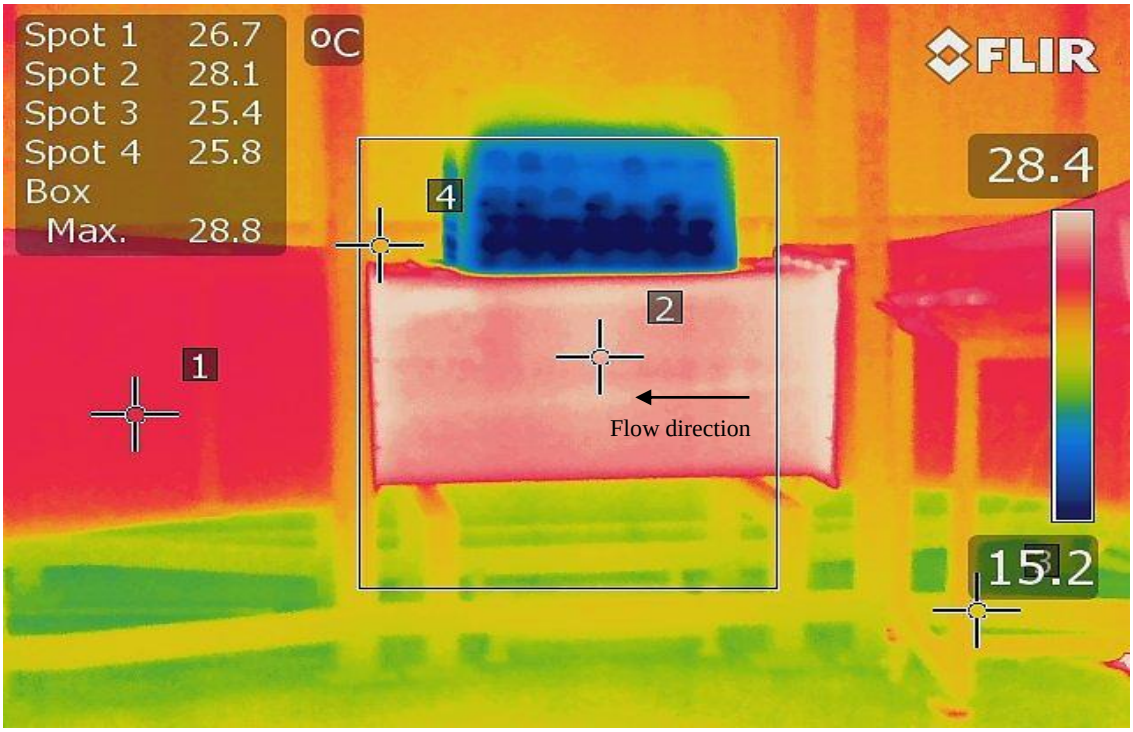

Figure 6.6 Thermal image taken at an inlet temperature of 35°C using FLIR $T650_{SC}$ thermal imaging camera

The visualisation of surface temperatures indicating the differential between the heated test section and the cold sink in relation to the room temperature is displayed in Figure 6.6. The figure displays the infrared image captured using the thermal imaging camera at an inlet source temperature of 35°C. The image was taken at the surfaces of both evaporator and condenser sections to qualitatively illustrate the difference in working temperatures at both ends of the heat pipes. As observed, the cold sink (top of the image) temperature was recorded at approximately between 15°C and 17°C while the heating elements increased the temperature of test section (bottom of the image) surface to a maximum of 28.4°C.

6.4 Design parameters

Subsequent to the temperature visualisation, this section of the chapter describes the quantitative test results achieved for the investigated design parameters. Thermal performances of water and R134a were compared to each other and both fluids were used in different spanwise configurations between the heat pipes in order to determine the most suitable arrangement.

6.4.1 Comparison between water and R134a as heat pipe working fluids

The tests were conducted using an inlet velocity of 2.3m/s in the test section of the wind tunnel. K-type thermocouples were positioned at the inlet and outlet as per the measurement locations (Chapter 4, Section 4.8.3). A comparison between water and R134a was determined at three different source temperatures of 32°C (305K) to 41°C (314K) replicating the monthly temperature of November, April and June (The Weather Channel, 2012).

Table 6.1 displays the air temperature values downstream of the heat pipes for three inlet source temperatures. The temperatures were obtained along the radial length of the test section. As observed, the temperatures at either side of the bank of the heat pipe tubes were similar to the inlet temperatures. This was because the regions near the walls of the test section did not incorporate heat pipes. At a source temperature of 32°C, water displayed a greater reduction in air temperatures in comparison to R134a. The maximum reduction was calculated at 0.92°C for water in comparison to 0.84°C for R134a. However, both working fluids displayed a very similar thermal profile at the

source temperature of 35°C. The largest reduction in inlet temperature using water was 1.18°C, which was only 0.06°C higher than R134a.

Table 6.1 Air temperature distribution downstream across the radial length of the heat pipes using water and R134a as internal working fluids

Radial length (m)	Source (°C)	Water (°C)	R134a (°C)	Source (°C)	Water (°C)	R134a (°C)	Source (°C)	Water (°C)	R134a (°C)
0.00		31.95	31.96		34.95	34.97		40.96	40.97
0.08		31.34	31.51		34.24	34.43		39.60	40.36
0.17		31.07	31.30		33.82	34.15		39.40	40.11
0.25	32.00	31.08	31.16	35.00	34.01	33.88	41.00	39.70	39.85
0.33		31.32	31.42		34.24	34.05		40.02	39.98
0.42		31.50	31.53		34.41	34.27		40.23	40.18
0.50		31.99	31.98		34.97	34.98		40.98	40.97

A superior thermal performance of water was observed when the source temperature was increased to 41°C with a maximum reduction of 1.60°C. The maximum reduction in air temperatures using R134a as the working fluid was only 1.15°C thereby confirming its inferior performance in comparison to water. An in-depth tabulation of the temperature differentials for both fluids is displayed in Table 6.2.

Table 6.2 Air temperature variation downstream across the radial length of the heat pipes using water and R134a as internal working fluids

Radial length (m)	Source (°C)	Water ΔT	R134a ΔT	Source (°C)	Water ΔT	R134a ΔT	Source (°C)	Water ΔT	R134a ΔT
0.00		0.05	0.05		0.05	0.05		0.05	0.05
0.08		0.66	0.49		0.76	0.57		1.40	0.64
0.17		0.93	0.70		1.18	0.85		1.60	0.89
0.25	32.00	0.92	0.84	35.00	0.99	1.12	41.00	1.30	1.15
0.33		0.68	0.58		0.76	0.95		0.98	1.02
0.42		0.50	0.47		0.59	0.73		0.77	0.82
0.50		0.02	0.02		0.02	0.02		0.02	0.02

The graphical representation of the thermal profiles using water and R134a as heat pipe internal fluids is displayed in Figure 6.7. A parabolic trend was noted across the radial length of the test section with largest temperature reductions along the centre of the section.

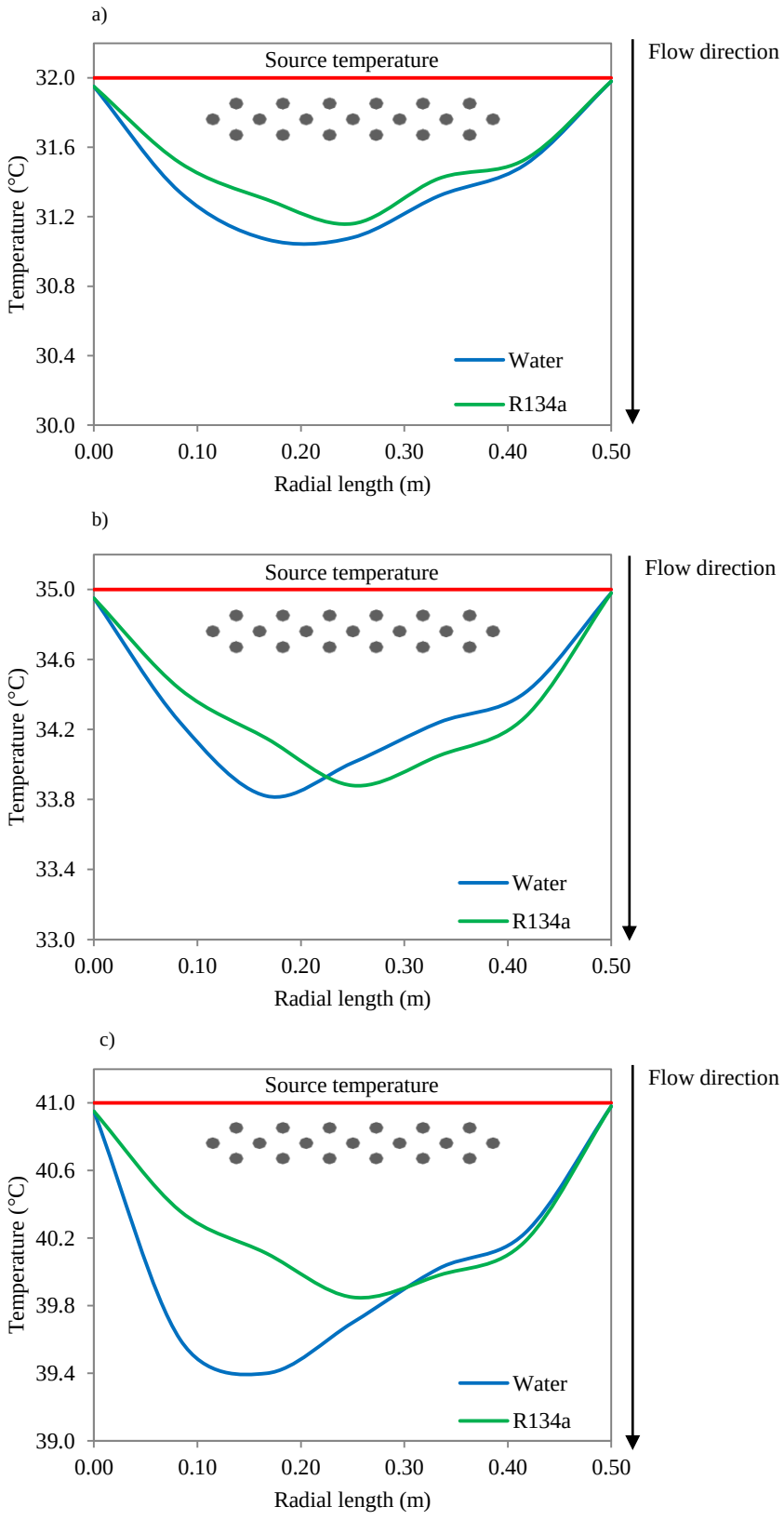

Figure 6.7 Thermal profile of water and R134a at air temperature of: a) 32°C b) 35°C c) 41°C

The mean temperature drop at the source temperature of 32°C was 0.74°C for water while R134a displayed a temperature drop of 0.62°C (Figure 6.7 a). The reduction in air

temperature increased for both working fluids when the source temperature was increased to 35°C (Figure 6.7 b) with water displaying a mean temperature drop of 0.86°C while R134a displaying 0.84°C. The largest reduction in air temperatures were achieved for both fluids when the source temperature was increased to 41°C (Figure 6.7 c). Water displayed a superior heat transfer capability compared to R134a as a mean temperature reduction of 1.21°C was achieved while R134a displaying a reduction of only 0.91°C.

A comparison between water and R134a at different source temperatures and heat pipe spanwise thickness is presented in Figure 6.8. The bar chart plot indicates the air temperature reductions that were obtained using the two internal fluids. As observed, water displayed a higher temperature drop than 1°C or 1K during 6 out of the 9 experimental test-runs. The maximum temperature drop was calculated at 1.6K at a source temperature of 314K using a span length of 50mm (St_{50} model). R134a displayed a temperature reduction of higher than 1°C on 3 out of the 9 experimental testing runs with a maximum drop of 1.15°C. In general, the St_{52} model indicated the lowest temperature differentials for both fluids.

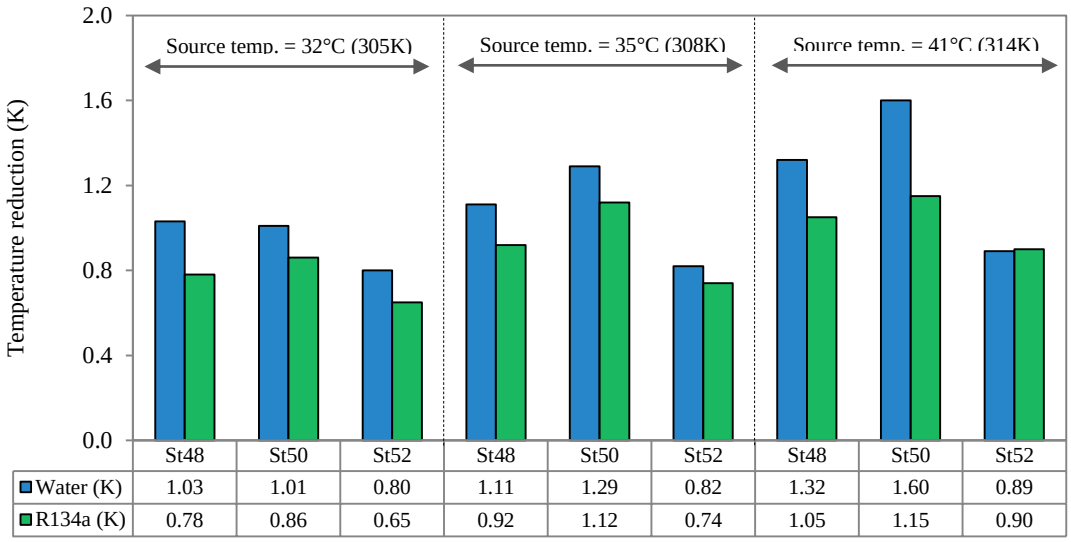

	St48	St50	St52	St48	St50	St52	St48	St50	St52
Water (K)	1.03	1.01	0.80	1.11	1.29	0.82	1.32	1.60	0.89
R134a (K)	0.78	0.86	0.65	0.92	1.12	0.74	1.05	1.15	0.90

Figure 6.8 Comparison between water and ethanol in terms of temperature reductions at increasing source temperatures

The comparison between heat transfer rates for both fluids at varying source temperatures is illustrated in Figure 6.9. The mean transfer of thermal energy using water was calculated at 726W which was 124W higher than the mean obtained for R134a. The highest rate of heat transfer for both fluids was obtained at a source

temperature of 41°C (314K) with water achieving 1,045W in comparison to 751W for R134a. The St_{50} model displayed superior heat transfer for R134a at all three inlet source temperatures. In the case of water, the St_{50} model determined superior heat transfer results at 35°C (308K) and 41°C (314K) while the St_{48} model showed greater heat transfer at a source temperature of 32°C (305K).

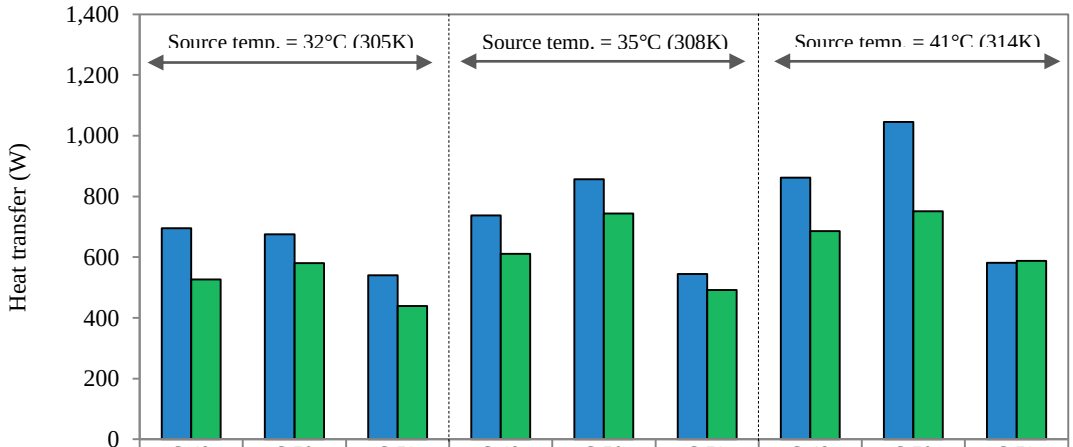

	St48	St50	St52	St48	St50	St52	St48	St50	St52
Water (W)	695.49	675.23	540.19	737.27	856.85	544.66	862.24	1,045.13	581.36
R134a (W)	526.69	580.70	438.90	611.08	743.93	491.52	685.87	751.19	587.89

Figure 6.9 Comparison between water and ethanol in terms of heat transfer at increasing source temperatures

This section of the experimental results described the comparison between water and R134a as heat pipe internal fluids in terms of its thermal performance. The findings revealed that water has a higher heat transferring ability in comparison to R134a at the operative range of inlet temperatures. At an inlet velocity of 2.3m/s the maximum temperature drop was recorded at 1.60K using water as heat pipe working fluid which was 0.45K or approximately 28% higher than R134a working fluid. Following the comparison between water and R134a, both fluids were tested under varying spanwise thicknesses to determine the optimum arrangement.

6.4.2 Geometrical variation using water as the working fluid

Subsequent to the comparison between water and R134a, this section of the chapter details the results obtained for the optimum spanwise thickness between heat pipes using water as the working fluid. The set-up comprised of 19 cylindrical heat pipes arranged vertically at an angle of 90° with respect to ground. Each test run was carried

out at an inlet velocity of 2.3m/s for a duration of 200 seconds following the stabilisation of heating elements at the set-point level.

The tests were carried out at three normalised source temperatures, namely 32°C (305K), 35°C (308K) and 41°C (314K) in order to validate the CFD models at the same source temperatures for the months of November, April and June (The Weather Channel, 2012). All temperature readings were recorded using the data logging system connected to the K-type thermocouples which were positioned at the upstream and downstream measurement locations as defined in Chapter 4, Section 4.8.3.

Three perspex base-plate templates for the arrangement of heat pipes were manufactured with heat pipe holes measuring spanwise thicknesses of 48mm, 50mm and 52mm. The three arrangements were built to replicate the St_{48}, St_{50} and St_{52} numerical models. Thermocouple locations upstream and downstream of the heat pipes were kept identical to the numerical model in order to generate comparative experimental results.

Using eqn.27 and eqn.28 (as detailed in Chapter 5, Section 5.2.3), the rate of heat transfer in the evaporator section and the overall effectiveness of the system was determined. The air density was taken as 1.165kg/m^3, 1.146kg/m^3 and 1.127kg/m^3 at 305K, 308K and 314K while the specific heat capacity was taken as 1,005kJ/kgK. The tests were conducted within the stabilised time of the cold sink which was maintained between 288K and 291K.

The normalised air temperature values upstream and downstream of the heat pipes at inlet temperatures of 32°C (305K), 35°C (308K) and 41°C (314K) using water as the heat pipe working fluid were investigated for the duration of 200 seconds. Figure 6.10 displays the air temperature results for the month of November when the heat pipes were arranged with a span length of 48mm. A mean temperature reduction of 0.92°C was obtained when the source temperature was approximately 32.5°C, corresponding to a mean heat transfer of 624.1W.

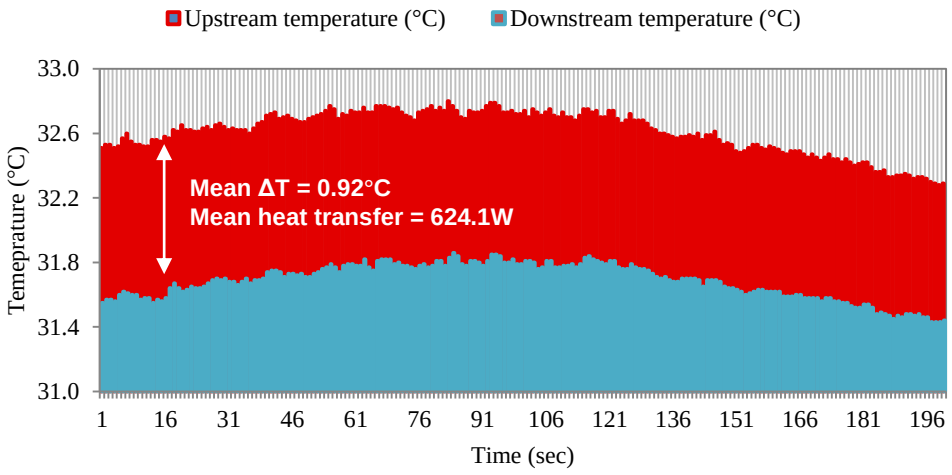

Figure 6.10 Normalised upstream and downstream air temperatures for the month of November using water heat pipes arranged in a span length of 48mm

The temperature differential between upstream and downstream locations was found to be directly proportional to the increasing source temperature as the mean heat transfer increased from 624.1W to 686.0W when the source temperature increased to 35.6°C (Figure 6.11).

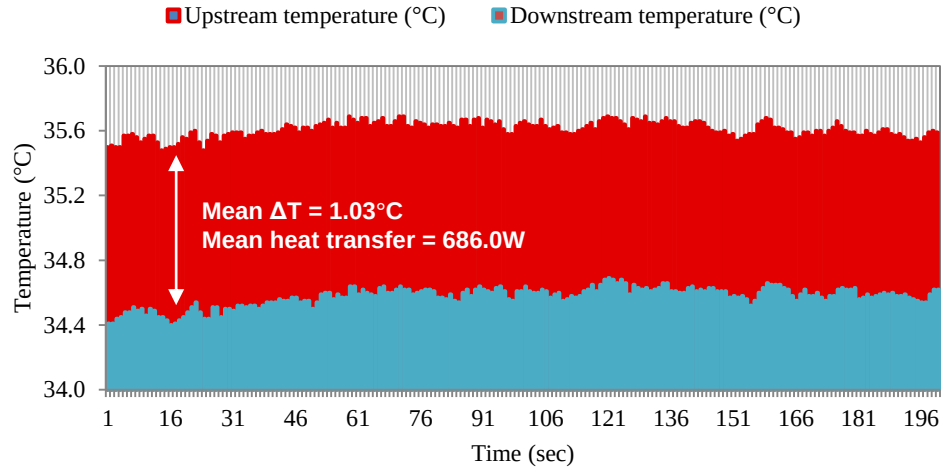

Figure 6.11 Normalised upstream and downstream air temperatures for the month of April using water heat pipes arranged in a span length of 48mm

The highest temperature reduction was obtained when the inlet air temperature was increased to approximately 40.6°C with a mean reduction of 1.14°C recorded over the 200 seconds run-time (Figure 6.12). The corresponding mean heat transfer was calculated at 742.8W. The downstream temperatures were directly proportional to the upstream values upon normalisation of the heating elements for all experimental cases.

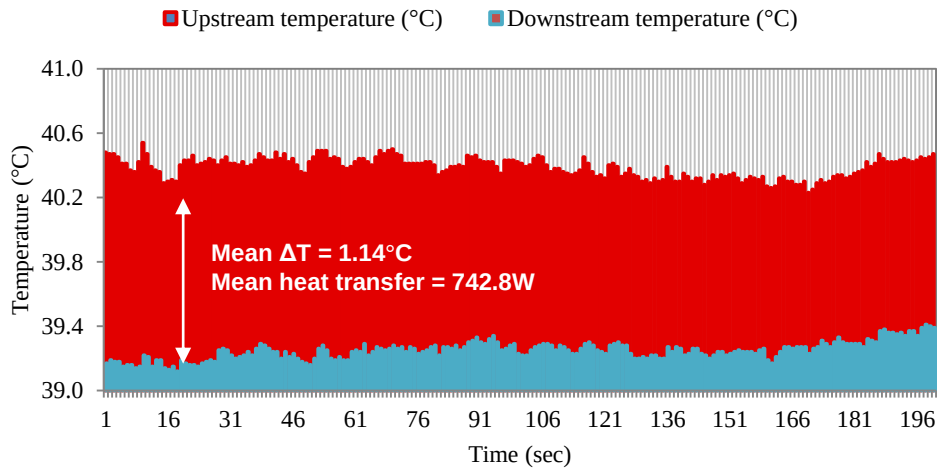

Figure 6.12 Normalised upstream and downstream air temperatures for the month of June using water heat pipes arranged in a span length of 48mm

The experimental tests were repeated with an increased heat pipe span length of 50mm, the results of which are displayed in Figure 6.13 for the month of November. The minimum temperature drop of 0.96°C was noted when the source temperature was normalised at 33.4°C. This was due to a low temperature differential between the source and sink conditions.

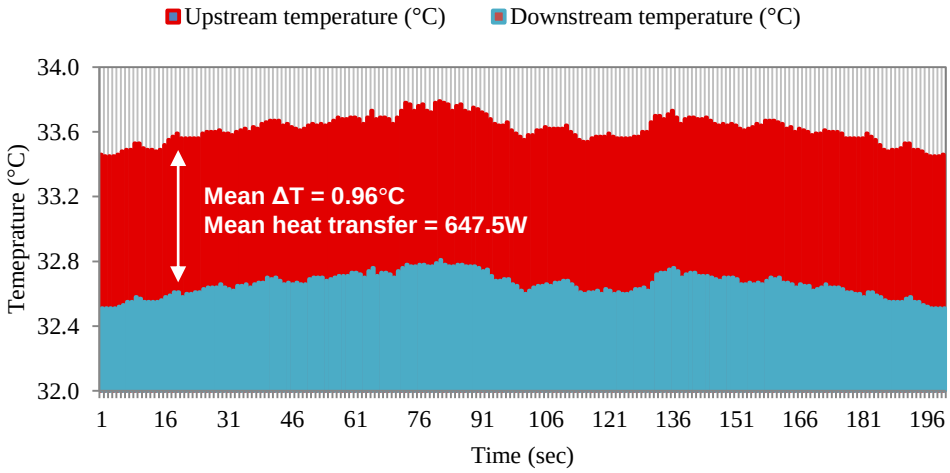

Figure 6.13 Normalised upstream and downstream air temperatures for the month of November using water heat pipes arranged in a span length of 50mm

It was observed that the mean heat transfer increased by 101.7W when the source temperature was increased from 33.6°C to 36.3°C. Figure 6.14 illustrates the graphical representation of the normalised temperature profiles for the month of April over the testing duration of 200 seconds.

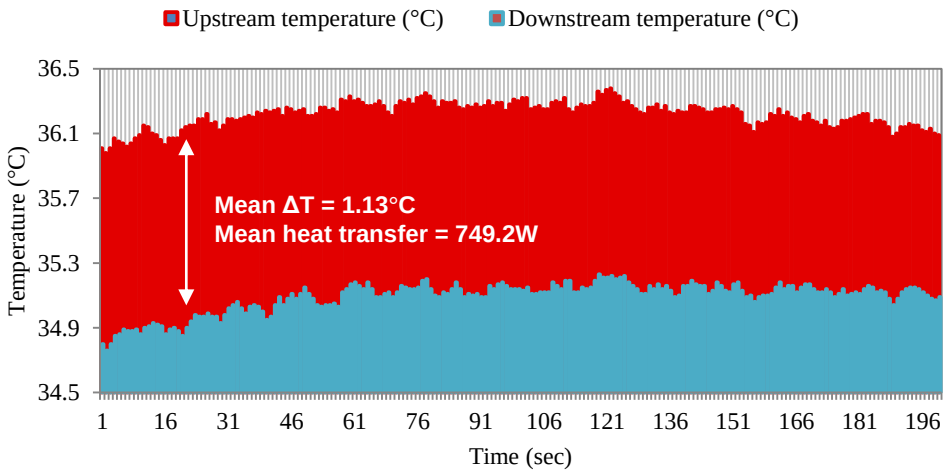

Figure 6.14 Normalised upstream and downstream air temperatures for the month of April using water heat pipes arranged in a span length of 50mm

The highest downstream temperature drop was obtained at a source temperature of 41°C, displaying a mean reduction of 1.35°C (Figure 6.15) across the experimental run-time. In general, the spanwise thickness of 50mm (St_{50} model) displayed the highest temperature drop and the corresponding convective heat transfer in comparison to the other two arrangements.

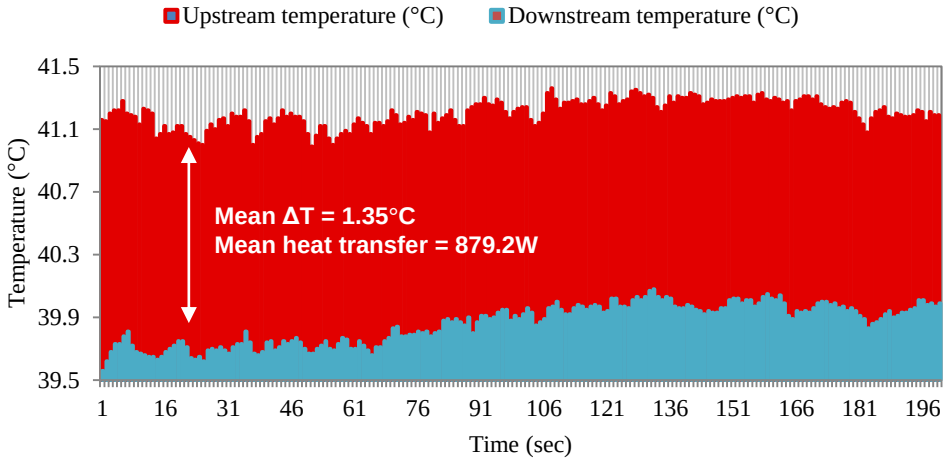

Figure 6.15 Normalised upstream and downstream air temperatures for the month of June using water heat pipes arranged in a span length of 50mm

The final analysed heat pipe span length was 52mm and Figure 6.16 displays the transient air temperature results replicating the month of November. As predicted by the numerical analysis in the previous chapter (Chapter 5, Section 5.4), this configuration produced the lowest temperature differential from all compared models. A mean

temperature differential (ΔT) of 0.72°C was produced resulting in a heat transfer of 488.8W.

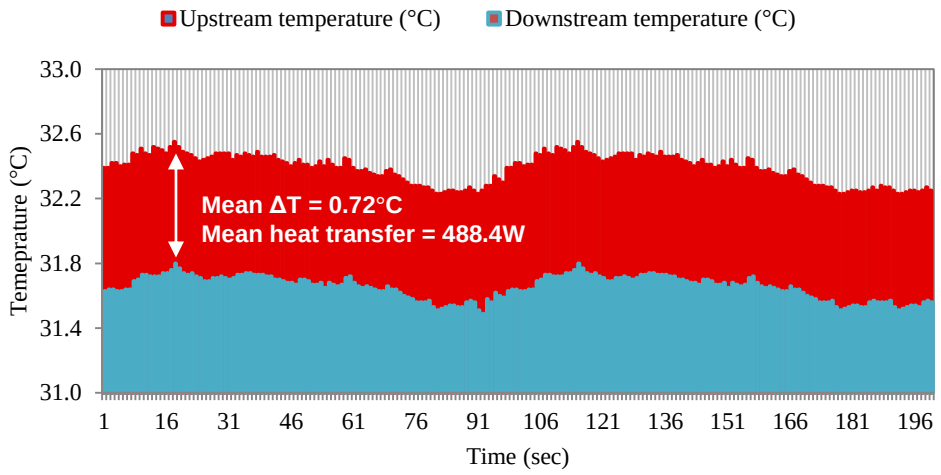

Figure 6.16 Normalised upstream and downstream air temperatures for the month of November using water heat pipes arranged in a span length of 52mm

Figure 6.17 displays the normalised air temperature findings for the month of April (source temperature of 34.8°C). A similar trend between upstream and downstream temperatures was perceived and the mean temperature differential was observed to increase by 0.06K subsequently increasing the heat transfer by 31W.

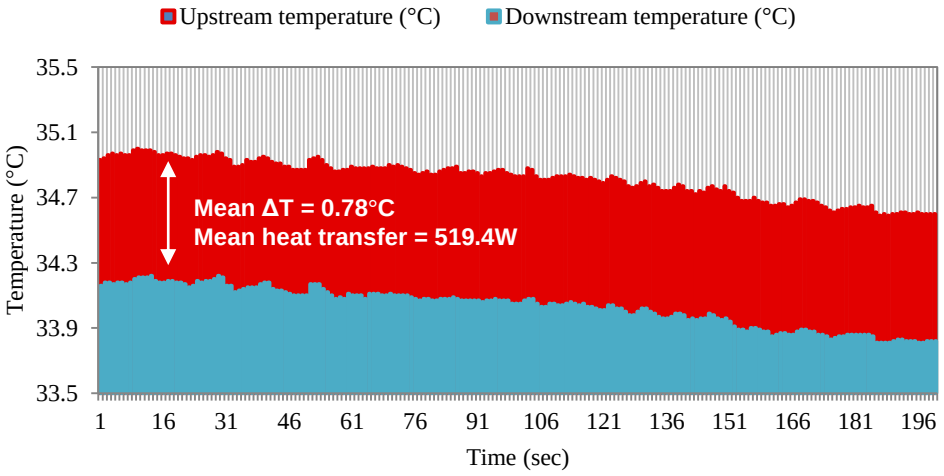

Figure 6.17 Normalised upstream and downstream air temperatures for the month of April using water heat pipes arranged in a span length of 52mm

The maximum temperature reduction was recorded at 0.85°C when the inlet temperature was increased to 41°C (Figure 6.18). The highest mean rate of heat transfer

was calculated at 554.1W which was significantly lower than that achieved for the other two spanwise arrangements.

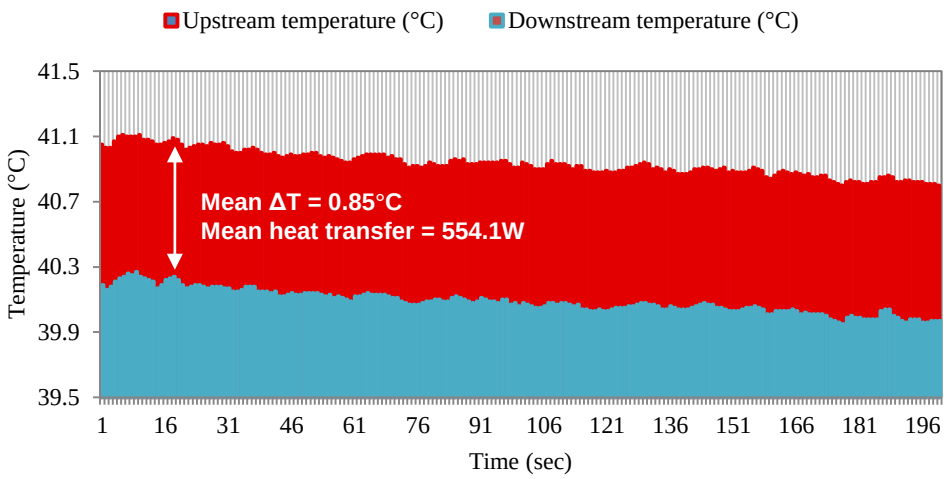

Figure 6.18 Normalised upstream and downstream air temperatures for the month of June using water heat pipes arranged in a span length of 52mm

The experimental duration was kept constant at 200 seconds for all three analysed spanwise configurations. A direct comparison between the three heat pipe arrangements at a source temperature of 32°C (305K) is displayed in Figure 6.19.

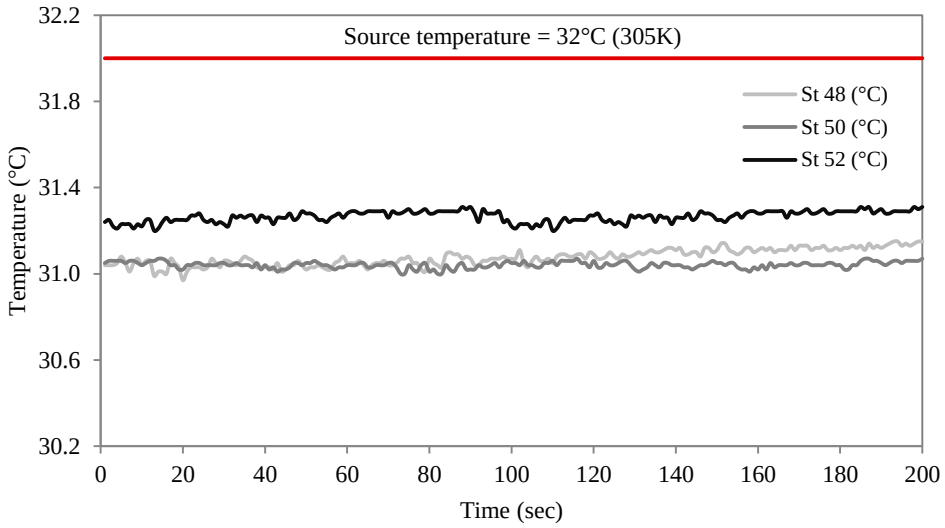

Figure 6.19 Comparison between St_{48}, St_{50} and St_{52} models using water pipes at a source temperature of 32°C

The highest mean temperature drop was obtained at 0.96°C using the spanwise thickness of 50mm (St_{50} model) while the lowest temperature drop was recorded at 0.72°C using the spanwise thickness of 52mm (St_{52} model). The St_{48} model (spanwise thickness of 48mm) consistently indicated intermediate findings between the other two compared configurations.

Figure 6.20 displays the comparison between the three configurations at an inlet temperature of 35°C (308K). It was noted that in general, the temperature reductions increased in direct proportionality to the increase in source temperatures. The greatest mean temperature drop was again recorded at 1.13°C for the St_{50} model which was 0.35°C higher than that achieved for the St_{52} model.

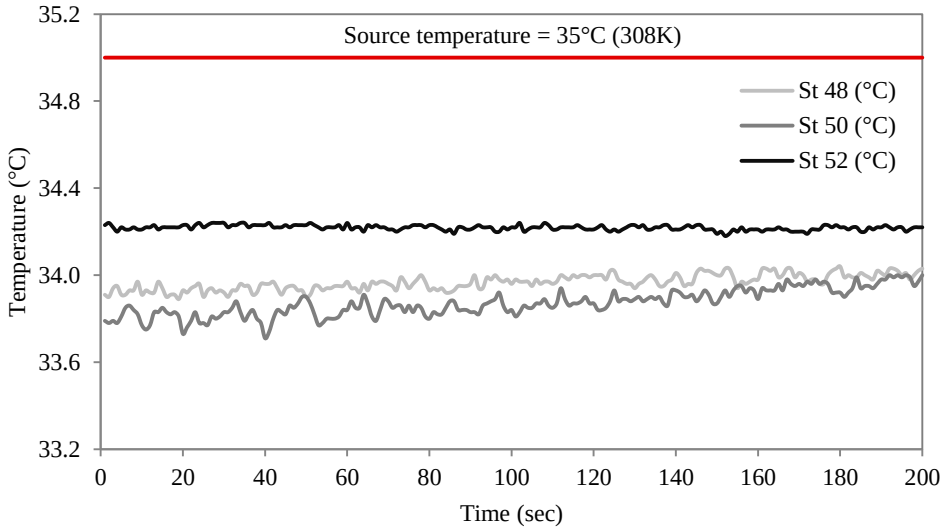

Figure 6.20 Comparison between St_{48}, St_{50} and St_{52} models using water pipes at a source temperature of 35°C

All three investigated spanwise configurations displayed the highest reduction in air temperatures when the source or inlet temperature was increased to 41°C (314K) as displayed in Figure 6.21. Greater downstream temperature fluctuations were noted for this source temperature. However, a similar trend was observed between the three arrangements with the St_{50} model giving the highest reduction between upstream and downstream temperatures at 1.35°C which was superior to the other two analysed cases.

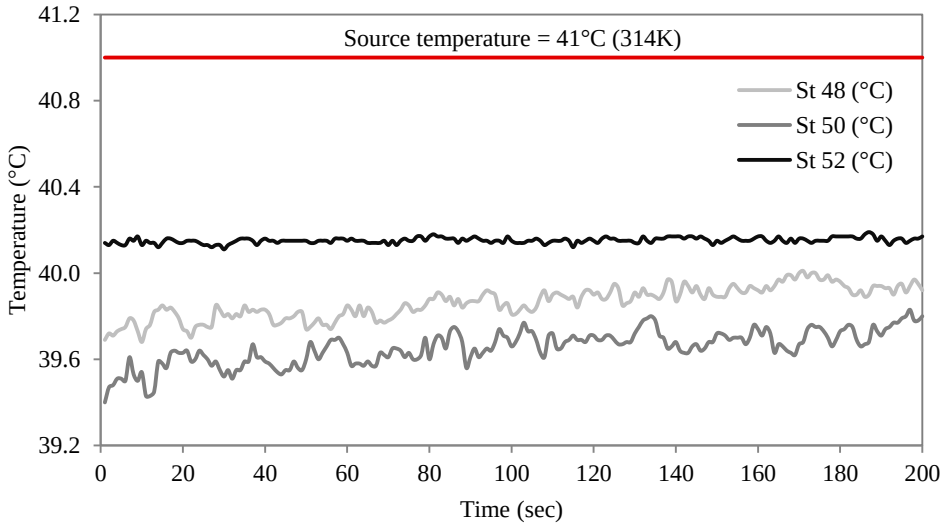

Figure 6.21 Comparison between St_{48}, St_{50} and St_{52} models using water pipes at a source temperature of 41°C

The summary of the experimental results highlighting the maximum heat transfer and heat pipe heat exchanger effectiveness using eqn.27 and eqn.28 (Chapter 5, Section 5.2.3) are tabulated in Table 6.3.

Table 6.3 Heat transfer and heat pipe heat exchanger effectiveness for the three spanwise arrangements using water as the internal fluid

Source temperature	**Model**	**Downstream temp. (°C)**	**ΔT (°C)**	**Heat transfer (W)**	**Effectiveness (%)**
	St_{48}	30.97	1.03	695.49	6.06%
32°C	St_{50}	31.00	1.00	675.23	5.88%
	St_{52}	31.20	0.80	540.19	4.71%
	St_{48}	33.89	1.11	737.27	5.55%
35°C	St_{50}	33.71	1.29	856.85	6.45%
	St_{52}	34.18	0.82	544.66	4.10%
	St_{48}	39.68	1.32	862.24	5.08%
41°C	St_{50}	39.40	1.60	1,045.13	6.15%
	St_{52}	40.11	0.89	581.36	3.42%

The maximum heat transfer was recorded for the St_{50} model at 1,045W at a source temperature of 41°C (314K) indicating the effectiveness of the heat pipe system to be 6.15%. The values of effectiveness were low due to a high inlet air velocity of 2.3m/s which was the lowest that could be achieved using the current wind tunnel facility. The highest effectiveness was calculated for the St_{50} model at 6.45% for the month of April at a source temperature of 35°C (308K). The maximum reduction in air temperature was

recorded at 1.60°C for the St_{50} model which was approximately two times higher than that achieved with the St_{52} model.

6.4.3 Geometrical variation using R134a as the working fluid

The experimentation was repeated using R134a as the internal working fluid in order to further confirm the most suitable heat pipe spanwise configuration. The spanwise thicknesses between the heat pipes were kept fixed at 48mm (St_{48} model), 50mm (St_{50} model) and 52mm (St_{52} model). Figure 6.34, Figure 6.35 and Figure 6.36 display the normalised air temperature values upstream and downstream of the heat pipes at source temperatures of 32°C (305K), 35°C (308K) and 41°C (314K) using R134a as the heat pipe working fluid arranged in a span length of 48mm.

Figure 6.22 shows the normalised air temperature variations upstream and downstream of the heat pipes for the run-time of 200 seconds at a spanwise thickness of 48mm. The stabilised profiles ensured that the source temperatures remained at the desired set-point levels. In general, R134a produced inferior temperature differential or heat transfer results in comparison to water for all analysed temperatures. The minimum temperature reduction of 0.74°C was noted at this source temperature which was 31.4°C, indicating a heat transfer of 497.9W.

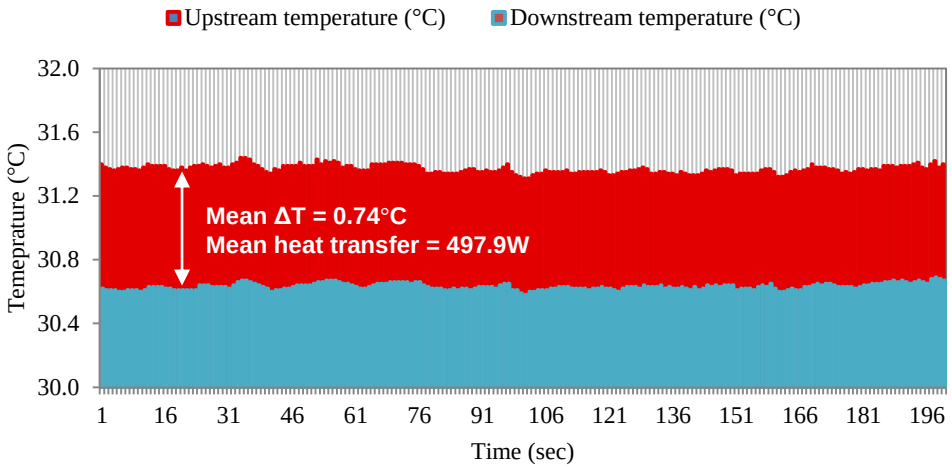

Figure 6.22 Normalised upstream and downstream air temperatures for the month of November using R134a heat pipes arranged in a span length of 48mm

The mean temperature differential (ΔT) increased from 0.74°C to 0.88°C when the source temperature was increased to 36.1°C replicating the month of April. The graphical illustration of the normalised temperature results are displayed in Figure 6.23.

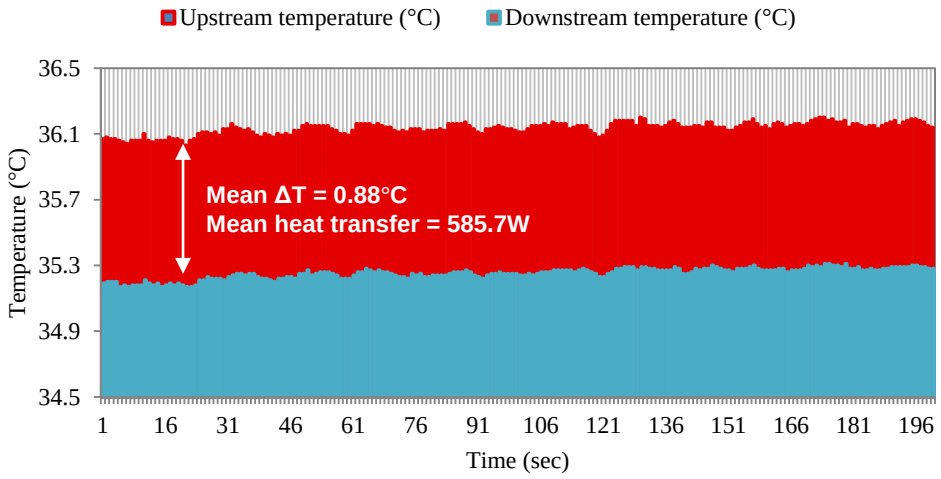

Figure 6.23 Normalised upstream and downstream air temperatures for the month of April using R134a heat pipes arranged in a span length of 48mm

The highest mean temperature drop was recorded at 1.00°C at an inlet temperature of 41.8°C (Figure 6.24) providing a heat transfer of 655.2W which was 157.3W higher than the one obtained at a source temperature of 31.4°C.

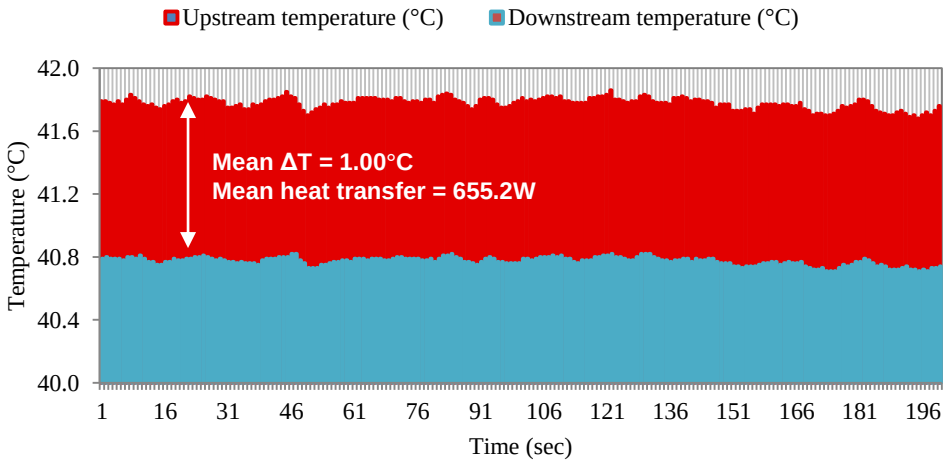

Figure 6.24 Normalised upstream and downstream air temperatures for the month of June using R134a heat pipes arranged in a span length of 48mm

All recordings were taken at the measurement locations which were identical to the CFD measurement points (Chapter 4 Section 4.8.3). Figure 6.25 displays the normalised

air temperature values when the heat pipes were arranged in a span length of 50mm. In general, the highest rate of heat transfer and temperature drop using R134a as the working fluid was produced using this arrangement. The mean heat transfer was determined at 563.3W when the source temperature was 32°C replicating the month of November.

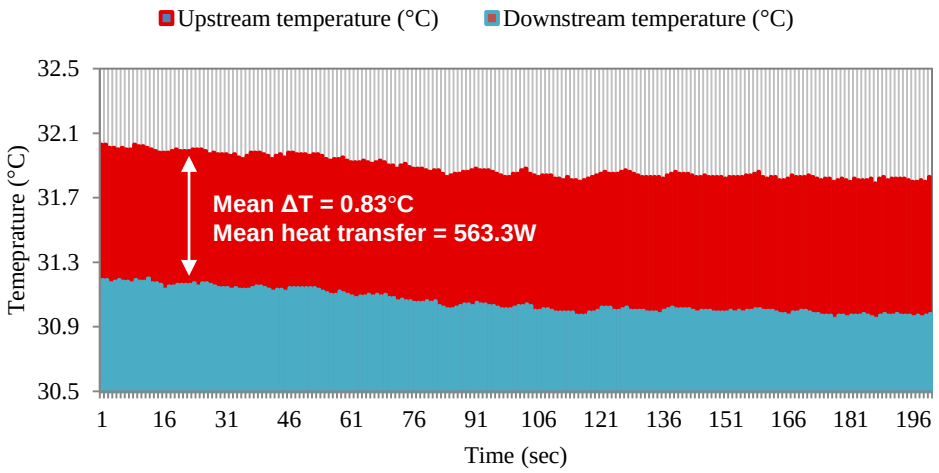

Figure 6.25 Normalised upstream and downstream air temperatures for the month of November using R134a heat pipes arranged in a span length of 50mm

The mean differential between upstream and downstream temperatures increased from 0.83°C to 1.04°C when the source temperature was increased to 36°C with the corresponding heat transfer recorded at 687.6W. Figure 6.38 displays the normalised air temperature results for the duration of 200 seconds.

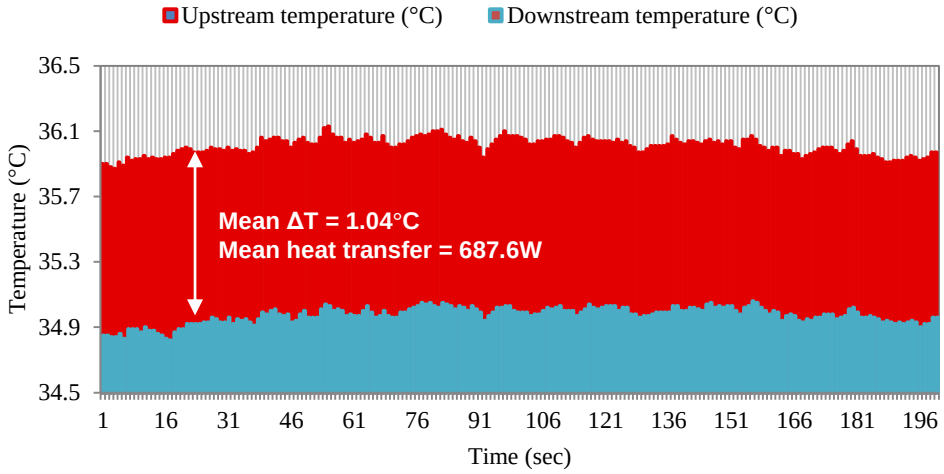

Figure 6.26 Normalised upstream and downstream air temperatures for the month of April using R134a heat pipes arranged in a span length of 50mm

The maximum temperature reduction was noted at 1.09°C when the inlet temperature was 41°C (314K), at which the heat transfer was calculated at 714.6W (Figure 6.27). As observed for all cases, the downstream temperatures were directly proportional to the upstream values upon normalisation of the heating elements.

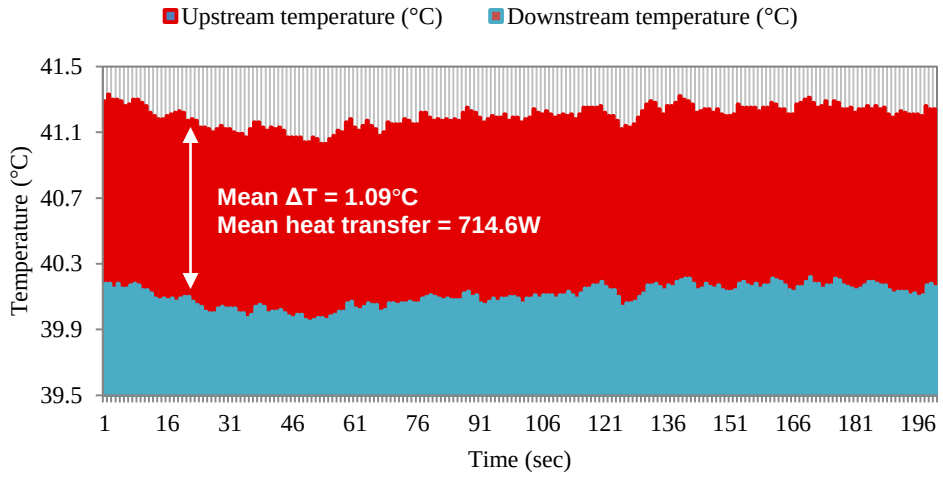

Figure 6.27 Normalised upstream and downstream air temperatures for the month of June using R134a heat pipes arranged in a span length of 50mm

Similar to the experimentation with water, the final analysed spanwise thickness for R134a was 52mm. With respect to Figure 6.28, the normalised air temperature result for the month of November is displayed. The mean temperature differential was 0.62°C indicating a heat transfer of 417.3W.

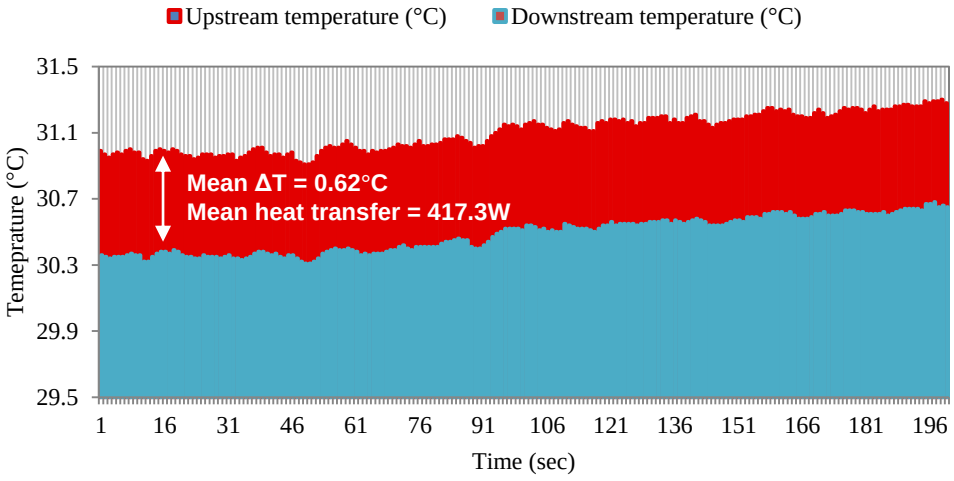

Figure 6.28 Normalised upstream and downstream air temperatures for the month of November using R134a heat pipes arranged in a span length of 52mm

Generally, this arrangement highlighted the lowest temperature differentials for all three analysed source temperatures. Figure 6.29 illustrates the normalised air temperature results when the source temperature was increased to 36°C replicating the month of April. An increase of 44.7W was obtained for the mean heat transfer at the temperature differential of 0.7°C.

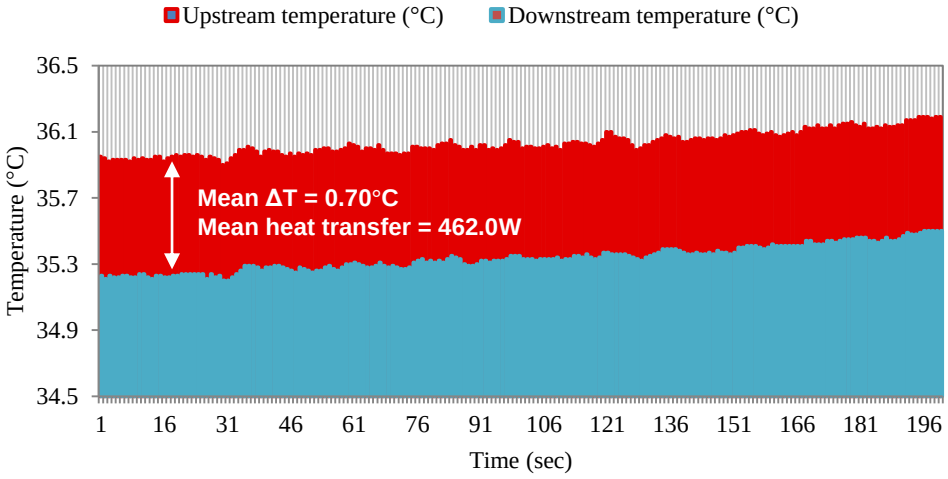

Figure 6.29 Normalised upstream and downstream air temperatures for the month of April using R134a heat pipes arranged in a span length of 52mm

For a spanwise thickness of 52mm, the highest reduction of 0.87°C was achieved at an inlet temperature of 41.6°C corresponding to a mean heat transfer of 567.1W (Figure 6.30). It was observed that the St_{52} model consistently produced the lowest heat transfer for all analysed cases.

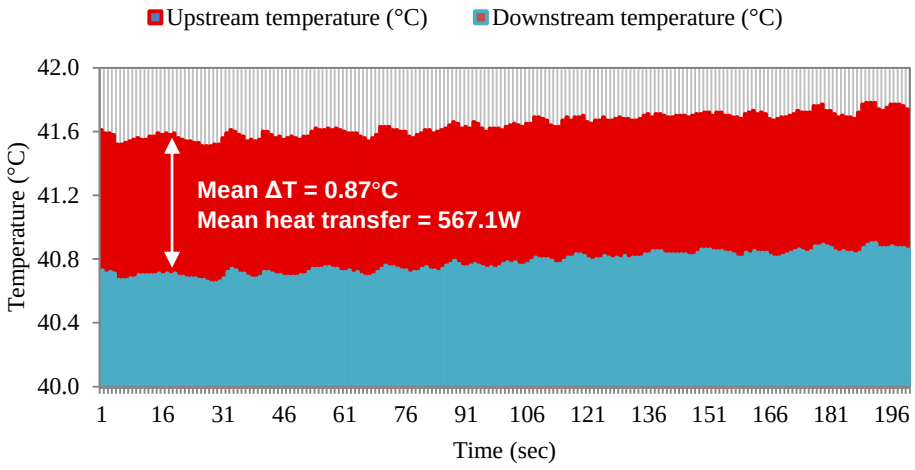

Figure 6.30 Normalised upstream and downstream air temperatures for the month of June using R134a heat pipes arranged in a span length of 52mm

The source temperature values at the test section were stabilised to 32°C (305K) and the corresponding downstream temperatures were plotted for R134a heat pipes. This was done in order to achieve a direct comparison between the three compared spanwise arrangements. A similar trend to water heat pipe was observed as the St_{50} model gave the highest reduction in air temperatures. The highest mean temperature drop was 0.83°C from the St_{50} model while the lowest temperature drop was recorded at 0.62°C from the St_{52} (spanwise thickness of 52mm) numerical model. The graphical representation of the comparison between St_{48}, St_{50} and St_{52} models using R134a as the working fluid is displayed in Figure 6.31.

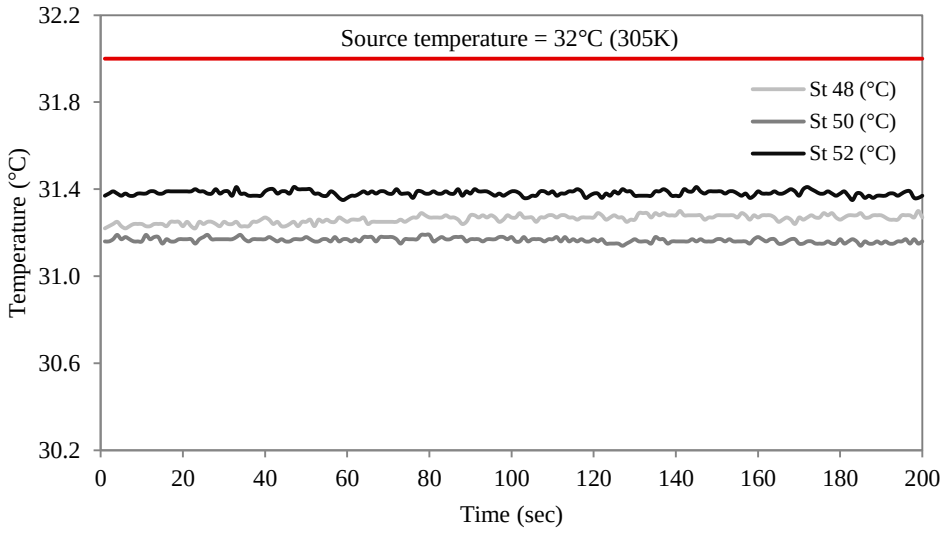

Figure 6.31 Comparison between St_{48}, St_{50} and St_{52} models using R134a pipes at a source temperature of 32°C

Figure 6.32 displays the comparison between the three heat pipe arrangements at a source temperature of 35°C (308K). The highest temperature drop at this source temperature was achieved at 1.04°C corresponding to a heat transfer of 687.6W using the spanwise thickness of 50mm. Overall, the reduction in air temperatures increased as the source temperatures were raised. This was anticipated as the temperature difference between source and sink were increased simultaneously.

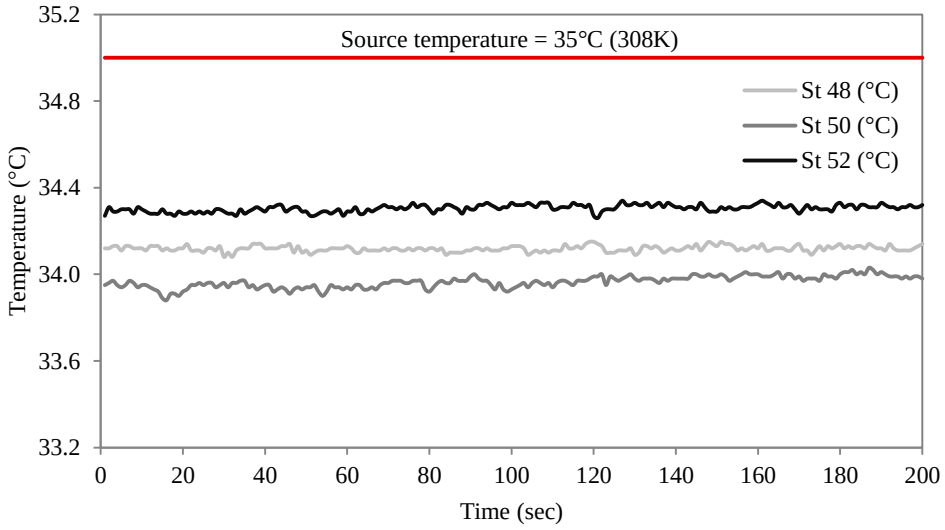

Figure 6.32 Comparison between St_{48}, St_{50} and St_{52} models using R134a pipes at a source temperature of 35°C

The largest temperature reductions were recorded for all models when the source temperature was increased to 41°C (Figure 6.33), replicating the monthly mean temperature of June in the city of Doha, Qatar.

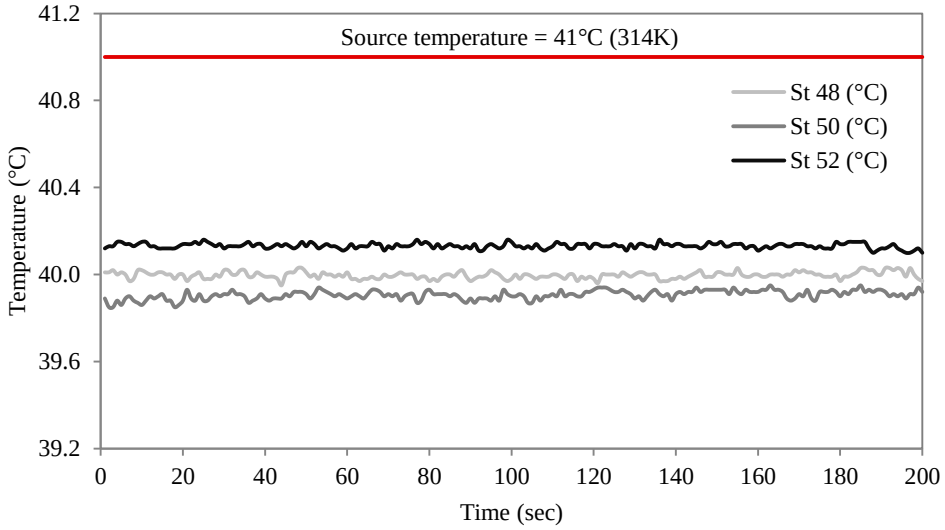

Figure 6.33 Comparison between St_{48}, St_{50} and St_{52} models using R134a pipes at a source temperature of 41°C

The St_{52} model indicated a temperature drop of 0.87°C, while the St_{48} model indicated a temperature reduction of 1.00°C. However, the highest airside temperature reduction was recorded at 1.09°C using the St_{50} model. The experimental analysis using R134a

confirmed the span length of 50mm as the most suitable spanwise arrangement to be used for the heat pipes within this physical domain.

The summarised results of heat transfer and heat pipe heat exchanger effectiveness are tabulated in Table 6.4. The highest rate of heat transfer was calculated at 751.19W at a source temperature of 41°C (314K) using the St_{50} model, corresponding to a maximum temperature drop of 1.15°C. The heat pipe system was found to be the most effective during the month of April with an overall effectiveness of 5.60%. It was noted that the St_{50} displayed the greatest airside temperature drop with a maximum reduction of 1.15°C, which was 0.25°C higher than what was achieved using the St_{52} numerical model.

Table 6.4 Heat transfer and heat pipe heat exchanger effectiveness for the three spanwise arrangements using R134a as the internal fluid

Source temperature	Model	Downstream temp. (°C)	ΔT (°C)	Heat transfer (W)	Effectiveness (%)
	St_{48}	31.22	0.78	526.69	4.59%
32°C	St_{50}	31.14	0.86	580.70	5.06%
	St_{52}	31.35	0.65	438.90	3.82%
	St_{48}	34.08	0.92	611.08	4.60%
35°C	St_{50}	33.88	1.12	743.93	5.60%
	St_{52}	34.26	0.74	491.52	3.70%
	St_{48}	39.95	1.05	685.87	4.04%
41°C	St_{50}	39.85	1.15	751.19	4.42%
	St_{52}	40.10	0.90	587.89	3.46%

6.4.4 Thermal behaviour of heat pipes in response to variation in external temperatures

A transient air temperature test was performed following the steady-state evaluation of heat pipes. The test was carried out for a period of 24 hours with varying inlet source temperatures at 30 minute intervals. The inlet temperature profile was taken as a reference to match the conditions experienced during a typical hot day in the state of Doha, Qatar. The hourly temperature values were taken for June 21st, 2012 (Weather History for Doha, Qatar, 2012). The purpose of conducting this test was to determine the climatic response characteristics of heat pipes at varying temperature gradients and investigate the periods when maximum and minimum temperature differentials are

obtained. Figure 6.34 displays the air temperature results upstream and downstream of the heat pipes for a period of 24 hours.

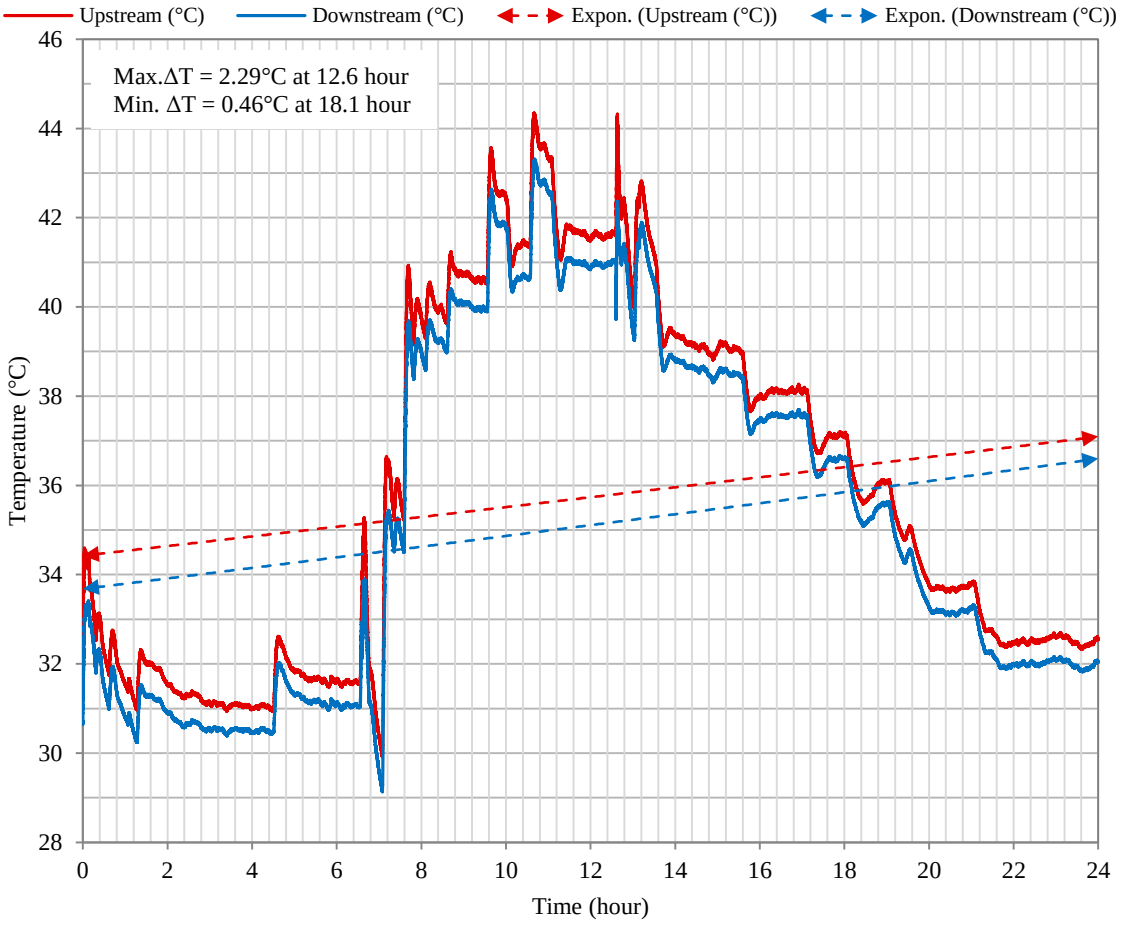

Figure 6.34 Transient thermal behaviour of heat pipes under convection over a period of 24 hours

Increasing source (inlet) temperature peaks induced greater thermal performance of the heat pipes as a maximum ΔT of 2.29°C (or 2.29K) was measured at the 12.6 hour mark when the upstream temperature was approximately 44°C. The temperature differentials were the lowest when the upstream temperatures were reduced in a downward gradient. The lowest temperature drop was measured at 0.46°C at the 18.1 hour mark when the upstream temperature was decreased from 37°C to 36°C. The dotted lines represent the exponential trendlines associated with the two temperature streams.

For the purpose of this test, thermocouples were located on the heat pipe surface, both in the evaporator and condenser sections. This was done in order to monitor the behaviour of the heat pipes under conduction. Larger temperature differentials were

obtained under the conduction mode with a maximum ΔT measured at 4.84°C at the 10.7 hour mark. The lowest temperature drop was 0.26°C at the 4.4 hour point as the sink temperature increased when the upstream temperature was increased from 31°C to 32°C. The downward troughs are formed due to the reloading of the ice pockets at the cold sink in order to maintain appropriate conditions at the cold interface. The dotted lines represent the exponential trendlines associated with the two temperature streams. Figure 6.35 displays the obtained temperature trends.

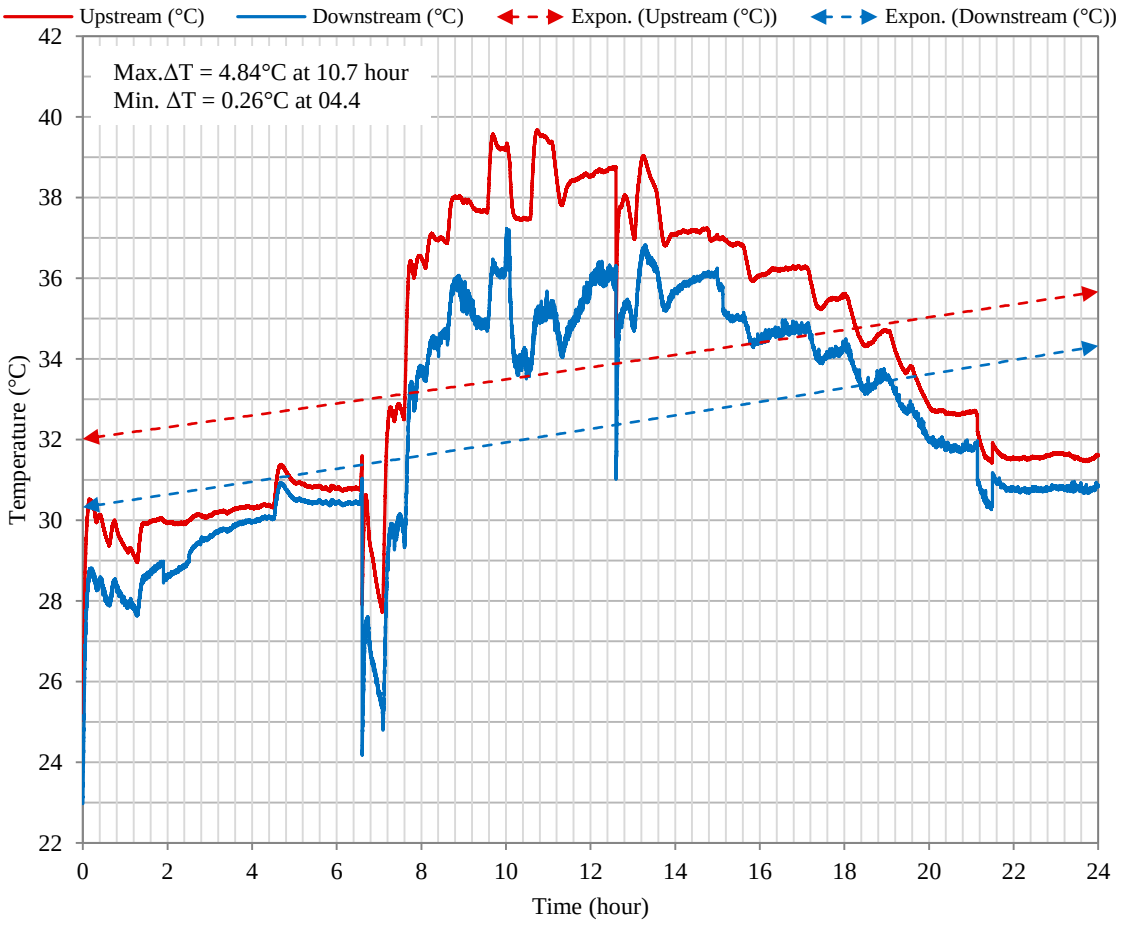

Figure 6.35 Transient thermal behaviour of heat pipes under conduction over a period of 24 hours

The infrared camera was used for detecting and capturing the transient formation of surface temperature images as displayed in Figure 6.36. The thermal profile of the heat pipes was recorded at source temperatures ranging from 22°C to 45°C.

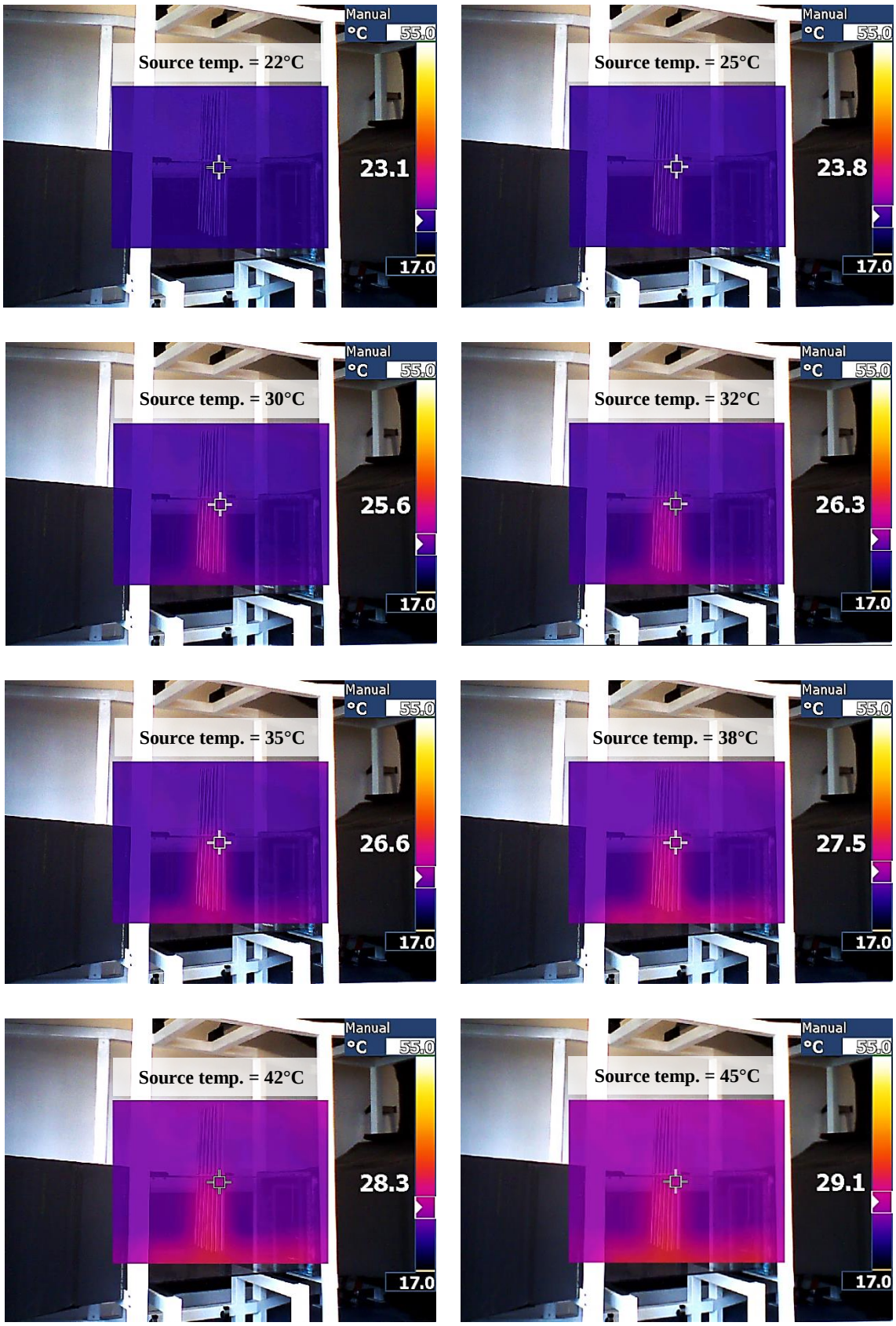

Figure 6.36 Transient formation of surface temperatures using FLUKE Tir1 thermal imaging camera

A steady increase in heat pipe surface temperatures was observed over the duration of the experiment as the heating elements increased temperatures to 45°C or 318K at the end of the run-time. The evaporator section temperature (bottom of the figure) of the heat pipes was higher than the condenser section temperature (top of the figure) due to constant dissipation of the heat to the ambient. An overall increase of 6°C in room temperature was recorded varying between 23.1°C at the start of the experimental run-time to 29.1°C at the end of the experiment.

An illustration of the temperature reduction trends are illustrated in Figure 6.37 a) for the duration of 24 hours. Regular peaks were formed at the 6^{th}, 7^{th} and 8^{th} hour mark when the upstream temperature was in an increasing gradient starting from 30°C to approximately 40°C. The highest temperature peak of 2.29°C is formed at 12.6 hours when the upstream temperature was increased up to 44.2°C. The average temperature differentials were measured at 0.76°C. This was mainly due to the upstream temperatures being under 40°C for most part of the test.

The thermal response of heat pipes during the temperature peak between 7.08 and 7.15 hours is displayed in Figure 6.37 b). During this time, the upstream temperature was increased by 6°C from 30°C to 36°C. Correspondingly, it was recorded that the temperature reduction increased in direct proportion from 0.8°C to 1.5°C. The change in upstream and downstream temperature during a decreasing source temperature pattern between 12.62 and 13.03 hours is displayed in Figure 6.37 c). The upstream temperature was reduced from 44°C to approximately 39°C and the corresponding heat pipe thermal response was underlined. It was observed that the temperature reduction decreased as the upstream temperature was reduced, indicating direct proportionality between two quantities.

As a third case in the analysis of thermal response from heat pipes, a normalised temperature stream was considered between 11.42 and 11.50 hours (Figure 6.37 d). The mean upstream air temperature was 41.8°C with a variation of ±0.1°C, while the mean downstream temperature was recorded at 41.0°C. It was observed that the temperature differential trend continued to be similar throughout the duration of the test.

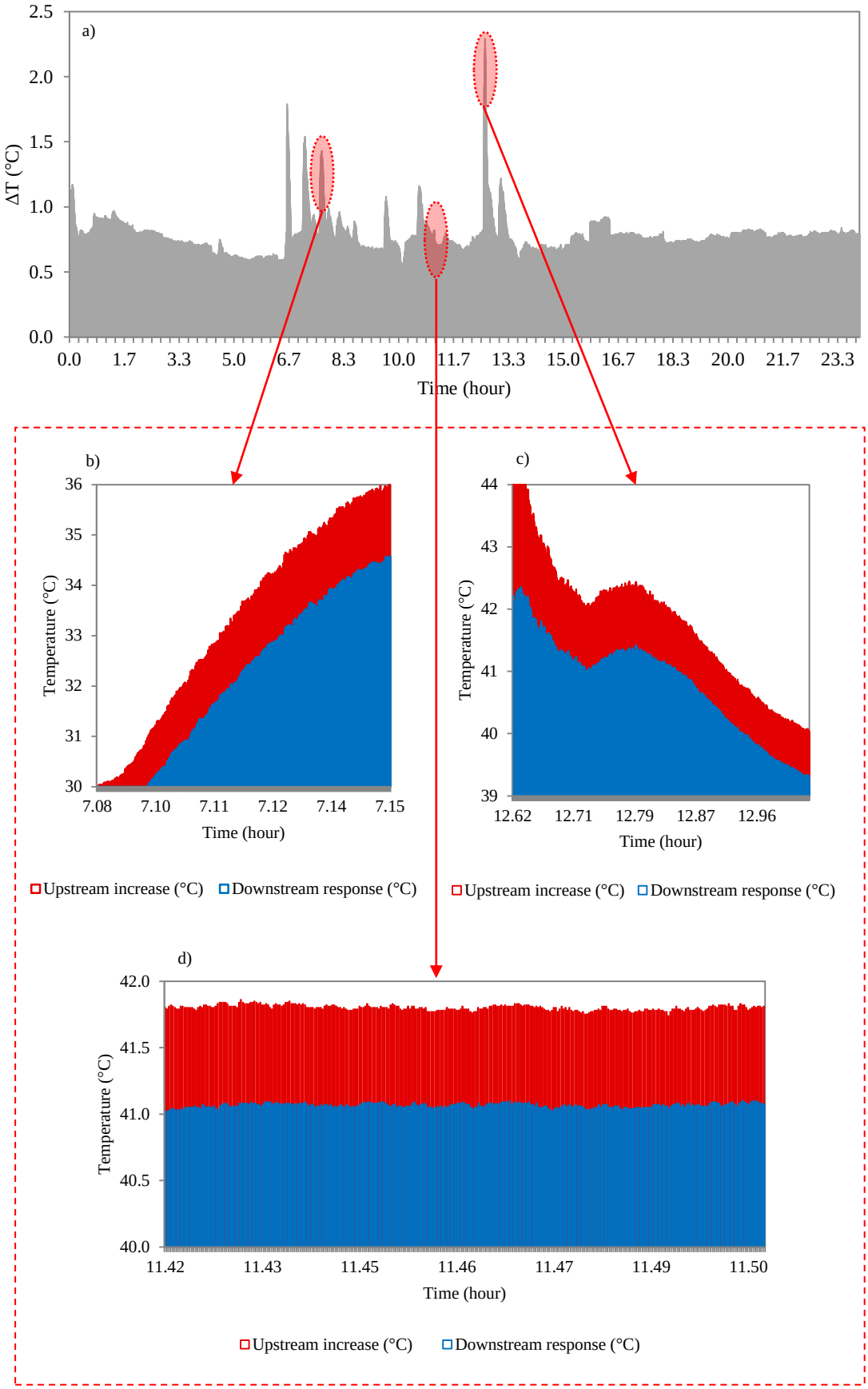

Figure 6.37 a) Temperature reduction trend over 24 hours b) Formation of upstream and downstream temperatures between 7.08-7.15 hours c) 12.62-13.03 hours d) 11.42-11.50 hours

Having considered three scenarios including an increasing temperature stream, a decreasing temperature stream and a normalised temperature stream, the detailed thermal responses for all cases were discussed in the following sections. The ratio of increasing source temperatures to increasing downstream temperature reduction is graphically displayed in Figure 6.38.

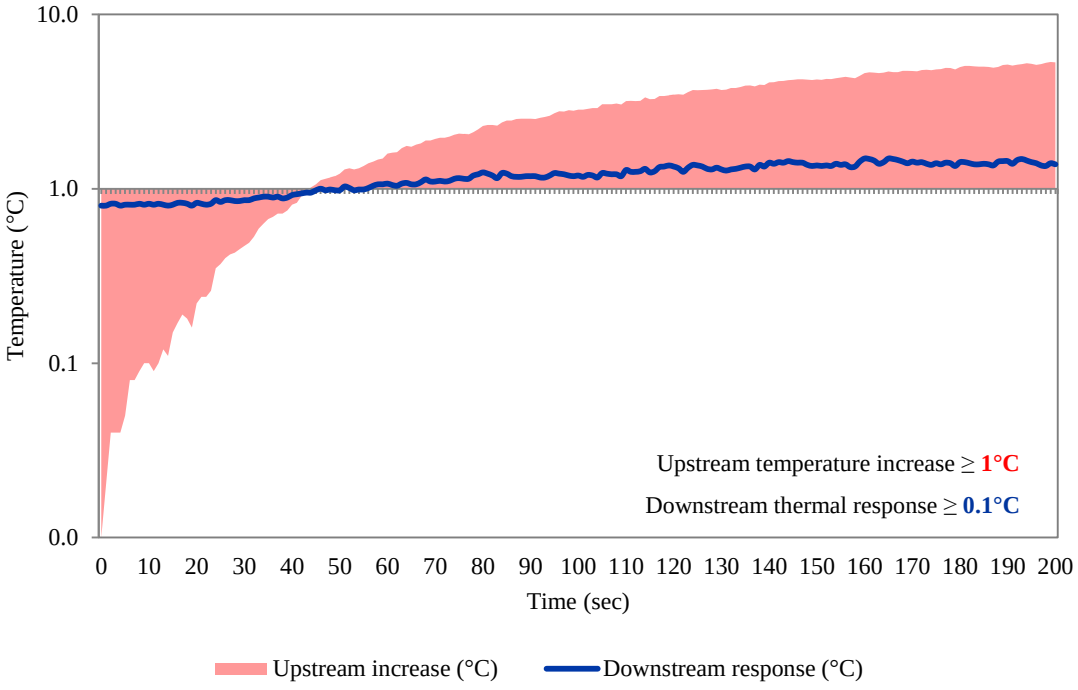

Figure 6.38 Ratio of increasing source temperatures to increasing downstream temperature differentials

The base temperature was set to 30°C and upstream temperatures were increased by 6°C. It was determined that for upstream temperature rise below 1°C, the downstream temperature reduction or thermal response of heat pipes was less than 1°C as well with a minimum temperature drop of 0.8°C. The trend in direct proportionality between the two parameters was noticeable when the upstream temperatures were increased above 1°C from the base temperature. This was because when the temperature rises in a constant pressure process, the amount of molecular activity of air particles increases thereby increasing the internal energy of the system and subsequently enhancing the heat transfer of the system.

The maximum increase in upstream temperature was 6°C, at which the maximum downstream temperature reduction was 1.5°C, indicating a faster thermal response from

heat pipes. Therefore, with every 1°C increase in upstream temperatures, the downstream temperature reduction using heat pipes increased by approximately 0.1°C.

Figure 6.39 displays the relationship between heat pipe temperature differentials in response to decreasing temperature gradient. The base temperature in this case was 44°C and temperatures were decreased by 4°C till reaching 40°C. The maximum temperature differential between upstream and downstream temperatures was 1.9°C at 44°C, which was reduced to 0.7°C at 40°C depicting a slower response from heat pipes. It was revealed that with every 1°C decrease in upstream temperatures, the downstream temperature reduction using heat pipes decreased by approximately 0.3°C.

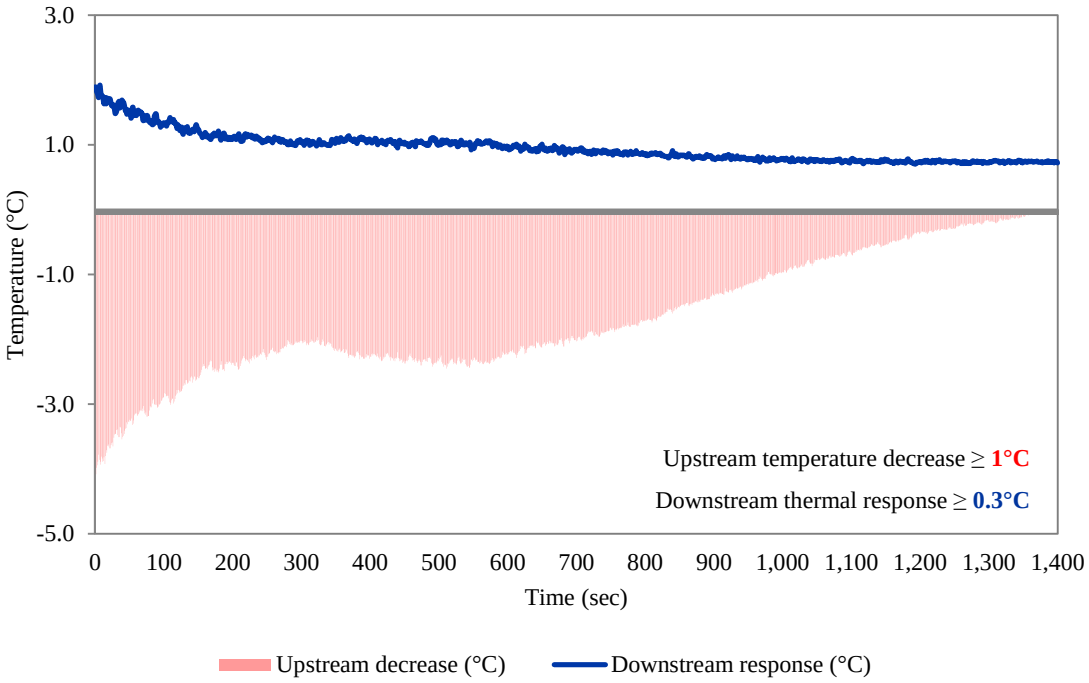

Figure 6.39 Ratio of decreasing source temperatures to decreasing downstream temperature differentials

The proportionality between normalised upstream air temperature and the corresponding downstream response from heat pipes is obtained in Figure 6.40. At upstream temperatures varying less than or equal to 0.1°C, it was recorded that the temperature drop due to heat pipes performed in a similar pattern with a maximum 0.1°C variation. It was concluded that a steady response from heat pipes is observed when the upstream air temperatures are stable.

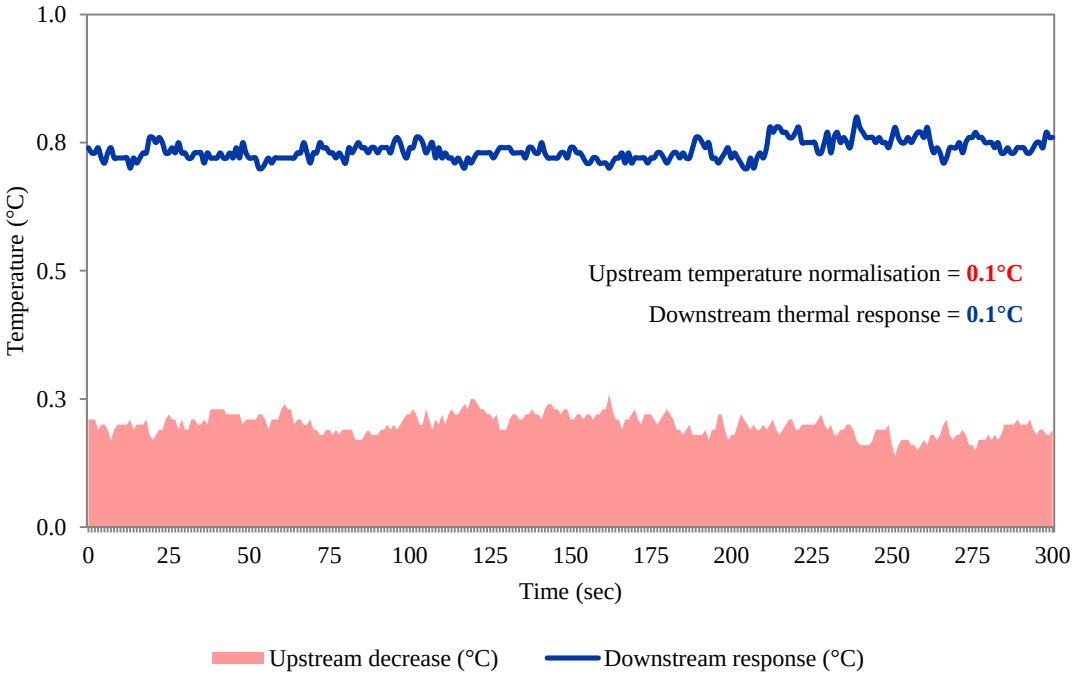

Figure 6.40 Ratio of normalised source temperatures to downstream temperature differentials

The findings from this section of the chapter identified the transient performance of heat pipes during a period of 24 hours at different operating temperatures. At varying upstream temperature gradients, the thermal response of the heat pipes and the corresponding trend in downstream temperatures was determined. The experimental study confirmed that heat pipes behave differently when exposed to fluctuating temperature streams and the thermal response is directly proportional to the upstream temperature gradient.

The maximum, minimum and mean temperature differentials for each hour are tabulated in Table 6.5. The two greatest temperature reductions of 1.79°C and 2.29°C were recorded at 07:00 hour and 13:00 hour. The average downstream temperature drop was 1.28°C between 08:00 hour and 14:00 hour when the upstream or source temperature was above 40°C. This value was however dropped to 0.83°C for the remainder of the day when source temperatures fell below 40°C indicating a superior thermal performance of heat pipes at high temperatures.

Table 6.5 Hourly maximum, minimum and mean air temperature differentials

Time (hour)	Maximum ΔT (°C)	Minimum ΔT (°C)	Mean ΔT (°C)
0:00	1.14	0.72	0.93
1:00	0.97	0.75	0.87
2:00	0.89	0.76	0.82
3:00	0.81	0.68	0.74
4:00	0.74	0.59	0.68
5:00	0.75	0.56	0.61
6:00	0.64	0.55	0.59
7:00	1.79	0.56	0.91
8:00	1.43	0.69	0.87
9:00	0.89	0.60	0.68
10:00	1.08	0.46	0.70
11:00	1.16	0.64	0.79
12:00	0.90	0.61	0.76
13:00	2.29	0.66	0.94
14:00	0.73	0.55	0.65
15:00	0.80	0.61	0.69
16:00	0.92	0.67	0.82
17:00	0.80	0.71	0.77
18:00	0.81	0.68	0.73
19:00	0.79	0.68	0.72
20:00	0.82	0.71	0.76
21:00	0.83	0.72	0.78
22:00	0.80	0.73	0.76
23:00	0.84	0.75	0.78
24:00	0.83	0.74	0.76

6.5 Experimental uncertainties

Additional care was taken in constructing the experimental set-up and in measuring the velocity, pressure and temperatures to minimise inaccuracies. However, individual given parameters were limited to possible inaccuracies in each case. The maximum allowable error of the K-type thermocouples at 0°C was 0.5°C while the maximum error increased to 0.6°C at a temperature of 50°C. The accuracy of the sensor used for velocity measurements was ±0.08m/s for a velocity value of 1m/s and ±0.43m/s for the velocity reading of 8m/s while the measurement uncertainties associated with the pressure measurements were ±1.0% of the reading at 22°C. The summary of the data acquisition devices used along with their measuring parameters and accuracies are tabulated in Table 6.6.

Table 6.6 Summary of the accuracies associated with the data acquisition devices

Illustration	Data acquisition device	Measuring parameter	Accuracy
	PICO K-type exposed wire thermocouples	Air temperature	±0.6°C at 50°C
	TESTO 425 digital hot-wire anemometer	Air velocity	±0.08m/s at 1m/s
	DPM ST650 ellipsoidal pitot tube	Air pressure	±1% of reading at 22°C
	FLUKE Tir1 thermal imager	Infrared images	±2°C from -20°C to 100°C
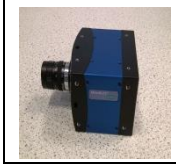	Mikotron MotionBlitz Cube 7	High-speed images	1280 x 1024 pixels at 500fps

Despite great attention being provided in ensuring the laboratory conditions remained stable for the duration of the experimentation, there were steady fluctuations in ambient temperatures. The heating elements were influenced by the room conditions and wind tunnel ambient temperatures at the start of the experiment when normalising to a set-point temperature level. This allowed for the variation of normalisation temperatures from the desired set-point temperatures of 32°C, 35°C and 41°C. The range of normalisation was ±1.5°C with minimum and maximum temperatures ranging between 30°C and 42°C.

6.6 Summary

A detailed description and discussion of experimental results related to the study were presented in this chapter. Full-scale wind tunnel experimentation was carried out using the test section as the evaporator section of the heat pipes. Copper/Water and Copper/R134a heat pipes tested under various spanwise arrangements replicating the CFD models. The experimental findings confirmed that that the St_{50} model

incorporating a span length of 50mm resulted in the highest reduction of air temperatures for both working fluids. At a fixed inlet velocity of 2.3m/s the maximum temperature drop was recorded at 1.60K using water as heat pipe working fluid which was 0.45K or 28% higher than R134a working fluid.

In addition, a transient test was carried out over a period of 24 hours in order to determine the response characteristics of heat pipes to varying temperature gradients. A direct proportionality was obtained between the heat pipe thermal response and the upstream temperature gradient. It was concluded that the reduction in air temperatures increased by 0.1°C or 0.1K for every 1.0K increase in upstream temperature from its base value. Consequently, the findings determined that decreasing the upstream temperature gradient has an inverse effect on the working of heat pipes and the temperature reduction decreased by 0.3°C or 0.3K for every 1.0K decrease in upstream temperatures from the peak value. The chapter concluded by quantifying the uncertainties associated with the experimental set-up and operation.

Chapter 7
Comparison between CFD and Experimentation

7.1 Introduction

This chapter details the evaluation of the CFD findings of this study by using quantitative methods. A comparison between the CFD results and the experimental wind tunnel testing results was carried out to determine the error between the two techniques. Velocity, pressure and temperatures were used as the flow characterisation parameters and the profiles were analysed using three different heat pipe spanwise arrangements (St_{48}, St_{50} and St_{52} models) and two different working fluids (water and R134a). The purpose of conducting the comparative study for different heat pipe configurations was to analyse the error patterns associated with each parameter and whether it was independent from the type of fluid and geometry.

In addition, this chapter displays the temperature trends obtained downstream of the heat pipes in order to determine the consistency of error variations at different source conditions. Source temperatures of 32°C, 35°C and 41°C were used for both water and R134a as the working fluids to investigate the comparative trends. Following the analyses of steady-state models, the results achieved using the transient 24-hour experimental test was compared with the CFD findings. The analysis yielded the accuracy of the CFD model in predicting the downstream temperatures in response to varying upstream temperatures. The chapter concludes by evaluating the error range obtained from the current study and validates them against common errors and uncertainties associated with CFD modelling reported in literature.

7.2 Geometrical variation using water as the working fluid

This section illustrates the CFD and experimental results using water as the working fluid. The findings are analysed based on a quantitative evaluation of the flow characteristics including velocity, pressure and temperature at the designated measurement locations.

7.2.1 Velocity profile

The comparison of velocity profiles was carried out for the three spanwise configurations using an inlet velocity if 2.3m/s. The analysis determined the accuracy of the CFD model in relation to the experimental testing. Measurement points at the inlet (I_1 and I_2) and outlet (O_1 – O_5) locations (detailed in Chapter 3, Section 3.6.4 and Chapter 4, Section 4.8.3) were used for the results. Figure 7.1 displays the bar-chart representation between CFD and experimental air velocity results for the St_{48} model. It was observed that the inlet velocity using the wind tunnel at points I_1 and I_2 was lower than its CFD equivalent. The mean inlet velocity using CFD was 2.18m/s which was 0.32m/s higher than the mean value obtained using experimentation. The velocity profiles obtained downstream of the heat pipes were found to be in good correlation to each other with a mean error of 11.2%.

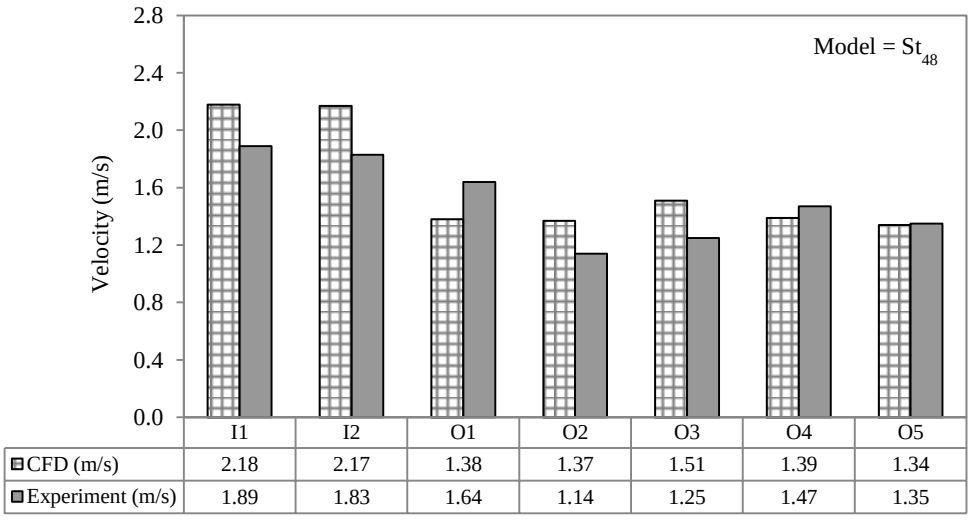

	I1	I2	O1	O2	O3	O4	O5
CFD (m/s)	2.18	2.17	1.38	1.37	1.51	1.39	1.34
Experiment (m/s)	1.89	1.83	1.64	1.14	1.25	1.47	1.35

Figure 7.1 Comparison of CFD and experimental results of air velocity for the St_{48} model using water

Figure 7.2 illustrates the results drawn for the St_{50} model. A similar trend was observed to the St_{48} model with the CFD values of air velocity and pressure overestimating the experimental results at the upstream locations. The lowest downstream velocity using CFD was 1.44m/s while the lowest downstream velocity using experimentation was 1.25m/s with the lowest values of velocity obtained at the point O_2 for both methodologies. The mean error was calculated at 8.7% for all measurement locations.

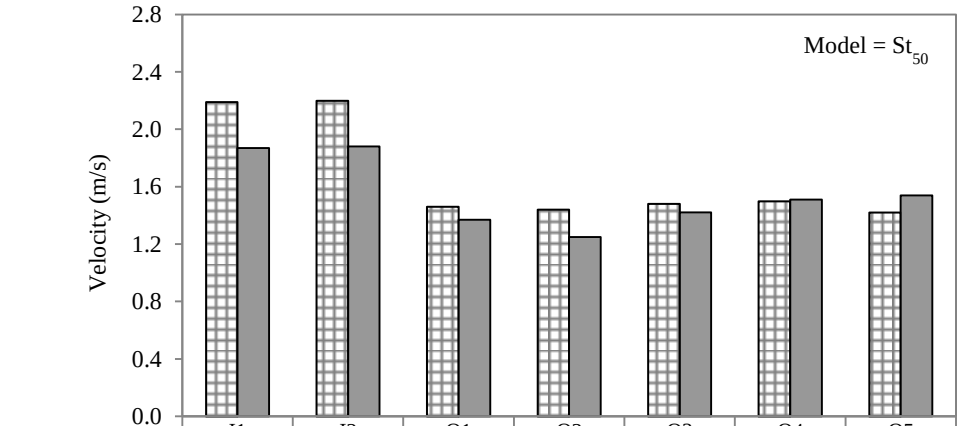

	I1	I2	O1	O2	O3	O4	O5
CFD (m/s)	2.19	2.20	1.46	1.44	1.48	1.50	1.42
Experiment (m/s)	1.87	1.88	1.37	1.25	1.42	1.51	1.54

Figure 7.2 Comparison of CFD and experimental results of air velocity for the St_{50} model using water

Figure 7.3 displays the velocity distribution for the St_{52} model at the measurement locations. The mean inlet air velocity using CFD was 2.21m/s while the mean inlet air velocity using the wind tunnel was 1.90m/s indicating a difference of 0.31m/s and an error of 14%. A more consistent result was achieved at the downstream locations with a mean differential of 0.02m/s between the two parameters. The maximum error percentage was recorded for point O_4 at 10.2% with the velocity difference of 0.16m/s.

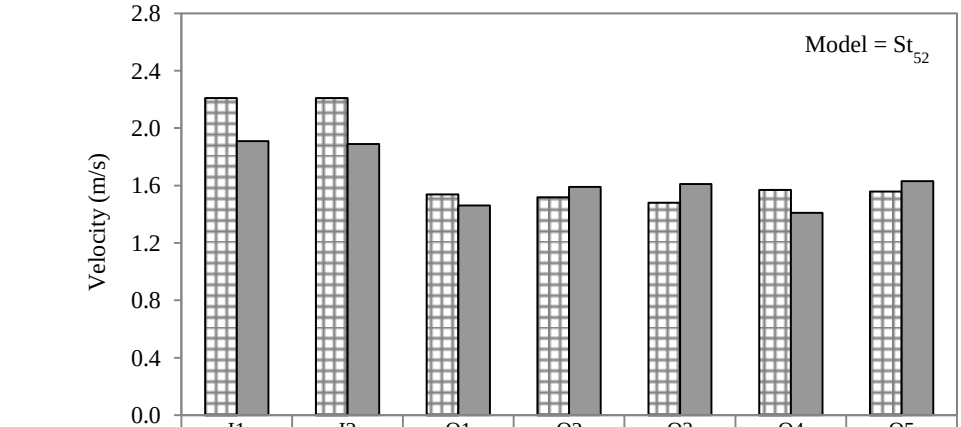

	I1	I2	O1	O2	O3	O4	O5
CFD (m/s)	2.21	2.21	1.54	1.52	1.48	1.57	1.56
Experiment (m/s)	1.91	1.89	1.46	1.59	1.61	1.41	1.63

Figure 7.3 Comparison of CFD and experimental results of air velocity for the St_{52} model using water

7.2.2 Pressure profile

Following the evaluation of air velocity, this section of the chapter highlights the variation in air pressures. Using the St_{48} model, the trend in pressure obtained from Figure 7.4 indicated that the CFD values over-estimated the experimental values by 0.52Pa. Good agreement was observed at the downstream locations with both methodologies indicating a difference of only 0.04Pa between the maximum values. The maximum CFD obtained downstream pressure was 1.44Pa while the experimentally obtained pressure was 1.40Pa with an error of 1.4%.

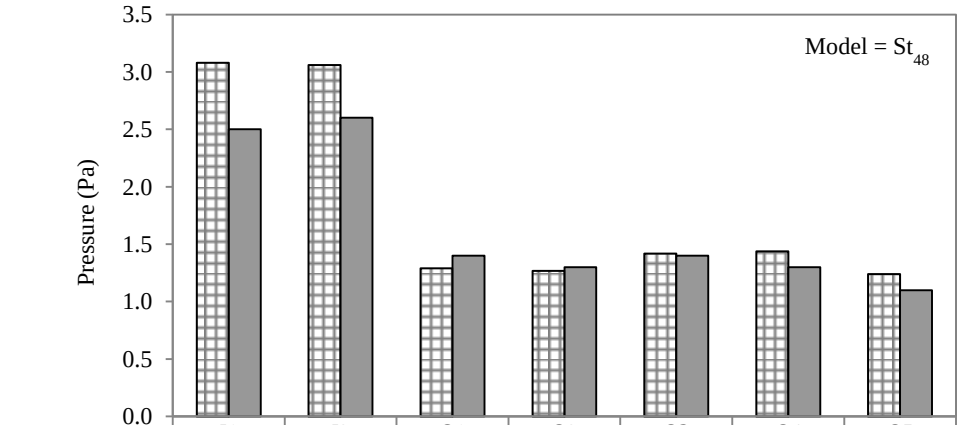

	I1	I2	O1	O2	O3	O4	O5
CFD (Pa)	3.08	3.06	1.29	1.27	1.42	1.44	1.24
Experiment (Pa)	2.50	2.60	1.40	1.30	1.40	1.30	1.10

Figure 7.4 Comparison of CFD and experimental results of air pressure for the St_{48} model using water

The St_{50} model showed the largest downstream value at point O_3 with the experimental result of 1.60Pa overestimating the CFD by 0.1Pa (Figure 7.5). The inlet points (I_1 and I_2) displayed the highest difference between the two methodologies with an error of 14.5%. It was observed that the CFD overestimated the pressures at the upstream locations of the heat pipes. A mean error percentage of 7.9% was estimated across all measurement locations.

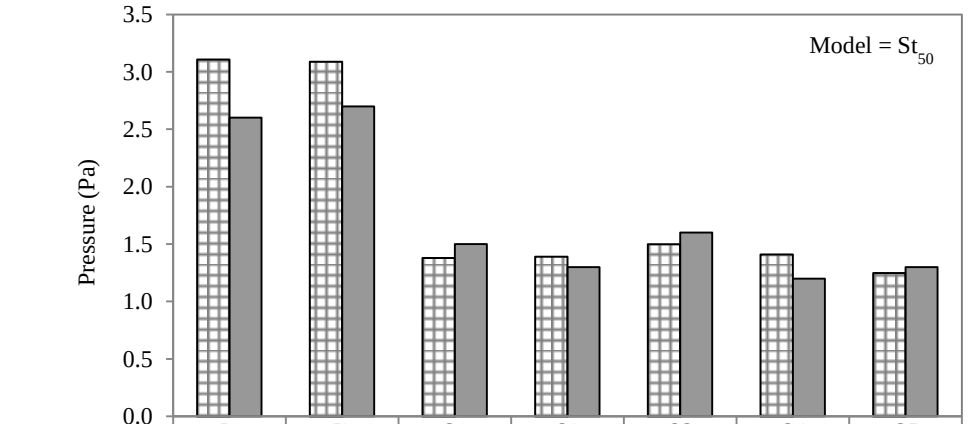

	I1	I2	O1	O2	O3	O4	O5
CFD (Pa)	3.11	3.09	1.38	1.39	1.50	1.41	1.25
Experiment (Pa)	2.60	2.70	1.50	1.30	1.60	1.20	1.30

Figure 7.5 Comparison of CFD and experimental results of air pressure for the St_{50} model using water

Figure 7.6 illustrates the air pressure profile for a span length of 52mm. It was observed that the air pressure reduced by approximately half upstream and downstream of the heat pipes and this trend was represented using both CFD and experimental techniques. The lowest pressure using CFD was 1.44Pa while the lowest experimental pressure was found to be 1.30Pa. A mean error of 12.2% was recorded at the upstream locations (points I_1 and I_2) while it was observed that the error dropped to 10.3% for the downstream locations (points $O_1 – O_5$).

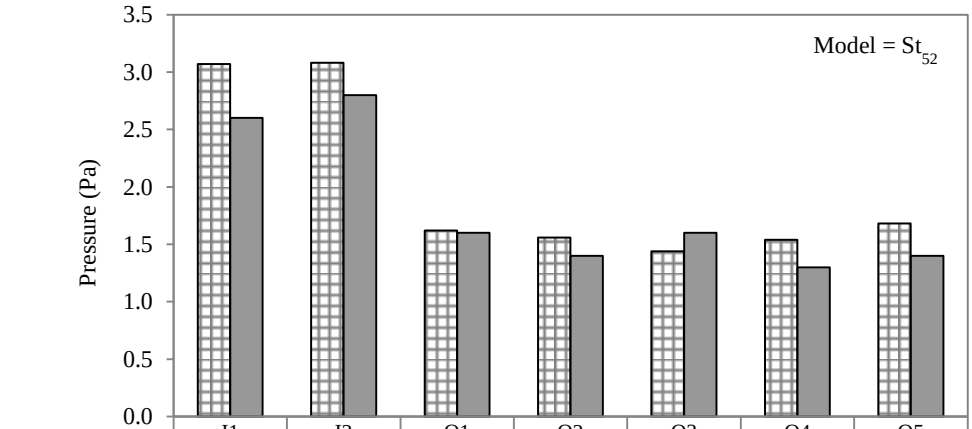

	I1	I2	O1	O2	O3	O4	O5
CFD (Pa)	3.07	3.08	1.62	1.56	1.44	1.54	1.68
Experiment (Pa)	2.60	2.80	1.60	1.40	1.60	1.30	1.40

Figure 7.6 Comparison of CFD and experimental results of air pressure for the St_{52} model using water

7.2.3 Temperature profile

Using water as the heat pipe working fluid, the evaluation of air temperature profiles for the three spanwise configurations are displayed in Figure 7.7, Figure 7.8 and Figure 7.9. Overall, the temperature parameter indicated the most consistent results at both upstream and downstream measurement locations. Figure 7.7 shows the results for the St_{48} model. The maximum difference between the two parameters was 1.01°C at measurement point O_4 with an error of 2.5%. The highest reduction in temperature using CFD was 1.82°C, which was 0.99°C greater than the highest reduction obtained using the experimental investigation.

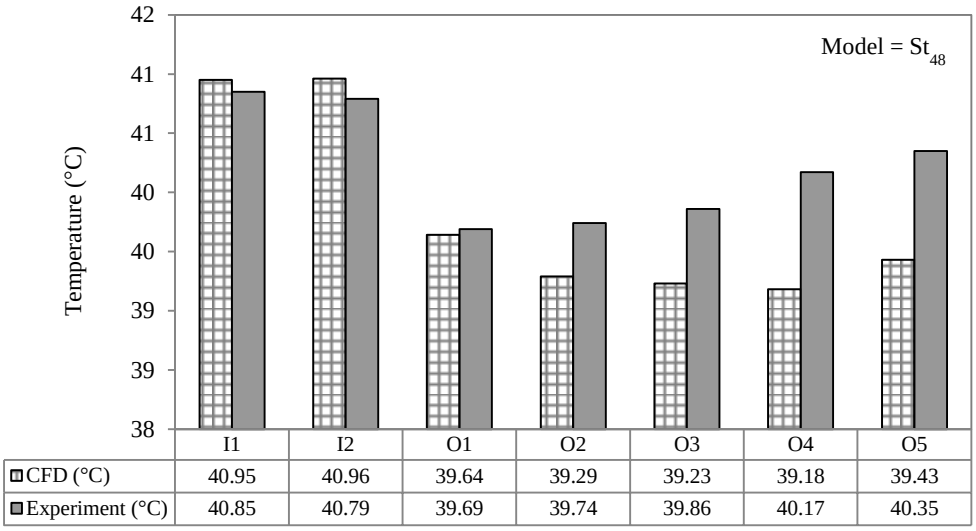

	I1	I2	O1	O2	O3	O4	O5
CFD (°C)	40.95	40.96	39.64	39.29	39.23	39.18	39.43
Experiment (°C)	40.85	40.79	39.69	39.74	39.86	40.17	40.35

Figure 7.7 Comparison of CFD and experimental results of air temperature for the St_{48} model using water

Figure 7.8 displays the temperature distribution for the St_{50} model. The highest consistency in the findings was achieved for air temperatures as both models correlated well with each other. Point O_2 displayed the largest reduction in air temperature with the CFD value overestimating the experimental findings by 0.38°C. In general, the CFD under-predicted the temperature values with the highest error percentage of 1.6% recorded for points O_4 and O_5.

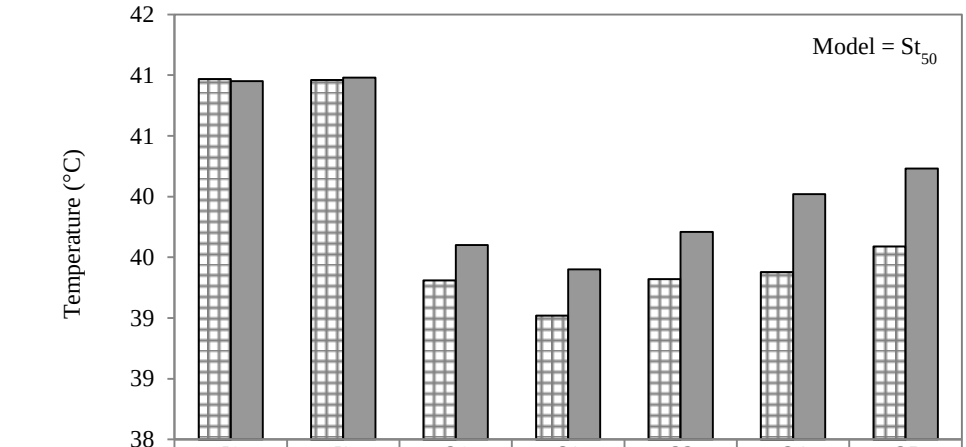

	I1	I2	O1	O2	O3	O4	O5
CFD (°C)	40.97	40.96	39.31	39.02	39.32	39.38	39.59
Experiment (°C)	40.95	40.98	39.60	39.40	39.71	40.02	40.23

Figure 7.8 Comparison of CFD and experimental results of air temperature for the St_{50} model using water

Figure 7.9 illustrates the graphical representation of the air temperature profiles and the St_{52} model displayed the lowest consistency of results in relation to other models. The error range was found to be independent of the other two analysed configurations (St_{48} and St_{50} model). A maximum error of 2.77% was recorded at point O_4 with the CFD under-predicting the air temperature value by 1.12°C in relation to the experimentally recorded temperature finding.

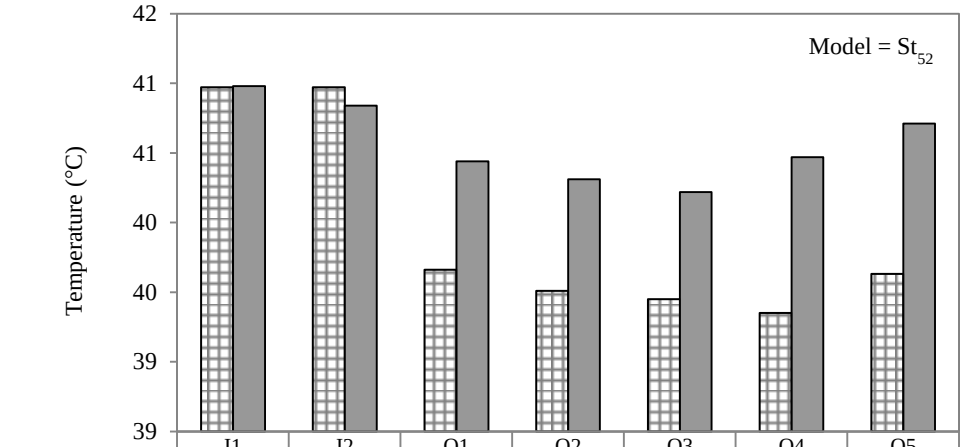

	I1	I2	O1	O2	O3	O4	O5
CFD (°C)	40.97	40.97	39.66	39.51	39.45	39.35	39.63
Experiment (°C)	40.98	40.84	40.44	40.31	40.22	40.47	40.71

Figure 7.9 Comparison of CFD and experimental results of air temperature for the St_{52} model using water

Table 7.1 displays the summarised results for the air velocity, pressure and temperatures for the St_{48} model.

Table 7.1 Error percentage between CFD and experimental results for St_{48} model using water as the working fluid

Point	CFD (°C)	Exp. (°C)	Error	CFD (m/s)	Exp. (m/s)	Error	CFD (Pa)	Exp. (Pa)	Error
I_1	40.95	40.85	0.24%	2.18	1.89	13.3%	3.08	2.50	18.8%
I_2	40.96	40.79	0.42%	2.17	1.83	15.7%	3.06	2.60	15.0%
O_1	39.64	39.69	0.13%	1.38	1.64	15.9%	1.29	1.40	7.9%
O_2	39.29	39.74	1.13%	1.37	1.14	16.8%	1.27	1.30	2.3%
O_3	39.23	39.86	1.58%	1.51	1.25	17.2%	1.42	1.40	1.4%
O_4	39.18	40.17	2.46%	1.39	1.47	5.4%	1.44	1.30	10.8%
O_5	39.43	40.35	2.28%	1.34	1.35	0.7%	1.24	1.10	12.7%

The maximum error for the temperature was 2.46% at point O_4 while the highest error for the velocity was obtained at 16.8% at point O_2. Measurement location I_1 indicated the highest difference in terms of pressure with an error percentage of 18.8%. The total error range for velocity was between 0.7% and 16.8% while the error range recorded for pressure was found to lie between 1.4% and 18.8%.

The error percentage at each measuring location for the St_{50} model is tabulated in Table 7.2. The most consistent temperature results were obtained for this model with a maximum differential of only 1.63%. Measurement location I_1 indicated the highest variation in air velocity and pressure readings with the CFD values overestimating the experimental results by 14.6% and 16.4%. Good correlation was obtained for air velocity between the two methodologies at the downstream locations with a mean error percentage of 6.4%.

Table 7.2 Error percentage between CFD and experimental results for St_{50} model using water as the working fluid

Point	CFD (°C)	Exp. (°C)	Error	CFD (m/s)	Exp. (m/s)	Error	CFD (Pa)	Exp. (Pa)	Error
I_1	40.97	40.95	0.05%	2.19	1.87	14.6%	3.11	2.60	16.4%
I_2	40.96	40.98	0.05%	2.20	1.88	14.5%	3.09	2.70	12.6%
O_1	39.31	39.60	0.74%	1.46	1.37	6.2%	1.38	1.50	8.0%
O_2	39.02	39.40	0.97%	1.44	1.25	13.2%	1.39	1.30	6.9%
O_3	39.32	39.71	0.99%	1.48	1.42	4.1%	1.50	1.60	6.3%
O_4	39.38	40.02	1.63%	1.50	1.51	0.7%	1.41	1.20	14.9%
O_5	39.59	40.23	1.62%	1.42	1.54	7.8%	1.25	1.30	3.8%

Table 7.3 highlights the error distribution for the St_{52} model. A mean error of 14.0% and 12.2% was obtained for air velocity and pressure at the upstream locations. However, this variation was reduced to 6.4% and 10.3% at the downstream locations after the heat pipes. With respect to air temperature, the largest error in the findings was noted for point O_4 at 2.77%. It was observed that the error patterns for all parameters remained independent when analysing different spanwise configurations.

Table 7.3 Error percentage between CFD and experimental results for St_{52} model using water as the working fluid

Point	CFD (°C)	Exp. (°C)	Error	CFD (m/s)	Exp. (m/s)	Error	CFD (Pa)	Exp. (Pa)	Error
I_1	40.97	40.98	0.02%	2.21	1.91	13.6%	3.07	2.60	15.3%
I_2	40.97	40.84	0.32%	2.21	1.89	14.5%	3.08	2.80	9.1%
O_1	39.66	40.44	1.93%	1.54	1.46	5.2%	1.62	1.60	1.3%
O_2	39.51	40.31	1.98%	1.52	1.59	4.4%	1.56	1.40	10.3%
O_3	39.45	40.22	1.91%	1.48	1.61	8.1%	1.44	1.60	10.0%
O_4	39.35	40.47	2.77%	1.57	1.41	10.2%	1.54	1.30	15.6%
O_5	39.63	40.71	2.65%	1.56	1.63	4.3%	1.68	1.40	16.7%

7.3 Geometrical variation using R134a as the working fluid

The study was repeated using R134a as the working fluid to show that the results were independent of the fluid properties. This section of the chapter illustrates the quantitatively compared results of air velocity, pressure and temperatures parameters at the specified inlet and outlet measurement locations.

7.3.1 Velocity profile

Repeating the same process as the water working fluid, this section displays the variation in velocity profiles for the three analysed spanwise models. The recorded air velocities for the St_{48} model at the measurement points is illustrated in Figure 7.10. It was observed that the CFD over-estimated the velocities at both inlet and outlet locations. The mean upstream error (points I_1 and I_2) was calculated at 14.7% while the mean downstream error (points O_1 – O_5) was recorded as 10.4%. On average, the experimentally air velocities were 0.11m/s lower than the CFD values.

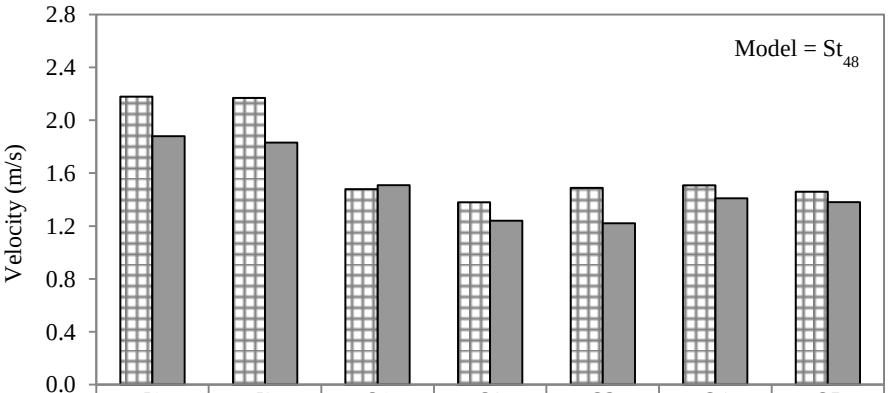

	I1	I2	O1	O2	O3	O4	O5
CFD (m/s)	2.18	2.17	1.48	1.38	1.49	1.51	1.46
Experiment (m/s)	1.88	1.83	1.51	1.24	1.22	1.41	1.38

Figure 7.10 Comparison of CFD and experimental results of air velocity for the St_{48} model using R134a

Figure 7.11 shows the graphical representation of the velocity profiles for the St_{50} model. The air velocities were found to be lower than the ones obtained using water. The maximum error was noted upstream for the point I_2 with 13.7% while the minimum error percentage was recorded for the point O_1 with 2.2%. The mean difference in velocity and error across all measurement points was calculated at 0.1m/s and 5.8%.

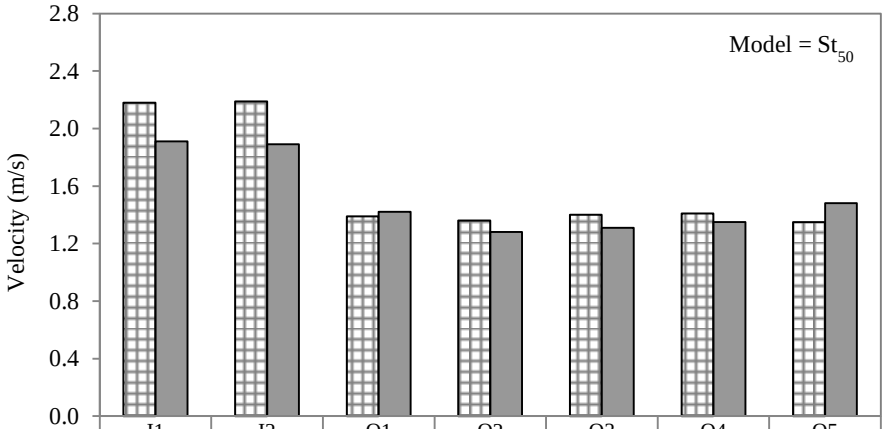

	I1	I2	O1	O2	O3	O4	O5
CFD (m/s)	2.18	2.19	1.39	1.36	1.40	1.41	1.35
Experiment (m/s)	1.91	1.89	1.42	1.28	1.31	1.35	1.48

Figure 7.11 Comparison of CFD and experimental results of air velocity for the St_{50} model using R134a

Figure 7.12 displays the velocity distribution for the St_{52} model. The maximum recorded CFD velocity was 2.24m/s while the maximum recorded experimental velocity was 1.98m/s indicating an error of 11.6%. The difference in downstream velocities between the two methodologies was 0.12m/s with the experimental findings under-

predicting the values. Good correlation was observed at point O_3 with an error of 0.6%. The mean error across the measurement points was calculated at 9.4%.

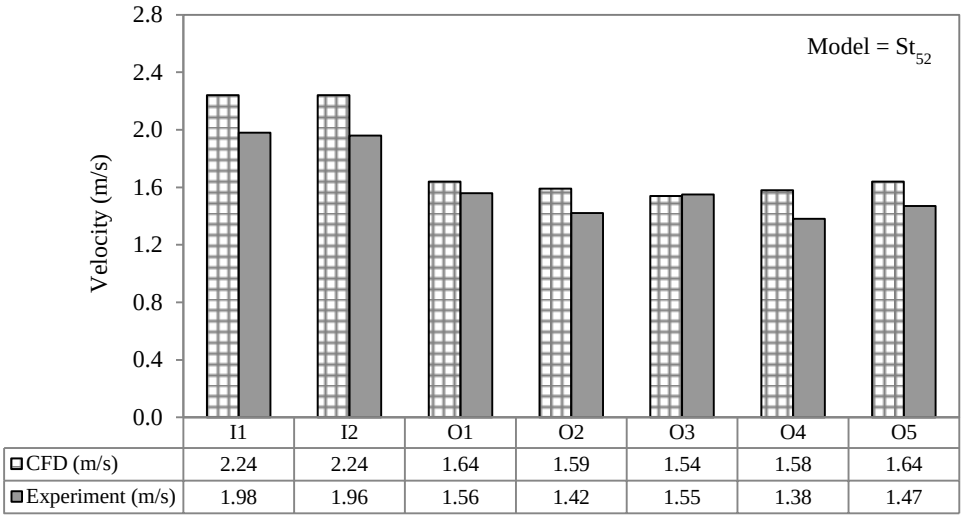

	I1	I2	O1	O2	O3	O4	O5
CFD (m/s)	2.24	2.24	1.64	1.59	1.54	1.58	1.64
Experiment (m/s)	1.98	1.96	1.56	1.42	1.55	1.38	1.47

Figure 7.12 Comparison of CFD and experimental results of air velocity for the St_{52} model using R134a

7.3.2 Pressure profile

Subsequent to the velocity profiles, the pressure distribution was evaluated at the measurement locations. With respect to Figure 7.13, the comparison of results between the two methodologies is illustrated for the St_{48} model.

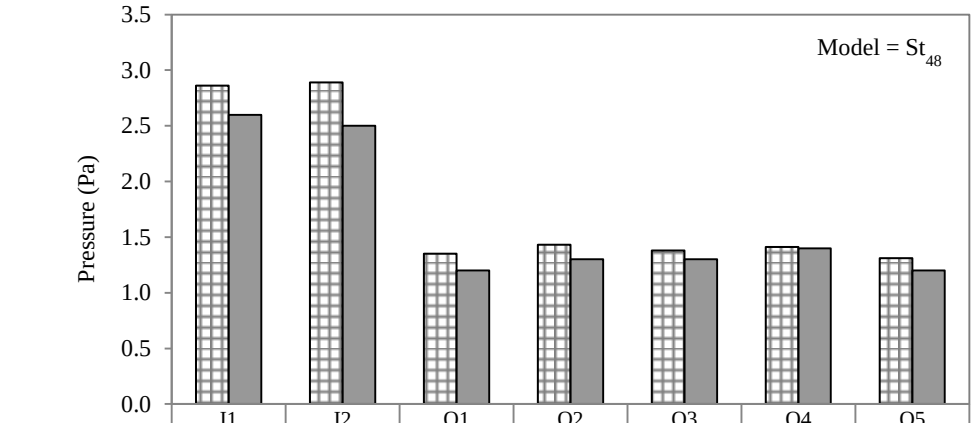

	I1	I2	O1	O2	O3	O4	O5
CFD (Pa)	2.86	2.89	1.35	1.43	1.38	1.41	1.31
Experiment (Pa)	2.60	2.50	1.20	1.30	1.30	1.40	1.20

Figure 7.13 Comparison of CFD and experimental results of air pressure for the St_{48} model using R134a

The maximum error of 13.5% was recorded for the point I_2 at which the CFD predicted pressure result was 0.39Pa higher than the experimentally measured value. However, a good agreement was obtained between the two parameters at the downstream locations with the mean error percentage dropping down to 7.7%.

Figure 7.14 highlights the pressure profiles for the St_{50} model. A good agreement was obtained between the upstream values with a mean error of 6.5% and a variation of 0.19Pa. The maximum error percentage was recorded for point O_4 at 14.8% with the CFD under-predicting the value by 0.18Pa. In general, the CFD under-predicted the pressure values by 0.08Pa across all downstream measurement locations highlighting a mean error of 7.3%.

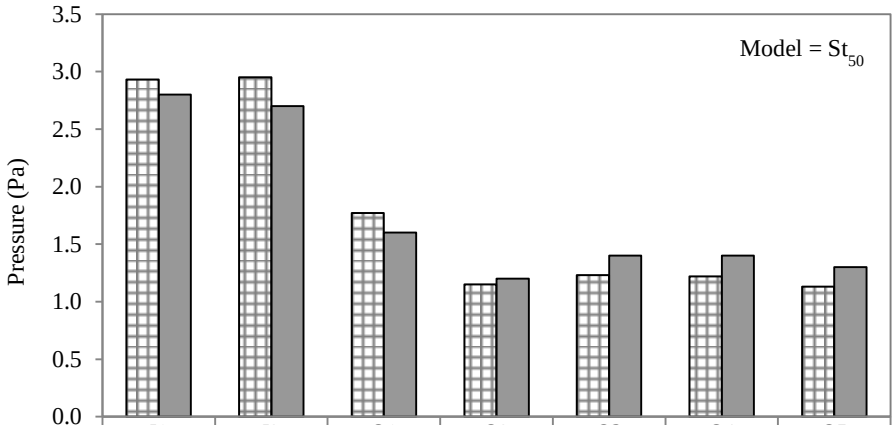

	I1	I2	O1	O2	O3	O4	O5
CFD (Pa)	2.93	2.95	1.77	1.15	1.23	1.22	1.13
Experiment (Pa)	2.80	2.70	1.60	1.20	1.40	1.40	1.30

Figure 7.14 Comparison of CFD and experimental results of air pressure for the St_{50} model using R134a

The final analysed model in terms of pressure values was the St_{52} model indicating a span length of 52mm (Figure 7.15). The mean pressure predicted by the CFD upstream of the heat pipes was 2.99Pa, which was greater than the experimentally recorded value of 2.65Pa. In addition, the CFD code over-estimated the pressure values across the downstream locations as well displaying a mean value of 1.58Pa which was 0.12Pa higher than the experimentally obtained mean recording of 1.46Pa. The mean error percentage between the two methodologies was thus determined at 9.1%.

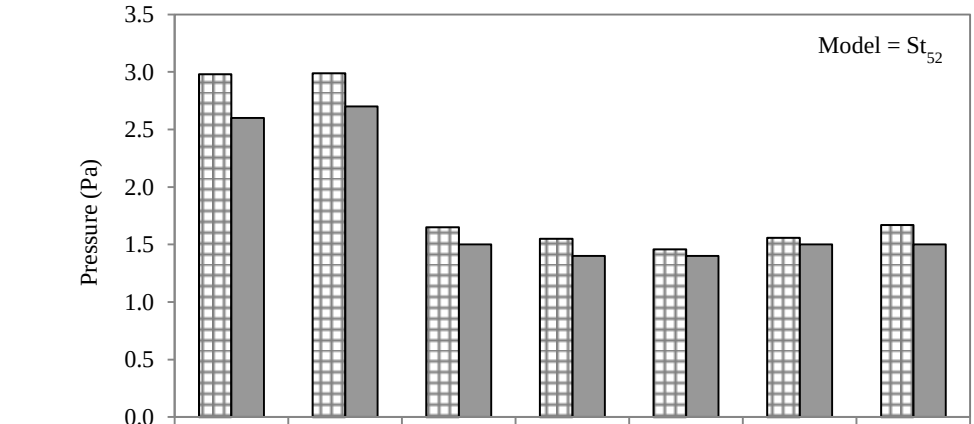

	I1	I2	O1	O2	O3	O4	O5
CFD (Pa)	2.98	2.99	1.65	1.55	1.46	1.56	1.67
Experiment (Pa)	2.60	2.70	1.50	1.40	1.40	1.50	1.50

Figure 7.15 Comparison of CFD and experimental results of air pressure for the St_{52} model using R134a

7.3.3 Temperature profile

Temperature values at the measurement locations were the final assessed parameter in terms of their distribution at the measurement points. Figure 7.16 displays the graphical representation of the temperature values obtained from the St_{48} model.

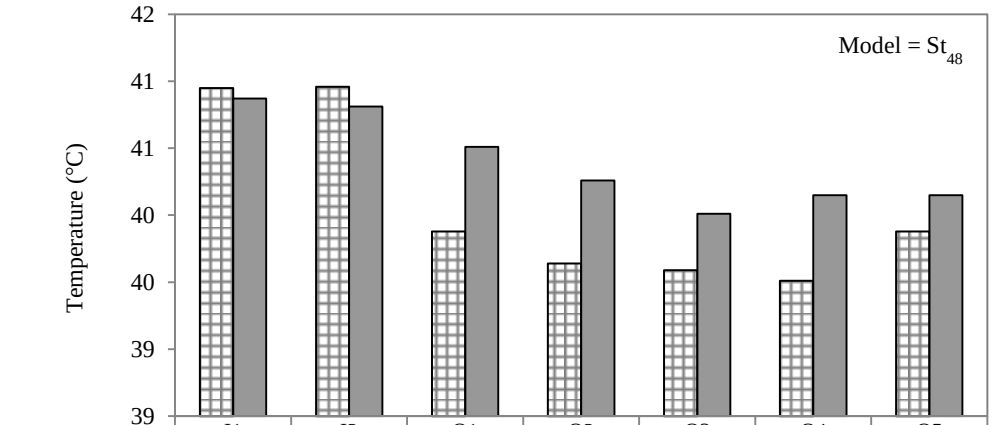

	I1	I2	O1	O2	O3	O4	O5
CFD (°C)	40.95	40.96	39.88	39.64	39.59	39.51	39.88
Experiment (°C)	40.87	40.81	40.51	40.26	40.01	40.15	40.15

Figure 7.16 Comparison of CFD and experimental results of air temperature for the St_{48} model using R134a

A good agreement was observed between the temperature readings both upstream and downstream of the heat pipes with a maximum error of 1.62%. However, the CFD code was found to consistently under-predict the temperature by 0.53°C across all

measurement locations. Point O_5 displayed the most accurate reading of the downstream temperatures with an error percentage of 1.06%.

Figure 7.17 shows the temperature profiles for the St_{50} model. As observed, the CFD code under-predicted the values once again and a maximum error of 2.5% was recorded at the measurement location O_2. The minimum predicted temperature value using CFD was 39.13°C which was approximately 1°C lower than the experimentally obtained value of 40.11°C.

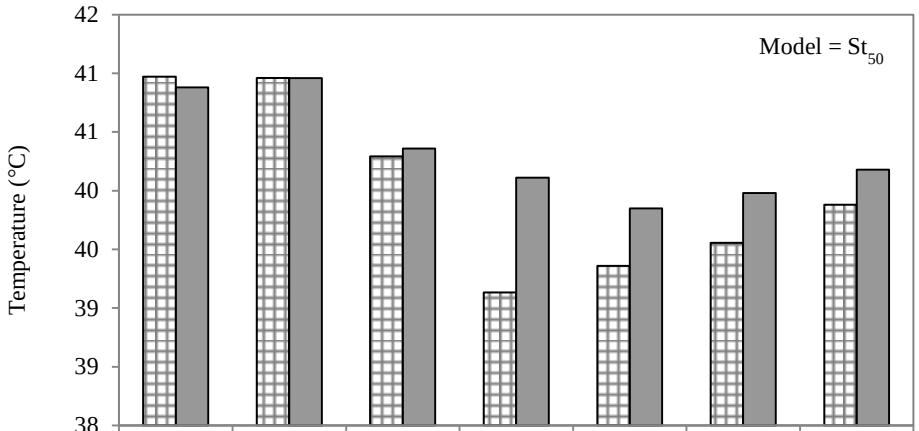

	I1	I2	O1	O2	O3	O4	O5
CFD (°C)	40.97	40.96	40.29	39.13	39.36	39.55	39.88
Experiment (°C)	40.88	40.96	40.36	40.11	39.85	39.98	40.18

Figure 7.17 Comparison of CFD and experimental results of air temperature for the St_{50} model using R134a

The St_{52} model was the final model analysed in terms of air temperatures and the bar-chart representation is displayed in Figure 7.18. The maximum error percentage was recorded at 1.7% for point O_1. On average, the CFD generated values were 0.53°C lower than the experimental values across all downstream measurement points.

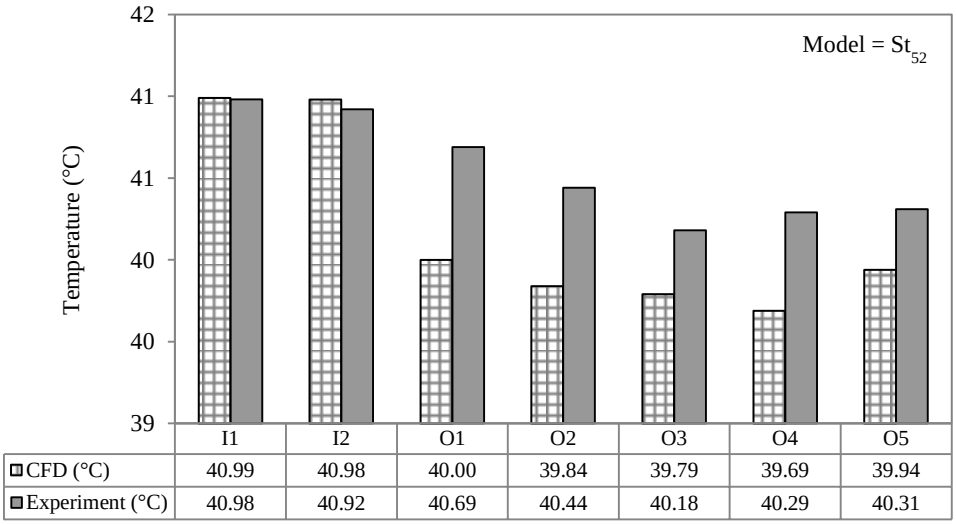

Figure 7.18 Comparison of CFD and experimental results of air temperature for the St_{52} model using R134a

The summarised results for the three spanwise configurations using R134a as the working fluid are tabulated in Table 7.4, Table 7.5 and Table 7.6. With respect to Table 7.4, the errors for air velocity, pressure and temperature are displayed for the St_{48} model. The maximum error for air velocity was obtained for point O_3 at 18.1% while the minimum error was obtained for point O_1 at 2.0%. With regards to air pressure values, the mean error across all measurement locations was 8.7% with point O_4 highlighting the minimum difference of 0.7%. As observed for water, temperature variations for R134a were also found to be consistent at all points depicting a maximum error of 1.62%.

Table 7.4 Error percentage between CFD and experimental results for St_{48} model using R134a as the working fluid

Point	CFD (°C)	Exp. (°C)	Error	CFD (m/s)	Exp. (m/s)	Error	CFD (Pa)	Exp. (Pa)	Error
I_1	40.95	40.87	0.20%	2.18	1.88	13.8%	2.86	2.60	9.1%
I_2	40.96	40.81	0.37%	2.17	1.83	15.7%	2.89	2.50	13.5%
O_1	39.88	40.51	1.58%	1.48	1.51	2.0%	1.35	1.20	12.5%
O_2	39.64	40.26	1.56%	1.38	1.24	10.1%	1.43	1.30	10.0%
O_3	39.59	40.01	1.06%	1.49	1.22	18.1%	1.38	1.30	6.2%
O_4	39.51	40.15	1.62%	1.51	1.41	7.1%	1.41	1.40	0.7%
O_5	39.88	40.15	0.68%	1.46	1.38	5.8%	1.31	1.20	9.2%

The summary of the error measurements for the St_{50} model is tabulated in Table 7.5. The temperature results were found to be consistent with a maximum error of 2.5%.

Measurement location I_2 indicated the highest variation in air velocity with an error of 13.7% while the maximum error for pressure was recorded at the measurement location O_4 at 14.8%. A good agreement was observed for air velocity between the two methodologies at the downstream locations with a mean and maximum error percentage of 5.5% and 8.8%.

Table 7.5 Error percentage between CFD and experimental results for St_{50} model using R134a as the working fluid

Point	CFD (°C)	Exp. (°C)	Error	CFD (m/s)	Exp. (m/s)	Error	CFD (Pa)	Exp. (Pa)	Error
I_1	40.97	40.88	0.22%	2.18	1.91	12.4%	2.93	2.80	4.4%
I_2	40.96	40.96	0.00%	2.19	1.89	13.7%	2.95	2.70	8.5%
O_1	40.29	40.36	0.17%	1.39	1.42	2.2%	1.77	1.60	10.6%
O_2	39.13	40.11	2.50%	1.36	1.28	5.9%	1.15	1.20	4.2%
O_3	39.36	39.85	1.25%	1.40	1.31	6.4%	1.23	1.40	12.1%
O_4	39.55	39.98	1.08%	1.41	1.35	4.4%	1.22	1.40	14.8%
O_5	39.88	40.18	0.75%	1.35	1.48	8.8%	1.13	1.30	13.1%

Table 7.6 illustrates the error distribution for the St_{52} model. Mean error percentages of 12.1% and 11.2% were obtained for air velocity and pressure at the upstream measurement locations. However, this was reduced to 8.4% and 7.6% at the downstream locations after the heat pipes. The temperature validation error remained consistent with a maximum error of 1.7% recorded for measurement points O_1. The error ranges were found to be independent of the working fluid with the CFD code under-predicting the air temperatures by 0.53°C across all measurement locations.

Table 7.6 Error percentage between CFD and experimental results for St_{52} model using R134a as the working fluid

Point	CFD (°C)	Exp. (°C)	Error	CFD (m/s)	Exp. (m/s)	Error	CFD (Pa)	Exp. (Pa)	Error
I_1	40.99	40.98	0.02%	2.24	1.98	11.6%	2.98	2.60	12.8%
I_2	40.98	40.92	0.15%	2.24	1.96	12.5%	2.99	2.70	9.7%
O_1	40.00	40.69	1.70%	1.64	1.56	4.9%	1.65	1.50	10.0%
O_2	39.84	40.44	1.61%	1.59	1.42	12.0%	1.55	1.40	9.7%
O_3	39.79	40.18	1.22%	1.54	1.55	0.6%	1.46	1.40	4.3%
O_4	39.69	40.29	0.87%	1.58	1.38	12.7%	1.56	1.50	3.8%
O_5	39.94	40.31	0.93%	1.64	1.47	11.6%	1.67	1.50	10.2%

A good correlation was observed between the CFD and experimental results for all analysed cases involving water and R134a as working fluids, therefore the comparison outcome was deemed independent of the type of heat pipe fluid.

7.4 Temperature trends using water and R134a

Subsequent to the point measurements of the air velocity, pressure and temperature parameters at specific measurement points, this section of the chapter displays the trend of the CFD and experimentally obtained temperatures measured downstream of the heat pipes. The profiles of both water and R134a as heat pipe internal fluids along the radial length of the test section were compared. The analysis was conducted in order to determine the consistency associated with the error trends in relation to varying inlet temperature boundary conditions.

The analysis was carried out at inlet temperatures of 32°C, 35°C and 41°C in order to establish the independence of the CFD model for a range of temperatures. Figure 7.19 displays the thermal profile of air using water and R134a as heat pipe working fluids at an inlet temperature of 32°C. It was observed that while the CFD predicted a temperature drop of approximately 1.5°C for water and 1.0°C for R134a, the experimental values for both water and R134a were very similar to each other at approximately 1.0°C. The highest experimental air temperature reduction using water was 0.93°C while the largest temperature reduction using R134a was 0.84°C.

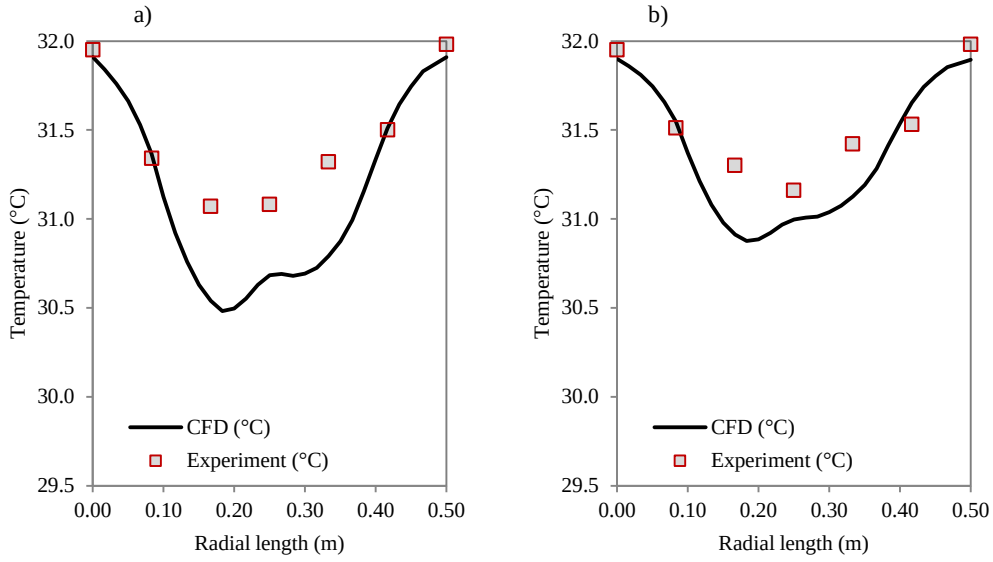

Figure 7.19 Thermal profile of air using: a) water b) R134a as heat pipe internal fluid at an inlet temperature of 32°C

Downstream air temperature profiles at the source temperature of 35°C are displayed in Figure 7.20. Water displayed a higher reduction in air temperatures using CFD with a reduction of approximately 1.7°C. The maximum reduction using experimentation was recorded at 1.16°C. Good correlation was obtained between the temperature results using R134a as the working fluid. The largest experimental temperature differential was 1.12°C, which was 0.12°C lower than the CFD predicted value.

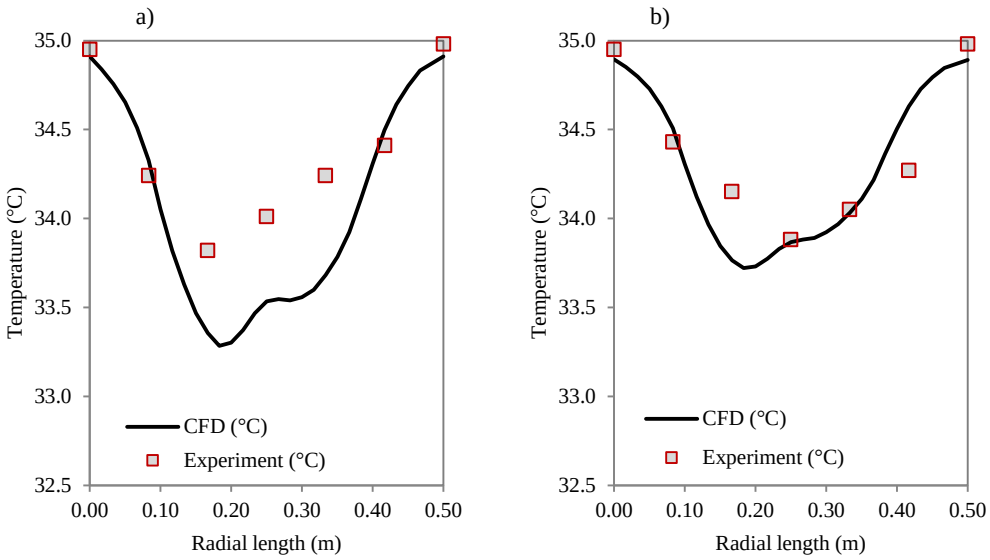

Figure 7.20 Thermal profile of air using: a) water b) R134a as heat pipe internal fluid at an inlet temperature of 35°C

The final evaluation of the CFD and experimental air temperature values was made at an inlet temperature of 41°C. Figure 7.21 displays the thermal profile as predicted by the numerical model and the experimental test-run. The temperature trend revealed maximum differential between upstream and downstream values close to the centre of the test section (between 0.2m and 0.3m). It was observed that both working fluids displayed the largest reduction in air temperatures at a source temperature of 41°C. Water indicated a temperature reduction of approximately 2°C which was 0.4°C higher than the value obtained using experimentation. This performance was superior in relation to R134a which indicated a maximum temperature reduction of 1.48°C using CFD while the experimental testing indicated a drop of 1.15°C.

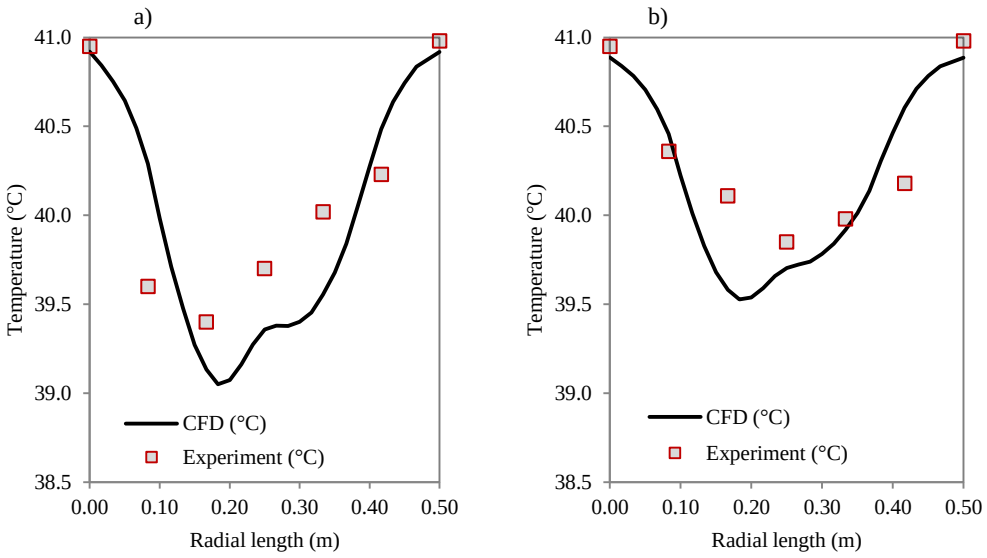

Figure 7.21 Thermal profile of air using: a) water b) R134a as heat pipe internal fluid at an inlet temperature of 41°C

Consistent results were obtained for all analysed cases indicating good agreement between CFD and experimental techniques, therefore the trend was deemed independent of the type of the boundary conditions.

7.5 Transient thermal response model

The final step in the validation phase was the evaluation of the heat pipe thermal response model. A transient model was developed using CFD wherein inlet temperatures to the test section were varied every 30 minutes or 1,800 seconds according to the supplied weather data (Weather History for Doha, Qatar, 2012). The time-step size was taken as 120 seconds and the temperature information was collected for the entire period of 86,400 seconds or 24 hours. The purpose of creating a transient CFD model was to analyse its accuracy in determining the outlet air temperatures or the performance of heat pipes in response to varying inlet temperatures at 30-minute intervals. Figure 7.22 displays the thermal profile obtained during the entire day using the numerical and experimental model.

The CFD model incorporated fewer fluctuations in temperatures in relation to the experimental model. This was expected due to the experimentation being conducted under real-time set-up. The maximum reduction in temperature using CFD was estimated at 3.74K or 3.74°C around the 10^{th} hour mark when the inlet temperatures were increasing. At a similar position, the maximum temperature reduction using the

experimental testing was calculated at 1.08°C. The CFD results displayed inconsistencies after the 14th hour mark when the inlet temperatures started to decrease. It was noted that the numerical model was incapable of predicting the thermal profile of heat pipes when the inlet temperatures decreased from a base value. However, in general, the CFD model successfully determined that the thermal response of heat pipes improves as the inlet temperatures are increased.

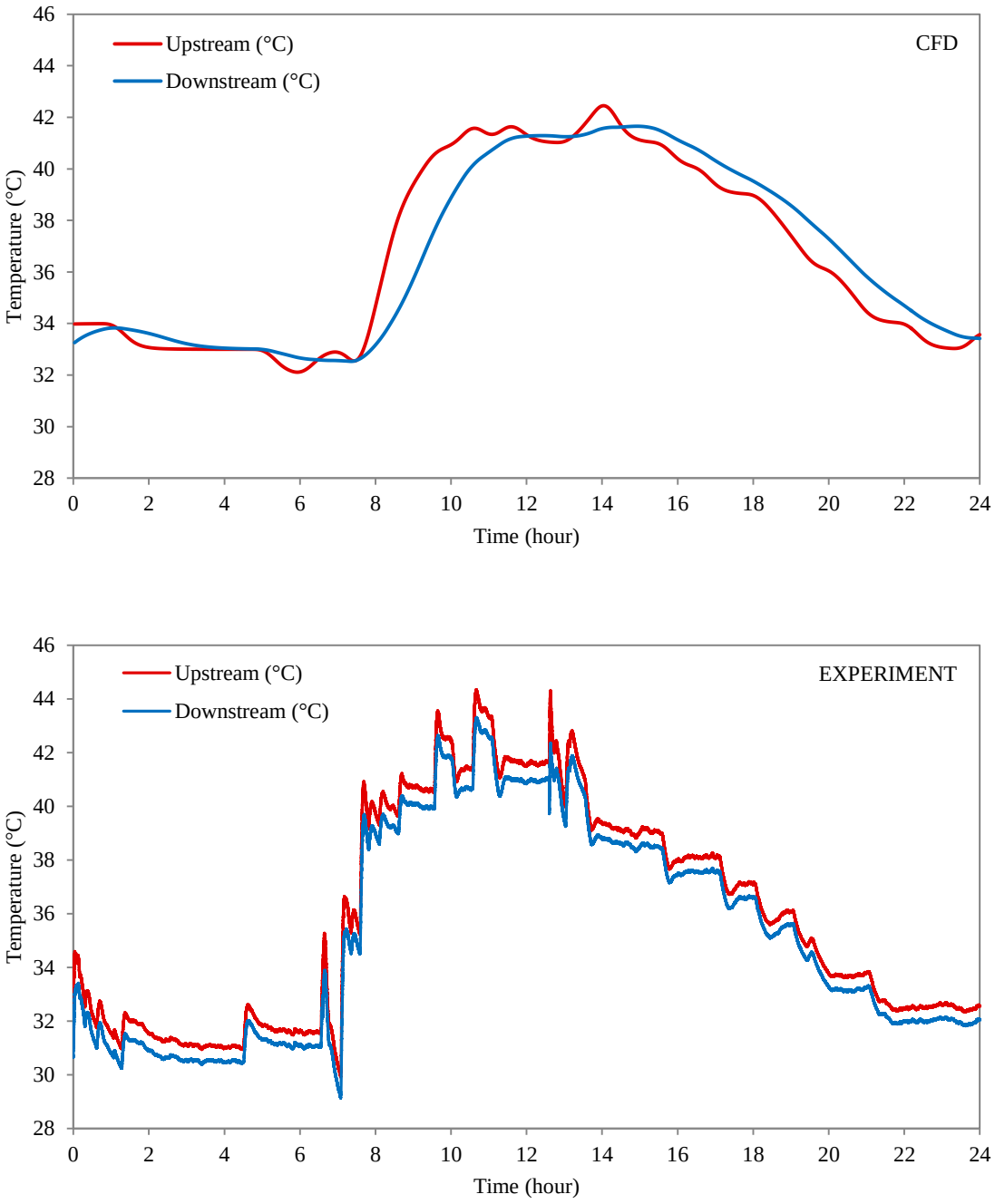

Figure 7.22 Temperature profile over a period of 24 hours

A breakdown of the upstream and downstream temperature profiles obtained using CFD and experimentation is displayed in Figure 7.23, Figure 7.24 and Figure 7.25. The duration of 24 hours was split into three sections of 8 hours each in order to determine the accuracy of the CFD model during each section. Figure 7.23 displays the temperatures from the 1st hour to the 8th hour. The maximum temperature differential using CFD was estimated at 0.73°C while the maximum temperature differential using the experimentation was recorded at 1.94°C. It was observed that the CFD under-predicted the temperature differentials by a mean of 0.55°C during the duration of 8 hours.

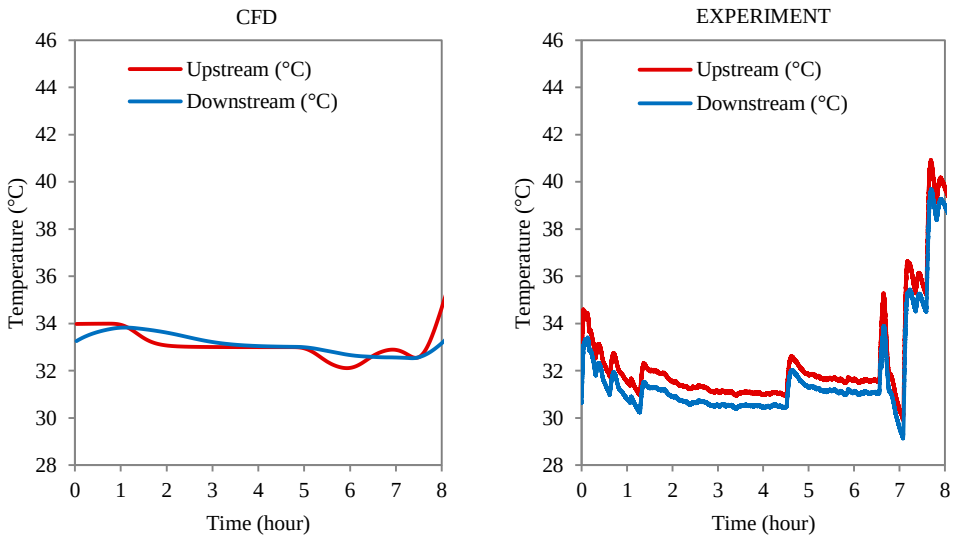

Figure 7.23 Breakdown of the thermal profiles from 1st hour to the 8th hour period

Figure 7.24 displays the profile from the 8th hour to the 16th hour of the day. The mean temperature differential using CFD was estimated at 1.04°C while the mean temperature differential using experimental profile was recorded at 1.17°C. The maximum temperature differential using CFD was 3.74°C at the 9.5 hour mark which was 1.45°C higher than the experimentally recorded temperature differential of 2.29°C at the 12.6 hour mark.

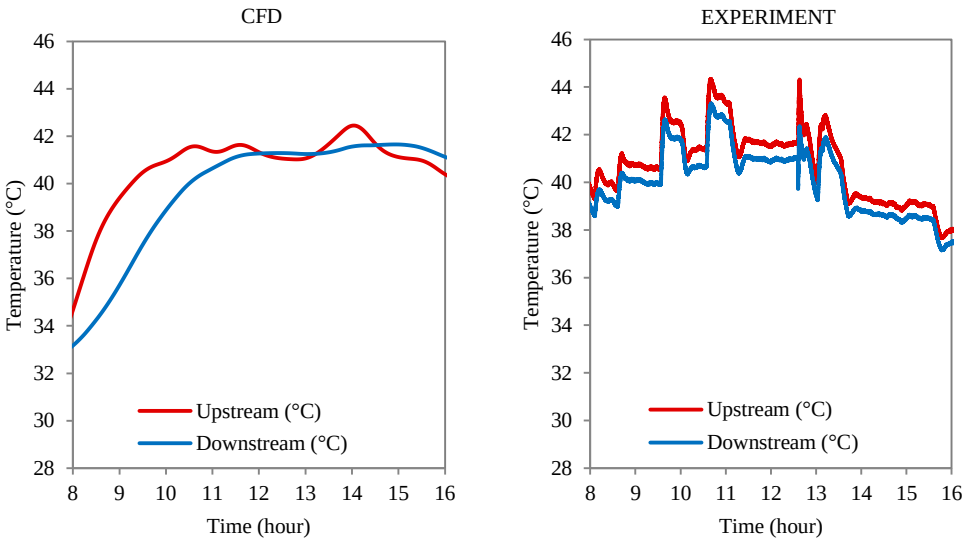

Figure 7.24 Breakdown of the thermal profiles from 8th hour to the 16th hour period

It was observed that the CFD predicted temperatures did not correlate well with the experimental results when the source temperatures were in a decreasing gradient as illustrated in Figure 7.25. The duration from the 16th hour to the 24th indicated a mean temperature drop of 0.52°C from the experimental obtained results. The CFD code predicted a rise of 0.9°C in air temperatures during this duration. The results revealed that the response time of the CFD model correlated well with the experimental results during increasing temperature gradients but was less effective during decreasing temperature gradients.

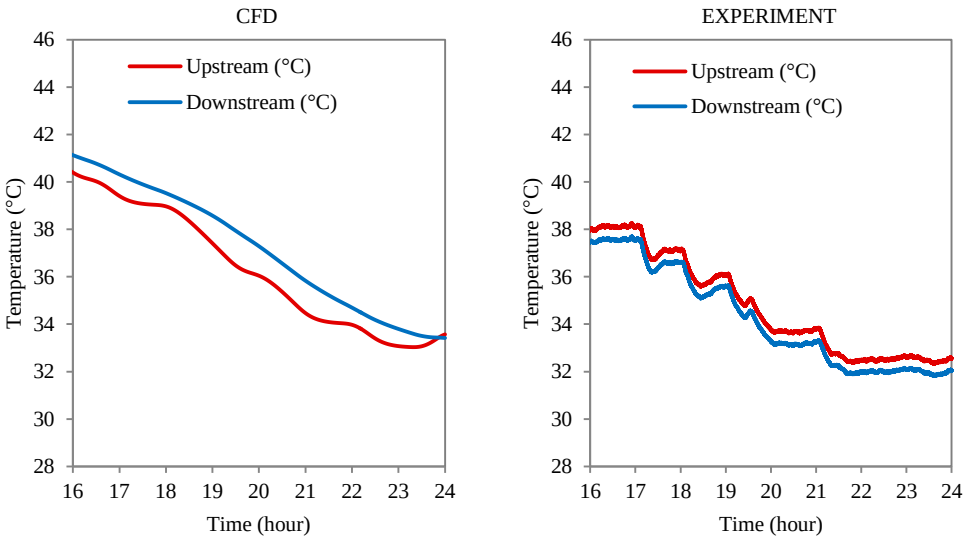

Figure 7.25 Breakdown of the thermal profiles from 16th hour to the 24th hour period

7.6 Assessment of CFD and experimental results

The current study used air velocity, pressure and temperature for flow characterisation between the CFD and experimentally generated values located at the measurement locations. The analysis was conducted using water and R134a as heat pipe working fluids across the three models. Figure 7.26 displays the distribution of error across all measurement locations. The region between 5% and 17% was highlighted in grey to signify the common error percentages found in previous literature (Ekambara *et al.*, 2008, Wang, 2012). The error for velocity ranged from a minimum of 0.7% to a maximum of 17.2%. The difference in pressure distribution resulted in error percentages between 1.3% and 18.8%. The error range for the temperature parameter was found to be between 0.02% and 2.8%. As observed, the current study's range of error distribution correlated well with previous work. The validation results indicated mean error percentages of 9.8% for air velocity, 10.3% for air pressure and 1.2% for air temperature.

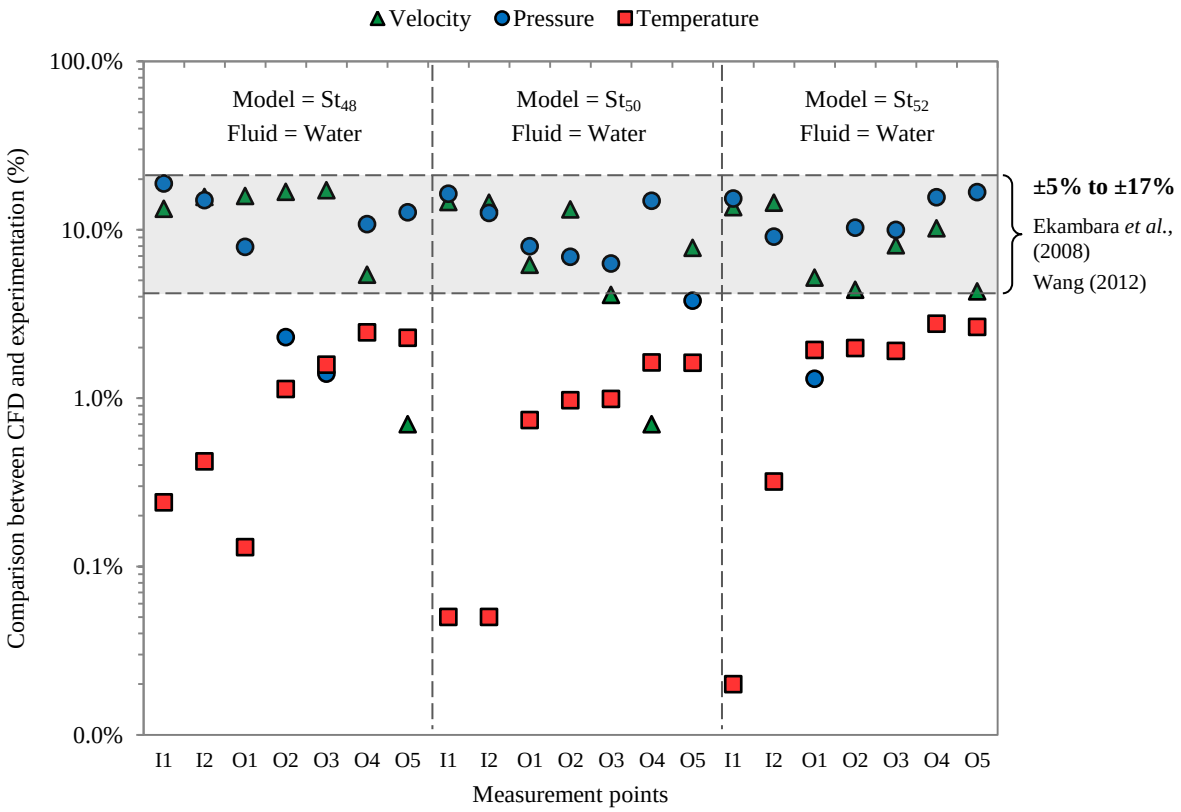

Figure 7.26 Summary of variations between CFD and experimentation using water

The graphical representation of the summarised validation results using R134a as the working fluid is illustrated in Figure 7.27. A good agreement was observed between the CFD and experimentally obtained error when evaluated alongside common ranges found from previous literature. In relation to water, the mean error percentages increased to 9.2% for air velocity and decreased to 9.0% for air pressure and 1.0% for air temperature. The maximum error was recorded for the air velocity parameter at 18.1% using the St_{48} model while the minimum error was obtained at 0.6% for the St_{52} model. The error range for pressure was found to be between 0.7% and 14.8% across all measurement points. Temperature variations were observed to highlight an error range from a minimum of 0.02% to a maximum of 2.5%. As highlighted in the figure, the error range between 5% and 17% was found in literature (Ekambara *et al*., 2008, Wang, 2012) and the error range from the current investigation were found to be similar to previous studies.

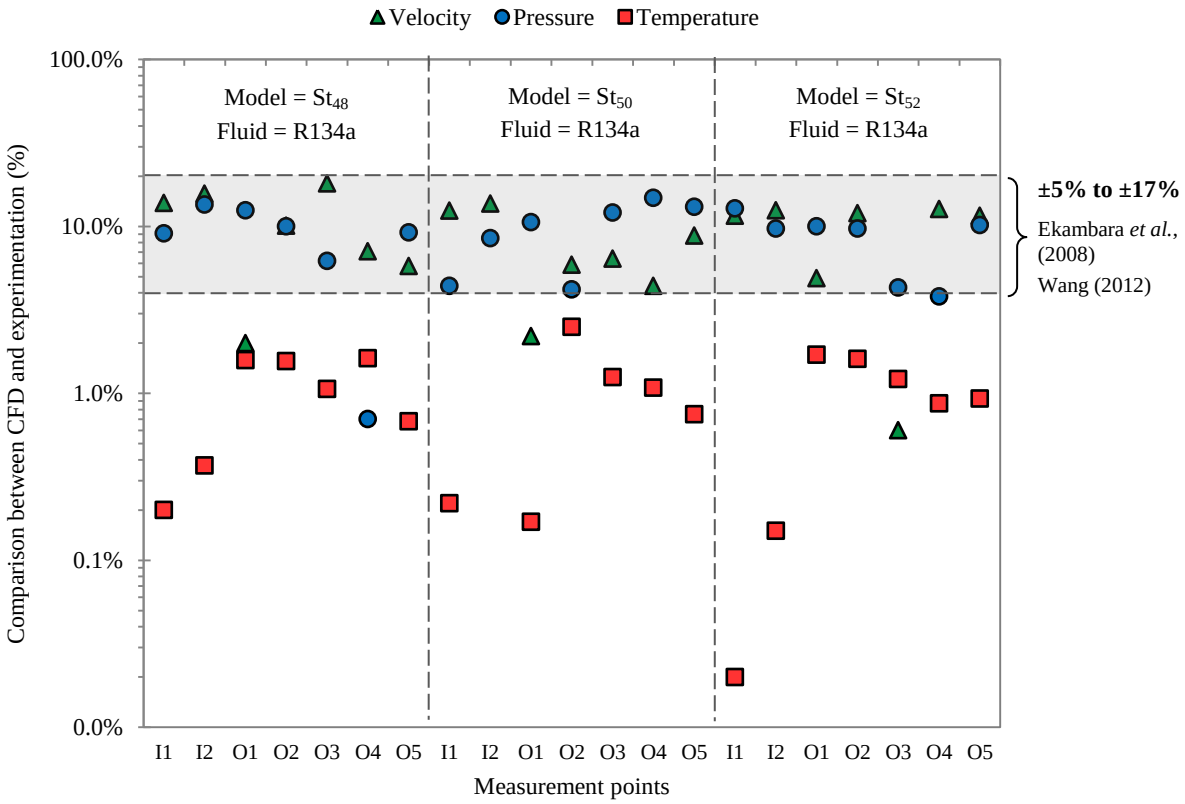

Figure 7.27 Summary of variations between CFD and experimentation using R134a

In summary, the comparison between CFD and experimental findings indicated a good agreement for all three parameters indicating a mean error of 9.5% for velocity, 9.7% for pressure and 1.1% for temperature fields. Since the experimental differences were

low and the findings were in line with common uncertainties reported in existing literature for using multiphase modelling techniques in conjunction with wind tunnel experimentation, thus ensuring confidence in the reliability of the CFD models.

Furthermore, the analyses determined the CFD and experimentally obtained temperature trends across the radial length of the test section downstream of the heat pipes. Three source temperatures (32°C, 35°C and 41°C) were used in order to highlight the CFD and experimental variations at different inlet boundary conditions. A similar trend was recorded for both methodologies with maximum temperatures near the walls and minimum temperatures at the immediate downstream of the central heat pipe. Additionally, the study showed that the CFD consistently under-predicted the thermal profiles in relation to the experimental results by a mean value of 0.83°C corresponding to 2.32% for all investigated source temperatures.

7.7 Common error ranges found in current literature

Common error ranges associated with multiphase modelling couples with *k-e* turbulence models have resulted in error percentages ranging from ±5% to ±17% in comparison with experimental data as indicated in the work of Ekambara *et al*., (2008). When dealing with experimentation involving low-speed wind tunnel testing, a previous study by Wang (2012) established an error percentage of 5% between CFD and experimental results. The current study determined an error range between 0.6% and 18.1% for velocity, 0.7% and 18.8% for pressure and 0.01% and 2.8% for temperature. The error patterns were found to be independent of the geometrical arrangement and fluid properties across the three compared body forces (velocity, pressure and temperature).

For ventilation processes involving heat transfer, an analysis highlighting an example of validation of a CFD based *k-e* turbulence model was presented by Srebric and Chen, (2002) using air temperature. The work illustrated that the CFD code under-predicted the air temperatures with an uncertainty of 0.4°C (0.4K) in comparison with the experimental data. This trend was observed in the current study as well as the CFD model consistently under-predicted the air temperature by a mean value of 0.83K across all measurement locations for all investigated models. Hence, the findings from the current study indicated that the CFD model was validated.

7.8 Summary

In this chapter, the findings from the CFD model were compared and evaluated against full-scale wind tunnel experimental testing. Point values of air velocity, pressure and temperature were systematically compared at the fixed measurement locations. Good agreement was obtained for all three parameters indicating a mean error of 9.5% for velocity, 9.7% for pressure and 1.1% for temperature fields. It was observed that the error variations for all analysed models were in agreement with similar studies found in published literature. In addition, the trend between CFD and experimental methodologies was analysed by highlighting the temperature profile across the radial length of the test section. The trend was established using water and R134a as working fluids and indicated a mean error percentage of 2.32% between air temperature values. In general, a good correlation was observed between all measured flow characterisation parameters as the error was found to be independent of the geometry and the working fluid, thus the CFD results were deemed validated.

Chapter 8
Conclusions and Future Work

8.1 Conclusions

This chapter draws the conclusions from the current study. The broad objective of this research was to advance knowledge in the field of passive cooling by investigating the effectiveness of heat pipes operating under natural ventilation conditions for cooling of fresh air streams in areas of extreme climatic conditions. The conclusions are made in the logical sequence to establish a direct comparison with the objectives of this research (detailed in Chapter 1, Section 1.3). The study comprised of numerical and experimental procedures in order to analyse the internal and external flow and thermal characteristics of heat pipes operating under the required range of operating temperatures.

1. The study investigated the performance of available working fluids used in heat pipes. Water, ethanol and R134a were systematically compared and their effectiveness in delivering the maximum cooling capability was analysed. At an inlet temperature of 314K and an inlet velocity of 2.3m/s, downstream temperature profiles were drawn to comprehend the ideal candidate working fluid. Heat transfer due to convection was calculated at 977W using water, 763W using R134a and 571W using ethanol. The corresponding effectiveness of the heat pipe heat exchanger was found to be 6.5% for water, 4.9% for R134a and 3.7% for ethanol. The findings established that water incorporated the greatest capability of reducing incoming airside temperatures by approximately 24% higher than the refrigerant R134a and 42% higher than ethanol which was found to be the least effective working fluid under the range of investigated temperatures (detailed in Chapter 5, Section 5.2.3).

2. In order to increase the performance of heat pipes, individual physical properties of the working fluid were analysed as part of the study. Using properties of water as the benchmark, the investigated properties included density, thermal conductivity; dynamic viscosity and specific heat capacity were varied one at a time keeping other parameter constant to determine the property that had the greatest influence on heat transfer. From the prospect of cooling a low-speed

natural airstream carrying a high temperature of 314K, the findings determined that the specific heat capacity was found to be the most influential parameter with a 39% enhancement in convective cooling while fluid density was found to increase heat transfer by approximately 28%. Dynamic viscosity and thermal conductivity were the least dominant parameters with both affecting an increase of approximately 17% (detailed in Chapter 5, Section 5.3.5).

3. The way in which heat pipes are arranged plays an important role on the overall effectiveness of the system. Using the heat pipe diameter (D) of 20mm, the spanwise thicknesses were varied from 44mm (St/D ratio of 2.2) to 52mm (St/D ratio of 2.6). Keeping the boundary conditions constant for all modes (inlet velocity of 2.3m/s and inlet temperature of 314K), the rate of heat transfer was found to be directly proportional to the temperature difference between inlet and outlet interface. The findings determined that the spanwise thickness of 50mm (St/D ratio of 2.5) provided the highest heat transfer in comparison to the other analysed models at 768W. The overall effectiveness of the system was found to decrease by from 5.6% to 4.7% when the spanwise thickness reduced from 50mm to 44mm (detailed in Chapter 5, Section 5.4.2).

4. Subsequent to the determination of the most suitable spanwise thickness, the effects of streamwise distance (Sd) between columns of heat pipes was analysed in this study. Using a fixed array of heat pipes, the streamwise distances were varied from 20mm (Sd/D ratio of 1.0) to 40mm (Sd/D ratio of 2.0). The results for air velocity distribution illustrated two regions of increased concentration when the Sd/D (streamwise distance to pipe diameter) ratio exceeded 1.0, thus indicating a reduction in contact time. As a result, the overall effectiveness of heat pipes decreased as the streamwise distances was increased. The overall effectiveness of the heat pipe heat exchanger was the highest for the streamwise distance of 20mm at 5.6% and decreased to 5.0% at a streamwise distance of 40mm (detailed in Chapter 5, Section 5.5.2).

5. Following a range of steady-state analyses, a transient experimental test was conducted to determine the thermal behaviour of heat pipes in response to continuously varying external temperatures. The city of Doha, Qatar was used as a case-study reference and the test was conducted over a period of 24 hours,

using hourly temperatures for June 21st, 2012 (Weather History for Doha, Qatar, 2012). The purpose of carrying out the test was to establish the climatic response characteristics of heat pipes in relation to increasing and decreasing outdoor temperature gradients. The findings from the investigation depicted that the thermal response of heat pipes was directly proportional to the inlet air temperatures with an increase of 0.1°C or 0.1K evaluated for every 1K rise in external temperature. In contrast, the working performance of heat pipes reduced by 0.3°C or 0.3K for every 1K decrease in external air temperatures. The test confirmed that in general, the heat pipes performed better during the day-time when external temperatures reached over 40°C in comparison to night-time operation when external temperatures dropped below 35°C. This was primarily because of the temperature differential between the evaporator and condenser ends of the pipe which increased during the day-time, thereby indicating a superior effectiveness of the heat pipes (detailed in Chapter 6, Section 6.4.4).

6. The findings of the present study are based on categorising the heat pipe design parameters for low-velocity airstreams by achieving a full-scale wind tunnel validation of the CFD findings within the accepted error range of ±5% and ±17% (Ekambara *et al*., 2008, Wang, 2012). Point values of fluid flow parameters, namely velocity, pressure and temperature were systematically compared at the fixed measurement locations and the error variation was quantified. The comparison was established at three different spanwise configurations (St_{48}, St_{50} and St_{52} models) along with two different working fluids (water and R134a) to highlight the consistency in error patterns in relation to varying geometrical and boundary conditions. The analysis determined an error range between 0.6% and 18.1% for velocity, 0.7% and 18.8% for pressure and 0.01% and 2.8% for temperature. The findings from the validation study determined a good correlation for all three parameters indicating a mean error of 8.9% for velocity, 9.7% for pressure and 1.1% for temperature fields which were found to be in line with previous studies (detailed in Chapter 7, Section 7.7).

In conclusion, the maximum temperature drop calculated for steady-state conditions was approximately 2K at a source temperature of 314K (or 41°C). This was because of the speed of the external airstream which was kept fixed at 2.3m/s due to it being the minimum supply velocity possible using the wind tunnel. The relevance of this data

however indicates that if the heat pipe technology is applied under typical indoor conditions incorporating fresh air requirements of 0.8L/s/m^2 (BS5952:1991, Hughes and Ghani, 2008), the effectiveness of the device can be improved due to the increased contact duration, thereby providing a higher cooling performance.

8.2 Contribution to knowledge

This study used numerical and experimental techniques identified through literature in order to fill the research gap (as detailed in Chapter 2, Section 2.8). The following points present a summary of the contributions of the study's findings in the field of heat transfer, passive cooling and in particular, the effectiveness of heat pipes operating under extreme temperatures.

- Extensive numerical data has been provided on the behaviour of heat pipe working fluids in response to hot temperature conditions. The CFD model determined the internal and external flow and thermal profiles of water, ethanol and R134a and their subsequent heat transfer capabilities when operating under convection airstreams (Chapter 5).

- Computational models were established to investigate the influence of physical properties of the heat pipe working fluid on its heat transfer ability. The relationship between individual properties (density, thermal conductivity, dynamic viscosity and specific heat capacity) and convective heat transfer has been determined (Chapter 5).

- The investigation presented the effect of the varying spanwise and streamwise configurations on the corresponding effectiveness of heat pipes. The study analysed different characteristic lengths in order to scrutinise the trends obtained for thermal performance of the device (Chapter 5).

- By carrying out the transient experimental testing, the present work characterised the dynamic response of heat pipes working under different source temperatures for the duration of 24 hours. The study showed that the thermal behaviour of heat pipes varies considerably depending on external temperature gradients (Chapter 6).

- The numerical models were validated using full-scale experimental testing. The work established the level of accuracy of using wind tunnel testing techniques to validate the CFD models using quantitative (measurement point comparison) data analysis (Chapter 7).

8.3 Scope for future work

After meeting the aims and objectives of this research, the following scope of future work was identified during the course of the study:

- This research highlighted the effectiveness of heat pipes using the standard cylindrical tubes available with a circular cross-section. As an extended study, customised design of heat pipes could be manufactured in varying profiles including elliptical, triangular and square cross-sections. This could help determine the effect of the shape of the heat pipe on the overall effectiveness of the system.

- Flexible ice blankets were used in the present study in order to maintain the temperatures at the cold sink or condenser section of the heat pipes. The stabilisation experimental time from the current method was 2.2 hours. An automated solution to control the temperatures at the cold interface would be a useful addition to the work to allow maintaining the sink conditions for a longer length of time at any desirable temperature.

- It was necessary that the current study incorporated a fixed physical domain in order to determine the optimum heat pipe design parameters. However, there is scope to investigate the effect of aluminium fins on heat pipes to enhance the thermal performance of the system. Quantification of increase in heat transfer by increasing the contact time between the incoming airstream and the surface area of the heat exchanger could a future point of interest.

- Conducting an in-depth analysis into the variation in latent heat capacity of working fluids in order to determine its impact on the airside cooling capacity of heat pipes. This will provide further scope of work in the subject area of fluid properties covered in the present study.

- Designing an automated process optimisation technique in order to evaluate the cooling capacity and effectiveness of heat pipes in response to external geometrical configurations and internal working fluids. This will assist in yielding an accurate assessment of the overall performance of the device.

List of References

Abou-Zian HZ, Helali A, Fatouh M, El-Nasr MMA, 2000. *Performance of stationary and vibrated thermosiphon working with water and R134a*, Applied Thermal Engineering 21 813-830

AIAA Guide for the Verification and Validation of Computational Fluid Dynamics Simulations (G-077-1998e), ISBN: 978-1-56347-354-8

Alizadehdakhel A, Rahimi M and Alsairafi AA, 2010. *CFD modeling of flow and heat transfer in a thermosiphon,* International Communications in Heat and Mass Transfer 37, 312–318.

ANSYS Fluent User's Guide, 2011. ANSYS, Inc. Southpointe November 2011, 275 Technology Drive, Canonsburg, PA 15317 Release 14.0

Aris MS, McGlen R, Owen I and Sutcliffe CJ, 2011. *An experimental investigation into the deployment of 3-D,finned wing and shape memory alloy vortex generators in a forced air convection heat pipe fin stack,* Applied Thermal Engineering 31, 2230-2240

ASHRAE Standard 55-2004. Thermal Environmental Conditions for Human Occupancy (ANSI approved)

Asif M, Muneer T and Kelley R, 2007. *Life cycle assessment: a case study of a dwelling home in Scotland.* Building and Environment 2007;42.

Awbi H, 2010. *Basic concepts for natural ventilation of buildings*, CIBSE BSG Seminar: Natural and Mixed-Mode Ventilation Modelling, University of Reading 2010

Bakker A, 2002. A*pplied Computational Fluid Dynamics*, Lecture 7 - Meshing, Available from: http://www.bakker.org

Barlow JB, Rae WH Jr. and Pope A, 1999. *Low-speed wind tunnel testing*, 3rd edition, Wiley-Interscience publication, ISBN-0-471-55774-9, USA

Beckert K and Herwig H, 1996. *Inclined air to air heat exchangers with heat pipes: comparing experimental data with theoretical results*, Energy Conversion Engineering Conference1996, Vol.2 -1441 - 1446

Bowen RM, 1976. *Theory of Mixtures*, In A.C.Enrigen, editor, C0ntinuum Physics, pages 1-127, Academic Press, New York

British Standards, 1991. Ventilation principles and designing for natural ventilation, BS5952:1991

Calautit JK, Chaudhry HN, Hughes BR and Ghani SA, 2013. *Comparison between evaporative cooling and heat pipe assisted thermal loop for a commercial wind tower in hot and dry climatic conditions,* Applied Energy 101, 740-755

Cengel Y, 2006. *Heat and Mass Transfer-A Practical Approach*, (p592-597), Third Edition 2006, McGraw-Hill, New York, NY 10020, USA

Chaudhry HN, Hughes BR and Ghani SA, 2012. *A review of heat pipe systems for heat recovery and renewable energy applications,* Renewable and Sustainable Energy Reviews 16, 2249-2259

Chen QY and Srebric J, 2002. *A procedure for verification, validation, and reporting of indoor environment CFD analyses,* HVAC&R Research 8, 201-216

Chung TJ, 2002. *Computational Fluid Dynamics*, Cambridge University Press; illustrated edition edition, ISBN-0521594162

Chyu M, Hsing Y and NatarajanV, 1998. *Convective heat transfer of cubic fun arrays in a narrow channel*, ASME J. Turbomach 120 362-367

Cokljat D, Slack M and Vasquez SA, 2003. *Reynolds-Stress model for Eulerian Multiphase*, Proceedings of the 4th International Symposium on Turbulence Heat and Mass Transfer, pages 1047-1054, Begell House, Inc.

Cooper JT, 1996. *Heat pipe impact on dehumidification, indoor air quality and energy savings*, Tenth Symposium on Improving Building Systems, FT.Worth,Texas, May13-14, 1996

De Leeuw B, Hagens H, Brand S, Grooten M, Ganzevles F, van der Geld C and van Kemenade E, 2006. *Generator cooling using heat pipes,* 13th Intl. Conference on Modelling Flow Technologies, Hungary, September 6-9

Do KH, Kim SJ and Garimella SV, 2008. *A mathematical model for analyzing the thermal characteristics of a flat micro heat pipe with a grooved wick,* International Journal of Heat and Mass Transfer 51, 4637–4650.

Duan Z, Zhan C, Zhang X, Mustafa M, Zhao X, Alimohammadisagvand B, Hasan A, 2012. *Indirect evaporative cooling: Past, present and future potentials*, Renewable and Sustainable Energy Reviews 16: 6823-6850

Easa M, Barigou M, 2009. *CFD investigation of the pipe transport of coarse solids in laminar power law fluids*, Chemical Engineering Science 64, 322-333

Ekambara K, Dhotre MT, Joshi JB, 2006. *CFD simulation of homogeneous reactions in turbulent pipe flows-Tubular non-catalytic reactors,* Chemical Engineering Journal 117, 23-29

Ekambara K, Sanders RS, Nandakumar K, Masliyah JH, 2008. *CFD simulation of bubbly two-phase flow in horizontal pipes*, Chemical Engineering Journal 144, 277-288

El-Baky MA and Mohamed MM, 2007. *Heat pipe heat exchanger for heat recovery in air conditioning*, Applied Thermal Engineering 27, 795–801.

Elnaggar MHA, Abdullah MZ and Mujeebu MA, 2011. *Experimental analysis and FEM simulation of finned U-shape multi heat pipe for desktop PC cooling*, Energy Conversion and Management 52, 2937-2944

Energy Efficiency in Buildings, 2009. World Business Council for Sustainable Development, August 2009, Atar Roto Presse SA, Switzerland

Energy Efficiency in Buildings, World Business Council for Sustainable Development (Online) 2013 (cited July 02, 2013). Available from: http://www.wbcsd.org/work-program/sector-projects/buildings/overview.aspx

Energy Efficient Solutions, 2011. Heat Pipes Dehumidification and Heat Recovery, S & P Coil Products Limited, Leicester, U.K.

Energy On Demand, 2008. Middle East Energy and Resources Managing scarcity for the future, Deloitte & Touche (M.E.)

Enertron Total Thermal Management Solutions (Online) 2012 (cited February 26, 2013). Available from http://www.enertron-inc.com/enertron-products/heat-pipe-basics.php

F2 Chemicals Limited, Technical Article (Online) 2012 (cited June 13, 2013). Available from http://www.fluoros.co.uk/pdf/technical/Rankine.pdf

Faghri A, 1986. *Vapor flow analysis in a double walled concentric heat pipe*, Numer. Heat Transfer 10, 583–595

Fang X and Xia L, 2010. *Heating performance investigation of a bidirectional partition fluid thermal diode*, Renewable Energy 35, 679–684.

Firouzfar E and Attaran M, 2008. *A review of heat pipe heat exchangers activity in Asia*, World Academy of Science, Engineering and Technology 23, 2008

Gan G and Riffat SB, 1996. *Measurement and computational fluid dynamics prediction of diffuser pressure-loss coefficient*, Applied Energy, Vol.54, 181-195

Gan G and Riffat SB, 1998. *A study of heat pipe heat recovery for natural ventilation*, Building Services Engineering Research and Technology, 20:57

Gaugler RS, 1944. Heat transfer device, U.S. Patent No. 2,350,348, 1944

Givoni B, 2009. *Indoor temperature reduction by passive cooling system,* Solar Energy 85, 1692-1726

Hagens H, Ganzevles FLA, van der Geld CWM and Grooten MHM, 2007. *Air heat exchangers with long heat pipes: experiments and predictions*, Applied Thermal Engineering 27: 14-15

Hager WH, *Wilfrid Noel Bond and the Bond number*, 2012. Journal of Hydraulic Research, 50:1, 3-9

Hellevang K, 2009. Air-to-air heat exchangers for healthier energy-efficient homes, North Dakota State University Fargo, North Dakota 58108, March 2009

Hemadri VA, Gupta A and Khandekar S, 2011. *Thermal radiators with embedded pulsating heat pipes: Infra-red thermography and simulations,* Applied Thermal Engineering 31, 1332-1346.

Hirt CW and Nichols BD, 1981. *Volume of Fluid (VOF) method for the dynamics of free boundaries,* Journal of Computational Physics 39 (1) 201–225.

Holman JP, 1997. Heat Transfer, (p517-518), Eighth Edition 1997, McGraw-Hill, New York, NY 10020, USA

Hsieh SS and Huang DC, 1990. *Comparisons of thermal performance and pressure drop of counterflow and parallel-flow heat pipe heat exchangers with aligned/staggered tube rows*, Energy Conversion and Management 30, 357-368

Hughes BR, Chaudhry HN and Calautit JK, 2013. Passive energy recovery from natural ventilation air streams, Applied Energy 113, 127-140

Hughes BR, Chaudhry HN and Ghani SA, 2011. *A review of sustainable cooling technologies in buildings*, Renewable and Sustainable Energy Reviews 15, 3112-3120

Hughes BR and Ghani SA, 2008. *Investigation of a windvent passive ventilation device against current fresh air supply recommendations*, Energy and Buildings 40, 1651-1659

Hung YM and Seng Q, 2011. *Effects of geometric design on thermal performance of star-groove micro-heat pipes,* International Journal of Heat and Mass Transfer 54, 1198–1209

Industrial Technologies Program Energy Efficiency and Renewable Energy U.S. Department of Energy Washington, DC, 2011, 20585-0121 http://www.eere. energy.gov/industry.

Jabardo JMS, da Silva EF, Ribatski G and de Barros SF, 2004. Evaluation of the Rohsenow Correlation through experimental pool boiling of halocarbon refrigerants on cylindrical surfaces, Journal of the Brazilian Society of Mechanical Sciences and Engineering 26, 218-230

Joudi KA and Witwit AM, 2000. *Improvements of gravity assisted wickless heat pipes,* Energy Conversion & Management 41, 2041-2061.

Kakac S, Vasiliev LL, Bayazitoglu Y, Yener Y, 2004. *Microscale heat transfer - Fundamentals and Applications*, NATO Science Series, Springer Vol. 193 ISBN: 1-4020-3359-1

Karthikeyan R, Rathnasamy R, 2011. *Thermal performance of pin-fin arrays, International Journal of Advanced Engineering Sciences and Technologies* 10, 125-138

Kaya T and Goldak J, 2006. *Numerical analysis of heat and mass transfer in the capillary structure of aloop heat pipe*, International Journal of Heat and Mass Transfer 49, 3211–3220.

Kays WM and London AL, 1984. *Compact heat exchanger design*, third ed., McGraw-Hill, New York

Klein GJ, Tupper KF and Green JJ, 1930. *The design of corners in fluid channels*, Canadian Jounrnal of Research, Vol.3, 272-285

Laboratories for the 21st Century, U.S. Environmental Protection Agency, October 2003, National Renewable Energy Laboratory, U.S.A.

Landry CM, 2004. *The impact of air conditioning design on the power plant*, Turbine Air Systems Power-Gen Middle East, 13-15 September, Manama, Bahrain

Lane HJ and Heggs PJ, 2005. *Extended surface heat transfer - the dovetail fin*, Applied Thermal Engineering 25, 2555-2565

Launder BE and Spalding DB, 1972. *Lectures in mathematical models of turbulence*, Academic Press, London, England

Lee WH, 1979. *A Pressure Iteration Scheme for Two-Phase Modeling*, Technical Report LA-UR 79-975, Los Alamos Scientific Laboratory, Los Alamos, New Mexico

Lee YS, 2003. *Trend Validation of CFD Prediction Results for Ship Design*, Dissertation for the degree of Doctor of Philosophy, Institute of Naval Architecture, Marine and Ocean Engineering of Technical University of Berlin, Germany

Lefe`vre F and Lallemand M, 2006. *Coupled thermal and hydrodynamic models of flat micro heat pipes for the cooling of multiple electronic components,* International Journal of Heat and Mass Transfer 49: 1375–1383.

Liang TS and Hung YM, 2010. *Experimental investigation on the thermal performance and optimization of heat sink with U-shape heat pipes*, Energy Conversion and Management 51, 2109-2116

Liao Q, Jen TC, Chen Q, Li L and Cui W, 2007. *Heat transfer performance in 3D internally finned heat pipe*, International Journal of Heat and Mass Transfer 50, 1231–1237.

Lin S, Broadbent J and McGlen R, 2005. *Numerical study of heat pipe application in heat recovery systems,* Applied Thermal Engineering 25, 127–133.

Lin WK, Liaw KC, Tsai MZ and Chu MG, 2012. *Heat transport study of the laminar heat pipe heat exchanger*, Smart Grid and Renewable Energy 3, 348-354

Living Planet Report 2012, World Wide Fund for Nature, May 2012, WWF International, Gland, Switzerland

Majumder CH, Yuen DA, Sevre EO, Boggs JM, Bergeron SY, 2002. *Finite Prandtl number 2-D convection at high Rayleigh numbers*, Electronic Geosciences, 7: 11-30

Mathur GD, 1991. *Indirect-direct evaporative cooling with heat pipe heat exchangers*, ASME National Heat Transfer Conference, 91-HT-20.

Mathur GD, 1996. *Using heat-pipe heat exchangers for reducing high energy costs of treating ventilation air*, Energy Conversion Engineering Conference, 1996. IECEC 96., Proceedings of the 31st Intersociety, Vol.2 1447-1452

Mathur GD, 2000. *Controlling space humidity with heat-pipe heat exchangers*, The American Institue of Aeronautics and Astronautics, AIAA-2000-2949

Mehta RD and Bradshaw P, 1979. *Design rules for small low speed wind tunnels*, Aeronautical Journal, Paper No. 718

Mehta RD, 1985. *Turbulent boundary layer perturbed by a screen,* AIAA Journal, Vol. 23, No.9

Mehta UB, 1996. *Guide to Credible Computer Simulations of Fluid Flows,* AIAA Journal of Propulsion and Power 12, 940-948.

Metzger D, Fan C and Haley S, 1984. Effects of pin shape and array orientation on heat transfer and pressure loss in pin fin arrays, Journal of Engineering for Power 106(1) 252-257

Mishra M, Das PK and Sarangi S, 2006. *Transient behaviour of crossflow heat exchangers due to perturbations in temperature and flow,* International Journal of Heat and Mass Transfer 49, 1083-1089

Mochizuki M, Nguyen T, Mashiko K, Saito Y, Nguyen T and Wuttijumnong V, 2011. *A review of heat pipe application including new opportunities*, Frontiers in Heat Pipes 2, 013001

Montgomery RB, 1947. *Viscosity and thermal conductivity of air and diffusivity of water vapor in air*, Journal of Meteorology, Vol. 4, Contribution No. 388

Morel T, 1977. Design of two-dimensional wind tunnel contractions, Journal of fluids engineering, ASME transactions, Series I, Vol.99, 371-378

Naphon P, 2010. *On the performance of air conditioner with heat pipe for cooling air in the condenser*, Energy Conversion and Management 51, 2362-2366

Nasrin R, Alim MA, Chamkha AJ, 2012. *Buoyancy-driven heat transfer of water–Al2O3 nanofluid in a closed chamber:Effects of solid volume fraction, Prandtl number and aspect ratio,* International Journal of Heat and Mass Transfer 55, 7355-7365

Nemec P, Caja, A and Lenhard R, 2010. *Visualization of heat transport in pipes using thermocamera*, Archives of Thermodynamics, Vol. 31, No.4, 125-132

Noie-Baghban SH and Majideian GR, 2000. *Waste heat recovery using heat pipe heat exchanger (HPHE) for surgery rooms in hospitals,* Applied Thermal Engineering 20, 1271-1282.

Oberkampf WL and Trucano TG, 2002. *Verification and validation in computational fluid dynamics*, Progress in Aerospace Sciences 38, 209-272

Omer SA, Riffat SB and Ma X, 2001. *Experimental investigation of a thermoelectric refrigeration system employing a phase change material integrated with thermal diode*, Applied Thermal Engineering 1, 1265-1271.

Peace Software International, Saturation properties of R134a (Online) 2013, (Cited March 2, 2013) Available from http://www.peacesoftware.de/einigewerte/calc_r134a.php5

Peng H, Li J and Ling X, 2013. *Study on heat transfer performance of an aluminum flat plate heat pipe with fins in vapor chamber*, Energy Conversion and Management 74, 44-50

Perspex For Glazing (Online) 2013, (Cited December 12, 2013) Available from http://www.bayplastics.co.uk/PDFs/datasheets/perspex-glazing.pdf

Qu W and Ma HB, 2007. *Theoretical analysis of startup of a pulsating heat pipe*, International Journal of Heat and Mass Transfer 50, 2309–2316.

Rahmat M and Hubert P, 2010. *Two-phase simulations of micro heat pipes*, Computers & Fluids 39, 451–460.

Rallabandi AP, Liu YH and Han JC, 2011. *Heat transfer in trailing edge wedge shaped pin fin channels with slot ejection under high rotation numbers*, Journal of Thermal Science and Engineering Applications, 3 021007-1-9

Ranjan R, Murthy JY, Garimella SV and Vadakkan U, 2011. *A numerical model for transport in flat heat pipes considering wick microstructure effects,* International Journal of Heat and Mass Transfer 54, 153–16.

Rao YVC, 2001. *Heat Transfer*, University Press, Sangam Books Ltd., ISBN-8173713847

Reay D and Kew P, 2006. *Heat Pipes-Theory, Design and Applications*, Fifth Edition, Butterworth-Heinemann, Oxford OX2 8DP, USA

Rennie TJ and Raghavan VGS, 2005. *Experimental studies of a double-pipe helical heat exchanger*, Experimental Thermal and Fluid Science 29, 919-924

Rhee J, Campbell A, Mariadass A and Morhous B, 2010. *Temperature stratification from thermal diodes in solar hot water storage tank*, Solar Energy 84, 507–511.

Ridley P, 2010. *Guide to partitioning unstructured meshes for parallel computing*, Numerical Algorithms Group Ltd., Oxford OX2 8DR, United Kingdom

Riffat S and Zhu J, 2003. *Experimental investigation of an indirect evaporative cooler consisting of a heat pipe embedded in porous ceramic*, The Journal of Research 1 (2004) 46-52

Roache PJ, 1997. *Quantification of uncertainty in Computational Fluid Dynamics*, Annu. Rev. Fluid. Mech 29,123–160

Ruch MA, 1976. *Heat pipe exchagers as energy recovery devices*, ASHRAE Transactions, Vol 8, No 1, 1008-1014.

Saber MH, Ashtiani HM, 2010. *Simulation and CFD Analysis of heat pipe heat exchanger using Fluent to increase of the thermal efficiency*, Proceedings of the 7th WSEAS International Conference on Heat and Mass Transfer, Cambrdige, 2010

Sahin B, Ward-Smith AJ and Lane D, 1995. *The pressure drop and flow characteristics of wide-angle screened diffusers of large area ratio*, Journal of Wind Engineering and Industrial Aerodynamics, Vol.58, 33-50

Sahiti N, Krasniqi F, Fejzullahu Xh, Bunjaku J and Muriqi I, 2008. *Entropy generation minimization of a double-pipe pin fin heat exchanger*, Applied Thermal Engineering 28, 2337-2344

Sahu AK, Chhabra RP, Eswaran V, 2009. *Effects of Reynolds and Prandtl numbers on heat transfer from a square cylinder in the unsteady flow regime*, International Journal of Heat and Mass Transfer 52, 839-850

Sanaye S and Talaee MR, 2009. *Thermal-economic analysis of a heat pipe heat exchanger for energy recovery in air conditioning applications*, Journal of Power and Energy - Part A: 223:925

Sargison JE, Walker GJ, Rossi R, Design and calibration of a wind tunnel with a two dimensional contraction, 15th Australasian Fluid Mechanics Conference, The University of Sydney, 13-17 December, 2004

Savino R, Cecere A and Paola RD, 2009. *Surface tension-driven flow in wickless heat pipes with self-rewetting fluids*, International Journal of Heat and Fluid Flow 30, 380–388.

Sedov LI, 1997. *Mechanics of Continuous Media* Vol.2, Series in Theoretical and Applied Mechanics, World Scientific Publishing Co. Pte. Ltd. ISBN-981-02-3982-3

Shabgard H, Faghri A, 2011. *Performance characteristics of cylindrical heat pipes with multiple heat sources*, Applied Thermal Engineering 31, 3410-3419

Shao L and Riffat SB, 1997. *Flow loss caused by heat pipes in natural ventilation stacks*, PII: S13594311(96)00029-4.

Singh R, Mochizuki M, Nguyen T and Akbarzadeh A, 2011. *Applications of heat pipes in energy conservation and renewable energy based systems*, Frontiers in Heat Pipes, 2, 033003

Soltani MR, Ghorbanian K and Manshadi MD, 2010. *Application of screens and trips in Enhancement of flow characteristics in subsonic wind tunnels*, International Journal of Scientia Iranica, 17 (1)

Song F, Ewing D and Ching CY, 2008. *Heat transfer in the evaporator section of moderate-speed rotating heat pipes*, International Journal of Heat and Mass Transfer 51, 1542-1550

Srebric J and Chen QY, 2002. *An example of verification, validation, and reporting of indoor environment CFD analyses*, ASHRAE Transactions 108, 185-194

The Weather Channel, (Online) 2011, (Cited December 12, 2011) Available from http://www.weather.com/weather/today/Doha+Qatar+QAXX0003

Van Fossen G, 1981. *Heat transfer coefficients for staggered arrays of short pin fins*, NASA STI/Recon Technical Report No. 81

Varga S, Oliveira AC and Afonso CF, 2002. *Characterisation of thermal diode panels for use in the cooling season in buildings,* Energy and Buildings 34, 227-235.

Vasiliev LL and Vasiliev LL Jr., 2004. *The sorption heat pipe—a new device for thermal control and active cooling,* Superlattices and Microstructures 35, 485–495.

Vasiliev LL and Vasiliev LL Jr., 2005. *Sorption heat pipe - a new thermal control device for space and ground application*, International Journal of Heat and Mass Transfer 48, 2464-2472

Vasquez SA and Ivanov VA, 2000. *A phase coupled method for solving Multiphase problems on unstructured meshes,* ASME 2000, Fluids Engineering division, Boston

Versteeg HK and Malalasekera V, 2007. *An Introduction to Computational Fluid Dynamics: The Finite Volume Method,* Second Edition, Pearson Education Limited 1995, 2007

Wan JW, Zhang JL and Zhang WM, 2007. T*he effect of heat-pipe air-handling coil on energy consumption in central air-conditioning system*, Energy and Buildings 39, 1035-1040

Wang JC, 2012. *3-D numerical and experimental models for flat and embedded heat pipes applied in high-end VGA card cooling system*, International Communications in Heat and Mass Transfer 39, 1360-1366

Wang S, Lin Z, Zhang W and Chen J, 2009. *Experimental study on pulsating heat pipe with functional thermal fluids*, International Journal of Heat and Mass Transfer 52, 5276–5279.

Wang S, Zhang W, Zhang X and Chen J, 2011. *Study on start-up characteristics of loop heat pipe under low-power,* International Journal of Heat and Mass Transfer 54, 1002–1007.

Wang Z, Yi L and Gao F, 2009. *Night ventilation control strategies in office buildings*. Solar Energy;8 3:1902–13.

Weather History for Doha, Qatar, (Online) 2012, (Cited December 4, 2012) Available from: http://www.wunderground.com/history/airport/OTBD/2012/6/21/DailyHistory.html

Wei H and Hongjun Y, 2010. *Recovery energy from the seperated and gravity type of heat pipe exchanger in China,* Journal of Petroleum and Gas Engineering, Vol. 2 (1) 1-6

Welty J, Wicks C, Wilson R and Rorrer G, 2007. *Fundamentals of Momentum, Heat and Mass Transfer,* Fifth Edition, John Wiley & Sons, Inc., 111 River Street, Hoboken, USA

Wong SC, Lin YC, Liou JH, 2011. *Visualization and evaporator resistance measurement in heat pipes charged with water, methanol or acetone,* International Journal of Thermal Sciences, 52, 154-160

Wu XP, Mochizuki M, Mashiko K and Nguyen T, 2011. *Cold energy storage systems using heat pipe technology for cooling data centres,* Frontiers in Heat Pipes, 2, 013005

Yang H, Khandekar S and Groll M, 2008. *Operational limit of closed loop pulsating heat pipes,* Applied Thermal Engineering 28, 49–59.

Yau YH and Ahmadzadehtalatapeh M, 2010. *A review on the application of horizontal heat pipe heat exchangers in air conditioning systems in the tropics,* Applied Thermal Engineering 30, 77–84.

Yau YH and Foo YC, 2011. *Comparative study on evaporator heat transfer characteristics of revolving heat pipes filled with R134a, R22 and R410A,* International Communications in Heat and Mass Transfer, 38, 202-211

Yau YH, 2008. *The heat pipe heat exchanger: a review of its status and its potential for coolness recovery in tropical buildings,* Building Serv. Eng. Res. Technol. 29,4, 291–310

Yodrak L, Rittidech S, Poomsa-ad N and Meena P, 2010. *Waste Heat Recovery by Heat Pipe Air-Preheater to Energy Thrift from the Furnace in a Hot Forging Process,* American Journal of Applied Sciences 7, 675-681

Zhang J, Diao, YH, Tang X, Yu WJ and Wang S, 2013. Experimental study on the heat recovery characteristics of a new-type flat micro-heat pipe array heat exchanger using nanofluid, Energy Conversion and Management 75, 609-616

Zhang L, Du W, Wu J, Li Y and Xing Y, 2012. *Fluid flow characteristics for shell side of double-pipe heat exchanger with helical fins and pin fins,* Experimental Thermal and Fluid Science 36, 30-43

Zhao X, Yang S, Duan Z and Riffat SB, 2009. *Feasibility study of a novel dew point air conditioning system for China building application.* Building and Environment; 44:1990–9

List of Abbreviations

CFD	Computational Fluid Dynamics
COP	Coefficient of Performance
EEB	Energy Efficiency in Buildings
FPHP	Flat Pipe Heat Pipe
GCC	Gulf Cooperation Council
IEA	International Energy Agency
IPCC	Intergovernmental Panel on Climate Change
LHP	Loop Heat Pipe
MHP	Micro Heat Pipe
NREL	National Renewable Energy Laboratory
PCM	Phase Change Material
SIMPLE	Semi-Implicit Method for Pressure Linked Equations
WBCSD	World Business Council for Sustainable Development

Appendix A
Wind Tunnel Calculations

A.1 Introduction

A wind tunnel is a research tool designed and constructed to visualise and study the effects of controlled fluid flow over and around objects. In order to avoid high expenditures of full-scale testing, scaled wind tunnels are utilised to study the airflow around structures. The principle components for manufacture of a wind tunnel include the contraction, the test section and the diffuser section. The contraction section is used to ensure the uniform passage of flow into the test section. The test section is the chamber in which observations and measurements are made and its shape and size is principally determined by the testing requirements. Simple test section designs are of rectangular or square cross-section. Diffusers are chambers that expand along their length, allowing fluid pressure to increase with decreasing fluid velocities. Each wind tunnel is designed according to the available working space in order to suit a certain application. The pressure loss from each section defines the forces that need to be overcome in order to supply the required set-point velocity in the test-section. The following sections describe the losses associated with each section of the closed-loop wind tunnel.

A.2 The test section

The test-section is a closed chamber measuring 500mm x 500mm with a length of 1,000mm.

Area of test-section (mm^2)	250,000
Height of test-section (mm)	500
Length of test-section (mm)	1,000

Hydraulic diameter (D_H) = $\frac{4wh}{4w}$ = 0.5m

Cross-section of wind tower specimen = 150x150x150mm

Initial conditions:

Density of air at 60°C = 1.067kg/m^3

Kinematic viscosity =18.9x10^{-6}m^2/s

Velocity in the test-section = 10m/s

$R_e = \frac{\mathrm{v} \times D_H}{v}$ $\therefore R_e = \frac{10 \times 0.5}{18.9 \times 10^{-6}} = 264 \times 10^3$

$Q_{air} = \left(A_{test} - A_{specimen}\right) \times v \therefore Q_{air} = (0.25 - 0.0225) \times 10 = 2.28 m^3/s$ *(8,208m^3/hr)*

Pressure loss coefficient, $k = 1 - \frac{A_{specimen}}{A_{test}}$ $\therefore k = 1 - \frac{0.0225}{0.25} = 0.91$

Test-section pressure loss, $h = k \times \frac{v^2}{2g}$ $\therefore h = 0.91 \times \frac{10^2}{2(9.81)} = 4.64m$

A.3 The diffuser section

The equivalent cone angle for the diffuser is selected as 8° while the area ratio is kept at 3 which is under the typical guidelines *(Barlow JB, Rae WH Jr., Pope A, Low-speed wind tunnel testing, 3rd edition, 1999, Wiley-Interscience publication, ISBN-0-471-55774-9, USA, Mehta RD, Bradshaw P, Design rules for small low speed wind tunnels, Aeronautical Journal, Paper No. 718, 1979).*

Area of diffuser inlet (mm^2)	250,000
Area of diffuser outlet (mm^2)	700,000
Height of diffuser inlet (mm)	500.0
Height of diffuser outlet (mm)	700.0
Diffuser area ratio	3.0
Cone angle ° (diffuser)	8.0

Pressure loss coefficient *(k)* at an angle of 8° with an area ratio of 3 = 0.445 (interpolated value)

Velocity at diffuser, $v_{diffuser} = \frac{Q}{A}$ $\therefore v_{diffuser} = \frac{2.28}{0.70} = 3.26 m/s$

Diffuser section pressure loss, $h = k \times \frac{v^2}{2g}$ $\therefore h = 0.445 \times \frac{3.26^2}{2(9.81)} = 0.24m$

A.4 The contraction section

The contraction area ratio is kept at 6 which is under the typical values under the guidelines ranging from 6-10 *(Barlow JB, Rae WH Jr., Pope A, Low-speed wind tunnel testing, 3rd edition, 1999, Wiley-Interscience publication, ISBN-0-471-55774-9, USA).*

Area of contraction inlet (mm^2)	1,000,000
Area of contraction outlet (mm^2)	250,000
Length of contraction (mm)	882.0
Height of contraction inlet (mm)	1,000.0
Contraction area ratio	4.0
Contraction curvature ratio	0.0

Using venturi flow equation, diffuser pressure loss can be written as:

$$P_{in} - P_{out} = \frac{1}{2}\rho v_{out}^2 = \rho v_{in}^2$$

From continuity, outlet velocity can be substituted out of the above equation as:

$$\Delta P = \frac{1}{2}\rho v_{in}^2 \left[\left(\frac{A_{in}}{A_{out}}\right)^2 - 1\right]$$

Velocity at contraction, $v_{contraction} = \frac{Q}{A}$ $\therefore v_{contraction} = \frac{2.28}{1.0} = 2.28m/s$

$$\therefore \Delta P = \frac{1}{2}1.067 \times 2.28^2[(4)^2 - 1] = 41.6Pa$$

Contraction section pressure loss, $h = \frac{P}{\rho g}$ $\therefore h = \frac{41.6}{1.067 \times 9.81} = 3.97m$

A.5 Upstream and downstream horizontal sections

The upstream straight duct is a rectangular duct measuring 1000 x 700mm with a length of 1,631mm.

Length of the duct (mm)	1,631
Area of the duct (mm^2)	700,000

Velocity at upstream straight duct, $v_{upduct} = \frac{Q}{A}$ $\therefore v_{upduct} = \frac{2.28}{0.7} = 3.26m/s$

Upstream straight duct pressure loss, $h = k \times \frac{v^2}{2g}$ $\therefore h = 1 \times \frac{3.26^2}{2(9.81)} = 0.54m$

The downstream straight duct is a rectangular duct measuring 1000 x 700mm with a length of 1,613mm.

Length of the duct (mm)	1,613
Area of the duct (mm^2)	700,000

Velocity at upstream straight duct, $v_{upduct} = \frac{Q}{A}$ $\therefore v_{upduct} = \frac{2.28}{0.7} = 3.26m/s$

Upstream straight duct pressure loss, $h = k \times \frac{v^2}{2g}$ $\therefore h = 1 \times \frac{3.26^2}{2(9.81)} = 0.54m$

A.6 Upstream and downstream vertical sections

The upstream vertical duct is a rectangular duct measuring 1000 x 700mm with a length of 951mm.

Length of the duct (mm)	951
Area of the duct (mm^2)	700,000

Velocity at upstream straight duct, $v_{upduct} = \frac{Q}{A}$ $\therefore v_{upduct} = \frac{2.28}{0.7} = 3.26m/s$

Upstream straight duct pressure loss, $h = k \times \frac{v^2}{2g}$ $\therefore h = 1 \times \frac{3.26^2}{2(9.81)} = 0.54m$

The downstream vertical duct is a rectangular duct measuring 1000 x 700mm with a length of 801mm.

Length of the duct (mm)	801
Area of the duct (mm^2)	700,000

Velocity at upstream straight duct, $v_{upduct} = \frac{Q}{A}$ $\therefore v_{upduct} = \frac{2.28}{0.7} = 3.26m/s$

Upstream straight duct pressure loss, $h = k \times \frac{v^2}{2g}$ $\therefore h = 1 \times \frac{3.26^2}{2(9.81)} = 0.54m$

A.7 First corner

The first corner is designed to achieve flow uniformity upstream to the vertical duct. The height was 700m and width of this corner was 1,000mm generating a cross-section area of 490,000 mm^2. Radius of the corner was 200mm.

Outer radius (mm)	200
Ratio of height to width	1.4
Ratio of radius to width	0.3

Pressure loss coefficient for elbow *(Cp)* = 0.65 (table value)

Angle correction factor *(Af)* = 1.00 (table value) since its 90 degrees bend

Pressure loss coefficient in the contraction corner *(k)* $= 0.65 \times 1 = 0.65$

Velocity at first corner, $v_{fircorner} = \frac{Q}{A}$ $\therefore v_{fircorner} = \frac{2.28}{0.7} = 3.26m/s$

Upstream straight duct pressure loss, $h = k \times \frac{v^2}{2g}$ $\therefore h = 0.65 \times \frac{3.26^2}{2(9.81)} = 0.35m$

A.8 Second corner

The second corner was created to direct air flow around the bend upstream of the contraction section. Furthermore, it also acts as the settling chamber to regain pressure. The height was 700m and width of this corner was 1,000mm generating a cross-section area of 490,000 mm^2.

Outer radius (mm)	200
Ratio of height to width	1.4
Ratio of radius to width	0.3

Pressure loss coefficient for elbow *(Cp)* = 0.65 (table value)

Angle correction factor *(Af)* = 1.00 (table value) since its 90 degrees bend

Pressure loss coefficient in the contraction corner *(k)* $= 0.65 \times 1 = 0.65$

Velocity at first corner, $v_{seccorner} = \frac{Q}{A}$ $\therefore v_{seccorner} = \frac{2.28}{0.7} = 3.26m/s$

Upstream straight duct pressure loss, $h = k \times \frac{v^2}{2g}$ $\therefore h = 0.65 \times \frac{3.26^2}{2(9.81)} = 0.35m$

A.9 Third corner

The third corner was created to direct air flow around the bend downstream of the diffuser section. The height was 700m and width of this corner was 1,000mm generating a cross-section area of 490,000 mm^2.

Outer radius (mm)	200
Ratio of height to width	1.4
Ratio of radius to width	0.3

Pressure loss coefficient for elbow *(Cp)* = 0.65 (table value)

Angle correction factor *(Af)* = 1.00 (table value) since its 90 degrees bend

Pressure loss coefficient in the contraction corner *(k)* $= 0.65 \times 1 = 0.65$

Velocity at first corner, $v_{thicorner} = \frac{Q}{A}$ $\therefore v_{thicorner} = \frac{2.28}{0.7} = 3.26m/s$

Upstream straight duct pressure loss, $h = k \times \frac{v^2}{2g}$ $\therefore h = 0.65 \times \frac{3.26^2}{2(9.81)} = 0.35m$

A.10 Fourth corner

The fourth corner is designed to achieve flow uniformity downstream to the horizontal duct. The height was 700m and width of this corner was 1,000mm generating a cross-section area of 490,000 mm^2.

Outer radius (mm)	200
Ratio of height to width	1.4
Ratio of radius to width	0.3

Pressure loss coefficient for elbow *(Cp)* = 0.65 (interpolated value)

Angle correction factor *(Af)* = 1.00 (table value) since its 90 degrees bend

Pressure loss coefficient in the contraction corner *(k)* $= 0.65 \times 1 = 0.65$

Velocity at first corner, $v_{foucorner} = \frac{Q}{A}$ $\therefore v_{foucorner} = \frac{2.28}{0.7} = 3.26m/s$

Upstream straight duct pressure loss, $h = k \times \frac{v^2}{2g}$ $\therefore h = 0.65 \times \frac{3.26^2}{2(9.81)} = 0.35m$

A.11 Guide vanes

The guide vanes were added to the corner to enhance the flow around the 90 degrees bend. The radius of the vanes along with the spacing between each vane was 100mm. The total numbers of vanes were 9 on the 1st, 3rd and 4th bend while the 2nd bend had 11 vanes. The k value was interpolated from the guide vane pressure loss coefficient table at 0.3.

Velocity at first corner, $v_{fircorner} = \frac{Q}{A}$ $\therefore v_{fircorner} = \frac{2.28}{0.7} = 3.26m/s$

Guide vanes pressure loss, $h = k \times \frac{v^2}{2g}$ $\therefore h = 0.3 \times \frac{3.26^2}{2(9.81)} = 0.16m$

A.12 Annular inlet

The annular outlet connects the downstream horizontal duct to the fan. The height and width of the cut was 700mm by 1000mm and the fan mouth diameter is taken as 650mm.

$$\Delta P = \frac{Q^2 \rho \left[1 - \frac{A_2}{A_1}^2\right]}{2A_2^2}$$

$$\Delta P = \frac{2.28^2 \times 1.22[1 - 0.6^2]}{2 \times 0.18} = 11.27Pa \approx 0.94m$$

A.13 Annular outlet

The annular outlet connects the downstream horizontal duct to the fan. The height and width was 700mm by 1000mm and the fan mouth diameter is taken as 650mm.

$$k = \frac{1}{AR^2} - 1 + k_d$$

$$\sigma = \frac{A_2}{A_1} \qquad AR = \frac{1}{\sigma} \qquad k_d = 1 - c_p$$

Therefore *AR=1.6* and k_d*=0.7*. The loss coefficient *(k)* = 0.09

Velocity at upstream straight duct, $v_{upduct} = \frac{Q}{A}$ $\quad \therefore v_{upduct} = \frac{2.28}{0.7} = 3.26m/s$

Annular outlet pressure loss, $h = k \times \frac{v^2}{2g}$ $\quad \therefore h = 0.09 \times \frac{3.26^2}{2(9.81)} = 0.05m$

A.14 Total head loss summary

Duct section	**Velocity (m/s)**	**Pressure loss coefficient**	**Pressure head loss with guide vane (m)**
First corner	3.26	0.65	0.35
Upstream horizontal duct	3.26	1.0	0.54
Upstream vertical duct	3.26	1.0	0.54
Downstream horizontal duct	3.26	1.0	0.54
Downstream vertical duct	3.26	1.0	0.54
Second corner	3.26	0.65	0.35
Contraction	2.28	-	3.97
Test section	10.0	0.91	4.64
Diffuser	3.26	0.445	0.24
Third corner	3.26	0.65	0.35
Fourth corner	3.26	0.65	0.35
Guide vanes	3.26	0.30	0.16
Annular inlet	-	-	0.05
Annular outlet	3.25	0.09	0.94
Total pressure head loss (m)			**13.4**
Total pressure head loss (Pa)			**140.1**

Appendix B
Wind Tunnel CFD Modelling

B.1 Introduction

The commercial ANSYS Fluent 14.0 numerical code was used for predicting the flow, pressure, turbulence and temperature profiles inside the subsonic wind tunnel. The analytical model for estimating the pressure losses were directed as input boundary conditions for the CFD model. The steady-state simulations were conducted using the *k-e* turbulence model. An attempt was made to combine the advantages of a structured (superior accuracy near wall boundaries) with those of an unstructured grid at the other sections of the domain to minimize the computational expense. Sections of the wind tunnel that were of simple geometry such as the horizontal and vertical duct work were meshed with structured prismatic mesh. In the sections of complex geometry such as the diffuser, test section and in the areas of the guiding vanes, tetrahedral/mixed-mode cells are used. The patch independent mesh algorithm for tetrahedron elements is based on the subsequent spatial subdivision algorithm which ensures refinement of the mesh where essential, but retains larger elements where feasible, therefore allowing faster computing times.

B.2 Grid generation and verification

The complete meshed model comprised of 768,655 nodes and 4,245,896 elements. Modelling the flow conditions in the entire wind tunnel requires more effort than only modelling the flow in the test section. The grid resolution was determined taking into account an acceptable value of wall y^+ (average value of 222), the cell equiangle skewness (average value of 0.38) and the cell equivolume skewness (average value of 0.39). A very high mesh resolution was applied at the walls of the turning vanes at all four corners where a mixed grid was used in order to increase the accuracy of capturing the flow passing through. Figure B.1 displays the complete meshed model alongside the areas of refinement.

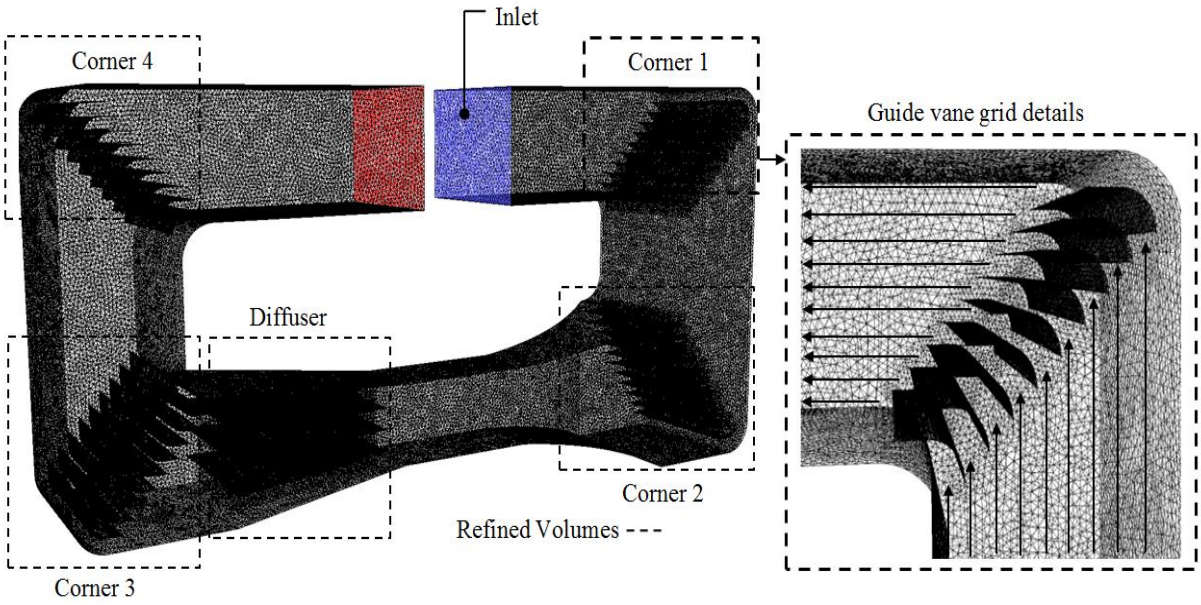

Figure B.1 Grid design highlighting areas of refinement

Grid verification was carried out using the *h*–method in order to optimise the distribution of mesh size *h* over a finite element with a posterior error indicator. Average velocity and static pressure in the test-section were taken as error indicators as the grid was refined from 1,622,108 to 7,149,235 elements. The grid was evaluated and refined until the posterior estimate error becomes insignificant between the number of nodes and elements, computational iterations and the posterior error indicator. The discretisation error was found to be the lowest at over 7 million cells for both indicated variables. In order to achieve a balance between accuracy and computational times, the element sizing of 0.025 was selected.

Figure B.2 displays the posterior error percentage for average velocity and static pressure in the test-section at increasing grid sizes. The maximum error for average velocity was recorded 4.38%. The errors between variables reduced as the grid was refined and dropped to below 1% for average velocity at the element sizing of 0.025 respectively.

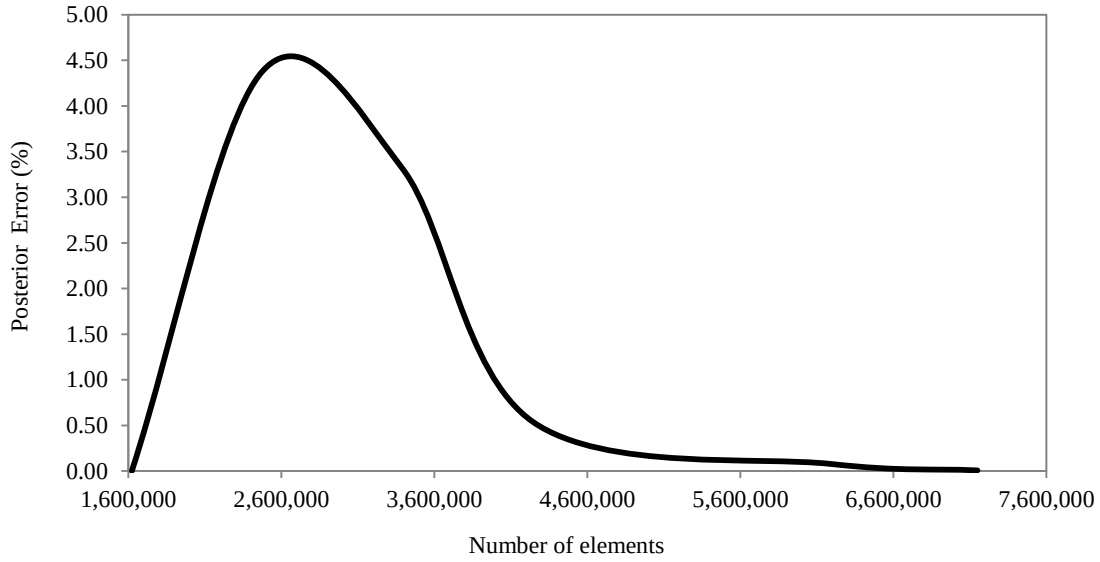

Figure B.2 Posterior error on the average velocity in the test-section using h-p grid adaptation method

A pressure of 140Pa was applied at the inlet from the fan in order to overcome the overall loss from the wind tunnel as identified. Standard wall functions were used with a roughness constant (CKS) of 0.5 applied on the walls. Pressure–velocity coupling was achieved using the SIMPLEC algorithm. The QUICK discretisation scheme and second-order pressure interpolation was used to achieve higher accuracy of the solutions and as recommended from literature.

B.3 Pressure and velocity profiles

The numerical simulation was carried out on the empty wind tunnel to determine the flow characteristics. Figure B.3 displays the static pressure contours across the cross-section of the wind tunnel. At an applied inlet pressure of 140Pa from the fan, the average static pressure in the test-section was estimated at -2.8Pa due to the high velocity. A static pressure drop of 27% was observed after corner 1 upstream of the contraction section where the pressure reduced to 103Pa. The pressure increased to 54Pa at the end of the diffuser which was located downstream of the test-section. In total, the decrease in static pressure was found to be 91.2% from supply to recovery. The recovered pressure after corner 4 was 13Pa which was then fed back to the axial fan in order to re-start the wind-tunnel cycle.

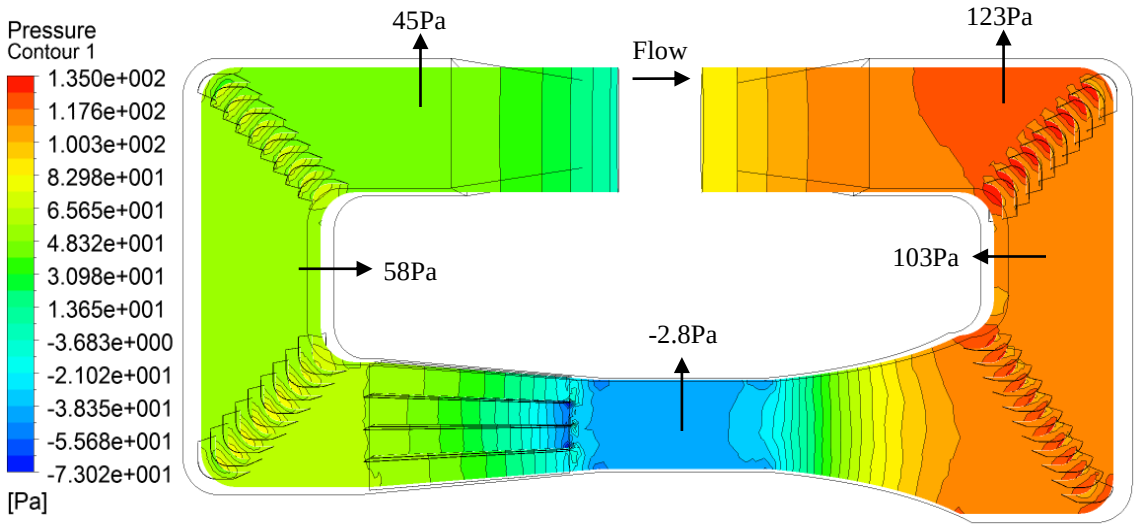

Figure B.3 Static pressure contour of a cross sectional plane in the wind tunnel

With respect to B.4, the air velocity profile in the X (horizontal) direction within the top plane of an empty wind tunnel is depicted. At an inlet pressure of 140Pa from the fan, the mean velocity variation within the test-section was 2.5%.

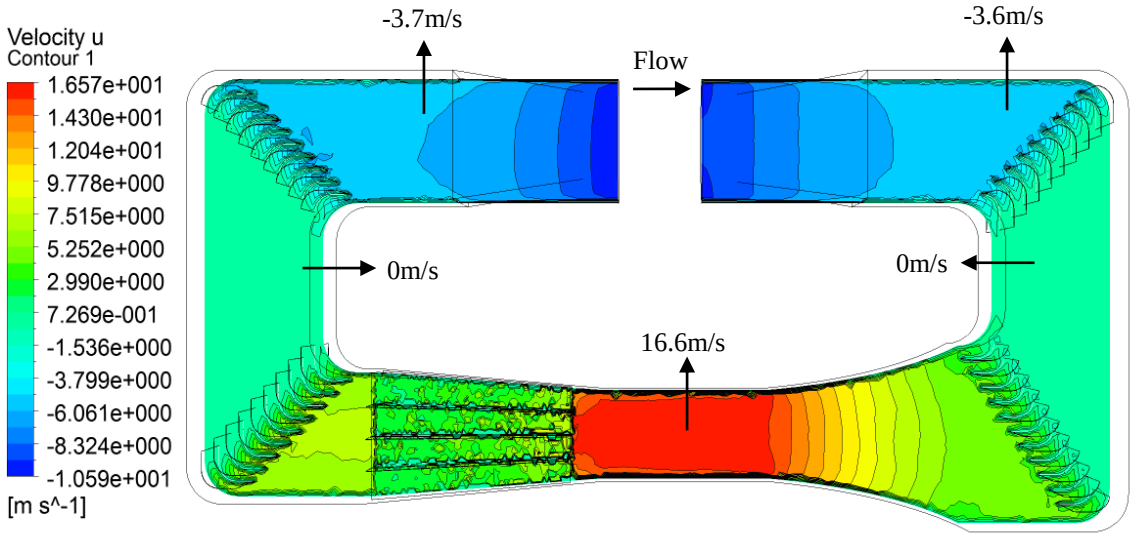

Figure B.4 Velocity contour in the X (horizontal) direction in the wind tunnel

The average velocity in the test-section was recorded at 16.1m/s. An increase in mean velocity from 3.9m/s to 16.6m/s was observed from the contraction to the test-section, highlighting an increase factor of approximately 4 and thereby confirming the correct operation of the contraction section. It was observed that the velocity was increased after the contraction section and was subsequently reduced as it passed through the guide vanes installed in the diffuser section. The 90° turning vanes located at all four

corners aided in reducing the re-circulation of the flow at the bends as there was no velocity rotation in the horizontal axis between corners 1 and 2 and between corners 3 and 4.

The velocity profile across the plane in the Z (vertical) direction is indicated in B.5. As observed, the velocity values were negative between corners 1 and prior to the contraction section highlighting that the movement of the flow particles were in the downward direction. On the other side, the highest recorded values of the velocities were observed between corners 3 and 4 thereby depicting that the entire movement of the flow particles was in the upward direction. The minimum and maximum velocity values were recorded at -6.31m/s (between corners 1 and 2) and 6.28m/s (between corners 3 and 4). As expected, the values of the velocity contours in the test-section were approximately 0m/s, thereby suggesting that no rotational velocity sites were created in the test-section.

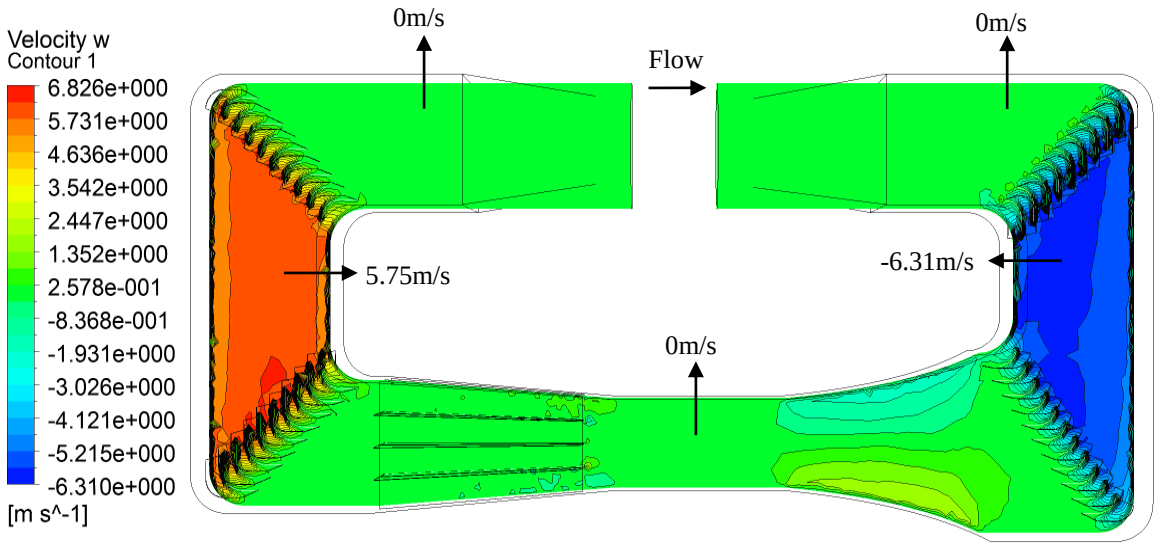

Figure B.5 Velocity contour in the Z (vertical) direction in the wind tunnel

Velocity contours at the inlet and outlet of the test-section are displayed in Figure B.6. The uniformity of the velocity is highlighted by taking the mean values of both planes. The area averaged mean velocity recorded at the inlet plane was 13.72m/s while the outlet plane recorded 13.71m/s respectively. The difference from inlet to outlet was therefore 0.01m/s. The mean values of the velocities were smaller compared to the free-stream due to the effects of the wall. However, it can be observed from the figure that

the wall effects across both planes are similar thereby indicating that the velocity pattern across the entire length of the test-section is uniform.

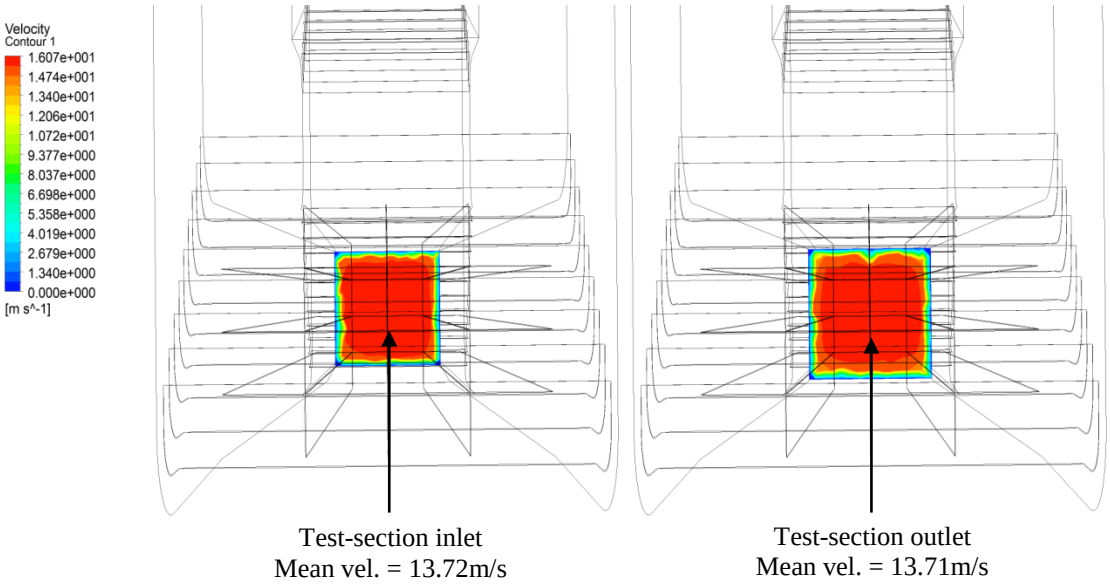

Figure B.6 Velocity contours at the inlet and outlet of the test-section

Figure B.7 illustrates the three-dimensional view of the velocity streamlines in the cross-sectional plane for the entire empty wind tunnel.

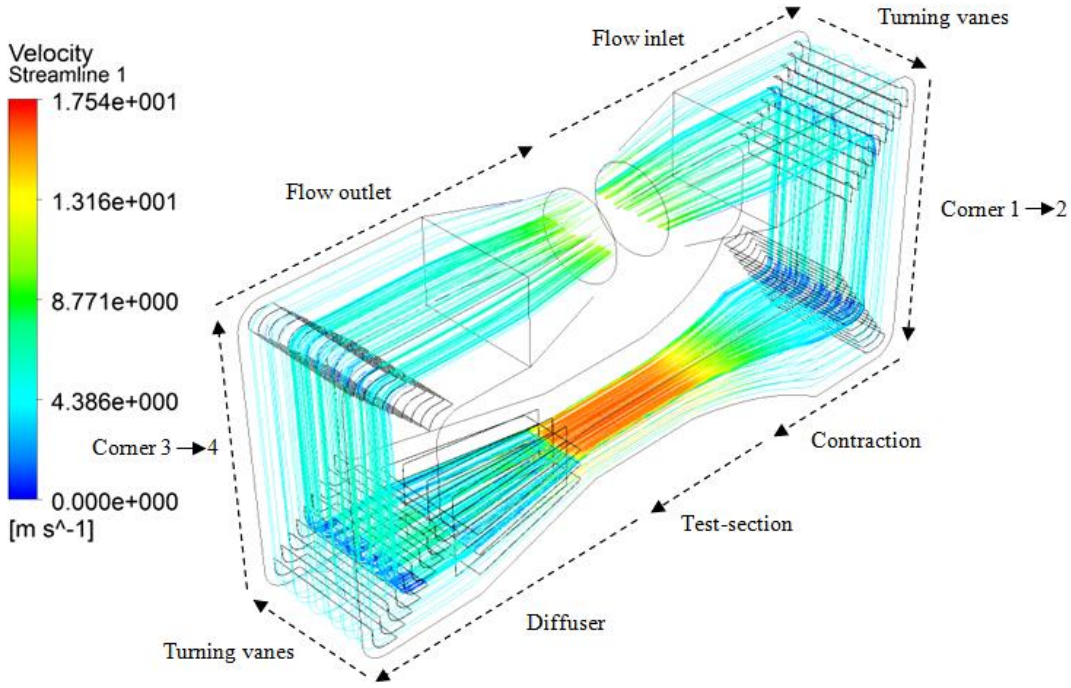

Figure B.7 Velocity streamlines of a cross sectional plane in the wind tunnel

The formation of velocity rotations were eliminated by adding turning vanes to all four 90° corners. The effect of the turning vanes fitted with leading and trailing edges is evident as it significantly decreased the areas of high re-circulations or eddy formations both upstream and downstream of the four corners. The horizontal and vertical guide vanes in the diffuser aided in reducing the re-circulation and further improving the flow in the diffuser section.

B.4 Turbulence and temperature profiles

The turbulence intensity across the frontal plane of the wind tunnel is displayed in Figure B.8. The maximum region of turbulence was found close to the walls with the maximum turbulence value recorded at 5.19%. However, the mean turbulence in the test-section was calculated at 1.29%. The purpose of carrying out the CFD simulations was to ensure accurate flow and turbulence characterization of the wind tunnel prior to manufacturing. Since the numerical investigation was carried out prior to the installation of the honeycomb section, the turbulence values were expected to have a reduction to below 1% after the addition of the flow straightener, which will be discussed in the following section.

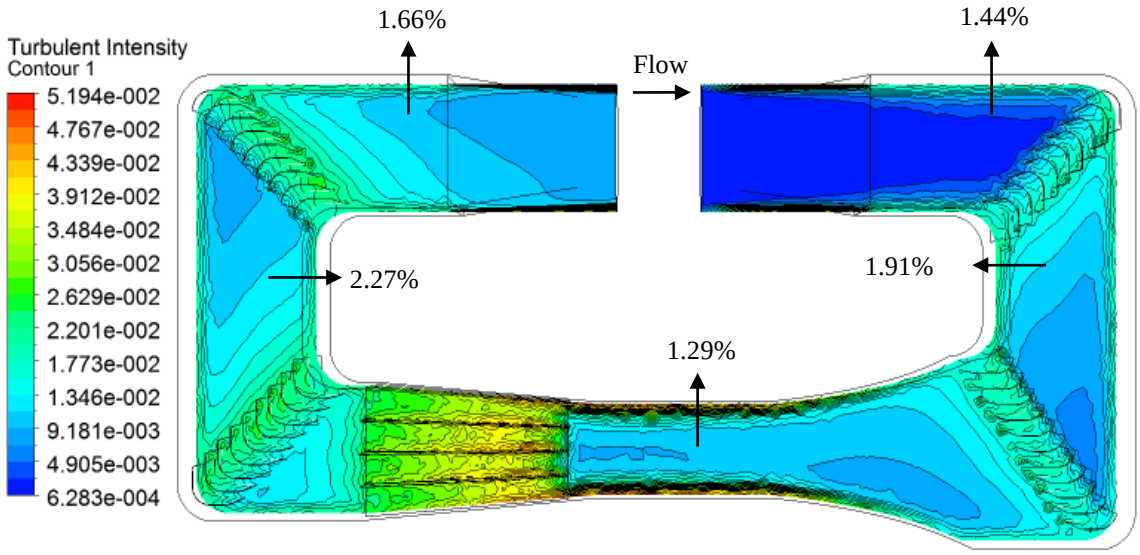

Figure B.8 Turbulence intensity across the frontal plane of the wind tunnel

Thermal profiles across the wind tunnel were further determined in order to depict the thermal stratification in the test-section. Figure B.9 displays the temperature contours at an inlet temperature of 323K or 50°C across the frontal plane. The total rise in temperature from the inlet was 0.15K achieved due to shear from the walls and turning vanes. Temperature stratification effects in the test-section were depicted although the general profile across the section was linear.

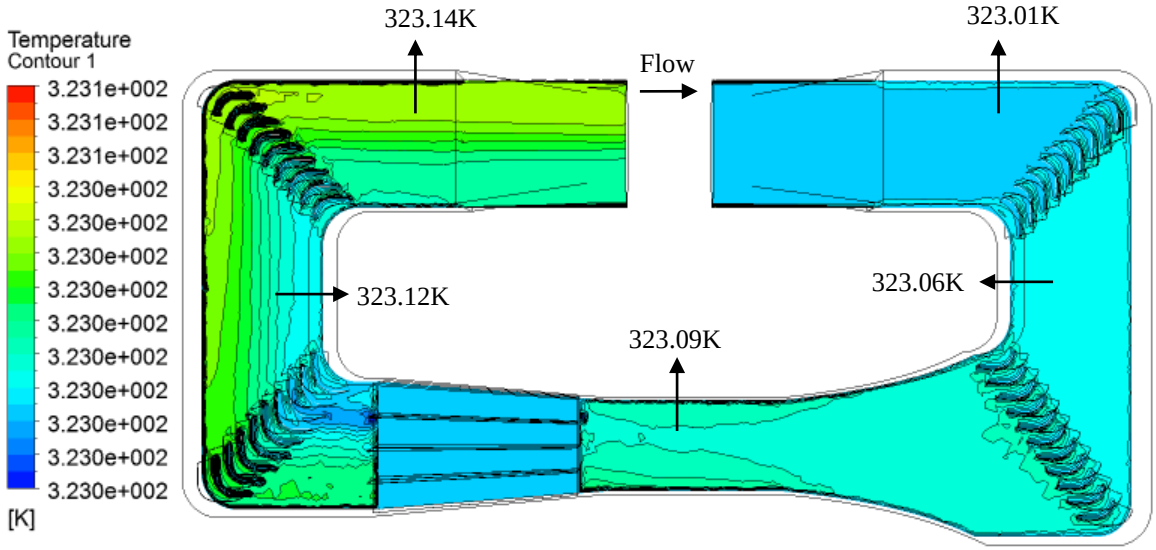

Figure B.9 Temperature distributions across the frontal plane of the wind tunnel

Furthermore, inlet temperature in the wind tunnel was varied starting from the 20°C under ambient conditions and will increased up to 50°C. The wall effects on temperature distribution in the test-section are highlighted in Figure B.10.

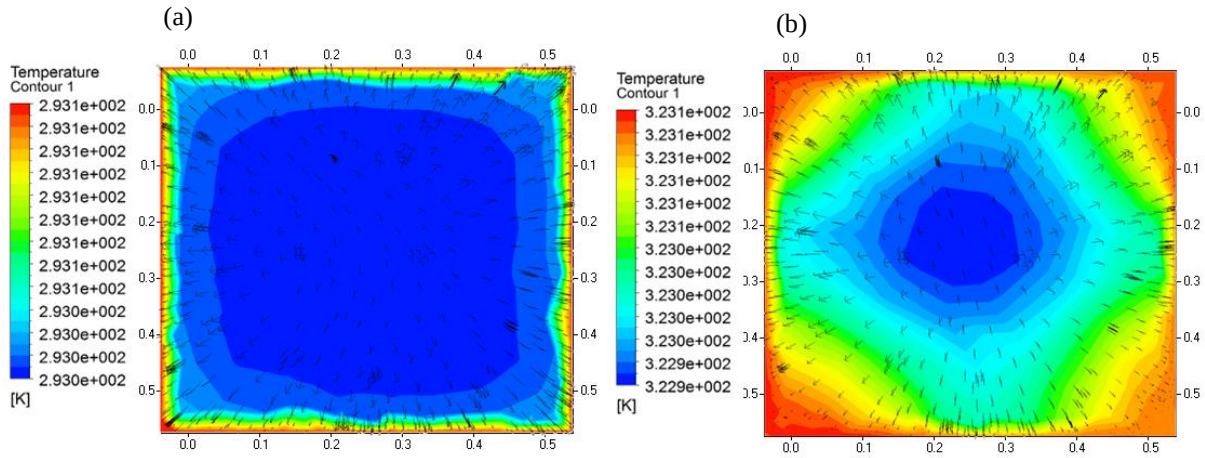

Figure B.10 Temperature distribution in the test-section at: (a) 293K or 20°C (b) 323K or 50°C

It was imperative to note that the thermal boundary layer was lower when the inlet temperature was 20°C while thermal stratification effects were greater when the inlet temperature was increased to 50°C. However, the overall variations in both cases were under 0.5% when the temperatures stabilised.

A graphical illustration of the comparison between CFD and experimentally obtained air velocities is displayed in Figure B.11. On average, the CFD predicted test-section velocity values depicted an increase of 1.1m/s in comparison to the experiments. The variation in velocity using the CFD predicted findings was calculated at 2.52% with a difference of 0.41m/s between the highest and lowest recorded value. The experimental tests showed lower consistency in results with a variation of 6.56% between the highest and lowest measured value of the velocity and a difference of 0.96m/s between the highest and lowest recorded value of the respective. The non-uniformity and turbulence intensity in the test-section was however reduced to acceptable values after the addition of the honeycomb and screen section as discussed in the earlier section.

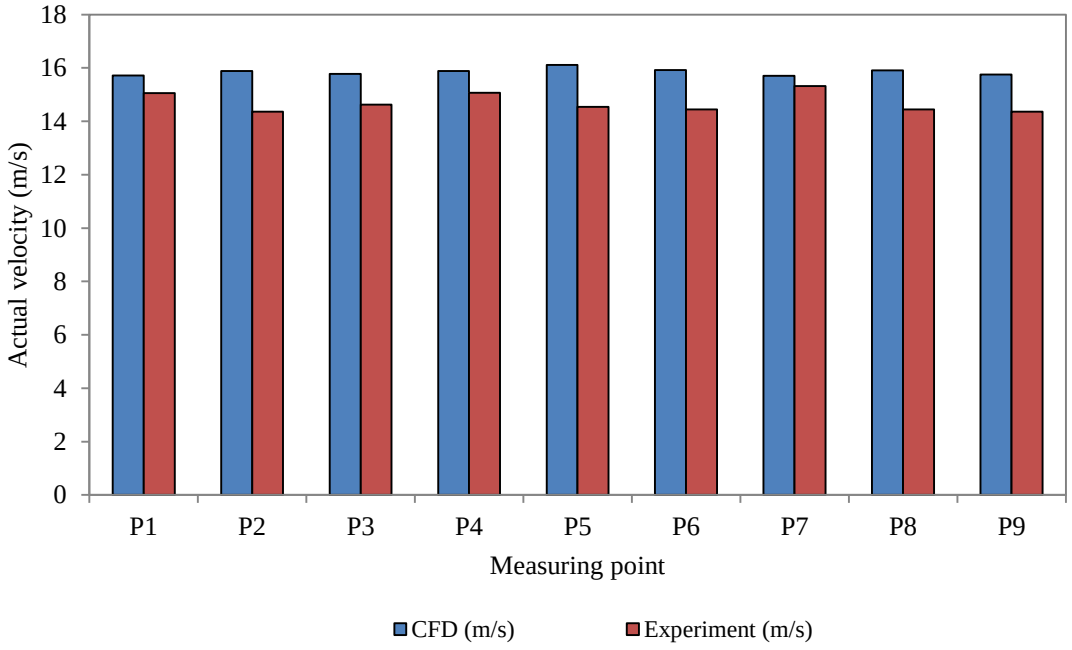

Figure B.11 Comparison between CFD and experimentally obtained air velocities

Appendix C
Wind Tunnel Calibration

C.1 Pressure data sheet

CLOSED-LOOP WIND TUNNEL - BUILDING SERVICES LAB, SCHOOL OF CIVIL ENGINEERING, UNIVERSITY OF LEEDS

TEST-SECTION ACTUAL PRESSURE (Pa) READINGS

Vertical Orientation	Frequency (Hz)	Inlet (left)	Inlet (centre)	Inlet (right)	Cl (left)	Cl (centre)	Cl (right)	Centre (left)	Centre (centre)	Centre (right)	CO (left)	CO (centre)	CO (right)	Outlet (left)	Outlet (centre)	Outlet (right)	Variation	Mean (Pa)
125mm	10.0	4.30	4.00	4.30	4.10	4.00	4.10	4.10	4.00	4.00	4.10	4.00	4.10	4.40	4.50	4.30	2.47%	4.056
250mm	10.0	4.20	4.10	4.30	4.20	4.10	4.00	4.10	4.10	4.20	4.30	4.20	4.10	4.50	4.40	4.10	7.24%	4.144
375mm	10.0	4.40	4.10	4.30	4.20	4.30	4.20	4.20	4.20	4.20	4.20	4.30	4.60	4.50	4.40	4.20	9.37%	4.267
125mm	20.0	18.70	18.00	18.20	18.60	18.30	18.70	18.60	18.20	18.40	18.50	18.40	18.90	17.10	18.60	19.80	3.78%	18.511
250mm	20.0	18.90	18.00	18.20	18.80	18.20	18.50	18.70	18.50	18.60	18.70	18.40	18.80	18.20	18.40	19.90	3.23%	18.578
375mm	20.0	19.30	18.70	19.00	19.40	18.90	18.90	19.20	18.80	19.00	19.40	18.90	19.30	19.60	19.40	20.80	3.14%	19.089
125mm	30.0	39.90	38.30	39.10	38.90	38.50	38.50	38.60	38.00	38.80	39.30	38.10	38.80	39.50	39.90	41.10	3.37%	38.611
250mm	30.0	40.10	38.10	39.70	39.90	38.60	39.30	39.90	38.80	39.70	39.80	39.20	39.80	39.40	39.80	42.80	3.30%	39.444
375mm	30.0	41.10	39.50	40.10	40.80	40.00	40.30	40.70	39.60	40.10	41.10	40.60	40.70	42.60	40.80	43.70	3.71%	40.433
125mm	40.0	68.30	65.90	68.20	68.80	66.20	67.90	68.40	67.60	68.00	68.50	67.30	68.80	62.10	66.90	69.80	3.83%	67.944
250mm	40.0	68.90	65.60	67.20	68.90	66.50	68.30	69.00	68.80	68.10	68.80	67.80	69.20	67.50	67.60	71.80	3.95%	68.378
375mm	40.0	70.10	65.80	69.20	69.40	69.20	68.40	69.80	69.60	69.40	70.40	69.40	69.60	72.50	72.70	75.10	2.88%	69.467
125mm	50.0	104.00	98.40	103.00	101.00	100.00	102.00	101.00	100.00	101.00	102.00	99.00	104.00	99.80	102.00	112.00	4.95%	101.111
250mm	50.0	106.00	97.20	101.00	104.00	101.00	103.00	103.00	101.00	102.00	103.00	101.00	105.00	101.00	104.00	110.00	3.90%	102.556
375mm	50.0	108.00	100.00	103.00	102.00	103.00	103.00	106.00	104.00	104.00	108.00	105.00	106.00	110.00	104.00	122.00	5.74%	104.556

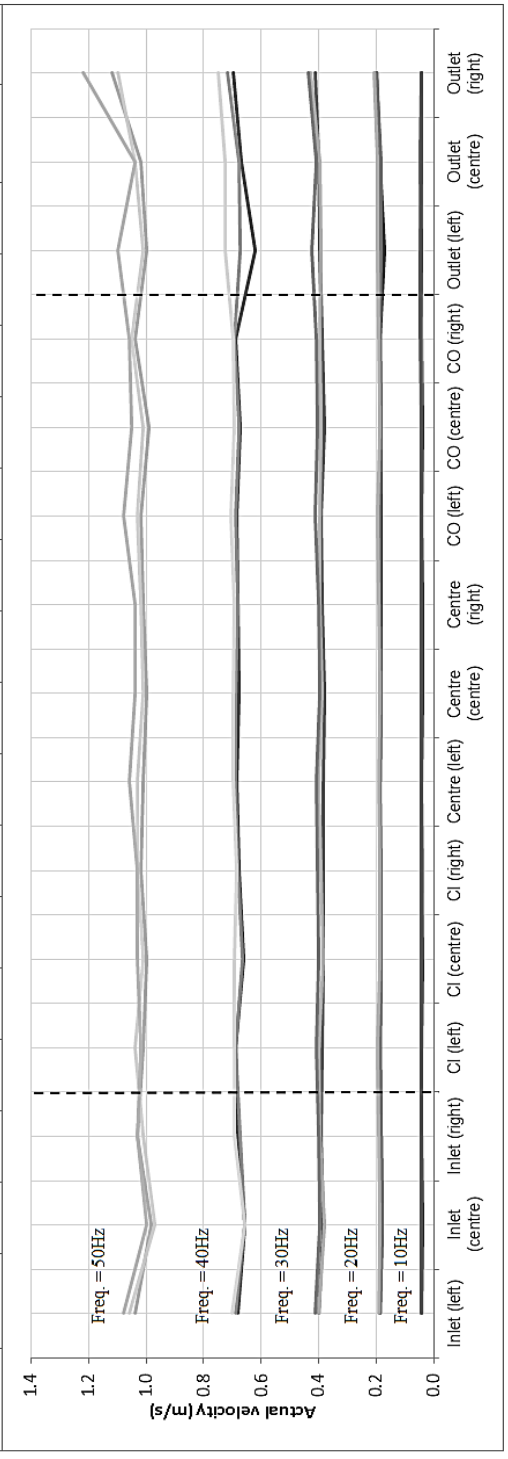

C.2 Velocity data sheet

CLOSED-LOOP WIND TUNNEL - BUILDING SERVICES LAB, SCHOOL OF CIVIL ENGINEERING, UNIVERSITY OF LEEDS

TEST-SECTION ACTUAL VELOCITY (m/s) READINGS

Vertical Orientation	Frequency (Hz)	Inlet (left)	Inlet (centre)	Inlet (right)	CI (left)	CI (centre)	CI (right)	Centre (left)	Centre (centre)	Centre (right)	CO (left)	CO (centre)	CO (right)	Outlet (left)	Outlet (centre)	Outlet (right)	Mean	Max.	Min.
125mm	10.0	2.24	2.19	2.22	2.22	2.17	2.21	2.22	2.24	2.23	2.21	2.17	2.21	1.97	2.00	2.26	2.21	2.24	2.17
		-1.41%	0.86%	-0.50%	-0.50%	1.76%	-0.05%	-0.50%	-1.41%	-0.96%	-0.05%	1.76%	-0.05%	10.81%	9.46%	-2.31%			
250mm	10.0	2.31	2.23	2.23	2.28	2.26	2.27	2.30	2.27	2.28	2.27	2.26	2.29	2.06	2.23	2.38	2.28	2.30	2.26
		-1.51%	2.00%	2.00%	-0.20%	0.68%	0.24%	-1.07%	0.24%	-0.20%	0.24%	0.68%	-0.63%	9.47%	2.00%	-4.59%			
375mm	10.0	2.36	2.30	2.31	2.36	2.32	2.33	2.36	2.32	2.36	2.39	2.36	2.38	2.16	2.39	2.43	2.35	2.39	2.32
		-0.28%	2.27%	1.84%	-0.28%	1.42%	0.99%	-0.28%	1.42%	-0.28%	-1.56%	-0.28%	-1.13%	8.22%	-1.56%	-3.26%			
125mm	20.0	4.85	4.75	4.81	4.77	4.69	4.78	4.74	4.71	4.75	4.64	4.62	4.69	4.05	4.44	4.84	4.71	4.78	4.62
		-2.97%	-0.85%	-2.12%	-1.27%	0.42%	-1.49%	-0.64%	0.00%	-0.85%	1.49%	1.91%	0.42%	14.01%	5.73%	-2.76%			
250mm	20.0	4.43	4.62	4.84	4.78	4.76	4.79	4.72	4.72	4.76	4.74	4.74	4.73	4.74	4.56	4.65	4.75	4.79	4.72
		6.72%	2.71%	-1.92%	-0.66%	-0.23%	-0.87%	0.61%	0.61%	-0.23%	0.19%	0.19%	0.40%	0.19%	3.98%	2.08%			
375mm	20.0	4.89	4.79	4.77	4.81	4.83	4.84	4.85	4.79	4.83	4.89	4.83	4.86	4.87	4.80	4.94	4.84	4.89	4.79
		-1.10%	0.96%	1.38%	0.55%	0.14%	-0.07%	-0.28%	0.96%	0.14%	-1.10%	0.14%	-0.48%	-0.69%	0.76%	-2.14%			
125mm	30.0	7.08	6.89	7.07	6.82	6.84	6.94	6.89	6.92	6.88	6.91	6.84	6.94	6.47	6.58	7.11	6.89	6.94	6.82
		-2.81%	-0.05%	-2.66%	0.97%	0.68%	-0.77%	-0.05%	-0.48%	0.10%	-0.34%	0.68%	-0.77%	6.05%	4.45%	-3.24%			
250mm	30.0	6.78	6.67	6.80	7.03	6.90	6.95	7.02	6.93	7.01	6.94	6.90	7.05	6.58	6.72	7.13	6.97	7.05	6.90
		2.73%	4.30%	2.44%	-0.86%	1.00%	0.29%	-0.72%	0.57%	-0.57%	0.43%	1.00%	-1.15%	5.60%	3.59%	-2.30%			
375mm	30.0	6.77	6.85	6.81	6.96	6.92	6.95	6.94	6.91	6.90	6.93	6.93	6.96	6.94	6.97	6.98	6.93	6.96	6.90
		2.36%	1.20%	1.78%	-0.38%	0.19%	-0.24%	-0.10%	0.34%	0.48%	0.05%	0.05%	-0.38%	-0.10%	-0.53%	-0.67%			
125mm	40.0	9.09	9.08	9.15	9.16	9.08	9.18	9.13	9.08	9.08	9.04	9.06	9.04	8.85	8.96	9.11	9.09	9.18	9.04
		0.05%	0.16%	-0.61%	-0.72%	0.16%	-0.94%	-0.39%	0.16%	0.16%	0.60%	0.38%	0.60%	2.69%	1.48%	-0.17%			
250mm	40.0	9.14	8.98	9.04	9.20	9.04	9.19	9.16	9.06	9.16	9.12	9.06	9.27	8.82	8.91	9.14	9.14	9.27	9.04
		0.00%	1.75%	1.09%	-0.66%	1.09%	-0.55%	-0.22%	0.88%	-0.22%	0.22%	0.88%	-1.42%	3.50%	2.52%	0.00%			
375mm	40.0	9.24	8.87	8.95	9.12	9.06	9.09	9.10	9.09	9.14	9.16	9.06	9.18	9.18	9.16	9.22	9.11	9.18	9.06
		-1.41%	2.65%	1.77%	-0.10%	0.56%	0.23%	0.12%	0.23%	-0.32%	-0.54%	0.56%	-0.76%	-0.76%	-0.54%	-1.20%			
125mm	50.0	11.63	11.28	11.45	11.63	11.53	11.61	11.57	11.46	11.57	11.54	11.44	11.66	10.31	11.22	11.89	11.45	11.63	11.44
		-1.55%	1.51%	0.02%	-1.55%	-0.68%	-1.38%	-1.03%	-0.07%	-1.03%	-0.76%	0.11%	-1.81%	9.98%	2.03%	-3.82%			
250mm	50.0	11.68	11.36	11.18	11.52	11.49	11.53	11.62	11.48	11.50	11.62	11.46	11.54	11.47	11.35	12.21	11.57	11.62	11.46
		-0.99%	1.78%	3.34%	0.40%	0.66%	0.31%	-0.47%	0.74%	0.57%	-0.47%	0.92%	0.22%	0.83%	1.87%	-5.57%			
375mm	50.0	11.64	11.47	11.34	11.66	11.63	11.62	11.62	11.57	11.43	11.68	11.59	11.78	11.68	11.58	11.75	11.62	11.68	11.43
		-0.17%	1.29%	2.41%	-0.34%	-0.09%	0.00%	0.00%	0.43%	1.64%	-0.52%	0.26%	-1.38%	-0.52%	0.34%	-1.12%			

C.3 Turbulence data sheet

CLOSED-LOOP WIND TUNNEL - BUILDING SERVICES LAB, SCHOOL OF CIVIL ENGINEERING, UNIVERSITY OF LEEDS

TEST-SECTION ACTUAL TURBULENCE READINGS

Vertical Orientation	Frequency (Hz)	CI (left)	CI (centre)	CI (right)	Centre (left)	Centre (centre)	Centre (right)	CO (left)	CO (centre)	CO (right)	Variation	Max.
125mm	**10.0**	0.73%	0.58%	0.67%	0.77%	0.71%	0.50%	0.76%	0.73%	0.56%	**0.67%**	**0.77%**
250mm	**10.0**	0.47%	0.60%	0.75%	0.43%	0.76%	0.97%	0.58%	0.81%	0.98%	**0.71%**	**0.98%**
375mm	**10.0**	0.96%	0.53%	0.43%	0.49%	0.46%	0.58%	0.42%	0.33%	0.44%	**0.52%**	**0.96%**
125mm	**20.0**	0.27%	0.32%	0.32%	0.43%	0.22%	0.34%	0.70%	0.45%	0.48%	**0.39%**	**0.70%**
250mm	**20.0**	0.65%	0.31%	0.24%	0.24%	0.28%	0.31%	0.44%	0.34%	0.50%	**0.37%**	**0.65%**
375mm	**20.0**	0.61%	0.26%	0.38%	0.45%	0.47%	0.69%	0.29%	0.23%	0.34%	**0.41%**	**0.69%**
125mm	**30.0**	0.28%	0.22%	0.32%	0.47%	0.33%	0.25%	0.56%	0.31%	0.49%	**0.36%**	**0.56%**
250mm	**30.0**	0.27%	0.28%	0.23%	0.35%	0.22%	0.28%	0.37%	0.17%	0.34%	**0.28%**	**0.37%**
375mm	**30.0**	0.23%	0.32%	0.51%	0.25%	0.43%	0.21%	0.20%	0.27%	0.19%	**0.29%**	**0.51%**
125mm	**40.0**	0.32%	0.23%	0.25%	0.43%	0.25%	0.32%	0.37%	0.51%	0.30%	**0.33%**	**0.51%**
250mm	**40.0**	0.22%	0.30%	0.25%	0.25%	0.17%	0.24%	0.31%	0.21%	0.16%	**0.23%**	**0.31%**
375mm	**40.0**	0.14%	0.22%	0.16%	0.24%	0.25%	0.33%	0.31%	0.34%	0.26%	**0.25%**	**0.34%**
125mm	**50.0**	0.30%	0.78%	0.38%	0.25%	0.43%	0.21%	0.20%	0.27%	0.19%	**0.33%**	**0.78%**
250mm	**50.0**	0.23%	0.26%	0.33%	0.23%	0.27%	0.37%	0.28%	0.20%	0.22%	**0.27%**	**0.37%**
375mm	**50.0**	0.30%	0.40%	0.29%	0.24%	0.36%	0.32%	0.23%	0.34%	0.17%	**0.29%**	**0.40%**

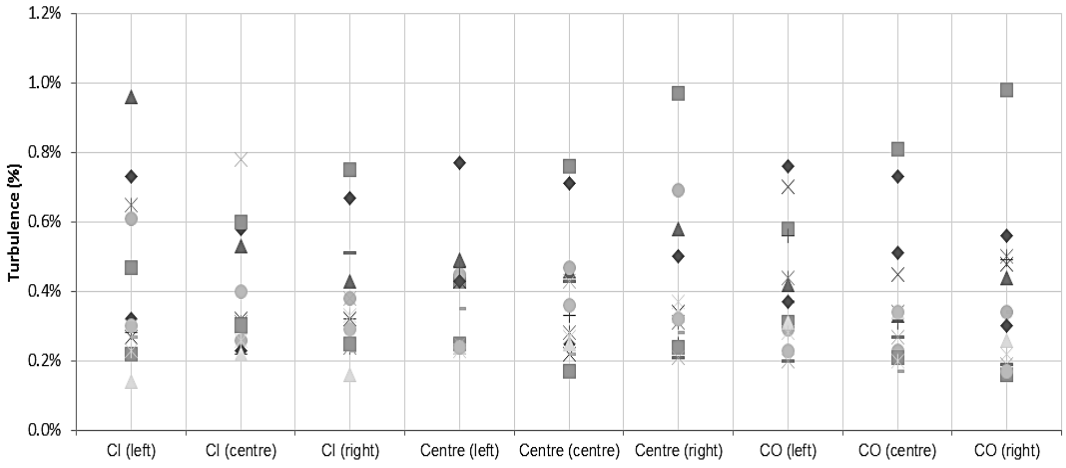

Northern Fan Supplies Ltd

Drawing and Dimensions

JM Aerofoil

Date: : Monday, August 6, 2012
Fan Code : 71JM/20/4/6/14
Item Reference: :

Project Name :
Quotation Number :
Customer :

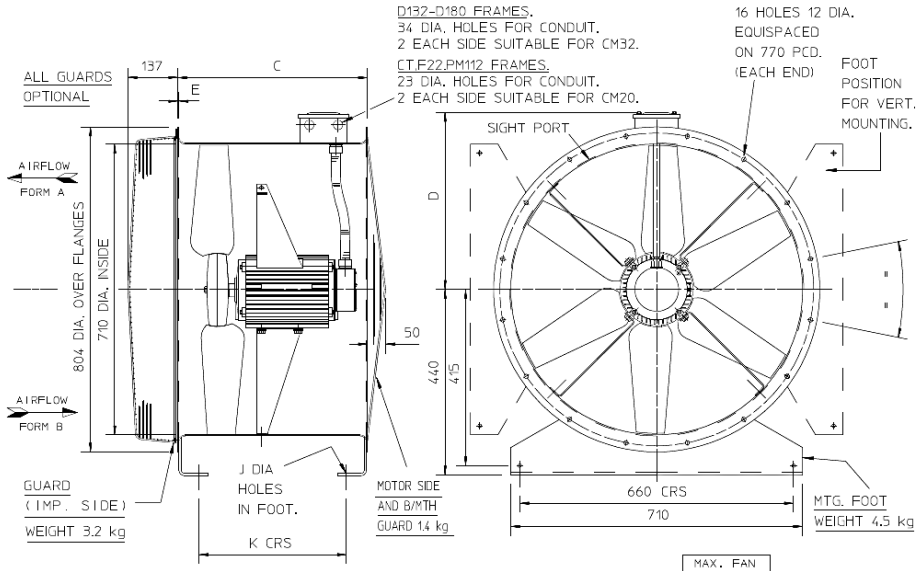

SIZE	FRAME	C	D	E	J	K	MAX. FAN WEIGHT kg
710	CT5/9	375	443	3	10	259	54
	F22	520	443	3	10	404	80
160mm	PM112	520	443	3	10	404	87
to	D132	520	480	4	10	402	168
315mm	D160/18-34	625	480	5	10	505	205
hubs	DF160/LKE D160/40 D160-TECO	711	480	6	10	589	258
	DF180	711	480	6	16	589	303

Notes : Dimensions shown in mm / Weight in kg

Reference :D248977

This drawing shows dimensions that should be used as a guide only and are subject to change. Certified drawings are available on request.

Unit 32 Longford trading Estate
Thomas Street, Stretford, Manchester, , M32 0JT
Tel: 0161 864 1777 Fax: 0161 964 2777

Website: www.nfan.co.uk
Email: kyle@nfan.co.uk

Printed on 07 August 2012

Selection Engine: 2.8.1.7a(1)(UK.3.6.0)

C.5 15kW heating elements drawing and dimensions

A4

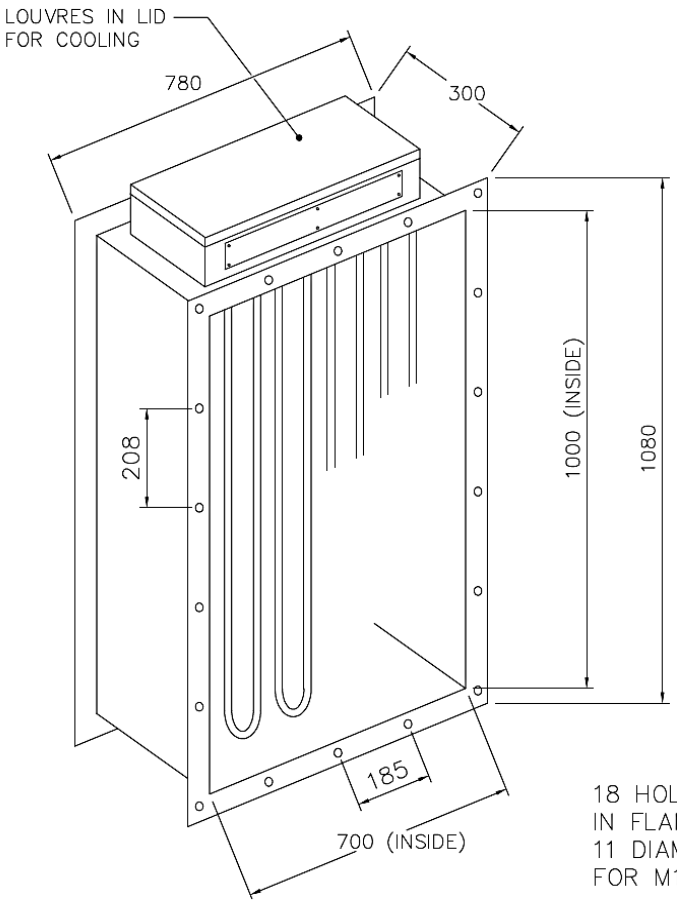

18 HOLES TOTAL
IN FLANGES
11 DIAMETER?
FOR M10 BOLTS?

- NUMBER OF ELEMENTS: 9–OFF (U–BENDS), FIXED TO DUCT USING COMPRESSION FITTINGS. (15KW TOTAL) 240V PER ELEMENT? FOR 240V OR 415V 3–PH. (NO LINKING SUPPLIED BY ELMATIC).
- STAT: 1 FITTED, TYPE: TO BE ADVISED (AUTO OR MANUAL RESET)
- LOUVRED TERMINAL BOX WITH REMOVABLE GLAND–PLATE WHICH YOU CAN DRILL FOR WHATEVER GLAND(S) YOU PREFER (OR WE CAN SUPPLY WITH SPECIFIED DIAMETER HOLE(S) IF YOU PREFER

MODIFICATIONS			
REV	MOD	SIG	DATE

CUSTOMER: LEEDS UNIV.

DRG NO:

DRAWN: P.DONOVAN | DATE: 17/8/12

ELMATIC DRG/PART NO: (FOR APPROVAL PURPOSES)

C.6 K-type thermocouples calibration certificate

pico® Technology

James House,Colmworth Business,Park
Eaton Socon,St Neots,Cambs,PE19 8YP
Tel: 01480 396395 Fax: 01480 396296

Certificate of Calibration

Certificate number: 9022
Calibration Date: 15th November 2012
Model: USB TC-08
Serial Number: AZ810/578
Invoice/Report No: 78231/22553
Pico Calibration Reference: Thermospeed Type K Thermocouple simulator s/n 17219
Calibration Number: 34648

Accreditations & Procedure
The following measurements were carried out using working standards which are periodically verified, and are traceable to National Standards where these exist.

Ambient temperature: 23.61 °C (23°C ±2°C)

Measurement Results

Simulator Setting (°C)	TC-08 Reading (°C)	Error (°C)	Max Allowable Error (°C)
-100	-99.74	0.26	0.70
-50	-49.79	0.21	0.60
-10	-9.89	0.11	0.52
0	0.04	0.04	0.50
50	49.90	-0.10	0.60
100	99.80	-0.20	0.70
200	199.60	-0.40	0.90
400	399.76	-0.24	1.30
600	599.69	-0.31	1.70
800	799.78	-0.22	2.10
1000	999.51	-0.49	2.50
1200	1199.32	-0.68	2.90

The uncertainties of the TC-08 under test include those that are attributable to the standards used together with those contributed by personnel, procedures and environment and are estimated not to exceed ±0.1%.

Calibrated Signature: _____
Checked Signature: _____

Authorised Signature: Alan Tong ☐ Adrian Lawes ☐ Brian Fosh ☐

 Issue 3

C.7 TESTO 425 hot-wire anemometer calibration certificate

testo

Kalibrier-Protokoll
Certificate of conformity • Protocole d'étalonnage
Certificato di taratura • Informe de calibración

Gerät / Module type / Modèle / Modelo:	**testo 425**
Serien-Nr. / Serial no. / No. de série / Número de serie:	**02415595**
Segmenttest / Display test / Test d'affichage / Test del visualizador:	**ok**
Tastaturtest / Keyboard test / Testes de clavier / Test del teclado:	**ok**

Messwerte mit externe Messfühler / Measured values with external probe / Valeurs mesurées avec sonde de mesure externe / Valores medidos con sonda externa:

Sollwert / Reference / Référence / Referencia:	**Toleranz / Tolerance / Tolérance / Tolerancia:**	**Istwert / Actual Value / Valeur réelle / Valor medido:**
Temperatur / Temperature / Température / Temperatura (NTC)		
22.0 °C	± 0.5 °C	22.0 °C
Strömung/Velocity/Vitesse d'air/Velocidad		
1.00 m/s	± 0.08 m/s	1.01 m/s
8.00 m/s	± 0.43 m/s	7.95 m/s
20.0 m/s	± 1.03 m/s	20.1 m/s

07.11.2012
Datum / Date / Date / Fecha

(1414)
Prüfer / Inspector / Vérificateur / Verificador

C.8 DPM ST650 micro manometer calibration certificate

DP MEASUREMENT
Unit 11, Top Angel, Buckingham Industrial Park, Buckingham. MK18 1TH
Tel/Fax: 01280 817122 e-mail: dpm@ttseries.com www.ttseries.com

CALIBRATION CERTIFICATE

CALIBRATION DETAILS:		**INSTRUMENT DETAILS:**		**TEST ROOM CONDITIONS:**	
Date Of Calibration:	20/11/2012	**Model:**	ST650 M	**Temperature:**	20°C ± 2°C
Due Date:	20/11/2013	**Serial Number:**	301	**Manufacturer:**	DP Measurement

Specification
Pressure & Velocity: Readings < 100 counts ± 2 counts. Readings > 100 counts ± 1% of reading ± 1 count.
Temperature: Instrument only ± 2°C

TEST RESULTS:

Calibration Points Pa:	0	40.0	160.0	800.0	4000	-40.0	-160.0	-800.0	-4000
Indicated Readings:	0	39.8	160.0	799.0	4007	-40.3	-160.0	-799.0	-4014
Error:	0	-0.5%	0.0%	-0.1%	0.2%	0.7%	0.0%	-0.1%	0.4%
Calibration Points mbar:	0	0.400	1.60	8.00	40.0	-0.400	-1.60	-8.00	-40.0
Indicated Readings:	0	0.398	1.60	7.99	40.1	-0.399	-1.59	-7.99	-40.1
Error:	0	-0.5%	0.0%	-0.1%	0.3%	-0.3%	-0.6%	-0.1%	0.3%
Calibration Points mmH_2O:	0	4.08	16.3	81.6	408	-4.08	-16.3	-81.6	-408
Indicated Readings:	0	4.07	16.3	81.6	409	-4.03	-16.3	-81.5	-410
Error:	0	-0.2%	0.0%	0.0%	0.2%	-1.2%	0.0%	-0.1%	0.5%
Calibration Points mmHg:	0	0.299	1.20	5.98	29.9	-0.299	-1.20	-5.98	-29.9
Indicated Readings:	0	0.297	1.20	6.00	30.1	-0.299	-1.19	-5.99	-30.1
Error:	0	-0.7%	0.0%	0.3%	0.7%	0.0%	-0.8%	0.2%	0.7%
Calibration Points m/sec:	0	5.00	8.16	11.5	15.0	16.3	25.8	36.5	50.0
Indicated Readings:	0	5.00	8.14	11.5	15.0	16.3	25.8	36.5	50.0
Error:	0	0.0%	-0.2%	0.0%	0.0%	0.0%	0.0%	0.0%	0.0%

Calibration Points °C	0.0	50.0	150.0	250.0	500.0	750.0	1000.0
Indicated Readings:	-0.3	50.0	150.6	249.1	499.8	750.0	1000.0
Error:	-0.3	0.0	0.6	-0.9	-0.2	0.0	0.0

Traceablity:
Equipment: The instrument detailed above the pressure range has been calibrated against equipment whose serial number 2288 which in turn has been calibrated against instruments and equipment that are traceable to National Standards.
(UKAS Calibration Laboratory N° 0157)

Velocity Range: Is calibrated for the ellipsoidal nose (NPL Type) Pitot Static Tubes used at air density 1.20kg/m³. 16°C, 1000 mbar.

Temperature Range: Is calibrated against equipment whose serial number is 13724. Which in turn has been calibrated against instruments and equipment that are traceable to National or International Standards. (K026-10P4495)

Calibrated by Hussein Khimji:

Associated Instrument Repairs Ltd. Trading as DP Measurement.
Company Reg. No: 3485904 VAT No: 685 868 755
Registered Office: Ebenezer House, Poole Road, Bournemouth, Dorset. BH2 5QJ.

Appendix D
Heat Pipe Fluid Properties

Fluids listed in the order of appearance: Ammonia, Pentane, Acetone, Methanol, Flutec PP2, Ethanol, Heptane and Water (*Reay D and Kew P, 2006. Heat Pipes-Theory, Design and Applications, Fifth Edition, Butterworth-Heinemann, Oxford OX2 8DP, USA*)

Ammonia

Temp °C	Latent heat kJ/kg	Liquid density kg/m³	Vapour density kg/m³	Liquid thermal conductivity W/m °C	Liquid viscos. cP	Vapour viscos. cP × 10²	Vapour press. Bar	Vapour specific heat kJ/kg °C	Liquid surface tension N/m × 10²
−60	1343	714.4	0.03	0.294	0.36	0.72	0.27	2.050	4.062
−40	1384	690.4	0.05	0.303	0.29	0.79	0.76	2.075	3.574
−20	1338	665.5	1.62	0.304	0.26	0.85	1.93	2.100	3.090
0	1263	638.6	3.48	0.298	0.25	0.92	4.24	2.125	2.480
20	1187	610.3	6.69	0.286	0.22	1.01	8.46	2.150	2.133
40	1101	579.5	12.00	0.272	0.20	1.16	15.34	2.160	1.833
60	1026	545.2	20.49	0.255	0.17	1.27	29.80	2.180	1.367
80	891	505.7	34.13	0.235	0.15	1.40	40.90	2.210	0.767
100	699	455.1	54.92	0.212	0.11	1.60	63.12	2.260	0.500
120	428	374.4	113.16	0.184	0.07	1.89	90.44	2.292	0.150

Pentane

Temp °C	Latent heat kJ/kg	Liquid density kg/m³	Vapour density kg/m³	Liquid thermal conductivity W/m °C	Liquid viscos. cP	Vapour viscos. cP × 10²	Vapour press. Bar	Vapour specific heat kJ/kg °C	Liquid surface tension N/m × 10²
−20	390.0	663.0	0.01	0.149	0.344	0.51	0.10	0.825	2.01
0	378.3	644.0	0.75	0.143	0.283	0.53	0.24	0.874	1.79
20	366.9	625.5	2.20	0.138	0.242	0.58	0.76	0.922	1.58
40	355.5	607.0	4.35	0.133	0.200	0.63	1.52	0.971	1.37
60	342.3	585.0	6.51	0.128	0.174	0.69	2.28	1.021	1.17
80	329.1	563.0	10.61	0.127	0.147	0.74	3.89	1.050	0.97
100	295.7	537.6	16.54	0.124	0.128	0.81	7.19	1.088	0.83
120	269.7	509.4	25.20	0.122	0.120	0.90	13.81	1.164	0.68

Acetone

Temp °C	Latent heat kJ/kg	Liquid density kg/m^3	Vapour density kg/m^3	Liquid thermal conductivity W/m °C	Liquid viscos. cP	Vapour viscos. cP × 10^2	Vapour press. Bar	Vapour specific heat kJ/kg °C	Liquid surface tension N/m × 10^2
−40	660.0	860.0	0.03	0.200	0.800	0.68	0.01	2.00	3.10
−20	615.6	845.0	0.10	0.189	0.500	0.73	0.03	2.06	2.76
0	564.0	812.0	0.26	0.183	0.395	0.78	0.10	2.11	2.62
20	552.0	790.0	0.64	0.181	0.323	0.82	0.27	2.16	2.37
40	536.0	768.0	1.05	0.175	0.269	0.86	0.60	2.22	2.12
60	517.0	744.0	2.37	0.168	0.226	0.90	1.15	2.28	1.86
80	495.0	719.0	4.30	0.160	0.192	0.95	2.15	2.34	1.62
100	472.0	689.6	6.94	0.148	0.170	0.98	4.43	2.39	1.34
120	426.1	660.3	11.02	0.135	0.148	0.99	6.70	2.45	1.07
140	394.4	631.8	18.61	0.126	0.132	1.03	10.49	2.50	0.81

Methanol

Temp °C	Latent heat kJ/kg	Liquid density kg/m^3	Vapour density kg/m^3	Liquid thermal conductivity W/m °C	Liquid viscos. cP	Vapour viscos. cP × 10^2	Vapour press. Bar	Vapour specific heat kJ/kg °C	Liquid surface tension N/m × 10^2
−50	1194	843.5	0.01	0.210	1.700	0.72	0.01	1.20	3.26
−30	1187	833.5	0.01	0.208	1.300	0.78	0.02	1.27	2.95
−10	1182	818.7	0.04	0.206	0.945	0.85	0.04	1.34	2.63
10	1175	800.5	0.12	0.204	0.701	0.91	0.10	1.40	2.36
30	1155	782.0	0.31	0.203	0.521	0.98	0.25	1.47	2.18
50	1125	764.1	0.77	0.202	0.399	1.04	0.55	1.54	2.01
70	1085	746.2	1.47	0.201	0.314	1.11	1.31	1.61	1.85
90	1035	724.4	3.01	0.199	0.259	1.19	2.69	1.79	1.66
110	980	703.6	5.64	0.197	0.211	1.26	4.98	1.92	1.46
130	920	685.2	9.81	0.195	0.166	1.31	7.86	1.92	1.25
150	850	653.2	15.90	0.193	0.138	1.38	8.94	1.92	1.04

Flutec PP2

Temp °C	Latent heat kJ/kg	Liquid density kg/m^3	Vapour density kg/m^3	Liquid thermal conductivity W/m °C	Liquid viscos. cP	Vapour viscos. cP × 10^2	Vapour press. Bar	Vapour specific heat kJ/kg °C	Liquid surface tension N/m × 10^2
−30	106.2	1942	0.13	0.637	5.200	0.98	0.01	0.72	1.90
−10	103.1	1886	0.44	0.626	3.500	1.03	0.02	0.81	1.71
10	99.8	1829	1.39	0.613	2.140	1.07	0.09	0.92	1.52
30	96.3	1773	2.96	0.601	1.435	1.12	0.22	1.01	1.32
50	91.8	1716	6.43	0.588	1.005	1.17	0.39	1.07	1.13
70	87.0	1660	11.79	0.575	0.720	1.22	0.62	1.11	0.93
90	82.1	1599	21.99	0.563	0.543	1.26	1.43	1.17	0.73
110	76.5	1558	34.92	0.550	0.429	1.31	2.82	1.25	0.52
130	70.3	1515	57.21	0.537	0.314	1.36	4.83	1.33	0.32
160	59.1	1440	103.63	0.518	0.167	1.43	8.76	1.45	0.01

Ethanol

Temp °C	Latent heat kJ/kg	Liquid density kg/m^3	Vapour density kg/m^3	Liquid thermal conductivity W/m°C	Liquid viscos. cP	Vapour viscos. cP × 10^2	Vapour press. Bar	Vapour specific heat kJ/kg °C	Liquid surface tension N/m × 10^2
−30	939.4	825.0	0.02	0.177	3.40	0.75	0.01	1.25	2.76
−10	928.7	813.0	0.03	0.173	2.20	0.80	0.02	1.31	2.66
10	904.8	798.0	0.05	0.170	1.50	0.85	0.03	1.37	2.57
30	888.6	781.0	0.38	0.168	1.02	0.91	0.10	1.44	2.44
50	872.3	762.2	0.72	0.166	0.72	0.97	0.29	1.51	2.31
70	858.3	743.1	1.32	0.165	0.51	1.02	0.76	1.58	2.17
90	832.1	725.3	2.59	0.163	0.37	1.07	1.43	1.65	2.04
110	786.6	704.1	5.17	0.160	0.28	1.13	2.66	1.72	1.89
130	734.4	678.7	9.25	0.159	0.21	1.18	4.30	1.78	1.75

Heptane

Temp °C	Latent heat kJ/kg	Liquid density kg/m^3	Vapour density kg/m^3	Liquid thermal conductivity W/m °C	Liquid viscos. cP	Vapour viscos. cP × 10^2	Vapour press. Bar	Vapour specific heat kJ/kg °C	Liquid surface tension N/m × 10^2
−20	384.0	715.5	0.01	0.143	0.69	0.57	0.01	0.83	2.42
0	372.6	699.0	0.17	0.141	0.53	0.60	0.02	0.87	2.21
20	362.2	683.0	0.49	0.140	0.43	0.63	0.08	0.92	2.01
40	351.8	667.0	0.97	0.139	0.34	0.66	0.20	0.97	1.81
60	341.5	649.0	1.45	0.137	0.29	0.70	0.32	1.02	1.62
80	331.2	631.0	2.31	0.135	0.24	0.74	0.62	1.05	1.43
100	319.6	612.0	3.71	0.133	0.21	0.77	1.10	1.09	1.28
120	305.0	592.0	6.08	0.132	0.18	0.82	1.85	1.16	1.10

Water

Temp °C	Latent heat kJ/kg	Liquid density kg/m^3	Vapour density kg/m^3	Liquid thermal conductivity W/m °C	Liquid viscos. cP	Vapour viscos. cP × 10^2	Vapour press. Bar	Vapour specific heat kJ/kg°C	Liquid surface tension N/m × 10^2
20	2448	998.2	0.02	0.603	1.00	0.96	0.02	1.81	7.28
40	2402	992.3	0.05	0.630	0.65	1.04	0.07	1.89	6.96
60	2359	983.0	0.13	0.649	0.47	1.12	0.20	1.91	6.62
80	2309	972.0	0.29	0.668	0.36	1.19	0.47	1.95	6.26
100	2258	958.0	0.60	0.680	0.28	1.27	1.01	2.01	5.89
120	2200	945.0	1.12	0.682	0.23	1.34	2.02	2.09	5.50
140	2139	928.0	1.99	0.683	0.20	1.41	3.90	2.21	5.06
160	2074	909.0	3.27	0.679	0.17	1.49	6.44	2.38	4.66
180	2003	888.0	5.16	0.669	0.15	1.57	10.04	2.62	4.29
200	1967	865.0	7.87	0.659	0.14	1.65	16.19	2.91	3.89